



GSJ Interim Report No.EQ/00/1  
(地質調査所速報 No.EQ/00/1 )



USGS Open-file Report 00-129

Proceedings of  
THE INTERNATIONAL WORKSHOP ON THE NOJIMA FAULT CORE  
AND BOREHOLE DATA ANALYSIS

November 22-23, 1999  
Tsukuba, Japan

As a part of Twin Institute Program between  
Geological Survey of Japan and United States Geological Survey

Edited by  
Hisao Ito<sup>1</sup>, Koichiro Fujimoto<sup>1</sup>, Hidemi Tanaka<sup>2</sup> and David Lockner<sup>3</sup>

1. Hisao Ito, Geological Survey of Japan, 1-1-3 Higashi, Tsukuba 305-8567 Japan
1. Koichiro Fujimoto, Geological Survey of Japan, 1-1-3 Higashi, Tsukuba 305-8567 Japan
2. Hidemi Tanaka, Ehime University, Ehime University, Bunkyo-cho 2-5, Matsuyama, 790-8577 Japan
3. David Lockner, United States Geological Survey, 345 Middlefield Road, MS 977, Menlo Park, CA 94025 U.S.A.

This report is preliminary and has not been reviewed for conformity with Geological Survey of Japan or U.S. Geological Survey editorial standards, or with the North American stratigraphic Code. Any use of trade, firm, or product names is for descriptive purposes only and does not imply endorsement by the Japanese or U.S. Government.

Proceedings of  
THE INTERNATIONAL WORKSHOP ON THE NOJIMA FAULT CORE  
AND BOREHOLE DATA ANALYSIS

November 22-23, 1999  
Tsukuba, Japan

as a part of Twin Institute Program between  
Geological Survey of Japan and United States Geological Survey

Edited by  
Hisao Ito<sup>1</sup>, Koichiro Fujimoto<sup>1</sup>, Hidemi Tanaka<sup>2</sup> and David Lockner<sup>3</sup>

GSJ Interim Report No.EQ/00/1  
(地質調査所速報 No.EQ/00/1)

USGS Open-File Report 00-129

1. Hisao Ito, Geological Survey of Japan, 1-1-3 Higashi, Tsukuba 305-8567 Japan
1. Koichiro Fujimoto, Geological Survey of Japan, 1-1-3 Higashi, Tsukuba 305-8567 Japan
2. Hidemi Tanaka, Ehime University, Ehime University, Bunkyo-cho 2-5, Matsuyama, 790-8577 Japan
3. David Lockner, United States Geological Survey, 345 Middlefield Road, MS 977, Menlo Park, CA 94025 U.S.A.

This report is preliminary and has not been reviewed for conformity with Geological Survey of Japan or U.S. Geological Survey editorial standards, or with the North American stratigraphic Code. Any use of trade, firm, or product names is for descriptive purposes only and does not imply endorsement by the Japanese or U.S. Government.

## Table of contents

<b>Preface</b> .....	vi
<b>Program</b> .....	xix

### **Introduction**

#### **Microscopic and macroscopic physics of earthquakes\***

Hiroo Kanamori and Thomas H. Heaton.....	1
<b>Thermal pressurization, fluidization and melting of fault gouge during seismic slip recorded in the rock from Nojima fault</b>	
Kenshiro Otsuki, Nobuaki Monzawa and Toshiro Nagase .....	43
<b>Seismogenic zone drilling and monitoring of OD21/IODP</b>	
Kiyoshi Suyehiro.....	51

### **Outline of the Drilling Activities on the Nojima Fault**

#### **Geologic and geophysical drilling at the Nojima fault: Fault trace of the 1995 Hyogoken-Nanbu earthquake, $M_s7.2$**

Masataka Ando.....	55
--------------------	----

#### **Outline of the Nojima Fault Scientific Drilling by NIED**

Ryuji Ikeda.....	65
------------------	----

#### **Outline of the Nojima Fault Drilling by GSJ: Structure, physical properties and permeability structure from borehole measurements in GSJ borehole crossing the Nojima fault, Japan**

Hisao Ito, Yasuto Kuwahara, Tsutomu Kiguchi, Koichiro Fujimoto and Tomoyuki Ohtani.....	71
---	----

### **Geological Studies on the Nojima Core**

#### **Distribution, deformation and alteration of fault rocks along the GSJ core penetrating the Nojima fault, Awaji Island, Southwest Japan**

Hidemi Tanaka, Naoto Tomida, Norie Sekiya, Yuichi Tsukiyama, Koichiro Fujimoto, Tomoyuki Ohtani and Hisao Ito.....	81
<b>Characterization of fault gouge from GSJ Hirabayashi core samples and implications for the activity of the Nojima fault</b>	
Koichiro Fujimoto, Hidemi Tanaka, Naoto Tomida, Tomoyuki Ohtani and Hisao Ito.....	103
<b>Deformation mechanisms in granodiorite from the hanging-wall of the Nojima fault</b>	
Anne-Marie Boullier, Benoît Ildefonse, Jean-Pierre Gratier, Koichiro Fujimoto, Tomoyuki Ohtani and Hisao Ito.....	111
<b>Characters of the fracture zones of the Nojima fault at depths of 1140, 1300 and 1800m viewed from NIED core analyses and well logging</b>	
Kenta Kobayashi, Takashi Arai, Ryuji Ikeda, Kentaro Omura, Takashi Sawaguchi, Koji Shimada, Hidemi Tanaka, Tomoaki Tomita, Naoto Tomida, Satoshi Hirano, Tatsuo Masuda and Akiko Yamazaki.....	119
<b>Isotope analysis of carbonates in the Nojima fault cores</b>	
Akira Ueda, Akiko Kawabata, Koichiro Fujimoto, Hidemi Tanaka, Naoto Tomida, Tomoyuki Ohtani and Hisao Ito.....	127
<b>Dynamic analysis based on 3-D orientation distribution of microcracks in quartz from the Cretaceous granodiorite core samples drilled along the Nojima fault, southwest Japan</b>	
Toru Takeshita and Koshi Yagi.....	133
<b>Fault rock distribution analysis based on chemical composition, water contents and fracture density</b>	
Naoto Tomida, Hirokazu Tsukiyama, Hidemi Tanaka, Koichiro Fujimoto, Tomoyuki Ohtani and Hisao Ito.....	141

### Permeability and Physical Properties

#### **Permeability and strength of the Nojima core samples from the Nojima fault of the 1995 Kobe earthquake**

David Lockner, Hisanobu Naka, Hidemi Tanaka, Hisao Ito and Ryuji

<b>Ikeda.....</b>	<b>147</b>
<b>Permeability of the deep drillhole core samples</b>	
Carolyn A. Morrow.....	153
<b>Correlation of deformation textures with laboratory measurements of permeability and strength of Nojima fault zone core samples</b>	
Diane E. Moore, David A. Lockner, Hisao Ito and Ryuji Ikeda.....	159
<b>Laboratory study of fluid migration and fault growth</b>	
Koji Masuda, Mai Lin Doan, Osamu Nishizawa, Xinglin Lei and Hisao Ito.....	167

**Hydraulic Properties**

<b>Hydraulic properties at the GSJ Hirabayashi borehole in the Nojima fault from analysis of pump test and time series data</b>	
Evelyn A. Roeloffs and Norio Matsumoto.....	173
<b>Earthquake-induced hydrological changes and possible permeability enhancement due to the January 17, 1995 Kobe Earthquake, Japan*</b>	
Tomochika Tokunaga.....	179
<b>Chemical and isotopic compositions of groundwater obtained from the GSJ Hirabayashi well</b>	
Tsutomu Sato and Makoto Takahashi.....	187
<b>Deep surface-water flow near the Nojima earthquake fault</b>	
Shinichi Uda, Aiming Lin and Keiji Takemura.....	193

**Thermal Disturbance, Age**

<b>Thermal history analysis of the Nojima fault borehole samples by fission-track thermochronology</b>	
Takahiro Tagami, Masaki Murakami, Noriko Hasebe, Hidenori Kamohara and Keiji Takemura.....	203
<b>Inspection of resetting state of ESR signals and elucidation of radioactive disequilibria in the fault gouge zone using the Nojima Fault GSJ 750m drilling</b>	

**core samples**

Tatsuro Fukuchi, Noboru Imai and Natsumi Tanaka.....	211
<b>Decay of E<sub>1</sub>' center in quartz from the Nojima fault gouge by the contact of H<sub>2</sub> gas - Possible indicator for H<sub>2</sub> generation and seismic activity</b>	
Hiroshi Matsumoto, Makoto Hirai, Chihiro Yamanaka and Motoji Ikeya...	219
<b>A survey of thermal disturbance on the GSJ Nojima core samples by Electron Spin Resonance (ESR)</b>	
Atsushi Tani, Hiroshi Matsumoto and Motoji Ikeya.....	223

**Geophysical Measurements on Cores**

<b>Anisotropy of elastic and anelastic properties of granites from the Hirabayashi hole, Japan</b>	
Maria Zamora, Philippe A. Pezard and Hisao Ito.....	227
<b>Borehole wall geometry across the Nojima fault: BHTV acoustic scans analysis from the GSJ Hirabayashi hole, Japan</b>	
Bernard P. Célérier, Philippe A. Pezard, Hisao Ito and Tsutomu Kiguchi.....	233
<b>Stress state around the Nojima fault estimated from core measurements</b>	
Kiyohiko Yamamoto, Namiko Sato and Yasuo Yabe.....	239
<b>Estimation of in-situ stress on cores retrieved from a deep borehole at the Arima-Takatsuki tectonic line</b>	
Ziqiu Xue, Hisao Ito and Osamu Nishizawa.....	247

**Analysis of Logging Data**

<b>Electrical properties and alteration of granodiorites from the GSJ Hirabayashi hole, Japan</b>	
Philippe A. Pezard, Hisao Ito, Daniel Hermitte and Andre Revil.....	255
<b>Fracture system in the Nojima fault</b>	
Tsutomu Kiguchi, Hisao Ito, Yasuto Kuwahara and Tomoyuki Ohtani.....	263
<b>Reorientation of cores and distribution of macroscopic fractures along the GSJ borehole penetrating the Nojima fault zone</b>	

Tomoyuki Ohtani, Teruki Miyazaki, Hidemi Tanaka, Takayuki Higuchi, Koichiro Fujimoto and Hisao Ito.....	271
--	-----

**Monitoring**

<b>Temperature monitoring in a borehole drilled into the Nojima fault and radioactive heat production of core samples</b>
---

Tohru Yamaguchi, Makoto Yamano, Toshiyasu Nagao and Shusaku Goto..	277
--	-----

<b>Deep structure of the Nojima fault zone by trapped wave analysis</b>
---

Yasuto Kuwahara and Hisao Ito.....	283
------------------------------------	-----

\* Duplications of already published paper.

# PREFACE

## To the Proceedings of the International Workshop on the Nojima Fault Core and Borehole Data Analysis

Hisao Ito (Geological Survey of Japan)  
Koichiro Fujimoto (Geological Survey of Japan)  
Hidemi Tanaka (Ehime University)  
David Lockner (US Geological Survey)

### **I. Introduction**

The International Workshop on the Nojima Fault Core and Borehole Data Analysis was held in November 22-23, 1999 at Geological Survey of Japan (GSJ) in Tsukuba. It is based on the core and borehole data analysis on the borehole drilled by GSJ just after the 1995 Hyogo-ken Nanbu (Kobe) earthquake of January 17 ( $M_{JMA}=7.2$ ; the Japan Meteorological Agency (JMA) Magnitude). The GSJ borehole penetrated the active fault just after the large earthquake for the first time in the world.

Because of this unique opportunity, great interests in core and borehole data analysis have been taken by researchers from GSJ, United States Geological Survey (USGS), Japanese universities, National Institutes and private companies, and French researchers. The core and borehole data analysis was motivated by the sampling party held at the GSJ Hirabayashi drill site in January 1996. This was followed by several core viewings and samplings in Tsukuba, and the acceptance of research proposals from Japan and other countries.

GSJ and USGS recently started the Twin Institute Program on earthquake research supported by the Agency of Industrial Science and Technology, Ministry of International Trade and Industry of Japan. The Twin Institute Program covers the following four research areas;

- 1) Study of deposits and hazards of tsunamis
- 2) Evaluation of earthquake potential using geologic methods
- 3) Study of earthquake source process in near source region
- 4) Study of structure and physical properties of fault

As a part of these activities, we already had an International Workshop on Paleoseismology at GSJ on March 15, 1999, and published the proceedings (Satake and Schwartz, 1999).

We also held the International Workshop on the Nojima Fault Core and Borehole Data Analysis at GSJ, Tsukuba, on November 22-23, 1999. Thirty oral presentations and five poster presentations were made at the workshop with about 90 participants; not only from GSJ and USGS, but also from universities, National Institutes and companies in Japan and from France.

### **The 1995 Kobe Earthquake**

The 1995 Kobe Earthquake,  $M_{JMA}=7.2$ , occurred beneath the Akashi Strait on January 17, 1995, and formed a surface break about 10 km long with 1-2 m offset along the Nojima fault (Lin et al., 1995; Nakata et al., 1995; Lin and Uda, 1996; Awata et al., 1996). Lin et al., (1995) and Lin and Uda (1996) documented that the surface break extends southwestward with small offset.

The Nojima fault is a component of the Arima-Takatsuki-Rokko fault zone, which is a branch of the Median Tectonic Line. In a broad sense, the fault systems near Osaka Bay form a boundary between pre-Neogene basement and Neogene and Quaternary sedimentary rocks.

The Nojima fault is a NE-SW striking, active right-lateral strike-slip fault with a minor reverse component (Mizuno et al., 1990). Although they estimated the length of the Nojima fault as 7km, the surface break during the 1995 Kobe earthquake was longer than this.

The total displacement of the Nojima fault is

unknown; the total vertical displacement is 230 m at the southern part of the Nojima fault (Murata et al., 1998). The Miocene sedimentary rocks (Iwaya Formation) and Plio-Pleistocene sediments (Osaka Group) are distributed to the west of the Nojima fault and the Cretaceous granodiorites are distributed to the east.

Surface rupture was found only on Awaji Island southwest of the mainshock epicenter, and surface displacement from the Kobe earthquake was generally a right-lateral reverse shear with east side up (Lin and Uda, 1996). The maximum net slip was 2.15 m with 1.80 m of right slip and 1.30 m of reverse slip and occurred at Nojima-Hirabayashi in the central part of the surface rupture (Lin and Uda, 1996). From the trench survey, the recurrence time of the earthquake is estimated to be about 2000 years (Awata and Suzuki, 1996).

Ide et al. (1996), Yoshida et al. (1996), Spudich et al. (1998) and Bouchon et al. (1998) made inversion analysis on the 1995 Kobe earthquake based on seismic and geodetic data. They showed dynamic behavior of the earthquake.

Ito and Kuwahara (1996), Li et al. (1998) and Ito et al. (1999) observed significant trapped waves from the aftershocks on the Nojima fault. They did not observe any trapped wave for adjacent active faults, and they interpret this as an evidence of the segmentation of the Nojima fault and adjacent faults. They estimated the velocity and Q of the low velocity zone of the Nojima fault, and compared with the drilling results (Ito et al., 1996; Ito et al. 1999).

#### Outline of the Drilling Activities on the Nojima Fault

After the 1995 Kobe earthquake, three major research groups initiated fault drilling projects and conducted experiments in boreholes around Kobe and the Nojima fault.

The three research groups are, 1) the University Group (UG), led by Prof. Masataka Ando, and funded by the Ministry of Education, 2) the National Research Institute for Earth Science and Disaster Prevention (NIED), led by

Dr. Ryuji Ikeda, and funded by the Science and Technology Agency, and 3) GSJ, led by Dr. Hisao Ito, and funded by the Agency of Industrial Science and Technology, Ministry of International Trade and Industry. The groups have been working somewhat independently, and are conducting similar types of geological and geophysical investigations, *in situ* experiments, and downhole monitoring of crustal activities.

The GSJ and NIED have completed several boreholes located close to the epicenter, near the ends of the earthquake rupture, and on the Nojima fault near the epicenter and on the places where the maximum surface displacements were observed. These latter boreholes, GSJ Hirabayashi and NIED Hirabayashi are located 75 m and 320 m, respectively, from the surface trace of the Nojima fault and cross the fault zone at depth (Fig. 1). The GSJ hole is 747 m deep and the NIED is 1800 m deep. The six other boreholes range between 300 m and 1300 m in depth. The three UG boreholes are also located on the Nojima fault at a location where both the main Nojima fault and a subsidiary fault is observed (Fig. 1). The depth range of these boreholes is 500 m to 1800 m.

Continuous core has been collected from almost all of the boreholes. GSJ has had close to 100% core recovery in all their boreholes. At Hirabayashi, continuous core was taken between the depth 150 m-746 m, with 98% recovery across the fault zone. The core shows a deformed zone between 557 and 713 m, with clay gouge between 623.1 and 625.3 m. This depth interval corresponds to a fault zone thickness of approximately 30 m.

The NIED and UG also have collected cores from the boreholes across the Nojima fault. For the Hirabayashi core, the GSJ has photographed the core using a core scanning system (Miyazaki et al., 1997), made in-situ stress measurements (Ito et al., 1997a) and measurements on core samples (Ito et al., 1997b, Kudo et al., 1997). Physical properties including seismic velocity, density, permeability, and fracture strength are also measured. In addition, petrographic studies, analysis of fractures and core deformation, fluid inclusion analysis, and dating core materials are in progress. The NIED and UG are conducting

similar studies of their core materials.

All groups have completed a number of downhole measurements, particularly in the holes across the Nojima fault. The research activities on the GSJ Hirabayashi borehole are described in Fig. 2 and the publication list is shown in the Appendix.

## ***II. Summary of the workshop***

### ***Introduction***

Kanamori (Kanamori and Heaton) summarized the role of microscopic and macroscopic physics of earthquakes. They emphasize the importance of the role of frictional melting and that fluid pressurization can play a key role in rupture dynamics of large earthquakes. The microscopic state of stress caused by local melting and pressurization can be tied to macroscopic seismic parameters such as seismic moment and radiated energy by averaging the stresses in the microscopic states. They also suggest that the dynamics of small and large earthquakes can be very different, because the thermal process is important only for large earthquakes.

Otsuki et al. found rock composed of thinly laminated fault gouge and pseudotachylite layers, and they considered the detail of physical processes during the seismic slip; thermal pressurization, fluidization and melting, is recorded. They characterized degrees of melting and fragmentation quantitatively, and presented a possible mechanism of pseudotachylite formation.

Suyehiro introduced a seismogenic zone drilling and monitoring of OD21/IODP with a new scientific drill ship equipped with riser capability that allows deep drilling beneath ocean floors. The new drill ship will be constructed by Japan, and will drill through the seismogenic part of the subduction plate boundary to collect samples, make in-situ measurements, and set up observatory to understand earthquake mechanics and physico-chemical processes operating in this environment.

### ***Geological Studies on the Nojima Core***

Comprehensive work on core analysis is performed by Tanaka et al. including the detailed petrological and fault-rock chemistry analysis of the Nojima fault zone. They described seven shear zones including main Nojima fault surface (MSZ) at 625.3m depth. Those shear zones are surrounded by weakly pulverized and altered granodiorite (WPAR). They insisted on the importance of WPAR as fault gouge, fault breccia or cataclasite be considered to be evolved from WAPR. They strictly define the fault zone thickness of 30 m for hanging wall based on microstructure and volatile contents. One of the most important findings is that there are two fault cores, one of which shows a distinct characteristics of mass-loss and very fine grained nature and referred to as a co-seismic fault core, the other is characterized by flow texture and preferred alignment of clay minerals and referred to as interseismic fault core.

Fujimoto et al. described the fault core, where deformation and alteration are intensively localized within 30cm thickness. The fault core is composed of three types of fault gouges, which preserve texture, and mineralogy of the ancient activity of the Nojima fault. The formation temperature is higher than 130-200 °C, which corresponds to the depth of 4-7 km if the geotherm is not different from the present. Deformations of both seismic and interseismic period are recognized. Carbonate minerals are main sealing minerals and isotope chemistry suggests that the carbonates are probably connate seawater origin (Ueda et al.). They represent different age and depth of activity of the Nojima fault.

Boullier et al. described deformation textures and attributed them to aseismic or seismic deformation mechanisms. Aseismic deformation is characterized by kinked biotites, which are distributed from low strain rocks to ultracataclasite. The textures of quartz and calcite suggest that the most deformation occur not at present depth but at 3 to 5 km.

Kobayashi et al. described the lithology of the NIED core and compared the lithology and physical properties such as sonic velocity and

density. Three fracture zones are distributed at 1800, 1300 and 1140m depth. Alteration is most intense at 1140m fracture zone and it may have developed most recently in the three.

Ueda et al. performed isotopic studies on the carbonate minerals, which are typical alteration minerals in GSJ core samples. The results imply that the carbonates were formed from seawater penetrating along the fault.

Takeshita and Yagi measured orientation of healed microcracks and kink band in quartz to elucidate paleostress field. The inferred paleostress field (Jurassic in age) is apparently different from that of Quaternary.

Tomida et al. tried to quantify degrees of deformation and alteration based on the loss of ignition data and fracture density.

#### **Permeability and Physical Properties**

The permeability of fault zone is key to understanding fluid movements and its relation to earthquake generation.

Lockner et al. measured the matrix permeability for core samples from GSJ and NIED Hirabayashi boreholes. They found a strong correlation between permeability and proximity to the fault zone shear axes. The width of the high permeability zone is in good agreement with fault zone width inferred from trapped wave analysis (Li et al., 1998; Ito and Kuwahara, 1996) and borehole logging data (Ito et al., 1996). The shear zone axis, due to its high clay content and fine gouge grain size, has relatively low permeability in the microdarcy range (Darcy =  $10^{-12} \text{ m}^2$ ). Flanking the shear zone axis, the damage zone has high permeability. Father away from the shear zone axis, the permeability returns to the protolith permeability value. They also pointed out that because of the strong sensitivity of permeability, *in situ* permeability in the Nojima fault zone will decrease rapidly with depth.

Kiguchi et al. (1999) and Ito et al. estimated permeability structure from the borehole tube wave and Stoneley wave analysis. Ito et al. observed several highly permeable layers with very thin thickness that correspond to cataclasite, gouge. They estimated the highly permeable fault core thickness as 0.1 m, and estimated extremely

high permeability as 40 Darcy. Both the core permeability measurements and borehole tube wave and Stoneley wave analysis results are consistent with the fault zone model that the highly permeable zones in the fracture zone act as a conduit for fluids parallel to the fault but acts as barrier for movement across the fault.

Morrow reviewed the core sample permeability measurements from four different scientific drill holes (Cajon Pass, Kola, KTB and Illinois UPH 3), and concluded that most fluid flow at depth will occur through discrete joints and faults rather than through bulk of the rock.

The results by Ito et al. and Kiguchi et al. (1999) are based on the fracture permeability. If we consider the strong pressure dependence of the matrix permeability, the matrix permeability will be extremely low and fracture permeability dominates at depth.

Moore et al. made a detailed observation of the fault rocks in relation with the physical properties such as permeability and strength. In the permeable zone, the rock exhibits dilatant deformation whereas; micro shear bands are characteristic features in the less permeable zone. They confirmed that the GSJ and shallowest NIED fault strands appear to be currently active, whereas the deepest NIED fault strand was abandoned and has been thoroughly sealed with mineral deposits.

Masuda et al. studied the effect of fluid migration on fracture process using the Nojima core samples. They showed that the internal structure of the rock affects the location of fracture surface.

#### **Hydraulic Properties**

Roeloffs and Matsumoto analyzed data from the pumping test conducted in March 1996, and groundwater-level data for the period from June 1996 through October 1999. Analysis of the pump test data yields the transmissivity that is consistent with the borehole measurements. The tidal variations in the groundwater level suggest that the tidal response is governed by deformation of a fracture zone, rather than of a uniform porous material.

Sato and Takahashi analyzed the chemical and

stable isotopic compositions of water from the GSJ Hirabayashi well. Both ionic and isotopic characteristics of the water are similar to that of the local spring water of meteoric origin.

Tokunaga constructed a simple horizontal flow model to explain the observed hydrological changes associated with the 1995 Kobe earthquake; (1) large drop of water table in the mountainous area, (2) rapid increase of discharge along active faults, and (3) change in chemistry of discharged water. According to his model, the hydraulic conductivity increased at least 5 times at the earthquake and the change of chemical composition of discharged water could be caused by movement of deeper water into the aquifer.

Uda et al. described the cracks filled with clay and/or carbonate minerals. They considered these crack fillings are the evidence of rapid surface water flow into the fault zone at the earthquake event.

Célérier et al. observed a few deformed cross sections in the ultrasonic borehole televiewer data obtained in the GSJ Hirabayashi borehole. They interpret these as slips on pre-existing fractures and estimated the fault slip vector.

Yamamoto et al. estimated the stress from the core sample from Toshima (University Group) and GSJ Hirabayashi. They found that the maximum horizontal stress direction is almost perpendicular to the strike of the Nojima fault. Ito et al. (1997) pointed out the stress direction at Takarazuka, located at the intersection of the Arima-Takatsuki tectonic line and Nojima fault system, is NE-SW. This maximum stress direction is also confirmed by careful measurements for core samples by Xue et al. This is different from the general trend of the stress direction along the Nojima fault system, and is not consistent with the right lateral movement of neither Arima-Takatsuki tectonic line nor Nojima fault system.

### **Thermal Disturbance, Age**

Tagami et al. analyzed thermal history of the fault zone using fission-track thermochronology. They found shortening of track length in zircon around the fault surface probably due to recent thermal anomaly around the fault.

Fukuchi et al. found scarce thermal effect of 1995 event at the fault core based on ESR signals. They also found chemical anomaly at the fault core attributed to the inflow of calcium rich fluid.

Matsumoto et al. performed ESR study on the quartz from the fault core. They suggested the possible generation of hydrogen gases in the fault zone.

Tani et al. performed ESR studies to elucidate the thermal disturbance. They found a thermal anomaly at 250 m depth.

### **Geophysical Measurements on Cores**

Zamora et al. measured the ultrasonic P-wave velocities to investigate the effect of the alteration and the fracturing intensity on the velocity and velocity anisotropy. The preliminary results show that P-wave velocity and anisotropy strongly depends on the porosity and suggests that thin cracks play an important role.

### **Analysis of Logging Data**

Pezard et al. made an integrated analysis of core measurements and logging results on electrical properties of GSJ Hirabayashi borehole. They found correlation between electrical properties to alteration and fracturing intensity.

Kiguchi et al., analyzed the fracture distribution in the GSJ Hirabayashi borehole by FMI images. They found that almost all the resistive fractures are distributed in the shallower depth than the coaxial zone, and the strike and dip of fractures at the coaxial zone are consistent with those of the Nojima fault.

Ohtani et al. reoriented the core by comparing the FMI logging image and core scanner image to characterize macroscopic fractures. Distribution and orientation of sealed fractures are controlled by porphyry intrusion and faulting activity.

### **Monitoring**

University group has installed seismometer, tiltmeter, strainmeter, accelerometer, pressure gauge and thermometer in the 800 m borehole and multi-level seismometer and optical fiber temperature sensor in the 1760 m borehole

(Ando). They have plan to make repeated injection experiments to study possible permeability change, induced seismicity and trapped wave.

In the NIED borehole, they made precise temperature measurements after the completion of the borehole (Ikeda) and estimated heat flow (Kitajima et al., 1999).

GSJ has been installing downhole seismometers, continuously monitoring water level, and making repeated pumping tests in the GSJ Hirabayashi borehole. One of the purposes of water level monitoring is to detect any changes in hydraulic properties after the 1995 Kobe earthquake related to healing of the Nojima fault (Roeloffs and Matsumoto). Kuwahara and Ito are making trapped wave observation with multi-level downhole seismometers to detect any changes in trapped waves related to healing of the Nojima fault.

### **III. Discussion**

During the workshop, we discussed about the following important issues;

- 1) The study of microscopic structure of the fault is essential to better understand macroscopic earthquake mechanism.
- 2) Integration of borehole logging and laboratory data has begun, but needs to be continued; for example permeability, velocity, resistivity, etc.
- 3) What is healing/strength recovery of fault zone? Geochronology, numerical modeling and further monitoring and repeated experiments should be planned.
- 4) What is fault structure in 3D? How complex is the fault structure? Can relatively shallow borehole observation be used to constrain deep fault structure (especially in seismogenic region)?
- 5) Scale effect in space and time; core logging data remote observation.
- 6) Can the observations from this workshop be synthesized into a more general model of (a) fault zone structure, (b) fault zone hydrology, (c) earthquake cycle / inter-event time / strength recovery rate, (d) evolution of active faults,(e) fault related stress state?
- 7) How are the observation at Nojima fault to be

applied to other fault zones and active seismic regime?

- 8) What useful measurements / analysis are not being done at the present time?
- 9) What could have done better at Nojima fault study area?
- 10) Is some kind of review/overview paper desirable?
- 11) Regular contact is essential — More workshop? Newsletter? Website? Other?

As a whole, geological core analysis, in-situ and experimental geophysical measurements provide excellent answers to the above questions which clarify precise nature of seismogenic fault zone at shallow depth. However, there still remains some controversial issues, such as 1) origin of the fluids in the fault zone (Fujimoto et al., Ueda et al. and Uda et al.) and fluid balance problem (Lockner et al., Tanaka et al. and Fukuchi et al.), 2) frictional heating, 3) distinction between rapid process at seismic stage and slow process at interseismic stage, and 4) large differences in permeability between is-situ estimated from Stoneley and Tube wave analysis and core measurements (Ito et al., Lockner et al., Kiguchi et al., 1999.).

As the drilling into the fault zone just after the big earthquake is a first trial in the world, the results presented in this issue could be potential candidates of primary standard for future drilling projects and core analysis, such as San Andreas drilling projects. Direct observations of seismic activities through material in the fault zone are a recent developed research and referred to here as "material seismology". However, it will become a more essential work for understanding earthquake generation mechanism in near future, since the earthquake can be regarded as a response of natural fault rocks to loading elastic rocks which surrounds the fault zone rocks at the seismogenic depth.

#### ***Suggestions to the future drilling***

In this particular drilling project, we have been fortunately successful in penetrating the fault zone, recovering samples from the fault zone, making almost complete borehole experiments. It is also noteworthy that integrated study on core-

log-remote data analysis began.

We have learned a lot about technique for drilling through and recovering cores from the fault zone, core processing ( in our case, we used resin, and made Archive Half, Working Half and Slab for preservation; Tanaka et al.), distribute and keep the core samples.

We hope that our experiences will be applied in the future scientific drilling works.

#### **IV. Available data on GSJ Hirabayashi borehole**

Core images, Core scanner data on CD-ROM;  
(Miyazaki, T., H. Ito, H. Tanaka, and T. Higuchi,

Core image data of Nojima-Hirabayashi borehole (v 1.0), Open-file Report, Geol. Surv. Japan, no.1997-306, 1997.)

Logging Data (including Schlumberger FMI, DSI data, BHTV data, and conventional logging data)

Core samples

Are available. Please contact with Hisao Ito at

Hisao ITO

Earthquake Research Department  
Geological Survey of Japan

1-1-3 Higashi, Tsukuba, Ibaraki 305-8567, Japan

Tel: 81-298-61-3757

Fax: 81-298-55-1298

E-mail : g0193@gsj.go.jp

According to the request during the workshop to open a Website, we opened the site:

<http://www.gsj.go.jp/~ohtani/nojima/Nojima1.html>

#### **Acknowledgements**

We thank all the participants of the workshop and contributors of this proceedings, who worked on volunteer base, very hard to make the workshop successful and this proceedings very meaningful. The research at GSJ, workshop and publication of the proceedings are funded by AIST, STA, Twin Institute program, The Science and Technology Promotion Foundation of Ibaraki

Prefecture and TCI Tsukuba Center Inc.

The drilling and borehole experiments were made possible by the efforts of Sumicon consultant, Schlumberger KK, and Geophysical Surveying Co. Ltd. People in Awaji Island gave us opportunity of making this project possible. We also thank encouragement from Yoshihiro Kinugasa, Tetsuro Noda, Masataka Ando and Ryuji Ikeda.

#### **References**

Awata, Y., and Y. Suzuki, Paleoseismology and activity study of the Nojima fault system, which generated the Hyogo-ken Nanbu earthquake of January 17, 1995 (in Japanese), Geol. Surv. Japan. Open File Rep., 250, 4-8, 1996.

Awata, Y., K. Mizuno, Y. Sugiyama, R. Imura, K. Shimokawa, K. Okumura, and E. Tsukuda, Surface fault ruptures on the northwest coast of Awaji Island associated with the Hyogoken Nanbu earthquake of 1995, Japan (in Japanese with English abstract), J. Seismol. Soc. Japan. 49, 113-124, 1996.

Bouchon, M., H. Sekiguchi, K. Irikura and T. Iwata, Some characteristics of the stress field of the 1995 Hyogo-ken Nanbu (Kobe) earthquake, J. Geophys. Res., 103, 24271-24282, 1998.

Ide S., M. Takeo, and Y. Yoshida, Source process of the 1995 Kobe earthquake: Determination of Spatio-temporal slip distribution by Bayesian modeling, Bull. Seismol. Soc. Am. 86, 547-566, 1996.

Ito, H., and Y. Kuwahara, Trapped waves along the Nojima fault from the aftershock of Kobe Earthquake, 1995, Proceedings of VIIth International Symposium on the observation of the Continental Crust Through Drilling, 399-402, 1996.

Ito, H., Y. Kuwahara, T. Miyazaki, O. Nishizawa, T. Kiguchi, K. Fujimoto, T. Ohtani, H. Tanaka, T. Higuchi, S. Agar, A. Brie and H. Yamamoto, Structure and Physical Properties of the Nojima Fault by the Active fault Drilling (in Japanese), Butsuri-tansa, 49, 522-535, 1996.

Ito, H., Y. Kuwahara and O. Nishizawa, Stress Measurements by the Hydraulic Fracturing in the 1995 Hyogo-ken Nanbu earthquake Source Region, in *Rock Stress*, K. Sugawara and Y. Obara (eds.), Balkema, Rotterdam, 351-354, 1997a.

Ito, H., O. Nishizawa, Ziqiu Xue and O. Sano, Estimation of In-situ Stresses from ASR and DSCA Measurements on Drilled Cores in the 1995 Hyogo-ken Nanbu earthquake Source Region, in *Rock Stress*, K. Sugawara and Y. Obara (eds.), Balkema, Rotterdam, 355-358, 1997b.

Ito, H., Y. Kuwahara and S. Ito, Evaluation of subsurface structure of the Nojima fault by trapped waves, Proc. 2nd International Workshop on the Application of Geophysics to Rock Engineering, August 24th, 1999, Paris, France, 48-53, 1999.

Kiguchi, T., H. Ito, Y. Kuwahara, and T. Miyazaki, Estimate of permeability of the Nojima fault by hydrophone VSP experiment, submitted to Island Arc, 1999.

Kitajima, T., Y. Kobayashi, R. Ikeda, Y. Iio and K. Omura, Terrestrial heat flow in Hirabayashi, Awaji, Island, submitted to Island Arc, 1999.

Kudo, R., T. Yokoyama, H. Ito, Y. Kuwahara, O. Nishizawa and K. Yamamoto, Stress Measurements with the Core Samples by AE-DRA Methods in the 1995 Hyogoken-nanbu Earthquake Source Region, in *Rock Stress*, K. Sugawara and Y. Obara (Des), Balkema, Rotterdam, 359-362, 1997.

Li, Y.G., K. Aki, J.E. Vidale and M. G. Alvarez, A delineation of the Nojima fault ruptured in the  $M7.2$  Kobe, Japan, earthquake of 1995 using fault zone trapped waves, *J. Geophys. Res.*, 103, 7247-7263, 1998.

Lin, A., H. Imiya, S. Uda, K. Iimura, T. Misawa, T. Yoshida, Y. Abematsu, T. Wada, and K. Kawai, Investigation of the Nojima earthquake fault occurred on Awaji Island in the southern Hyogo prefecture earthquake (in Japanese with English abstract), *J. Geograp.*, 104, 113-126, 1995.

Lin, A., and S. Uda, Morphological characteristics of the earthquake surface ruptures on Awaji Island, associated with the 1995 Southern Hyogo Prefecture earthquake, *Isl. Arc.*, 5, 1-15, 1996.

Miyazaki, T., H. Ito, H. Tanaka, and T. Higuchi, Core image data of Nojima-Hirabayashi borehole (v 1.0), Open-file Report, Geol. Surv. Japan, no.1997-306, 1997.

Mizuno, K., H. Hattori, A. Sangawa, and Y. Takahashi, Geology of the Akashi district, quadrangle-series (in Japanese with English abstract), scale 1:50,000, 90pp. Geol. Surv. Japan. Tsukuba, Japan., 1990.

Murata, A., K. Takemura, T. Miyata, and A. Lin, Stratigraphy and cumulative displacement in the Nojima fault 500 m drilling core (in Japanese), *Earth Mon. Spec. Issue*, 21, 137-143, 1998.

Nakata, T., K. Yomogida, J. Odaka, T. Sakamoto, K. Asahi, and N. Chida, Surface fault ruptures associated with the 1995 Hyogo-ken Nanbu earthquake (in Japanese with English abstract), *J. Geograp.*, 104, 127-142, 1995.

Satake, K., and D. Schwartz (eds.), Proceedings of the Paleoseismology Workshop, GSJ Interim Report No. EQ/99/2; USGS Open-File Report 99-400, 1999.

Spudich, P., M. Guatteri, K. Otsuki, and J. Minagawa, Use of fault striations and dislocation models to infer tectonic shear stress during the 1995 Hyogo-ken Nanbu (Kobe) earthquake, *Bull. Seismol. Soc. Am.* 88, 413-427, 1998.

Yoshida, S., K. Kotetsu, B. Shibasaki, T. Sagiya, T. Kato, and Y. Yoshida, Joint inversion of near- and far-field waveforms and geodetic data for the rupture process of the 1995 Kobe earthquake, *J. Phys. Earth*, 44, 437-454, 1996.

## Appendix: Publication list of research on GSJ Nojima borehole

( Chronological Order)

Ito, H., and Y. Kuwahara, Trapped waves along the Nojima fault from the aftershock of Kobe Earthquake, 1995, Proceedings of VIIIth International Symposium on the observation of the Continental Crust Through Drilling, 399-402, 1996.

Ito, H., Research on the Kobe earthquake; Surveying, trenching and drilling, Proceedings of VIIIth International Symposium on the observation of the Continental Crust Through Drilling, 17-19, 1996.

Miyazaki, T. and H. Ito, Preliminaries on core image analysis using samples from a fault zone drilling, Proceedings of VIIIth International Symposium on the observation of the Continental Crust Through Drilling, 313-315, 1996.

Ito, H., Y. Kuwahara, T. Miyazaki, O. Nishizawa, T. Kiguchi, K. Fujimoto, T. Ohtani, H. Tanaka, T. Higuchi, S. Agar, A. Brie and H. Yamamoto, Structure and Physical Properties of the Nojima Fault by the Active fault Drilling, *Butsuri-tansa*, 49, 522-535, 1996.

Ito, H., Scientific drilling into the Hyogo-ken Nanbu earthquake rupture, Nojima fault, Awaji island, Japan, *Physical Properties of Earth Materials Newsletter* October, pp. 9-10, 1996. (AGU Committee on Mineral and Rock Physics)

Miyazaki, T., H. Ito, H. Tanaka, and T. Higuchi, Core image data of Nojima-Hirabayashi borehole (v 1.0), Open-file Report, *Geol. Surv. Japan*, no.1997-306, 1997.

Ito, H., Y. Kuwahara and O. Nishizawa, Stress Measurements by the Hydraulic Fracturing in the 1995 Hyogo-ken Nanbu earthquake Source Region, in *Rock Stress*, K. Sugawara and Y. Obara (eds.), Balkema, Rotterdam, 351-354, 1997.

Ito, H., O. Nishizawa, Ziqiu Xue and O. Sano, Estimation of In-situ Stresses from ASR and DSCA Measurements on Drilled Cores in the 1995 Hyogo-ken Nanbu earthquake Source Region, in *Rock Stress*, K. Sugawara and Y. Obara (eds.), Balkema, Rotterdam, 355-358, 1997.

Kudo, R., T. Yokoyama, H. Ito, Y. Kuwahara, O. Nishizawa and K. Yamamoto, Stress Measurements with the Core Samples by AE-DRA Methods in the 1995 Hyogoken-nanbu Earthquake Source Region, in *Rock Stress*, K. Sugawara and Y. Obara (Des), Balkema, Rotterdam, 359-362, 1997.

Tanaka, H., R. Ikeda, H. Ito, T. Arai, T. Ohtani, K. Omura, K. Kobayashi, H. Sano, T. Sawaguchi, T. Tomita, N. Tomida, T. Higuchi, S. Hirano, K. Fujimoto, T. Matsuda and A. Yamazaki, Mode of occurrence of fault rocks in the drilled cores (GSJ and NIED) penetrating the Nojima Earthquake fault, *Jour. Geol. Soc. Japan*, 104, 6, XIII-XVI, 1998.

Kiguchi, T., H. Ito, Y. Kuwahara and T. Miyazaki, Estimation of permeability of Nojima fault by hydrophone VSP experiment, Proceedings the 4th SEGJ International Symposium -FRACTURE IMAGING-, 335-342, 1998.

Kuwahara, Y., H. Ito, T. Kiguchi and T. Miyazaki, Characterization of damaged zone of Nojima fault by means of hydrophone VSP, Proceedings the 4th SEGJ International Symposium -FRACTURE IMAGING-, 365-368, 1998.

Brie, A., T. Endo, H. Ito, and M. Badri, Evaluation of a Fault Zone from Sonic Waveforms Data, Proceedings the 4th SEGJ International Symposium -FRACTURE IMAGING-, 191-197, 1998.

Ito, H., Y. Kuwahara and S. Ito, Evaluation of subsurface structure of the Nojima fault by trapped wave, Proceedings the 4th SEGJ International Symposium -FRACTURE IMAGING-, 177-183, 1998.

Higuchi, T., H. Tanaka, H. Ito, K. Fujimoto and T. Ohtani, Mode of deformation and hydrothermal alteration of the drilling cores from the Nojima earthquake fault, GSJ Open-file Report, No. 325, 1998.

Tomida, N., H. Tanaka, Higuchi, T., H. Ito, K. Fujimoto and T. Ohtani, The analysis of fault profile by Nojima fault drilling core, GSJ

Open-file Report, No. 325, 1998.

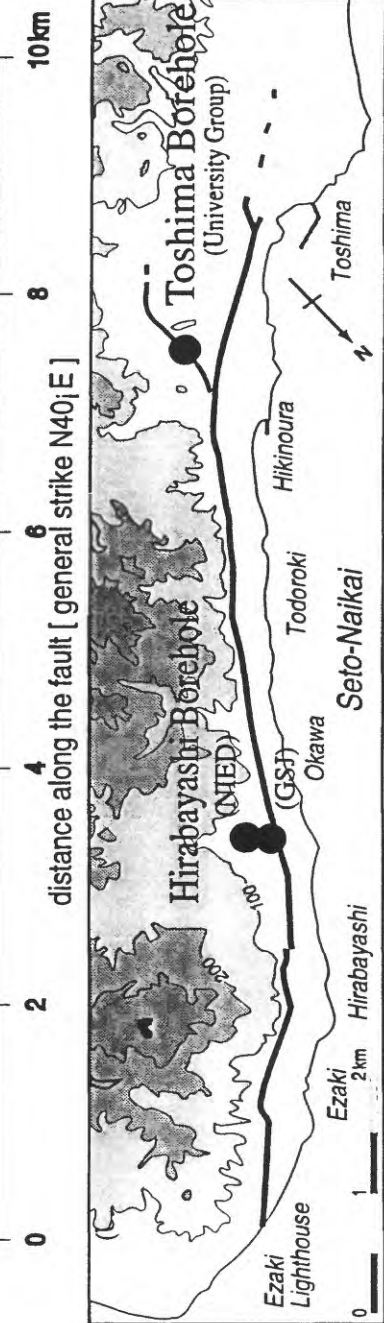
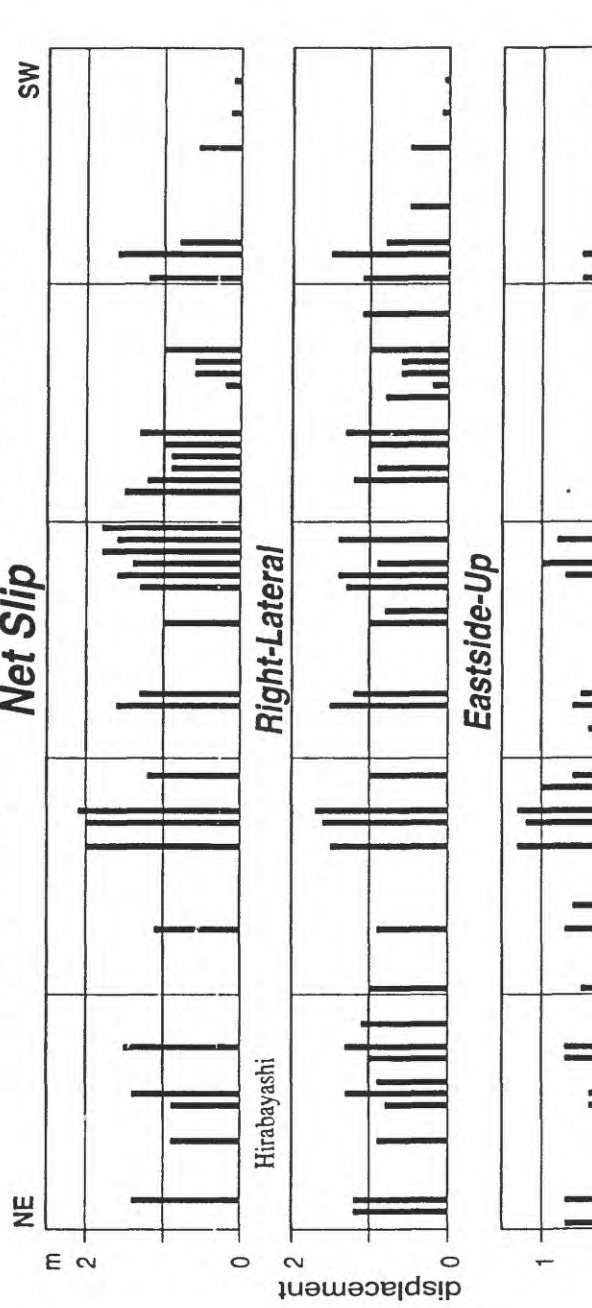
Tanaka, H., T. Higuchi, N. Tomida, K. Fujimoto, T. Ohtani and H. Ito, Distribution, deformation and alteration of fault rocks along the GSJ core penetrating the Nojima Fault, Awaji Island, Southwest Japan, *Jour. Geol. Soc. Japan*, 105, 1, 72-85, 1999.

Ito, H., Y. Kuwahara and S. Ito, Evaluation of subsurface structure of the Nojima fault by trapped waves, *Proc. 2nd International Workshop on the Application of Geophysics to Rock Engineering*, August 24th, 1999, Paris, France, 48-53, 1999.

Ohtani, T., K. Fujimoto, H. Ito, H. Tanaka, N. Tomida and T. Higuchi, Fault rocks and past to recent fluid characteristics from the borehole survey of the Nojima fault ruptured in the 1995 Kobe earthquake, southwest Japan, *J. Geophys. Res.*, 2000, in press.

## Coseismic Slip of the Nojima Fault in Awaji Island

### Net Slip



Geological Survey of Japan 1995

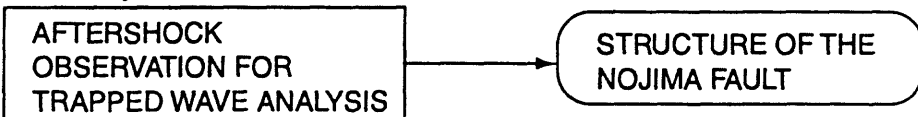
by Y. Awata, K. Mizuno, Y. Sugiyama, K. Shimokawa, and T. Imura

Fig. 1 Location of the Nojima Hirabayashi Borehole

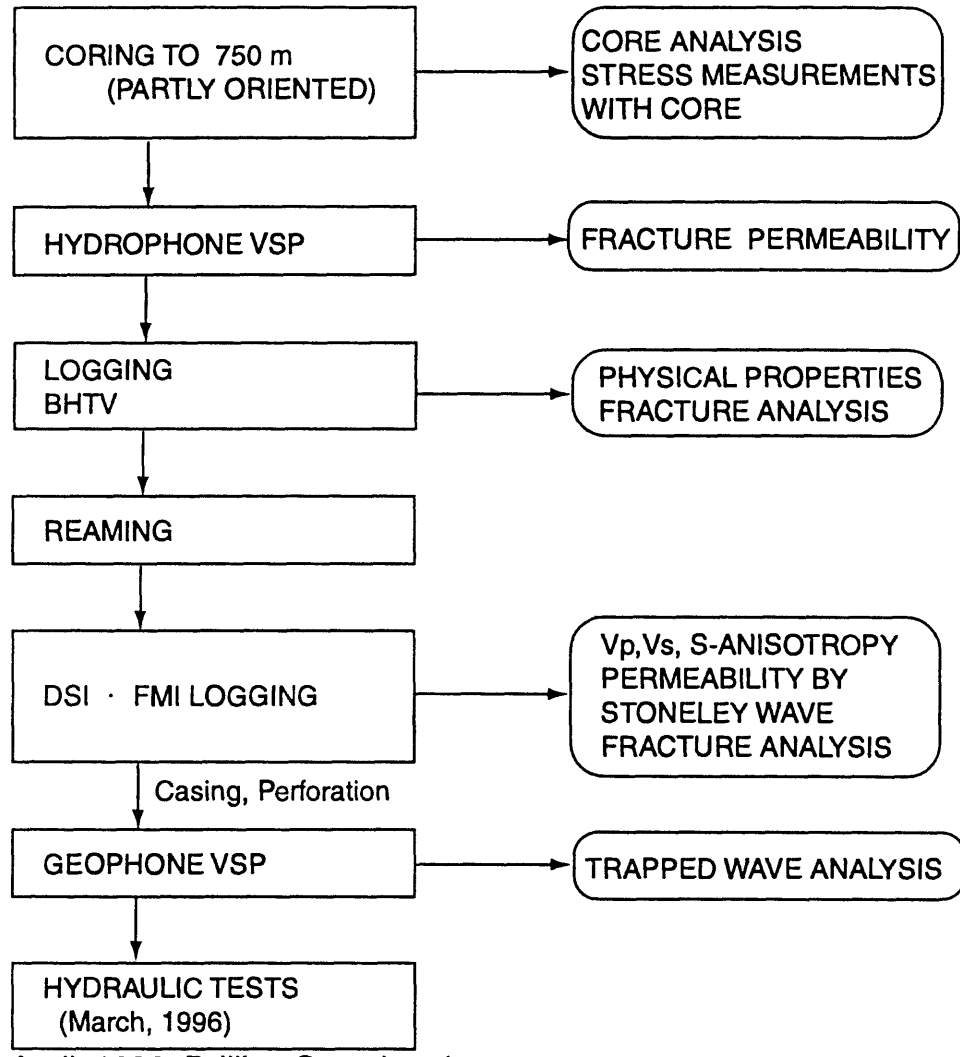
# STUDIES AT GSJ HIRABAYASHI BOREHOLE

January 17, 1995 Earthquake Ms 7.2

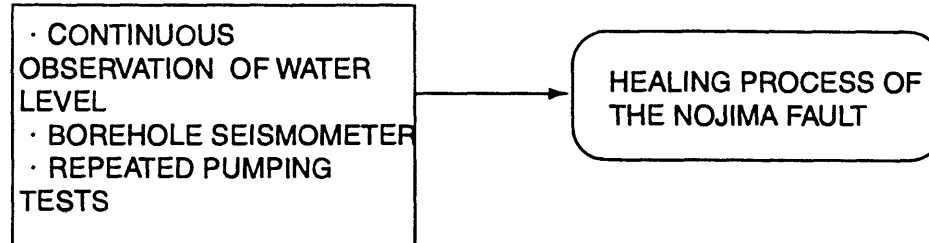
February~March, 1995



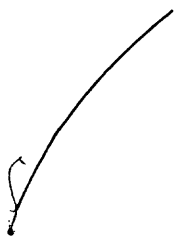
November, 1995 Drilling Started



April, 1996 Drilling Completed



BLANK



XVIII

**Workshop on Nojima Core and Borehole Data Analysis**  
**2 nd Circular, Program**  
**(at the Conference Room, GSJ, Tsukuba)**

**November 21, 17:00- Ice Breaker (Conference Room, GSJ)**

**November 22,**

9:30-10:30 Kanamori, H. (Caltech)  
Implications for core and borehole data for earthquake rupture dynamics.

10:30-11:00 Suehiro, K. (JAMSTEC)  
Seismogenic zone drilling and monitoring of OD21.

11:00-11:30 Ando, M. (DPRI, Kyoto Univ.)  
Outline of the Nojima Fault Drilling by University Group.

11:30-12:00 Ikeda, R. (NIED)  
Outline of the Nojima Fault Scientific Drilling by NIED.

12:00-13:00 **Lunch**

13:00-13:30 Ito, H., et al. (GSJ)  
Outline of the Nojima Fault Drilling by GSJ.

13:30-14:00 Tanaka, H. et al. (Ehime Univ.)  
Distribution, deformation and alteration of fault rocks along the GSJ core penetrating the Nojima fault, Awaji Island, Southwest Japan.

14:00-14:30 Lockner, D. (USGS)  
Permeability and strength of the Nojima core samples.

14:30-15:00 Morrow, C. (USGS)  
Permeability of the deep drillhole core samples.

15:00-15:30 **Coffee Break**

15:30-16:00 Moore, D. (USGS)  
Correlation of deformation textures with laboratory measurements of permeability and strength of Nojima fault zone core samples.

16:00-16:30 Pezard, P. et al. (CEREGE)  
Electrical properties and alteration of granites from the Hirabayashi hole, Japan.

16:30-17:00 Otsuki, K. and N. Kadosawa (Tohoku Univ.)  
Physical processes during seismic slip recorded in Nojima fault rock.

17:00-17:30 Takeshita, T. and K. Yagi (Hiroshima Univ.)  
Dynamic analysis based on 3-D orientation distribution of microcracks in deformed quartz from the Cretaceous granodiorite core samples drilled along the Nojima fault, southwest Japan.

17:30-20:00 **Poster Session and Welcome Party**

**November 23,**

9:00-9:20 Fujimoto, K. et al. (GSJ)  
Characterization of fault gouge from GSJ Hirabayashi core samples and implications for the activity of the Nojima fault.

9:20-9:40 Kobayashi, K. (Niigata Univ.) et al.  
Characters of the fracture zones of the Nojima fault at depths of 1140, 1300 and 1800m viewed from NIED core analyses and well logging.

9:40-10:00 Ueda, A. (Mitsubishi Material Co. Ltd.) and K. Fujimoto(GSJ)  
Isotope analysis of the Nojima fault core.

10:00-10:10 ***Coffee Break***

10:10-10:40 Roeloffs, E. (USGS) and N. Matsumoto (GSJ)  
Changes of water level and stress condition around Nojima fault.

10:40-11:00 Tokunaga, T. (Univ. of Tokyo)  
Modeling of earthquake-induced hydrological changes and possible permeability enhancement due to the January 17, 1995 Kobe Earthquake, Japan.

11:00-11:20 Sato, T. and M. Takahashi (GSJ)  
Chemical and isotopic compositions of groundwater obtained from the GSJ Hirabayashi well.

11:20-11:40 Uda, S. (Univ. of Tokyo)  
Deep surface-water flow near the Nojima earthquake fault.

11:40-12:00 Masuda, K. et al. (GSJ)  
Laboratory study of fluid migration and fault growth.

12:00-13:00 ***Lunch Break***

13:00-13:20 Tagami, T. (Kyoto Univ.) and N. Hasebe (Kanazawa Univ.)  
Thermal history analysis of the Nojima fault using fission-track thermochronology.

13:20-13:40 Fukuchi, T. (Yamaguchi Univ.) and N. Imai (GSJ)  
Inspection of resetting state of ESR signals and elucidation of radioactive disequilibria in the fault gouge zone using the Nojima Fault GSJ 750m drilling core samples.

13:40-14:00 Matsumoto, H. (Osaka Univ.)  
Property of Nojima core samples studied by ESR.

14:00-14:20 Tani, A. (Osaka Univ.)  
The geothermal and crushing effects to ESR signals in the Nojima core samples.

14:20-14:40 Tomida, N. and Y. Tsukiyama (Ehime Univ.)  
Fault rock distribution analysis based on chemical composition, water contents and fracture density.

14:40-15:00 Yamamoto, K. et al. (Tohoku Univ.)  
Stress state around the Nojima fault estimated from core measurements.

15:00-15:20 ***Coffee Break***

15:20-15:40	Ohtani, T. et al. (GSJ) Reorientation of cores and distribution of macroscopic fractures along the GSJ borehole penetrating the Nojima fault zone.
15:40-16:00	Boullier, A.-M. (Univ. Montpellier II) et al. Deformation mechanisms in granodiorite from the hanging-wall of the Nojima fault.
16:00-16:20	Zamora, M. (IPG) et al. (presented by P. Pezard) Anisotropy of elastic and anelastic properties of granites from the Hirabayashi hole, Japan.
16:20-16:40	Celerier, B. (Univ. Montpellier II) et al.; Borehole deformation along the Nojima fault after the 1995 Hyogoken-Nanbu Earthquake; BHTV acoustic scans analyses from the Hirabayashi hole, Japan.
16:40-17:00	Discussion

### ***Poster Session***

**Yamaguchi, T. (RIKEN) et al.;**

Temperature monitoring in a borehole drilled into the Nojima fault and radioactive heat production of core samples.

**Kuwahara, Y. and H. Ito (GSJ)**

Deep structure of the Nojima fault zone by trapped wave analysis.

**Kiguchi, T. (GSJ) et al.**

Fracture and permeability system in the Nojima fault.

**Xue, Z., H. Ito and O. Nishizawa,**

Estimation of in-situ stress on cores retrieved from a deep borehole at the Arima-Takatsuki tectonic line.

blank page

# Microscopic and Macroscopic Physics of Earthquakes

Hiroo Kanamori and Thomas H. Heaton

Seismological Laboratory, California Institute of Technology, Pasadena California 91125

## abstract

The thermal budget during seismic slip suggests that frictional melting and fluid pressurization can play a key role in rupture dynamics of large earthquakes. In a simple model of faulting under frictional stress  $\sigma_f$ , the temperature increases with  $\sigma_f$  and the earthquake magnitude,  $M_w$ . If the slip plane is thin and heat transfer is mainly by diffusion, the thickness of the heated zone,  $w$ , is of the order of a few mm for a seismic time scale of about 10 sec. Then, even for a modest  $\sigma_f$ , the temperature rise,  $\Delta T$ , would exceed 1000° for earthquakes with  $M_w$  = 5 to 6, and melting is likely to occur, and reduce friction during faulting. Another important process is fluid pressurization. If fluid exists in a fault zone, a modest  $\Delta T$  of 100 to 200° would likely increase the pore pressure enough to significantly reduce friction for earthquakes with  $M_w$  = 3 to 4. The microscopic state of stress caused by local melting and pressurization can be tied to macroscopic seismic parameters such as the seismic moment,  $M_0$ , and the radiated energy,  $E_R$ , by averaging the stresses in the microscopic states. Since the thermal process is important only for large earthquakes, the dynamics of small and large earthquakes can be very different. This difference is reflected in the observed relation between the scaled energy  $\tilde{e} = E_R / M_0$  and  $M_w$ . The available seismic data show that  $\tilde{e}$  for large earthquakes is 10 to 100 times larger than for small earthquakes. According to this model, mature fault zones such as the San Andreas are at relatively moderate stress levels, but the stress in the plate interior can be high. The fault dynamics described here suggests that once slip exceeds a threshold, runaway rupture could occur. This could explain the anomalous magnitude-frequency relationship observed for some mature faults. Since the thermal state is controlled by the amount of slip, the slip behavior is controlled by the slip itself. This would produce a non-linear behavior, and under certain circumstances, the slip behavior at the same location may vary from event to event. Another important implication is that slip velocity during a large earthquake could be faster than what one would extrapolate from smaller earthquakes.

*This paper is in press in American Geophysical Union, Geophysical Monograph Series  
Physics of Earthquakes*

*Editors: John Rundle, D. L. Turcotte, and W. Klein*

## Introduction

Modern broad-band seismic data have allowed seismologists to determine important seismic source parameters such as seismic moment,  $M_0$ , radiated energy,  $E_R$ , rupture parameters, and stress drops of earthquakes over a large magnitude range. However, at short length scales, resolution of seismic methods is limited because of the complex propagation and wave attenuation effects near the Earth's surface, and it is difficult to determine the details of rupture process below some length scale. The complex wave forms at high frequency must be controlled by microscopic processes on a fault plane. Such microscopic processes include frictional melting [Jeffreys, 1942; McKenzie and Brune, 1972; Richards, 1977; Sibson, 1977; Cardwell et al., 1978], fluid pressurization [Sibson, 1973; Lachenbruch, 1980; Mase and Smith, 1985, 1987], acoustic fluidization [Melosh, 1979, 1996], dynamic unloading effects [Schallamach, 1971; Brune et al., 1993; Weertman, 1980; Ben-Zion and Andrews, 1998; Mora and Place, 1998, 1999] and geometrical effects [Scott, 1996].

The importance of thermal processes in earthquake mechanics has long been recognized. Sibson [1977] discussed the implication of frictional heating for fault dynamics. He suggested that melt formation and transient increases in fluid pressure caused by frictional heating may decrease the friction to near-zero values once slip is initiated. Here, we extend the model discussed by Sibson in light of recent seismological data. A recent study of the deep Bolivian earthquake ( $M=8.3$ , depth=637 km) [Kanamori et al., 1998] presented an interesting observational case which suggests a dominant role of thermal processes during faulting. For this earthquake, the released potential energy,  $1.4 \times 10^{18}$  J, is at least 30 times larger than the radiated energy, with a large amount of non-radiated energy (comparable to the total thermal energy released during the 1980 Mount St. Helens eruption) deposited in a relatively small fault zone over a time scale of less than a minute.

The thermal process during faulting would cause a complex sequence of events including local melting, freezing, fluid pressurization, micro-fracturing and injection of fluids. Although these microscopic processes are important for understanding rupture dynamics, it is difficult to determine how these processes work in detail during faulting, because of the limited resolution of seismic methods.

In this paper, we investigate the effects of frictional melting and fluid pressurization and relate them to macroscopic seismic source parameters such as  $M_0$  and  $E_R$ . This approach is somewhat similar to that of statistical mechanics in which the physics applied to

small-scale processes is used to determine the average macroscopic parameters such as pressure and temperature.

## Thermal Budget during Faulting

The possibility of frictional melting during faulting has been suggested by several investigators. In particular, McKenzie and Brune [1972] quantitatively investigated this problem as a one-dimensional heat conduction problem. They assumed that the fault surface is simultaneously heated during slippage (i.e. infinite rupture speed) over a finite time, and concluded that if both the frictional and driving stresses are of the order of 1 kbar, melting can occur for fault slips as small as one millimeter. Richards [1977] solved elasto-dynamic equations for a propagating elliptical crack, estimated frictional heating rate behind the rupture front, and showed that if the driving stress is 100 bars and the fault particle velocity is 10 cm/sec at nucleation, a temperature rise of about 1000° can occur within a few seconds. These studies indicate that frictional melting is likely to occur during seismic faulting, at least locally.

Here we consider a gross thermal budget during faulting under a frictional stress  $\sigma_f$ . Let  $S$  and  $D$  be the fault area and the displacement offset respectively. Then the total heat generated during faulting is  $Q = \sigma_f D S$ . If we assume that the heat is distributed during seismic faulting within a layer of thickness  $w$  around the rupture plane, the average temperature rise  $\Delta T$  is given by

$$\Delta T = Q / C \rho S w = \sigma_f D / C \rho w \quad (1)$$

where  $C$  is the specific heat, and  $\rho$  is the density. In general  $D$  increases with the earthquake magnitude,  $M_w$ . Here we use a simple circular model in which the static stress drop is  $\Delta \sigma_s$  [Eshelby, 1957]. Then,

$$D = (16/7)^{2/3} (1/\pi) M_0^{1/3} \Delta \sigma_s^{2/3} / \mu \quad (2)$$

where  $M_0$  is the seismic moment and  $\mu$  is the rigidity. From (1) and (2), we obtain

$$\Delta T = (16/7)^{2/3} (1/\pi) \sigma_f \Delta \sigma_s^{2/3} M_0^{1/3} / \mu C \rho w \quad (3)$$

The seismic moment  $M_0$  is related to  $M_w$  by

$$\log M_0 = 1.5M_w + 9.1 \quad (M_0 \text{ in Nm}) \quad (4)$$

The static stress drop,  $\Delta\sigma_s$ , for most earthquakes is in the range of 10 to 100 bars, as shown in Figure 1 [Kanamori and Anderson, 1975, Hanks, 1977, Abercrombie and Leary, 1993]. However, higher stress drops have been reported for some earthquakes for which the source dimension was determined well [e.g. Kanamori et al., 1990; Wald, 1992]. Also, there is evidence that the stress drop can be locally very high (up to 25 kilobar) around small asperities [Nadeau and Johnson, 1998]. Since the thermal process considered here is most important at high-stress spots, we use  $\Delta\sigma_s = 100$  bars and  $\mu = 0.3$  Mbar for estimation of  $\Delta T$ .

The thickness  $w$  cannot be determined with seismological methods. Here,  $w$  refers to the thickness of the coseismic slip plane, not the width of the shear zone along a fault. Fault surface breaks in bed rocks are often extremely sharp suggesting that the coseismic slip must have occurred in a very narrow zone. An example of a thin slip surface within a fault zone is described in Hubbert and Rubey [1959]. Laboratory studies by Goldsby and Tullis [1998, 1999] found that when the displacement is large, slip tends to be localized in a thin layer. Also, some pseudotachylytes layers are very thin, less than a millimeter [Otsuki, 1998], suggesting that the slip plane is thin at least locally.

It is true that wide shear zones are often found along a fault. Otsuki [1978] and Hull [1988] have shown that the width of the shear zone is about 1 % of the total offset of the fault. Also, recent seismological studies suggest a 40 to 200 m thick zone with a low seismic velocity along several major faults [Li et al. 1994, 1997]. However, these wide fault-zone structures are probably formed by long-term processes involving deformation, chemical alteration, and aftershocks, and are not directly involved in coseismic slip.

If the slip plane is thin and heat is carried by thermal diffusion, then  $w$  would be of the order of  $\sqrt{k\tau_0}$ , the thermal diffusion distance, where  $k$  is the thermal diffusivity, and  $\tau_0$  is the time scale of faulting. Since  $\tau_0$  is less than 10 sec for most seismic events,  $w$  would be at most a few mm. A simple scaling shows that  $D$  is proportional to the time scale of faulting,  $\tau_0$ , while  $w$  is proportional to  $\tau_0^{1/2}$ ; then, we obtain from (1),  $\Delta T \propto D^{1/2}$ . This means that the thermal process would become increasingly important for large earthquakes.

Figure 2 shows  $\Delta T$  calculated from (3) as a function of magnitude  $M_w$  for two representative values of  $w$ , 1 mm and 1 cm. We used  $C = 1 \text{ J/g}^\circ\text{C}$ , and  $\rho = 2.6 \text{ g/cm}^3$ . If  $w = 1 \text{ mm}$ ,  $\Delta T$  exceeds  $1000^\circ\text{C}$  at  $M_w = 5$  even for a modest value of friction,  $\sigma_f = 100$  bars. Even for  $w = 1 \text{ cm}$ ,  $\Delta T$  exceeds  $1000^\circ\text{C}$  at  $M_w = 7$  for the same value of friction. If

$\sigma_f > 100$  bars,  $\Delta T$  exceeds 1000 °C at a lower  $M_w$ . Thus, thermal process becomes important for large earthquakes.

Depending on whether fluid exists or not in a fault zone, two distinct thermal processes can happen. If there is no fluid in a fault zone, the temperature can rise to cause frictional melting. Figure 2 shows that if no fluid exists, frictional melting is likely to occur for earthquakes with  $M_w = 5$  to 7. This general conclusion appears unavoidable even if the values of  $\Delta\sigma_s$ ,  $\sigma_f$ , and  $w$  used in (3) are varied over fairly large, but plausible, ranges.

Many investigators have found pseudotachylytes in cataclasites and presented them as evidence for frictional melting. Although pseudotachylytes are not commonly found [Sibson, 1975], the following are well-documented examples. Lin [1994a, 1994b] reported on glassy pseudotachylytes from the Fuyun fault zone, China, which he believed to have been formed during seismic faulting at a minimum temperature of 1,450 °C. Obata and Karato [1995] examined ultramafic pseudotachylytes from the Ivrea-Verbano zone, Italy, which are about 1 cm thick, and exhibit evidence for melting and cooling on a time scale of about 100 sec or less under a differential stress of 3 kbar. Otsuki [1998] examined cataclasites from the Nojima fault, Japan, on which the 1995 Kobe earthquake occurred. According to Otsuki [1998], these cataclasites were not formed during the recent Kobe earthquake, but they were formed from granites at a depth of about 3 km, and the original texture is exceptionally well preserved. They have a sandwich structure with alternating layers of pseudotachylytes (amorphous phase) and fine-grained rock. The pseudotachylyte layer, about 0.2 to 1 mm thick, exhibits evidence for melting at temperatures above 1,100 °C followed by rapid cooling.

Some pseudotachylytes are believed to be formed by crushing during faulting rather than melting [Lin et al., 1994; Lin, 1996]. It is also possible that pseudotachylytes were formed during faulting but they have been altered to clay minerals or crystallized into some kind of mylonites. We do not necessarily think that seismic faulting always causes melting. If a fault zone is highly crushed, the thermal energy can be distributed over a large volume and no melting occurs. Also, if fluid exists in a fault zone or some dynamic process such as acoustic fluidization or dynamic unloading occurs, the friction may drop before melting occurs. However, the existence of pseudotachylytes indicates that melting is an important process, at least locally, during faulting.

Melting does not necessarily mean reduction of friction. Once a thin melt layer is formed, high viscous friction may prevail depending on the thickness of the layer and the viscosity of the melt [Scholz, 1980]. In fact, Tsutsumi and Shimamoto [1997] performed high-velocity friction experiments and found a sharp increase in friction at the initiation of visible frictional melting. However, as shown by Spray [1993], the viscosity of molten

pseudotachylytes is low and drops rapidly with the temperature so that friction is likely to drop eventually, though the details can be complex. Recent laboratory studies by Beeler et al. [1996] and Goldsby and Tullis [1998, 1999] demonstrated that friction dropped significantly when displacement was large. Goldsby and Tullis [1998, 1999] (details described in Tullis and Goldsby [1998]) found that, at a normal pressure of 1.12 kbar, the coefficient of friction dropped to 0.14 when a large displacement, 1.6 m, occurred at a relatively high slip velocity of 3.2 mm/sec. These experiments were performed under confining pressure and the condition is close to that of natural earthquakes. From the observations of the sliding surface, they suggested that melting may have occurred during sliding.

Whether fluid exists in fault zones or not is still a matter of debate, but it is generally believed that some fault zones contain fluids and many mechanisms have been proposed to maintain high fluid pressure in fault zones [e.g. Irvine and Barnes, 1975; Byerlee, 1990; Rice, 1992]. If fluid exists in a fault zone, fluid pressurization could occur. This concept was introduced to seismology by Sibson [1973], and analyzed in great detail by Lachenbruch [1980], and Mase and Smith [1985, 1987]. Under the pressure-temperature conditions at the seismogenic depths, the thermal expansivity of water is of the order of  $10^{-3}$  °C, and significant increase in pore pressure with temperature could occur. If fluid does not escape (small permeability) and the surrounding rock is not compressive, the pressure increase would be of the order of 10 bars/deg [Lachenbruch, 1980]. In actual fault zones, permeability and compressibility vary and the pressure increase may be less. The most important parameter controlling the pressure change is the permeability. The analysis of Lachenbruch and Mase and Smith suggests that if permeability is less than  $10^{-18}$  m<sup>2</sup>, fluid pressurization is most likely to occur with a temperature rise of less than 200 °C, and friction will drop significantly. Permeability in the crust varies over a very wide range, more than a factor of  $10^{10}$ . Figure 3 shows the results for the samples taken from the Cajon drilling site in California [Morrow and Byerlee, 1992], and the Nojima fault, Japan [Ito et al., 1998]. Ito et al. [1998] show that permeability is very small near the middle of the shear zone, where the grain size of rocks is small. Ito et al.'s results are at a pressure of 500 bar (corresponding to a depth of 1.5 km), and suggest even smaller values in the deeper seismogenic zone. Although the distribution of permeability can be complex, these results suggest that pressure fluidization can play an important role, at least locally, in reducing friction. A modest  $\Delta T$  of 100 to 200° would likely increase the pore pressure enough to significantly reduce friction. Figure 2 shows that this can occur for earthquakes with  $M_w$  = 3 to 5. According to Chester and Chester [1998], the internal structure of the Punchbowl fault, California, implies that earthquake ruptures were not only confined to the

ultracataclasite layer, but also largely localized to a thin prominent fracture surface. They suggest that mechanisms that are consistent with extreme localization of slip, such as thermal pressurization of pore fluids, are most compatible with their observations.

Since a fault zone is probably complex and heterogeneous in stress, fluid content, permeability, porosity, and compressibility, no single process is likely to dominate. In other words, we do not necessarily expect a single continuous layer of melting and pressurization; we envision, instead, a fault zone that consists of many microfaults (subfaults) where different mechanisms are responsible for slip at different stress levels, producing complex rupture patterns as observed.

### Earthquake Energy Budget

We consider the energy budget for each subfault. The energy budget of earthquakes has been extensively studied by many investigators [e.g. Knopoff, 1958; Dahlen, 1977; Kostrov, 1974; Savage and Walsh; 1978]. Following these studies, and referring to Orowan [1960] and Savage and Wood [1971], here we consider a simple stress-release model. The simplest case is shown in Figure 4a which shows the stress on the fault plane as a function of slip. An earthquake is viewed as a stress release process on a surface  $S$  where, at the initiation of an earthquake, the initial (before an earthquake) shear stress on the fault plane  $\sigma_0$  drops to a constant dynamic friction  $\sigma_f$ . If the condition for instability is satisfied [Brace and Byerlee, 1966; Scholz, 1990], rapid fault slip motion begins and eventually stops. At the end, the stress on the fault plane is  $\sigma_1$  (final stress) and the average slip (offset) is  $D$ . For the example shown in Figure 4a,  $\sigma_f = \sigma_1$ . The difference  $\Delta\sigma_s = \sigma_0 - \sigma_1$  is the static stress drop, and the difference  $\Delta\sigma_d = \sigma_0 - \sigma_f$  is the driving stress of fault motion and is usually called the dynamic stress drop or effective tectonic stress [Brune, 1970]. During this process, the potential energy (strain energy plus gravitational energy) of the system,  $W$ , drops to  $W - \Delta W$  where  $\Delta W$  is the strain energy drop, and seismic wave is radiated carrying energy  $E_R$ . Then the energy budget can be written as

$$\Delta W = E_R + E_F + E_G \quad (5)$$

where  $E_F$  is the frictional energy loss given by  $E_F = \sigma_f D S$ , and  $E_G$  is the fracture energy. Knopoff [1958], Dahlen [1977] and Kostrov [1974] showed that  $\Delta W = \bar{\sigma} D S$  where  $\bar{\sigma} = (\sigma_0 + \sigma_1)/2$  is the average stress during faulting. From (5), we obtain

$$E_R = (\sigma_0 + \sigma_1) D S / 2 - \sigma_f D S - E_G = (1/2)(2\Delta\sigma_d - \Delta\sigma_s) D S - E_G$$

$$= M_0(2\Delta\sigma_d - \Delta\sigma_s)/2\mu - E_G \quad (6)$$

where  $M_0 = \mu D S$  is the seismic moment, and  $\mu$  is the rigidity. This is a simple but fundamental relationship which does not involve major assumptions. As we will show later, the fracture energy  $E_G$  can be ignored for large shallow earthquakes, and (6) can be written as

$$E_R = M_0(2\Delta\sigma_d - \Delta\sigma_s)/2\mu \quad (6')$$

This relation can be derived with a simple analogous spring system, and can be shown to be consistent with that derived from more rigorous relations for continuum. A similar relation has been used in seismology [e.g. Savage and Wood, 1971], but this particular form introduced here is useful because  $E_R$  is expressed in terms of the specific physical parameters  $\Delta\sigma_s$  and  $\Delta\sigma_d$  which directly characterize the stress release process on the fault plane.

The variation of stress during faulting can be more complex than shown in Figure 4a. For example, the stress may increase in the beginning of the slip motion (curve (1) in Figure 4a) because of loading caused by advancing rupture, or of a specific friction law such as the state-rate dependent friction law [Dieterich, 1979a, 1979b]. In fact, seismological inversion studies have shown this increase [Quin, 1990; Miyatake, 1992; Mikumo and Miyatake, 1993; Beroza and Mikumo, 1996; Ide, 1997; Bouchon, 1997]. However, this increase is of short duration and the amount of slip during this stage is small so that little energy is radiated. Thus, we will not include it in our energy budget.

Also, the friction may not be constant during faulting. It may drop drastically in the beginning and later resume a somewhat larger value (curve (2) in Figure 4a), or it may decrease gradually to a constant level (Figure 4b). The latter is called a slip-weakening process. These models have been considered in Brune [1970], Heaton [1990], Kikuchi and Fukao [1988], Kikuchi [1992], Kanamori [1994], Winslow and Ruff [1999], and Thio [1996].

If the friction is not constant, the rupture dynamics is complicated, but for the energy budget considered here, we formulate this problem referring to a simple case shown in Figure 4b. The friction  $\sigma_f$  gradually drops to a constant value  $\sigma_{f0}$  until the slip becomes  $D_c$ . In general the final stress  $\sigma_i$  can be different from  $\sigma_{f0}$ . Then, we define the average friction  $\bar{\sigma}_f$  by

$$\bar{\sigma}_f = \frac{1}{D} \int_0^D \sigma_f(u) du \quad (7)$$

where  $u$  is the slip (offset) on the fault plane. Then, equation (6') can be written as

$$E_R = M_0 (2\Delta\bar{\sigma}_d - \Delta\sigma_s) / 2\mu \quad (8)$$

where

$$\Delta\bar{\sigma}_d = \sigma_0 - \bar{\sigma}_f \quad (9)$$

Here,  $\Delta\bar{\sigma}_d$  defined by (9) can be called the average dynamic stress drop. If friction drops rapidly,  $\Delta\bar{\sigma}_d$  is the same as  $\Delta\sigma_d$ , but if friction drops very gradually to  $\sigma_i$ , then fault motion becomes quasi-static with no energy radiation, and  $\bar{\sigma}_f$  defined above would be close to the average stress  $(\sigma_0 + \sigma_i)/2$ . Then  $\Delta\bar{\sigma}_d = (1/2)\Delta\sigma_s$ , and  $E_R = 0$  from (8). We will use  $\Delta\bar{\sigma}_d$  in this paper, but the following alternative interpretation is also useful.

We can interpret the slip weakening process in terms of the breakdown process at the advancing front of an earthquake rupture. Then the total energy loss,  $\bar{\sigma}_f DS$  can be divided into two parts,

$$\bar{\sigma}_f DS = S \left[ \sigma_{f0} D + \int_0^{D_e} (\sigma_f(u) - \sigma_{f0}) du \right] \quad (10)$$

The first term can be interpreted as frictional energy (cross-hatched area in Figure 4b), and the second term, the fracture energy (hatched area in Figure 4b). Then, equation (6') can be written as

$$E_R = M_0 (2\Delta\sigma_d - \Delta\sigma_s) / 2\mu - S \int_0^{D_e} (\sigma_f(u) - \sigma_{f0}) du \quad (11)$$

where

$$\Delta\sigma_d = \sigma_0 - \sigma_{f0} \quad (12)$$

Here, the definition of the dynamic stress drop is the same as the traditional one, but the fracture energy  $E_G = S \int_0^{D_0} (\sigma_f(u) - \sigma_{f0}) du$  needs to be subtracted from the right-hand side of (6') to obtain  $E_R$ .

## Fracture Energy

The estimates of fracture energy for earthquakes vary over a wide range. The specific fracture energy  $G^*$  (fracture energy per unit area) ranges from 1 to  $10^8$  J/m<sup>2</sup> [Kostrov and Das, 1988]. The largest values are derived from seismic data on the assumption that rupture is arrested by a barrier [Aki, 1979] and may not be representative of the average fracture energy of earthquakes. Husseini [1977] estimated  $G^*$  to be on the order of  $10^5$  J/m<sup>2</sup>. Scholz [1990] quotes a range  $10^6$  to  $10^7$  J/m<sup>2</sup>.

The fracture energy can be related to the rupture velocity. For simplicity, we use a Mode III (longitudinal shear) crack model in the following, but we can qualitatively develop a similar argument for other crack geometries.

We take a Cartesian coordinate system  $(x, y, z)$ , and consider an infinitely long crack extending in  $z$  direction. The crack growth is in  $x$  direction. Let  $2c$  be the width of the crack in  $x$  direction. The crack is under uniform stress  $\sigma_0$  and friction  $\sigma_f$ , both in  $z$  direction. In actual faulting,  $\sigma_f$  is likely to vary during faulting, but here we assume it to be constant. Then,

$$\Delta W = (\sigma_0 + \sigma_f) DS/2 = (\sigma_0 - \sigma_f) DS/2 + \sigma_f DS = \Delta W_1 + \sigma_f DS \quad (13)$$

where

$$\Delta W_1 = (\sigma_0 - \sigma_f) DS/2 = \pi c^2 (\sigma_0 - \sigma_f)^2 / 2\mu \quad (14)$$

In the above, the relations  $S=2c$  and  $(\sigma_0 - \sigma_f) = 2\mu D/\pi c$  (Knopoff, 1958) are used.

The static energy release rate (specific fracture energy)  $G^*$  is given by

$$G^* = K^2 / 2\mu = \pi c (\sigma_0 - \sigma_f)^2 / 2\mu \quad (15)$$

where  $K = (\sigma_0 - \sigma_f)(\pi c)^{1/2}$  is the stress intensity factor [Dmowska and Rice, 1986; Lawn, 1993; Freund, 1998]. From (14) and (15),

$$d(\Delta W_1) = 2G^* dc \quad (16)$$

Following Kostrov [1966], Eshelby [1969], and Freund [1972], the energy release rate,  $G$ , for a crack growing at a rupture speed  $V$  is given approximately by

$$G = G^* g(V) \quad (17)$$

where  $g(V)$  is a universal function of  $V$ . For a Mode III crack, it is given by

$$g(V) = [(\beta - V)/(\beta + V)]^{1/2} \quad (18)$$

where  $\beta$  is  $S$ -wave velocity.

Then, the fracture energy is

$$E_G = \int G dS = 2 \int_0^c G^* g(V) dc = g(V) \int d(\Delta W_1) = g(V) \Delta W_1 \quad (19)$$

which becomes small compared with the strain energy involved as  $V$  increases to the limiting velocity  $\beta$ , because  $g(V)$  approaches 0 in this limit. For most large shallow earthquakes, it is generally established that the rupture velocity is about 75 to 85 % of  $\beta$ , [Heaton, 1990] and we can neglect  $E_G$ .

### Link between Microscopic and Macroscopic Processes

Our fault model consists of many faults (microfaults or subfaults) each one of which radiates seismic energy following the stress release process described above. We cannot distinguish every fault, but what we observe seismologically is the total energy radiated from all of them. Using equation (8), the total energy is given by

$$E_R = \sum E_{R_i} = \sum M_{0i} (2\Delta\bar{\sigma}_d - \Delta\sigma_s) / 2\mu = M_0 (2\Delta\bar{\sigma}_d - \Delta\sigma_s) / 2\mu \quad (20)$$

where the average dynamic stress drop,  $\Delta\bar{\sigma}_d$ , and the average static stress drop,  $\Delta\sigma_s$ , are the macroscopic parameters defined by

$$\Delta\bar{\sigma}_d = \sum M_{0i} \Delta\bar{\sigma}_d / M_0 \quad (21)$$

and

$$\Delta\sigma_s = \sum M_{0i} \Delta\sigma_s / M_0 \quad (22)$$

Here subscript  $i$  denotes the  $i$ -th subfault. Equations 21 and 22 show that the macroscopic stress drops  $\Delta\bar{\sigma}_d$  and  $\Delta\sigma_s$  are given as weighted averages of the stress drops for each subfault. The weight is the seismic moment of each subfault.

With this interpretation, we can tie the microscopic processes occurring on a fault plane to the macroscopic parameters, such as  $M_0$  and  $E_R$ , measurable with seismological methods. This is similar to the treatise in the kinetic theory of gas, in which macroscopic thermodynamic parameters like temperature and pressure are tied to the kinetic energy of molecules.

Since the rupture pattern on a fault plane is so complex that we cannot use a simple stress pattern shown in Figure 4 to represent the entire faulting. However, we can use the static and dynamic stress drops defined by (21) and (22) to represent the overall state of stress during seismic rupture.

## Interpretation

We use the macroscopic seismic parameters,  $M_0$  and  $E_R$ , which are now tied to microscopic processes through equations 20, 21 and 22 for interpreting seismic data. Specifically, we use the ratio  $\tilde{e} = E_R/M_0$ . This ratio,  $\tilde{e}$ , multiplied by  $\mu$  was introduced in seismology in the 1960's as "apparent stress" [Aki, 1966; Wyss and Brune; 1968, Wyss, 1970a, 1970b]. It is usually expressed as a product of the efficiency  $\eta$  and the average stress  $\bar{\sigma} = (\sigma_0 + \sigma_1)/2$ , neither of which can be directly determined seismologically. Nevertheless, the apparent stress, combined with static stress drop, provided useful information for the state of stress in different regions. Wyss [1970a] showed that the apparent stress of earthquakes on ridges do not differ much from those in trenches. The difficulty with the apparent stress was in difficulty in accurately computing the radiated energy. Although this difficulty still exists [e.g. Singh and Ordaz, 1994], the accuracy of energy estimates has improved [Choy and Boatwright, 1995], and we revive the use of  $\tilde{e}$ . In this paper, using equation 20, the relationship is cast in terms of the static and dynamic stress drops as follows.

$$\tilde{e} = E_R/M_0 = (2\Delta\bar{\sigma}_d - \Delta\sigma_s)/2\mu \quad (23)$$

The quantity  $\tilde{e}$  can be interpreted as a non-dimensional radiated energy scaled with  $M_0$ , the static size of the earthquake, and is called the scaled energy.

Qualitatively, if the friction drops rapidly, fault motion would be accelerated rapidly, and more energy will be radiated for a given  $M_0$ , and results in large  $\tilde{e}$ . In contrast, if the friction drops gradually, the fault motion is accelerated slowly thereby radiating less energy than the case for sudden drop in friction; this would result in small  $\tilde{e}$ . Thus,  $\tilde{e}$  which can be determined with the conventional seismological method can be used to infer the rupture behavior.

We can state the above behavior more quantitatively as follows. As shown in Figure 4a, if the friction drops rapidly,  $\Delta\bar{\sigma}_d$  is comparable, or larger than  $\Delta\sigma_s$ , and  $\tilde{e}$  given by equation 23 is of the order of  $\Delta\sigma/2\mu$ . In contrast, if friction drops gradually,  $\bar{\sigma}_f$  defined by (7) approaches the average stress  $(\sigma_0+\sigma_1)/2$ ; then  $\Delta\bar{\sigma}_d \approx (1/2)\Delta\sigma_s$ , and  $\tilde{e} \approx 0$ .

Figure 5a shows the observed relation between  $E_R$  and  $M_0$ , and Figure 5b shows  $\tilde{e}$  as a function of  $M_w$ . Although the determination of  $M_0$  can be made accurately, the determination of  $E_R$  is still subject to large uncertainties. The values of  $E_R$  estimated for the same earthquake by different investigators often differ by more than a factor of 10 [Singh and Ordaz, 1994; Mayeda and Walter, 1996]. In particular, the values determined from teleseismic data tend to be consistently smaller than those determined from regional data. This difficulty is mainly due to the complex propagation effects. Because of these uncertainties, the relation between  $E_R$  and  $M_0$  has not been given close attention.

Figures 5a and 5b include two data sets. The data for large earthquakes ( $M_w \geq 3.5$ ) are obtained in southern California using broad-band seismic data. The results obtained by Kanamori et al. [1993] have been slightly revised and updated using more recent data from TriNet, a broad-band seismic network in southern California [Mori et al. 1998]. In these studies, broad-band data at relatively short distances were used, and the propagation and site effects were removed empirically. The results of a recent study by Mayeda and Walter [1996] who used coda waves to determine the radiated energy agree with those of Kanamori et al. [1993] within a factor of 2, with Mayeda and Walter's values being slightly larger. With the recent deployment of a large number of broad-band instruments in southern California (TriNet, Mori et al.[1998]), the propagation and site effects can be calibrated more accurately with many high-quality data at short distances. The new calibration data suggest that the results obtained earlier with TERRAscope are probably accurate within a factor of 3.

The data for smaller earthquakes in Figures 5a and 5b were obtained by Abercrombie [1995] using the down-hole (2.5 km deep) seismic data recorded in the Cajon drilling site in southern California [Zoback and Lachenbruch, 1992]. A distinct advantage of using down-hole data is that they are free from the complex free-surface effects and the large attenuation near the recording site. These are the main factors that cause the large

uncertainties in the results obtained with surface instruments, especially for small earthquakes. Although only one station was available, the data set covers a fairly large azimuthal range (approximately 150°) so that the effects of radiation pattern and directivity were averaged out. Most events are within relatively short distances, 25 km, and the wave forms exhibit clean impulsive characters. Thus, these observations are considered among the most reliable for small earthquakes.

#### *Large ( $M_w \geq 4.5$ ) Earthquakes*

Figure 5b shows that the values of  $\tilde{e}$  is about  $5 \times 10^{-5}$  to  $2 \times 10^{-4}$  for large earthquakes. If the static stress drop  $\Delta\sigma_s$  is 10 to 100 bars, this result indicates (equation 8) that the dynamic stress drop,  $\Delta\bar{\sigma}_d$ , is 20 to 110 bars for large earthquakes, comparable to, or slightly larger than, the static stress drop  $\Delta\sigma_s$ .

Our interpretation is that, for large earthquakes, melting and fluid pressurization reduce dynamic friction thereby causing rapid brittle failure resulting in a relatively large  $\tilde{e}$ . Since both  $\Delta\sigma_s$  and  $\Delta\bar{\sigma}_d$  are of the order of 100 bars, and the friction is low, the entire process must be occurring at a stress level comparable to the static and dynamic stress drops, about 100 bars (Figure 4a). This is consistent with the result of Beroza and Zoback [1993] and Zoback and Beroza [1993] who found from the diversity of aftershock mechanisms that the friction during the 1969 Loma Prieta, California, earthquake was very low. Also Spudich [1992] and Spudich et al. [1998] inferred from the rotation of slip vectors that the absolute stress during faulting of several earthquakes is comparable to stress drops. The assumption in these studies is that the slip direction is subparallel to the frictional stress on the fault plane.

#### *Small ( $M_w < 2$ ) Earthquakes*

A striking feature seen in Figures 5b is that the ratio,  $\tilde{e}$ , for small earthquakes is approximately 10 to 100 times smaller than that for large earthquakes, i. e. small earthquakes appear to be less efficient in wave radiation than large earthquakes. Even if we allow for the potentially large uncertainties in energy estimation, this difference appears to be too large to be attributed to experimental errors, and probably reflects the real difference in the rupture dynamics between small and large earthquakes. The transition occurs between  $M_w = 2.5$  and 5. Although Figures 5a and 5b show the results only from the two specific data sets, many other studies show a similar transition over this magnitude range [e.g. Thatcher and Hanks, 1973; Fletcher and Boatwright, 1991; Boatwright et al., 1991; Mayeda and Walter, 1996; Thio, 1996; Zhu, 1998]. It is interesting to note that figure 7 of

Thatcher and Hanks [1973] showing the relation between  $M_0$  and  $M_L$ , if combined with their figure 10 ( $E_R$  vs.  $M_L$ ), could be interpreted as showing this transition.

Referring to equations 7 and 9, we interpret this result in terms of a gradual drop in friction. Because the thermal energy involved is not large enough to reduce friction, the stress change can be gradual as shown in Figure 4b. This means that fracture energy,  $E_G$ , defined by the second term of equation 10 is high for small earthquakes. As mentioned earlier, the fracture energy for large earthquakes is considered to be small but, for small earthquakes, there is no direct evidence for small fracture energy, i.e. small earthquakes could be significantly less brittle than large earthquakes.

McGarr [1999] suggests, on the basis of the data for the apparent stress, that the upper bound of efficiency of earthquakes is about 0.06. Our conclusion on small earthquakes is qualitatively consistent with McGarr's [1999]. However, our conclusion suggests that the efficiency for large earthquakes (e.g.  $M_w > 6$ ) could be considerably higher than that for small earthquakes.

### *Models for Small and Large Earthquakes*

Using the results obtained above, we present here a schematic model contrasting small and large earthquakes.

First we assume that  $\sigma_0$  is the same everywhere along a fault zone. Then, Figure 6 illustrates representative stress variations for small and large earthquakes. We assume that the stress on the fault plane drops linearly from  $\sigma_0$  until the slip reaches a critical value,  $D_C$ , where the stress is equal to a constant frictional stress  $\sigma_{f0}$ . The stress eventually drops to almost 0 if slip exceeds  $D_T$  when melting or pressurization reduces friction. Figure 5b shows that this transition occurs at  $M_w = 3$  to 6, which suggests that  $D_T = 3$  to 100 cm (equation 2).

We let  $D_s$  and  $D_L$  be the total displacement for small and large earthquakes, respectively. For small earthquakes,  $D_C < D_s < D_T$ , and for large earthquakes,  $D_L \gg D_T$ .

Then for large earthquakes,

$$E_R = \Delta W - E_F - E_G = D_L S \left[ \frac{\sigma_0 + \sigma_1}{2} - \sigma_{f0} \left( \frac{D_T}{D_L} \right) - \frac{\sigma_0 - \sigma_{f0}}{2} \left( \frac{D_C}{D_L} \right) \right] \quad (24)$$

Since  $D_L \gg D_T > D_C$ , and  $\sigma_1 = 0$ ,

$$\bar{c} = \frac{\Delta \sigma_s}{2\mu}, \quad \text{where} \quad \Delta \sigma_s = \sigma_0 \quad (25)$$

In contrast, for small earthquakes,

$$\begin{aligned}
 E_R &= \Delta W - E_F - E_G = D_s S \left[ \frac{\sigma_0 + \sigma_{f0}}{2} - \sigma_{f0} - \frac{\sigma_0 - \sigma_{f0}}{2} \left( \frac{D_C}{D_s} \right) \right] \\
 &= D_s S \frac{(\sigma_0 - \sigma_{f0})}{2} \left( 1 - \frac{D_C}{D_s} \right)
 \end{aligned} \tag{26}$$

Thus,

$$\tilde{e} = \frac{\Delta \sigma_s}{2\mu} \left( 1 - \frac{D_C}{D_s} \right), \text{ where } \Delta \sigma_s = \sigma_0 - \sigma_{f0} \tag{27}$$

In this case,  $\Delta \sigma_s$  (small earthquakes)  $< \Delta \sigma_s$  (large earthquakes), but the difference would be small, about a factor of 2 or so. On the other hand, the scaled energy,  $\tilde{e}$ , can be very different. If  $D_s$  is comparable to  $D_C$  for small earthquakes, then  $\tilde{e}$  can be very small.

This is the reason why we have the large difference in  $\tilde{e}$  between large and small earthquakes, even if the static stress drop is about the same. Actually,  $\sigma_0$  may vary considerably along a fault zone. If  $\sigma_0$  is large for small earthquakes, then we can have  $\Delta \sigma_s$  (small)  $= \Delta \sigma_s$  (large), yet  $\tilde{e}$  can be still very small for small earthquakes if  $D_s \approx D_C$ .

Actually, a large  $\sigma_0$  for small earthquakes may not be unreasonable considering the possibility of local stress concentration. In any case, the actual condition can be very heterogeneous, but as a whole, some mechanism as illustrated in Figure 6 is probably responsible for the difference between large and small earthquakes.

## Implications

### *State of Stress*

The results obtained for large earthquakes suggest that the average stress level along mature faults where large earthquakes occur must be low because of the dominant thermal effects such as frictional melting and fluid pressurization. Because of melting or pressurization, a fault zone is self-organized into a low stress state. That is, even if the stress was high in the early stage of fault evolution, it would eventually settle in a low stress state after many large earthquakes. This state of stress is consistent with the generally held view that the absence of heat flow anomaly along the San Andreas fault

suggests a shear strength of about 200 bars or less [Brune et al., 1969; Lachenbruch and Sass, 1980].

The stress in the crust away from active mature faults can be high as has been shown by many in-situ measurements of stress [McGarr, 1980; Brudy et al., 1997]. The stress difference is large, and a kbar type stress may be involved in small earthquakes, but the events are in general so small that it is hard to determine the stress parameters accurately. What is important, though, is that as long as the length of the fault is small, the state of stress in the fault zone would not affect the regional stress drastically. However, as the fault grows to some length (e.g. Japanese intra-plate earthquakes like Tango, Tottori, Nobi etc), then some sort of self-organization occurs and the fault settles at a stress level somewhat higher than that on more active plate boundaries.

This type of stress distribution has been suggested from seismic data [Figure 7, Kanamori, 1980], and from stress orientations near major plate boundaries [Mount and Suppe, 1987; Zoback et al., 1987].

#### *Magnitude-Frequency Relationship for Mature Faults*

One probable consequence of sudden reduction in friction when slip exceeds a threshold value would be runaway rupture. In this context, an interesting observation is the magnitude-frequency relationship for some mature plate boundaries such as the San Andreas fault and some subduction zones. For example, the absence of events with magnitude between 6.5 and 7.5 on the San Andreas fault in southern California, despite the occurrence of magnitude 8 earthquake in 1957 (Fort Tejon earthquake) and the average repeat time of about a few hundred years [Sieh, 1984], has been thought somewhat odd. Figure 8a shows the magnitude-frequency relation taken from Wesnousky [1994]. Earthquakes with  $M$  from 6 to 7 appear to be fewer than expected for the conventional magnitude-frequency relationship. A similar observation has been made for the Nankai trough in Japan [Masataka Ando, 1999, personal communication] as shown in Figure 8b. In this region, many earthquakes with  $M \geq 8$  are documented well (Figure 9), but almost no earthquakes with  $7 < M < 8$  have occurred there since 1900. These observations can be interpreted in terms of the runaway process discussed above. As the magnitude exceeds a threshold value, about 6.5 for the San Andreas and 7 for the Nankai trough, the friction drops and fault slip cannot stop until it reaches some limit imposed by the regional seismogenic structure or loading geometry. This is a runaway situation caused by dynamic effects of faulting.

If the specific fracture energy,  $G^*$ , is constant, the Griffith type cracks are inherently unstable, *i.e.* if the crack length exceeds a threshold, the crack will runaway.

So, in this sense all earthquakes, small and large, can get into runaway rupture. However,  $G^*$  is not constant in real fault zones, and the place where  $G^*$  is large acts as a barrier to stop rupture propagation [Aki, 1979]. Then the question is what is the probability of some barriers stopping the rupture. The easiest way to look at this situation is to use the stress intensity factor  $K$  which is given by  $(\sigma_0 - \sigma_f)(\pi l)^{1/2}$  for a Mode III crack [e.g. Dmowska and Rice, 1986] where  $l$  is the crack length. As the fault grows,  $l$  and  $D$  increase. When  $D$  exceeds  $D_T$ , friction,  $\sigma_f$ , drops (see Figure 6). The combined effect of the decreasing  $\sigma_f$  and increasing  $l$  increases  $K$ . Since the crack extension force is proportional to  $K^2$ , the fault rupture becomes harder to stop and runaway rupture is more likely to occur.

The magnitude-frequency relationship is usually understood as a manifestation of heterogeneity of fault structure [Scholz and Aviles, 1986; Okubo and Aki, 1987; Aviles et al., 1987]. In addition to this static feature, slip-controlled dynamic runaway process could be an important element that determines the earthquake statistics for mature faults.

### *Seismic Breakaway Phase*

In a series of papers, Ellsworth and Beroza [1995, 1998] and Beroza and Ellsworth [1996] showed that the moment rate of many earthquakes is initially low but after some time it grows rapidly. They called this sudden increase in the moment rate a breakaway phase. The breakaway phase could be a manifestation of the slip-controlled runaway rupture. However, our model has a highly heterogeneous distribution of strength and would not explain the scaling relation proposed by Ellsworth and Beroza [1995, 1998] and Beroza and Ellsworth [1996]. Similar observations, on various time scales, have been made by Umeda [1990, 1992], and Kikuchi [1997].

### *Slip Behavior of a Plate Boundary*

The thermally-controlled model discussed above is inherently non-linear in the sense that slip controls the slip behavior. In such a non-linear system, it is possible that an infinitesimally small perturbation in the initial condition may lead to a significantly different behavior. In this context, the historical sequence along the Nankai trough is interesting. Figure 9 shows the sequence determined by a series of studies of Imamura [1928], Ando [1975], and Ishibashi [1998]. An interesting event is the one in 1605. This event caused widespread tsunami along the Japanese coast, but no significant evidence for shaking has been documented [Ishibashi, 1981]. Although the evidence is qualitative, the historical data for this region are generally considered reliable. This evidence suggests that the 1605 earthquake was a tsunami earthquake in the sense defined by Kanamori [1972]. We suggest that the general style of earthquakes along a plate boundary (i.e. brittle ordinary

earthquake, slow tsunami earthquake, or creep) is determined by the properties of the boundary (e.g. age of the subducting plate, sediment structure, roughness of the subducting plate, convergence rate etc, [Ruff and Kanamori, 1983; Uyeda and Kanamori, 1979; Scholz and Campos, 1995]), but considerable perturbation from the average behavior could occur because of the non-linear nature of thermally-controlled mechanism. A slow tsunami earthquake could occasionally occur at a plate boundary where ordinary earthquakes regularly occur. This is a speculative interpretation, and the possibility that the 1605 earthquake was caused by some other mechanisms remains, but considering the significant thermal effects on fluid-filled subduction boundary, this interpretation is plausible. Yamashita [1998] showed that fluid migration in a porous fault zone with spatially heterogeneous fracture strength can produce irregular event sequences. Although Yamashita's model is for a quasi-static case, and is not directly applicable to dynamic rupture propagation, a similar model would produce variable dynamic rupture patterns.

#### *Ground Motion from Large Earthquakes*

The effect of a pulse-like near-field ground motion on large structures is becoming an important engineering problem [Heaton, 1990; Heaton et al., 1995; Hall et al., 1995]. However, very few recordings of near-field ground motion from large earthquakes exist. In modeling studies, the records from small earthquakes are used to estimate ground motions from hypothetical large earthquakes. This is a reasonable approach but the possibility exists that the slip velocity during very large earthquakes could be significantly larger than that for small earthquakes because of reduction of friction caused by large displacement.

#### **Conclusion**

The thermal budget during seismic slip suggests that frictional melting and fluid pressurization can play a key role in rupture dynamics of large earthquakes. In a simple model of faulting under frictional stress  $\sigma_f$ , the temperature increases with  $\sigma_f$  and the earthquake magnitude,  $M_w$ . If the slip plane is thin and heat transfer is mainly by diffusion, the thickness of the heated zone,  $w$ , is of the order of a few mm for a seismic time scale of about 10 sec. Then, even for a modest  $\sigma_f$ , the temperature rise,  $\Delta T$ , would exceed 1000° for earthquakes with  $M_w = 5$  to 7, and melting is likely to occur, and reduce friction during faulting. Another important process is fluid pressurization. If fluid exists in a fault zone, a modest  $\Delta T$  of 100 to 200° would likely increase the pore pressure enough to significantly reduce friction for earthquakes with  $M_w = 3$  to 5. The microscopic state of stress caused by local melting and pressurization can be tied to macroscopic seismic

parameters such as,  $M_0$ , and  $E_R$ , by averaging the stresses in the microscopic states. Since the thermal process is important only for large earthquakes, the dynamics of small and large earthquakes can be very different. This difference is reflected in the observed relation between the ratio  $\bar{e} = E_R / M_0$  and  $M_W$ . The available seismic data show that  $\bar{e}$  for large earthquakes is 10 to 100 times larger than for small earthquakes. According to this model, mature fault zones such as the San Andreas are at relatively moderate stress levels, but the stress in the plate interior can be high. The fault dynamics described here suggests that once slip exceeds a threshold, runaway rupture could occur. This could explain the anomalous magnitude-frequency relationship observed for some mature faults. Since the thermal state is controlled by the amount of slip, the slip behavior is controlled by the slip itself. This would produce a non-linear behavior, and under certain circumstances, the slip behavior at the same location may vary from event to event. Another important implication is that slip velocity during a large earthquake could be faster than what one would extrapolate from smaller earthquakes.

### Acknowledgments

We thank Kenshiro Otsuki for sharing his insight into cataclasites and pseudotachylytes with us. Discussions with Rachel Abercrombie helped us assess the accuracy of energy measurements for small earthquakes. We benefited from the comments on the early version of the manuscript by Yoshio Fukao, Masayuki Kikuchi, Minoru Takeo, and Emily Brodsky. We also thank Toshihiko Shimamoto, Lee Silver, and Yuri Fialko for helpful discussions at various stages of this work. We thank Masataka Ando and Hisao Ito for allowing us to use some of their unpublished figures. This research was partially supported by the U. S. Geological Survey grant 99HQGR0035. Contribution #8635, Division of Geological and Planetary Sciences, California Institute of Technology.

## References

Abercrombie, R., Earthquake source scaling relationships from -1 to 5  $M_L$  using seismograms recorded at 2.5-km depth, *J. Geophys. Res.*, 100, 24,015-24,036, 1995.

Abercrombie, R., and P. Leary, Source parameters of small earthquakes recorded at 2.5 km depth, Cajon Pass, Southern California: Implications for earthquake scaling, *Geophys. Res. Lett.*, 20, 1511-1514, 1993.

Aki, K., Generation and propagation of G waves from the Niigata earthquake of June 16, 1964. Part 2. Estimation of earthquake moment, from the G wave spectrum, *Bull. Earthquake Res. Inst. Tokyo Univ.*, 44, 73-88, 1966.

Aki, K., Characterization of barriers on an earthquake fault, *J. Geophys. Res.*, 84, 6140-6148, 1979.

Ando, M., Source mechanisms and tectonic significance of historical earthquakes along the Nankai trough, Japan, *Tectonophysics*, 27, 119-140, 1975.

Aviles, C. A., C. H. Scholz, and J. Boatwright, Fractal analysis applied to characteristic segments of the San Andreas fault, *J. Geophys. Res.*, 92, 331-344, 1987.

Beeler, N. M., T. E. Tullis, M. L. Blanpied, and J. D. Weeks, Frictional behavior of large displacement experimental faults, *J. Geophys. Res.*, 101, 8697-8715, 1996.

Ben-Zion, Y., and D. J. Andrews, Properties and implications of dynamic rupture along a material interface, *Bull. Seismol. Soc. Am.*, 88, 1085-1094, 1998.

Beroza, G. C., and W. L. Ellsworth, Properties of the seismic nucleation phase, *Tectonophysics*, 261, 209-227, 1996.

Beroza, G. C., and T. Mikumo, Short slip duration in dynamic rupture in the presence of heterogeneous fault properties, *J. Geophys. Res.*, 101, 22,449-22,460, 1996.

Beroza, G. C., and M. D. Zoback, Mechanism diversity of the Loma Prieta aftershocks and the mechanics of mainshock-aftershock interaction, *Science*, 259, 210-213, 1993.

Boatwright, J., J. B. Fletcher, and T. Fumal, A general inversion scheme for source, site and propagation characteristics using multiply recorded sets of moderate-sized earthquakes, *Bull. Seismol. Soc. Am.*, 81, 1754-1782, 1991.

Bouchon, M., The state of stress on some faults of the San Andreas system as inferred from near-field strong motion data, *J. Geophys. Res.*, 102, 11,731-11,744, 1997.

Brace, W. F., and J. D. Byerlee, Stick slip as a mechanism for earthquakes, *Science*, 153, 990-992, 1966.

Brudy, M., M. D. Zoback, K. Fuchs, F. Rumell, and J. Baumgartner, Estimation of the complete stress tensor to 8 km depth in the KTB scientific drill holes: Implications for crustal strength, *J. Geophys. Res.*, 102, 18,453-18,475, 1997.

Brune, J. N., Tectonic stress and spectra of seismic shear waves from earthquakes, *J. Geophys. Res.*, 75, 4997-5009, 1970.

Brune, J. N., S. Brown, and P. A. Johnson, Rupture mechanism and interface separation in foam rubber models of earthquakes: A possible solution to the heat flow paradox and the paradox of large overthrusts, *Tectonophysics*, 218, 59-67, 1993.

Brune, J. N., T. L. Henyey, and R. F. Roy, Heat flow, stress, and the rate of slip along the San Andreas fault, California, *J. Geophys. Res.*, 74, 3821-3827, 1969.

Byerlee, J. D., Friction, overpressure and fault normal compression, *Geophysical Research Letters*, 17, 4,741-4,750, 1990.

Cardwell, R. K., D. S. Chinn, G. F. Moore, and D. L. Turcotte, Frictional heating on a fault zone with finite thickness, *Geophys. J. Roy. Astron. Soc.*, 52, 525-530, 1978.

Chester, F. M., and J. S. Chester, Ultracataclasite structure and friction processes of the Punchbowl fault, San Andreas system, California, *Tectonophysics*, 295, 199-221, 1998.

Choy, G. L., and J. L. Boatwright, Global patterns of radiated energy and apparent stress, *J. Geophys. Res.*, 100, 18205-18228, 1995.

Dahlen, F. A., The balance of energy in earthquake faulting, *Geophys. J. R. astr. Soc.*, 48, 239-261, 1977.

Dieterich, J. H., Modeling of rock friction 1. Experimental results and constitutive equations, *J. Geophys. Res.*, 84, 2161-2168, 1979a.

Dieterich, J. H., Modeling of rock friction 2. Simulation of preseismic slip, *J. Geophys. Res.*, 84, 2169-2175, 1979b.

Dmowska, R., and J. R. Rice, Fracture theory and Its seismological applications, in *Theories in Solid Earth Physics*, edited by R. Teisseyre, pp. 187-255, PWN-Polish Publishers, Warzawa, 1986.

Ellsworth, W. L., and G. C. Beroza, Seismic evidence for an earthquake nucleation phase, *Science*, 268, 851-855, 1995.

Ellsworth, W. L., and G. C. Beroza, Observation of the seismic nucleation phase in the Ridgecrest, California, earthquake sequence, *Geophys. Res. Lett.*, 25, 401-404, 1998.

Eshelby, J. D., The determination of the elastic field of an ellipsoidal inclusion and related problems, *Proceedings of the Royal Soc. London*, 241, 376-396, 1957.

Eshelby, J. D., The elastic field of a crack extending non-uniformly under general anti-plane loading, *J. Mech. Phys. Solids*, 17, 177-199, 1969.

Fletcher, J. B., and J. Boatwright, Source parameters of Loma Prieta aftershocks and wave propagation characteristics along the San Francisco peninsula from a joint inversion of digital seismograms, *Bull. Seismol. Soc. Am.*, 81, 1783-1812, 1991.

Freund, L. B., *Dynamic Fracture Mechanics*, Cambridge Univ. Press, New York, 1-563, 1998.

Goldsby, D. L., and T. E. Tullis, Experimental observations of frictional weakening during large and rapid slip (abstract), *EOS, Transactions, American Geophysical Union*, 79, F610, 1998.

Goldsby, D. L., and T. E. Tullis, Dramatic reduction in friction of quartz at rapid but subseismic slip (abstract), *Seismological Research Letters*, 70, 247, 1999.

Guatteri, M., and P. Spudich, Coseismic temporal changes of slip direction: the effect of absolute stress on dynamic rupture, *Bull. Seismol. Soc. Am.*, 88, 777-789, 1998.

Hall, J. F., T. Heaton, M. W. Halling, and D. J. Wald, Near-source ground motion and its effects on flexible buildings, *Earthquake Spectra*, 11, 569-605, 1995.

Hanks, T. C., Earthquake stress drops, ambient tectonic stresses and stresses that derive plate motions, *Pure Appl. Geophys.*, 115, 441-458, 1977.

Heaton, T., Evidence for and implications of self-healing pulses of slip in earthquake rupture, *Physics of the Earth and Planetary Interiors*, 64, 1-20, 1990.

Heaton, T., J. F. Hall, D. J. Wald, and M. W. Halling, Response of high-rise and base-isolated buildings to a hypothetical  $M_w$ 7.0 blind thrust earthquake, *Science*, 267, 206-211, 1995.

Hubbert, M. K., and W. W. Rubey, Role of fluid pressure in mechanics of overthrust faulting, *Bull. Geol. Soc. Am.*, 70, 115-166, 1959.

Hull, J., Thickness-displacement relationships for deformation zones, *Journal of Structural Geology*, 10, 431-435, 1988.

Husseini, M. I., Energy balance for formation along a fault, *Geophys. J. R. astr. Soc.*, 49, 699-714, 1977.

Ide, S., and M. Takeo, Determination of constitutive relations of fault slip based on seismic wave analysis, *J. Geophys. Res.*, 102, 27,379-27,391, 1997.

Imamura, A., On the seismic activity of central Japan, *Jap. J. Astron. Geophys.*, 6, 119-137, 1928.

Irwin, W. P., and I. Barnes, Effect of geologic structure and metamorphic fluids on seismic behavior of the San Andreas fault system in central and northern California, *Geology*, 3, 713-716, 1975.

Ishibashi, K., Specification of a soon-to-occur seismic faulting in the Tokai district, central Japan, based upon seismotectonics, in *Earthquake Prediction, An International Review*, edited by D. W. Simpson and P. G. Richards, pp. 297-332, American Geophysical Union, Washington, D. C., 1981.

Ishibashi, K., Inferred Tokai earthquake paired with the 1361 Shohei Nankai earthquake (abstract), *Programme and Abstracts, The Seismological Society of Japan, 1998, Fall Meeting*, P125, 1998.

Ito, H., H. Naka, D. Lockner, T. Kiguchi, H. Tanaka, R. Ikeda, T. Ohtani, K. Fujimoto, and Y. Kuwahara, Permeability of the Nojima fault: Comparison of borehole results with

core measurements (abstract), *Programme and Abstracts, The Seismological Society of Japan, 1998, Fall Meeting, B20*, 1998.

Jeffreys, H., On the mechanics of faulting, *Geol. Mag.*, 79, 291-295, 1942.

Kanamori, H., Mechanism of tsunami earthquakes, *Phys. Earth Planet. Inter.*, 6, 346-359, 1972.

Kanamori, H., The state of stress in the Earth's lithosphere, in *Phys. Earth's Int., Course LXXVIII*, edited by A. M. Dziewonski and E. Boschi, pp. 531-554, North-Holland Pub. Co., Amsterdam, 1980.

Kanamori, H., Mechanics of Earthquakes, *Ann. Rev. Earth & Planetary Sciences*, 22, 207-237, 1994.

Kanamori, H., and D. L. Anderson, Theoretical basis of some empirical relations in seismology, *Bull. Seis. Soc. Amer.*, 65, 1073-1095, 1975.

Kanamori, H., T. H. Anderson, and T. H. Heaton, Frictional melting during the rupture of the 1994 Bolivian Earthquake, *Science*, 279, 839-842, 1998.

Kanamori, H., E. Hauksson, L. K. Hutton, and L. M. Jones, Determination of Earthquake Energy Release and  $M_L$  Using TERRAscope, *Bull. Seismol. Soc. Am.*, 83, 330-346, 1993.

Kanamori, H., J. Mori, and T. H. Heaton, The 3 December 1988, Pasadena earthquake ( $M_L=4.9$ ) recorded with the very broadband system in Pasadena, *Bull. Seismol. Soc. Am.*, 80, 483-487, 1990.

Kikuchi, M., Strain drop and apparent strain for large earthquakes, *Tectonophysics*, 211, 107-113, 1992.

Kikuchi, M., Size dependence of moment-rate function (abstract), in *1997 IASPEI meeting*, Thesaloniki, Greece, 1997.

Kikuchi, M., and Y. Fukao, Seismic wave energy inferred from long-period body wave inversion, *Bull. Seismol. Soc. Am.*, 78, 1707-1724, 1988.

Knopoff, L., Energy release in earthquakes, *Geophysic. Jour.*, 1, 44-52, 1958.

Kostrov, B. V., Unsteady propagation of longitudinal shear cracks, *J. Appl. Math. Mech. (transl. P. M. M.)*, 30, 1241-1248, 1966.

Kostrov, B. V., Seismic moment and energy of earthquakes, and seismic flow of rock (translated to English), *Izv. Earth Physics*, 1, 23-40, 1974.

Kostrov, B. V., and S. Das, *Principles of Earthquake Source Dynamics*, Cambridge University Press, Cambridge, 1-286, 1988.

Lachenbruch, A. H., Frictional heating, fluid pressure, and the resistance to fault motion, *J. Geophys. Res.*, 85, 6097-6112, 1980.

Lachenbruch, A. H., and J. H. Sass, Heat flow and energetics of the San Andreas fault zone, *J. Geophys. Res.*, 85, 6185-6222, 1980.

Lawn, B., *Fracture of Brittle Solids - Second Edition*, Cambridge University Press, Cambridge, 1-378, 1993.

Li, Y. G., K. Aki, D. Adams, A. Hasemi, and W. H. K. Lee, Seismic guided waves trapped in the fault zone of the Landers, California, earthquake of 1992, *J. Geophys. Res.*, 99, 11,705-11,722, 1994.

Li, Y. G., K. Aki, and F. L. Vernon, San Jacinto fault zone guided waves: A discrimination for recently active fault strands near Anza, California, *J. Geophys. Res.*, 102, 11,689-11,701, 1997.

Lin, A., Glassy pseudotachylite veins from the Fuyun fault zone, northwest China, *Journal of Structural Geology*, 16, 71-83, 1994a.

Lin, A., Microlite morphology and chemistry in pseudotachylite from the Fuyun fault zone, China, *Journal of Geology*, 102, 317-329, 1994b.

Lin, A., Injection veins of crushing-originated pseudotachylite and fault gouge formed during seismic faulting, *Engineering Geology*, 43, 213-224, 1996.

Lin, A., T. Matsuda, and T. Shimamoto, Pseudotachylite from the Iida-Matsukawa fault, Nagano prefecture: Pseudotachylite of crush origin? (in Japanese), *Kozo Chishitsu (Structural Geology)*, 39, 51-64, 1994.

Mase, C. W., and L. Smith, Pore-fluid pressures and frictional heating on a fault surface, *Pure and Applied Geophysics*, 122, 583-607, 1985.

Mase, C. W., and L. Smith, Effects of frictional heating on the thermal, hydrologic, and mechanical response of a fault, *J. Geophys. Res.*, 92, 6249-6272, 1987.

Mayeda, K., and W. R. Walter, Moment, energy, stress drop, and source spectra of western United States earthquakes from regional coda envelopes, *J. Geophys. Res.*, 101, 11,195-11,208, 1996.

McGarr, A., Some constraints on levels of shear stress in the crust from observations and theory, *J. Geophys. Res.*, 85, 6,231-6,238, 1980.

McGarr, A., On relating apparent stress to the stress causing earthquake fault slip, *J. Geophys. Res.*, 104, 3,003-3,011, 1999.

McKenzie, D. P., and J. N. Brune, Melting on fault planes during large earthquakes, *Geophys. J. R. astr. Soc.*, 29, 65-78, 1972.

Melosh, J., Acoustic fluidization: a new geologic process?, *J. Geophys. Res.*, 84, 7513-7520, 1979.

Melosh, H. J., Dynamical weakening of faults by acoustic fluidization, *Nature*, 379, 601-606, 1996.

Mikumo, T., and T. Miyatake, Dynamic rupture processes on a dipping fault, and estimates of stress drop and strength excess from the results of waveform inversion, *Geophys. J. Int.*, 112, 481-496, 1993.

Miyatake, T., Dynamic rupture process of inland earthquakes in Japan: Weak ad strong asperities, *Geophys. Res. Lett.*, 19, 1041-1044, 1992a.

Miyatake, T., Reconstruction of dynamic rupture process of an earthquake with constraints of kinematic parameters, *Geophys. Res. Lett.*, 19, 349-352, 1992b.

Mora, P., and D. Place, Numerical simulation of of earthquake faults with gauge: Towards a comprehensive explanation for the heat flow paradox, *J. Geophys. Res.*, 103, 21,067-21,089, 1998.

Mora, P., and D. Place, The weakness of earthquake faults, *Geophys. Res. Lett.*, 26, 123-126, 1999.

Mori, J., H. Kanamori, J. Davis, E. Hauksson, R. Clayton, T. Heaton, L. Jones, and A. Shakal, Major improvements in progress for southern California earthquake monitoring, *EOS Trans. American Geophysical Union*, 79, 217-221, 1998.

Morrow, C. A., and J. D. Byerlee, Permeability of core samples from Cajon Pass scientific drill hole: Results from 2100 to 3500 m depth, *J. Geophys. Res.*, 97, 5145-5151, 1992.

Mount, V., and J. Suppe, State of stress near the San Andreas fault: Implications for wrench tectonics, *Geology*, 15, 1143-1146, 1987.

Nadeau, R. M., and L. R. Johnson, Seismological studies at Parkfield VI: Moment release rates and estimates of source parameters for small repeating earthquakes, *Bull. Seismol. Soc. Am.*, 88, 790-814, 1998.

Obata, M., and S. Karato, Ultramafic pseudotachylite from the Balmuccia peridotite, Ivrea-Verbano zone, northern Italy, *Tectonophysics*, 242, 313-328, 1995.

Okubo, P. G., and K. Aki, Fractal geometry in the San Andreas fault system, *J. Geophys. Res.*, 92, 345-355, 1987.

Orowan, E., Mechanism of seismic faulting in rock deformation, *Geol. Soc. Am. Mem.*, 79, 323-345, 1960.

Otsuki, K., On the relationship between the width of shear zone and the displacement along fault, *Jour. of Geolog. Soc. Japan*, 84, 661-669, 1978.

Otsuki, K., Physical process of seismic frictional sliding observed in samples from fault zones (translated from Japanese), *Chikyu Monthly*, 213-224, 1998.

Quin, H., Dynamic stress drop and rupture dynamics of the October 15, 1979 Imperial Valley, California, earthquake, *Tectonophysics*, 175, 93-117, 1990.

Richards, P. G., Dynamic motions near an earthquake fault: a three-dimensional solution, *Bull. Seismol. Soc. Am.*, 66, 1-32, 1976.

Rice, J. R., Fault stress states, pore pressure distributions, and the weakness of the San Andreas fault, in *Fault Mechanics and Transport Properties of Rocks: A Festschrift in Honor of W. F. Brace*, edited by B. Evans and W. Teng-fong, pp. 475-503, Academic Press, New York, 1992.

Ruff, L., and H. Kanamori, Seismic coupling and uncoupling at subduction zones, *Tectonophysics*, 99, 99-117, 1983.

Savage, J. C., and J. B. Walsh, Gravitational energy and faulting, *Bull. Seismol. Soc. Am.*, 68, 1613-1622, 1978.

Savage, J. C., and M. D. Wood, The relation between apparent stress and stress drop, *Bull. Seismol. Soc. Am.*, 61, 1381-1388, 1971.

Schallamach, A., How does rubber slide?, *Wear*, 17, 301-312, 1971.

Scholz, C. H., Shear heating and the state of stress on faults, *J. Geophys. Res.*, 85, 6174-6184, 1980.

Scholz, C. H., *The mechanics of earthquake faulting*, Cambridge University Press, New York, 1-438, 1990.

Scholz, C. H., and C. Aviles, The fractal geometry of faults and faulting, in *Earthquake Source Mechanics, AGU Geophys. Mono.* 37, edited by S. Das, J. Boatwright and C. Scholz, pp. 147-155, American Geophysical Union, Washington, D. C., 1986.

Scholz, C., and J. Campos, On the mechanism of seismic decoupling and back-arc spreading at subduction zones, *J. Geophys. Res.*, 100, 22103-22115, 1995.

Scott, D. R., Seismicity and stress rotation in a granular model of the brittle crust, *Nature*, 381, 592-595, 1996.

Sibson, R. H., Interactions between temperature and fluid pressure during earthquake faulting -- A mechanism for partial or total stress relief, *Nature*, 243, 66-68, 1973.

Sibson, R. H., Generation of pseudotachylite by ancient seismic faulting, *Geophys. J. R. astr. Soc.*, 43, 775-794, 1975.

Sibson, R. H., Kinetic shear resistance, fluid pressures and radiation efficiency during seismic faulting, *Pure and Applied Geophysics*, 115, 387-400, 1977.

Sibson, R. H., Power dissipation and stress levels on faults in the upper crust, *J. Geophys. Res.*, 85, 6239-6247, 1980.

Sieh, K., Lateral offsets and revised dates of large prehistoric earthquakes at Pallett Creek, southern California, *J. Geophys. Res.*, 89, 7641-7670, 1984.

Singh, S. K., and M. Ordaz, Seismic energy release in Mexican subduction zone earthquakes, *Bull. Seismol. Soc. Am.*, 84, 1533-1550, 1994.

Spray, J. G., Viscosity determinations of some frictionally generated silicate melts - Implications for fault zone rheology at high-strain rates, *J. Geophys. Res.*, 98, 8053-8068, 1993.

Spudich, P. K. P., On the inference of absolute stress levels from seismic radiation, *Tectonophysics*, 211, 99-106, 1992.

Spudich, P., M. Guatteri, K. Otsuki, and J. Minagawa, Use of fault striations and dislocation models to infer tectonic shear stress during the 1995 Hyogo-ken Nanbu (Kobe) earthquake, *Bull. Seismol. Soc. Am.*, 88, 413-427, 1998.

Thatcher, W., and T. Hanks, Source parameters of southern California earthquakes, *J. Geophys. Res.*, 78, 8547-8576, 1973.

Thio, H. K., 1 - Using Short-Period Surface Waves to Study Seismic Source and Structure. 2 - Source Complexity of Large Strike-Slip Earthquakes, Ph.D thesis, pp., California Institute of Technology, 1996.

Tsutsumi, A., and T. Shimamoto, High-velocity frictional properties of gabbro, *Geophys. Res. Lett.*, 24, 699-702, 1997.

Tullis, T. E., and D. L. Goldsby, Laboratory experiments on rock friction focussed on understanding earthquake mechanics, USGS Technical Report, Vol. 40, <http://erp-web.er.usgs.gov/reports/VOL40/pt/g3034.htm>, 1998.

Umeda, Y., High-amplitude seismic waves radiated from the bright spot of an earthquake, *Tectonophysics*, 141, 335-343, 1990.

Umeda, Y., The bright spot of an earthquake, *Tectonophysics*, 211, 13-22, 1992.

Uyeda, S., and H. Kanamori, Back-arc opening and the mode of subduction, *J. Geophys. Res.*, 84, 1049-1061, 1979.

Wald, D. J., Strong motion and broadband teleseismic analysis of the 1991 Sierra Madre, California, earthquake, *J. Geophys. Res.*, 97, 11,033-11,046, 1992.

Weertman, J., Unstable slippage across a fault that separates elastic media of different elastic constants, *J. Geophys. Res.*, 85, 1455-1461, 1980.

Wesnousky, S. G., The Gutenberg-Richter or Characteristic Earthquake Distribution, Which is it?, *Bull. Seismol. Soc. Am.*, 84, 1940-1959, 1994.

Winslow, N., and L. Ruff, A hybrid method for calculating the radiated wave energy of deep earthquakes, *Physics of the Earth and Planetary Interiors*, submitted, 1997.

Wyss, M., Apparent stress of earthquakes on ridges compares to apparent stresses of earthquakes in trenches, *Geophys. J. R. astr. Soc.*, 19, 479-484, 1970a.

Wyss, M., Stress estimates for south American shallow and deep earthquakes, *J. Geophys. Res.*, 75, 1529-1544, 1970b.

Wyss, M., and J. N. Brune, Seismic moment, stress, and source dimensions for earthquakes in the California-Nevada region, *J. Geophys. Res.*, 73, 4681-4694, 1968.

Yamashita, T., Simulation of seismicity due to fluid migration in a fault zone, *Geophys. J. Int.*, 132, 674-686, 1998.

Zhu, L., Broadband Waveform Modeling and Its Application to the Lithospheric Structure of the Tibetan Plateau, Ph.D thesis, pp., California Institute of Technology, 1998.

Zoback, M. D., and G. C. Beroza, Evidence for near-frictionless faulting in the 1989 (M 6.9) Loma Prieta, California, earthquake and its aftershocks, *Geology*, 21, 181-185, 1993.

Zoback, M., and A. H. Lachenbruch, Introduction to the special section on the Cajon Pass scientific drilling project, *J. Geophys. Res.*, 97, 4991-4994, 1992.

Zoback, M. D., M. L. Zoback, V. S. Mount, J. Suppe, J. Eaton, D. Healy, P. Oppenheimer, L. Reasenberg, L. Jones, B. Raleigh, I. Wong, O. Scotti, and C. Wentworth, New evidence on the state of stress of the San Andreas fault system, *Science*, 238, 1105-1111, 1987.

## Figure caption

### Figure 1.

Static stress drop of earthquakes [Modified from Abercrombie and Leary, 1993].

### Figure 2.

Temperature rise,  $\Delta T$ , in a fault zone as a function of magnitude,  $M_w$ , with the frictional stress,  $\sigma_f$ , as a parameter. The static stress drop  $\Delta\sigma_s$  is assumed to be 100 bars. The upper and lower figures correspond to the cases of  $w$  (thickness of the heated zone)=1 mm and 1 cm, respectively.

### Figure 3

Permeability near a fault zone. a) Nojima fault, Japan [Ito et al. 1998]. b) Cajon Pass, California [Morrow and Byerlee, 1992].

### Figure 4.

Illustration of simple stress release patterns during faulting. a) Simple case. b) Slip-weakening model. Hatched and cross-hatched areas indicate the fracture energy and frictional energy loss, respectively.

### Figure 5.

a). Relation between the radiated energy  $E_R$  and the seismic moment  $M_0$ . The data for large earthquakes (solid circle) are from southern California [updated from Kanamori et al. 1993], and those for small earthquakes (open triangles) are taken from Abercrombie [1995]. b) The scaled energy,  $\bar{e} = E_R / M_0$ , computed as a function of  $M_w$ . Note that the values of  $\bar{e}$  for small earthquakes are 10 to 100 times smaller than those for large earthquakes.

### Figure 6.

Schematic stress release patterns for small (left) and large earthquakes (right). Hatched, cross-hatched, and dotted areas represent the fracture energy, frictional energy loss and radiated energy, respectively.

### Figure 7.

Schematic diagram showing the magnitude of the stresses in Earth's crust [Modified from Kanamori, 1980].

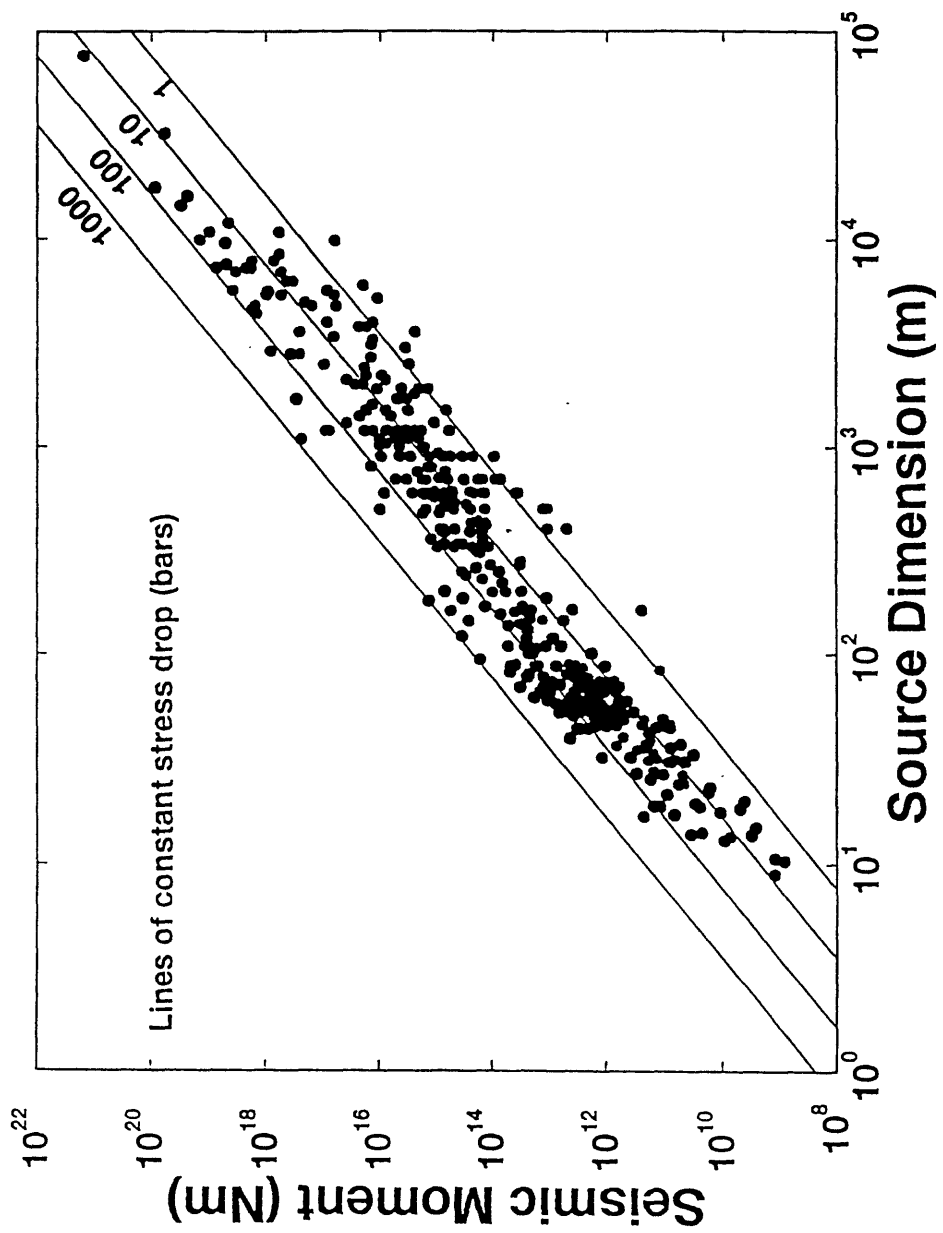
### Figure 8.

a). Magnitude-frequency relationship for the San Andreas fault, California [Wesnousky, 1994]. b). The same for the Nankai trough, Japan [Masataka Ando, written communication, 1999].

### Figure 9.

Large earthquakes along the Nankai trough, Japan [Ishibashi and Satake, 1998].

Figure 1



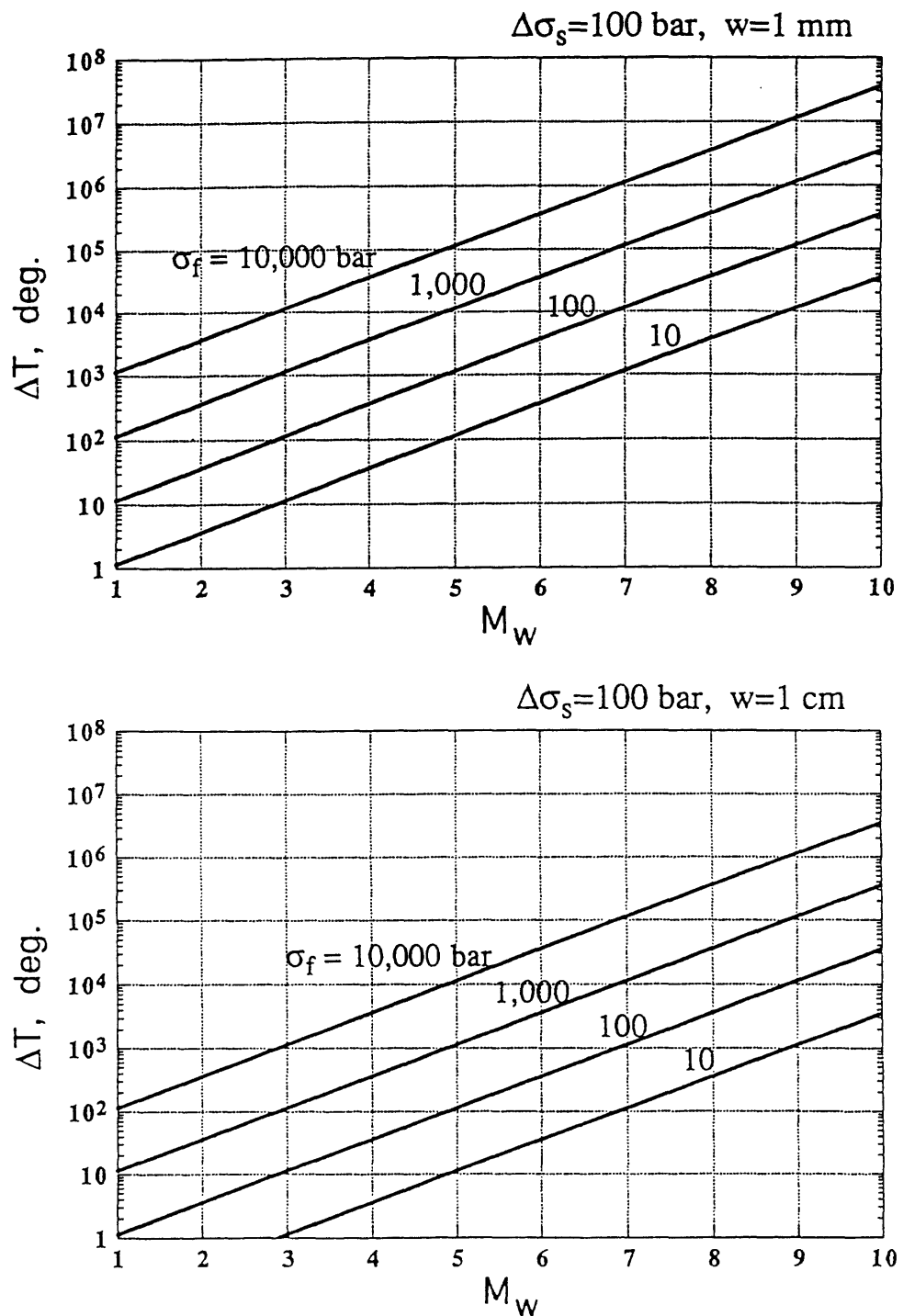


Figure 2

Permeability of Cajon Pass Rocks  
Morrow and Byerlee [1992]

PERMEABILITY OF NOJIMA FAULT CORE  
(at 50 MPa) Ito et al. (1998)

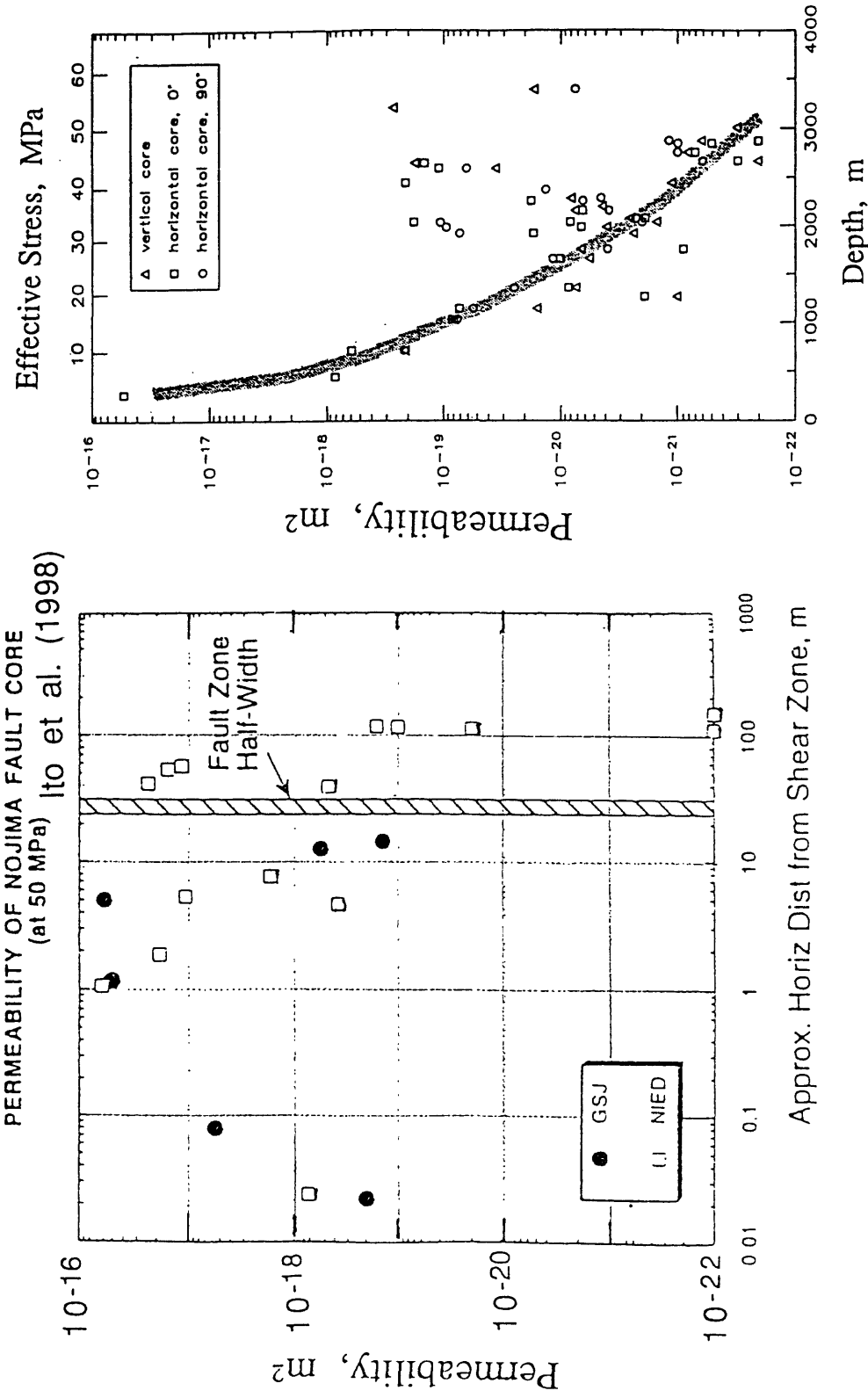
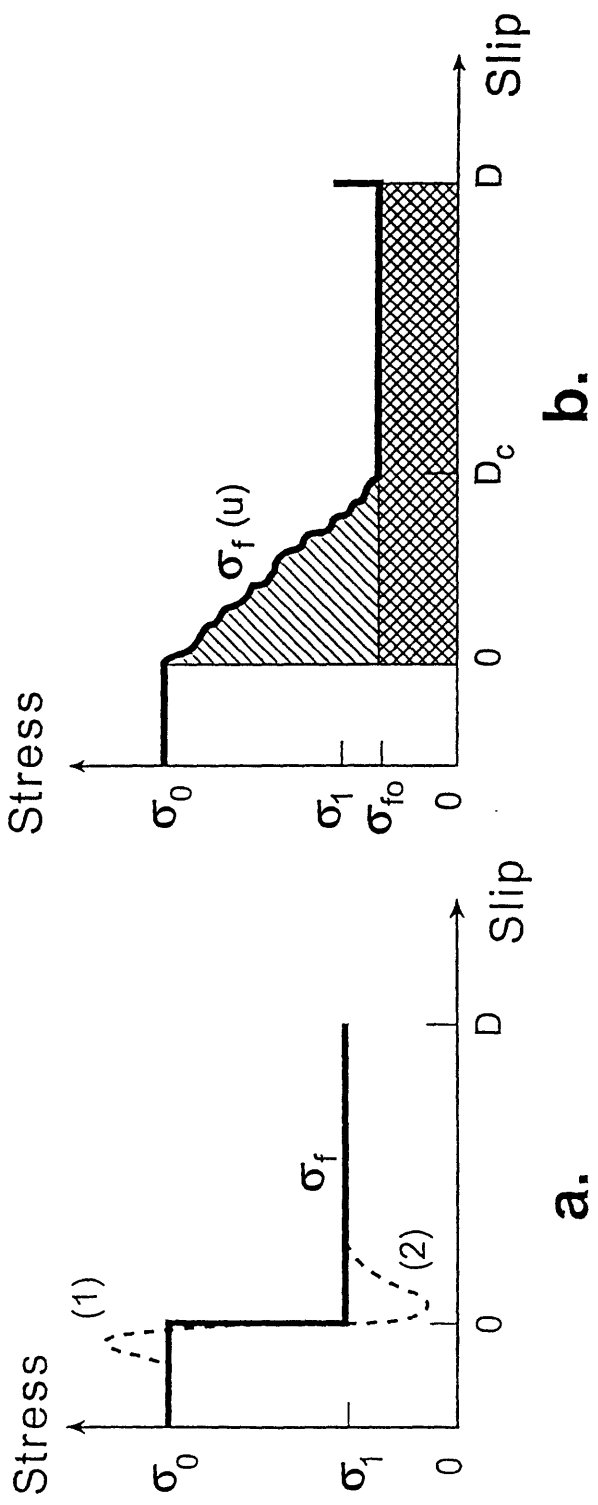


Figure 2

Figure 4



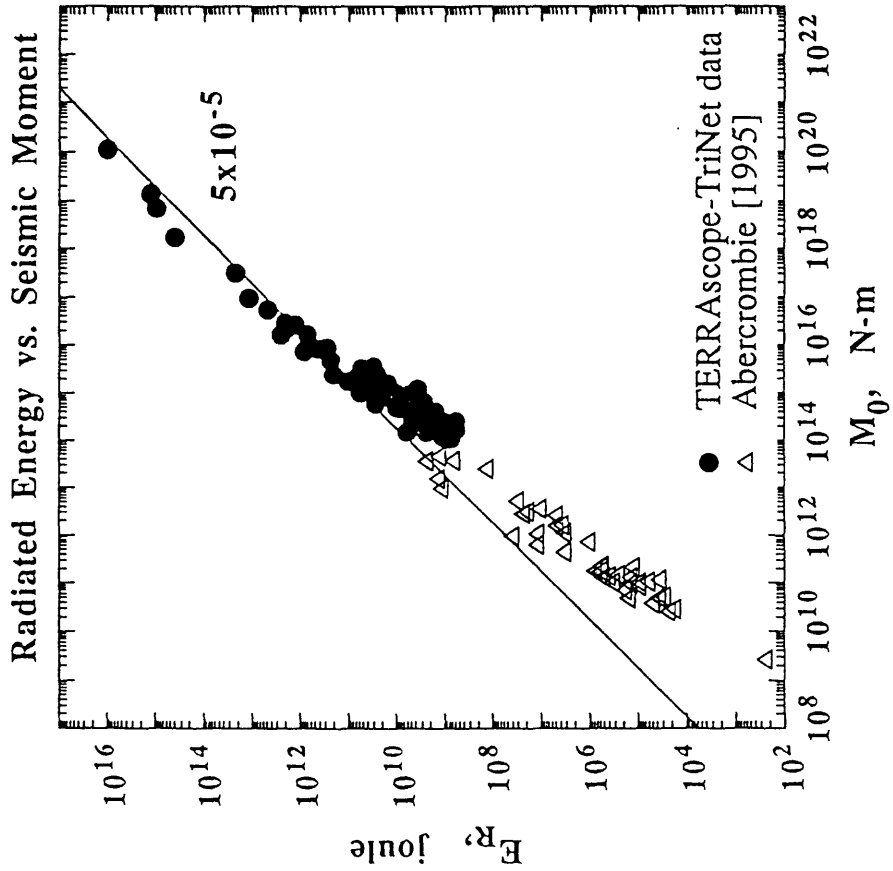


Figure 5a

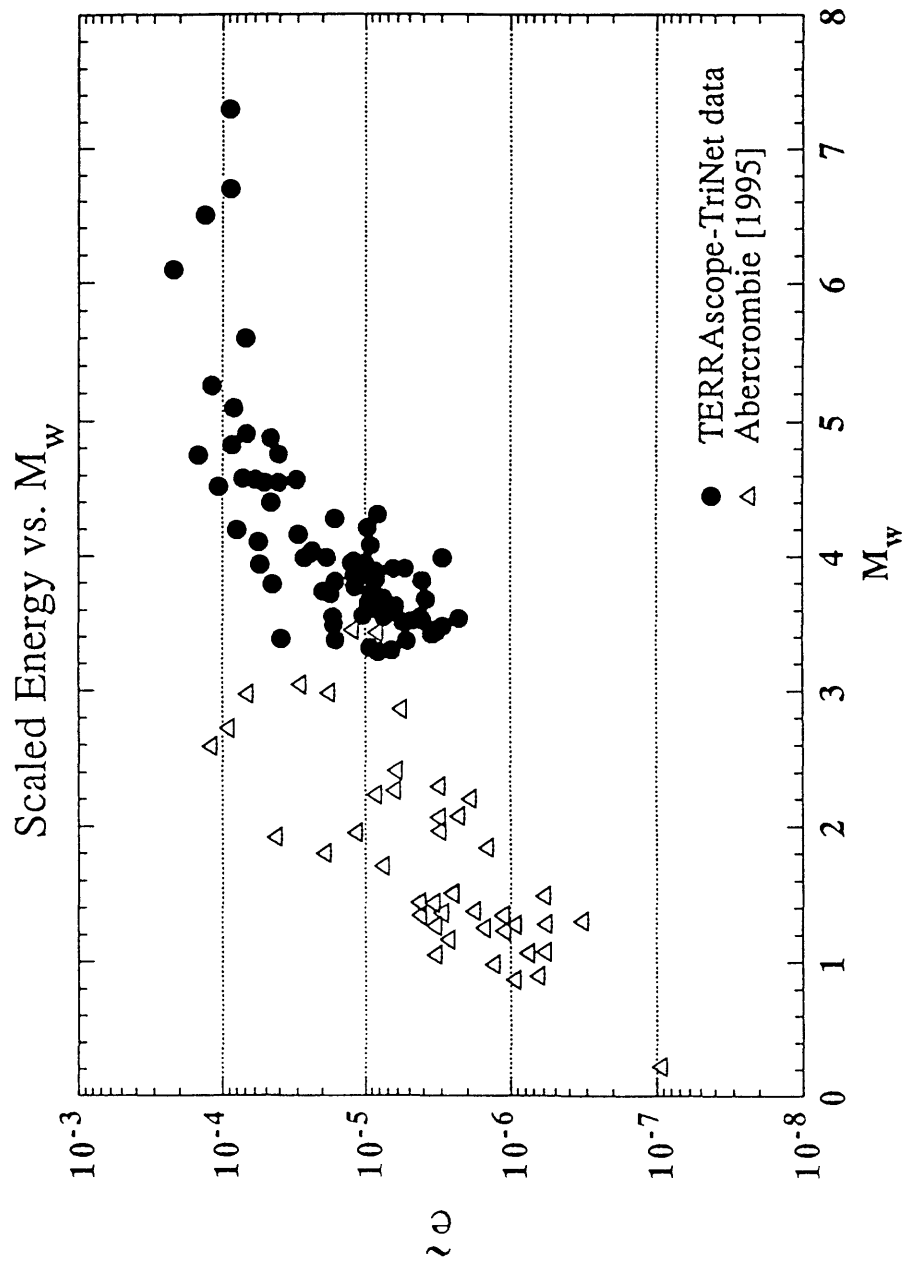


Figure 5b

## Energy Budget of Earthquakes

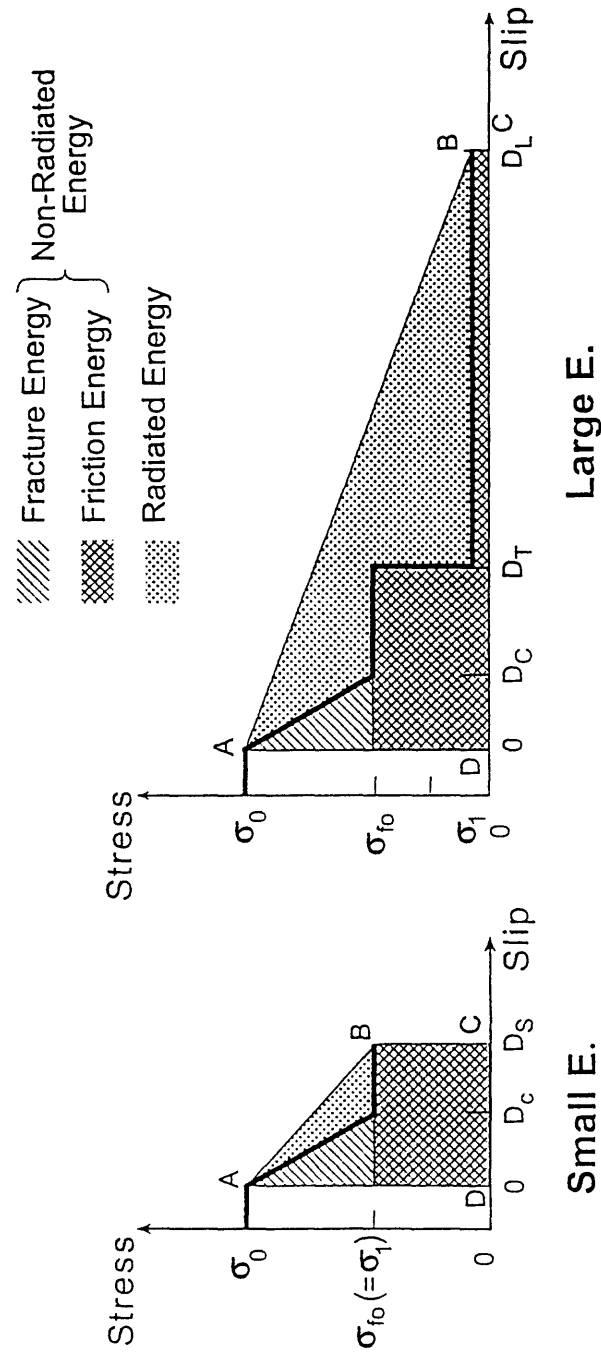
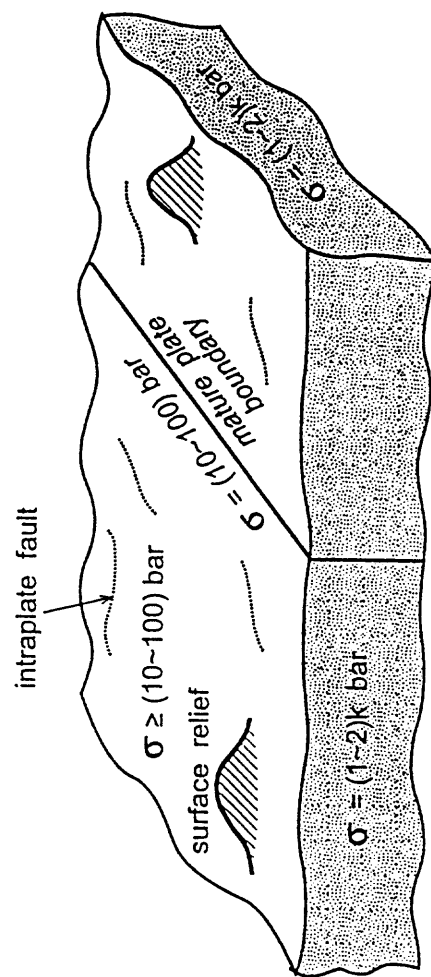


Figure 6

Figure 7



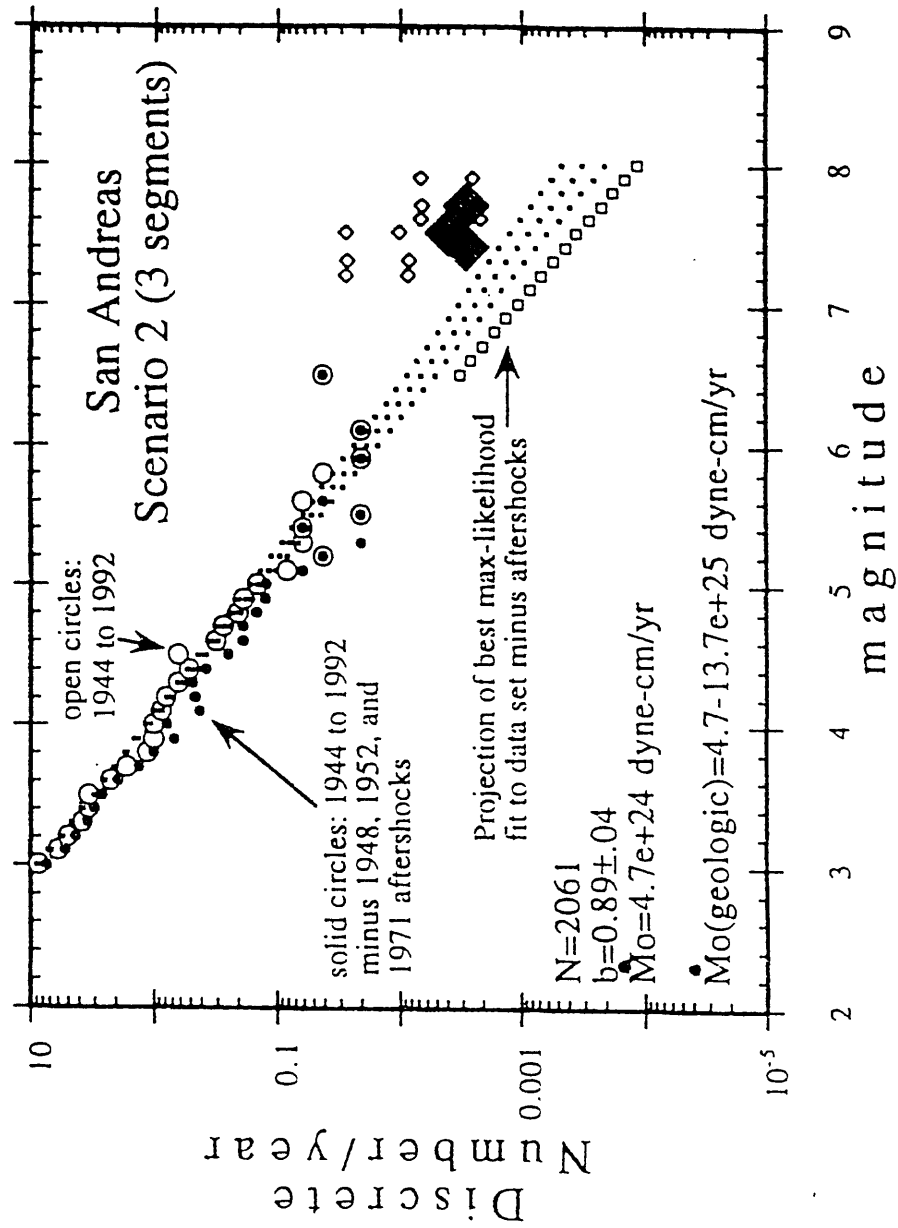
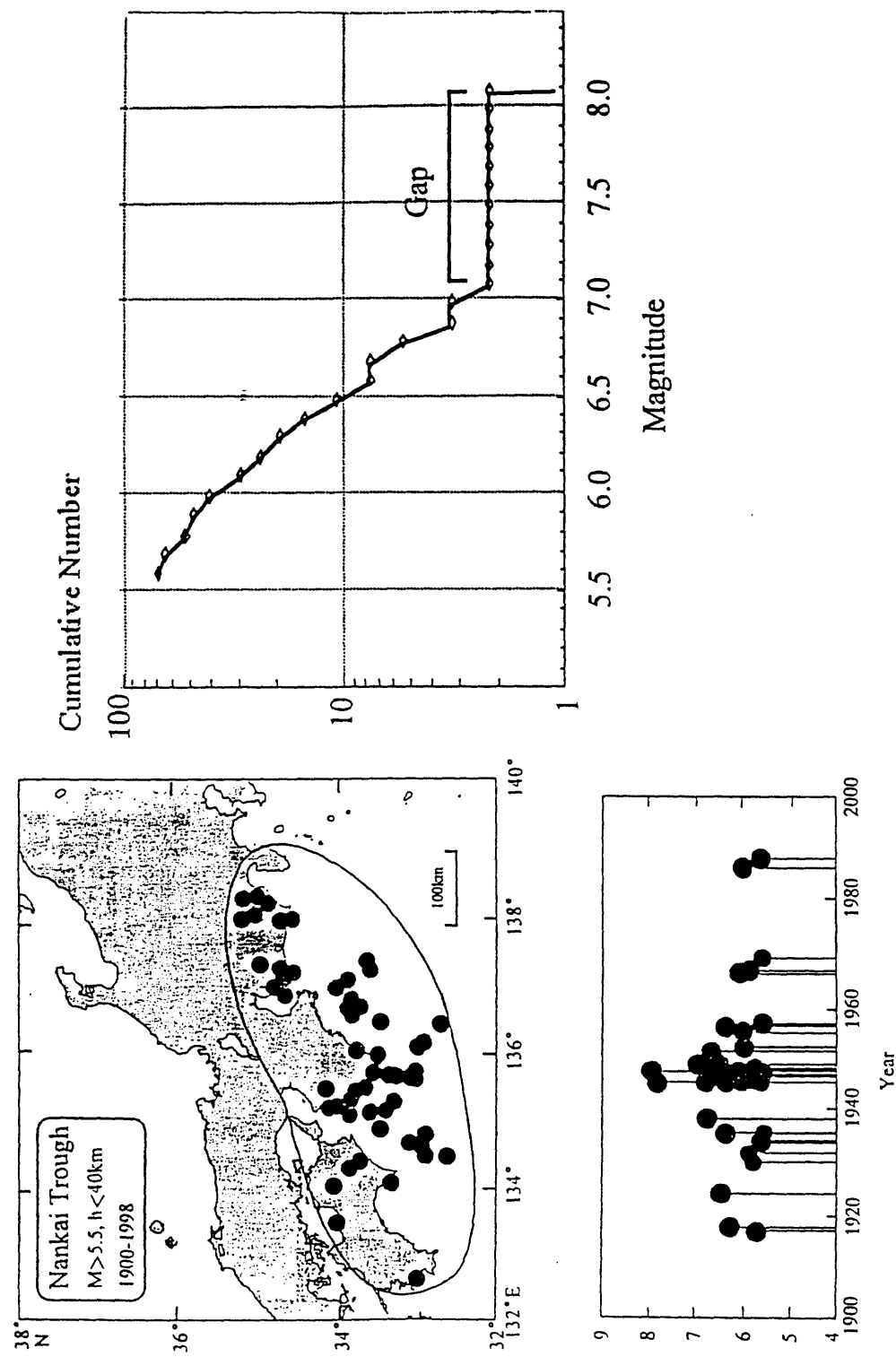


Figure 8a

Figure 8b



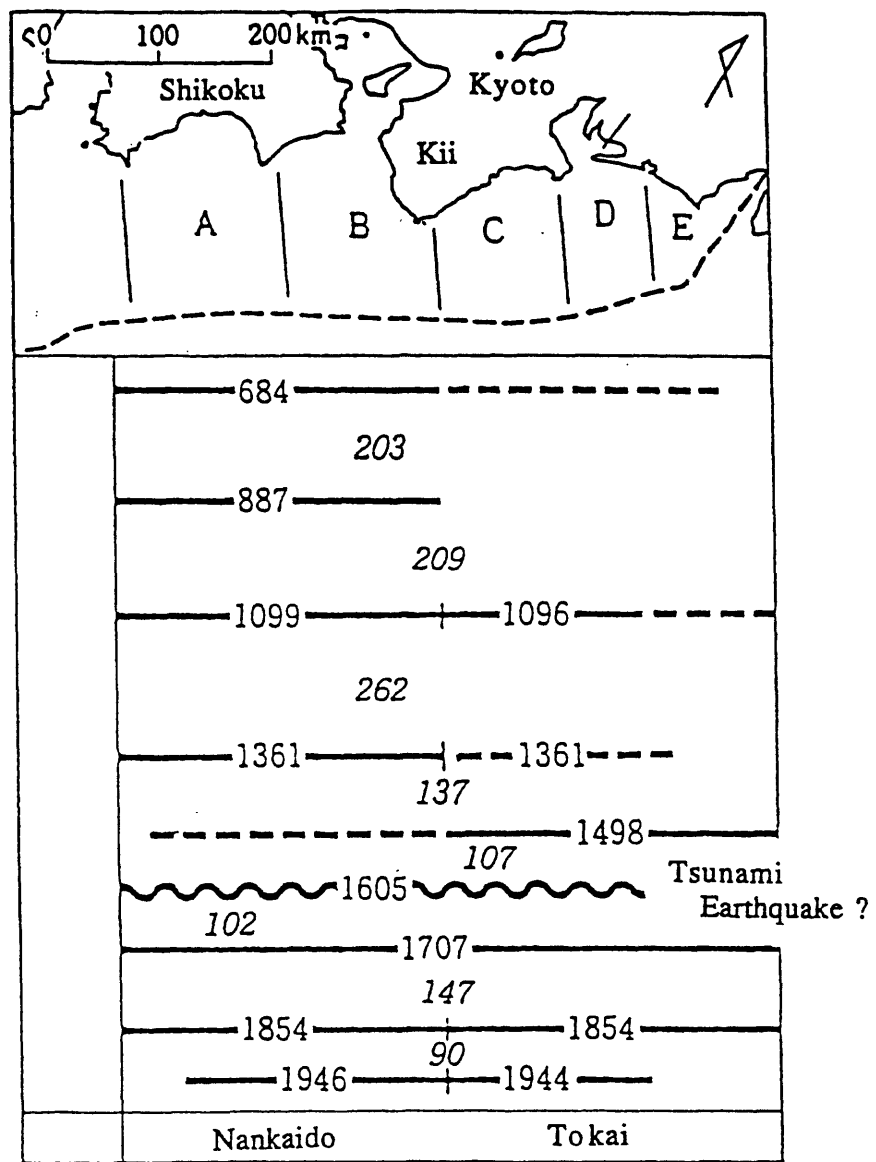


Figure 9

blank page

# Thermal Pressurization, Fluidization and Melting of Fault Gouge During Seismic Slip Recorded in the Rock from Nojima Fault.

Kenshiro Otsuki, Nobuaki Monzawa and Toshiro Nagase

Graduate School of Science, Tohoku University

## 1. Occurrence

At the 1995 Hyogo-ken Nanbu earthquake, the surface fault about 10 km long appeared along the northwestern coast of Awaji island near Kobe City. Along this fault at Hirabayashi village, we found very interesting fault rock in which the detail of physical processes during seismic slip is recorded. This fault rock about 20 cm wide are composed of thinly laminated fault gouge and pseudotachylite layers, and sandwiched by altered cataclastic granite on the southeast and Pliocene to Quaternary mud stone on the northwest. The seismic slip at the Hyogo-ken Nanbu earthquake occurred in the thin and soft fault clay layer between the laminated fault rock and Pliocene to Quaternary mud stone. Smectite, kaolinite and laumontite are detected by XRD analysis not only from cataclastic granite but also the laminated fault rock. Laumontite is stable in the temperature range from 110°C to 160°C, which is correlated to the depth of 3-5 km by the temperature measurement for NIED bore hole (Kitashima et al., 1998) at Hirabayashi. This suggests that the fault rock concerned was formed not at the ground surface at the 1995 Hyogo-ken Nanbu earthquake (Enomoto and Zheng, 1998), but at a 3-5 km depth at an ancient time, and has been uplifted associated with the lower temperature alteration.

The laminated fault rock is composed of very thinly (thinner than few mm) alternating layers of very fine grained gouge and pseudotachylite. These layers are in erode-eroded relationship, suggesting each layer to correspond to one seismic event, and 11 events are identified within a 15 mm wide thin section. Fault gouge and pseudotachylite coexist sometimes in one layer, and the former grades into the latter through a sintered zone, suggesting the melting after comminution of rock. The solid grains in the fault gouge and pseudotachylite are mainly quartz, K-feldspar, and fragments of old pseudotachylite. The bulk chemical compositions of gouge and pseudotachylite are nearly same as the host granite. Therefore, the root of them are granite, and their direct origin is old pseudotachylite and/or fault gouge.

## 2. Characteristics of pseudotachylite and temperature attained by frictional heating

Pseudotachylite is a mixture of glass matrix and many solid grains smaller than  $100 \mu\text{m}$ . By TEM and XRD analysis the diffraction hallow and the broad peak at  $2\theta$  about  $24^\circ$  ( $0.36 \text{ nm}$ ), both of which are proper to aluminosilicate glass, are observed. The increase in degree of melting is reflected in the EPMA back scatter images, namely solid grains become rounded and the volume fraction of glass matrix increases. For the layer of the highest melting, the volume fraction of solid grains is only 9 %, and the

cumulative size frequency shows a power law in the size range from 3 to 20  $\mu$  m with 2.74 power value and associated with the cut-off in the smaller size range within the limit of resolution. we classified the pseudotachylyte layers tentatively into 6 based on the texture in EPMA back scatter images. Vesicles about 1  $\mu$  m diameter are found and they arrange with a preferred orientation, suggesting viscous flow of melt and degassing of interstitial fluid. Within the pseudotachylyte layers, very complicated fold structures are developed, suggesting turbulent flow. Shear parallel to the layer is suggested also by the rotated snow ball structures whose core is the fragments of old pseudotachylyte softened by high temperature. Melt sometimes intruded into old layers.

The volume fraction of solid grains can be measured by layer-by-layer XRD analysis (Fig.1). X-axis is the peak height of pseudotachylyte glass, and Y-axis denotes the peak heights of quartz, K-feldspar and plagioclase. As the peak height of glass increases, the peak heights of these minerals linearly decrease. However, when the peak heights of K-feldspar and plagioclase become zero, about 40 % of quartz grains survives, suggesting the non-equilibrium melting. This can be testified by plotting the chemical composition of the pseudotachylyte glass on the  $\text{SiO}_2$ - $\text{NaAlSi}_3\text{O}_8$ - $\text{KAlSi}_3\text{O}_8$  diagram for the equilibrium melting of hydrous granite at 1 kb. All of the pseudotachylytes of different degree of melting are scattered around the granite melt at minimum temperature of 720°C, suggesting that the minimum temperature of pseudotachylyte melt was 720°C. It is sure that the maximum temperature was higher than 900 or 1000°C, because mullite was detected in a pseudotachylyte layer of the highest degree of melting (degree of melting: 6).

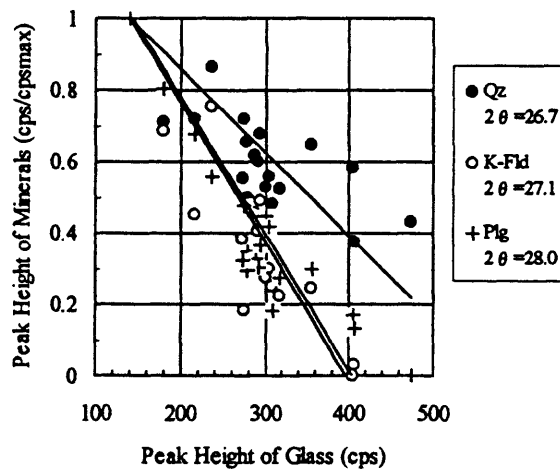


Fig 1 Layer by layer XRD analysis of pseudotachylyte. X-axis is the peak height of glass matrix and Y-axis is the normalized peak heights of quartz, K-feldspar and plagioclase.

Plastically deformed grain margin which was softened by the temperature very close to the breakdown temperature of the mineral species concerned is useful to estimate the temperature during the non-equilibrium melting. For example, the breakdown temperature of K-feldspar is 1150°C, and that of plagioclase varies from 1100°C to 1550°C corresponding to its anorthite component. The K-feldspar

grains with plastically deformed margin are found in the pseudotachylyte layers of the degree of melting 3 to 6. The plagioclase grains with plastically deformed margin are contained in the layers of the degree of melting 5 and 6. The maximum anorthite component among them is about 30 %, suggesting 1200°C. The breakdown temperatures of zircon and quartz are 1695°C and 1730°C, respectively, and the plastically deformed margin cannot have been found yet for these minerals.

As already noted, the fragments of old pseudotachylyte are contained in pseudotachylyte layers. They are sometimes plastically deformed to be elongated. The softening ( $10^{6.6}$  Pas) and working ( $10^3$  Pas) temperature of aluminosilicate glass are 900°C and 1200°C, respectively (Bansal and Doremus, 1986). The pseudotachylyte fragments in the layers of the degree of melting 1 are not elongated. Those in the layers of the degree of melting 2 to 4 are more elongated as the degree of melting becomes higher, and finally they are assimilated into the melt to be disappeared in the layers of the melting degree 5 and 6.

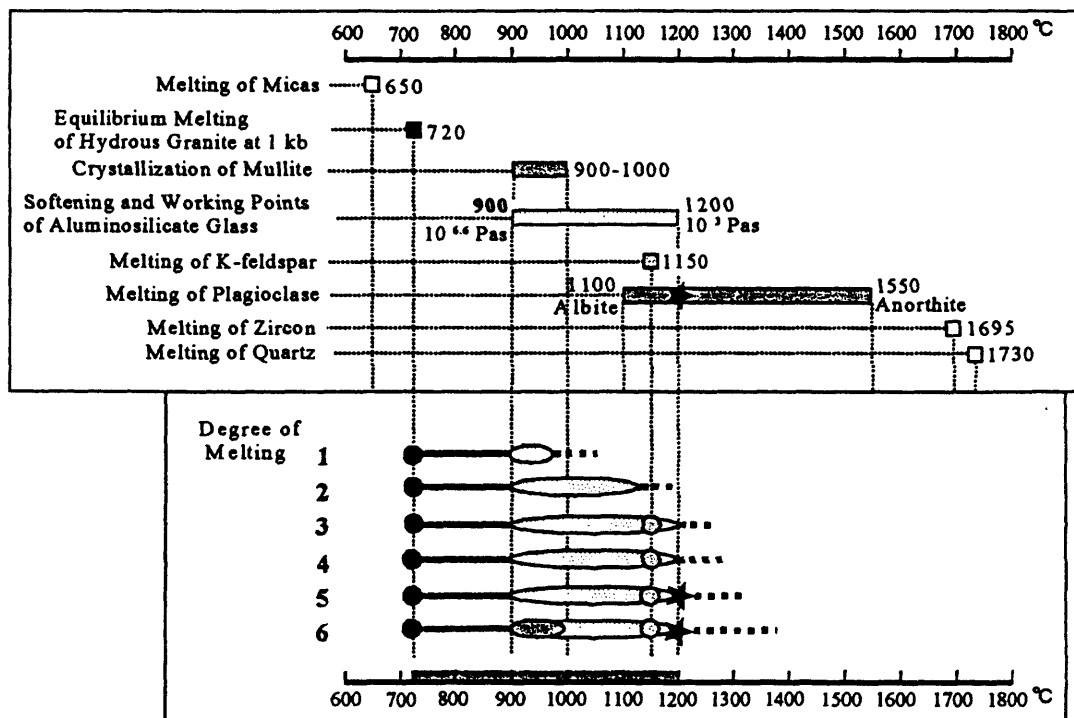


Fig.2 Temperature markers (above) and temperature range estimated for pseudotachylyte layers of degree of melting from 1 to 6.

The temperature estimations above are synthesized in Fig.2. From these data, we can conclude that the minimum temperature of the pseudotachylyte is just higher than 720°C and the maximum temperature is about 1200°C or little higher. The purpose of the temperature estimation is of course to answer to the question whether the melting promotes or restrains seismic slip. The viscosity of silicate melt depends mainly on temperature,  $\text{SiO}_2$  content and  $\text{H}_2\text{O}$  content. The temperature of the layers of

degree of melting 1, 2, 3, 4, 5 and 6 is assumed as 800, 900, 1000, 1100, 1200 and 1300°C from the temperature estimation shown in Fig.2. The SiO<sub>2</sub> content of the pseudotachylite glass is within the range from 61 to 63 %. This is nearly equal to those of sample LG-24 and WG-1 by Spray (1993), then we can use his temperature-viscosity relationship for the melt matrix with a modification below. The ignition loss of the EPMA analysis for the pseudotachylite glass from Hirabayashi attains to about 7 to 8 %, but the H<sub>2</sub>O content when it was melting is essentially unknown. Then we assume it as 4 % on the basis of H<sub>2</sub>O solubility in a granite minimum melt at 800°C and 1kb (Dingwell et al., 1984) and high-silica rhyolite at 850°C and 1 kb (Silver et al., 1989). On the other hand, the H<sub>2</sub>O content of the two samples of Spray (1993) is 2.0 and 2.5 wt %. The increase in the H<sub>2</sub>O content from 1.5 % or 2.0 % to 4 % decreases the viscosity of rhyolite melt at 850°C and 2 kb to about 1/100 (Shaw, 1963). The 4 % H<sub>2</sub>O content assumed is of course overestimated for the pseudotachylite of high degree of melting, because H<sub>2</sub>O solubility decreases as temperature increases.

Viscosity of granular material (melt + solid grains) depends strongly on the volume fraction of solid grains. Regarding to the viscosity-volume fraction relationship for monodisperse spherical granular materials, several formulations have been proposed. Among them, the equation below can well explain the well-controlled experiments (Frith et al., 1996),

$$\frac{\eta_s}{\eta_\infty} = \left(1 - \frac{\phi}{\phi^*}\right)^{-K\phi^*} \quad K = 3.12, \quad \phi^* = 0.647 \quad (1)$$

where  $\eta_s/\eta_\infty$  is the ratio between suspension viscosity and the viscosity of interstitial fluid, and  $\phi$  and  $\phi^*$  are a given volume fraction of solid grains and the maximum volume fraction attainable, respectively. When the equation (1) is applied to the pseudotachylite, two difficulties arise. In addition to the fact that grains in the pseudotachylite are not spherical, the size frequency is fractal associated with cut-off in the range of small size. Therefore both  $\phi$  and  $\phi^*$  cannot be estimated precisely. Based on the very rough measurement of  $\phi$ ,  $\phi/\phi^*$  is assumed as 0.8, 0.65, 0.65, 0.35, 0.2 and 0.1 for the layers of degree of melting 1, 2, 3, 4, 5 and 6, respectively.

From the temperature, melt viscosity and volume fraction of solid grains estimated and assumed above, the viscosity of pseudotachylite containing solid grains are calculated to be 1.5x10<sup>6</sup>, 1x10<sup>4</sup>, 2000, 60, 10 and 1.5 Pas for the layers of degree of melting 1, 2, 3, 4, 5 and 6, respectively. When we assume the thickness of melt layer and the seismic slip velocity to be 1 mm and 1m/s, shear resistance is calculated to be 1500, 10, 2, 0.06, 0.01 and 0.0015 MPa for the layer of degree of melting 1, 2, 3, 4, 5 and 6. As a result, we can conclude that seismic slip is surely restrained at the initial stage of melting, but after getting over this mechanical barrier, seismic slip is promoted. This conclusion is consistent with the frictional melting experiment by Tsutsumi and Shimamoto (1997).

### 3. Texture of fault gouge and its fluidization

The gouge layers are composed of very fine (sub- $\mu$ m to  $600\ \mu$ m) grains mainly of quartz, K-feldspar, plagioclase and the fragments old pseudotachylite. The cumulative size frequency is well fitted to a fractal distribution, and the fractal dimension is very large (2.3), suggesting very large input energy density. The gouge layers are very homogenous and lack any structures of shear localization. It is very strange, because stick-slip experiments for simulated gouge layers are commonly associated with shear localization on Reidel shear. It is sometimes found the droplets flying into gouge. These characteristic phenomena suggest that the state of dynamic granular flow was not grain friction controlled but fluidization, in which grains fly about and collide each other with a mean free path like gaseous molecules. Fluidization will be realized when the volume fraction of grains is decreased beyond the maximum volume fraction attainable. The decrease in volume fraction of grains in a gouge layer is attributed to the expansion of interstitial fluid by frictional heating and/or dilatation due to comminution of gouge.

Another characteristic texture of the gouge layers in the laminated fault rock is that the counter parts of fragmented grains are rarely found. Suppose that we are observing a thin section of fault gouge by photo-microscope, where  $n$  grains with radius  $r$  are seen and  $n_f$  of  $n$  are identified to be fragmented counterparts. The identification probability  $P(r)$  is defined as

$$P(r) = \frac{n_f(r)}{n(r)} \propto \frac{1}{v_r t_s} \quad \dots \quad (2)$$

where  $v_r$  is the relative velocity between the fragmented counterparts and  $t_s$  is the survival time interval (a reciprocal of fragmentation rate). When fluidized,  $v_r$  is much faster than that in non-fluidized state, and  $t_s$  is much longer than that in non-fluidized state, because the collision velocity of about 100 m/s is needed for 0.1 mm quartz grains to be fragmented. As a result,  $P(r)$  for the fluidized state is expected to be much smaller than that for the non-fluidized state.  $P(r)$  for the gouge layers in the laminated fault rock from Hirabayashi is, in fact, more than two order smaller than that for the non fluidized granitic cataclasite from other place. This surely verifies the gouge in the Hirabayashi fault rock to have been fluidized.

According to the experimental and theoretical knowledge in the fields of physics and technology, viscosity of fluidized granular materials follows the equation (1). Just before the gouge is molten (about  $720^\circ\text{C}$ ), the interstitial water attains super-critical phase at which viscosity of the fluid is smaller than  $10^4$  Pas at 1 kb. Even if the volume fraction  $\phi$  of solid grains attains to 0.9 of its critical value  $\phi^*$ , viscosity of fluidized gouge is not larger than the 1 Pas. Therefore the shear resistance is smaller than the order of 1000 Pa when the thickness of gouge layer and slip velocity are assumed to be 1 mm and 1m/s, respectively. This suggests the nearly complete stress drop at the fluidization.

#### 4. Fundamental physical processes deciphered and their implication to earthquake

Melting and fluidization of fault gouge are of course preceded by thermal pressurization in which gouge layer is heated up and interstitial fluid is expanded by frictional heating. This process is well studied by Mase and Smith (1987). After the seismic nucleation, seismic slip proceeds from thermal pressurization to melting of fault gouge through fluidization of gouge (Fig.3), all of which are positive feedback processes governing different deformation phases. In the phase of thermal pressurization, pore pressure increased by frictional heating decreases the effective normal stress on fault plane and it accelerates the seismic slip. Bulk mechanical properties in this phase are governed by friction among grains and fracturing of granular material.

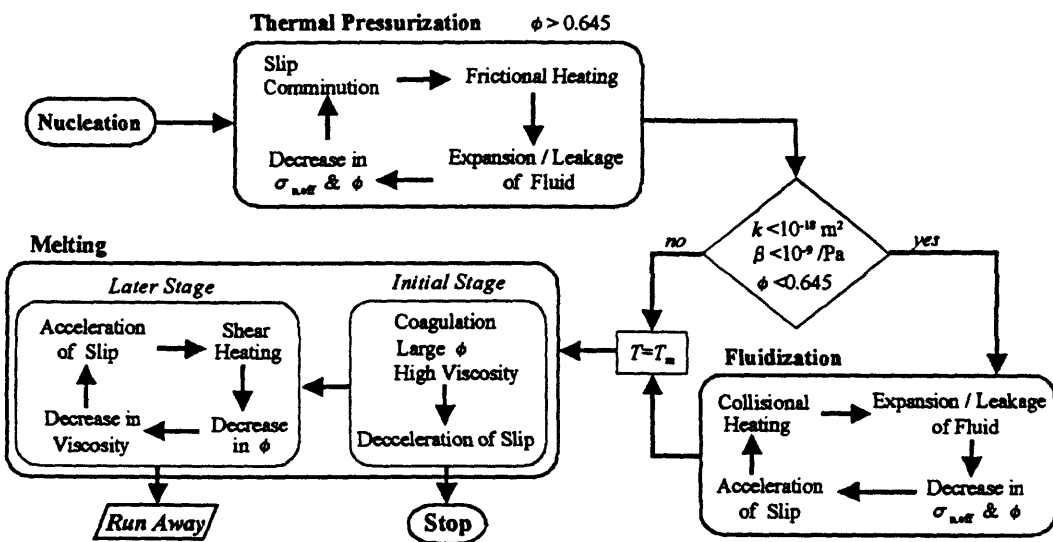


Fig.3 Elementary processes during seismic slip.  $k$  and  $\beta$  are permeability and compressibility of wall rock,  $\phi$  is volume fraction of solid grains of gouge layer.  $\sigma_{\text{eff}}$  is the effective normal stress on the fault plane.  $T_m$  is melting temperature of gouge.

When the porosity and permeability of wall rock are smaller than the critical values, the thermal pressurization works so effectively that volume fraction of solid grains in gouge layer becomes smaller than the critical value  $\phi^*$  (0.647 when monodisperse spherical granular materials) by thermal expansion of interstitial fluid. At this moment, fluidization, another positive feedback mechanism, starts. Frictional resistance becomes very small, then an abrupt and nearly complete decrease in shear resistance is expected at the transition from thermal pressurization to fluidization. The heat generation rate in this phase is due to the grain collision and is very small. Then the fluidization is thought to be unstable phase and is easily turned back to the phase of thermal pressurization, because leaking rate of interstitial fluid from gouge layer is tend to exceed the thermal expansion rate of fluid.

Anyway, soon or later, gouge is molten by heat produced by grain to grain collision. When the

permeability and compressibility of wall rock are greater than the critical values, thermal pressurization is turned directly into melting phase. As discussed above, seismic slip is restrained by the very high viscosity of melt, and may be stopped at some cases. However, frictional melting is also a positive feedback process, then slip thereafter is accelerated as melting proceeds and the seismic slip will run away.

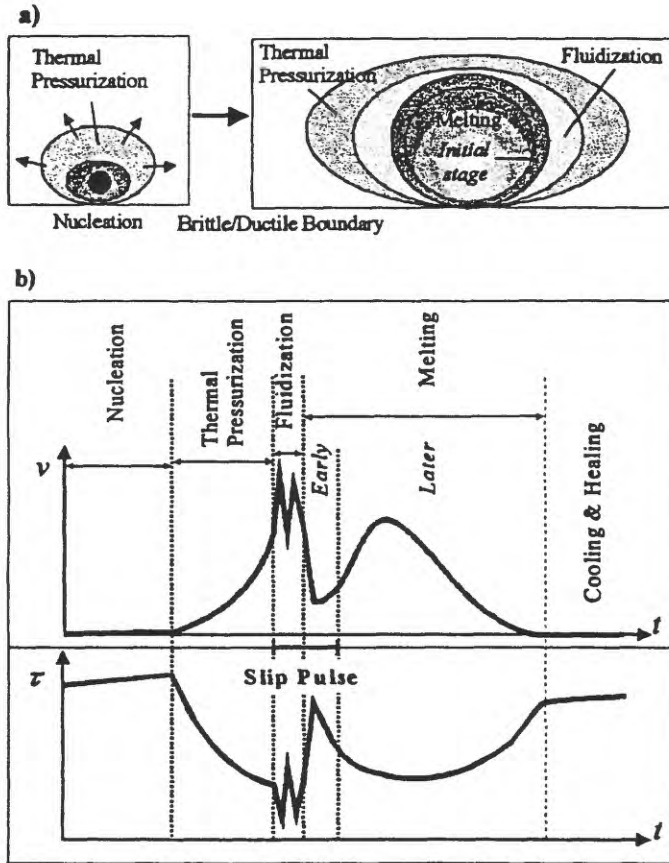


Fig.4 a): Concentric distribution of areas in which thermal pressurization, fluidization, and initial and advanced stages of melting work.  
 b): Schematic time functions of slip velocity and shear stress during seismic slip estimated from the fault rock.

The processes during seismic slip deciphered here are microscopic views, but seismic faulting is a macro-system. Leaving this out of consideration, we have some conclusions below. Thermal pressurization, fluidization, and initial and advanced stages of melting are the processes working successively, then they will work in the concentric regions in a extending rapture plane (Fig.4a). Frictional resistance is decreased suddenly to nearly zero when fault gouge is fluidized, and in contrast, seismic slip is restrained by the mechanical barrier of initial melting just after the fluidization. This process will radiate strong slip pulse (Heaton, 1990) from the outer region of a rapture plane (Fig.4b). Pseudotachylite melt is cooled and consolidated with in short time duration just after seismic slip, and it is a main process to heal the fault plane.

## References

Bansal, N.P. and Doremus, R.H., 1986, *Handbook of Glass Properties*. Academic Press Inc.

Dingwell, D.B., Harris, D.M., and Scarfe, C.M., 1984, The solubility of H<sub>2</sub>O in melts in the system SiO<sub>2</sub>-Al<sub>2</sub>O<sub>3</sub>-Na<sub>2</sub>O-K<sub>2</sub>O at 1 to 2 kbar. *J. Geol.*, **92**, 387-395.

Enomoto, Y., and Zheng, Z., 1998, Possible evidences of earthquake lightning accompanying the 1995 Kobe earthquake inferred from the Nojima fault gouge. *Geophys. Res. Lett.*, **25**, 2721- 2724.

Frith, W.J., d'Haene, P., Buscall, R. and Mewis, J., 1996, Shear thickening in model suspensions of sterically stabilized particles. *J. Rheol.*, **40**, 531-548.

Heaton, T.H., 1990, Evidence for and implications of self-healing pulses of slip in earthquake rupture. *Phys. Earth Planet. Inter.*, **64**, 1-29.

Kitashima, T., Kobayashi, Y., Ikeda, R., Iio, Y. and Kobayashi, K., 1998, Heat flow measurement for the bore hole at Hirabayashi, Awaji island. *Gekkan Chikyu*, Special Issue, no.21, 108-113 (in Japanese).

Mase, C.W. and Smith, L., 1987, Effects of frictional heating on the thermal, hydrologic, and mechanical response of a fault. *J. Geophys. Res.*, **92**, 6249-6272.

Show, H.R., 1963, Obsidian-H<sub>2</sub>O viscosities at 1000 and 2000 bars in the temperature range 700- 900°C. *J. Geophys. Res.*, **68**, 6337-6343.

Silver, L. and Stolper, E., 1989, Water in albitic glasses. *J. Petrol.*, **30**, 667-709.

Tsutsumi, A. and Shimamoto, T., 1997, High-velocity frictional properties of gabbro. *Geophys. Res. Lett.*, **24**, 699-702.

# Seismogenic Zone Drilling and Monitoring of OD21/IODP

Kiyoshi Suyehiro, JAMSTEC

2-15 Natsushima-cho Yokosuka

[suyehiro@jamstec.go.jp](mailto:suyehiro@jamstec.go.jp)

## ABSTRACT

A new scientific drill ship equipped with riser capability that allows deep drilling beneath ocean floors will be constructed by Japan. This new opportunity after more than 30 years of successful scientific deep sea drilling programs (DSDP/IPOD/ODP) will mark a major step forward in better understanding of the earth's complex system inter-linking life and dynamics of the environment and deep interior. The first target agreed upon by scientists internationally is the seismogenic zone. The new drill ship will drill through the seismogenic part of the subduction plate boundary to collect samples, make in-situ measurements, and set up observatory to understand earthquake mechanics and physico-chemical processes operating in this environment.

## Introduction

New exciting scientific objectives to be pursued by the proposed drill ship have been discussed both within Japan and internationally. In particular, the CONCORD meeting held in Tokyo in 1997 attracted more than 150 scientists from around the globe to discuss scientific foci together with technological requirements. Among diverse but key questions to be addressed centered around the drill ship, "a comprehensive study of an active seismogenic zone within a seismogenic zone within a subduction zone system" was unanimously selected as the first experiment.

It is well known fact that major earthquakes occur in subduction zones and that actual faultings occur beneath the sea. Until the '70's investigations of these seismogenic zones were mainly made by teleseismic observations. Marine geological and geophysical (MG&G) survey technology was not quite advanced enough to image the seismogenic zone due to its complex heterogeneity and large depth. However, recent MG & G results are beginning to reveal the complexities of seismogenic zone in far more detail than before. This is an important but sometimes not well recognized aspect of drilling science. One cannot go and drill into a spot without knowing what to expect. Once the drilling provides the ground truth, then immediately a much wider area should become "illuminated" through extrapolation using existing remotely sensed data.

## Scientific Rationale

We share many of our scientific objectives with those attempted or planned on the continents. The

objectives are "an improved understanding of the physical and chemical processes responsible for earthquakes, and seismic hazard reduction for the very destructive great earthquakes that occur on these faults" (Seismogenic Zone Detailed Planning Group Report, 1999). This group of international scientists specifically addressed following questions:

1. What controls the earthquake cycle of elastic strain build-up and sudden rupture: stress, pore pressure and chemical changes?
2. Are there changes with time, of stress, pore pressure, pore fluid chemistry or other parameters that define times of increasing probability of great earthquakes?
3. What controls the parts of subduction thrusts that are seismic and aseismic, especially the seaward updip and landward downdip limits?
4. What is the nature of asperities on the megathrust faults that are inferred to be stronger and generate large earthquake slip compared to areas that may have significant aseismic creep?
5. What is the nature of "tsunami earthquakes?" Why do some large slip events have most stress release in the seismic motion of great earthquakes, whereas others have slower slip that generates only moderate earthquakes but large tsunamis?

Some questions are pertinent to the realm of plate subduction boundary, but any significant contribution in answering these questions will undoubtedly have broad application to earthquakes in general.

### **OD21 Drill Ship**

What makes the proposed OD21 drill ship different from the existing drilling vessel *JOIDES Resolution* is that it is equipped with a riser for mud circulation and with a blow-out prevention device. This method conventionally used in the oil field will, in essence, enable deeper drilling. The proposed vessel will be capable of drilling in up to 2,500 m water depth using riser and drilling 7,000 m below the seafloor. The ship is scheduled to become available for international scientific community as part of IODP (Integrated Ocean Drilling Program) from 2006. IODP is planned to operate more than two drilling platforms to bring about new directions in drilling science. After gaining initial experiences, the ship is to be further advanced to enable drilling in 4,000 m water depths with riser. The OD21 drill ship has started its construction in FY1999 and is expected to start its shakedown operations in 2003/04.

### **Subduction Seismogenic Zone**

Already the *JOIDES Resolution* made a number of drillings in subduction zones. In particular, the drillings in the Barbados and the Japan Trench and instrumenting the holes can be considered as steps towards reaching the seismogenic zone. In the Barbados Ridge, where Caribbean and North

American plates are bordered, drilling were made into different zones of fluid condition that were seismically estimated and were instrumented with long-term pressure and temperature sensors. In the Japan Trench, where the Pacific plate is subducting beneath northeast Japan, two holes were instrumented with strain, tilt, seismic and temperature sensors. Technical successes of and the results from these experiments indicate that we are steadily stepping forward to be ready for the seismogenic zone drilling.

Careful consideration of the requirements for site selection is probably the most important aspect in the initial stage of the drilling project. The requirements listed by the DPG are abridged here:

1. A subduction zone where the tectonics, structure, thermal regime, and earthquakes are very well studied and well known. Previous shallow drilling of the subduction thrust and on the continental slope in the area of the proposed deep site would be essential. The region should be structurally simple with an inferred decollement that is fairly stable in position and depth with time.
2. Shallow plate dip and shallow trench such that the subduction thrust fault can be reached by OD21 drilling in a reasonable time, i.e. less than 5 km penetration. This appears to require sites where young oceanic plates are being subducted. It is recognized that young plates also usually means high thrust temperatures.
3. Accretionary prism sediments or other formation that it is expected to be readily penetrated by the OD21 drilling. A low temperature gradient is desirable.
4. The subduction thrust should be accessible to non-riser drilling seaward from the main deep riser site that penetrates the seismogenic zone.
5. A recent great earthquake within the seismogenic zone that has been well studied is needed to characterize the seismogenic zone.
6. The subduction thrust should be well imaged by multichannel seismic data, especially in the area of the seismogenic zone to be drilled.
7. The locked part of the seismogenic zone should be defined

#### **Case of Nankai Trough**

In the vicinity of Japan, the Nankai Trough and Japan Trench areas are two contrasting seismogenic zones capable of generating M-8 class earthquakes. The former is considered to be 100 % locked in between the major events, which recur at about 120 years interval. The recurrence time is not well established in the Japan Trench. The background activity is much higher than in the Nankai Trough, however the seismic coupling (plate motion accommodated by earthquakes) is only about 1/4. Tectonic backgrounds are different between these areas. But, we do not yet know what makes this contrast.

Of the two zones, OD21 drilling vessel will not be able to reach the Japan Trench seismogenic zone. The likely target is in the Nankai Trough. But where? In order to select the best location, many investigations are ongoing including 3-D seismic surveys. The present understanding from MG&G investigations will be shown. The drilling proposal will have to be composed soon for careful peer reviews, however it is almost certain that drilling proposal in the Nankai Trough will be based on these site survey data.

### Summary

With the construction of a riser-equipped drilling vessel by Japan, a new opportunity arises to directly reach, sample, and monitor the subduction seismogenic zone from 2006. The first target is likely to be selected in the Nankai Trough area that satisfies the scientific requirements for addressing key questions for understanding earthquake cycle processes. Before actual drilling, many studies must be carried out based on careful planning. These include site surveys, geological sampling of exhumed subduction zones, and development of borehole tools for high temperature environment, which are already under way. Target sites should be proposed within a few years' time.

# Geological and Geophysical Drilling at the Nojima Fault: Fault Trace of the 1995 Hyogoken-Nanbu Earthquake, $M_s$ 7.2

MASATAKA ANDO

The Nojima Fault Zone Probe and Disaster Prevention Research Institute, Kyoto University, Kyoto  
611-0011, Japan

## ABSTRACT

The Nojima Fault-zone Probe was designed to study the properties and recovery processes of the Nojima fault which moved during the Hyogo-ken Nanbu earthquake ( $M_s$  7.2) of January 17, 1995 (JST, 9 hours +UT). Three holes, 500 m, 800 m and 1800 m deep, were drilled into or near the fault zone. The 800 m hole was drilled in November 1995, and in December 1996 the last hole reached its final depth of 1760 m. The significant results are: (1) Geological and geophysical reconstruction of the structure and evolution of the Nojima fault was obtained; (2) The maximum compression axis was found to be perpendicular to the fault, about 45° to the regional compression stress axis; (3) Micro-earthquakes ( $m = -2$  to +1) were induced by water injections 1 to 3 km from the injection points in the 1800 m hole; (4) The fault zone was measured to be 30 m wide from microscopic studies. 3-component seismometers, crustal deformation instruments, thermometer etc. were installed in the holes.

**Key words:** Hyogo-ken Nanbu earthquake, Nojima Fault, drilling, water injection

## INTRODUCTION

The Hyogoken Nanbu earthquake ( $M_s$  7.2) occurred at 5:42 on January 17 (JST), 1995 along the coast of Kobe and Awaji Island (Fig. 1). The

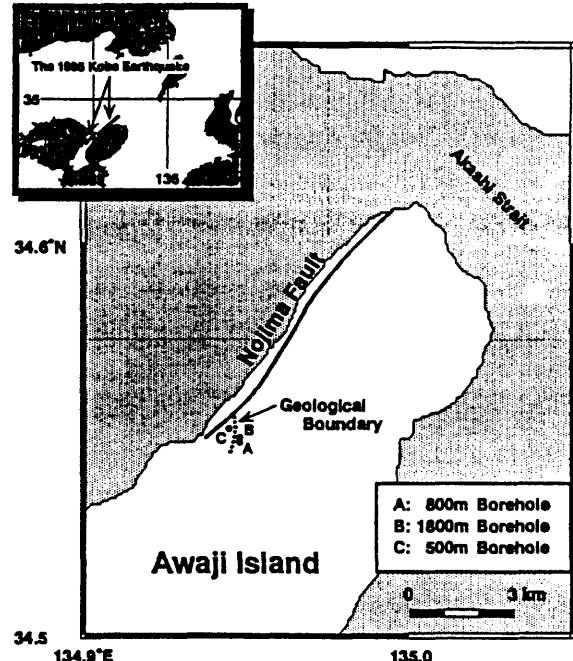


Fig. 1 Map showing the Nojima fault (thick solid line) associated with the 1995 Hyogo-ken Nanbu earthquake on Awaji Island. The thick dashed line represents the geological boundary between the Osaka series (Quaternary) and granite basement (Cretaceous), which moved slightly with a maximum vertical slip of 40 cm in 1995.

hypocenter was located beneath the Awaji straight and the rupture propagated bilaterally towards Kobe and Awaji Island (e.g. Ide *et al.* 1996; Hashimoto *et al.* 1996). Fault traces appeared on Awaji Island, but not in the Kobe city (Nakata *et al.* 1995). The present program of intensive studies of the Nojima fault started

three months after the earthquake. It consists of both a deep drilling plan of 500 m, 800 m, and 1800 m depth holes, and a plan for geophysical and geological investigations at the surface. This project was called the "Nojima Fault-zone Probe" and consisted of about 60 scientists and technicians with 14 universities (Table 1). In addition, the project cooperated with two national institutes, Geological Survey of Japan (Ito *et al.* 2000), and National Research Institute for Earth Sciences and Disaster Prevention (Ikeda *et al.* 2000), which engaged their own drilling programs of the Nojima fault and nearby active faults. The three groups collaborated throughout the study in exchanging information and data on site selection, drilling logs and techniques etc.

## OBJECTIVES

The objectives of this project are divided mainly in five items: (1) seismic reflection and refraction surveys (Sato *et al.* 1998; Ohmura *et al.* 2000) and geoelectric and geomagnetic surveys near and on the Nojima fault (Murakami *et al.* 2000), (2) geophysical

continuous monitorings such as seismicity (Nishigami *et al.* 2000), crustal deformation (Ishii *et al.* 2000), geochemical, geothermal (Yamano & Goto, 2000) and geoelectro-geomagnetic measurements, (3) active experiments were done in the 1800 m borehole such as hydro-fracturing (Tsukahara *et al.*, 2000) and experiments of water injection into the fault gouge (Shimazaki *et al.* 1997; Tadokoro *et al.* 2000a), and (4) microscopic analyses of core samples near and on the fault zone (Deformation mechanisms and fluid behavior in a shallow, brittle fault zone during coseismic and interseismic periods: results from drilling cores penetrating the Nojima fault, Japan, H. Tanaka, S. Hinoki, K. Kosaka, A. Lin, K. Takemura, A. Murata, and T. Miyata), and (5) ACROSS (Accurately Controlled Routinely Operated Seismic Source) experiment for measuring high sensitivity seismic velocity changes (Yamaoka *et al.*, 2000). The above observations and experiments will be carried out continuously or intermittently for at least 10 years. These experiments will reveal the mechanism of healing and recovery processes of the fault zone.

Table 1 Participants\* of the Nojima Fault Probe

Tohoku Univ.	Core stress memory (Deformation Rate Change Method)
Chiba Univ.	Seismic reflection survey around the drilling site
Univ. of Tokyo	Geochemistry near fault zone, Ground-water level change
Earthquake Res. Inst.	Physical properties and material science of fault zone
(Univ. of Tokyo)	Geothermal, Crustal deformation observation using down-hole instruments, Seismological observation
Shinshu Univ.	Hydrofracturing test, Gas geochemistry of fault zone
Kanazawa Univ.	Thermal history of drilling site using chronological data
Nagoya Univ.	ACROSS (Accurately Controlled Routinely Operated Seismic Source)
Kyoto Univ.	Material science of fault zone, Tectonic history, Geochronology of drilling site
Disaster Prevention Res. Inst.	Seismic observation using down-hole seismometers and accelerometer,
(Kyoto Univ.)	Ground water level change, Geoelectro-magnetic observation of fault zone and surrounding rock, Physical properties of fault zone
Kobe Univ.	Tectonic history of fault zone
Tokushima Univ.	Structural geology of drilling site
Kochi Univ.	Tectonic history of fault zone, Geoelectro-magnetism of fault zone and surrounding rock
Yamaguchi Univ.	Stress measurements of core samples
Ehime Univ.	Material science of fault zone rock
National Res. Inst. for Earth Sciences and Disaster Prevention (NEID)	Collaboration in several subjects
Geological Survey of Japan (GSJ)	Collaboration in several subjects

\*Only institutions' names are listed.

## DRILLING SITE

A perpendicular long seismic reflection survey was undertaken across northern Awaji Island (Sato *et al.* 1998). The seismic reflection profile reveals the fault geometry beneath the area. Sato *et al.* (1998) interpreted that Awaji Island uplifted by movement on the Nojima fault and a fault beneath the western coast of the Island. The basement of Awaji Island is bounded by these active faults.

The Nojima fault lies on the western coast of Awaji Island. The 1995 fault trace appeared mostly on narrow terraces between the coast and mountain slopes (Nakata *et al.* 1995). Because of the narrow area on the Island, sites available for drilling experiments were quite limited, but two inactive quarry sites were found to be available. We selected the "Toshima site" and the two national institutions (Geological Survey of Japan and National Research Institute for Earth Science Research and Disaster Prevention) chose the "Hirabayashi site", 5 km to the north of the Toshima site. The drilling site consists of granite, partly covered by Neogene or Quaternary marine sediments. The scientific attractions of this site were: (1) It is located near a branching of the Nojima fault, from which a geologic boundary fault splays to the southwest (Fig. 1). Therefore, there was a chance of hitting two faults with deep drilling, enabling a comparison of properties of the two fault zones at depth; (2) A relatively flat area was available for geophysical surveys, such as resistivity, geoelectro-potential, and seismic reflection surveys; (3) The depth of basement below the sedimentary layers can be estimated from the drilling, which enable us to estimate a total offset of the fault.

## THREE BOREHOLES

This project was based on drilling three boreholes, first a pilot hole of 500 m depth for determining the dip-angle of the fault at depth, second

an instrumentation hole of 800 m depth for passive observations of crustal deformation and earthquakes, and third an experimental hole of 1800 m depth for actively injecting water into the fault gouge and hydrofracturing tests. The 500 m hole was drilled with an inclination of 60°. In order to assure hitting the fault zone and determining its exact location at a depth about 300 m. In order to install tiltmeter, which have small inclination tolerances, the deviation of the drilling center from the vertical was 3° for the 800 m hole. The hole was cased with iron pipes from the surface to a depth of 785 m; the last 15 m above the bottom was left uncased in order to install a capsule that contains a 3-component seismometer, a 3-component accelerometer, a 3-component strainmeter, a 2-component tiltmeter, thermometer and pressure gauge. The strainmeter must be cemented to the surrounding rock with a special cement. The 1800 m hole was drilled 80 m away from the 800 m hole. The 1800 m hole was drilled vertically for the first 1200 m and then bent gradually with a maximum inclination of 20° from the vertical to reach the fault zone at depth. In the 1800 m hole, seismometers were also installed at three levels (Nishigami *et al.* 2000). The results of the hydrofracturing tests in the 1800 m hole indicate that the maximum compression axis was found to be perpendicular to the fault, about 45° to the regional compression stress axis (Tsukahara *et al.* 2000). Yamamoto & Yabe (2000) made a deformation rate analysis (DRA) of core samples from the 1800 m hole. Also, a system to accurately monitoring seismic wave velocities called ACROSS has been installed by a group from Nagoya University (Yamaoka *et al.* 2000). Signals from the ACROSS and boundary waves traveling through the fault zone from earthquakes occurring within or close to the fault below are of particular interested to this project. An observation vault was constructed near the drilling site. The concept of the present project is summarized in Fig. 2 and Table 2.

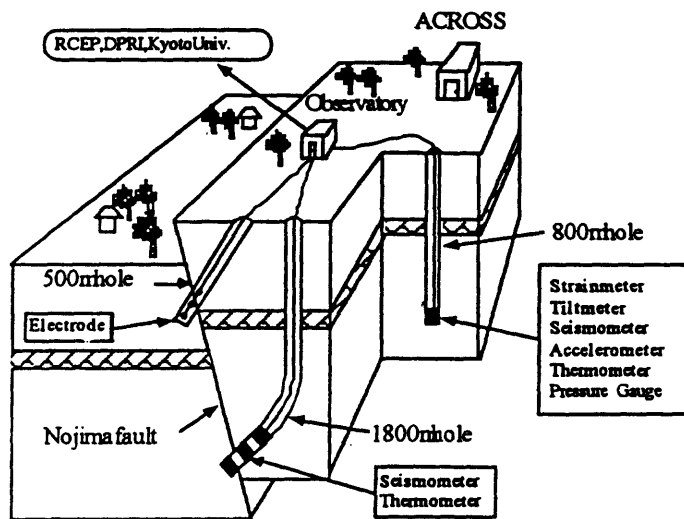


Fig. 2 The concept of the Nojima Fault-zone Probe. The three drill holes are shown in the figure. The 500 m hole is the pilot hole to determine the depth and location of the Nojima fault for planning the 1800 m hole. The 800 m hole is the installation hole for strainmeter, tiltmeter and seismometers. The data from these sensors are telemetered to Disaster Prevention Research Institute, Kyoto Univ. and Earthquake Research Institute, the University of Tokyo. The ACROSS station is located on granite basement, 200 m from the Nojima Fault Observatory.

Fig. 3 shows the drilling logs for the three holes. Because of the fragile nature of the fault zone, drilling heads of the 1800 m hole were recovered three times when they hit the fault zone. The drilling schedule was thus extended six months longer than initially planned. Fig. 4 represents the vertical geological cross-section reconstructed from the core samples of the 500 m hole (Quaternary vertical displacement and avarage slip rate of the Nojima fault in Awaji Island, Japan, A. Murata, K. Takemura, T. Miyata, and A. Lin). Two unconformities, one between the Osaka Group and the Kobe Group and the other between the Kobe Group and the granite basement, are found in the cross section. From this geological section, a 5mm/y dip-slip rate is

estimated by Quaternary vertical displacement and avarage slip rate of the Nojima fault in Awaji Island, Japan, A. Murata, K. Takemura, T. Miyata, and A. Lin. From the core samples, the Nojima fault zone was measured to be 30 m wide (Deformation mechanisms and fluid behavior in a shallow, brittle fault zone during coseismic and interseismic periods: results from drilling cores penetrating the Nojima fault, Japan, H. Tanaka, S. Hinoki, K. Kosaka, A. Lin, K. Takemura, A. Murata, and T. Miyata). Fig. 5 shows the three holes and the two faults and the geological cross-sections approximately

perpendicular to the fault, (Quaternary vertical displacement and avarage slip rate of the Nojima fault in Awaji Island, Japan, A. Murata, K. Takemura, T. Miyata, and A. Lin).

Fig. 6 shows geophysical sensors installed in the three holes. From the 500 m hole all cores were extracted and from the 800 m hole only core samples for the 10 m above the bottom were extracted. Results of logging tests, lithological profiles, and hydrofracturing experiment in the 1800 m hole are all summarized in Tadokoro *et al.* (2000b).

## ACROSS

The ACROSS (Accurately Controlled Routinely Operated Seismic Source) system has been developed by a group at Nagoya University in order to measure slight changes in seismic velocity (Yamaoka *et al.* 2000). The possibility of using the high sensitivity of seismic velocity for detecting stress variation in the earth's crust has long been discussed by seismologists. Many field experiments were performed using several kind of sources. In most of the experiments impulsive seismic signals were used, which lead to eventual failure of the medium around the source. To detect the velocity change without destroying the site it is natural to use vibrators which generate continuous sinusoidal

Table 2 Objectives, core sample and observation

500 m	
Objective	Pilot hole to define the location of fault
Inclination	30° from vertical (dip angle of 60°) and drilled straightway
Core sample	All cores retrieved with a diameter of 65 mm
Casing	
Long-term observation	Installing 3 electrodes in both sides of fault at depths 400-500 m to measure changes in telluric current and resistivity, Ground water level change near the surface
800 m	
Objective	Passive observations
Inclination	Vertical within an allowance of 3°
Core sample	Only 15 m section at the bottom (785-800 m) retrieved
Long-term observation	3-component seismometers (velocity and acceleration), 3-component horizontal strainmeter, 2-component tiltmeter and water-pressure gauge, thermometer Above are all installed in a capsule of 5 m length at the depth 795-800 m). Signals are transmitted through armored 100-core cable to the surface. The instrument capsule was mold with a special kind of cement to be coupled with borehole wall. Near the surface a discharge gage was installed in the hole.
1800 m	
Objective	Active experiments and passive observations
Inclination	Vertical down to 1000 m, around the 1200 m depth gently bent and then straightway with an inclination of 20°
Logging tests	500-1250m: Resistivity, temperature, sonic wave, density, caliper and borehole televiewer 1250-1800m: Resistivity, temperature, sonic wave, density, caliper, borehole televiewer and cement-bonding
Experiments	1) Hydrofracturing tests: several measurements at depths between 1100-1700 m 2) Water injection tests: injected twice after hydrofracturing tests, jet-percolation pin-holes were made near the fault zone 3) Geomagnetic measurement: using a downhole magnetometer measurements were carried out at depths shallower than 500 m within steel casing pipes.
Long-term observation	3-component seismometer (To=4.5 Hz, depth=1460 m), 2 vertical seismometers(depths 1568 and 1673 m), thermometer and a optical-fiber thermometer from the surface down to 1650 m depth

waves.

The ACROSS consists of such continuously vibrating sources which generate precisely controlled seismic signals. The source consists essentially of a servo motor and an eccentric mass which is fixed to the motor. The motor rotates the eccentric mass with the rate which is referenced to the precise pulses given by GPS. This produces centrifugal forces acting on the surrounding ground. This system can be used to monitor the long-term velocity changes associated with healing of the fault plane. It will hopefully be able to measure velocity changes of the order of  $10^{-6}$  near the ACROSS site.

#### WATER INJECTION EXPERIMENT

One of the major borehole experiments of the present project was water injection into the fault zone near the bottom of the 1800 m hole. Fig. 7 shows the concept of the water injection experiment proposed by Shimazaki *et al.* (1997). The idea shows that the healing process of a fault zone can be measured by monitoring its permeability derived from water injections into the fault zone.

The hole was cased from the surface down to the bottom at 1720 m. Between 14800 m and 1670 m depths, the casing pipes were pin-holed by shots in order to inject water into the surrounding rock. We injected water twice. The first experiment lasted for 5 days, and the second for 10 days, 1 month after the first experiment. In the first experiment, water was injected for 2 days, and then stopped for 24 hours. Then water

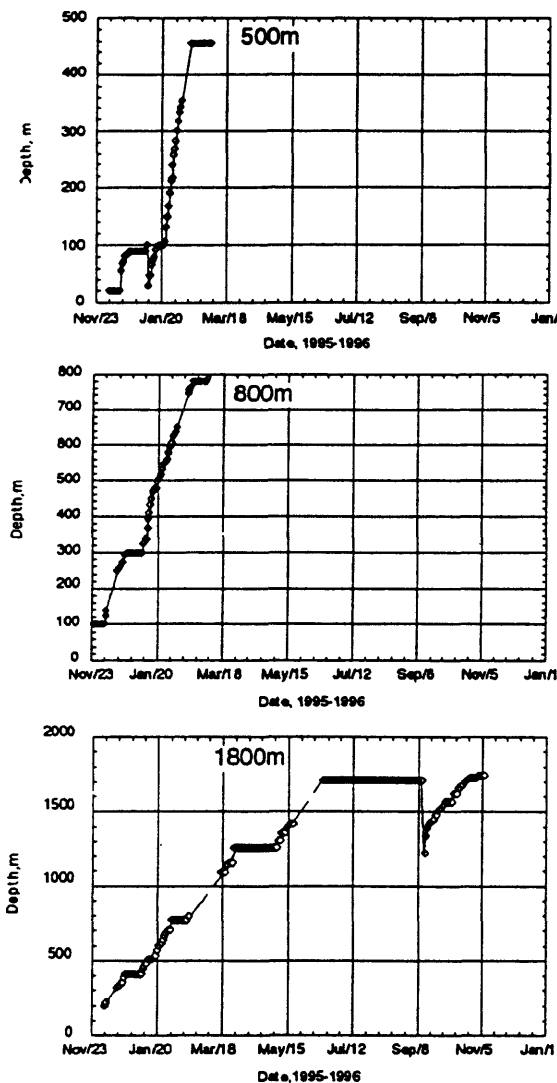


Fig. 3 Diagram showing drilling depths reached versus time for the three holes. The 1800m hole drilling was stacked three times near or in the fault zone of the Nojima fault.

injection was restarted, keeping the pressure at a constant level for 2 days. In the second experiment, water was injected for 10 days continuously.

At the start of each experiment, the water pressure was increased to preset levels (2.8 to 4.7 MPa). The injection pressure was controlled automatically with a valve connected to the casing head at the surface. The fluctuations of water pressure were kept within 5%. The inflow rate of water was about 20 l/min throughout the experiments. Excess water flowed out of the system

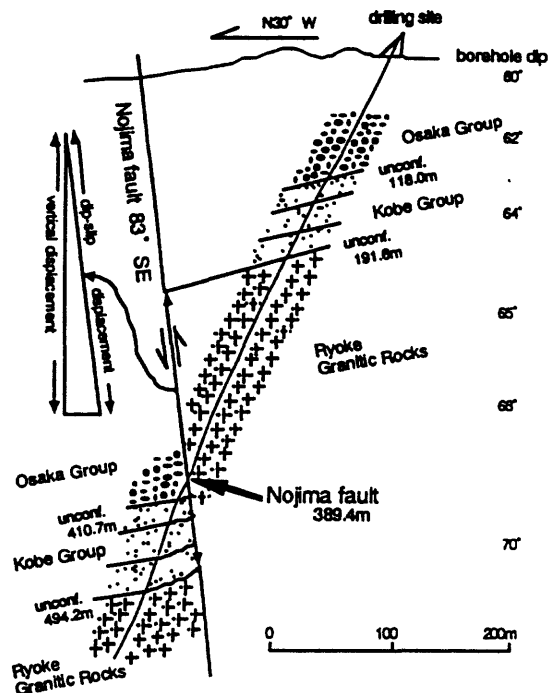


Fig. 4 Vertical geological cross-section derived from core samples of the 500 m hole. Two unconformities between the Osaka Group and the Kobe Group and between the Kobe Group and the granite basement are found in the cores. The Nojima fault dips 83° to the southeast (Murata *et al.*, 2000).

to keep the pressure level constant. The total water volume injected during both phases reached 258 cubic meters.

Subsurface ground water flow was monitored by geoelectrical or geomagnetic methods (Hashimoto *et al.* 2000). Seismicity changes caused by the water injection were monitored by installing seven temporary stations surrounding the drilling site, and borehole seismometers in the 800 m hole were used to monitor seismicity changes (Tadokoro *et al.* 2000a). The noise level at the seismometers was  $5 \times 10^{-6}$  cm/s, low enough to record nearby earthquakes of  $m=2$ .

Most earthquakes are located 2 to 4 km below

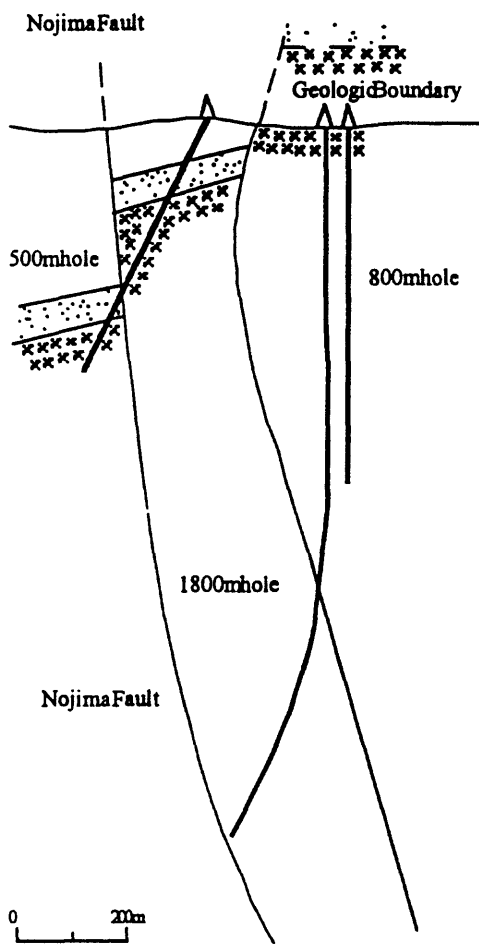


Fig. 5 Cross-section approximately perpendicular to the fault for the three boreholes and the two faults (Murata et al., 2000).

the surface, 1 to 3 km from the injection site. It should be noticed that earthquakes possibly induced by the injection spread away along the fault zone, instead of being concentrated near the injection sites. Earthquakes with S-P times at the bottom of the 800 m hole of about 0.3-0.5 s increased 4 to 5 days after the beginning of each injection. This activation delay is similar to the experiment in Matsushiro, Japan (Ohtake 1974).

The observation that microearthquakes can be triggered by small increases in pore pressure indicates that stress levels in the crust near the fault are almost at equilibrium with the frictional strength. The concentration of hypocenters at KTB (Zoback & Harjes

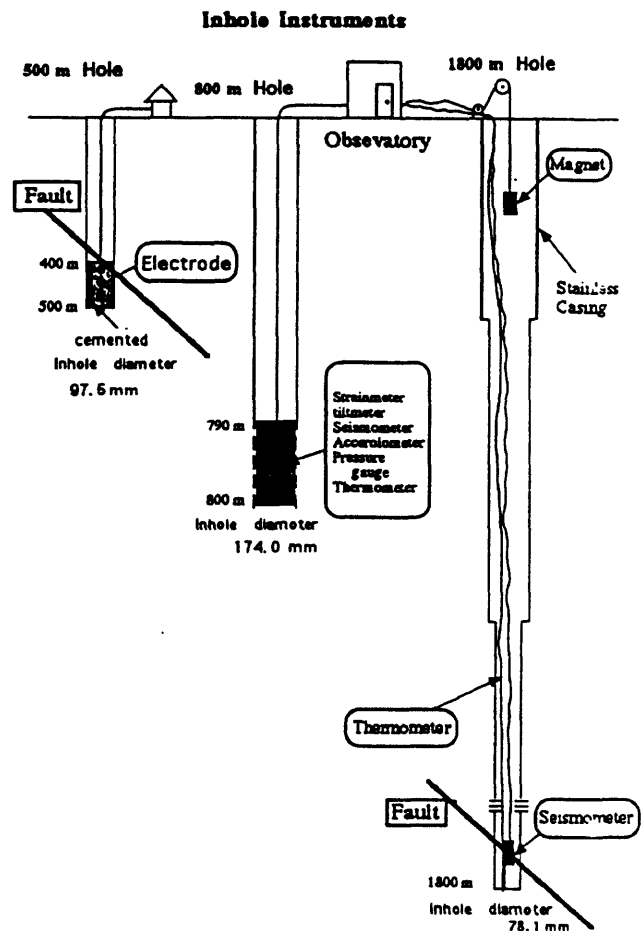


Fig. 6 Diagram showing sensors installed in the three boreholes

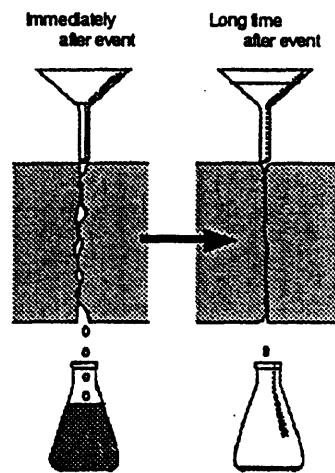


Fig. 7 Concept of the water injection experiment proposed by Shimazaki et al. (1997). The idea shows that the healing process of a fault zone can be measured by monitoring its permeability derived from water injections into the fault zone.

1997) differs from our case at Awaji. This suggests that the differential stress (shear stress) at the Nojima fault is extremely low. From hydrofracturing tests in the 1800 m hole (Tsukahara *et al.*, 2000), the frictional coefficient is estimated to be less than 0.3, under the assumption of "Coulomb Failure Criterion" (Tadokoro *et al.* 2000a). This frictional strength on the fault planes where the earthquakes were triggered is extremely low, compared to results from laboratory experiments, 0.6-0.7 (Byerlee 1978) and an induced test at KTB, 0.6-0.7 (Zoback & Harjes 1997). Further considerations are necessary to understand the mechanism of the earthquake cycle on the fault.

## CONCLUSIONS

The important results of the Nojima Fault-zone Probe, a consortium program of 14 universities and 2 national institutions, are: (1) Geological reconstruction of the evolution of the Nojima fault was obtained; (2) The maximum compressional axis was found to be perpendicular to the fault, about 45° to the regional compressional stress axis; (3) Micro-earthquakes ( $m = -2$  to  $+1$ ) were induced by water injections 1 to 3 km from the injection points in the 1800 m hole; (4) The fault zone was measured to be as thin as 30 m from microscopic studies. 3-component seismometer and accelerometer, 2-component tiltmeter, 3-component strainmeter were installed in the 800 m hole, and seismometers were installed at three depth levels in the 1800 m hole.

## ACKNOWLEDGEMENTS

I am indebted to Dr. Jim Mori for his reviewing of the manuscript. The Ministry of Education and Culture supported the Nojima Fault-zone Probe. The author also thanks to Dr. Ryuji Ikeda for providing facilities for our hydrofracturing test.

## REFERENCES

BYERLEE J. 1978. Friction of rocks. *Pure and Applied Geophysics* 116, 615-29.

HASHIMOTO M., SAGIYA T., TSUJI H., HATANAKA Y. & TADA T. 1996. Co-seismic displacements of the 1995 Hyogo-ken Nanbu earthquake. *Journal of Physics of the Earth* 44, 255-80.

HASHIMOTO T. 2000. Detection of crustal inhomogeneity in Nojima fault zone using the earth current noise. *The Island Arc*, in press.

IDE S., TAKEO M. & YOSHIDA Y. 1996. Source model of the 1995 Hyogo-ken Nanbu earthquake determined by near-field strong-motion records. *Journal of Physics of the Earth* 44, 649-53.

IKEDA R., IIO Y. & OMURA K. 2000. Scientific drilling and in-situ stress measurements in and around the fault zone in the vicinity of the 1995 Hyogo-ken-Nanbu earthquake, Japan. *The Island Arc*, in press.

ISHII H., MUKAI A., FUJIMORI K., NAKAO S., MATSUMOTO S. & HIRATA H. 2000. Multi-component observation of crustal activity in an 800m borehole close to an earthquake fault. *The Island Arc*, in press.

ITO H., KUWAHARA Y., MIYAZAKI T., KIGUCHI T. & NISHIZAWA O. 2000. Scientific drilling by GSJ in the Hyogo-ken Nanbu earthquake focal region. *The Island Arc*, in press.

MURAKAMI H., HASHIMOTO T., OSHIMAN N., YAMAGUCHI S., HONKURA Y. & SUMITOMO N. 2000. Electrokinetic phenomena associated with the water injection experiment at Nojima fault in Awaji Island, Japan. *The Island Arc*, in press.

NAKATA T., YOMOGIDA K., ODAKA J., SAKAMOTO T., ASAHI K., & CHIDA N. 1995. Surface fault ruptures associated with the 1995 Hyogoken-nanbu Earthquake, *Journal of Geography* 104, 127-42 (in Japanese).

NISHIGAMI K., TADOKORO K. & ANDO M. 2000.

Seismic observation at 1700m borehole drilled into the Nojima fault. *The Island Arc*, in press.

OHMURA T., MORIYA T., PIAO C., IWASAKI T., YOSHII T., SAKAI S., TAKEDA T., MIYASHITA K., YAMAZAKI F., ITO K., YAMAZAKI A., SHIMADA Y., TASHIRO K. & MIYAMACHI H. 2000. Crustal structure in and around the region of the 1995 Kobe earthquake deduced from a wide-angle and refraction seismic exploration. *The Island Arc*, in press.

OHTAKE M. 1974. Seismic activity induced by water injection at Matsushiro, Japan. *Journal of Physics of the Earth* 22, 163-76.

SATO H., HIRATA H., ITO T., TSUMURA N. & IKAWA T. 1998. Seismic reflection profiling across the seismogenic fault of the 1995 Kobe earthquake, southwestern Japan. *Tectonophysics* 286, 19-30.

SHIMAZAKI K., ANDO M., NISHIGAMI K., OSHIMAN N. & KITAGAWA Y. 1997. Water injection experiments of the scientific drilling program of the Nojima fault, Japan. *Seismological Society of Japan; abstracts* 2, P98 (in Japanese).

TADOKORO K., NISHIGAMI K., ANDO M., HIRATA N., IIDAKA T., HASHIDA Y., SHIMAZAKI K., OHMI S., KANO Y., KOIZUMI M., MATSUO S. & WADA H. 2000a. Seismicity changes related to a water injection experiment in the Nojima fault zone. *The Island Arc*, in press.

TADOKORO K., ANDO M., SHIMAZAKI K., TAKEMURA K., OSHIMAN N. & NISHIGAMI K. 2000. Geophysical logging in the boreholes drilled to the Nojima fault, Japan. *The Island Arc*, in press.

TSUKAHARA H., IKEDA R. & YAMAMOTO K. 2000. In situ stress measurements around 1500m depths in a borehole close to the earthquake fault of the 1995 Kobe earthquake. *The Island Arc*, in press.

YAMAMOTO K. & YABE Y. 2000. Stress at sites close to the Nojima earthquake fault measured on boring core samples. *The Island Arc*, in press.

YAMANO M. & GOTO S. 2000. Long-term temperature monitoring in a borehole drilled into the Nojima fault, southwest Japan. *The Island Arc*, in press.

YAMAOKA K., KUNITOMO T., MIYAKAWA K., KOBAYASHI K. & KUMAZAWA M. 2000. Trial for monitoring temporal variation of seismic velocity with ACROSS system. *The Island Arc*, in press.

ZOBACK M. & HARJES H. 1997. Injection-induced earthquakes and crustal stress at 9 km depth at the KTB deep drilling site, Germany. *Journal of Geophysical Research* 102, 18477-91.

blank page

# Outline of the Nojima Fault Scientific Drilling by NIED

Ryuji Ikeda

*National Research Institute for Earth Science and Disaster Prevention,  
Tennodai 3-1, Tsukuba, 305-0006 Japan. E-mail: ikeda@geo.bosai.go.jp*

## ABSTRACT

Three deep boreholes of 1,000 m to 1,800 m were drilled by NIED (National Research Institute for Earth Science and Disaster Prevention) in the vicinity of the epicenter of the 1995 Hyogoken-Nanbu (Kobe) earthquake for scientific research purposes. In particular, the Nojima-Hirabayashi borehole was drilled to a depth of 1,800 m and crossed the fault zones below the depth of 1,140 m. To investigate tectonic and material characteristics near and in active faults, we have been conducting an integrated study of crustal stress, heat flow, and fracture and material analyses on the cores.

A series of in-situ stress measurements by the hydraulic fracturing method was conducted in these boreholes. Measurement results revealed characteristic stress states around the fault system. The shear stress is very small at each site, and the orientation of the maximum horizontal compression was almost the same in the three boreholes, perpendicular to the surface trace of the faults. This result supports the finding that the magnitude of the shear stress along the Rokko-Awaji fault system was at a very low level after the earthquake. Terrestrial heat flow was also studied by using the temperature logging data and the thermal conductivity of the cores retrieved from the Nojima-Hirabayashi borehole. Amplifying the results of the heat flow value, the cutoff depth of aftershocks was estimated to be roughly 300 °C in temperature. Furthermore, to characterize the deformation and alteration of the fault fracture zone, rock cores retrieved from the fracture zone were studied for the relative density of micro-fractures, mafic minerals and chemical compositions. The core pieces were classified into five types of fault rocks, and the asymmetric distribution pattern of the fault rocks in the fracture zones was clarified.

## DRILLING, CORING AND LOGGING

We at the NIED drilled three boreholes in the vicinity of the epicenter of the Hyogoken-Nanbu earthquake, M=7.2, January 17, 1995. The main purpose of these drillings was to evaluate quantitatively the stress states, permeability, and heat flow in the fault vicinity just after the earthquake occurrence, while also investigating the fault structure and the physical and chemical properties of the fault rock. The earthquake occurred along the NE-SW trending fault network, the Rokko-Awaji fault system; and the Nojima fault appeared on the surface in Awaji Island when this rupture occurred (Katao et al., 1997). Figure 1 shows our borehole sites and the active fault distribution. The drilling sites and the state of each are outlined in Table 1. Each borehole is located at a characteristic site in relation to this earthquake's active fault system and aftershock distribution.

The Nojima-Hirabayashi borehole on Awaji Island was drilled to a depth of 1,838 m, at a quarry about 320 m SE from the surface trace of the Nojima fault, and it directly crossed the fault zones. Figure 2 indicates the relationship between the Nojima-Hirabayashi drilling trajectory, NIED Drilling Trace, and the Nojima fault together with a simplified lithological column obtained by rock core observations. The core recovery was almost 100 % from 1,000 m to the final depth of 1,838 m. Granodiorite and tonalite were found to be the basement rocks. Remarkable fractured zones of cataclasite with a fault gauge were confirmed at three depths, around 1,140 m, 1,313 m and 1,815 m. A drilling trace of GSJ (Geological Survey of Japan) is also shown in Fig. 2. In the GSJ well, the fault zone with a fault gauge was confirmed at the 623.3 m to 625.1 m depth (Ito et al. 1996). From these results, the dip of the Nojima fault is estimated to be about 70° to 85°. Geophysical logs recorded before the borehole experiments elucidate the in-situ variation in the physical

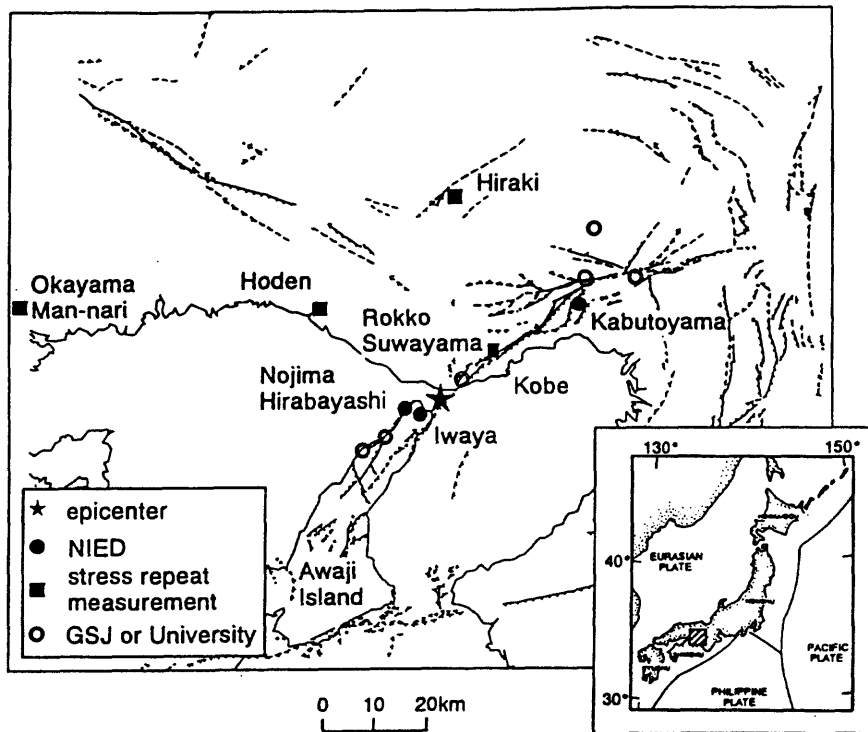


**Figure 1.** Scientific drilling sites around the epicenter of the 1995 Hyogoken-Nanbu earthquake (star symbol) on the map of active fault distribution (dotted line; after The Research Group for Active Faults of Japan, 1992). Black circles indicate the three deep boreholes discussed in this paper. Double circles denote the boreholes drilled by the Geological Survey of Japan and University Group. Black squares indicate stress repeat measurement sites (after Ikeda et al., 1996).

	NOJIMA-HIRABAYASHI (AWAJI ISLAND)	IWAYA (AWAJI ISLAND)	KABUTOYAMA (NISHINOMIYA)
Drilling Site	Hokudan, Tsuna, Hyogo Pref.		
Distance and Direction from Active Fault	320 m, S41° E, from Nojima-fault	1.7 km, S40° E, from Nojima-fault	1.5 km, E, from Ashiya-fault 1.5 km, W, from Koyo-fault
Drilling Depth	1,838.8 m	1,001.5 m	1,313.2 m
Drilling Diameter	193.7 mm (10-250 m) 149.2 mm (250-1,000 m) 97.5 mm (1,000-1,800 m)	193.7 mm (10-200 m) 149.2 mm (200-1,000 m)	149.2 mm (20-700 m)
Max. Inclination	7° 20' (at 993.9 m)	4° 00' (at 959.3 m)	11° 20' (at 934.0 m)
Lithology	tonalite, granodiorite, cataclasite, fault gauge	granodiorite, diorite, cataclasite	biotite granite
Coring	spot coring; 5 points (<1,000 m). all coring; (>1,000 m)	spot coring; 6 points in every 100 - 200 m	spot coring; 6 points in every 200 m
Casing	4" c.p. to 100.3 m deep	6" c.p. to 200 m deep	7" c.p. to 701 m deep, reaming 701-740 m by 175 mm dia.

**Table 1.** Drilling outline of the Hyogoken-Nanbu earthquake fault zone drilling project by NIED

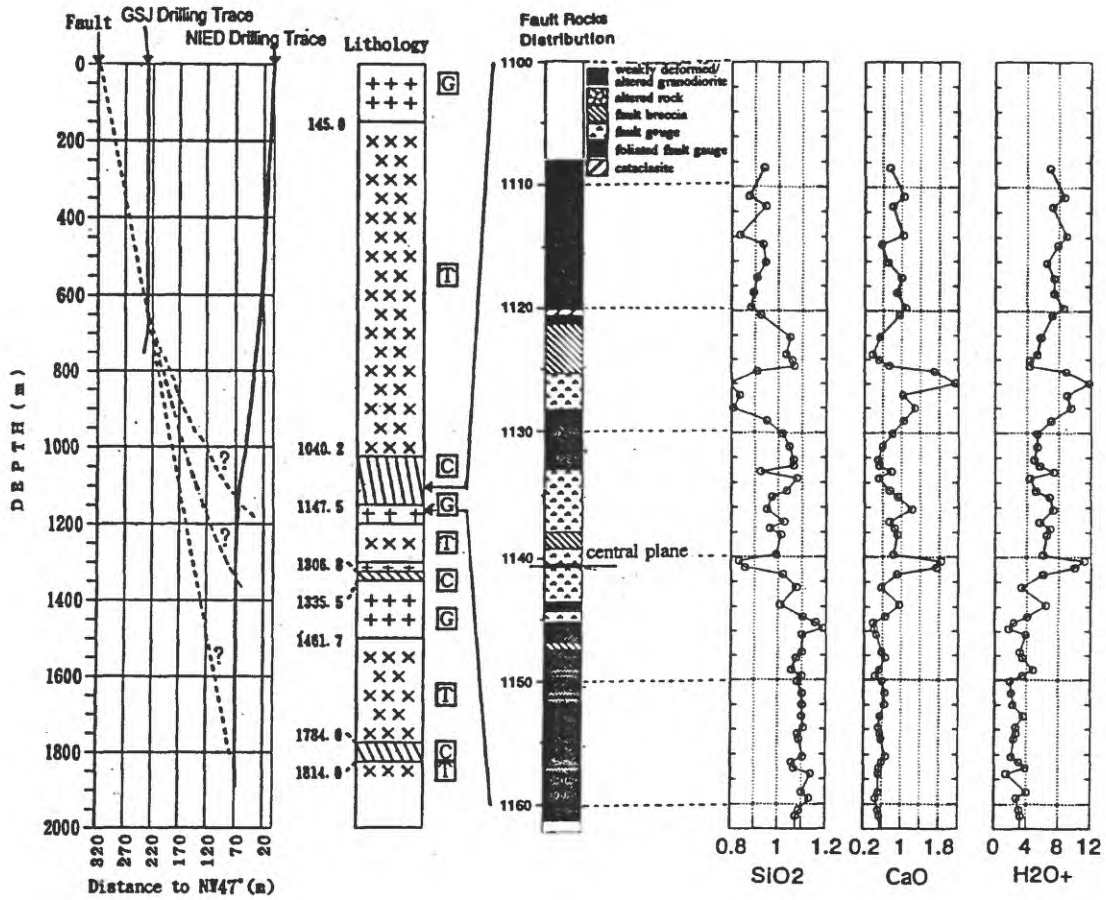


Figure 2. Vertical projection of the Nojima-Hirabayashi borehole and the Nojima fault with the lithological column as determined by the rock cores; G: Granodiorite, T: Tonalite and C: Cataclasite. NIED Drilling Trace is conducted by this study, and the GSJ one is conducted by the Geological Survey of Japan (after Ito et al., 1996). Some of the chemical components' variations found around the 1,140 m fault zone are also shown. The value of these components is shown in relation to the value of fresh Tonalite (compiled and modified Ikeda et al. (1998) and Kobayashi et al. (1998)).

properties. The composite log for the Nojima-Hirabayashi well is shown in Fig. 3. It was noted that at fracture zones including unconsolidated clay, the values of the p-wave velocity, resistivity and density sharply decrease to the value of 2~4 km/sec, 10~20 ohm-m and 1.5 g/cm<sup>3</sup>, respectively.

#### STRESS MEASUREMENT

In-situ stress measurement by the hydraulic fracturing method and a borehole televue survey, following techniques similar to those described by Ikeda and Tsukahara (1989), were conducted within selected intervals by the geophysical logs (Ikeda et al., 1998). They were conducted in almost only granitic rocks in these boreholes. At most measurement points, we could

detect clearly the reopening pressure and shut-in pressure from the pressure-time records. Stresses for each site are plotted against the respective depths in Fig. 4. At the Nojima-Hirabayashi site, a reverse fault type stress state can explain the local stress state located around the Nojima fault scarp, but this state changes to a strike-slip type at a deeper depth. On the other hand, the Iwaya site is situated in a normal type stress state, and the Kabutoyama site shows a strike-slip fault type stress state. Another characteristic state of stress relating to various fault fracture zones is observed in the Nojima-Hirabayashi borehole, that is the state where the differential stress decreases considerably beneath the 1,140 m fracture zone.

The average fracture direction, that is the SH<sub>max</sub> azimuth, is N49°W±15° for the

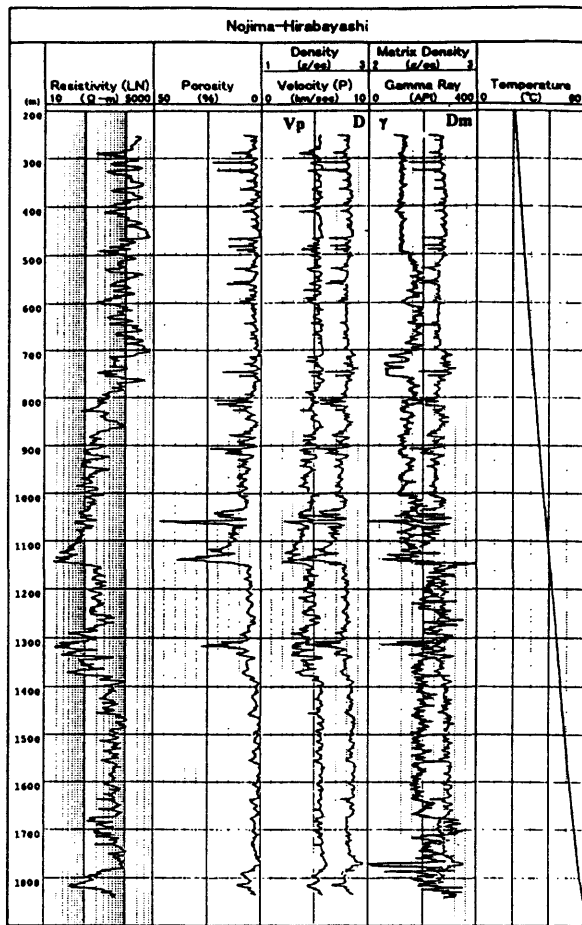


Figure 3. Geophysical well logging results of the Nojima-Hirabayashi borehole.

Nojima-Hirabayashi borehole,  $N45^{\circ}W \pm 10^{\circ}$  for the Iwaya borehole, and  $N33^{\circ}W \pm 10^{\circ}$  for the Kabutoyama borehole. It is very remarkable that this azimuth trending NW-SE is perpendicular to the Rokko-Awaji fault system, which includes the Nojima fault.

#### HEAT FLOW MEASUREMENT

Terrestrial heat flow at Hirabayashi was obtained based on the measurements of the thermal conductivity of the rock cores and the geothermal gradient from the temperature logging data in the borehole (Kitajima et al., 1998). Figure 5 shows the relationship between the thermal conductivity and bulk density of rocks, which are compared with data from 2,000 m class deep boreholes in the Kanto district, Japan, and from a 9,000 m hole of the German Continental Deep Drilling Program (KTB). By using these data, the value of the terrestrial heat flow is calculated as  $56.6 \pm 5.2$

( $10^{-3}$  W/m<sup>2</sup>) at the Nojima-Hirabayashi site. The temperature corresponding to the cutoff depth of the aftershocks was also investigated using these data. As a result, the cutoff depth caused by the Hyogoken-Nanbu Earthquake roughly corresponds to 300 °C in temperature (Kitajima et al., 1998).

#### FAULT ROCK CORE ANALYSES

Characteristics of the deformation and alteration of the rock cores retrieved from the fracture zone of the Nojima-Hirabayashi well were examined (Kobayashi et al., 1998). To study in more detail the fractures and core deformation, and to analyze chemical components by using an X-ray defraction meter, X-ray fluorescent meter and SEM, the fault zone cores were all coated by synthetic resin and half-split. Degrees of deformation and alteration were estimated based on the relative density of micro-fractures and on the relative disappearance of mafic minerals. Core pieces were classified into five types of fault rocks. Also, the asymmetric

distribution pattern of the fault rocks in the fracture zones was clarified, and a precise observation and chemical analyses of the fault gouge were conducted as shown in Fig. 2.

#### DISCUSSION

Stress measurement results have revealed characteristic stress states in and around active faults. Absolute stress magnitudes are relatively small when compared with values measured in plutonic rock bodies such as those found in the Ashio focal area (Tsukahara et al., 1996) and the Cajon Pass close to the San Andreas fault (Zoback and Healy, 1992). Similarly, shear stress is also very small at each site. This must be interpreted in terms of the stress drop found around the area after the earthquake. The SHmax direction at the three sites was almost the same, being perpendicular to the surface trace of the faults, in a NW-SE direction. This tendency was also observed

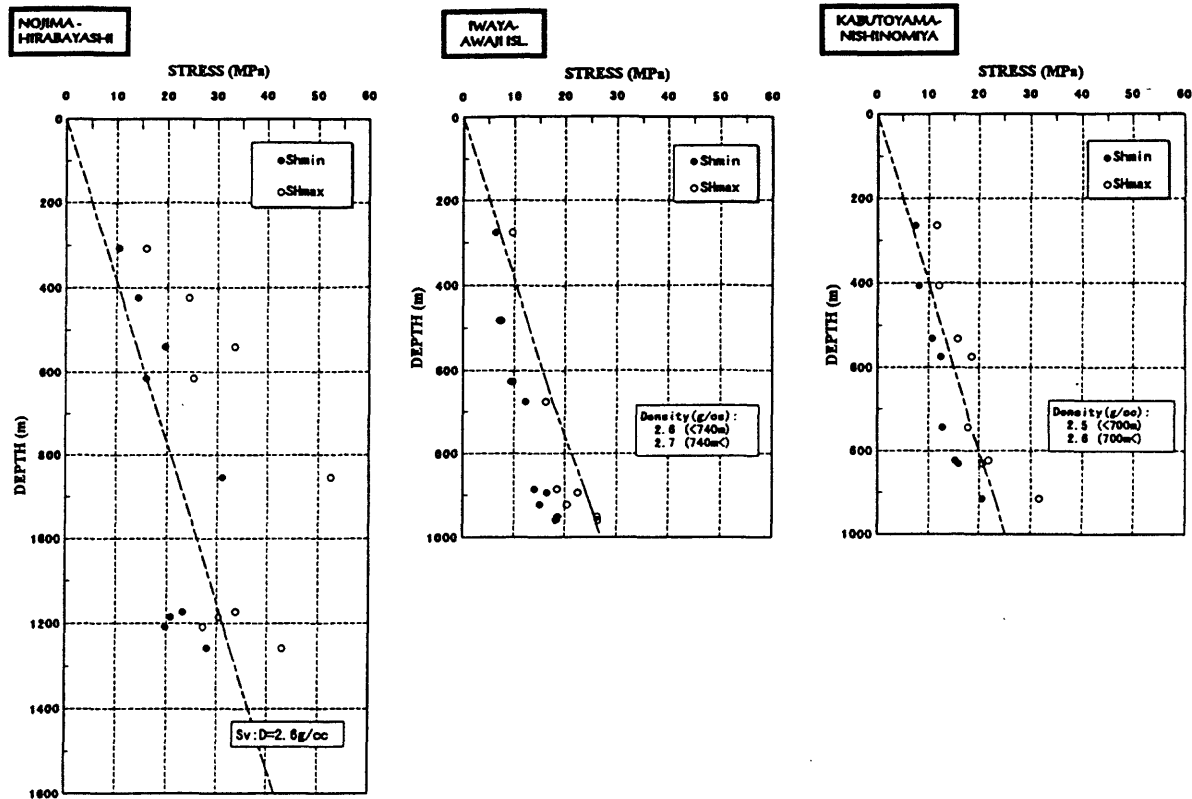


Figure 4. Stress-depth profiling in each borehole; the Nojima-Hirabayashi, Iwaya and Kabutoyama boreholes, respectively. (Ikeda et al., 1998)

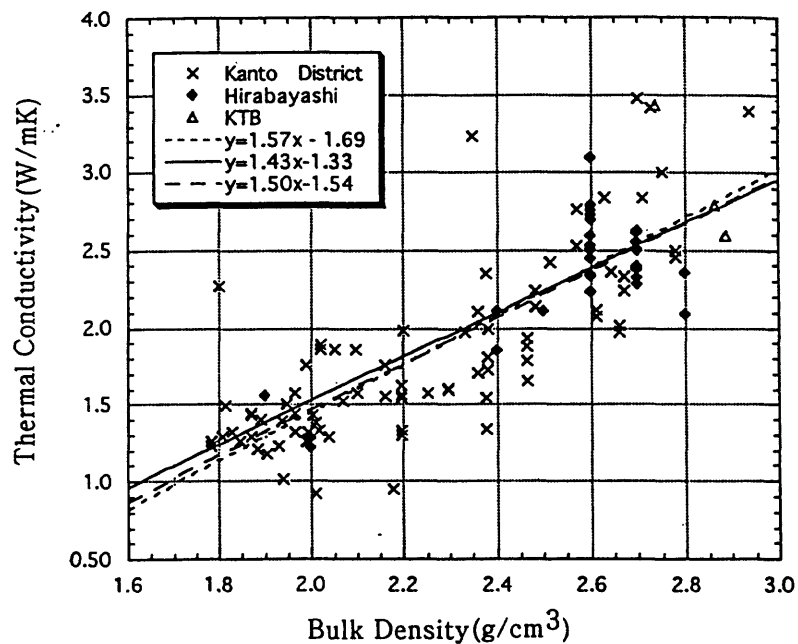


Figure 5. Relationship between thermal conductivity and bulk density of rocks, compared with data from the Kanto District and KTB boreholes by Rauen and Winter (1995). (after Kitajima et. al., 1998).

in the Nojima-Ogura borehole drilled by the university group (Tsukahara et al., 1998). Our measurement results revealed that the magnitude of shear stress along the Rokko-Awaji fault system is at a very low level, which agrees well with the Cajon Pass case (Zoback and Healy, 1992). It has been confirmed that the shear stress in the immediate vicinity of the Nojima fault became a very low value just after the Hyogoken-Nanbu earthquake. Fault types estimated from the stress condition are very contrastive among the three sites. It seems that in order to become such a characteristic stress state, the area must be strongly controlled by the active fault's distribution.

In the Hirabayashi hole, the shear stress value just beneath the fault fracture zone decreases abruptly to a value approximately one-half that of the above fault zone. It is believed that the material properties in and around the fault zones caused a weakening of the fracture zone which resulted in a characterization of the state of stress. In the Nojima fault, the fault gauge is very weak and collapses easily, and the strength difference from the granitic bedrock is quite large.

Scientific drilling into active fault zones could provide valuable insights for understanding the dynamic phenomena at deep positions. The fault structure, physical and chemical properties of the materials, and distribution of the fracture system are directly and continuously examined by geophysical logging in the borehole. The research conducted in the Nojima fault will be utilized to clarify the actual condition of various active faults which are found throughout the nation.

## REFERENCES

IKEDA R. and TSUKAHARA H., 1989, Hydraulic fracturing technique: Pore pressure effect and stress heterogeneity. *Int. J. Rock Mech. and Min. Sci. & Geomech. Abstr.* 26, 471-475.

IKEDA R., IIO Y., OMURA K. & TANAKA Y. 1996. In-situ crustal stress variation before and after the 1995 Hyogo-ken Nanbu Earthquake around the epicenter. *Proc. of The VIII-th Int'l. Symp. on the Observation of the Continental Crust through Drilling*, 393-398.

IKEDA R., OMURA K. and IIO Y., 1998, Stress measurements around active faults, *Chikyu Monthly*, No.21, 91-96. (in Japanese).

ITO H., KUWAHARA Y., MIYAZAKI T., NISHIZAWA O., KIGUCHI T., FUJIMOTO K., OHTANI T., TANAKA H., HIGUCHI T., AGAR S., BRIE A. & YAMAMOTO H., 1996. Structure and physical properties of the Nojima fault by the active fault drilling. *Geophysical Exploration* 49, 522-535. (In Japanese with English abstract).

KATAO H., MAEDA N., HIRAMATSU Y., IIO Y. & NAKAO S., 1997, Detail mapping of focal mechanisms in/around the 1995 Hyogo-ken Nanbu Earthquake rupture zone. *J. Phys. Earth* 45, 105-120.

KITAJIMA T., KOBAYASHI Y., IKEDA R., IIO Y. and OMURA K., 1998, Terrestrial heat flow in Nojima-Hirabayashi, Awaji Island, *Chikyu Monthly*, No.21, 108-113 (in Japanese).

KOBAYASHI K., MATSUDA T., ARAI T., IKEDA R., OMURA K., SANO H., SAWAGUCHI T., TANAKA H., TOMITA T., TOMIDA N., HIRANO S. and YAMAZAKI A., 1998, Distribution pattern of fault rocks, minerals and chemical elements at deeper part of the Nojima fault: analyses of 1,140 m fault zone cores drilled by NIED, *Chikyu Monthly*, No.21, 154-159 (in Japanese).

RAUEN A. and WINTER H., 1995, Petrophysical properties, KTB-Report, 95-2, *The German Continental Deep Drilling Program (KTB)*.

THE RESEARCH GROUP FOR ACTIVE FAULTS OF JAPAN, 1992, Maps of active faults in Japan with an explanatory text. Univ. of Tokyo Press, Tokyo.

TSUKAHARA H., IKEDA R. & OMURA K., 1996, In-situ stress measurement in an earthquake focal area. *Tectonophysics* 262, 281-290.

TSUKAHARA H., IKEDA R. and YAMAMOTO K., 1998, In-situ stress measurements at points close to Nojima Fault at the depths about 1500m: The maximum compressive stress perpendicular to the fault strike, *Chikyu Monthly*, No.21, 66-69 (in Japanese).

ZOBACK M. D. and HEALY J. H., 1992, In situ stress measurements to 3.5 km depth in the Cajon Pass scientific research borehole: Implications for the mechanics of crustal faulting. *J. Geophys. Res.* 97, 5039-5057.

# OUTLINE OF THE NOJIMA FAULT DRILLING BY GSJ: STRUCTURE, PHYSICAL PROPERTIES AND PERMEABILITY STRUCTURE FROM BOREHOLE MEASUREMENTS IN GSJ BOREHOLE CROSSING THE NOJIMA FAULT, JAPAN

Ito, H., Y. Kuwahara, T. Kiguchi, K. Fujimoto, T. Ohtani  
Geological Survey of Japan

## ABSTRACT:

After the 1995 Hyogoken-nanbu earthquake, three major research groups (Geological Survey of Japan (GSJ), the National Research Institute for Earth Science and Disaster Prevention (NIED), and the University Group) drilled boreholes into the Nojima fault and conducted experiments in the borehole. GSJ drilled a 747 m deep borehole at Nojima Hirabayashi penetrating the Nojima fault to elucidate the fine structure of the fault just after the large slip. The drill site is 74.6 m apart from the surface break of the fault. Cores were recovered for almost entire depth interval from 150 m to 746.6 m. The stratigraphy of the well is granodiorite from the surface. The fault zone is characterized by altered and deformed granodiorite from 426 m to 746.6 m, with fault gouge at 623.3 m to 625.1 m. The fault zone has low resistivity, low density, low velocities (both P and S wave; more than 50% decrease at the fault gouge), high porosity, and high Vp/Vs. The borehole observations, such as FMI logging, also revealed fine structure of the Nojima fault that corresponds to the changes in the degree of deformation within the fault zone, and the degree of deformation is more intense in the hanging wall side than in the footwall side of the Nojima fault. The width of the fault zone from the drilling result is consistent with that estimated from the surface trapped wave observations. This shows a good correlation between in-situ physical properties measured in boreholes with remote geophysical observations.

Permeability distribution in the fault zone were evaluated with very fine depth resolution from the tube wave analysis and Stoneley wave reflection, attenuation and slowness analysis. There are several permeable intervals in the fault zone, especially below the fault gouge. The fracture distribution and shear wave anisotropy show distinct changes within the fault zone.

Permeability of the Nojima fault just after the 1995 Kobe earthquake is estimated from the borehole measurements. The borehole was drilled by the Geological Survey of Japan to penetrate the Nojima fault. The depth of the borehole is 746.5 m. The fault zone is characterized by altered and deformed granodiorite from 426.1 m to 746.6 m, with coaxial zone of fault gouge at 623.3 m to 625.1 m. Permeability distribution in the fault zone was evaluated from the Stoneley wave analysis and hydrophone VSP results, and core measurements. The permeability of the fault core is estimated as 30 darcy and the thickness of the high permeable zone is about 0.1 m from the Stoneley wave analysis and hydrophone VSP results.

We find a strong correlation between permeability and proximity to the fault zone shear axes. The permeability observations are consistent with fault zone models in which a highly localized core or shear zone is surrounded by a damage zone of fractured rock. In this case, the damage zone will act as a high-permeability conduit for vertical and horizontal flow in the plane of the fault. The clay core region, however, will impede fluid flow across the fault.

## INTRODUCTION

After the 1995 Hyogoken-nanbu (Kobe) earthquake ( $M_s = 7.2$ ) on January 17, 10.5 km long distinguished surface breaks of the Nojima fault in Awaji island appeared (Awata et al., 1996). The Geological Survey of Japan drilled a 746.7 m deep borehole at Nojima-Hirabayashi, where the maximum surface slip at the 1995 Kobe earthquake was observed,

to penetrate the Nojima fault (Fig. 1). The drill site is 74.6 m apart from the trace of the surface break. The drilling, coring and borehole logging were completed in March, 1996: one year after the 1995 Kobe earthquake.

Cores were recovered for almost entire depth interval from 150 m to 746.6 m. The stratigraphy of the well is granodiorite from surface. The fault zone is

characterized by altered and deformed granodiorite from 426.1 m to 746.7 m, with fault core of fault gouge at 623.3 m to 625.1 m, fault gouge at 707.8 - 707.9 m, cataclasite at 525.5 - 525.7 m, 669.5 - 672.7 m (Ito et al., 1996, Tanaka et al., 1999, Ohtani et al., 1999).

We conducted conventional logging. The main shear zone observed by core inspection is characterized by low electrical resistivity, low density and high porosity. They gradually decrease towards the depth of fault gouge of 623.3 m to 625.1 m. The fault gouge at 623.3 m to 625.1 m has extremely low electrical resistivity of about several tens of ohm - m.

In addition to conventional logging, monopole and dipole sonic waveforms were acquired with a DS1\* (Dipole Sonic Imager) tool. Micro-resistivity images were also acquired with an FMI\* (Formation Micro Imager) tool. The location of the fault is clearly seen in the logs (Fig. 3). The zone below the fault appears to have been extensively broken up and became significantly porous and permeable.

Both P and S wave velocities were determined by the Schlumberger's DS1\* (Dipole Shear Sonic Imager):

\*Trademark of Schlumberger tool. Both the P and S velocities gradually decrease towards the depth of fault core of 623.3 m to 625.1 m, as in the case of electrical resistivity and density. P wave velocity drops from 4 km/s (just above the fault gouge at 623.3 m to 625.1 m) to 2.6 km/s. Because the S wave signal is so weak that the S wave velocities were not determined for several depth intervals, including the fault core at 623.3 m to 625.1 m.

BHTV (ultrasonic borehole televiwer) and FMI logging clearly detected the fault gouge at 623.3 m to 625.1 m. The strike and dip of the fault gouge zone by FMI is about 140 degrees and 80 degrees, respectively. These are in good agreement with the surface strike of the Nojima fault and the dip estimated from the angle between the surface trace and the depth of the fault gouge.

## PERMEABILITY STRUCTURE FROM SONIC MEASUREMENTS

Identification and evaluation of permeable fracture system is of primary importance to better understand the physical properties of the fault. Sonic measurements are sensitive to fractures and can contribute in many ways to their evaluation. Stoneley wave reflections and attenuation analysis are commonly used techniques. They have the advantage of showing open permeable

fractures. Permeability added Stoneley slowness is another useful technique. It compares the measured Stoneley slowness to the elastic slowness obtained from a model without permeability. The difference, the permeability added slowness, is an indication of the mobility of the pore fluid in the formation. Sonic techniques include Stoneley wave reflections evaluation (Hornby et al., 1989), and Stoneley attenuation (Brie et al., 1988). The advantage with Stoneley techniques is that they detect major open fractures. Recently, Stoneley fracture evaluation was improved through the use of Stoneley modeling which allows separation of the effect of borehole irregularities and lithology changes from permeable fractures (Tezuka et al., 1997). Permeability added Stoneley slowness is another technique which has proven useful in identifying permeable zones. It is based on the difference between a Stoneley slowness computed from elastic theory, without the effect of permeability and the measured Stoneley slowness (Winkler et al., 1989). The difference is an indicator of permeability in the formation.

Sonic waveforms were acquired with the DS1 (Dipole Sonic Imager) tool. This tool has one monopole transmitter which can be driven by a high frequency pulse at around 10 kHz to measure compressional and shear head waves, and by a low frequency source below 1 kHz to measure the Stoneley wave. The low frequency Stoneley wave, or tube wave, is sensitive to fractures and formation pore fluid mobility, and cause Stoneley wave reflections (Hornby et al., 1989), Stoneley attenuation (Brie et al., 1988) and Stoneley slowness increase (Winkler et al., 1989). Borehole discontinuities, and formation changes also cause attenuation and reflections of the Stoneley wave. To evaluate this effect a fast modeling technique was used (Tezuka et al., 1997). This technique uses the borehole size and the formation elastic properties from the compressional and shear measurements to generate synthetic waveforms representative of the effect of borehole and formation changes without fractures. These waveforms are then evaluated with the same process as the one used for real waveforms, and the results compared.

On a plot of the Stoneley waveforms (Fig. 3), we can clearly observe a time delay in the arrivals, associated with a reduction in amplitude caused by permeable zones. We also observe chevron patterns resulting from reflections either from open fractures or from borehole irregularities. The down going feature of

the chevron is caused by energy reflected from above the receivers, while the up going feature is energy reflected from below the transmitter. In a simple case these features should be symmetrical; however when the formation below or above the reflector is very attenuative one of the features is substantially reduced. Also in intervals with multiple fractures, the reflection from one fracture can be attenuated by nearby fractures.

Stoneley attenuation was evaluated with the Normalized Differential Energies (NDE) technique (Brie et al., 1988). The computation was made in the 0 to 1.5 kHz frequency band. Small cyclic irregularities can be observed on the caliper log, which clearly affect the Stoneley propagation. To reduce this effect the direct wave was separated from the reflections before computation using a velocity filter. A borehole compensation was achieved by calculating the average of the receiver and transmitter mode results. Model waveforms were processed in the same fashion to estimate borehole effects. In Fig. 3, the attenuation due to borehole variations and lithology is shown in white. The additional attenuation due to fractures and permeability is shown in black. Because of the extraordinary values of the measurement near the fault, the model waveforms could not be calculated in the interval of the fault core.

Up and down going reflected fields can be separated from the total waveform with a velocity filter (Fig. 3). Both down and up going Stoneley reflections were evaluated in the 0 to 1.5 kHz frequency band, for the real and model waveforms. The resulting reflection coefficients are presented in Fig. 4. The results for the down going reflections are shown on the left side, and for the up going reflection on the right side. Again here the model reflection coefficient is coded white, while the added reflection coefficient caused by fractures are shown in dark gray.

The Stoneley slowness was evaluated from the low frequency monopole waveforms using the STC technique. The computation was performed in the frequency band 0.5 to 1.5 kHz. The results are of very good quality except right in front of the fault where the hole is very damaged, and the signal too small to be evaluated. We clearly observe an increase in Stoneley slowness in some sections. This could be caused either by porous, permeable formation, or by the presence of open fractures.

In a non-permeable purely elastic formation, the Stoneley slowness is a function of the formation shear slowness and its density, the mud slowness and its

density, the borehole size, the Stoneley frequency. Let's call this slowness the elastic slowness or  $S_e$ . Fluid movement in a permeable formation causes an increase in the Stoneley slowness  $S$ . The elastic slowness can be calculated and compared with the measured one. The difference  $S - S_e$  is therefore indicative of permeability.  $S - S_e$  is very large below the fault and significant in the interval above the fault (Fig. 4). In the fault zone, there are also several short intervals in which  $S - S_e$  is very large: 667 m-674 m and 706 m-710 m. In these intervals, the Stoneley attenuation is large, but there is no Stoneley reflection from within the interval, but reflections are observed at the upper and lower boundaries, going away from the bed (up above, and down below). This is because the other side of the reflection pattern is very strongly attenuated. These beds can be porous, permeable zones, or zones where the porosity is filled with soft clay material.

In Fig. 4,  $S - S_e$  is shown as a function of the distance from the fault core zone. The shaded area shows the fault zone characterized by alteration and deformation. The permeability indicator  $S - S_e$  in the fault zone is larger than that outside of the fault zone, and it is larger in the footwall than that in the hanging wall of the Nojima fault. The high  $S - S_e$  zone is confined to several narrow zones which corresponds to cataclasite and gouge zones. As shown in Fig. 3 and Fig. 4, the Stoneley analysis has an advantage of obtaining continuous permeability structure with fine depth resolution.

## PERMEABILITY ESTIMATES FROM HYDROPHONE VSP

We carried out a multi-offset hydrophone VSP experiment to detect subsurface permeable fractures and permeable zones and to estimate permeability of the Nojima Fault. Our analysis is based on a model that tube waves are generated when incident P-wave compresses the permeable fractures (or permeable zones) intersecting the borehole and a fluid in the fracture is injected into the borehole. Permeable fracture (or permeable zone) is detected at the depth of tube wave generation, and fracture permeability is calculated from amplitude ratio of tube wave to incident P-wave. We detected several tube wave generations from VSP sections. Distinct tube waves were generated at the depths of the fault zone which was characterized by altered and deformed granodiorite with a fault gouge.

In order to evaluate permeability of the Nojima fault, we analyzed the amplitudes of the tube waves generated at the depths of fault gouges in the fault zone. To calculate permeability, we apply the model of Beydoun et al. (1985) for the permeable fracture and that of Li et al. (1994) for the permeable zone. In the model of Beydoun et al. (1985), tube wave is generated at isolated permeable fracture. In the model of Li et al. (1994), the source of tube wave generation corresponds to the permeable zone which has the width of the order of 10 cm to 1m. The main difference between two model is the oscillation of the width of fracture or permeable zone by incident P-wave.

We can calculate the theoretical curves of tube wave to P-wave amplitude ratio ( $A^T/A^P$ ) as a function of frequency for several permeability values for each model. The feature of the two model is in the frequency dependence of the theoretical curves. For the fracture model, the value of  $A^T/A^P$  decreases with frequency. Conversely, for the permeable zone model, amplitude ratio increases with frequency.

We show one example of estimating permeability in the fault core at 623.3 - 625.1m (Fig. 5). Judging from the frequency dependence of the amplitude ratio (Fig. 6), we applied the model by the permeable zone model. From this VSP data, it is difficult to determine the lower boundary depth of the permeable zone. So we apply other data for estimating the width of this permeable zone. One is tube wave attenuation in VSP section, another is Stoneley wave attenuation obtained from sonic logging.

The tube waves attenuate very strongly at 624m depth. The attenuation occurs within 1m of sensor spacing. We conclude that this attenuation of tube wave indicates this depth zone has a high permeable zone and the width of permeable zone is less than 1m (Kuwahara et al, 1999). Fig. 6 shows high permeable zone estimated from Stoneley wave attenuation. The width of high permeable zone is about 1m along the borehole at this fault gouge. From the analysis of tube wave attenuation and Stoneley wave attenuation, we assume that the true thickness of this permeable zone is 0.1 m, if we take into account that the angle between the borehole and the fault is about 84 degrees (Fig. 1). With this permeable zone thickness, the permeability of this zone can be estimated as about 30 d ( $30 \times 10^{-12} \text{ m}^2$ ).

## DISCUSSION AND CONCLUSIONS

Permeability distribution in the fault zone was evaluated from Stoneley wave reflection, attenuation and slowness analysis and the tube wave analysis. Stoneley wave analysis shows permeability increase in the fault zone. Both the hydrophone VSP data and the Stoneley wave analysis show several permeable zones at gouges and cataclasite within the fault zone. The tube wave analysis at 624 m shows the permeability of the coaxial zone is estimated as 30 darcies.

We measured matrix permeability of core samples. We find a strong correlation between permeability and distance from the fault coaxial zone. The width of the high permeable zone (approximately 20 to 40m) is in good agreement with fault zone width inferred from trapped wave analysis and borehole results. The fault coaxial zone contains clays with permeability of approximately 0.1 to 1 microdarcy at 50 Mpa confining pressure. Outside this zone, matrix permeability drops to sub-nanodarcy values.

Stoneley wave analysis has an advantage of obtaining continuous evaluation of permeability structure with fine depth resolution. However, it is difficult to estimate permeability values for the present case, because the theory is based on the Darcy's law, and it is not the case for the Nojima fault. The combined analysis with the Stoneley wave and tube wave made it possible us to estimate permeability of the fault core of the Nojima fault. The permeability of 30 darcies ( $30 \times 10^{-12} \text{ m}^2$ ) is considered to be the highest limit, because the measurements was made only one year after the earthquake.

These permeability observations are consistent with fault zone model in which a highly localized permeable zone is surrounded by a damage zone of fractured rock. In this case, the damage zone will act as a high permeable conduit for vertical and horizontal flow in the plane of the fault. The clay gouge, however, will impede fluid flow across the fault.

## REFERENCES

Awata, Y., K. Mizuno, Y. Sugiyama, R. Imura, K. Shimokawa, K. Okumura, E. Tsukuda and K. Kimura, Surface fault ruptures on the northwest coast of Awaji Island associated with the Hyogo-ken Nanbu earthquake of 1995, Japan, *Zisin, Suppl. 2*, 49, 113-124, 1996.  
 Beydoun, W. B., C. H. Cheng and M. N. Toksoz, Detection of open fractures with Vertical Seismic Profiling, *J. Geophys. Res.*, 90, 4557-4566, 1985.

Brie A., K. Hsu, and C. Eckersley, Using the Stoneley normalized differential energies for fractured reservoir evaluation, 29th Annual Logging Symposium of the SPWLA, paper XX, 1988.

Hornby, B.E., D.L. Johnson, K.W. Winkler and R. A. Plumb, Fracture evaluation using reflected Stoneley -wave arrivals, *Geophysics*, 54, 1274-1288, 1989.

Ito, H. and Y. Kuwahara, Trapped waves along the Nojima fault from the aftershock of Kobe Earthquake, 1995, Proceedings of VIIth International Symposium on the observation of the Continental Crust Through Drilling, 399-402, 1996.

Ito, H., Y. Kuwahara, T. Miyazaki, O. Nishizawa, T. Kiguchi, K. Fujimoto, T. Ohtani, H. Tanaka, T. Higuchi, S. Agar, A. Brie and H. Yamamoto, Structure and physical properties of the Nojima Fault, *BUTSURI-TANSA*, 49, 522-535, 1996.

Kuwahara, Y., H. Ito, T. Kiguchi, and T. Miyazaki, Characterization of damaged zone of the Nojima fault by means of hydrophone VSP, submitted to *The Island Arc*, 1999.

Li, Y. D., W. Rabbel and R. Wang, Investigation of permeable fracture zones by tube-wave analysis, *Geophys. J. Int.*, 116, 739-753, 1994.

Li, Y.-G., K. Aki, J. E. Vidale and M. G. Alvarez, A delineation of the Nojima fault ruptured in the M7.2 Kobe, Japan, earthquake of 1995 using fault zone trapped waves, *J. Geophys. Res.*, 7247-7263, 1998.

Tezuka, K., C. H. Cheng and X. M. Tang, Modeling of low-frequency Stoneley-wave propagation in an irregular borehole, *Geophysics*, 62, 1047-1058, 1997.

Tanaka, H., T. Higuchi, N. Tomida, K. Fujimoto, T. Ohtani and H. Ito, Distribution, deformation and alteration of fault rocks along the GSJ core penetrating the Nojima Fault, Awaji Island, Southwest Japan, *Jour. Geol. Soc. Japan*, 105, 1, 72-85, 1999.

Ohtani, T., H. Tanaka, K. Fujimoto, T. Higuchi, N. Tomida and H. Ito, Internal structure of the Nojima fault zone revealed from the GSJ borehole, submitted to *The Island Arc*, 1999.

Winkler, K. W., H.L. Liu and D. L. Johnson, Permeability and borehole Stoneley waves: comparison between experiments and theory, *Geophysics*, 54, 66-75, 1989.

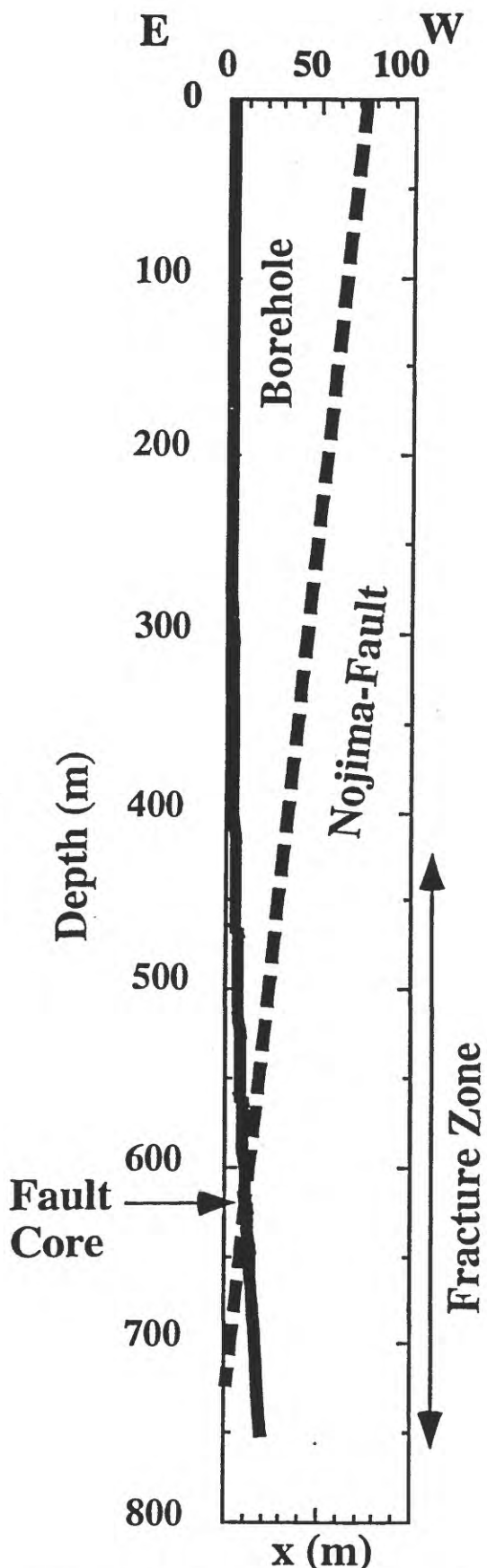


Fig. 1 Trajectory of the borehole and the Nojima fault.

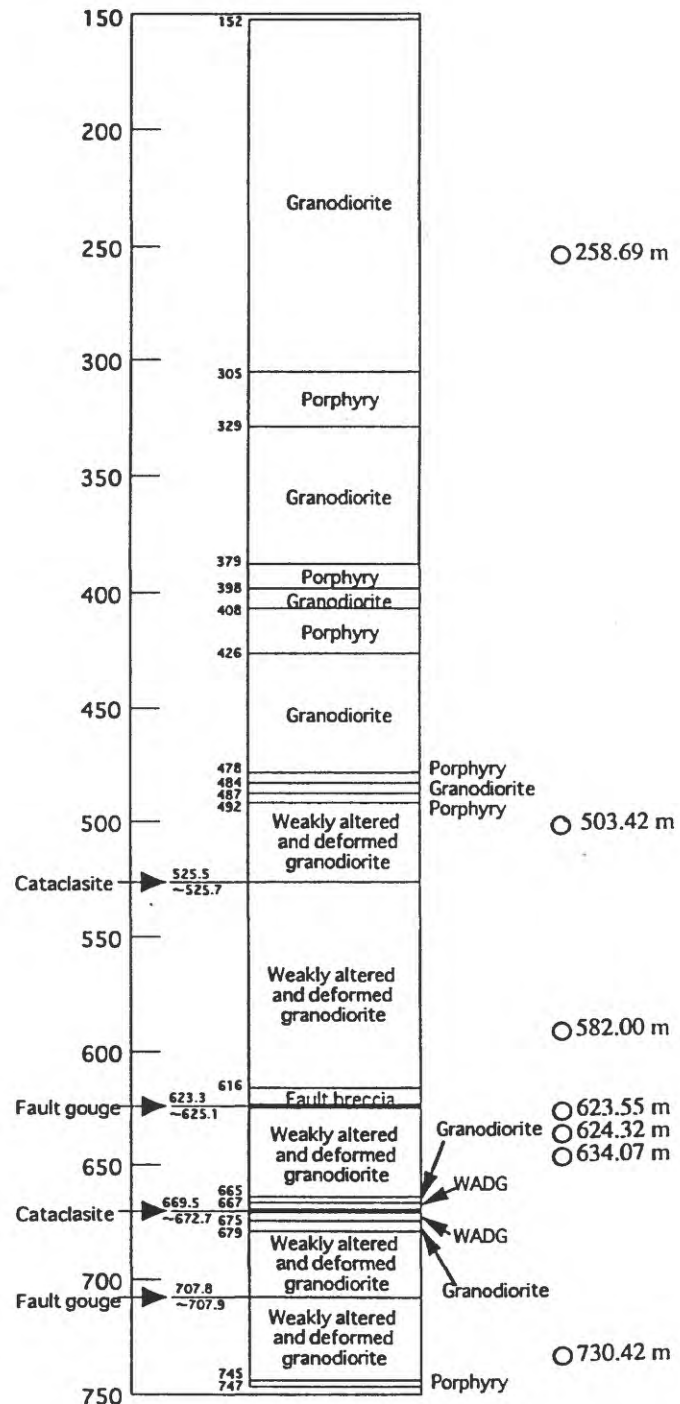


Fig. 2 The geological structure of the Nojima Hirabayashi borehole. The circles show the depths of the core samples for the permeability measurements.

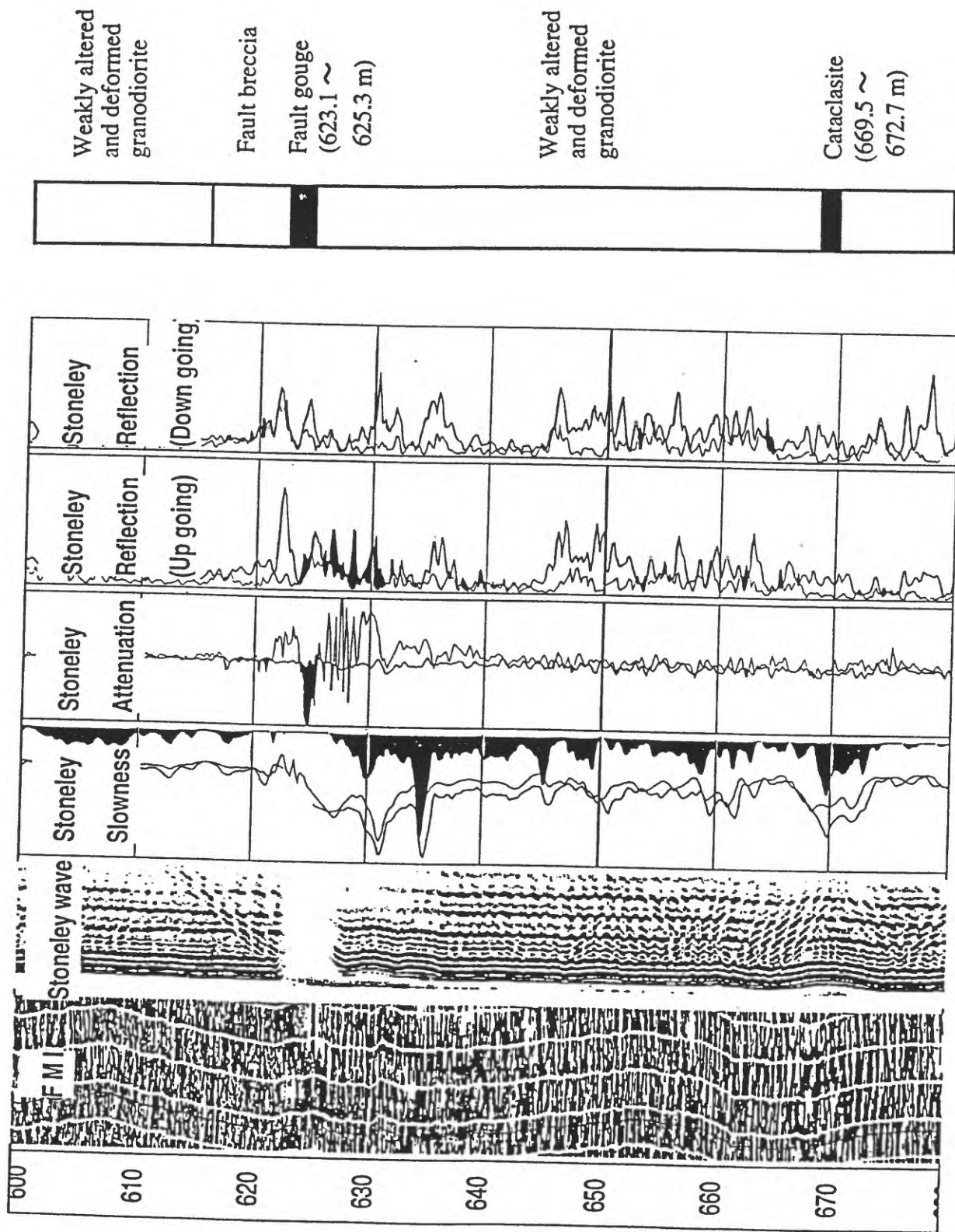


Fig. 3 FMI image, Stoneley waveforms, Stoneley slowness, Stoneley attenuation and Stoneley reflection around the fault core zone.

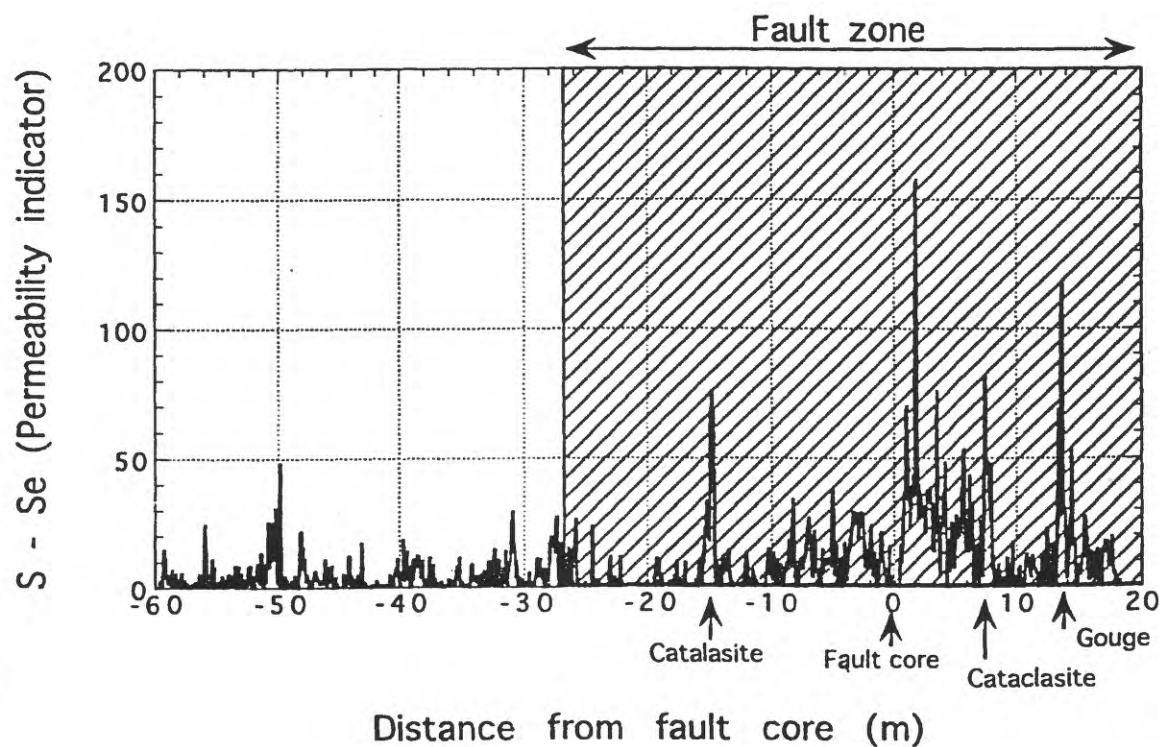
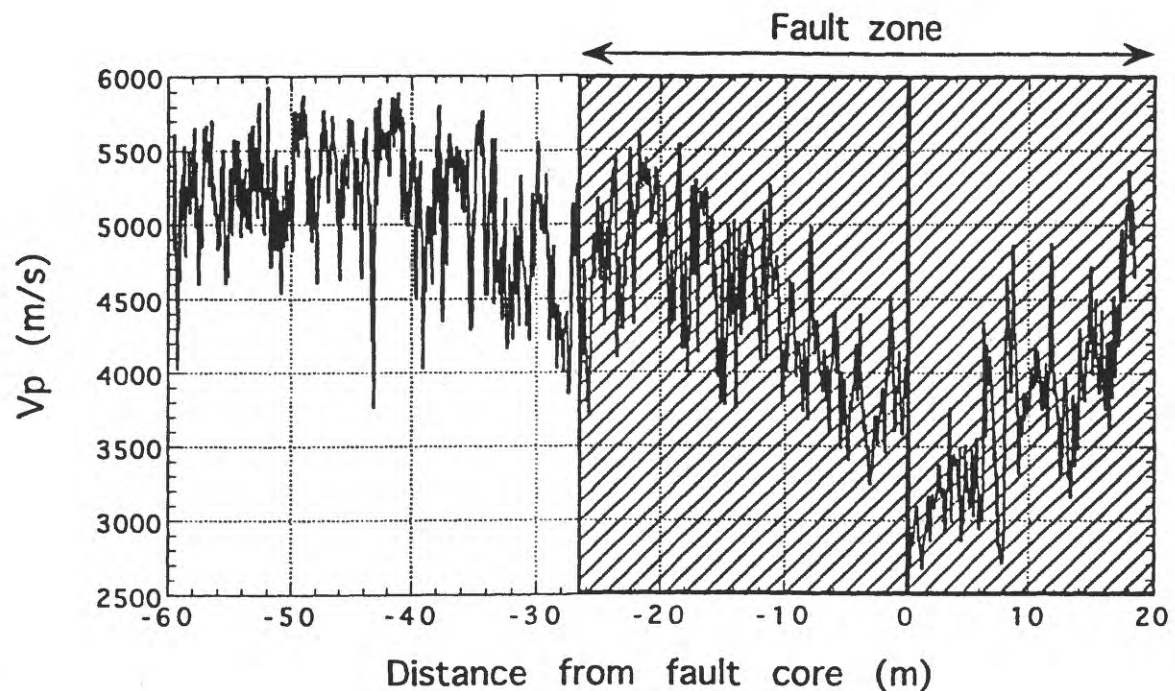


Fig. 4 Velocity (upper) and permeability (lower) structure of the GSJ Hirabayasi borehole as a function of distance from the coaxial zone of the fault.

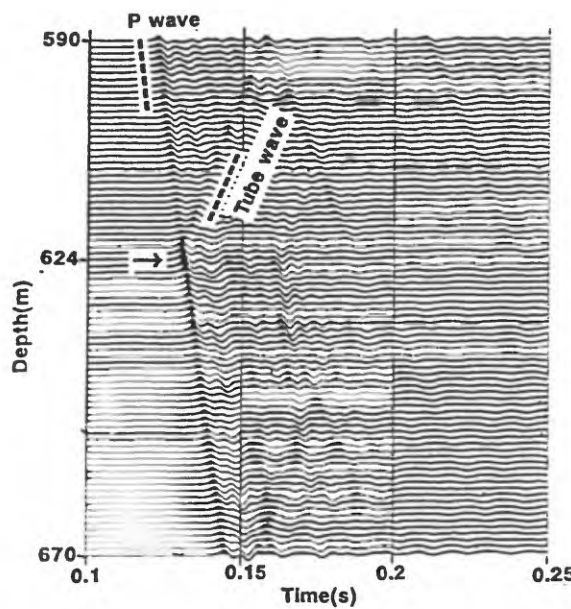


Fig. 5 VSP section around the fault core (623.3 - 625.1 m). The upgoing tube wave is clearly shown at 624 m depth, whereas the downgoing tube wave is not observed.

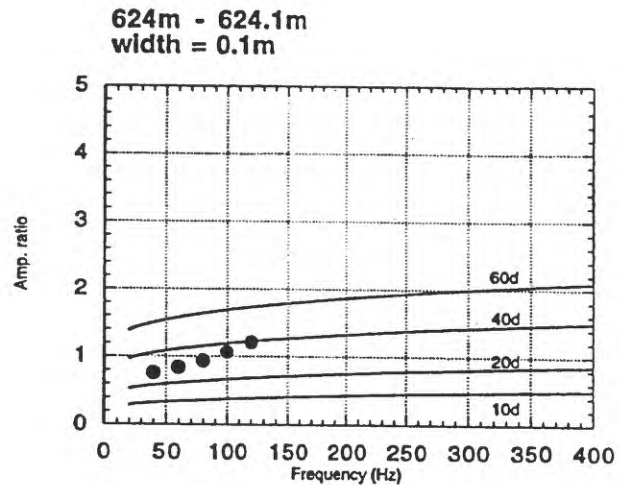


Fig. 7 The comparison between theoretical curves and VSP data for the depth of 623 - 624 m. The permeability is of this permeable zone is estimated as about 30 d.

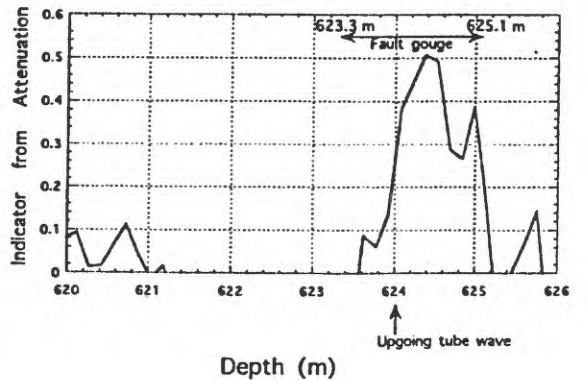


Fig. 6 The Stoneley attenuation around the fault core (623.3 - 625.1 m). The high attenuation zone is confined to narrow zone of 1 m depth interval within the fault core zone of 623.3 - 625.1 m.

blank page

# Distribution, deformation and alteration of fault rocks along the GSJ core penetrating the Nojima fault, Awaji Island, Southwest Japan

Hidemi Tanaka<sup>1</sup>, Naoto Tomida<sup>1</sup>, Norie Sekiya<sup>1</sup>, Yuichi Tsukiyama<sup>1</sup>, Koichiro Fujimoto<sup>2</sup>, Tomoyuki Ohtani<sup>2</sup> and Hisao Ito<sup>3</sup>

<sup>1</sup> Department of Geo / Biosphere Sciences, Faculty of Science, Ehime University, Bunkyo-cho 2- 5 Matsuyama, 790-8577 Japan,

<sup>2</sup> Geological survey of Japan, Geothermal Department, Higashi 3-3-1, Tsukuba 305-8567, Japan

<sup>3</sup> Geological survey of Japan, Earthquake Research Department, Higashi 3-3-1, Tsukuba 305-8567, Japan

## ABSTRACT

This paper presents results of petrographic and chemical characterization on a fault zone in the GSJ drill core penetrating the Nojima fault which was activated during the 1995 Hyogoken Nanbu Earthquake ( $M=7.2$ ). Based on these data, we will discuss the dynamic behavior and role of each shear zone in a shallow fault zone of granitic origin during seismic cycles. The GSJ core consists of granodiorite and porphyritic intrusive rocks including seven shear zones, MSZ (main shear zone: 625 m depth), UCZ, USZ, LSZ-1, LSZ-2, LCZ-1 and LCZ-2. These shear zones are generally surrounded by less pulverized and less altered fault related rocks (WPAR). Microscopic observation clarifies that centralized layers of MSZ are composed of fault gouges which had experienced high velocity frictional movement with heat generation, fault breccia in LSZ -1 shows explosion brecciation texture with zeolite matrix, fault gouge in LSZ-2 shows well defined folia presented by clay particle alignments possibly formed by low velocity movement or creeping. LCZ-1 and LCZ-2 are older cataclasite zones formed prior to the intrusion of porphyry dikes.

Major and trace element chemical composition analysis clarifies that many of the elements are depleted (referred to as C type elements) from widely distributed WPAR. The C type elements are more concentrated in MSZ and less in other shear zones than WPAR suggesting the C type elements are the candidates for high field strength (HFS) elements. Results of constant mass isocon analysis using the

three most stable C type elements ( $TiO_2$ ,  $P_2O_5$  and  $Zr$ ) indicate that mass loss occurred in the MSZ and mass gain occurred in the other shear zones. In centralized layer fault gouge in MSZ, graphite or organic carbon is anomalously concentrated, possibly indicating deoxidation of  $CO_2$  gas or carbonate minerals during frictional heating. These results lead to the following conclusions :

(1) All shear zones except the older cataclasite zones were evolved from the WPAR, indicating that pulverization and alteration of recent activity were more diffused at the initial stage of faulting and gradually localized to each shear zone undertaking a differentiation of function during seismic cycles.

(2) The MSZ shear zone can be regarded as a high velocity frictional zone with accompanying mass loss (compaction) and possibly with heat generation during co-seismic periods.

(3) The LSZ-1 shear zone, located just beneath the MSZ and typically showing explosion brecciation texture with few carbonate minerals, could have a function of trap zone of fluid or gas. Little compaction and dilatancy are detected in this zone leaving some ambiguities for this interpretation.

(4) The LSZ-2 shear zone contains foliated fault gouge enriched with clay minerals and characterized by a large degree of dilatancy, possibly undertaken a role of slow velocity motion or creep during the interseismic and/or post- seismic periods.

## Introduction

At 5:46 AM, on the date of 16th January, 1995, an  $M = 7.2$  earthquake struck the southern part of Kobe city and northwestern part of Awaji island (Hyogoken-Nanbu earthquake). The epicenter was located at the Akashi straight and the focal depth was reported to be 14 km. Surface rupture appeared more than 10 km long along the preexisting NE-SW striking Nojima fault (Awata *et al.*, 1996). Maximum displacement of surface rupture was observed at Nojima-Hirabayashi located at the northern part as 180 cm right lateral and 130 cm reverse components (Awata *et al.*, 1996). On 6th November, the Geological Survey of Japan began a drilling project in order to explore the natural state of fault zone just after the big earthquake at Nojima Hirabayashi, and successfully penetrated the fault zone at drilling depth of 625 m and recovered the drill core containing almost entire fault zone rocks at 19th, January 1996 (Ito *et al.*, 1996). The drill core of Geological Survey of Japan (GSJ core) has a total length of about 600 m (152.24 to 746.60 m depth), including several oriented portions.

Fault rock distribution is one of the most important issues for understanding the dynamics of the fault zone and chemical reactions during seismic cycles (Tanaka and Itaya 1998). However, previous studies of the natural fault rocks in a brittle regime, from the seismogenic depth to the surface have been limited for following two reasons, (1) processing the brittle fault rocks have some difficulties since they are generally very soft and fragile, and (2) outcrop observation is limited because they are easily eroded and if present, they are usually modified mechanically and chemically by weathering in a surface condition.

The GSJ core contains not only fault rocks that experienced a big earthquake but also a succession from host rock to fault rocks all of which have

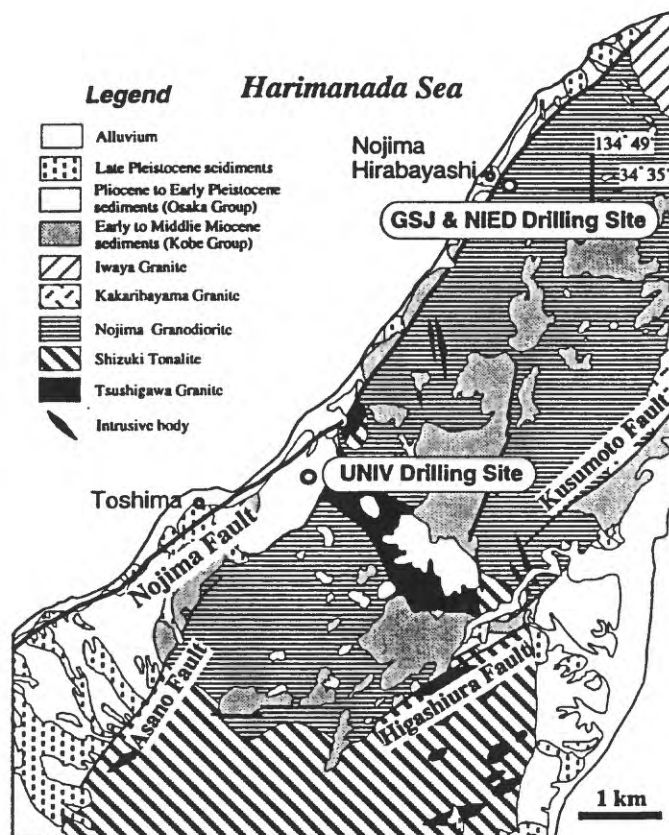


Fig.1 Geological map along the Nojima surface rupture

never been weathered at surface condition. The Cajon Pass Project is well known as a fault related drilling project (Zoback *et al.*, 1988). The main purpose of this project was to investigate the geothermal anomaly along the San Andreas Fault, and drilling was performed about 4 km northeast from the San Andreas Fault trace (Zoback and Lachenbruch, 1992). Therefore the GSJ core is the first drill core containing the complete fault zone which preserves the condition just after the earthquake. Detailed description and examination of the fault rocks, including distribution, characterization of deformation microscopic texture, almost in-situ fluid rock interaction should be recorded and these mechanisms should also be clarified for future development of fault rock research. In this paper, we will describe the fault rock distribution based on numerous polished surface observations, results of microscopic observation of deformation and alteration textures, and the results of measurements for major and trace chemical elements.

These data will lead us to figure out the role of each shear zone in an active fault during seismic cycles at shallow depths in granitic crust.

### Outline of geology along the Nojima surface rupture and drill core

The Nojima fault is an 8 km long right-lateral active fault with minor reverse component (The research group for active faults of Japan, 1991). This fault runs along the northwestern margin of Awaji Island (Fig.1), trending northeast and dipping southeastwards at a high angle (Mizuno *et al.* 1990). The fault juxtaposes Cretaceous granitic rocks (Nojima Granodiorite, 66 to 88 Ma; Takahashi 1992) partly overlain by Neogene and Quaternary sediments on the southeastern side with Neogene and Quaternary sediments on the northwestern side. The sediments on both sides belong to the middle Miocene Kobe Group and Plio-Pleistocene Osaka Group. These groups are composed mainly of sand and gravel beds intercalated with thin layers of mud (Mizuno *et al.*, 1990).

The surface rupture was generated basically along the Nojima fault but extended farther southwest. Total length was estimated as 10 km (Awata *et al.*, 1996) to 18 km (Lin and Uda 1996). The southwestern part of the surface rupture deviated from the Nojima fault to the west and extended into Neogene sediments (Awata *et al.*, 1996).

The GSJ drilling site was located about 74.6 m southeast of the surface rupture of the Nojima fault near Nojima-Hirabayashi. The drilling was performed down to 746.7 m in length along its direction with average inclination of about 84 degrees to the northwest, and succeeded in penetrating and recovering the drill core containing the surface of Nojima fault at the drilling depth of 625 m. The dip of the Nojima fault is inferred to be 83 degrees from a spatial relationship between the outcrop of surface rupture and the depth of the fault surface in the drilling hole. The GSJ core consists mainly of Nojima granodiorite accompanied by minor porphyry intrusions. The fault rocks (fault gouge, fault breccia and cataclasite) are distributed at an extent from 426 to 746.7 m depth (Ito *et al.*, 1996, Tanaka *et al.*, 1998).

Each shear zone in a fault zone is relatively narrow and surrounded by less deformed and altered, and widely distributed fault related rocks. This type of fault rock is referred to as weakly - pulverized/ altered rocks (WPAR) in this paper (Tanaka *et al.*, 1998).

### Fault rock distribution along the GSJ core

#### Analytical methods

Repeated failures during core processing led us to develop the method outlined in Fig.2. This is rather complicated but composed of seven steps mainly for two reasons, first is to avoid confusion during processing and second is to satisfy following three requirements. (1) Long term preservation for memorial of this earthquake, (2) the core volume necessary for basic research (as is described in this paper) should be minimum, and (3) maximum amount and volume of the core, which as much as preserves original conditions, should be remained for various research such as radiometric dating, thermal history analysis, permeability and strength measurements, and any other physical and chemical analysis requiring large volume of cores, at the time of distribution.

### Work flow of core processing

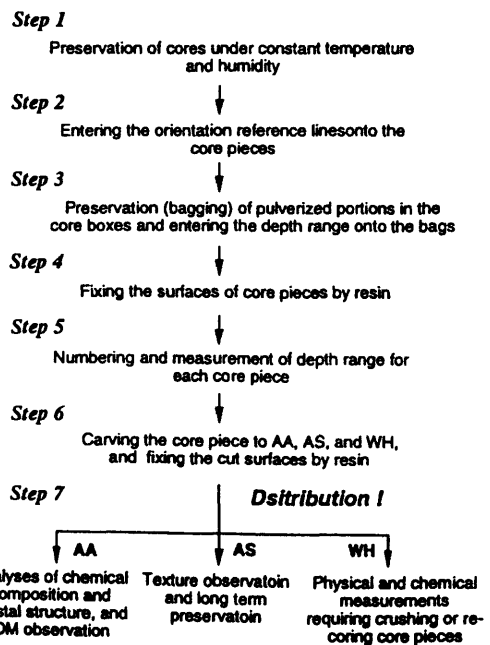


Fig. 2 Work flow of core processing

This method was applied to the depth extent from 553.39m to 718.20 m, where most of the core was composed of soft and fragile fault rocks.

Fig.3 shows the method of carving the core pieces into AH (Archive Half) and WH (Working Half) and further carving AH into AA (for Analyzing) and AS (Slab for preservation). After carving, again fixing the carved surface by resin (Step 6). AA was utilized mainly by chemical composition and crystal structure analysis, AS for texture observations and non-destructive measurements/analysis (such as color analysis) and long term preservation after polishing the surfaces, and WH for various kinds of measurements/observations and analysis (Step 7).

For understanding the whole trend of fault rock distribution in the GSJ core, surfaces of all drill core (154.24 to 746.60 m) were at first observed visually during a period between Steps 1 and 2 and prepared a rough fault rock distribution map. Rock types in the drill core were categorized into the following six types: (1) granodiorite (host rock), (2) porphyry intrusions, (3) weakly pulverized/ altered fault-related rocks (WPAR), (4) cataclasite, (5) fault breccia, and (6) fault gouge. Categories (3) - (6) correspond to the fault rock classification followed of Higgins (1971) and Sibson (1977) that was partly modified by Tanaka *et al.*(1995). Detailed occurrence of each

rock type will be described in a later section. After completion of core processing, fault rock distribution was re-examined through observation of about 2000 pieces of polished slabs (AS) in the depth extent from 553.39 m to 718.20 m. The original fault-rock distribution map was modified and prepared more detailed fault rock distribution map. About 120 thin sections were prepared throughout the core for observation of deformation / alteration microtextures.

### Petrographic characteristics of host and fault rocks from the GSJ drill hole

#### 1. Host rock (granodiorite)

The occurrence and texture of Nojima granodiorite was described by Mizuno *et al.*,(1990) in detail. Mesoscopic textural characteristics are as follows. Short, column-shaped hornblende crystals and thin crystals of biotite are scattered in larger quartz and feldspar crystals. Feldspars are milky white in color and quartz is relatively clear. Xenoliths of basic rocks, several cm in diameter, are occasionally included. The xenoliths have a relatively dark color, possibly due to a greater abundance of mafic minerals. Biotite K-Ar ages were reported to be 81 Ma for this rock (Takahashi, 1992). In the drilled core, although some feldspar grains are altered to an orange color, few other alteration and deformation features are observed on the polished surfaces.

Under the microscope, the host rock shows some intercrystalline cracks containing carbonate and zeolite minerals, although their density is quite low and they are usually very narrow. In these veins, coexisting euhedral zeolite and carbonate minerals are occasionally observed. Rare micro-shearzones contain matrix of crushed grains of the host granodiorite and carbonate micro-grains and clasts of quartz, feldspars, zeolites and carbonate minerals. In quartz grains, wavy and blocky extinction and healed intra-grain cracks are commonly observed. Feldspar grains are less deformed than quartz, but occasionally weak wavy extinction of the feldspars can be observed. However, core portions of plagioclase crystals are commonly altered to micrograins of carbonate, zeolite and sericite. Some biotite grains are partly altered to chlorite along their cleavages. Carbonate

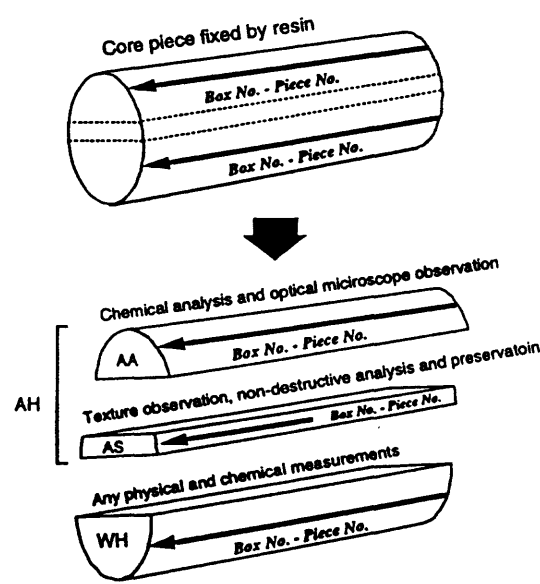


Fig.3 Carving method for core piece

minerals occasionally occur as microlenses or small columns along biotite cleavages. Kink bands are well developed in some grains of biotite at large angles to their cleavages. Hornblendes are well preserved but occasionally altered to carbonate minerals along their cleavages.

### 2. Host rock (*Porphyry intrusive body*)

Typical texture is that grayish gray colored phenocrysts are scattered in dark-green colored groundmass. Phenocrysts vary in color from milky white to light brown and grayish white vein appears with decreasing distance from the fault zone. Along the boundary between the porphyry and WPAR, veins in the WPAR cut the porphyry indicating porphyry was intruded before recent activity of the Nojima fault.

Under the microscope, the groundmass is composed of plagioclase, quartz, hornblende and biotite. Some of the plagioclase grains show the thin rectangle shape. Phenocrysts are dominated by plagioclase accompanied by quartz, biotite and hornblende. Ratio between groundmass and phenocrysts is arbitrary at places. The cores of plagioclase phenocrysts are commonly replaced by fine-grained carbonate and zeolite minerals especially at depths close to the fault zone. Very close to the fault zone, groundmass of the porphyry is commonly altered to cryptocrystalline materials. Few mafic minerals are preserved in these porphyritic rocks. All of these textures are commonly cut by carbonate and zeolite veins.

### 3. Weakly pulverized and altered fault rocks (WPAR)

This type of rock shows varying degrees of pulverization and alteration. General mesoscopic descriptions of WPAR are as follows. Host rock texture is disturbed and mafic minerals are generally reduced both in size and amount due to pulverization and alteration. The mafic minerals are generally replaced by grayish green to grayish brown colored minerals. The cores of feldspar grains are altered and generally change their color into grayish white or light orange. The density of shear surfaces is low, and the shears are generally filled with grayish white, brown and greenish gray materials. The disappearance of mafic

minerals and alteration of feldspar grains are common along these shear surfaces.

Under the microscope, intragranular cracks are prominent in quartz grains and they are commonly filled with carbonate (calcite and mafic carbonates) and zeolite (laumontite and stilbite) minerals. Intragranular cracks are less common in feldspar grains, but the filling materials are similar to those in quartz. Intergranular cracks are also prominent features. They are filled with the same minerals as the intragranular cracks, but contain relatively large, euhedral carbonate and zeolite crystals. Close relationship between carbonate and zeolite minerals are typical in the WPAR especially above the 625 m fault surface. Microscopic evidence, including crosscutting relationships among veins containing these minerals, indicate that they are precipitated almost at the same time. Micro-shear surfaces are abundant and commonly contain clasts of crushed igneous and carbonate minerals and a matrix of fine grained quartz, feldspar, carbonate and zeolite minerals. They commonly show a random fabric texture.

The cores of many feldspar grains are replaced by fine grained mafic carbonate and zeolite minerals. Comparison of alteration of feldspar grains on polished surfaces with those in thin sections clarifies that the brown or orange colored feldspar on the polished surfaces corresponds to substitution by mafic carbonate minerals and grayish white colored feldspar corresponds to substitution by zeolite minerals. Biotite grains are less abundant and smaller in size than those in host rocks, mainly due to pulverization and alteration. Mafic carbonate minerals showing a spindle shape or forming irregular aggregates are deposited between cleavages of biotite grains. Some biotite grains show complete pseudomorphic replacement by these carbonates. Other examples of deformation and alteration of biotite include (1) exfoliation brecciation along cleavages to fine grained crystals which are commonly incorporated into shear surfaces and cracks and (2) kink bands which bend the intra-cleavage carbonate and zeolite minerals. Hornblende crystals also show complete pseudomorphic replacement by cryptocrystalline dark materials.

These characteristics of pulverization and alteration, including density of intra- and inter-granular

cracks, micro-shear zones, degree of alteration of feldspar grains and mafic minerals are more intense with decreasing distance from the 625 m depth of Nojima fault zone. WPAR gradually changes to fault breccia at around 613.6 m depth.

In the hanging wall, crack filling minerals are characterized by the co-existence of carbonate with smaller amount of zeolite minerals. Hydraulic fracturing texture is not a common feature. Small numbers of their examples show that the crack filling minerals of hydraulic fracturing texture is composed of carbonate minerals. The similar textures can be observed in the footwall of the fault zone below 680 m depth.

However, the texture of WPAR is quite unique at the depths between 625 m and 656 m. The mesoscopic color of the WPAR in this extent is generally grayish white and occasionally mafic minerals or their alteration products are arranged parallel to the micro-shear zones. Under the microscope, zeolite is a typical mineral filling in intra- and inter-crystalline cracks. Few carbonate filled cracks are observed. Broken textures with blocky clasts and zeolite matrix are well observed, which is considered as evidence of hydraulic brecciation. Quartz grains are equant with little wavy extinction. Feldspar is commonly substituted by dominant zeolites. In biotite grains, small, lens-shaped mafic carbonate minerals are deposited between the cleavages. Some biotite grains are disaggregated along their cleavages and release oval grains of carbonates into the comminuted matrix along the shear surfaces. Kink bands are less common than those in WPAR in the hanging wall. Instead, cleavages of biotite show an undulating form, indicating more hydration than hanging wall. Alteration of hornblende is similar to that in the hanging wall WPAR.

#### 4. Fault breccia

Feldspar grains generally change in color to light brown or light orange and are greatly reduced in abundance. Few mafic minerals are remained in texture. Anastomosing development of micro shear zones more than 5 mm thick is commonly observed. They contain crushed fragments of host rock minerals surrounded by a matrix of brown-colored alter-

ation products. The mean size of the clasts is 3 mm, and the maximum is more than 50 mm. Some clasts are rounded in shape, possibly due to wearing and/or dissolution. The texture of the host rock or WPAR is occasionally preserved in the larger clasts. The fault breccia basically shows a random fabric but a foliated texture is observed where the fault breccia adjoins other types of fault rock, such as fault gouge and WPAR. Fault breccia is more intensely pulverized and altered with decreasing distance from the 625 m fault surface.

Under the microscope, host rock texture is no longer observed, and the typical texture is one in which larger clasts are surrounded by a finer-grained matrix, especially those in the hanging wall. The matrix is composed of fine-grained, crushed crystals of quartz and feldspars, mafic carbonate minerals and reddish-brown materials. Clasts include quartz, aggregates of healed quartz and feldspars, and carbonate minerals. Feldspar grains are heavily altered to carbonate minerals. Biotite grains are greatly reduced in their size and amount. Hornblendes and their pseudomorphic crystals are no longer observed. Foliation is recognized where reddish-brown materials, possibly iron hydroxide minerals, are concentrated, although random fabric is dominant texture. The foliations is cut by veins containing reddish-brown materials and mafic carbonate minerals.

Fault breccia occurred in lower shear zone in the footwall (711.7 m, Fig. 4) also shows a "clasts supported by matrix" texture. However, the matrix is composed of fine grained, crushed crystals of quartz and feldspar, and zeolites, and the clasts are composed predominantly of grains of quartz and feldspar derived from host rocks. The clasts have a subangular, blocky shape, suggesting that they were formed by hydraulic brecciation. Few carbonate minerals are observed.

#### 5. Cataclasite

Cataclasite is characterized by intense brecciation and minor alteration. Feldspar grains change their color to grayish white or light orange. Mafic minerals are not reduced in amount but reduced in size by brecciation. Veins are generally poorly developed.

Under the microscope, the host rock texture is almost completely obliterated by brecciation. The typical texture is a random fabric even if a foliation can be recognized at mesoscopic scale. Both clasts and matrix are composed of crushed grains derived from the host rock. Mafic minerals are well preserved. Kink bands are not observed in biotite grains, which, instead, are brecciated, reduced in size, and scattered in the matrix. Few mineral filling cracks are present. Microscopic observation of the contact between the cataclasite and the porphyry intrusion reveals that crushed grains in the cataclasite are incorporated into the intrusive rock with heavy alteration, indicating that cataclasite are formed prior to the intrusion of porphyry. Zeolite and carbonate veins are well developed in cataclasite close to the boundary with the WPAR. Feldspar grains are altered and hornblende crystals are generally obliterated close to the boundary with the WPAR, indicating that cataclasite had been formed prior to the WPAR.

#### *6. Fault gouge (light brown/greenish brown)*

Host rock texture and host rock derived minerals including feldspar and mafic minerals are completely obliterated. Instead, this type of fault gouge is composed of very fine grained materials showing various colors such as dark gray, grayish brown, light grayish green and dark green. Small amounts of fine-grained and rounded clasts are scattered in the variably colored matrix. This type of fault gouge gradually developed by overprinting the fault breccia. However, in some cases, direct contacts with other types of fault rocks bounded by shear surfaces are observed. Foliations are commonly recognized by color banding of these materials.

Under the microscope, this fault gouge shows typical "clasts supported by matrix" texture. The matrix is composed of very fine grained crystals of quartz, zeolites, carbonates, iron hydroxides and minor amounts of clay minerals. The clasts are composed of crushed quartz, aggregates preserving an inherited texture of hydraulic explosion, carbonate minerals and zeolites. The clasts are finer and more rounded in shape than those in fault breccia. Feldspars are hardly recognized but a small number of relict crystals, although they are generally replaced

by carbonate minerals. Mafic minerals are no longer observed even under high magnifications (x 1000). Random fabric is a common texture and foliations recognized at mesoscopic scales are basically the planar boundary between coarser- and finer-grained zones. Dark reddish-brown, irregularly shaped materials, possibly iron hydroxide minerals, are precipitated in the coarser-grained part, resulting in the formation of color banding in the fault gouge. The dark reddish-brown materials occur in veins in some parts of the coarse gouge and as matrix and in thin foliated shear zones in other parts. These textures are overprinted by veins containing dark reddish brown materials and mafic carbonate minerals. These complicated textures indicate that micro foliations are formed at the same time or after the precipitation of the dark reddish colored materials.

These textures are overprinted by a hydraulic explosion brecciation texture in some places. The matrix of this breccia is composed of very fine-grained, mafic carbonate minerals, and the clasts are composed of brecciated grains of this type of gouge itself. Even in the case that clasts are fine grain size, reconstruction of original grain by a method similar to puzzling can be possible since, in most case, neighboring grains has similar shape of grain boundaries. This texture indicates that dilatancy occurred at the time of brecciation. These foliation and dilatant textures cannot be observed in the finer grained gouge.

#### *7. Fault gouge (dark gray)*

This type of fault gouge is found only in the central layer of the Nojima fault zone. This occurrence of dark gray gouge is unique in the GSJ core. Few fragments are observed in the gouge. Thin, black colored materials are intercalated parallel to each other. Foliation is recognized by dark gray/black color banding. The foliation is cut at a large angle by micro shear surfaces. Observation at the boundary between the light brown and dark gray gouges indicate that both the foliation developed in the dark gray gouge and the shear surfaces cutting this foliation, are cut by the boundary shear surfaces between these two gouges. The foliation developed in the light brown gouge is almost parallel to the boundary, while that in the dark gray gouge is slightly diagonal to the bound-

ary, indicating that the dark gray gouge was generated prior to the light brown gouge.

Under the microscope, the fundamental texture is "clasts supported by matrix". The matrix is composed mostly of cryptocrystalline materials, with very fine grained quartz and minor amounts of very fine grained carbonates scattered in it. Clasts are smaller and much less abundant than those contained in the light-brown fault gouge. One of the most prominent feature of this gouge is that dark brown opaque materials develop as thin layers in some places. Wavy foliations with similar patterns to the trajectory lines generated by turbulence are preserved in these thin layers. The layered texture of dark brown and cryptocrystalline materials are in some places brecciated and in other places present in clasts, indicating that the deformation occurred more than once. Dark reddish-brown materials, which are concentrated in the light-brown gouge, are not contained in the dark gray gouge. As a whole, although this type of fault gouge seems to show a random fabric texture except the layered portion of opaque materials, the very fine-grained or cryptocrystalline nature of the gouge prevents definitive discrimination of random fabric from foliated texture. These textures are cut by thin and anastomosing shear surfaces containing clay minerals and also by relatively thick veins containing mafic carbonate minerals. In some parts, these shear surfaces become a matrix of hydraulic brecciation texture and include angular clasts of this type of fault gouge. Shear surfaces which develop at large angles to the foliation described above cut the whole structure of the gouge.

#### *8. Fault gouge (greenish gray)*

This type of gouge appears near the bottom of the GSJ bore hole. It is characterized especially by dilatant nature of the core. In other words, diameter of the core is larger in this part than that in other part. Shear surfaces and cracks are less developed than other types of fault gouges at the mesoscopic scale. Cracks occasionally contain reddish brown materials similar to those contained in the light-brown fault gouge. The host rock minerals are mostly altered to clays and other secondary minerals.

Under the microscope, the basic texture of

heavily deformed part of this fault gouge is "clasts supported by matrix" and host rock structure is completely obliterated. The matrix is composed of quartz, clay minerals, zeolites and minor amounts of carbonate minerals. Clasts consist of crushed grains of quartz, carbonates and zeolites. Clay minerals are generally oriented and form distinct foliations. Rotation textures such as asymmetric pressure shadows can be seen around the clasts contained in these clay layers. These textures are cut by veins containing euhedral zeolites and carbonate minerals. The dilatant nature and greenish gray color observed in the core at mesoscopic scale seem to result from crystal characteristics of these clay minerals.

#### **Distribution of shear zones and fault rocks in the GSJ core**

At the mesoscopic scale of observation, fault-related pulverization and alteration gradually increase in the GSJ core from the drilling depth of 426 m, just beneath the porphyry dikes, to the bottom of the drill hole. Fresh host rocks are present at shallower depths and consist of Nojima granodiorite and porphyry dikes. The host rocks also contain shear zones, but these zones are relatively thin, consolidated and isolated compared to those at the depths greater than 426 m. For these reasons, the extent from the depth of 426 m to the bottom of the core (747 m) is treated as the Nojima fault zone in this paper. However, because pulverization and alteration are observed even at the bottom of the core, the fault zone may extend to greater depths. In the Nojima fault zone, several shear zones with contrasting characteristics are present, as described above, and they are rather concentrated in the depth range from 489.57 to 746.70 m (Fig. 4). Thus, the detailed fault rock distribution is examined in this extent for further analysis.

The Nojima fault zone contains seven major shear zones, from shallower to deeper, they are: UCZ, USZ, MSZ, LSZ-1, LCZ-1, LCZ-2 and LSZ-2. Each shear zone is surrounded by WPAR. MSZ is regarded as the central zone of the Nojima fault for the following reasons. (1) The MSZ is one of the thickest shear zones and the only one with a thick fault breccia zone. (2) Density, porosity, elastic wave velocity and

other physical data show a distinct change or anomalies especially in this zone (Ito *et al.*, 1996). (3) Compaction or mass loss and possible evidence for heat generation have been detected in this zone by means of chemical measurements, as described later. These data suggest that the MSZ contains fault surfaces activated by earthquakes including the 1995 Hyogoken-Nanbu earthquake. Thus, we propose in this paper that the fault surface appeared at the bottom of the fault gouge zone in MSZ (625.27 m) as a Nojima fault surface. However, we cannot unambiguously determine that this surface is the main surface activated by the 1995 earthquake, because of the lack of clear evidence.

A regular arrangement of fault rocks is recognized in the hanging wall directly above the MSZ, downwards from host rock, WPAR through fault breccia and finally into fault gouge. Meanwhile, in the footwall, each shear zone has unique characteristics and is surrounded by WPAR. The Nojima fault zone in the hanging wall includes a shear zone characterized by explosion brecciation (LSZ-1), two cataclasite zones (LCZ-1 and LCZ-2) and a dilatant and oriented-clay dominated shear zone (LSZ-2). These facts suggest that (1) the hanging wall above the MSZ can be treated as a shear zone of the MSZ, and (2) the role of each shear zone in the footwall is distinctive.

A number of additional thin shear zones containing fault gouge and cataclasite are also recognized in the Nojima fault zone. Four relatively thick shear zones are recognized. Although they may be regarded as nucleations of shear localization, further examinations, including microtextural observations, chemical measurements, and comparison of the results between these and physical logging data are necessary for clarifying this question.

#### Chemical composition analysis

#### Methods

Powder samples were prepared from throughout the GSJ core in order to obtain the major and trace element compositions by whole rock X-Ray Fluorescence methods (XRF). Spot samples were obtained from the extent of host rock distribution (above 426

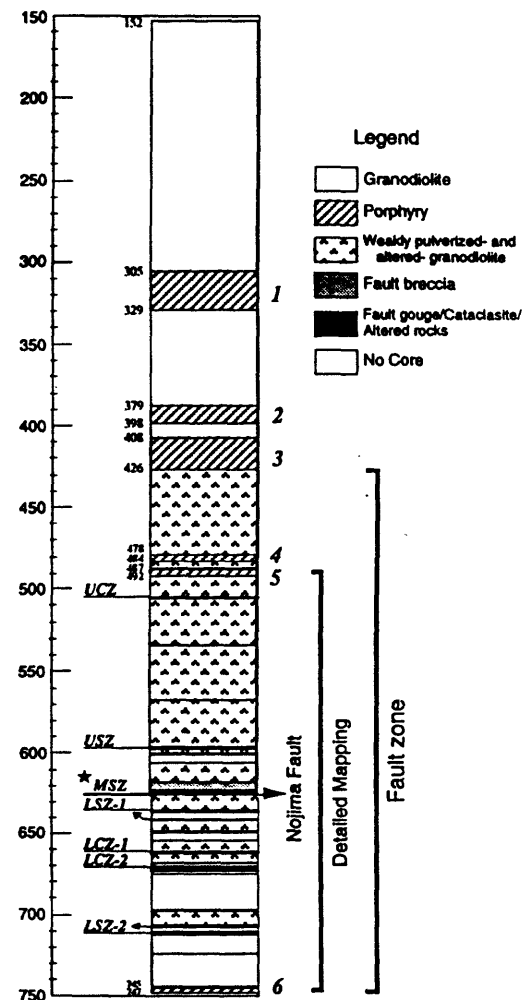


Fig.4 Fault rock distribution along the GSJ core

m depth). In the extent from 492 m to the bottom of the core (746.7 m), in which several shear zones are concentrated, samples were prepared at 50 cm intervals, and 80 samples were selected at average intervals of about 3 m and total 94 samples were analyzed. Many more samples are still waiting in a line to than we have analysed. Major elements are measured by fused glass bead method by using GSJ standard chemical composition materials and presented as oxide forms. Trace elements are quantified by direct press method. The volatile components are measured by gravity methods, samples were heated at 110°C for 3 hours and measuring the reduced weight. They are presented as  $H_2O$ . Loss of weight after ignition at 1000°C for 3 hours was also measured and presented

as LOI. The weight ratio of major elements,  $H_2O$  and LOI were combined and normalized to 100%. CHN measurements were also performed to quantify the volatile components. Only C is presented as  $CO_2$  wt% in this paper, since the abundant contents of C allow more accurate quantification than H and N.

These data are analyzed by the following methods. (1) Results from four fresh host rock samples are averaged and treated as the initial chemical components of fault rocks of granodiorite origin. Major and trace chemical compositions of all samples are normalized by host rock standard compositions, and the modes of chemical element distribution are examined by comparing with the fault rock distribution. (2) Diagrams of normalized values of loss of ignition versus each element are prepared and behavior of chemical elements are analyzed with respect to the fluids in the fault zone. (3) Isocon diagrams are prepared for typical fault rocks and mass loss/gain are estimated for each shear zone.

## Results

### 1. Comparison between normalized chemical elements and fault rock distribution

Results are shown graphically in Fig. 5. Two distinct trends were found.

(a) Behavior of chemical elements are classified basically into two types, one is depleted in the WPAR and increased in the MSZ (This type is referred to as C type elements in this paper), and another is increased in the WPAR and depleted in the MSZ (D type elements). C type elements are  $SiO_2$ ,  $K_2O$  and  $Na_2O$  for major elements and Rb, Th and Pb for trace elements. D type elements are  $TiO_2$ ,  $Al_2O_3$ ,  $Fe_2O_3$ ,  $MnO$ ,  $MgO$ ,  $CaO$  and  $P_2O_5$  for major elements and Ba, Nb, Zr, Y, Sr, Cu, Co, Cr, V and Sc for trace elements. Degree of increase/decrease in both C and D type elements is larger in the WPAR in the hanging wall than in the footwall. Ce and La seem to behave as an intermediate between these two types, that is, they are slightly increased in the WPAR and also slightly increased in the MSZ. These trends also indicate that the MSZ is the central zone for chemical behavior of the Nojima fault.

(b) Volatile contents are two to four times increased even in the most upper portion of WPAR

(465 m depth) and finally attained to almost 10 times in the MSZ compared to the standard host rock. This indicates that marginal part of the fault zone can be defined as fluid increase zone since other major and trace elements start to change their contents at the UCZ shear zone at around 500 m depth.

The chemical trends of each shear zone are as follows.

(c) Most of the C and D type elements start change their contents at the depth of the UCZ shear zone except Y.

(d) Little change in chemical compositions is observed in the USZ shear zone, compared to the surrounding WPAR.

(e) In the MSZ shear zone, both C and D type elements are gradually increased/decreased to the central layers of fault gouge in the hanging wall. They are suddenly decreased/increased to the similar level with hanging wall WPAR at the just beneath the MSZ.  $CO_2 + H_2O$  contents measured by the CHN method are well concordant with those measured by XRF method, except for the 99-1 sample which is part of the dark gray gouge in the MSZ shear zone. The contents measured by CHN method for this sample are much larger value than those measured by the XRF method ( $H_2O + LOI$ ). Therefore, this sample was treated in acidic solution to dissolve the carbonate minerals, and the  $H_2O + CO_2$  contents remeasured by the CHN method. C contents are 5.03 wt% before acidic treatment and 4.04 wt% after this treatment, indicating 0.99 wt% of C (3.63 wt% of  $CO_2$ ) was incorporated in the carbonate minerals. This results indicate that the remaining 4.04 wt% of C should be regarded as organic carbon or graphite.

(f) In the LSZ-1 shear zone,  $CaO$ ,  $CO_2$ , Y and Cu contents are twice as high as those of the surrounding WPAR. This trend suggests that the LSZ-1 shear zone is dominated by carbonate minerals.

(g) C type elements seem to be slightly depleted in the two cataclasite zones in the footwall (LCZ-1 and LCZ-2) but they show relatively similar values to the host rocks.

(h) C type elements are generally depleted and D type elements are increased in the LSZ-2 shear zones compared to those of surrounding WPAR.

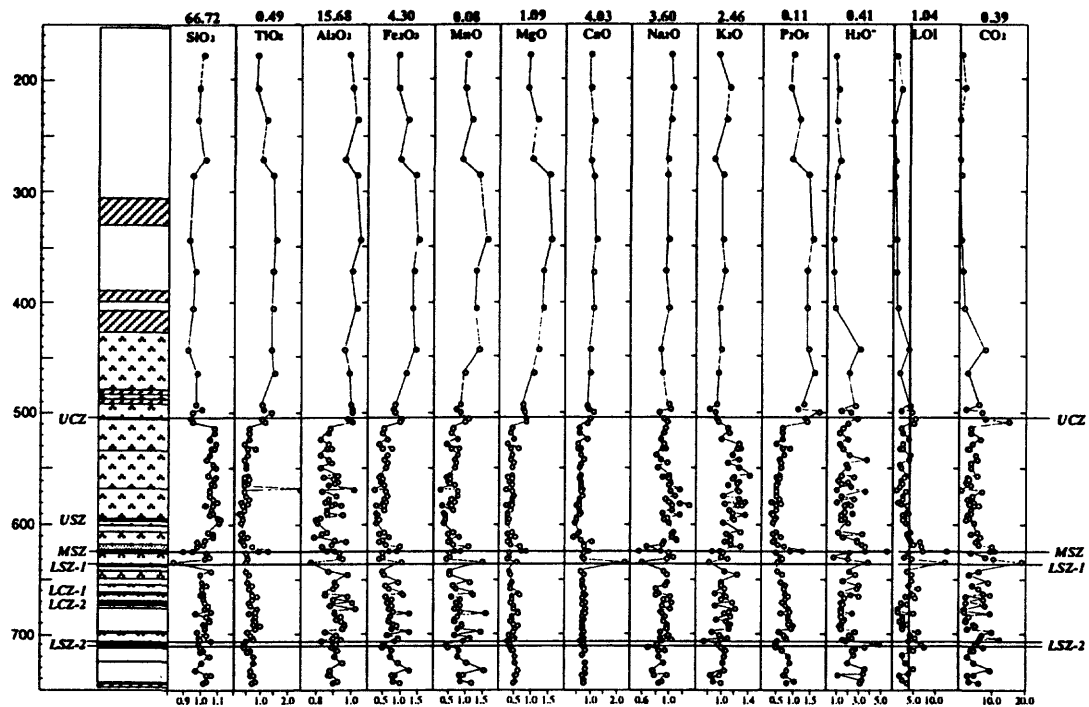


**Fig.5 Fault rock distribution and major element chemical composition**

## 2. Results from examinations of LOI vs each chemical elements

Results of volatile components ( $H_2O^-$ , LOI and  $CO_2$  in Fig.5) analysis show that they are generally more contained than host rocks (normalized value,  $>1.0$ ) and their distribution patterns are different from those of C and D type elements. Thus LOI is selected to represent the volatile components and examined the relationship between LOI values and major and trace chemical components (Figs.7,8). Ideally the host rock chemical component is indicated by (1.0, 1.0) in this diagram. The diagrams show two characteristic relationships that one is start from around (1.0, 1.0) and contents increases and attains to maximum at 2.5 to 4.0 of normalized LOI values followed by decrease the contents to around (1.0, 1.0) at the 6.0 to 7.0 of LOI, and another shows completely reverse trend but minimum values are also corresponds to 2.5 to 4.0 of LOI values. The former is referred to as convex type and the latter a concave type. The convex type elements are  $SiO_2$ ,  $K_2O$ ,  $Na_2O$ ,  $Rb$ ,  $Pb$ ,  $Ce$  and  $La$  and others belong to concave type. Most of the convex type elements correspond to D type ele-

ments and the concave types to C type elements. Therefore, the maximum/minimum values for convex / concave type elements implies the change in mode from precipitation to depletion or vice versa at these points in WPAR.

## 3. Results from examinations of isocon diagram

Mass loss/gain are estimated by chemical elements isocon method which has been applied to other shear zones (Evans and Chester 1995, Goddard and Evans 1995). Several high field strength elements (HFS elements) including  $TiO_2$ ,  $MgO$ ,  $MnO$ ,  $P_2O_5$ ,  $Zr$  and  $Y$ , have been proposed to be immobile even under the intense pulverization and alteration conditions (Evans and Chester 1995, Goddard and Evans 1995). Among these,  $TiO_2$  may be one of the most immobile elements. The most intense pulverization and alteration are observed in MSZ shear zone. Thus, the C type elements are candidates for HFS elements as well as  $TiO_2$ . From the examinations described below,  $TiO_2$ ,  $P_2O_5$  and  $Zr$  constitute a rather straight line. Other HFS elements are somewhat arbitrary. Thus we define a isocon line by using these three HFS elements and referred to as PTZ isocon in this paper.  $V$  and  $Nb$  are also the candidate for stable HFS

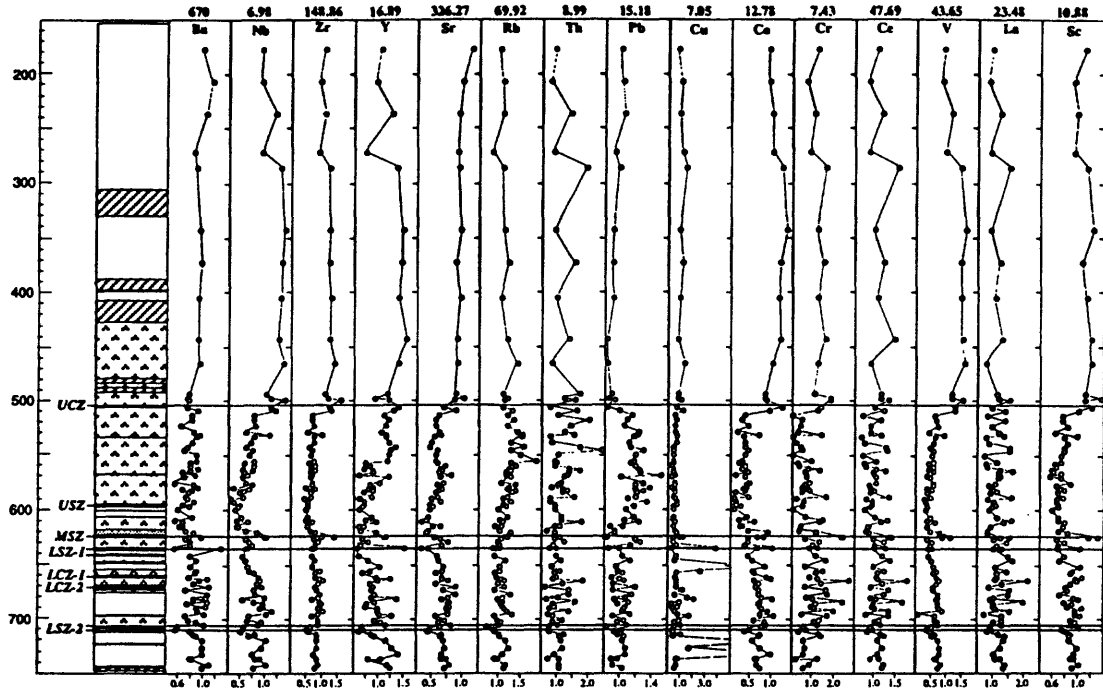


**Fig.6 Fault rock distribution vs trace elements chemical composition**

elements. However, more data are necessary for using these as HFS elements.

First, concentrations of chemical elements of three WPAR, just above the MSZ (average of 4 samples), LSZ-1 (average of 3 samples) and LSZ-2 (averages from 3 samples), are compared to those of host rock samples, since it is clear that these WPAR have evolved from the host rock. Figure 9 shows that PTZ isocon of the WPAR are all less than 1, indicating the mass gain (mass ratio = 1/ inclination of the isocon line) occurred generally in the WPAR. Among these diagram, largest mass gain is recognized in the WPAR samples just above the MSZ shear zone, and intermediate gain in those just above LSZ-1 and smallest gain in those just above LSZ-2, indicating that mass gain is largest in the hanging wall of MSZ and lesser degree to the depth in the hanging wall.

From chemical trend - fault rock distribution diagram and from microtexture observations, three shear zones (MSZ, LSZ-1 and LSZ-2) have evolved from surrounding WPAR and cataclasite zone (LCZ - 2) have evolved from host rock. The deficit of chemical data prevent us from examining other shear zones. Thus isocon diagrams are examined on WPAR vs

MSZ, LSZ-1 and LSZ-2 and host rock vs LCZ-2. The results of these examinations are as follows (Figs. 10 and 11). Four results from MSZ shear zone samples (Fig. 10) indicate mass loss occurred in this shear zone and the amount of mass loss increases with depth from the fault breccia (inclination of isocon = 1.15) to the light brown gouge (2.86) and then decreases in dark gray gouge (2.00). Three results from LSZ-2 shear zone samples indicate simmilar amounts of mass gain occurred. Every HFS elements seems to be rather on a straight line. One result from LSZ-1 shear zone sample shows slight mass gain occurred in this shear zone compared to the surrounding WPAR. However, Y and MnO are very different from the trend of other HFS elements.

In the case that density of fault rocks in each shear zone are constant, volume loss/gain can be estimated by using the value of 1/inclination of PTZ mass isocon line. However lack of information of density of fault rocks prevent us to analyze this issue in detail. Reasonable estimates of density of fault rocks is  $2500 \text{ kg/m}^3$  for fault gouge and fault breccia, which coincides with the density of a kind of clay minerals, WPAR for  $2700 \text{ kg/m}^3$  and host rock and cataclasites for  $3000 \text{ kg/m}^3$ . These densities suggests that volume gain occurs in WPAR compared to host

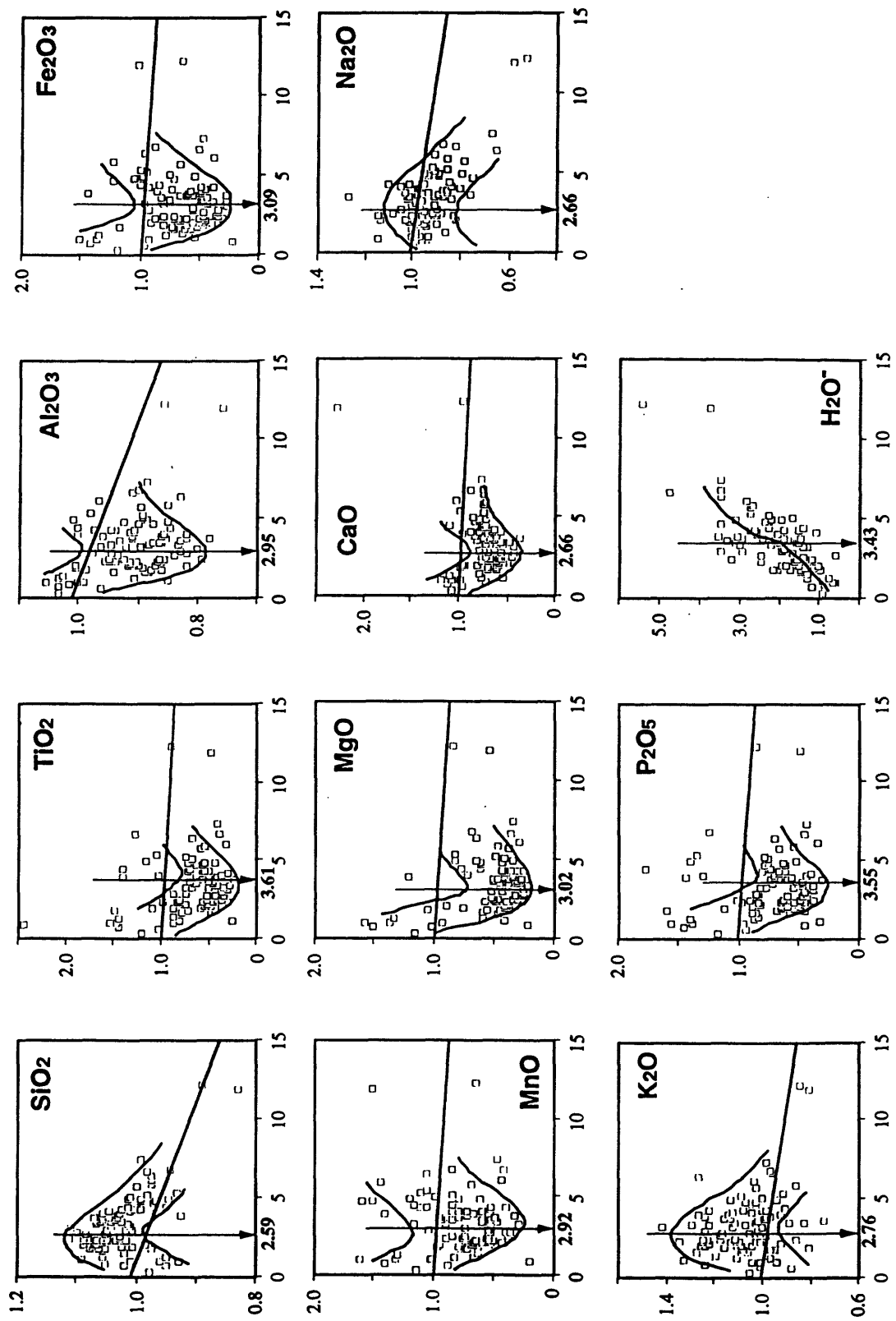


**Fig.7 Relationship between normalized LOI and major elements**

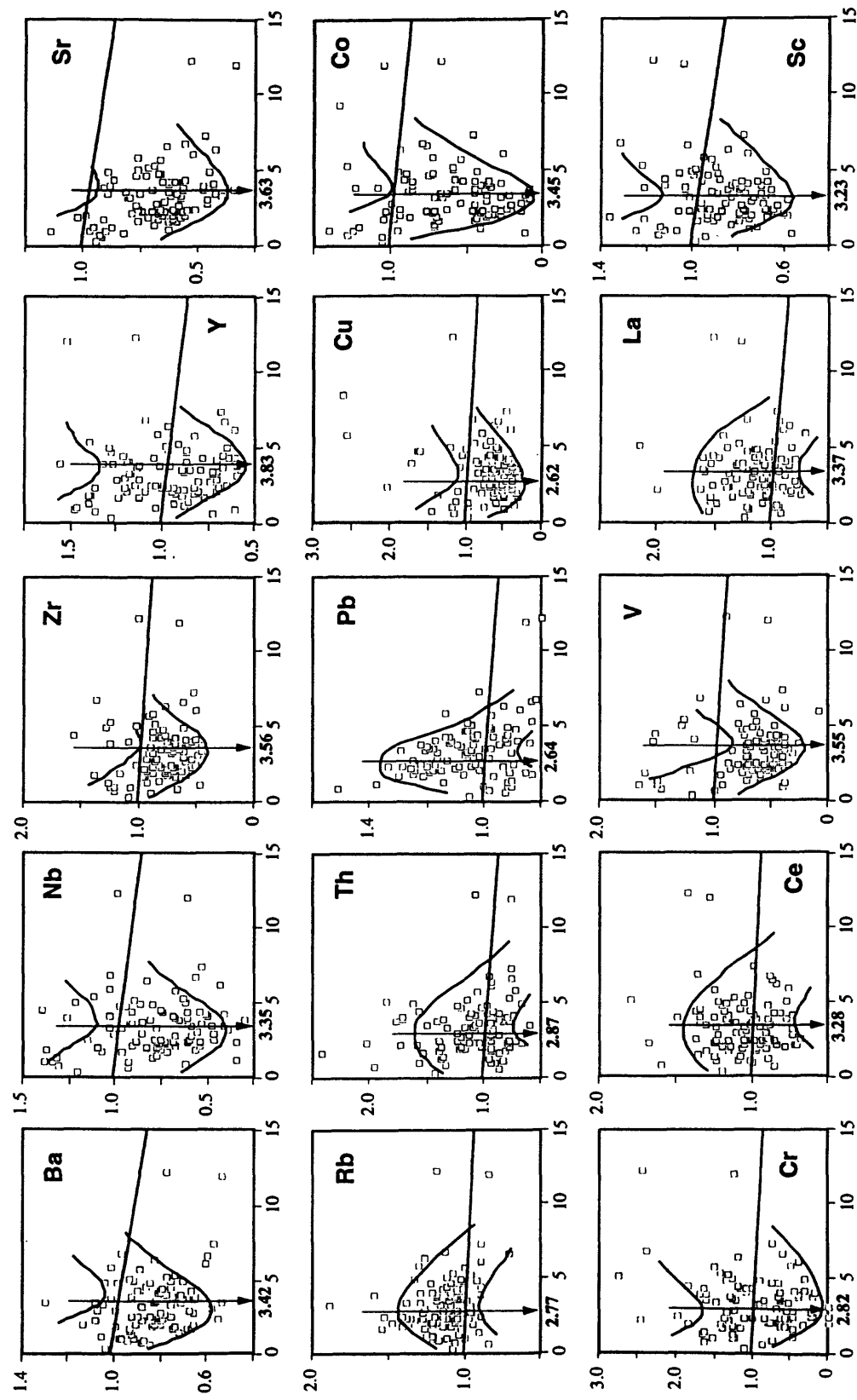


**Fig.8 Relationship between normalized LOI and minor elements**

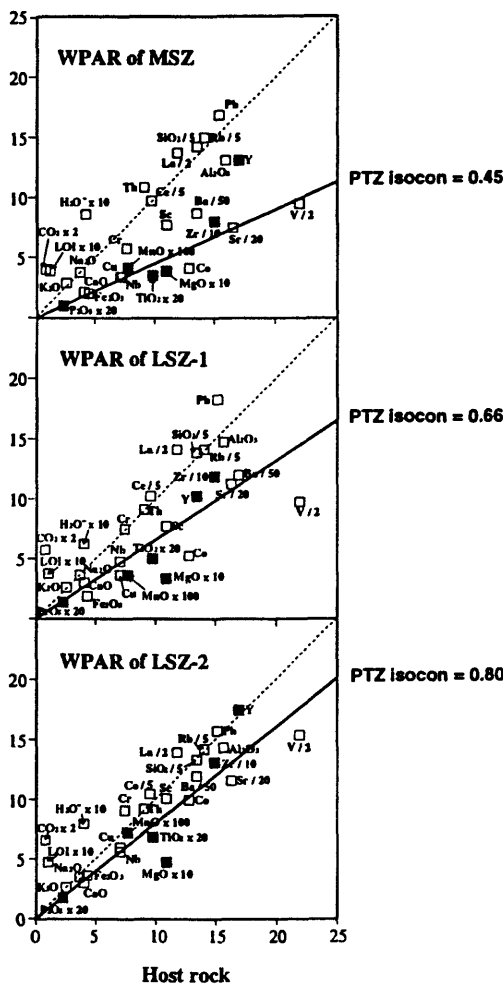


Fig.9 Isocon diagram for Host rock - WPAR

rock, volume loss occurs in MSZ shear zone compared to surrounding WPAR, volume gain occurs in LCZ-2 compared to the host rock. Almost no volume change occurred in LSZ-1 compared to the surrounding WPAR. Volume gain occurs in LSZ-2. Clearly volume gain implies dilatancy and volume loss implies compaction. Thus the MSZ-1 is the only zone showing compaction and other shear zones are regarded as dilatant shear zone except the LSZ-1 shear zone.

## Discussion

### Implications of maximum and minimum points in LOI - chemical elements diagram

From the LOI - chemical elements examination, turning points of depletion/concentration of the

most of the D and C type elements, presented as a maximum/minimum points in the Figs.7 and 8, exist within WPAR (normalized LOI values: 1 to 4), indicating that turning points of depletion/concentration of chemical elements do not coincide with the fault rock boundary. We interpret the values for maximum/minimum points of the curve in the Figs.7 and 8 imply the chemical potential for resistance to alteration and possibly to pulverization. In fact,  $TiO_2$ ,  $P_2O_5$  and  $Zr$ , which are selected as immobile HFS elements, have values larger than 3.5. In reported HFS elements,  $MnO$  and  $MgO$  are 2.92 and 3.02 respectively, suggesting that they are less immobile compared to the above elements. However,  $Y$  has a large value (3.83) but regarded as relatively unstable at the isocon diagram examination. One of the possible explanations for this is that  $Y$  may migrate together with  $Ca$  and/or  $CO_2$ , which can be seen in the chemical composition data in LSZ-1 shear zone (Figs. 5 and 6). From this view point, although the  $P_2O_5$  and  $TiO_2$ , and  $Zr$  are empirically determined to be immobile under the intense condition, this method is worthwhile to be tested in other fault zones.

### Characterization of each shear zone in the Nojima fault

Seven major shear zones are distinguished in the GSJ core penetrating the Nojima fault. They are UCZ, USZ, MSZ, LSZ-1, LCZ-1, LCZ-2 and LSZ-2. Among them the UCZ, USZ, LCZ-1 are less well characterized mainly due to the lack of microstructural (UCZ) and chemical data (USZ-1 and LCZ-1). Clearly, further work is necessary for characterizing these and other smaller shear zones, since they may have information of nucleation of shear zone. All data including detailed results of fault rock distribution, microtexture examination and results of chemical composition measurements are available for MSZ, LSZ-1, LCZ-2 and LSZ-2. However, the LCZ-2 had clearly been formed prior to the recent activity, as evidenced by overprinting relationship between porphyry intrusive dikes and the cataclasite. Although this zone should have some implications for the evolution of the Nojima fault, we eliminate this cataclasite zone from the present discussion in order to concentrate on clarifying the mechanisms of seis-

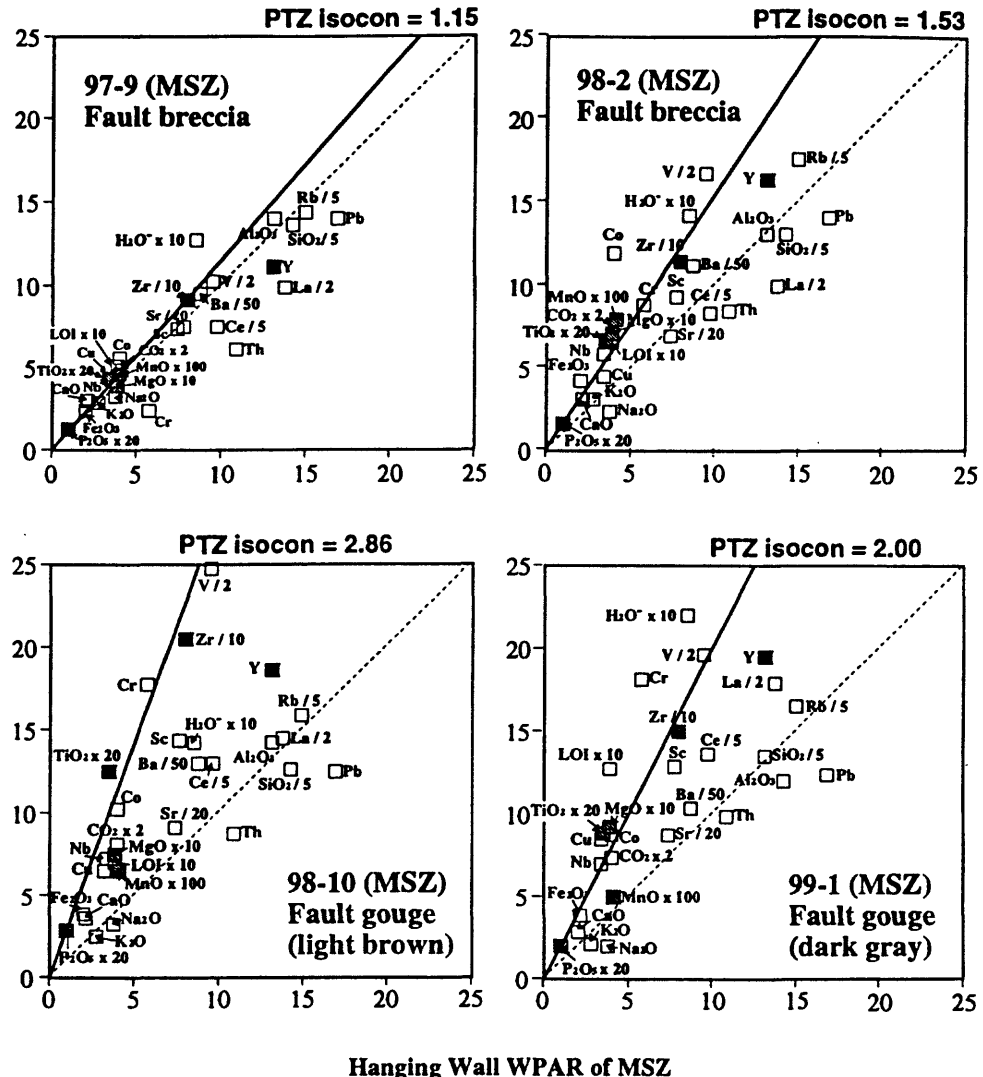


Fig.10 Isocon diagram for WPAR - MSZ

## mic faulting at shallow depths in granitic crust.

Fault rock distribution analysis clarifies that the MSZ is the most prominent and thickest shear zone in the Nojima fault zone and contains fault breccia and two kinds of fault gouge, each showing light brown and dark gray fault color. The light brown gouge overprints the fault breccia which further overprints the WPAR, indicating gradual shear localization had occurred in the MSZ. The light brown gouge also overprints the dark gray gouge, which indicate that the light brown gouge is the newest fault gouge in the MSZ and may have been activated during the 1995 Hyogoken-Nanbu earthquake. Microstructural observation reveals that (1) foliations are rarely ob-

served in this shear zone, except in thin and minor layers filled with reddish brown materials developed in fault breccia and light brown fault gouge. In other words, the most dominant texture is random fabric. (2) The wavy shape foliation, which is similar to the trajectory lines of turbulence composed of dark brown materials, occurred in the dark fault gouge. In these two zones, prominent compaction process possibly caused by mechanical wear and dissolution is suggested by constant mass isocon analysis. These observations and considerations lead us to conclude that the MSZ shear zone formed by high velocity motion of the fault. Both chemical composition and CHN measurements indicate that the dark brown materials contained in dark gray gouge are organic carbon or graphite. As it is clear that these fault rocks

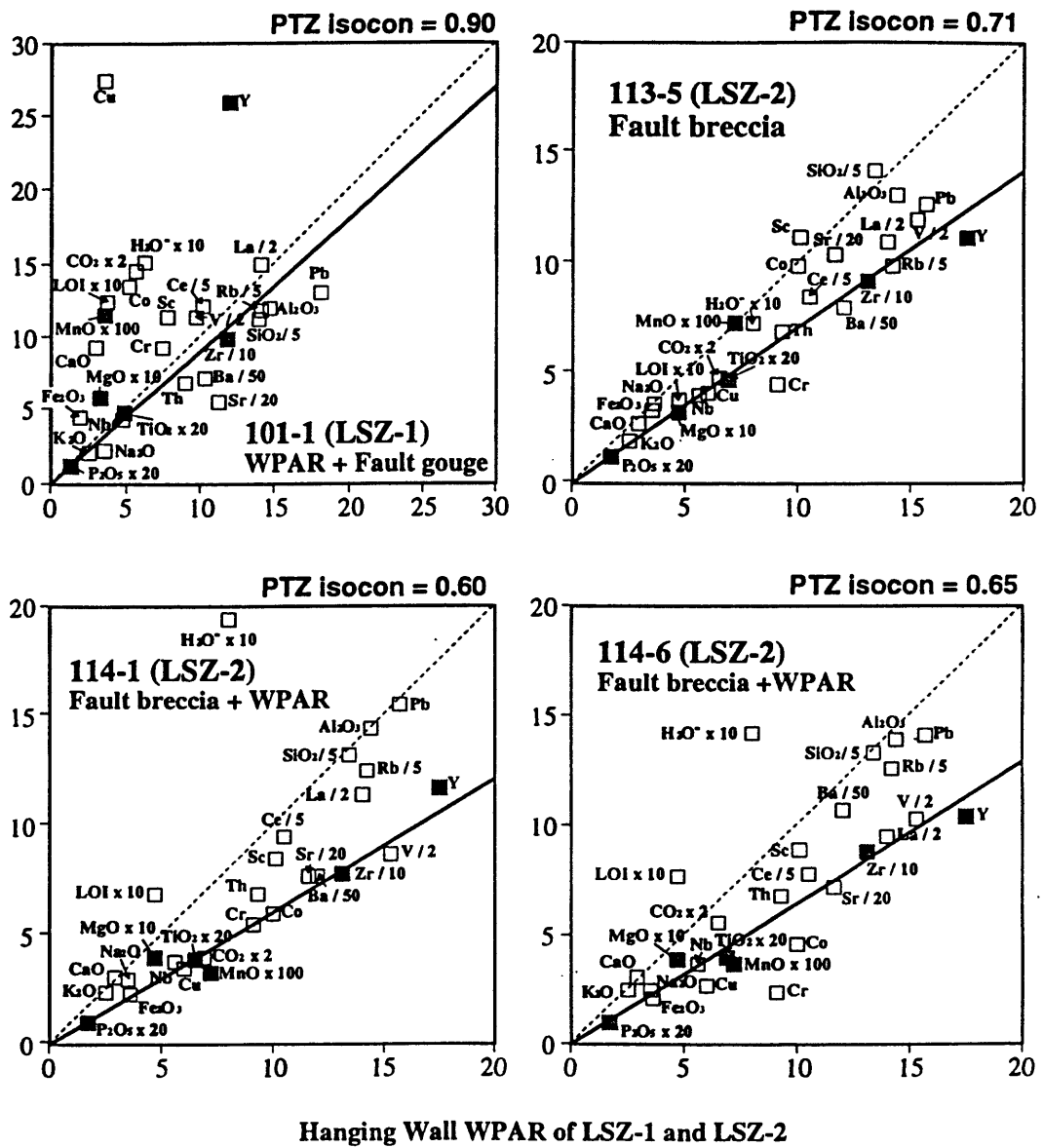


Fig.11 Isocon diagram for WPAR - LSZ-1, LSZ-2

had been derived from granodiorite, some difficulties arise about their origin if these materials are organic carbon. Thus, we treat these materials as graphite in this paper. If so, the only possible origin of graphite could be the carbonate minerals or  $\text{CO}_2$  gas, suggesting that deoxidation occurred in this gouge, possibly caused by frictional heating during the co-seismic period. Although this is not a concrete conclusion, it support the hypothesis that the MSZ is a high-velocity, and localized co-seismic shear zone that the wavy foliation in dark gray gouge is similar to the turbu-

lence trajectory may also support this hypothesis.

Microstructural observation reveals that LSZ-1 contains small amounts of carbonate minerals which are generally limited to intercalations between cleavages of relict biotites. In contrast, zeolite is abundant in the matrix of hydraulically brecciated rock and as an alteration product of feldspar. It still remains ambiguous for explaining the general lack of carbonate in this shear zone. However they are generally limited to be present in biotite crystals suggest slower rate of fluid flow containing  $\text{CO}_2$  gas than those flowing in cracks. Thus it is highly possible that they had been formed during the interseismic periods.

Co-seismic activity of this fault zone is clearly evidenced by dominant hydraulic brecciation texture which also implies the fluid dominant condition prior to seismic faulting. This fluid could be derived from slower rate flow thorough the biotite cleavage and/or intracrystalline path in feldspars, which is evidenced by alteration and substitution of feldspars by zeolites, and trapped in this shear zone. The fluid is possibly of deeper origin, because the relatively thick, impermeable layers of the MSZ preclude the down flow of fluids of meteoric origin. From these considerations, The LSZ-1 could have been a fluid-rich (possibly deeper origin), co-seismic brecciation zone during seismic cycles.

The distinctive characteristics of the LSZ-2 shear zone at mesoscopic scale is dilatancy of the core. Microscopic observation reveals that the fault rocks in this shear zone are dominated by fault gouge containing clay minerals and characterized by a foliation texture caused by preferred orientation of clay particles. The results of constant mass isocon analysis indicate that fault rocks in this zone show a strong dilatancy compared to those of surrounding WPAR. The facts that they contain abundant clay minerals and show dilatancy indicate that effective pressure in this shear zone is quite low compared to other shear zones. The asymmetric clay particle trails extending on both sides of the clasts indicate that the mode of deformation of the clay minerals is shear flow resulting in rotation of particles. This texture could be a candidate for slow creep structure based on the similarities between the textures in the clay gouge and those formed by viscous flow experiments. In a viscous flow experiment, flow trajectories develop parallel to each other if the flow velocity is quite slow ( $R < 1.0$ ) and in the case that a cylindrical column exists in such a flow, flow trajectories envelope the columns. Thus, we infer that these textures developed by slow creep motion during the interseismic period.

#### *Characterization of the WPAR*

The WPAR is widely distributed, surrounding the every shear zone in the GSJ core. It generally shows an intermediate pulverization and alteration textures between the host rock and fault breccia, except for the depth range from 625 m to 656 m where

the LSZ-1 shear zone appears. Constant mass isocon analysis suggests that the WPAR generally shows dilatancy and depletion of C type elements. However, in the extent between 426 m and 500 m, the uppermost part of the WPAR in the hanging wall is characterized chemically only by LOI increase. Thus, the WPAR can be regarded as a dilatancy zone or a fluid-increase zone. As described above, the MSZ and LSZ-1 are regarded as co-seismic high-velocity shear zones and LSZ-2 is regarded as an interseismic, low-velocity shear zone. The WPAR is involved in these shear zones, suggesting that they were generated during co-seismic periods at the marginal part of the shear zone. During interseismic periods they could be the conduit for fluid flow, due to crack opening and dilatancy. The presence of euhedral, large grains of carbonate and zeolite filling cracks may support this hypothesis.

#### *Differentiation of roles for shear zones during seismic cycle in the Nojima fault*

Recently the concept of a shear zone within a fault is greatly revised mainly based on micro structural observations and chemical measurements (Chester & Logan 1986, Chester et al., 1993, Evans & Chester 1995, Evans & Goddard 1995, Evans et al., 1997). Two distinct zones are recognized so far in the fault zone from these results. One is the fault core, which is characterized by relatively low shear strength and very low permeability. Another is the damaged zone, which has a tabular form and surrounds the fault core. The damaged zone is characterized by moderate strength and moderate to high permeability. These two zones are further surrounded by the host rock which shows higher shear strength and quite low permeability. The fault core - damaged zone model is quite reasonable for understanding the fault mechanics during seismic cycles. However, we will try to construct a revised model since we are now understanding a more detailed mechanism of fault activity during seismic cycles through a vast amount core observation on polished surfaces, micro structural observations on more than 100 thin sections and examinations both major and trace chemical elements of 94 samples, as described so far.

Physical logging results, mesoscopic and mi-

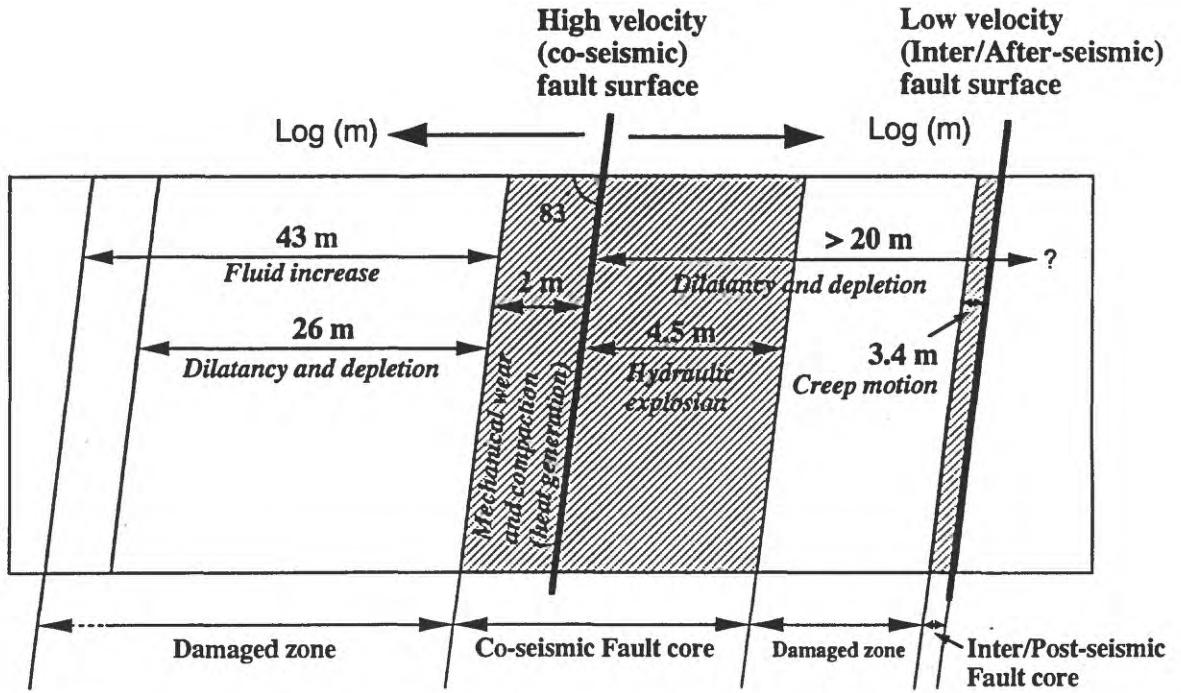


Fig.12 Distribution and role of shear zones

crostructural observations and the results of chemical analysis all indicate that the centralized shear zone in the Nojima fault zone is the MSZ, which shows a distinct compaction and mechanical wearing and/or dissolution possibly accompanying heat generating by friction with high velocity motion of fault surface. The width of this zone is measured as 2.0 m by projecting the extent of this shear zone to the line at right angles to the fault surface. LSZ-1 is located just beneath the MSZ and is also regarded as a co-seismic fault surface, based on dominant texture of explosion brecciation. The thickness of the LSZ-1 is 4.5 m. Thus we interpret that the fault core attains a total of 6.5 m thickness and is composed of two parts each of which played a different role during earthquakes. We refer to this as the co-seismic fault core. The co-seismic fault core is surrounded by a damaged zone composed of WPAR about 43 m thick if WPAR is defined as a fluid increase zone, or 26 m thick if it is defined by dilatancy and depletion of C type elements in the hanging wall. In the footwall the dilatancy and depletion zone is thicker than 20 m. The LSZ-2 shear zone is 3.4 m thick, isolated shear zone in the footwall damaged zone. This shear zone can be regarded as an

interseismic, creeping shear zone. Thus, we interpret that a different fault core is activated during interseismic periods. This fault core is referred to as the interseismic fault core.

### Conclusions

We have performed fault rock distribution analysis throughout the GSJ core, microstructural observations of deformation and alteration under the microscope and whole rock chemical analyses. These data lead to the following conclusions.

- (1) The whole fault zone is more than 63 m in thickness and contains seven major shear zones, each showing unique characteristics, are distinguished. They are referred to as, from shallower to deeper core, UCZ, USZ, MSZ, LSZ-1, LCZ-1, LCZ-2 and LSZ-2 respectively. Every shear zone is surrounded by weakly pulverized and altered fault-related rocks (WPAR). Detailed analyses have been performed for the MSZ, LSZ-1 and LSZ-2 shear zones.
- (2) The MSZ shear zone is located at 625 m depth and has 2.0 m in thickness and is the main shear zone in the GSJ core, characterized by random fabric fault breccia and two kinds of fault gouge. The microstructural examination and chemical composition analysis clarifies that this zone is regarded as the compaction

zone due to mechanical wear and dissolution, possibly associated with heat generation. Thus this zone is interpreted as the co-seismic fault zone.

(3) The 4.5 m thick LSZ-1 shear zone is located just beneath the MSZ shear zone, and it is characterized by dominant hydraulic brecciation texture. This zone is regarded as a fluid trapped zone during the interseismic period and hydraulic explosion zone during the co-seismic period.

(4) The 3.4 m thick LSZ-2 shear zone is located 16.6 m beneath the MSZ shear zone, and characterized by a great increase in volume and distinct foliation produced by preferred orientation of clay minerals. This shear zone is regarded as a dilatant, slow-velocity creeping zone of the interseismic periods.

(5) The WPAR surrounding these shear zones is characterized by volume increase and numerous cracks containing carbonate and zeolite minerals.

This zone is regarded as a dilatant, co-seismic zone at the marginal part of the main shear surfaces.

(6) The MSZ and LSZ-1 shear zones are regarded as the co-seismic fault core, in which each shear zone behaved differently as described above. The LSZ-2 shear zone is regarded as the inter/after seismic fault core. As a result, each shear zone which has a different role in the seismic cycle have been clarified in this paper.

## References

Awata Y., Mizuno K., Sugiyama Y., Imura R., Shimokawa K., Okumura K., Kimura K. & Tsukuda E. 1995. Surface fault ruptures associated with the Hyogo-ken Nanbu (Kobe) earthquake of 1995, Japan. *Eos Transactions, American Geophysical Union* 76, 46, Suppl., 372.

Chester F. M. & Logan J. M. 1986. Implications for mechanical properties of brittle faults from observations of the Punchbowl fault zone, California. *Pure and Applied Geophysics* 124, 79-106.

Chester F.M., Evans J.P. and Biegel R.L. 1993. Internal Structure and weakening mechanisms of the San Andreas Fault. *Journal of Geophysical Research*

98, 771-786.

Evans J. P. & Chester F.M. 1995. Fluid-rock interaction in faults of the San Andreas system: Inferences from San Gabriel fault rock geochemistry and microstructures. *Journal of Geophysical Research* 100, 13007-13020.

Evans J. P. & Goddard J. V. 1995. Chemical changes and fluid-rock interactions in faults of crystalline thrust sheets, northwestern Wyoming, U.S.A. *Journal of Structural Geology* 17, 553-547

Evans J. P., Forster C. B. & Goddard J. V. 1997. Permeability of fault-related rocks, and implications for hydraulic structure of fault zones. *Journal of Structural Geology* 19, 1391-1404.

Higgins, M. W., 1971, Cataclastic rocks. *Prof. Pap. U.S. Geol. Surv.*, 687.

Ito H., Kuwahara Y., Miyazaki M., Nishizawa O., Kiguchi T., Fujimoto K., Ohtani T., Tanaka H., Higuchi T., Agar S., Brie A., Yamamoto Y., 1996. Deep structure of the nojima fault investigated at drill hole penetraing the fault surface. *Phisical measurements*, 49, 522-535

Lin A. & Uda S. 1996. Morphological characteristics of the earthquake surface rupture which occurred on Awaji Island, associated with the 1995 Southern Hyogo Prefecture Earthquake. *The Island Arc* 5, 1-15.

Mizuno K., Hattori H., Ssangawa A. & Takahashi Y. 1990. Geology of the Akaishi District. With Geological Sheet Map at 1 : 50,000, Geological Survey of Japan. 90p.\*

Sibson, R. H., 1977, Fault rocks and fault mechanisms. *Jour. Geol. Soc. Lond.*, 133, 191-213.

The Research Group for Active Faults of Japan 1991. *Active Faults in Japan: Sheet Maps and Inventories (Revised Edition)*. University of Tokyo Press, Tokyo. 437p. \*

Takahashi Y. 1992. K - Ar ages of the granitic rocks in Awaji Island -with an emphasis on timing of mylonitization -. Gankou 87, 291 -299.\*

Tanaka H., Uehara N. and Itaya T., 1995. Timing of the cataclastic deformation along the Akaishi Tectonic Line, central Japan. Contribution to Mineralogy and Petrology 120, 150 - 158.

Tanaka, H. and Itaya T. 1998. Deep beneath the active fault. From the view point of structural petrology. Kagaku, 68, 246 - 254\*

Zoback, M.D. and Lachenbruch, A.H., 1992, Introduction to special section on the Cajon Pass scientific drilling project. Jour. Geophys. Res., 97, 4990 - 4994.

Zoback, M.D., Silver, L.T., Henyey, T. and Thatcher, W., 1988, The Cajon Pass scientific drilling experiment; Overview of Phase I. Geophys. Res. Lett., 15, 933 - 936.

\* in Japanese with English abstract

+ in Japanese

blank page

# Characterization of fault gouge from GSJ Hirabayashi core samples and implications for the activity of the Nojima fault

Koichiro Fujimoto<sup>1</sup>, Hidemi Tanaka<sup>2</sup>, Naoto Tomida<sup>2</sup>, Tomoyuki Ohtani<sup>1</sup> and Hisao Ito<sup>1</sup>

*1: Geological Survey of Japan, Tsukuba, 305-8567 Ibaraki, Japan. TEL: +81-298-54-3707, FAX: +81-298-54-3702. E-mail: fujimoto@gsj.go.jp*

*2: Department of Earth Sciences, Ehime University, 2-5 Bunkyo-cho, Matsuyama, Ehime 790-8577, Japan*

## ABSTRACT

The fault core of the Nojima Fault is investigated from structural and mineralogical point of view to elucidate the environment of the gouge formation. The fault core is about 30 cm thickness and deformation is intensively localized even there. It is composed of three types of fault gouges; type I, II and III. Type II gouge is the oldest from the cross cutting relations. It is very fine grained and contains melted material (relict of pseudotachylite?). This gouge was formed probably deeper than type II gouge. Type I gouge is also fine grained and foliated gouge. It is formed probably at the temperature ranges between 130 to 200°C. Type III gouge is random fabric and relatively coarse grained. It is formed probably the most recent and shallow level inferred from poor development of veins and sealing materials. These three types of gouge are considered to represent different age and depth of Nojima fault activity.

## Introduction

The active fault drilling at Nojima Hirabayashi after the 1995 Hyogoken-nanbu (Kobe) earthquake, SW Japan provides us with a unique opportunity to investigate subsurface fault structure and in-situ properties of the fault zone. We succeeded in penetrating through the active fault at depth immediately after the large earthquake almost for the first time in the world. This paper describes

the characteristics of the fault core and discusses on the activity of the Nojima fault.

## Outline of GSJ Hirabayashi core

Fig. 1 is a composite column showing the lithology, distribution of alteration minerals and ignition loss (LOI) (Fujimoto et al., 1999). We identified the fault core of the Nojima Fault between 623.1 to 625.3 m depth, because the thickest fault gouge in the borehole is distributed with a high dipping angle that is coincident with that of the surface rupture. Another evidence is that the results of geophysical logging (Ito et al., 1996) show various anomalies at this depth such as remarkable change of sonic wave velocity.

Core lithology is mostly Cretaceous granodiorite (Nojima granodiorite (Mizuno et al., 1990)) with some porphyry dikes. The rocks above 426 m depth are nearly intact granodiorite (Fig.2a). The borehole enters into the fault zone at 426 m depth and the rocks are affected by the fault activities even at the bottom of the borehole. We categorize four types of fault related rocks, which are weakly deformed and altered granodiorite, fault breccia, fault gouge and cataclasite based on degree of alteration and pulverization (Tanaka et al., 1999).

Characteristic alteration minerals in the fault zone are smectite, zeolites (laumontite, stilbite) and carbonate minerals (calcite, siderite, and dolomite). Alteration will be mentioned in detail in Fujimoto et

al (in prep.). Laumontite veins are inferred to have formed during the fault activity before precipitation of the carbonate minerals. Laumontite is stable at a temperature range between 130 and 200°C based on the active geothermal area data (Henley and Ellis, 1983). Calcite which is also a major sealing material at the fault core is probably the youngest authigenic mineral in the shallow level of the Nojima fault.

#### Characteristics of the fault core

Table 1 summarizes the lithology around the fault

core based on Tanaka et al. (1999). Core recovery is fairly well in this interval. Zones a and h correspond to weakly deformed and altered granodiorite, zone b corresponds to fault breccia and zones c, d, e, f and g correspond to fault gouge of the fault core, respectively. Fig. 2 shows typical polished slabs of the fault gouge. The a/b boundary is gradual and the b/c boundary is not clear, as the just boundary is not wholly recovered. The other boundaries are not gradual but shear surfaces (e.g., Fig. 2e and h).

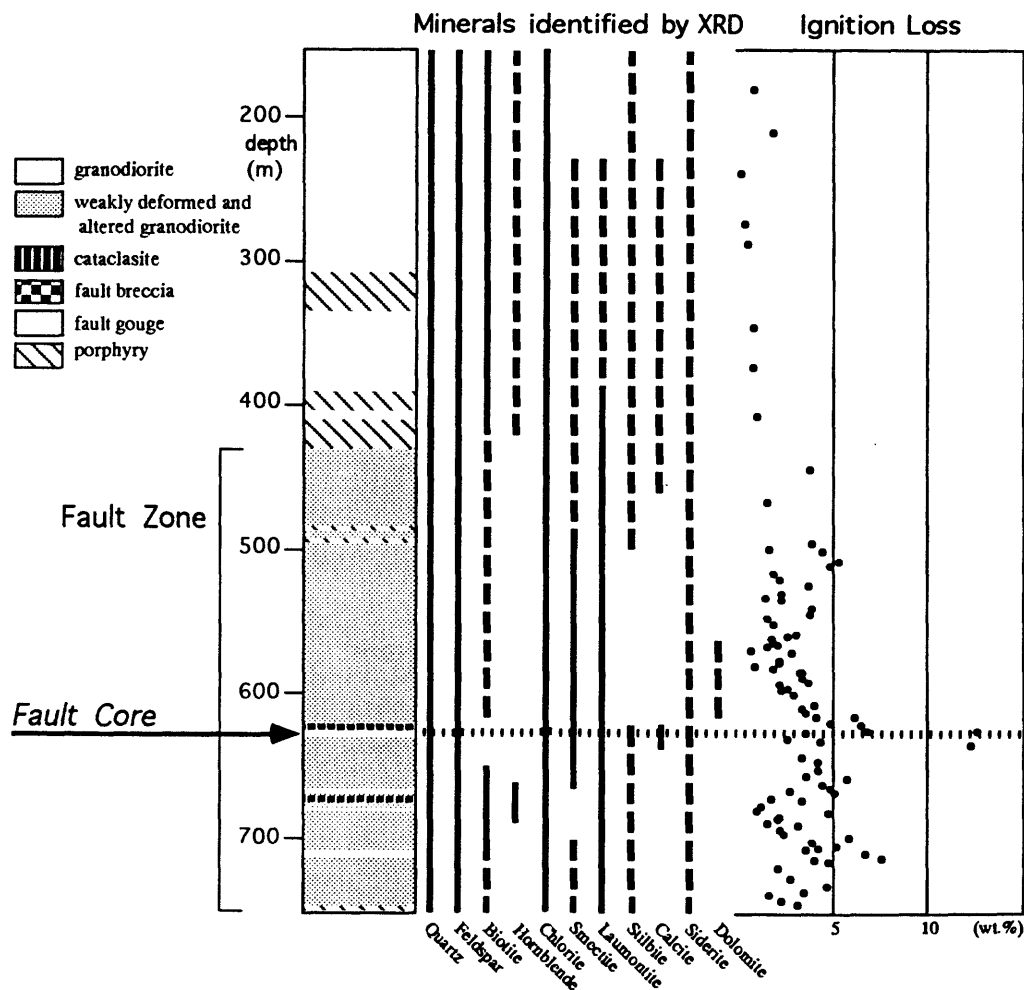


Fig.1 A composite column showing simplified lithology, distribution of mineral species by X-ray diffraction, ignition loss of the bulk rock composition after Fujimoto et al., (1999).

Zones d and f are quite similar in appearance and zones e and g are also similar except foliation. Thus, we categorize three types of fault gouge based on the texture and color as mentioned below. Type I gouge (zone a; Fig. 2c and d) is light bluish gray and foliated. Type II gouge (zone d and f; Fig 2f) is medium bluish gray and intensively foliated. Type III gouge (zone e and g; Fig.2g and h) is yellowish gray and foliation is weak. Horizontal shear surface is only recognized in type II gouge. Maximum clast size is about 1 mm in type I gouge, about 0.5 mm in type II, and about 2 mm in type III respectively. Veins of laumontite and siderite are

developed in type I gouge and laumontite and calcite veins are also developed in type II gouge, no veins are developed in type III gouge.

Crosscutting relations and development of carbonate and zeolite veins indicate that type II gouge is the oldest and type III gouge is the youngest among the three.

#### Microscopic characteristics

Occurrences of alteration minerals at the fault core are observed by scanning electron microscope (SEM).

zone	depth (m)	thickness (cm)	deformation grade / alteration grade	boundary between the lower zone	whole color	%relict of mafic mineral	color of felsic minerals	foliation	%matrix	maximum clast size	main minerals by XRD	veins	others	gouge type
a	609.12-616.34	119.0	1 / 1-2	gradual	dusky yellow	<50	orange	×	<10%	-	Qtz, Fd, Lm, Sd	laumontite & siderite		
b	616.34-623.07	114.5	2 / 2-3	gradual?	yellowish gray	0-30	orange	×	<30%	~3mm max 50 mm	Qtz, Fd, Lm, Sd	laumontite & siderite		
c	623.07-624.15	18.0	2-3 / 3	high angle shear plane	light bluish gray	0	-	○ color banding	~90%	<1mm	Qtz, Mont, Lm, Sd, Cc	laumontite & siderite		I
d	624.15-624.50	6.2	3 / 3	middle angle shear plane?	medium bluish gray	0	-	○ color banding	~100%	<0.5mm	Qtz, Mont, Lm, Cc	calcite	pseudotachylite? Lateral shear	II
e	624.50-624.65	2.6	3 / 3	low angle shear plane?	yellowish gray	0	-	×	~60%	~2mm max 10mm	Qtz, Mont, Lm, Sd, Cc	no		III
f	624.65-625.04	7.2	3 / 3	high angle shear plane	medium bluish gray	0	-	○ color banding	~100%	<0.5mm	Qtz, Mont, Lm, Cc	calcite	pseudotachylite? Lateral shear	II
g	625.04-625.27	3.7	3 / 3	middle angle shear plane	yellowish gray	0	-	○ clast alignment	~60%	~2mm max 10mm	Qtz, Mont, Lm, Sd, Cc	no		III
h	625.27-628.90	61.8	1 / 1-2	-	light gray	30-50	white	×		-	Qtz, Fd, Lm, St, Sd			

Table 1 Description of GSJ Hirabayashi core around the fault core modified from Tanaka et al., (1999). Grade of deformation and alteration is classified based on percentage of relict mafic minerals and density of shear surfaces based on naked eye observations respectively. 1 is weak, 2 is moderate and 3 is intense. Abbreviations: Qt. (quartz), Fd (feldspar), Mont (montmorillonite), Lm (laumontite), St (stilbite), Sd (siderite), and Cc (calcite).

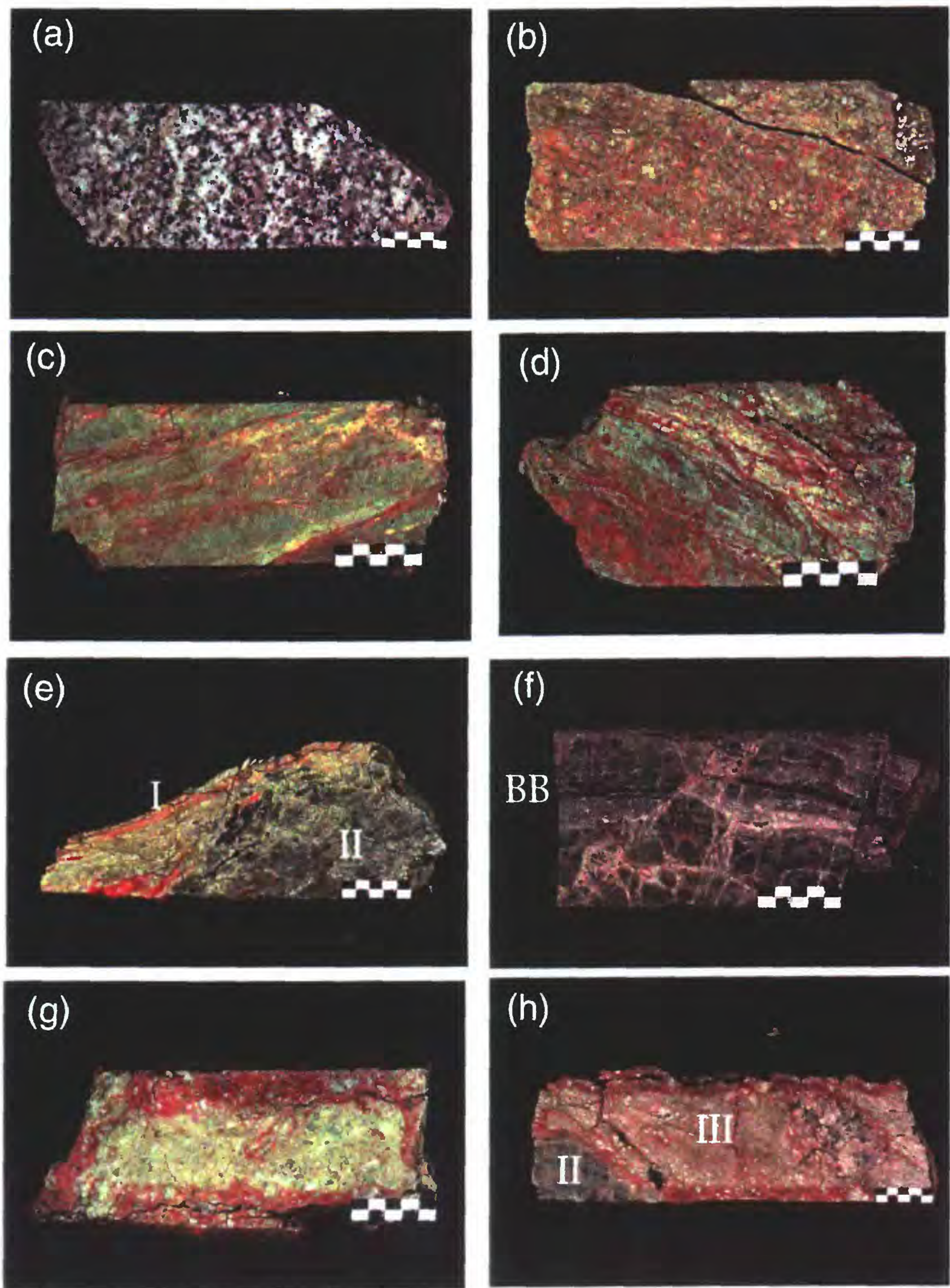


Fig.2 Polished surface of the typical samples. The scales in each photo is 25 mm long. Left side is upward direction.  
 (a) Intact granodiorite. (b) Fault breccia in zone b. (c) Type I fault gouge in zone c. (d) Type I gouge in zone c.  
 (e) Boundary between zones c and d. (f) Type II gouge in zone d. BB indicates black band possibly pseudotachylite band..  
 (g) Type III gouge in zone e. (h) Type III gouge in zone g. Characteristic features are given in Table 1.

A laumontite vein, which penetrates type I gouge at 623.5m depth, is cut by carbonate vein composed of siderite and calcite (Fig. 3a). Calcite and siderite also occur as a matrix component as shown in Fig. 3b. Calcite and siderite are both euhedral in shape in this case, which suggest that the minerals are precipitated from solution under hydrostatic condition. These facts indicate that the laumontite vein was formed before carbonate vein, after the formation of type I gouge. Laumontite also appears as a clast in the same fault gouge, which means that the laumontite formed before the fault activity. Thus, laumontite formed at multiple stages during the fault gouge formation. Considering that laumontite is formed at temperature range between 130 to 200°C (Henley and Ellis, 1983), the formation temperature of type 2 gouge is also in the same temperature range. If the temperature gradient did not vary so much from the present day (about 30°C/km), the formation depth of type II gouge should be about 4 to 7 km.

At 624.4 m depth, type II gouge was fractured with calcite filling (Fig. 3c). The texture indicates dilatation. At the same depth, a narrow cataclastic band composed of very fine materials without any carbonate sealing cuts the other structure with high angle (Fig. 3d). This unsealed cataclastic micro band may have formed in the 1995 earthquake. Type II gouge characteristically contains black band of a few mm thickness (Fig. 2f). The black band is transparent and cryptocrystalline under optical microscope as shown in Fig. 3e. The cryptocrystalline materials have granitic chemical composition and contain rounded shaped quartz as shown in Fig. 3f. The outline of the quartz is vague. They also contain elongated and oriented small bubbles (Fig. 3f). These facts indicate that the cryptocrystalline materials are formed by melting, that is, they are probably relict of pseudotachylite. They are not formed by 1995

Kobe earthquake as it is crushed and cemented with calcite. Probably they are formed below several kilometers depth as it is only recognized in type II gouge. Type II gouge formed prior to type I gouge which formed probably at about 4 to 7 km depth as mentioned before.

The vertical displacement of the Nojima fault in Quaternary age is estimated to 230m (Murata et al., 1998). Thus, the total vertical displacement should be more. The fault core of the Nojima fault experienced probably more than hundred earthquakes if the displacement is responsible for seismic activity. It is surprising that the texture of pseudotachylite remains during a few kilometers uplift and seismic activity in a fault core.

#### Pulverization and alteration

Almost continuous whole rock chemical analysis shows that the fault core is highly concentrated in  $H_2O$  and  $CO_2$ , represented by LOI (Ignition loss indicating total concentration of  $H_2O$  and  $CO_2$ ) due to formation of smectite, laumontite, siderite and calcite (Fig.1). Pulverization and alteration are strongly interactive in the fault zone

#### Concluding remarks

The fault core of the Nojima Fault is about 30 cm thickness and deformation is not homogeneous and intensively localized even in the fault core. It is composed of three types of fault gouges; type I, II and III. Type II gouge is the oldest from the cross cutting relations. It is very fine grained and contains cryptocrystalline materials (relict of pseudotachylite?). Horizontal shear surface is developed. This gouge was formed probably deeper than type II gouge. Type I gouge is also fine grained and foliated gouge. It is formed probably at the temperature ranges of laumontite stability (130 to 200 °C (Henley and Ellis, 1983)). This temperature corresponds to the about 4 to 7 km

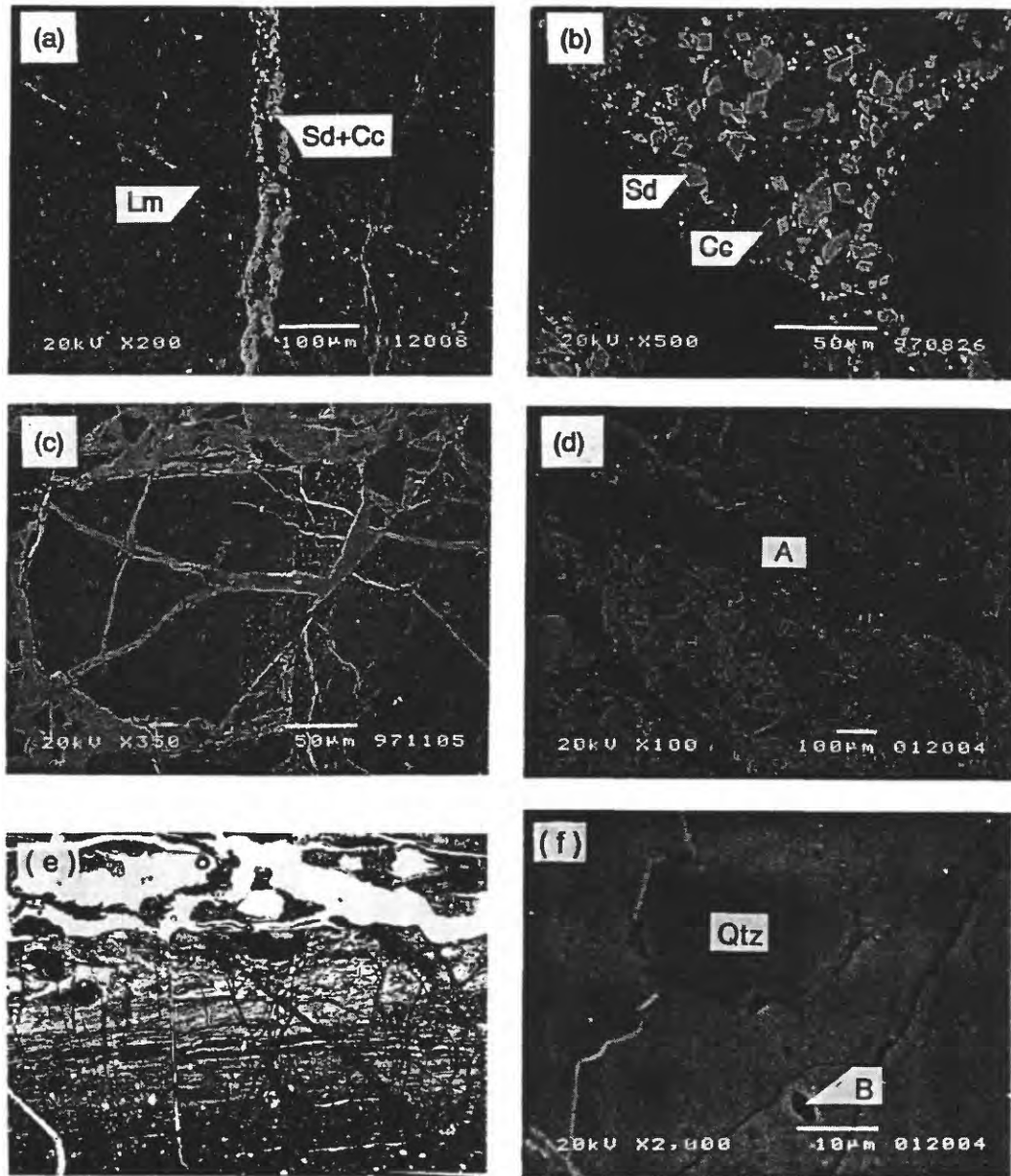


Fig.3 Secondary electron images (except e) showing the microstructure of the fault gouge in the fault core. Scale is shown in each photograph. (a) and (b) is type I gouge and (c), (d), (e) and (f) are type II gouge. The left side corresponds to the upper side of the original orientation. (a) 623.5 m depth. Laumontite vein (Lm) in pale grayish green fault gouge is cut by a carbonate vein (Sd+Cc) composed of siderite (white rim) and calcite (inner part in gray color). (b) 623.5 m depth. Rhombic shaped euhedral crystals of siderite (Sd) and calcite (Cc) are distributed as matrix components. A sub-rounded clast of laumontite (dark gray) exists in the right side. (c) 624.4 m depth. Calcite (white) fills fractures in dark grayish fault gouge. (d) 624.4 m depth. An unsealed cataclastic veinlet (A) runs through dark grayish fault gouge sealed by calcite. (e) 624.4 m depth. Optical microphotograph of the black band (BB). (f) 624.4 m depth. Rounded quartz (Qtz) and elongated bubble (B) in the cryptocrystalline material, which indicates that it is relict of pseudotachylite.

depth assuming the temperature gradient to be 30 °C/km. Type III gouge is random fabric and relatively coarse grained. It is formed probably the most recent and shallow level inferred from poor development of veins and sealing materials.

These three types of gouge are considered to represent different age and depth of Nojima fault activity.

#### References

Fujimoto, K., Ohtani, T., Tanaka, H., Tomida, N. and Ito, H., 1999, Characteristics of texture and mineralogy of fault rocks along the Nojima fault: analysis of continuous core from GSJ Hirabayashi borehole. *Geological Survey of Japan Interim Report no. EQ/99/1*, 50-53.

Henley, R.W. & Ellis, A.J., 1983, Geothermal systems, Ancient and modern: A geochemical review. *Earth Science Reviews* **19**, 1-50.

Ito, H., Kuwahara, Y., Miyazaki, T., Nishizawa, O., Kiguchi, T., Fujimoto, K., Ohtani, T., Tanaka, H., Higuchi, T., Agar, S., Brie, A. & Yamamoto, H. 1996. Structure and Physical Properties of the Nojima Fault. *BUTSURI-TANSA* **49**, 522-535\*

Mizuno, K., Hattori, H., Sangawa, A. & Takahashi, Y. 1990 Geology of the Akashi district. With Geological Sheet Map at 1:50,000, Geol. Surv. Japan, 90p.\*

Murata, A., Takemura, K., Miyata, T. & Lin, A-M., 1998, Stratigraphy and cummulative displacement in Nojima fault 500 m core, *Monthly Chikyu, Suppl.* **21**, 137-143. \*

Tanaka, H., Higuchi, T., Tomida, N., Fujimoto, K., Ohtani, T. & Ito, H. 1999. Mode of fault rocks distribution and their mode of deformation and alteration along GSJ drilling core penetrating the Nojima earthquake fault, northwest of Awaji Island, Southwest Japan. *Journal of Geological Society of Japan* **105**, 72-85. \*

(\* In Japanese with English abstract)

# Deformation textures and mechanisms in the granodiorite from the Nojima Hirabayashi borehole

Anne-Marie Boullier<sup>1</sup>, Benoît Ildefonse<sup>2</sup>, Jean-Pierre Gratier<sup>1</sup>, Koichiro Fujimoto<sup>3</sup>, Tomoyuki Ohtani<sup>3</sup> and Hisao Ito<sup>4</sup>.

1 - Laboratoire de Géophysique Interne et Tectonophysique, University Joseph Fourier, BP 43, 38041 GRENOBLE cedex, France

2 - Laboratoire de Tectonophysique, University of Montpellier II, Place E. Bataillon, 34095 MONTPELLIER cedex 5, France

3 - Geological Survey of Japan, Geothermal Department, 1-1-3 Higashi, Tsukuba, Ibaraki 305-8567, Japan

4 - Geological Survey of Japan, Earthquake Research Department, 1-1-3 Higashi, Tsukuba, Ibaraki 305-8567, Japan

## ABSTRACT

The deformation textures in the granodiorite from the Nojima Hirabayashi borehole are described and attributed to aseismic or seismic deformation mechanisms. Aseismic deformation appears to be non negligible even in the low-strain granodiorite (2-5%). It is also present in the cataclasites and ultracataclasites where it alternates with seismic episodes on the fault.

The observed textures throughout the borehole result from the mobility of quartz during the first stage of deformation, and of carbonates during the late ones. The same textures have been described also in the San Gabriel fault (California). This suggests that the textures may be attributed to decreasing temperature conditions and that the hanging wall of the Nojima fault has been uplifted, through time, from 3-5 km depth towards the first km of the crust.

## INTRODUCTION

Twenty-five horizontal thin sections from the core of the Hirabayashi borehole were examined in order to describe the small scale deformation textures related to the active Nojima fault. The objectives of this study were to compare the observed textures with what is known from other active fault systems such as the San Gabriel Fault (California), to interpret the textures in terms of deformation mechanisms and to attribute them, if possible, to the seismic or interseismic stages of the fault activity.

The borehole encountered granodiorite and porphyry dikes. Detailed structural, petrographical, mineralogical and geochemical studies of the borehole have been already achieved (Fujimoto et al., submitted; Ohtani et al., submitted, Tanaka et al., 1999). The present preliminary textural study focusses on granodiorite samples from one minor zone of

faulting (around 250 m) and from a few intervals above and below the main shear zone (624 m). Major magmatic minerals of these samples are amphibole, biotite, plagioclase, quartz and K-feldspar. In the following study, the textural classification of fault rocks by Sibson (1977) modified by Snee and Tullis (1998) has been used.

## DEFORMATION TEXTURES IN LOW-STRAIN ZONES

The granodiorite samples display varying degrees of internal deformation of minerals, fracturing and veining. The veins have not been studied in detail because only horizontal thin sections were available and it was not yet possible to decipher precisely the kinematics of these structures.

### BIOTITE

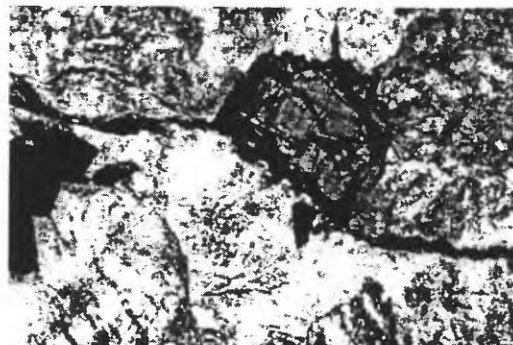


Figure 1. Microphotograph of a kinked biotite in the granodiorite at 352.3 m depth. Note the subhorizontal dark stylolitic plane compatible with the subvertical orientation of the shortened cleavage planes. Thin section is horizontal in the core reference frame. Plane polarized light. The width of the photograph is 3 mm.

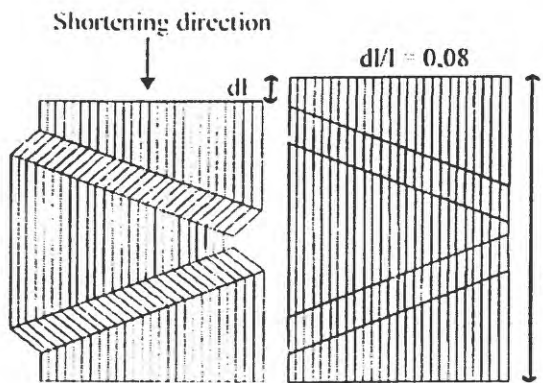


Figure 2. Schematic diagram showing the use of kinked biotites as markers of the shortening direction and of the finite shortening.

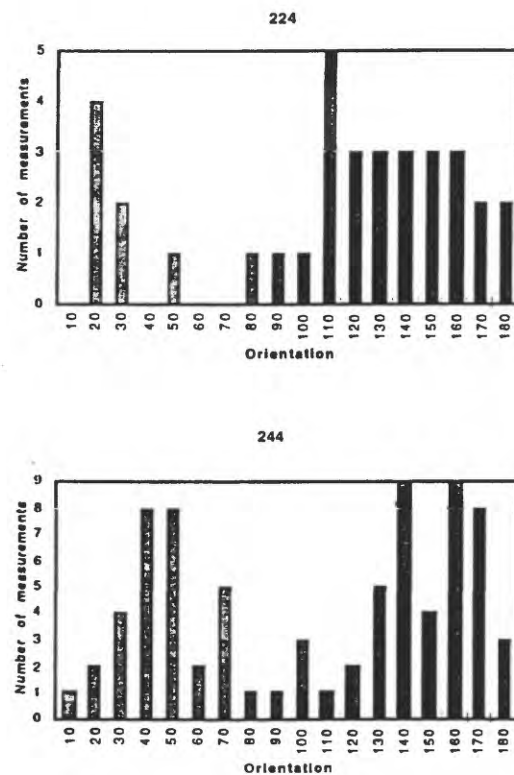


Figure 3. Examples of (001) orientation in kinked biotites for samples at 224.0 and 244.0 m depth. The histograms show two orthogonal directions corresponding to two shortening directions.

Biotite crystals display kink-bands (Figure 1) similar to those described by Kosaka et al. (1999). They indicate, first, the direction of shortening and, second, the finite strain (Figure 2). Generally, and assuming that biotites are randomly orientated

throughout the rock, two directions of shortening may be deduced from the orientation of (001) cleavages of the kinked biotite crystals (Figure 3). One direction is more clearly expressed than the other (sharp kink-band boundaries) and in most cases, this direction corresponds, chronologically, to the first one, as established with other structural criteria (veins, microcracks, etc..., see below).

Alteration of biotite may be present, together with kink-bands, and is expressed either by chloritisation along the cleavages or by crystallisation of calcite within the (001) cleavage planes.

The finite shortening of twelve biotites has been determined on one sample (224). Cleavages have been drawn on microphotographs and their length has been calculated using NIH Image program (U.S. National Institute of Health, 1998). The results depend on the location of the crystals: shortening may be as high as 40% for a biotite close to a shear fracture. Generally the shortening is between 2 and 5%.

In some samples, fractures link one biotite crystal to the others, a pattern which suggests that biotites act as soft minerals in the granodiorite.

## QUARTZ

Except in the immediate vicinity of the fault, quartz crystals scarcely exhibit classical features of plastic (intracrystalline) deformation such as undulose extinction, subgrains, dynamic recrystallisation (see Kosaka et al., 1999). On the contrary, quartz crystals are intensely fractured and several types of structures may be distinguished:



Figure 4. Microphotograph of the 256.2 m core sample (horizontal thin section). The contact between plagioclase (PI) and quartz (Qtz) has been outlined (thick black line), as well as the shortened (001) cleavage (black line) of biotite (Bt), fluid inclusion planes (thin black line) and flattened fluid inclusions (short thick black lines) in quartz. Fluid inclusion planes and biotite cleavages are radial around the plagioclase boundary which may have acted as a dissolution surface under compressive stress. Plane polarized light. Width of the microphotograph: 3mm.

(i) Fluid inclusion planes are mode I fractures which have been healed by dissolution-crystallisation processes (Tuttle, 1949). The orientation of these fluid inclusion planes is indicative of the stress tensor (Lespinasse and Pécher, 1986). In the studied samples, the principal orientation of the fluid inclusion planes is coincident with the first direction of shortening deduced from the biotite crystals (Figure 4) and with some small cracks crosscutting plagioclase or K-feldspar and sealed with clear albite or quartz.

(ii) The largest fluid inclusions located within these planes or isolated in the quartz crystals are deformed. They are flattened in short planes or cracks (Figure 4) which have a constant orientation throughout the thin section independantly of the lattice orientation of the quartz crystals.

(iii) Zeolite- or calcite-filled microcracks are present in most of the studied samples, these microcracks have similar orientation to the second shortening direction of (001) biotite cleavages. Generally the zeolite-filled cracks are older than the calcite-filled ones, as already observed by Fujimoto et al. (submitted).

## DEFORMATION TEXTURES IN HIGH-STRAIN ZONES

### CATACLASITES

Four samples of cataclasite (all cohesive) have been observed on horizontal thin sections: one in a minor fault zone at 249.9 m depth, two in the main fault zone at 619.8 and 622.6 m depth, and one, below, at 705.9 m depth. These samples fall into two classes: the silica-cemented (Si-) and the carbonate-cemented (Ca-) cataclasites, depending on the nature of the cementing matrix.

- 249.9 m: a Si-cataclasite is bounded by a sharp shear fracture. In the wall-rock and along this fracture, quartz displays slightly undulose extinction and biotite crystals are highly kinked and smeared out in the shear plane. An undeformed zeolite vein is emplaced along the shear fracture, but no carbonate vein has been observed.

- 619.8 m: quartz is highly fractured and shows only little internal plastic deformation (slight undulose extinction). Biotite is completely altered but the traces of the (001) cleavages are still recognisable and show large shortening (30-40%). K-felspar displays undulose extinction and plagioclase is almost completely replaced (zeolite?). In the preserved fragments of granodiorite, fluid inclusion planes are present and fluid inclusions are flattened perpendicular to these planes. Calcite- and zeolite-filled cracks crosscut the minerals and are approximately parallel to the fluid inclusion planes.

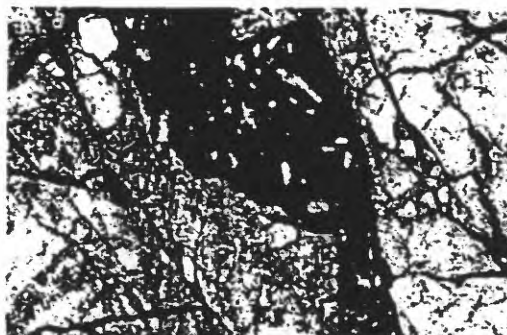


Figure 5. Microphotograph of the 619.8 m depth sample showing the Si-cataclasite (grey) containing some white fragments of quartz, cut by a Ca-cataclasite where small angular fragments of Si-cataclasite are embedded in black siderite cement. Thin section is horizontal in the core reference frame. Plane polarized light. Width of the view: 3 mm.

Twostages are recognized in the cataclastic zones at this level (Figure 5). The first one is a very fine-grained and compacted Si-cataclasite suggesting the activity of dissolution processes. In these Si-cataclasites, impurities and black material are concentrated on irregular stylolite-looking surfaces. Some of these planes are cut by other (younger) cataclastic events and by siderite-filled cracks. The second stage is a Ca-cataclasite with sideritic matrix; it also post-dates the Si-cataclasite



Figure 6. Microphotograph of the 622.6 m depth sample showing grey fragments of Si-cataclasite and quartz embedded in the black cement of the Ca-cataclasite. Thin section is horizontal in the core reference frame. Plane polarized light. Width of the view: 1.5 mm. - 622.6 m: This sample is almost completely cataclastic at the scale of the thin section. Both Si-cataclasites and Ca-cataclasites are observed. Fragments of Si-cataclasites are embedded in younger Si-cataclasites, and Si-cataclasites are themselves fragmented and embedded in Ca-cataclasite with highly variable percentage of carbonate cement. In the cement, euhedral crystals of carbonate may be observed within an unrecognized matrix, at high magnification on the petrographic microscope (see also description of fault gouge at 623.5m by Fujimoto et al., 1999).

Stylolitic planes are visible in the Si-cataclasite and are cut, in some places, by Ca-cataclasites. The latter are also cut by stylolitic planes.

- 705.9 m: this cataclastic sample appears to be more structured than the former ones, although the texture within the wall rock is very similar (highly fractured quartz, flattened fluid inclusions, etc...). The center of the high-strain zone is a foliated and colour-banded Si-cataclasite, displaying some C-S structures similar to those described by Lin (1999) (Figure 7). However, the foliation is defined by a compaction of the very fine-grained angular fragments rather than by internal deformation of them. Colour banding seems to be induced by the alternation of Ca-cataclasites in Si-cataclasites. Again irregular surfaces of dissolution are observed, and compaction appears to be higher in Si-cataclasites than in Ca-cataclasites.

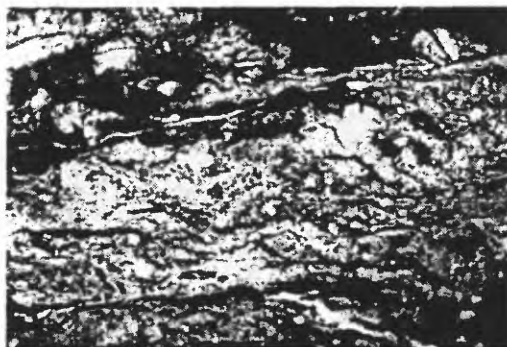


Figure 7. Microphotograph of the 705.9 m depth sample showing the cataclasite with a C (subhorizontal) and S (deeping to the right) structure. Thin section is horizontal in the core reference frame. Plane polarized light. Width of the view: 6 mm.

In summary, it appears that Si-cataclasites are formed first, and are subsequently followed by Ca-cataclasites and siderite-filled cracks. In the cataclasites, episodes of dissolution and veining seem to alternate with episodes of cataclasis.

#### DEFORMATION TEXTURES IN THE CORE OF THE MAIN SHEAR ZONE

Two very fragile samples of cohesive fault gouge have been observed at 624.30 and 624.60 m. They are very fine-grained and show a millimetric colour banding suggesting a succession of multiple cataclastic episodes. The banding of the ultracataclasite is cross-cut and displaced along fractures which are filled with zeolites(?) and different layers display varying degrees of fracturation (Figure 8). These samples correspond to the gouge type II as defined by Fujimoto et al. (1999).

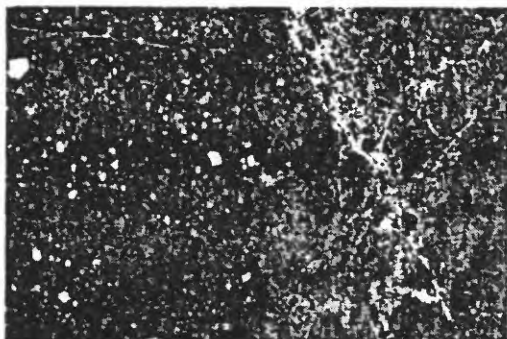


Figure 8. Microphotograph of the 624.6 m depth sample showing the colour banding (vertical). Note that each episode contains fragments of crystals or cataclasite and that the episode on the left is much less fractured than the one on the right. Plane polarized light. Width of the view: 6 mm.

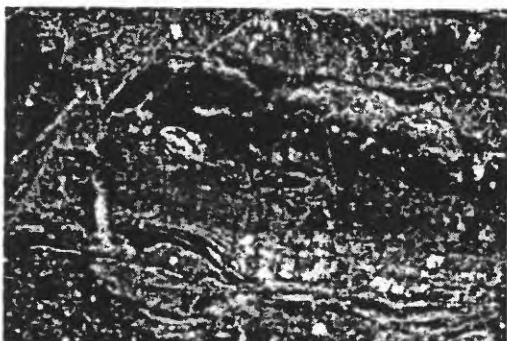


Figure 9. Microphotograph of the 624.6 m depth sample showing the colour banding (horizontal) and some stretched folded fragments within the central episode. Plane polarized light. Width of the view: 6 mm

Within the colour banding, it is possible to recognise elements of older ultracataclasite embedded in younger ultracataclasite. The fragments sometimes display folding suggesting structures described in pseudotachylites (Figure 9). The isotropic character (black under polarised and analysed light) of the very fine matrix in some of the bands, reinforce the similarity with pseudotachylite. However, this isotropic character may be due to very fine grain-size of the matrix and no absolute evidence has been found for the presence of glass under the petrographic microscope. Further detailed studies (SEM, TEM) are necessary to test the presence or absence of a molten phase.

#### COMPARAISON WITH TEXTURES IN THE SAN GABRIEL FAULT

In Southern California, recent uplifting of the San Gabriel mountains (along thrust faults) exposed crustal levels from about 2 to 5 km depth (Oakeshott, 1971).

Microstructures and mineral assemblages of the outcropping fault rocks are consistent with right lateral strike-slip faulting at depth (Jennings, 1994).

Samples were collected in granites several meters to hundreds of meters away from the central gouge zone. The crack orientation indicates the direction of shortening, and ranges from  $020^\circ$  to  $045^\circ$  with respect to the faults. This variation may be related to successive seismic events with associated crack sealing processes. Quartz is the most frequent mineral filling the sealed cracks. However, a network of very thin veins, filled with calcite, is seen by cathodoluminescence studies and is the latest episode of crack sealing.

Dissolution features can be distinguished in the samples. The sealed cracks (T) are associated with, and are perpendicular to, solution cleavage (S in Figure 10a). Most of the veins are interrupted against solution cleavage, this relation indicating their closed relationship (Figure 10). This solution cleavage can be seen at the scale of several grains or at the scale of a single grain boundary.

A schematic restored state, before solution along stylolites, (Figure 10b) shows the location of the transgranular zone of dissolution, and the associated veins which are interrupted against the zone of dissolution. Quartz and feldspar both show evidence for dissolution under stress. The aperture of the cracks (or at least the thickness of the filling material) may be estimate when the sealing mineral is different from the host mineral (for example quartz veins in feldspars); it ranges from 10 to 100  $\mu\text{m}$ . Apertures are more difficult to estimate when the sealing and the host mineral are not easily differentiated. Example of transgranular cracks in quartz shows that the two limits of the cracks are often outlined by two trails of fluid inclusions in the host mineral.

Other samples were collected from various sites in Southern California (Gratier et al., 1994) allowing the observation of pressure solution and crack sealing in rocks brought up from several kilometers depth (from 1-2 to 5-10 km). Mass change and mobile elements associated with pressure solution-deposition have been estimated by comparative chemical analysis. The relative mobility of quartz and calcite clearly evolves with depth. At low depth, calcite is more mobile than quartz, and this relative mobility reverses at larger depth. This is consistent with the theoretical evolution of pressure solution strain-rate with depth for these two mineral (Gratier, 1984, Figure 11). This evolution is related to two converging effects:

- the solubilities of quartz and calcite show an inverse evolution with increasing temperature (normal and reverse relation, respectively, for quartz and calcite),
- at low temperature the kinetics of quartz dissolution is very low and prevents significant pressure solution process (Oelkers et al., 1996; Renard et al., 1997).

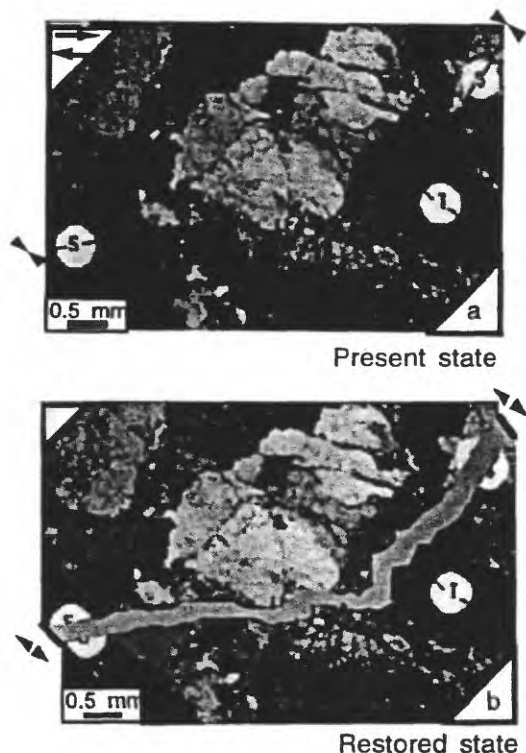


Figure 10. Microphotograph of an horizontal thin section from a granitic rock of the San Gabriel fault (Gratier et al., 1994). (a) present state: S is the stylolitic plane and T is a sealed crack. (b) restored state showing the dissolved mater along the stylolitic plane. Plane polarized and analysed light.

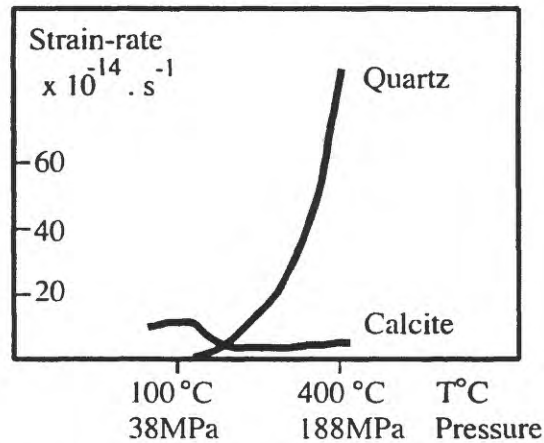


Figure 11. Theoretical diagram showing the strain-rate versus the P and T conditions for quartz or calcite aggregates (after Gratier, 1984).

## DISCUSSION

Several important facts must be pointed out. First, it is possible to recognize some deformation textures in the low-strain granodiorite, which indicate a succession of two-shortening directions (two stress tensors), each one corresponding to a few percent of strain (2-5%).

The first stage corresponds to temperature conditions in which silica is mobile since mode I cracks are healed (fluid inclusion planes) and fluid inclusions are flattened due to dissolution-crystallisation processes in quartz (Tuttle, 1949; Gratier and Jenatton, 1984). Microthermometric measurements on fluid inclusions in quartz from granodiorite core samples indicate relatively high homogenisation temperatures (ca 300°C, Ohtani et al. Submitted). The authors interpret these fluid inclusions as representing fluids trapped during cooling of the granodiorite. Moreover, the 3-D orientation of the fluid inclusion planes is not compatible with the present-day state of stress accompanying a reverse dextral sense of shear on the Nojima fault as demonstrated by Takeshita and Yagi (1999). Therefore, and following these authors, the fluid inclusion planes may represent Late Cretaceous microcracks healed at temperature above 300°C immediately after the solidification of the granodiorite in a tectonic setting corresponding to left-lateral movement on a "proto-Nojima" fault (Takeshita and Yagi, 1999).

The second event corresponds mostly to calcite-filled cracks and, therefore, to temperature conditions in which calcite is mobile. Since the two filling minerals (quartz and calcite) have opposite behaviours, we may deduced that the observed textures correspond to decreasing temperature conditions: above ca 180°C for quartz, and below that temperature for calcite (Gratier, 1984; Figure 11). A low temperature (ca 50°C) is also suggested for alteration and calcite deposition in cracks and veins by Ueda et al. (1999), on the basis of stable isotope data. These textures involve slow processes (dissolution, diffusion and crystallisation, Gratier & Gamond 1990) and therefore are assumed to be aseismic.

The second important point is that the same succession of mobile minerals may be observed in cataclasites, except in the 249.9 m sample, where no carbonate veins or cracks have been observed. In this zone, only Si-cataclasites are present. This suggests that this cataclastic zone has been active only at temperatures higher than ca 180°C and, therefore, that it is a to-day inactive and uplifted small fault zone. In the main shear zone, Ca-cataclasites post-date the Si-cataclasite, indicating that it has been uplifted through time, which is consistent with the reverse oblique movement on the Nojima fault.

The third important point is that, in all cataclasites and ultracataclasites, it was possible to observe

dissolution structures or mineralised fractures alternating with cataclastic episodes and mutual cross-cutting relations. This suggests that slow strain-rate (aseismic) processes such as dissolution-crystallisation alternate with high strain-rate (seismic) processes such as cataclasis and friction.

Finally, it was not yet possible to determine if melting occurred due to friction within the main shear zone. However, the flow structures (folds) suggest an intermediate viscous behaviour between a molten material (pseudotachylite) and a very finely crushed one (ultracataclasite) in the fault core.

## CONCLUSION

The deformation textures in the granodiorites from the Nojima Hirabayashi borehole are ascribed to aseismic or seismic deformation mechanisms (Gratier and Gamond, 1990; Gratier et al., 1999).

Aseismic deformation due to dissolution-crystallisation processes appears to be significant even in the low-strain granodiorite (2-5%). It is present also in the cataclasites and ultracataclasites where it alternates with seismic episodes on the fault. The observed textures result from the mobility of quartz during the first stages and of calcite during the late ones, which suggests that they may be attributed to decreasing temperature conditions and that the hanging wall of the fault has been uplifted through time, from 3-5 km depth towards the first kilometer of the crust.

The dissolution-crystallisation processes observed during aseismic intervals allow a modification of the permeability of rocks and, therefore, a variation in fluid pressure (Blanpied et al., 1992; Rice, 1992; Gratier et al. 1994). The fluctuations in fluid pressure may, in turn, enhance the seismic rupture on the high-angle reverse Nojima fault (Sibson et al., 1988).

## ACKNOWLEDGEMENTS

This study would not have been possible without the excellent thin sections realised on difficult material and in hurry by Christophe Nevado at the Montpellier University. This work is funded by GdR FORPRO (action 99.V, publication FORPRO 99/005 B).

## REFERENCES

Blanpied, M., Lockner, D. and Byerlee, J. 1992. An earthquake mechanism based on rapid sealing of faults. *Nature* **358**, 574-576.  
Chester, F. M., Evans, J. P. and Biegel, R. L. 1993. Internal structure and weakening mechanisms of the San Andreas fault. *Journal of Geophysical Research* **98**, 771-786.

Fujimoto, K., Tanaka, H., Tomida, N., Ohtani, T. and Ito, H. 1999. Characterization of fault gouge from GSJ Hirabayashi core samples and implications for the activity of the Nojima fault. In: *International workshop on the Nojima fault core and borehole data analysis*, Tsukuba, Japan. Extended abstracts.

Fujimoto, K., Tanaka, H., Higuchi, T., Tomida, N., Ohtani, T. and Ito, H. submitted. Alteration and mass transfer along the GSJ Hirabayashi borehole penetrating the Nojima earthquake fault, Japan. *Island Arc.*

Gratier, J. P. 1984. La déformation des roches par dissolution-cristallisation: aspects naturels et expérimentaux de ce fluage avec transfert de matière dans la croûte supérieure. Unpublished Thèse d'Etat thesis. Université Joseph Fourier.

Gratier, J. P., Chen, T. and Hellman, R. 1994. Pressure solution as a mechanism for crack sealing around faults. In: *Proceedings of Workshop LXIII: The Mechanical Involvement of Fluids in Faulting* Open-File Report 94-228. U.S. Geological Survey, 279-300.

Gratier, J. P. and Gamond, J. F. 1990. Transition between seismic and aseismic deformation in the upper crust. In: *Deformation mechanisms, rheology and tectonics* (edited by Knipe, R. J. & Rutter, E. H.) 54. Geological Society Special Publication, 461-473.

Gratier, J. P. and Jenatton, L. 1984. Deformation by solution - deposition and reequilibration of fluid inclusions in crystals depending on temperature, internal pressure and stress. *Journal of Structural Geology* 5, 329-339.

Gratier, J. P., Renard, F. and Labaume, P. 1999. How pressure-solution and fractures interact in the upper crust to make it behave in both a brittle and viscous manner. *Journal of Structural Geology* 21, 1189-1197.

Jennings, C. W. 1994. Fault activity map of California and adjacent areas with location and ages of recent volcanic eruptions. California Division of Mines and Geology.

Kosaka, K., Shimizu, M. and Takizawa, S. 1999. Delineation of deformation grades of low-strain granitoids using assemblages of elementary deformation textures. *Journal of Structural Geology* 21, 1525-1534.

Lespinasse, M. and Pêcher, A. 1986. Microfracturing and regional stress field : a study of the preferred orientations of fluid-inclusion planes in a granite from the Massif Central, France. *Journal of Structural Geology* 8(2), 169-180.

Lin, A. 1999. S-C cataclasite in granitic rock. *Tectonophysics* 304, 257-273.

Oakeshott, G. B. 1958. Geology and mineral deposits of San Fernando quadrangle. *California Division of Mines and Geology Bulletin* 172, 147pp.

Oakeshott, G. B. 1971. Geology of the epicentral area. *California Division of Mines and Geology Bulletin* 196, 19-30.

Oelkers, E. H., Bjørkum, P. A. and Murphy, W. M. 1996. A petrographic and computational investigation of quartz cementation and porosity reduction in North Sea sandstones. *American Journal of Science* 296, 420-452.

Ohtani, T., Tanaka, H., Fujimoto, K., Higuchi, T., Tomida, N. and Ito, H. submitted. Internal structure of the Nojima fault revealed by the GSJ borehole. *Island Arc.*

Renard, F., Ortoleva, P. and Gratier, J. 1997. Pressure solution in sandstones: Influence of clays and dependence on temperature and stress. *Tectonophysics* 280, 257-266.

Rice, J. R. 1992. Fault stress states, pore pressure distributions, and the weakness of the San Andreas Fault. In: *Fault mechanics and transport properties in rocks* (edited by Evans, B. & Wong, T. F.). Academic Press, 475-503.

Sibson, R. H. 1977. Fault rocks and fault mechanisms. *Journal of the Geological Society of London* 133, 191-213.

Sibson, R. H., Robert, F. and Poulsen, K. H. 1988. High angle reverse fault, fluid-pressure cycling and mesothermal gold quartz deposits. *Geology* 16, 551-555.

Snoke, A. W. and Tullis, J. 1998. An overview of fault rocks. In: *Fault-related rocks: a photographic atlas* (edited by Snoke, A. W., Tullis, J. & Todd, V. R.). Princeton University Press, Princeton, New Jersey, 3-18.

Takeshita, T. and Yagi, K. 1999. Dynamic analysis based on 3-D orientation distribution of microcracks in quartz from the Cretaceous granodiorite core samples drilled along the Nojima fault, southwest Japan. In: *International workshop on the Nojima fault core and borehole data analysis*, Tsukuba, Japan. Extended abstracts.

Tanaka, H., Tomida, N., Sekiya, N., Tsukiyama, Y., Fujimoto, K., Ohtani, T. and Ito, H. 1999. Distribution, deformation and alteration of fault rocks along the GSJ core penetrating the Nojima fault, Awaji Island, Southwest Japan. In: *International workshop on the Nojima fault core and borehole data analysis*, Tsukuba, Japan. Extended abstracts.

Tuttle, O. F. 1949. Structural petrology of planes of liquid inclusions. *Journal of Geology* 57, 331-356.

Ueda, A., Kawabata, A., Fujimoto, K., Tanaka, H., Tomida, N., Ohtani, T. and Ito, H. 1999. Isotopic study of carbonates in Nojima fault cores. In: *International workshop on the Nojima fault core and borehole data analysis*, Tsukuba, Japan. Extended abstracts.

blank page

# Characters of the fracture zones of the Nojima fault at depths of 1140, 1300 and 1800m viewed from NIED core analyses and well logging

Kenta Kobayashi<sup>1</sup>, Takashi Arai<sup>2</sup>, Ryuji Ikeda<sup>3</sup>, Kentaro Omura<sup>3</sup>, Takashi Sawaguchi<sup>4</sup>, Koji Shimada<sup>4</sup>, Hidemi Tanaka<sup>5</sup>, Tomoaki Tomita<sup>6</sup>, Naoto Tomida<sup>5</sup>, Satoshi Hirano<sup>7</sup>, Tatsuo Matsuda<sup>4</sup> and Akiko Yamazaki<sup>4</sup>

<sup>1</sup>*Graduate School of Science and Technology, Niigata University, Niigata 950-2181, Japan (E-mail address: kenkoba@gs.niigata-u.ac.jp)*

<sup>2</sup>*Graduate School of Science and Technology, Shinshu University, Matsumoto 390-8621, Japan.*

<sup>3</sup>*National Research Institute for Earth Science and Disaster Prevention, Tsukuba 305-0006, Japan*

<sup>4</sup>*Department of Earth Science, School of Education, Waseda University, Tokyo 169-8050, Japan*

<sup>5</sup>*Department of Geo/Biospheric Sciences, Faculty of Science, Ehime University, matsuyama 790-8577, Japan*

<sup>6</sup>*Graduate School of Science and Engineering, University of Tsukuba, Tsukuba 305-0006, Japan*

<sup>7</sup>*Frontier Research Program for Subduction Dynamics, Japan Marine Science and Technology Center, Yokosuka 237-0061, Japan*

**Abstract** Characteristics of deformation and alteration of the drill-core recovered from the fracture zone (1140 m in depth) of the Nojima fault (southwest Japan) are described. Degrees of deformation and alteration are estimated based on the relative density of fractures and shear planes and on the relative amount of mafic minerals. Based on the characteristics, the fault rocks in the core pieces are classified into following types, weakly deformed and altered granodiorite, altered granodiorite, fault breccia, fault gouge and cataclasite. Lithological column analysis clarified the distribution pattern of the fault rocks in the fracture zone. In addition, correlation to the logging data are conducted to clarify the physical property of the fault rocks. We refer decrease in P-wave velocity ( $V_p$ ) to deformation, and increase in porosity ( $\phi$ ) to alteration. In  $V_p$  versus  $\phi$  diagrams, most plots are scattered along the following line,  $V_p = -0.2\phi + 7$ .  $dV_p / d\phi = -0.2$  presents the mean rate of deformation versus alteration throughout the Nojima fracture zones. The fracture zones at depths of 1800, 1300 and 1140 m can be considered as strong, stronger and the strongest deformation and alteration zones. On the other hand,  $dV_p / d\phi = 0$  presents the strong alterations compared with the deformations, may have developed recently compared with others.

## INTRODUCTION

The Nojima fault, which has been known as one of the active faults in Japan, was reactivated at the time of the 1995 Hyogo-ken Nanbu earthquake. After the

earthquake, fault zone drilling was conducted by NIED (National Research Institute for Earth Science and Disaster Prevention, Japan), and all-core was recovered range from 1001 to 1838 m in depth, including remarkable fracture zones at depths of 1140, 1300 and 1800 m.

In this paper, we describe the characteristics of deformation and alteration of these fracture zones, mainly the zone at a depth of 1140 m. As a result of observation, the fault rocks in the zone are classified, and mode of distribution of the fault rocks are clarified. In addition, correlation to the logging data are conducted to clarify the physical property of the fault rocks.

## CLASSIFICATION OF FAULT ROCKS

The fracture zone at a depth of 1140 m is the thickest among the three fracture zones in the core. Based on the observations on the surfaces of core pieces, we selected the section range from 1108.1 to 1161.2 m in depth. In this section, the host rocks (Cretaceous granitic rocks) have undergone the most remarkable deformation and alteration.

Each core piece from the section was fixed by epoxy resin and split into two. Split surfaces are fixed again and observed by naked eyes to recognize the figures of deformation and alteration. Degree of deformation is estimated based on the relative density of fractures. Degree of alteration is estimated based on the relative amounts of residual mafic minerals (biotite and hornblende). Based on these two criteria, the fault rocks in the zone are classified.

Occurrence of each fault rocks are described as follows.

(1) *Weakly deformed and altered granodiorite*.

Texture of the original rocks (granodiorite) is preserved on hand-specimen scale. Shear and fissure (as mineral veins) surfaces are rarely developed. Along these surfaces, some grains of mafic minerals have been altered and changed into chlorite, or disappeared. Some grains of feldspar are also altered, and change in color from pale white to reddish brown.

(2) *Altered granodiorite*. Most grains of mafic minerals have disappeared. Yellow and white color mineral veins are developed. Degree of deformation is as same as that of the weakly deformed and altered granodiorite, not so many fractures are developed.

(3) *Fault breccia*. Degrees of deformation and alteration are moderate. Fragmentations are observed along shear surfaces.

(4) *Fault gouge*. Texture of the granodiorite is perfectly obliterated. Compositional color banding is observed in some gouges. They are referred to the *foliated fault gouge* in this paper.

(5) *Cataclasite*. Biotite grains are not altered, but elongated along the micro-shear surfaces, and preferred orientation of them is developed.

## DISTRIBUTION OF FAULT ROCKS

The fracture zone range from 1132.7 to 1145.3 m in depth consists of fault breccia and fault gouge (Figure 1). Two narrow foliated fault gouge zones occur 1140.6 and 1143.6 m in depths. In the hanging wall, there is a fracture zone which consists of fault breccia and fault gouge range from 1121.4 to 1128.4 m in depth. In the footwall, three thinner zones of the foliated fault gouge zones (1149.5, 1151.4 and 1156.9 m in depths) are distributed in the weakly deformed and altered granodiorite zone. Narrow zones of cataclasite occur both in the hanging wall and in the footwall.

### LEGEND

- Weakly deformed and altered granodiorite
- Altered granodiorite
- Fault breccia
- Fault gouge
- Foliated fault gouge
- Cataclasite

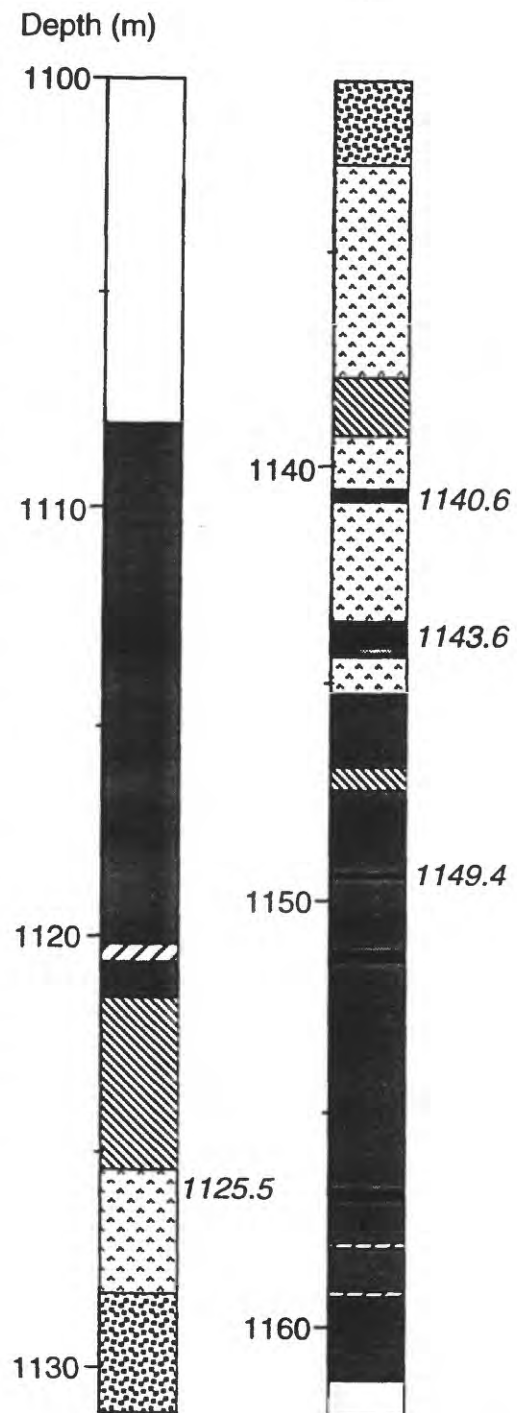


Figure 1. Fault rock profile of the fracture zone 1140 m in depth.

## CORRELATION TO THE LOGGING DATA

Geophysical logging data were measured from the borehole (Ikeda, 1999). The relationships between P-wave velocity and porosity (by neutron log) are shown on the cross plots (Figure 2). These relationships have been investigated to interpret structures of accretionary prism (e.g. Erickson and Jarrard, 1999) and oil field (e.g. Izumotani and Noguchi, 1996).

In Figure 2a (251.0-1834.8 m in depth), most plots are scattered along the line presented by the following equation,

$$Vp = -0.2\phi + 7 \quad (1)$$

where  $Vp$  is P-wave velocity (km/sec) and  $\phi$  is porosity (%). But some plots are scattered in the higher  $\phi$  area aside from the line (1).

In Figure 2b (1108.1-1161.2 m in depth), the lowest value of  $Vp$  is 2.1 km/sec, and the highest value of  $\phi$  is 40.0 %. In Figure 2c (1276.7-1336.7 m in depth), the lowest value of  $Vp$  is 2.9 km/sec, and the highest value of  $\phi$  is 34.7 %. In Figure 2d (1774.9-1828.4 m in depth), the lowest value of  $Vp$  is 4.4 km/sec, and the highest value of  $\phi$  is 17.7 %. In Figures 2b-d, tracks of the plots are shown, and continuous changes of physical properties can be recognized. Some parts of the tracks are along the line (1), others are aside from the line (1) and along the another lines of which  $dVp / d\phi$  are about zero (from -0.01 to 0.1).

Correlated pieces (fault gouges) to significant plots in the Figure 2b are selected, and their split surfaces are polished to be observed in detail (Figure 3). In addition, we made some thin sections to observe their micro-structural figures (Figure 4).

The fault gouges correlated to the plots on the peaks of low  $Vp$  along the line (1) are selected (1143.6 and 1125.5 m in depths). Weakly foliated or random fabrics are observed in hand-specimen scale (Figures 3b & c), but strongly fractured and altered in microscale (Figures 4c).

The fault gouges correlated to the plots on the peaks of high  $\phi$  along the lines of which  $dVp / d\phi = 0$  are selected (1140.6 and 1149.4 m in depths). Well foliated fabrics are observed in hand-specimen scale and microscale (Figures 3a & d, 4a & d). Fine grained clayey zone non-sealed with calcite is developed (Figures 4a).

## DISCUSSION AND CONCLUSIONS

We refer decrease in  $Vp$  to deformation, and increase in  $\phi$  to alteration. The line (1) is valid for all depths, and  $dVp / d\phi = -0.2$  presents the mean rate of deformation versus alteration throughout the Nojima fracture zones (Figure 2a). Based on the mean areas of plots on the line (1), the fracture zones at depths of 1800, 1300 and 1140 m can be considered as strong, stronger and the strongest deformation and alteration zones (Figures 2b-d).

The lines of which  $dVp / d\phi = 0$  presents the strong alterations compared with the deformations. The feature of the alterations is a narrow, isolated, fine grained clayey fault gouge zone which is non-sealed with calcite. These fault gouge zones may have developed recently compared with others.

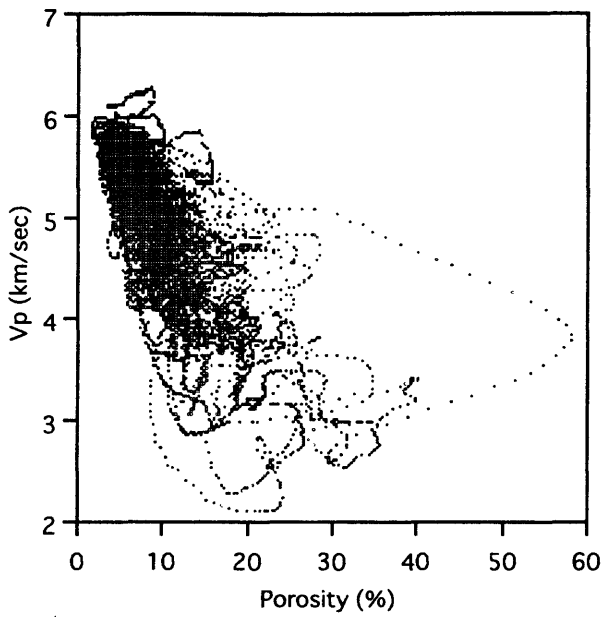
## REFERENCES

Erickson, S. N. and Jarrard, R. D., 1999, Porosity-formation factor and porosity-velocity relationships in Barbados prism. *Jour. Geophys. Res.*, **104**, 15391-15407.

Ikeda, 1999, Outline of the Nojima Fault Scientific Drilling by NIED. *This issue*.

Izumotani, S. and Noguchi, K., 1996, The relationship between velocity and porosity of rocks with the effects of the clay minerals. *Jour. Japan. Assoc. Petrol. Technol.*, **61**, 239-245.

(a)



(b)

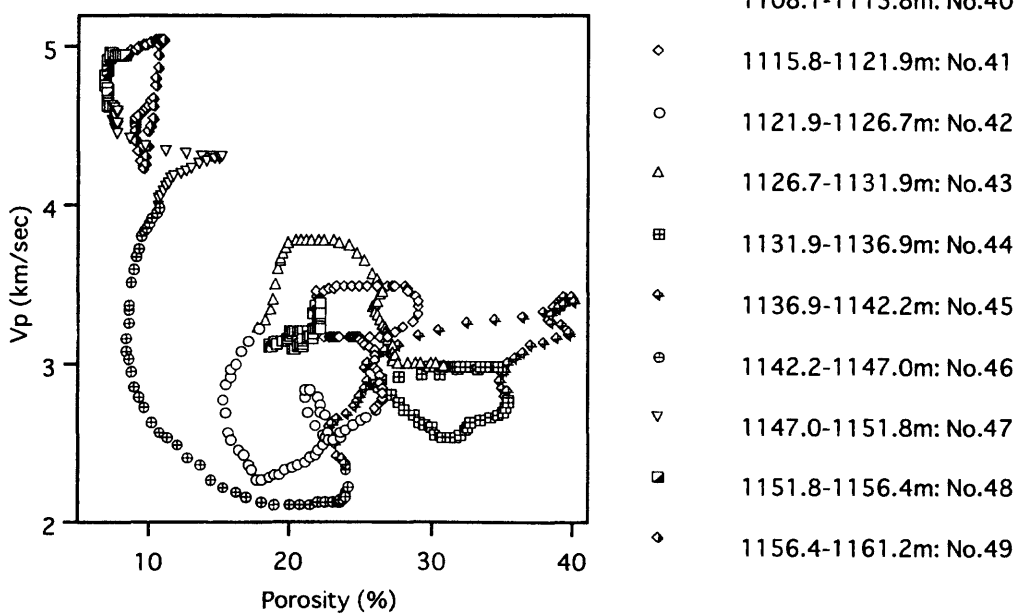
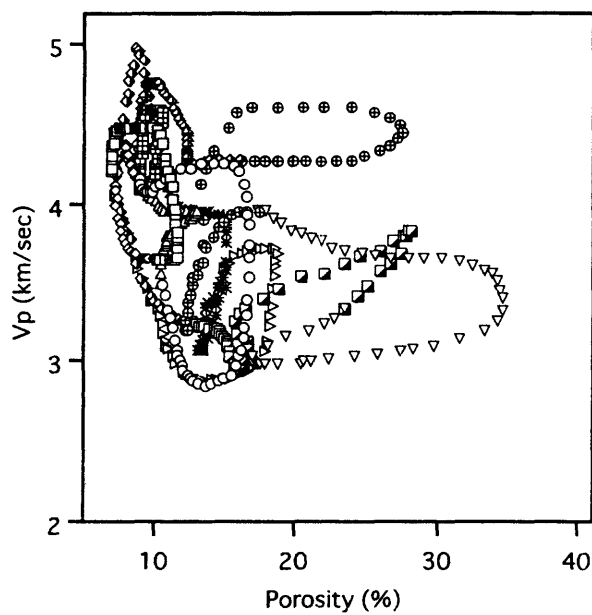


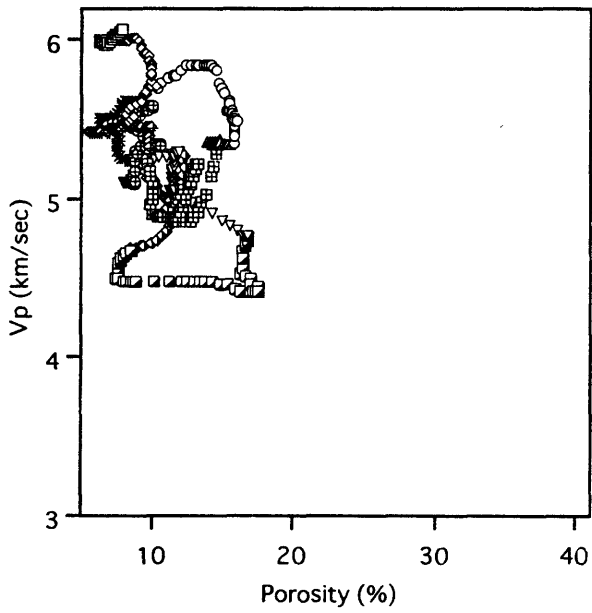
Figure 2. P-wave velocity versus porosity diagrams. Logging data were measured at 0.1 m intervals. (a) 251.0-1834.8 m in depth ( $n = 15838$ ). (b) 1108.1-1161.2 m in depth ( $n = 532$ ). (c) 1276.7-1336.7 m in depth ( $n = 601$ ). (d) 1774.9-1828.4 m in depth ( $n = 536$ ).

(c)



- 1276.7-1281.9m: No.74
- ◊ 1281.9-1286.4m: No.75
- 1286.4-1292.1m: No.76
- △ 1292.1-1297.0m: No.77
- 1297.0-1302.0m: No.78
- ◆ 1302.0-1306.6m: No.79
- ⊕ 1306.6-1311.4m: No.80
- ▽ 1311.4-1316.2m: No.81
- 1316.2-1321.2m: No.82
- ◊ 1321.2-1325.9m: No.83
- \* 1325.9-1330.9m: No.84
- ▷ 1330.9-1336.7m: No.85

(d)



- 1774.9-1778.7m: No.175
- ◊ 1778.7-1784.5m: No.176
- 1784.5-1789.4m: No.177
- △ 1789.4-1793.1m: No.178
- 1793.1-1799.0m: No.179
- ◆ 1799.0-1803.8m: No.180
- ⊕ 1803.8-1808.6m: No.181
- ▽ 1808.6-1813.5m: No.182
- 1813.5-1818.6m: No.183
- ◊ 1818.6-1823.4m: No.184
- \* 1823.4-1828.4m: No.185

Figure 2. (continued)

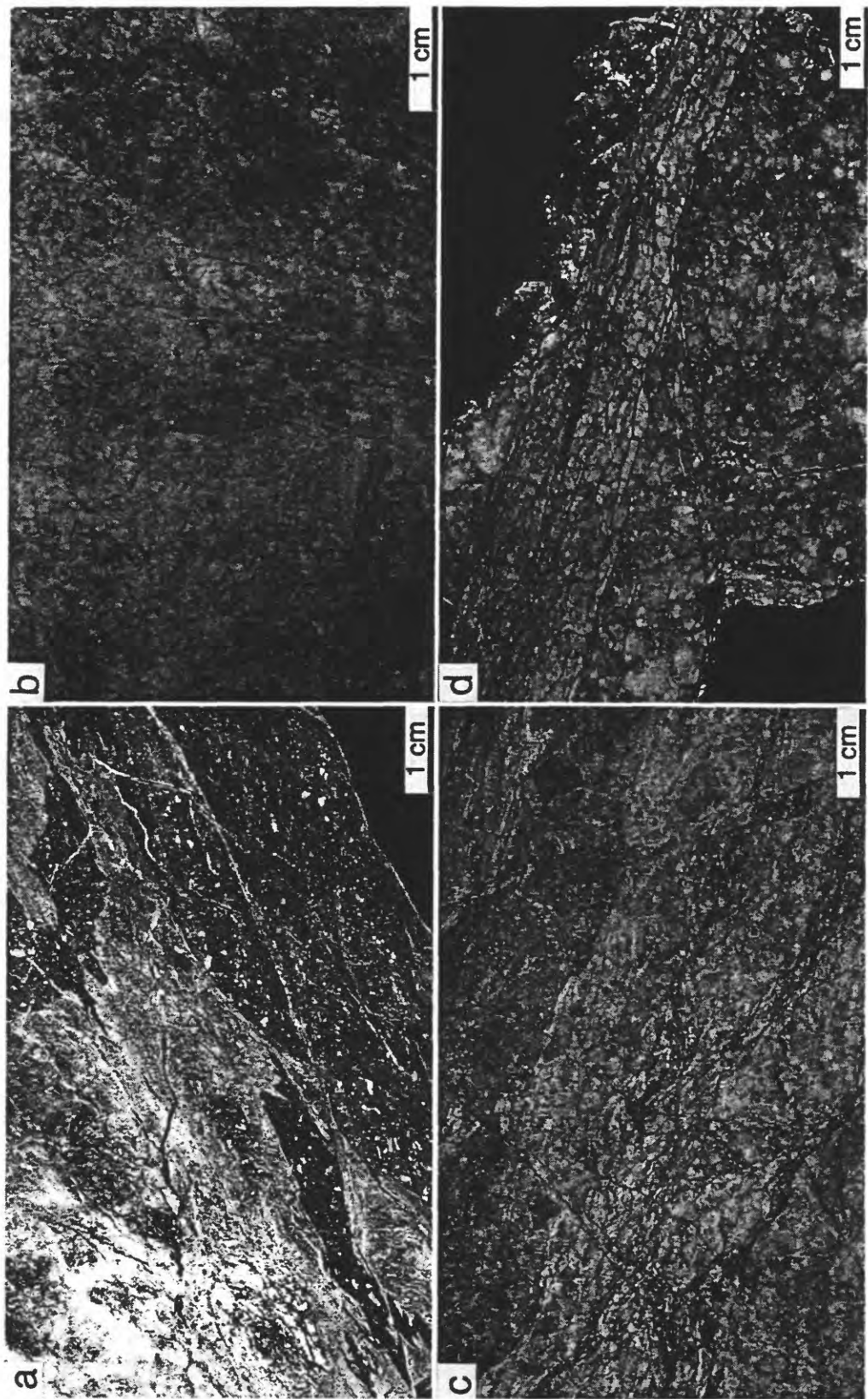


Figure 3. Photographs of polished split surfaces. (a) foliated fault gouge, 1140.6 m in depth. It is divided with moderately foliated part white and reddish-brown in color (upper) and well foliated part bluish gray in color (lower). Wedge shaped injection structure filled with the bluish gray fault gouge is developed in the reddish-brown fault gouge zone. (b) fault gouge with random fabric, 1125.5 m in depth. (c) weakly foliated fault gouge, 1143.6 m in depth. (d) well foliated fault gouge, 1149.4 m in depth.

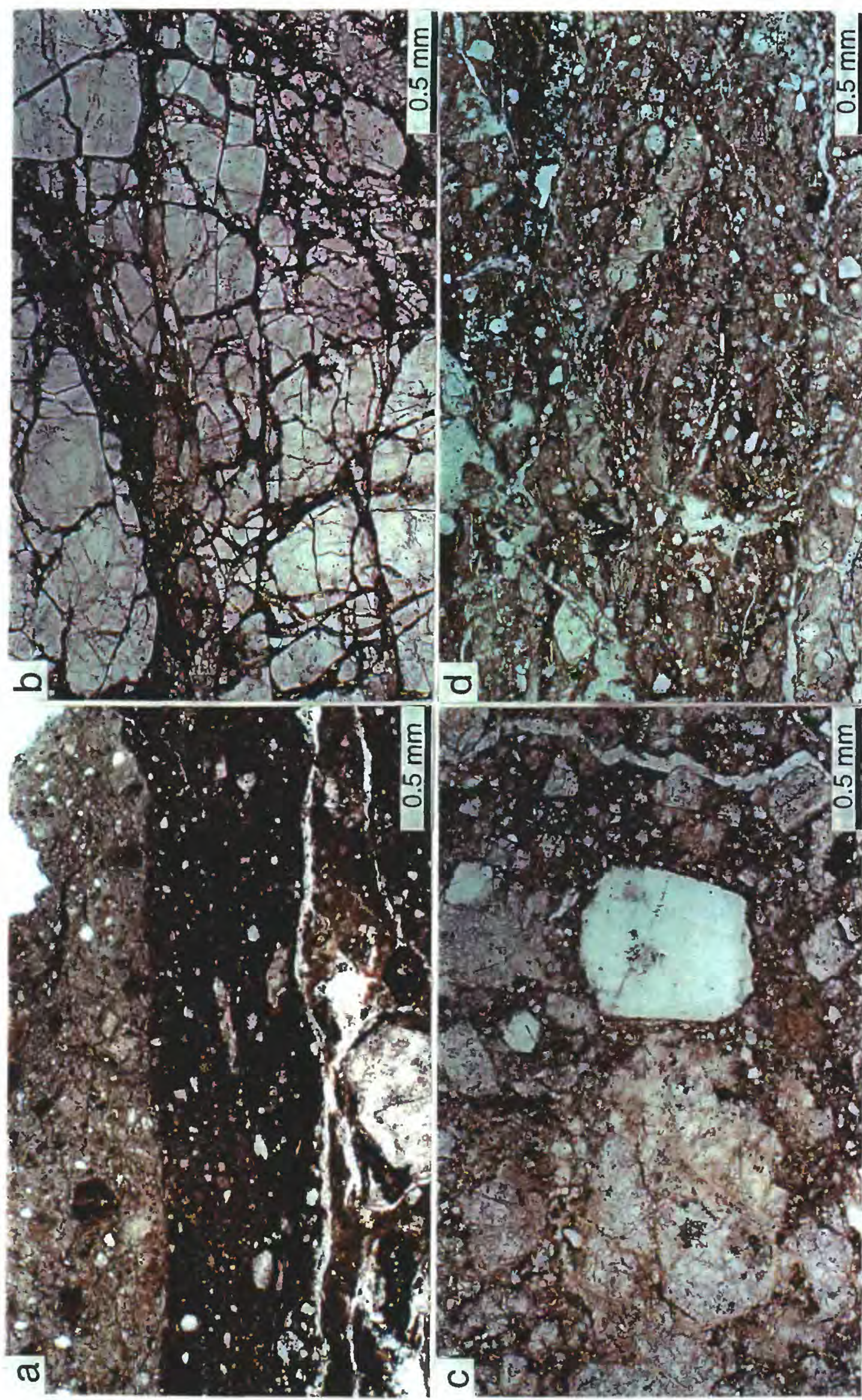


Figure 4. Photomicrographs of thin section. (a) foliated fault gouge, 1140.6 m in depth. It is divided with fine grained clayey part (upper, bluish gray by naked eye) and coarse grained part sealed with calcite (lower, white and reddish-brown by naked eye). (b) moderately foliated fault gouge (white and reddish-brown by naked eye), 1143.6 m in depth. Coarse grains of quartz and feldspar are preserved. (c) weakly foliated fault gouge, 1140.6 m in depth. Coarse and fine grained fragments are floated randomly in matrix sealed with calcite. Feldspar and mafic minerals have been altered and changed into clay minerals. (d) well foliated fault gouge, 1149.4 m in depth.

blank page

# Isotopic study of carbonates in Nojima Fault cores.

Akira Ueda<sup>1</sup>, Akiko Kawabata<sup>1</sup>, Koichiro Fujimoto<sup>2</sup>, Hidemi Tanaka<sup>3</sup>, Naoto Tomida<sup>3</sup>, Tomoyuki Ohtani<sup>2</sup> and Hisao Ito<sup>4</sup>

*1:Central Research Institute, Mitsubishi Materials Corporation, 1-297 Kitabukuro, Omiya, Saitama 330-8508, Japan*

*2:Geothermal Department, Geological Survey of Japan, Higashi 3-3-1, Tsukuba, Ibaraki 305-8567, Japan*

*3:Department of Geo/Biosphere Sciences, Faculty of Science, Ehime University, Bunkyo-cho 2-5, Matsuyama, Ehime 790-8577, Japan*

*4: Earthquake Research Department, Geological Survey of Japan, Higashi 3-3-1, Tsukuba, Ibaraki 305-8567, Japan*

## Abstract

Thirty six carbonate containing rock samples were collected from the Nojima Fault core and were analyzed for their carbon and oxygen isotopic compositions to investigate the mechanism of the carbonate formation from fluids along the fault. The  $\delta^{13}\text{C}$ (PDB) and  $\delta^{18}\text{O}$ (SMOW) values are  $-8.3$  to  $-0.6\text{\textperthousand}$  and  $21.6$  to  $30.4\text{\textperthousand}$ , respectively. The  $\delta^{13}\text{C}$ (PDB) values increase with increasing depth(up to 750m) whereas no good correlation is observed between the  $\delta^{18}\text{O}$ (SMOW) values and the depth. In contrast,  $\text{CO}_2$  and  $\text{H}_2\text{O}^+$  contents in rocks studied are almost constant above 500m depth. Below this level, their contents vary largely and increase with increasing depth, reaching to their maximum values (7wt % and 5wt %, respectively) around 625m depth (fault zone). The  $\delta^{13}\text{C}$ (PDB) values are almost constant( $\pm 1\text{\textperthousand}$ ) at the same depth independent of their  $\text{CO}_2$  contents. The formation fluids in equilibrium with these carbonates are calculated to be  $-0$  to  $+2\text{\textperthousand}$  for the  $\delta^{18}\text{O}$ (SMOW) values on the basis of the assumed temperature(25 to  $40^\circ\text{C}$ ). These results imply that the carbonates were formed from sea water penetrating along the fault.

## Introduction

An active fault drilling was performed by the Geological Survey of Japan at Nojima Hirabayashi, Awaji Island and was successful by penetrating the core of the Nojima Fault at 625m depth. The geological and petrographyical descriptions of the core have been done by many investigators (ex., Fujimoto, 1999, Fujimoto et al., 1999, Tanaka et al., 1999a). In the core, carbonates were commonly observed as veins and disseminated spots, and were especially concentrated along the active fault zone at 625m depth. The chemical compositions of rock powder samples were analyzed by Tanaka et al.(1999b). According to their results,  $\text{CO}_2$  contents in rocks reach to the maximum value (7wt%) around 625m depth.

This paper describes characteristics of their isotopic (carbon and oxygen) compositions of

carbonate containing rocks in the core and discuss their origin of the carbonate formation along the active fault. Isotopic study of carbonate samples in rocks have been mainly studied for cores and rocks from geothermal and hydrothermal fields (ex., Rye and Ohmoto, 1974, Olson, 1979, William and Elders, 1984, Sturchio et al., 1990, Morishita, 1990). In contrast, there are no detailed investigations for their isotopic compositions of rock samples along active faults. This paper reports a preliminary results for the isotopic characteristics of carbonates in the Nojima Fault core.

## Geological and petrological descriptions

According to Tanaka(1999a), the coaxial zone of the Nojima Fault exists between 623.1 to 625.3 m depth, because the thickest fault gouge in the borehole is distributed with a high dipping angle that is coincident with that of the surface rupture. Another evidence is that the results of geophysical logging (Ito et al., 1996) show various anomalies at this depth such as remarkable change of sonic wave velocity. Core lithology is of mostly Cretaceous granodiorite (Nojima granodiorite(Mizuno et al., 1990)) with some porphyry dikes. The rocks above 426m depth are nearly intact granodiorite. The borehole enters into the fault zone at 426 m depth and the rocks are affected by the fault activities even at the bottom of the borehole. Four types of faults are recognized for related rocks, which consist of weakly deformed granodiorite, fault breccia, fault gouge and cataclasite based on the degree of alteration and pulverization (Tanaka et al., 1999a).

Characteristic alteration minerals in the fault zone are smectite, zeolites (laumontite, stilbite) and carbonate minerals (calcite, siderite, and dolomite). Laumontite formation and fault activity is almost spontaneous at temperature about  $100^\circ\text{C}$  prior to precipitation of carbonate minerals. Calcite, which is one of the major sealing materials, is considered to be the most recent product in the shallow level of the Nojima fault zone.

Whole rock chemical analyses show that the

coaxial zone is highly concentrated in  $H_2O$  and  $CO_2$  due to formation of smectite, laumontite, siderite and calcite(Fujimoto, 1999, Fujimoto et al.,1999). This shows that the mineralogical and chemical changes in the fault zone strongly interact with pulverization.

Alteration can be briefly characterized by decomposition of primary minerals and formation of clay minerals, zeolite and carbonate minerals. Hornblende breaks down into carbonate and clay minerals deeper than 426.2 m depth except about 670 to 680 m depth. Biotite is decomposed into carbonate and clay minerals in the vicinity of the fault core. Plagioclase is partially replaced by zeolite, albite and sericite in the fault zone. Chlorite occurs as a replacement mineral of biotite and hornblende through out the whole depth. Smectite is distributed mainly deeper than 500 m as a replacement mineral of primary mafic minerals and the matrix component of fault rocks. Illite component is less than a few %. Calcium zeolite (laumontite and stilbite) occurs as a vein mineral through the whole depth. It also occurs as fracture filling and replacement of plagioclase in the fault zone (below 426.2m depth). In the vicinity of the two gouge zones, it is particularly rich in zeolite. Zeolite minerals show a zonal distribution; laumontite is distributed deeper than about 200m depth. Stilbite is distributed shallower than 480m depth and deeper than the fault core. Carbonate minerals occur as vein minerals and partial replacement of primary mafic minerals through the whole depth. They are also a major cement component of the fault core. Calcite is distributed shallower than about 460m depth and in the fault core as matrix cement. Siderite is distributed through the whole depth. Dolomite only occurs near the fault core(Fujimoto et al.,1999).

Alteration mineral assemblages and occurrences indicate multistage alterations under moderate temperatures (lower than about 300°C) and in nearly neutral solutions. Degree of alteration is indicated by ignition loss (LOI) that represents total concentrations of  $H_2O$  and  $CO_2$  in the bulk samples (Fujimoto et al.,1999). LOI profile clearly shows two peaks at the fault core and in the vicinity of low sonic zone, while it is about 1% outside of the fault zone and about 3 to 5 % in the fault zone.

#### Analytical procedures

36 carbonate containing rock samples were collected from the Nojima core and powdered. Then,  $\sim 100$ mg rock powders were reacted with phosphoric acid in vacuum at 25°C for 1 day

(McCrea, 1950) and the  $CO_2$  gas extracted was analyzed for the isotopic compositions by a Finnigan Mat Delta-E mass spectrometer. The uncertainties are within  $\pm 0.2\%$  for both carbon and oxygen isotopes.

Chemical data used in this study are quoted after Tanaka et al.(1999b), where  $CO_2$  and  $H_2O$  ( $H_2O^+ + H_2O^-$ ) contents were determined by two methods (wet chemical analyses (ignition loss) and CHN recorder analyses). The results are in good accordance with each other (Fig.4). From these results,  $H_2O^+$  contents are calculated by the difference between total  $H_2O$  and  $H_2O^-$  contents.

#### Results

Analytical results are shown in Table 1 and Figs. 1 to 6. The results are summarized as follows;

Table 1 Isotopic compositions of carbonate containing rocks from Nojima core.

Depth (m)	$\delta^{13}C_{PDB}(\text{‰})$	$\delta^{18}O_{SMOW}(\text{‰})$
177.68	-8.3	25.6
207.38	-5.8	25.8
271.37	-8.6	24.2
497.33	-2.1	28.4
531.58	-3.3	28.5
555.81	-6.0	21.6
559.55	-3.4	27.9
563.44	-4.0	27.1
568.41	-4.4	27.7
574.53	-4.5	28.1
579.49	-4.8	30.4
582.63	-5.4	24.8
587.83	-4.0	27.8
591.76	-4.9	26.8
596.09	-4.4	27.4
606.52	-5.3	25.8
610.79	-4.3	27.4
614.75	-3.7	24.8
623.75	-3.5	24.4
625.73	-1.0	29.0
629.13	-1.8	29.8
634.12	-0.9	21.9
645.48	-1.5	29.6
655.35	-1.4	28.1
663.05	-2.0	28.5
664.55	-0.6	28.0
670.12	-2.3	26.3
676.51	-1.5	24.7
683.13	-1.2	25.5
685.5	-1.1	24.5
691.98	-1.5	25.5
696.98	-0.5	25.8
700.24	-1.9	26.3
704.15	-0.9	26.8
708.83	-1.8	25.5
714.88	-2.1	27.9

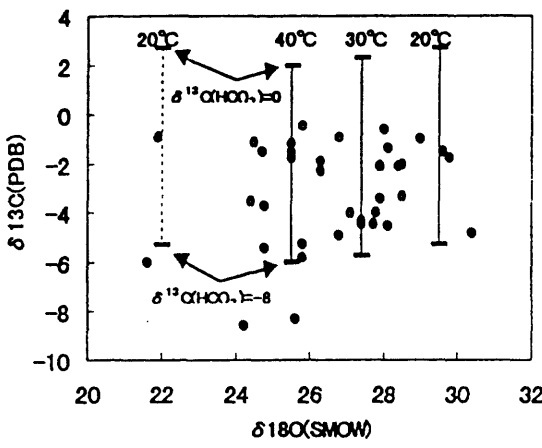


Figure 1 Isotopic compositions of carbonates and the calculated fluids in equilibrium with them

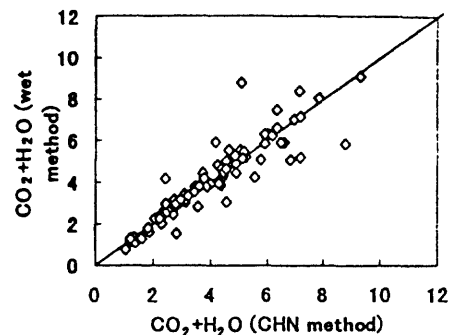


Figure 4 Comparison of  $\text{CO}_2 + \text{H}_2\text{O}$  contents in rocks by CHN and wet methods.

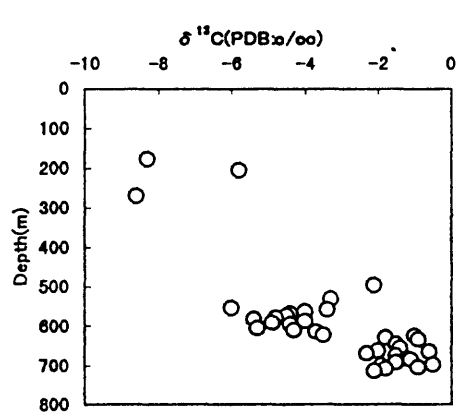


Figure 2  $\delta^{13}\text{C}$  values vs depth

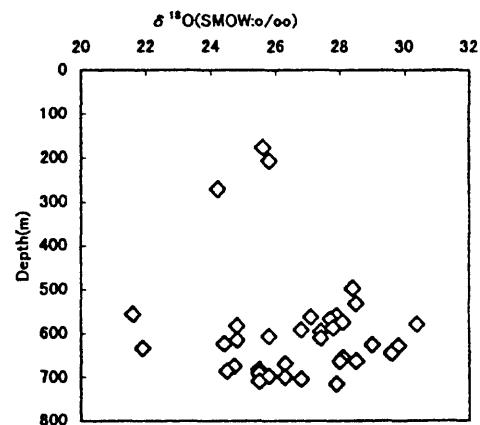


Figure 3  $\delta^{18}\text{O}$  value vs depth

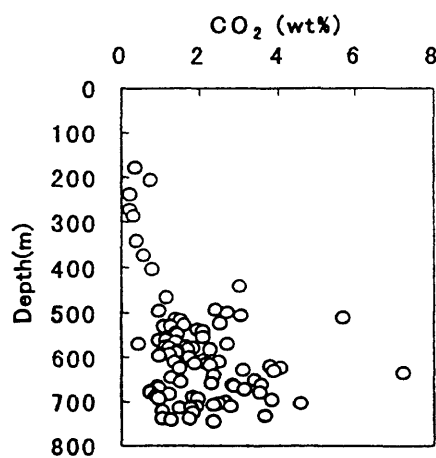


Figure 5  $\text{CO}_2$  contents in rocks.

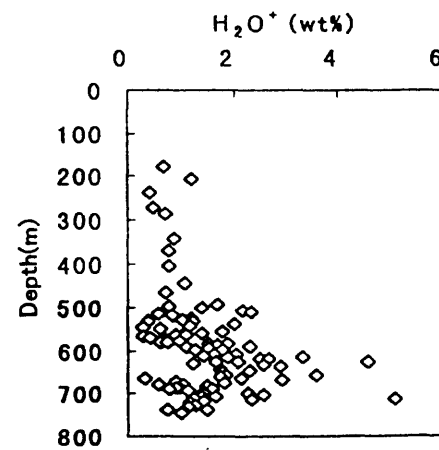


Figure 6  $\text{H}_2\text{O}^+$  contents in rocks.

- (1) The  $\delta^{13}\text{C}$ (PDB) and  $\delta^{18}\text{O}$ (SMOW) values are  $-8.3$  to  $-0.6\text{\textperthousand}$  and  $21.6$  to  $30.4\text{\textperthousand}$ , respectively.
- (2) The  $\delta^{13}\text{C}$ (PDB) values increase with increasing depth(up to 750m) whereas no good correlation is observed between the  $\delta^{18}\text{O}$ (SMOW) values and the depth.
- (3) The  $\delta^{13}\text{C}$ (PDB) values are almost constant ( $\pm 1\text{\textperthousand}$ ) at the same depth independent of their  $\text{CO}_2$  contents.

### Discussion

The significant characteristics of the isotopic compositions of carbonate containing rocks studied are that the  $\delta^{18}\text{O}$  values(21.6 to  $30.4\text{\textperthousand}$ ) are enriched in  $^{18}\text{O}$  compared to those of calcites from hydrothermal fields in the world(less than  $15\text{\textperthousand}$ ; ex., Olson, 1979, Mizutani et al., 1982, William and Elders, 1984, Sturchio et al., 1990, Morishita, 1991). Such high  $\delta^{18}\text{O}$  values are reported in calcites in the North Anatolian Fault zone, Germany, where the  $\delta^{18}\text{O}$  values of calcites in host limestones and vein calcites are  $24$  to  $30\text{\textperthousand}$  and  $19$  to  $26\text{\textperthousand}$ , respectively ( the  $\delta^{13}\text{C}$  values are  $0$  to  $5\text{\textperthousand}$  in both limestons and vein calcites).

It is also noted that rocks in the fault zone are enriched in  $\text{CO}_2$  and  $\text{H}_2\text{O}^+$ . These features mean that significant water-rock interactions occurred in site. As mentioned before, several stages of alteration are recognized by the petrographic studies (Fujimoto et al., 1999). Ohtani et al.(1999) measured filling temperature of fluid inclusions from the Nojima core and reported the temperature of  $100$  to  $300^\circ\text{C}$  and high salinity (5 to  $30$   $\text{NaCl}$  wt%). They also analyzed those in calcite at depth of 420m and reported the similar results to other minerals. These imply that the carbonates have been formed during several stages of alteration, especially during formation of the Nojima Fault. An observed temperature for the Nojima well at present is  $18^\circ\text{C}$  at 10m depth and it conductively increases up to  $30^\circ\text{C}$  at the bottom of the well (748m depth).

From these results, the  $\delta^{18}\text{O}$  values of fluids in equilibrium with these calcites are calculated by the following equations.

$$\begin{aligned} \alpha \text{CaCO}_3 \cdot \text{H}_2\text{O} &= \\ (\text{O}^{18}/\text{O}^{16}) \text{CaCO}_3 / (\text{O}^{18}/\text{O}^{16}) \text{H}_2\text{O} & \quad ① \\ 1000 \ln \alpha \text{CaCO}_3 \cdot \text{H}_2\text{O} &= \\ \delta^{18}\text{O}(\text{CaCO}_3) - \delta^{18}\text{O}(\text{H}_2\text{O}) &= \\ 2.78(10^6/T^2) - 2.89 & \quad ② \\ (\leq 500^\circ\text{C}; \text{O'Neil et al., 1969}) & \end{aligned}$$

where  $\alpha$  is a fractionation factor between two species.

The results are shown in Fig.1, where the  $\delta^{18}\text{O}$

values of sea water and meteoric waters are used to be  $0\text{\textperthousand}$  and  $-7.5\text{\textperthousand}$ , respectively. The latter value is an averaged value of those reported for groundwaters discharging anomalously after the 1995 Kobe earthquake and for hot spring waters in this area (Sato et al., 1999).

In Fig.1, the  $\delta^{13}\text{C}$  values of  $\text{HCO}_3^-$  in equilibrium with carbonates studied are also calculated by the following equations. In neutral pH fluids,  $\text{HCO}_3^-$  ion is a dominant species for carbonate ions.

$$\begin{aligned} \alpha \text{CaCO}_3 \cdot \text{HCO}_3^- &= \\ (\text{C}^{13}/\text{C}^{12}) \text{CaCO}_3 / (\text{C}^{13}/\text{C}^{12}) \text{HCO}_3^- & \quad ③ \\ 1000 \ln \alpha \text{CaCO}_3 \cdot \text{HCO}_3^- &= \\ \delta^{13}\text{C}(\text{CaCO}_3) - \delta^{13}\text{C}(\text{HCO}_3^-) &= \\ -8.914(10^6/T^3) + 10.716(10^6/T^2) - 38.27(10^3/T) + 43.97 & \quad ④ \\ (\leq 290^\circ\text{C}; \text{Bottinga, 1969}) & \end{aligned}$$

It is noted that the observed  $\delta^{18}\text{O}$  values for carbonate containing rocks are plotted in areas of those of calcites in equilibrium with sea water at  $20$  to  $40^\circ\text{C}$ , where the  $\delta^{13}\text{C}$  values of  $\text{HCO}_3^-$  are calculated to be  $0$  to  $-8\text{\textperthousand}$ . This results strongly demonstrates one possibility that the carbonates studied are precipitated from sea water mixed with/without meteoric water penetrating along the Nojima Fault. Another possibility is that meteoric water becomes to be enriched in  $^{18}\text{O}$  due to water-rock interaction (oxygen shift) in hydrothermal condition. This oxygen shift is commonly observed to be by 2 to  $8\text{\textperthousand}$  enrichment in geothermal fluids in the world (ex. Craig, 1963) as shown in Fig.7 as one example at the Sumikawa geothermal field (Ueda et al., 1995). At Sumikawa, geothermal fluids are of meteoric origin due to their similar  $\delta^{18}\text{O}$  values to those of local meteoric waters (Ueda et al., 1991), where 2 to  $3\text{\textperthousand}$  enrichment is observed as an oxygen shift. Calcites in the Sumikawa geothermal wells (900 to  $2700\text{m}$  depth) have  $\delta^{18}\text{O}$  values of by  $4\text{\textperthousand}$  higher than those of calcites in equilibrium with meteoric waters as shown in Fig.7.

In the North Anatolian Fault zone, Janssen et al. (1997) reported such high  $\delta^{18}\text{O}$  values for host limestones and by 5 to  $10\text{\textperthousand}$  lower values for vein calcites than the limestones as mentioned before. They concluded that host limestones were precipitated from sea water during the formation of sediments, in contrast, vein calcites are from meteoric water during the fault activity.

In the Nojima core, calcites are enriched along the fault zone and have the high  $\delta^{18}\text{O}$  values with  $\delta^{13}\text{C}$  values close to those of marine carbonates. From these results, the following models are possible for the origin of carbonates studied so far;

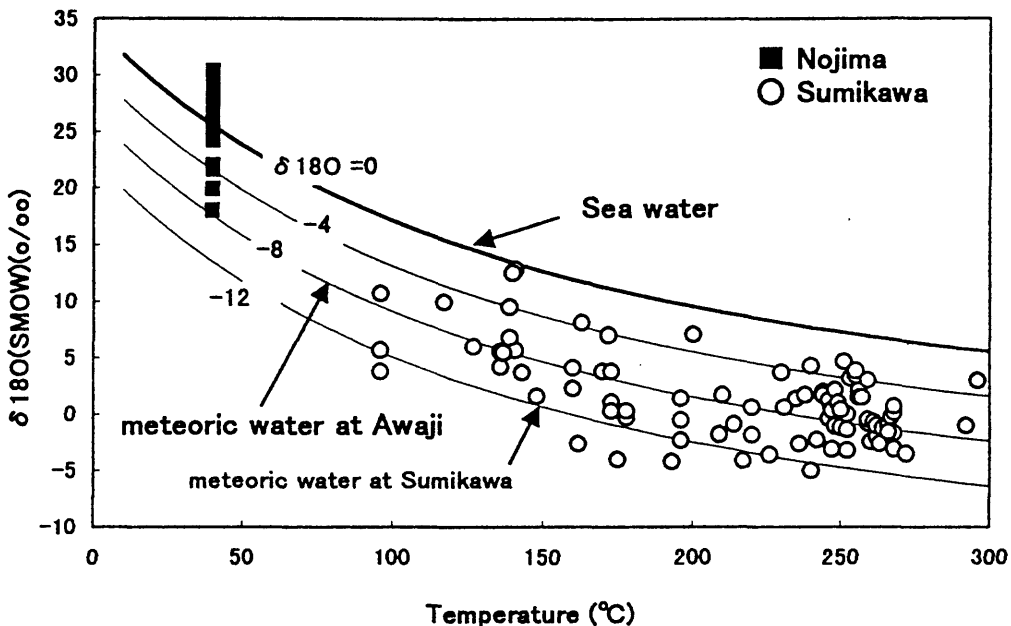


**Figure 7 Oxygen isotopic compositions of carbonates from the Nojima core and Sumikawa geothermal field.**

- (1) precipitation from sea water at temperature of 20 to 40°C,
- (2) precipitation from a mixture of sea water and meteoric water at  $\sim 20^\circ\text{C}$ ,
- (3) precipitation from meteoric water with oxygen shift (by 8‰) at temperature of 20 to 40°C,
- (4) precipitation from meteoric water with oxygen shift (by 30‰) at hydrothermal temperature,
- (5) precipitation of a mixture of sea water and meteoric water with oxygen shift (by 10 to 30‰) at hydrothermal temperature.

In these possibilities, significant degree of water-rock interaction should be occurred in the cases of (3) to (5). Especially, for possibility (3), it is unlikely to be occurred such oxygen shift around room temperature. For possibilities (4) and (5), such high enriched fluids in  $^{18}\text{O}$  have been not reported. From these results and observation of high  $\text{CO}_2$  contents along the Nojima Fault, the authors favor the possibilities (1) and (2).

#### Summary

Carbonate-rich rocks are observed along the Nojima Fault zone. Their isotopic compositions were studied and are characterized due to the high  $\delta^{18}\text{O}$  values. These features might be explained by a possibility that the carbonates were

precipitated from sea water with/without meteoric water. So far, sea water has not been recognized in groundwaters and the surrounding hot springs in the Nojima area. The possible source of such sea water is connate sea waters.

#### Acknowledgements

We are grateful to Dr. S. Sakata of Geological Survey of Japan for CHN analysis.

#### Reference

Bottinga, Y. (1969) Calculated fractionation factors for carbon and hydrogen isotope exchange in the system calcite-carbon dioxide-graphite-methane-hydrogen and water., *Geochim. Cosmochim. Acta*, 33, pp.49-64

Fujimoto, K. (1999) Water-rock interaction along fault rocks and the material transports., *Chikyu*, 21, 7-12.\*

Fujimoto, K., Ohtani, T., Tanaka, H., Tomida, N. and Ito, H. (1999) Characteristics of texture and mineralogy of fault rocks along the Nojima fault: Analysis of continuous core from the GSJ Hirabayashi borehole., *Geol. Surv. Japan Interim Report*, EQ/99/1, 50-53.

Ito, H., Kuwahara, Y., Miyazaki, T., Nishizawa, O., Kiguchi, T., Fujimoto, K., Ohtani, T., Tanaka, H.,

Higuchi, T., Agar, S., Brie, A. & Yamamoto, H. 1996. Structure and Physical Properties of the Nojima Fault. *Butsuri-Tansa* 49, 522-535.

Janssen,C., Michel,G.W., Bau,M., Luders,V. and Muhle,K. (1997) The north Anatolian fault zone and the role of fluids in seismogenic deformation., *J. Geol.*, 105, 387-403.

MacCrea,J.M.(1950) The isotopic chemistry of carbonates and a paleotemperature scale., *J. Chem. Phys.*, 18, 849.

Mizuno,K., Hattori,H., Scangawa,A. and Takahashi,Y. (1990) Geology of the Akashi district. With geological sheet map at 1:50,000., *Geol. Surv. Japan*, 90.

Mizutani,Y.,Akiyama,S., Kimura,M., Kusakabe,M., Satake,H., Usui,K. and Maeda,I. (1982) Mineralogy and isotopic geochemistry of hydrothermally altered rocks from the 54-NK-1 well, Nakao geothermal area, Gifu., Japan *Geotherm. Soc.*, 5, 121-138.

Morishita,Y.(1990) Fluid evolution and geobarometry on the Ohtani and Kaneuchi tungsten-quartz vein deposits, Japan: oxygen and carbon isotopic evidence., *Mineral Deposita*, 26, 40-50.

Olson,E.R. (1979) Oxygen and carbon isotope studies of calcite from the Cerro Prieto geothermal fields., *Geothermics*, 8, 245-251.

O'Neil,J.R., Clayton, R.N. and Mayeda, T.K.(1969) Oxygen isotope fractionation in divalent metal carbonates., *J. Chem.Phys.*,51, 5547.

Rye,R.O. and Ohmoto,H.(1974) Sulfur and carbon isotopes and ore genesis, A review., *Econ. Geol.*,61, 1399.

Sato,T., Sakai,R., Osawa,H., Furuya,K. and Komada,T.(1999) Oxygen and hydrogen isotopic ratios of the anomalously discharged groundwater after the 1995 Kobe earthquake in Awaji Island, Japan., *Japan aquifer Soc.*,29, 13-24.\*

Sturchio,N.C., Keith,T.E.C. and Muchlenbachs,K. (1990) Oxygen and carbon isotope ratios of hydrothermal minerals from Yellowstone drill cores., *J. Volcanol.Geotherm.Res.*, 40, 23-37.

Tanaka, H., Higuchi,T., Tomida, N., Fujimoto,K., Ohtani,T. and Ito,H. (1999a) Distribution deformation and alteration of fault rocks along the GSJ core penetrating the Nojima Fault, Awaji Island, Southwest Japan., *J. Geol. Soc. Japan*, 105, 72-85.\*

Tanaka, H., Higuchi,T., Tomida, N., Fujimoto,K., Ohtani,T. and Ito,H. (1999b) Distribution deformation and alteration of fault rocks along the GSJ core penetrating the Nojima Fault, Awaji Island, Southwest Japan., (in this text).

Ueda, A., Kubota, Y., Katoh,H., Hatakeyama, K. and Matsubaya, O. (1991) Geochemical characteristics of the Sumikawa geothermal system, Japan., *Geochem. Jour.*, 25, 223-244.

Ueda, A., Kubota, Y., Ajima S. and Yamamoto, M. (1995) Isotopic study of calcites from the Sumikawa geothermal area., *Abst. Japan Geochem. Soc.*,C48.\*

William,A.E. and Elders,W.A.(1984) Stable isotope systematics of oxygen and carbon in rocks and minerals from the Cerro Prieto geothermal anomaly, Baja California, Mexico., *Geothermics*, 13, 49-63.

\*: in Japanese with English abstract  
+: in Japanese

# Dynamic analysis based on 3-D orientation distribution of microcracks in quartz from the Cretaceous granodiorite core samples drilled along the Nojima fault, southwest Japan

TORU TAKESHITA and KOSHI YAGI

*Department of Earth and Planetary Systems Science, Faculty of Science, Hiroshima University, Higashi-Hiroshima 739-8526, Japan*

**Abstract** The orientations of both extension healed microcracks recognized as arrays of fluid inclusions (fluid inclusion plane, FIP) and open microcracks sealed mostly by clay minerals in quartz grains were measured with a universal stage for mutually perpendicular three thin sections from the Cretaceous granodiorite core samples drilled along the Nojima fault, southwest Japan. The preferred orientations of both healed and open microcracks approximately consist of three orthogonal sets (components) A, B and C: A strikes N-S~NW-SE and dips vertically, B strikes E-W~NE-SW and dips vertically, and C is horizontal. The microcracking in the mutually orthogonal directions could have been caused by the successive release of residual stresses in the principal stress directions (Takeshita 1995). The quartz grains were also very moderately plastically deformed which is indicated by the occurrence of kink bands and wavy extinction. The association of healed microcracks and kink bands in the quartz suggests that these microstructures formed under subgreenschist facies conditions (ca. 300 °C) during a hydrothermal activity which could have occurred immediately after the emplacement of the granodiorite (during Late Cretaceous). Based on both the preferred orientation of healed microcracks, and *c*-axis fabric of kinked and unkinked grains (so called kink method), it is inferred that the  $\sigma_1$ - and  $\sigma_3$ -axis were oriented horizontally in N-S~NW-SE and E-W~NE-SW directions, respectively. The inferred paleostress field does not conform to the E-W trending compression in Quaternary, but to the activation of E-W~NE-SW trending left-lateral strike-slip faults in Cretaceous in southwest Japan.

## INTRODUCTION

The preferred orientation of extension healed microcrack (explained below) in quartz has long been analyzed in relation to regional geologic structures and paleostress directions. As far as we know, Tuttle (1949) for the first time performed an extensive work on the orientation distribution of healed microcracks in deformed quartz from granite, metamorphic rocks and veins, and noted that it in general consists of two or three orthogonal sets. Bonham (1957) showed that although microfractures in quartz grains from sandstones are dominantly oriented perpendicular to a regional axis of anticline, a secondary orientation of

microfractures parallel to the fold axis is also predominant in some samples.

Some modern interpretations have been given for the development of microcracks in quartz since 1990. Both Jang and Wang (1991) and Vollbrecht *et al.* (1991) argued that microcracks in quartz from granite formed by thermal contraction during the cooling of granite (i.e. cooling joint). Since the thermal expansion coefficients of quartz are so high that a high tensional stress can be created in quartz by thermal contraction during its cooling, resulting in the formation of extension microcracks. Takeshita (1995) on the other hand argued that the formation of healed microcracks was not caused by thermal contraction of quartz, but by the buildup of pore fluid pressure (hydrofracturing). If the stress field is non-lithostatic, the tensile strength of quartz is first exceeded in the minimum principal stress ( $\sigma_3$ ) direction irrespective of the origin of tensile stress in quartz, which leads to the microcracking perpendicular to the regional  $\sigma_3$ -axis. Accordingly, it is expected that a very strong preferred orientation of microcracks perpendicular to the  $\sigma_3$ -axis becomes developed in quartz under non-lithostatic stress fields, which was in fact shown by Jang and Wang (1991). However, as already noted, the orientation distribution of microcracks in deformed quartz is much more complex, and often consists of two or three orthogonal sets (e.g. Tuttle 1949; Dula 1981; Lespinasse & Pecher 1986; Vollbrecht *et al.* 1991; Takeshita 1995, Takeshita *et al.* 1996, 1997). It has been found that each of two or three orthogonal sets of microcracks in quartz is oriented perpendicular to one of the principal paleostress directions, although different ideas were proposed for the origin (Vollbrecht *et al.* 1991; Takeshita 1995).

In this study, we analyzed the orientation distribution of microcracks in deformed quartz from the granodiorite core samples drilled along the Nojima fault, and documented that three orthogonal sets of microcracks are developed in the quartz. Based on the results, we inferred the paleostress fields and histories for microcracking in the quartz in the light of movement of the Nojima fault.

## SAMPLE DESCRIPTION AND ANALYTICAL PROCEDURES

We collected 7 oriented granodiorite (Ryoke younger granite; the amphibole K-Ar ages were dated as 87.7 Ma by Takahashi 1992) samples from the Ogura 1800 m (5 samples) and Hirabayashi 750 m (2 samples) cores drilled along the Nojima fault (Table

1). These two cores were drilled by the Disaster Prevention Research Institute of Kyoto University (DPRIK) and the Geological Survey of Japan (GSJ), respectively.

Sample No.	No.1 (DPK)	No.2 (DPK)	No.3 (DPK)	No.4 (DPK)	No.5 (DPK)	No.6 (GSJ)	No.7 (GSJ)
Depth (m)	532.3	785.5	893.5	898.0	1003.4	538.0	631.1
Rock type	Dr.	Grd.	Grd.	Grd.	Grd.	Grd.	Grd.
Key orient.	E	S38°W	N31°E	S16°E	N24°E	N	N

Table 1. Depth, rock type and key direction of the drilled core samples

DPK: Disaster Prevention Research Institute of Kyoto University, GSJ: Geological Survey of Japan, Dr.: Diorite, Grd.: Granodiorite

For the 5 core samples retrieved by the DPRIK, the localities are far from the Nojima fault plane which is penetrated at the depth of ca. 400 m by the Ogura 500 m core drilled in the vicinity of the 1800 m core. On the other hand, for the 2 core samples retrieved by the GSJ, the localities are rather close to the main shear zone (MSZ, Tanaka et al., 1999) at the depth of 625 m, within 50 m vertical distance from the fault plane. The granodiorite core samples are significantly hydrothermally altered; plagioclase and biotite underwent a saussuritization and muscovitization, and chloritization, respectively. Except for sample 1 in which the volume fraction of quartz is small, mutually perpendicular three thin sections (one is horizontal, and the other two, one of which includes the key direction, are vertical) were prepared for microfabric analyses. For each of the mutually perpendicular three thin sections from samples 2 to 7, at least 100 orientations of healed and open microcracks in quartz were measured, respectively with a universal stage under a microscope.

Here, the definition of healed and open microcracks is as follows. For healed microcracks, the open space created by microcracking is healed by crack healing processes (Smith & Evans 1984). Since

fluids which circulated through microcracks were trapped by the crack healing processes, healed microcracks are only recognized as arrays of fluid inclusions (fluid inclusion plane, FIP). On the other hand, for open microcracks the open space was sealed by minerals (mostly clay and mica minerals in the present samples) precipitated from the solution.

For each measurement of microcrack orientation, the unit vector normal to microcrack was calculated. Those unit vectors obtained for the mutually perpendicular two vertical thin sections were transformed to those in the frame of horizontal thin section. This way the orientation data from the mutually perpendicular three thin sections were combined (e.g. Vollbrecht et al. 1991; Takeshita 1995).

#### PREFERRED ORIENTATION OF MICROCRACKS IN QUARTZ

##### HEALED MICROCRACKS

The orientation distribution for each sample was presented in Figs. 1a, 2a, 3a, 4a, 5a and 6a.

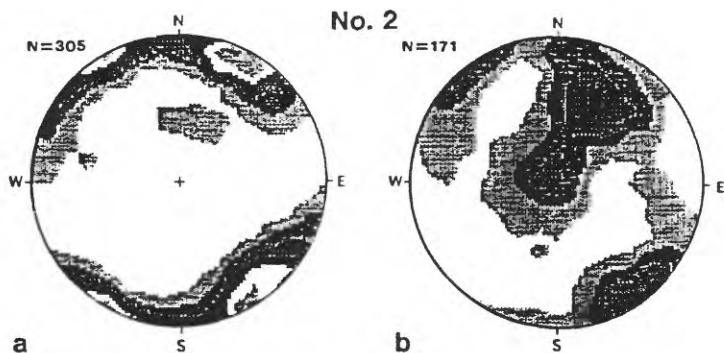


Fig. 1. Upper-hemisphere and equal-area projections of (a) 305 healed and (b) 171 open microcracks in the quartz grains from sample 2 in horizontal plane. Kamb contours and contour intervals are  $2\sigma$ . All the fabric diagrams have been plotted and contoured using the stereonet program by Allmendinger (1988).

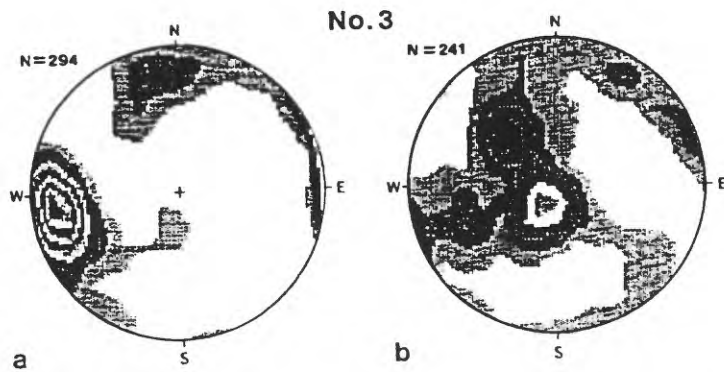


Fig. 2. Upper-hemisphere and equal-area projections of poles of (a) 294 healed and (b) 241 open microcracks in the quartz grains from sample 3 in horizontal plane. Kamb contours and contour intervals are  $2\sigma$ .

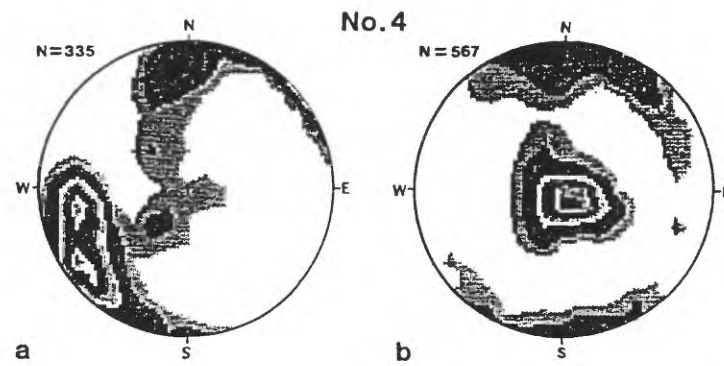


Fig. 3. Upper-hemisphere and equal-area projections of poles of (a) 335 healed and (b) 567 open microcracks in the quartz grains from sample 4 in horizontal plane. Kamb contours and contour intervals are  $2\sigma$ .

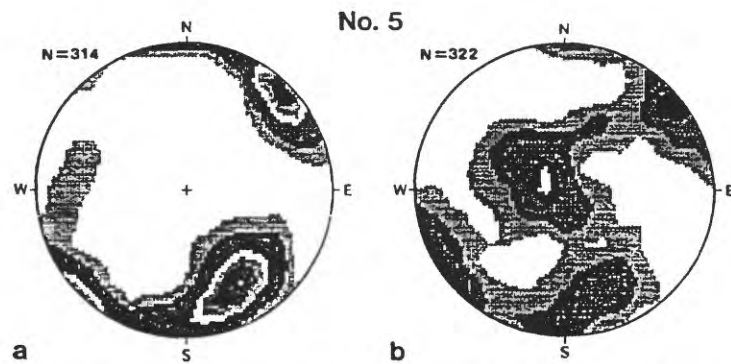


Fig. 4. Upper-hemisphere and equal-area projections of poles of (a) 314 healed and (b) 322 open microcracks in the quartz grains from sample 5 in horizontal plane. Kamb contours and contour intervals are  $2\sigma$ .

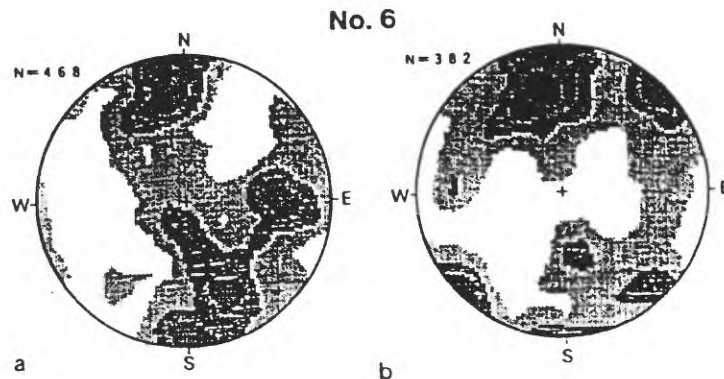


Fig. 5. Upper-hemisphere and equal-area projections of poles of (a) 468 healed and (b) 382 open microcracks in the quartz grains from sample 6 in horizontal plane. Kamb contours and contour intervals are  $2\sigma$ .

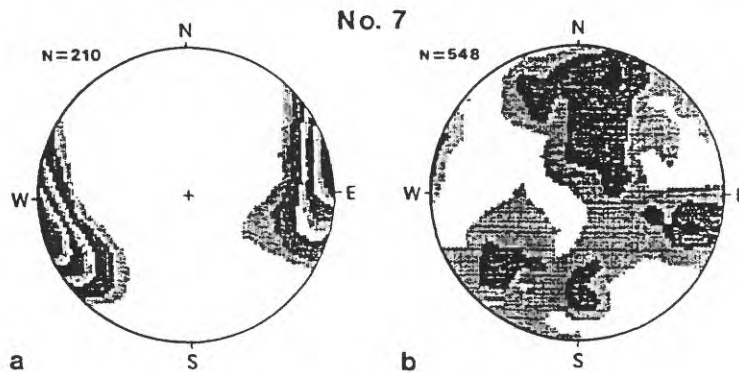


Fig. 6. Upper-hemisphere and equal-area projections of poles of (a) 210 healed and (b) 548 open microcracks in the quartz grains from sample 7 in horizontal plane. Kamb contours and contour intervals are  $2\sigma$ .

In samples 3, 4 and 5, healed microcracks which strike N-S-NW-SE and dip vertically (here referred to as orientation component A) most dominate, those which strike E-W-ENE-WSW and dip vertically (B) are also dominant, and a very small number of horizontally oriented microcracks (C) exists. These three orientation components of healed microcracks are roughly mutually perpendicular. The orientation distribution of healed microcracks in sample 2 is somewhat different from those in samples 3 through 5. In sample 2, vertical healed microcracks dominate, the strike of which greatly varies from NW-SE through E-W to NE-SW. In sample 6, the E-W-trending vertical component (B) is more dominant than the N-S-trending vertical component (A). In sample 7, only the component A dominates.

Note that there is no displacement of markers such as and grain boundaries (some of healed microcracks are transgranular) along healed microcracks, indicating that these microcracks are extension cracks. Hence, it is impossible to infer the chronological order of formation of differently oriented sets of microcracks.

#### OPEN MICROCRACKS

The orientation distribution of open microcracks for each sample was presented in Figs. 1b, 2b, 3b, 4b, 5b and 6b. The overall pattern (referring to fabric skeleton, not to the density of each component) of orientation distribution of open microcracks is similar to that of healed microcracks for each sample. Although components A, B and C also more or less appear in the orientation distribution of open microcracks in all the samples, their densities greatly differ from those of healed microcracks. In samples 3, 4 and 5, open microcracks oriented horizontally (C) are most dominant in contrast to a low frequency of this component for healed microcracks. Open microcracks belonging to component B are also dominant in all the samples. Open microcracks belonging to component A which is most dominant for healed microcracks are dominant in samples 3, 5 and 7, but are scarce in samples 2, 4 and 6. Note however that the degree of concentration of component A is much higher for healed than for open microcracks in samples 3, 5 and 7. In samples 2 and 3, microcracks which strike WNW-ESE and NE-

SW and dip northward at 50° and 60°, respectively are also dominant. Also, in sample 6, NW-SE trending vertical microcrack is dominant. Such oriented components are almost absent for healed microcracks in the same samples. Note that there is no displacement of any markers along open microcracks, indicating that these microcracks are extension cracks.

#### DYNAMIC ANALYSIS USING THE KINK METHOD

The deformed quartz from the granodiorite core samples is very moderately plastically deformed which is indicated by the occurrence of kink bands and wavy extinction. The fact that kink band boundaries are in most cases parallel to the *c*-axis in grains containing kink bands suggests that the operative slip system was basal (0001) slip (e.g.

Carter & Raleigh 1969). When basal (0001) slip is the dominant slip system, one can infer the paleostress directions based on the preferred *c*-axis orientations of kinked and unkinked grains (so called the kink method, Takeshita 1995). Namely, grains with *c*-axis oriented at the intermediate orientation between the  $\sigma_1$  (maximum principal stress)- and  $\sigma_3$  (minimum principal stress)-axis most tend to kink because the highest shear stress is resolved on basal (0001) plane, while grains with *c*-axis oriented parallel to the principal stress directions least tend to kink because no shear stress is resolved on it.

*c*-axis orientations of both kinked and unkinked grains from sample 3 were measured separately with a universal stage (Figs. 7a & b).

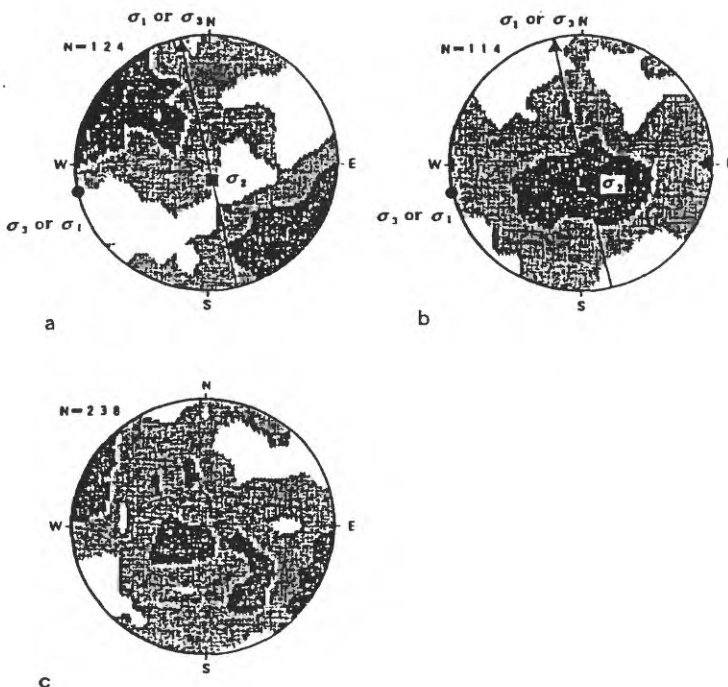


Fig. 7. Upper-hemisphere and equal-area projections of *c*-axes of (a) 124 kinked, (b) 114 unkinked and (c) all of the 238 quartz grains from sample 3 in horizontal plane. Kamb contours and contour intervals are  $2\sigma$ . The inferred  $\sigma_1$  (or  $\sigma_3$ )-,  $\sigma_2$ -,  $\sigma_3$  (or  $\sigma_1$ )-axis and  $\sigma_1$  (or  $\sigma_3$ )- $\sigma_2$  plane from the kink method are denoted by solid triangles, squares, circles and straight lines, respectively in Figs. 7a and b.

They are somewhat complementary indicating the favorable and unfavorable *c*-axis orientations, respectively for basal (0001) slip under stress. The *c*-axis orientations of kinked grains are most concentrated in NW-SE horizontal directions. The maximum *c*-axis orientation must coincide with one of the intermediate directions between the  $\sigma_1$ - and  $\sigma_3$ -axis. Although two maxima are supposed to be distributed symmetrically at the intermediate directions between the  $\sigma_1$ - and  $\sigma_3$ -axis, no

symmetrical disposition of the maxima is found in the *c*-axis fabric of kinked grains perhaps due to the very weak *c*-axis preferred orientation in all the grains (Fig. 7c).

Along the great circle almost parallel to the E-W trending vertical plane, *c*-axis orientations of kinked grains are sparsely populated, while those of unkinked grains are densely populated (Figs. 7a & b). Therefore, it is inferred that the nearly E-W trending vertical plane is the  $\sigma_2$ - $\sigma_3$  or  $\sigma_1$ - $\sigma_2$  plane, because the resolved shear stress on basal (0001) plane is

relatively low in these  $c$ -axis orientations. The orientation of the maximum  $c$ -axis concentration nearly parallel to the vertical direction in unkkinked grains could be parallel to the  $\sigma_2$ -axis. This way the  $\sigma_1$ -,  $\sigma_2$ - and  $\sigma_3$ -axis are inferred to be nearly N-S or E-W trending and horizontal, nearly vertical, and nearly E-W or N-S trending and horizontal, respectively (Fig. 7).

## DISCUSSION AND CONCLUSIONS

The association of intracrystalline gliding and healed microcracking in the quartz suggests that the deformation in the quartz probably occurred at subgreenschist conditions around 300 °C (also the conditions for brittle-ductile transition in quartz, e.g. Takeshita 1995) closely associated with a hydrothermal activity. There are neither volcanoes nor hot springs in the Nojima district. Hence, assuming a geothermal gradient of 30 °C/km it seems unlikely that during the Quaternary period high temperature fluids around 300 °C circulated at the depth of less than 1 km (2-3 km even considering the uplift during the Quaternary period) where the granodiorite core samples were collected. Hence, the intracrystalline gliding and healed microcracking in the quartz under subgreenschist conditions could have occurred during a hydrothermal event before Quaternary. It can be most reasonably concluded that healed microcracks in the quartz formed in Late Cretaceous (around 85 Ma) immediately after the solidification of the granodiorite when it was still hot enough.

Based on the fact that healed microcracks striking N-S-NW-SE and dipping vertically (component A) most dominate, it could be inferred that the  $\sigma_3$  direction trended E-W-NE-SW and plunged horizontally at the time of microcracking (Fig. 8).

Considering also the result of the kink method, the  $\sigma_1$ -axis perhaps trended N-S-NW-SE and plunged horizontally (parallel to the pole of B-component of microcrack) at the time of healed microcracking and moderate plastic deformation in the quartz (Fig. 8).

The inferred paleo- $\sigma_1$  direction does not agree not only with the well known E-W trending compression in southwest Japan during Quaternary (e.g. Okada & Ando 1979), but with the result of in-situ measurement of stress orientation at the vicinity of the Nojima fault using the borehole breakout method (the  $\sigma_1$ -axis is oriented horizontally in N45°W direction, Tsukahara *et al.* 1998). Rather, the inferred paleostress field conforms to that in southwest Japan during Late Cretaceous, which caused a pervasive left-lateral transcurrent faulting along E-W-NE-SW trending faults in southwest Japan (e.g. Otsuki and Ehiro 1978; Hara *et al.* 1980).

The intense microcracking in the quartz grains may have been related with the formation of the proto-Nojima fault which could have been activated as a left-lateral fault (Fig. 8).

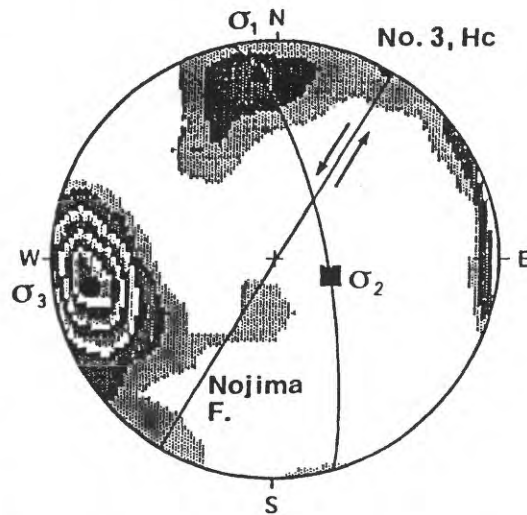


Fig. 8. Projection of the inferred principal stress directions from the preferred orientation of healed microcracks in the quartz grains in horizontal plane, superposed on the orientation distribution of poles of healed microcracks in sample 3. Upper-hemisphere and equal-area projections. The inferred  $\sigma_1$ -,  $\sigma_2$ - and  $\sigma_3$ -axis are denoted by solid triangle, square and circle, respectively. Solid curved and straight lines denote the projections of the inferred  $\sigma_1$ - $\sigma_2$  plane and the proto-Nojima fault plane, respectively. The arrows indicate the inferred sense of shear along the proto-Nojima fault under the paleostress field.

Since the overall patterns of preferred orientation of open and healed microcracks are similar, it is inferred that both types of microcracks could have formed under the same paleostress field at the same time. However, for healed microcracks both the orientation components which strikes N-S-NW-SE and dips vertically (A), and strikes NE-SW-E-W and dips vertically (B) dominate, whereas for open microcracks both the orientation components B and C (those oriented horizontally) dominate. We interpreted these differences in the dominant orientation between healed and open microcracks in the following way.

The time necessary for crack healing in quartz strongly depends on temperature conditions. According to Smith and Evans (1984) a crack which heals completely in 2 days at 400 °C would require several months at 200 °C. It is likely that the fluids which penetrated into fault zones were cooled rapidly by relatively cooler host rocks unless the fault zones

were extremely wide. For example, the time constant for cooling for a fault zone of 10 m width heated by hot fluids is an order of year (here a thermal diffusivity of  $10^{-6} \text{ m}^2/\text{s}$  is assumed). Therefore, the healing of microcracks could have occurred immediately after the microcracking and injection of hot fluids into the fault zone when the fluids were so hot that crack healing occurred very rapidly.

The tensile strength in the quartz was first exceeded in the direction of the  $\sigma_3$ -axis as pore fluid pressure increased, resulting in the formation of microcracks perpendicular to the  $\sigma_3$ -axis. However, since the formation of numerous healed microcracks perpendicular to the  $\sigma_3$ -axis may have led to an almost complete release of residual stresses in this direction, the subsequent microcracking probably occurred perpendicular to the  $\sigma_2$ -axis (and further perpendicular to the  $\sigma_1$ -axis), as the tensile strength in the quartz was exceeded in these directions by the buildup of pore fluid pressure (successive release of residual tectonic stress in the principal stress directions as proposed by Takeshita 1995).

As the time went on, the temperatures in the fault zone were decreased below say  $200^\circ\text{C}$ , resulting in the sluggishness of formation of healed microcracks. Hence, minerals (mostly clay minerals) which were dissolved in the fluids precipitated in the open spaces created by microcracking, leading to the formation of sealed open microcracks below  $200^\circ\text{C}$ . During the formation of open microcracks, the residual stresses in the  $\sigma_1$  and  $\sigma_2$  directions were mostly released, resulting in the development of such preferred orientation of open microcracks that both the components B and C dominate.

## REFERENCES

ALLMENDINGER, R. W. 1988. Stereonet 4.3a - Academic version; a plotting program for orientation data. Computer program.

BONHAM, L. C. 1957. Structural petrology of the Pico Anticline, Los Angeles Co., California. *Journal of Sedimentary Petrology* 27, 251-264.

CARTER, N. L. & RALEIGH, C. B. 1969. Principal stress directions from plastic flow in crystals. *Bulletin of the Geological Society of America* 80, 1231-1264.

DULA, W. F. 1981. Correlation between deformation lamellae, microfractures, macrofractures, and in situ stress measurements, White River Uplift, Colorado. *Bulletin of the Geological Society of America* 92, 37-46.

HARA, I., SHOJI, K., SAKURAI, Y., YOKOYAMA, S. & HIDE, K. 1980. Origin of the Median Tectonic Line and its initial shape. *The memoirs of Geological Society of Japan* No. 18, 27-49.

JANG, BO-AN & WANG, H. F. 1991. Micromechanical modeling of healed crack orientations as a paleostress indicator: application to Precambrian granite from Illinois and Wisconsin. *Journal of Geophysical Research* 96, 19655-19664.

LESPINASSE, M. & PECHER, A. 1986. Microfracturing and regional stress field: a study of the preferred orientations of fluid-inclusion planes in a granite from the Massif Central, France. *Journal of Structural Geology* 8, 169-180.

OKADA, A. & ANDO, M. 1979. Active faults and seismicity. *Kagaku* 49, 158-169 (in Japanese).

OTSUKI, K. & EHIRO, M. 1978. Major strike-slip faults and their bearing on spreading in the Japan Sea. *Journal of Physics of the Earth* 26, 537-555.

SMITH, D. L. & EVANS, B. 1984. Diffusional crack healing in quartz. *Journal of Geophysical Research* 89, 4125-4135.

TAKAHASHI, H. 1992. K-Ar ages of granites in the Awaji island, southwest Japan: constraints on the timing of mylonitization. *Journal of Mineralogy, Petrology and Economic Geology* 87, 291-299 (in Japanese with English abstract).

TAKESHITA, T. 1995. Dynamic analysis of deformed quartz grains from the folded Middle Miocene Momonoki Subgroup of central Japan: origin of healed microcracks. *Tectonophysics* 245, 277-297.

TAKESHITA, T., NAOMOTO, K. & YAGI, K. 1997. Studies on the deformed rock samples collected by Department of Earth and Planetary Systems Science, Hiroshima University, Part 3: Dynamic analysis of deformed quartz grains in en echelon quartz veins and their formation temperatures. *Report of the Hiroshima University Museum* No. 3, 41-49 (in Japanese with English abstract).

TAKESHITA, T., TORIGOE, Y., HASHIMOTO, S., ETO, A., SAKAUE, A., OHTOMO, J., TAGAMI, M., NISHIKAWA, O. & ENDO, H. 1996. Dynamic analysis of deformed quartz grains from fractured Jurassic sandstones in the Southern Kitakami belt, NE Japan. *Tectonics and Metamorphism* (The Hara Volume), SOUBUN CO., Ltd., Tokyo, pp. 261-279 (in Japanese with English abstract).

TANAKA, H., HIGUCHI, T., TOMIDA, N., FUJIMOTO, K., OHTANI, T. & ITO, H. 1999. Distribution, deformation and alternation of fault rocks along the GSJ core penetrating the Nojima Fault, Awaji Island, southwest Japan. *Jour. Geol. Soc. Japan*, 105, 72-85 (in Japanese with English abstract).

TSUKAHARA, H., IKEDA, R. & YAMAMOTO, K. 1988. Crustal stress measurement in the vicinity of the Nojima fault at the depth of 1500 m: a small maximum horizontal compressional stress perpendicular to the fault. *Earth Monthly*, Special Issue No. 21, 66-69 (in Japanese).

TUTTLE, O. F. 1949. Structural petrology of planes of liquid inclusions. *Journal of Geology* 57, 331-356.

VOLLBRECHT, A., RUST, S. & WEBER, K. 1991. Development of microcracks in granites during cooling and uplift: examples from the Variscan basement in NE Bavaria, Germany. *Journal of Structural Geology* 13, 787-799.

# Fault rock distribution analysis based on chemical composition, water contents and fracture density

Naoto Tomida<sup>1</sup>, Hirokazu Tsukiyama<sup>1</sup>, Hidemi Tanaka<sup>1</sup>, Koichiro Fujimoto<sup>2</sup>, Tomoyuki Ohtani<sup>2</sup> and Hisao Ito<sup>3</sup>

<sup>1</sup>Department of Earth Sciences, Faculty of Sciences, Ehime University, Bunkyo-cho 2-5, Matsuyama, Ehime 790-8577 Japan, E-mail address ntomida@sci.sci.ehime-u.ac.jp

<sup>2</sup>Geological Survey of Japan, Geothermal Department, Higashi 3-3-1, Tsukuba 305-8567, Japan

<sup>3</sup>Geological Survey of Japan, Earthquake Research Department, Higashi 3-3-1, Tsukuba 305-8567, Japan

## ABSTRACT

We investigate chemical composition of GSJ core and compared with geological columnar based on naked observation. And then it become clear that the necessity of suitable geological columnar to compare with chemical composition exactly. For the purpose of it, we considered a method that determined the quantity of fault rocks. Fault rocks were formed under influence of both of deformation and alteration, or either of them. Therefore, we try to determine the quantity of GSJ core using two axes of deformation and alteration (the vertical axis; alteration, the horizontal axis; deformation). As deformation is action of destruction, we use the fracture density of surface of the core as an index of deformation. Fault gouge and altered rocks that have notable alteration contain plenty of clay minerals and carbonate minerals. Clay minerals contain a large quantity H<sub>2</sub>O and carbonate minerals contain CO<sub>2</sub> in the structure. So we use the content of (H<sub>2</sub>O+CO<sub>2</sub>) of the core as an index of alteration. In this study, we use the Loss of ignition (LOI) of the core as an index of alteration. As a result, it is considered that division of fault rocks by naked observation and by measurement of the fracture density, LOI are almost correspond. However, we can not get clear border of division. It is suspected that we need to increase samples, and we must investigate the way that give suitable quantitatively estimation.

### 1. Outline of fault rock distribution in GSJ core

To begin with, we observed all core of GSJ core (152.24m~746.60m), investigated fault rock distribution, and made geological columnar (Tanaka et al. 1999, Fig.1).

GSJ core is mainly composed of granodiolite, and with porphyry as a intrusive rock. On the main shear zone, weakly pulverized-and altered granodiolite, cataclasite, fault breccia, altered rocks, fault gouge are distributed (Ito et al. 1996; Tanaka et al. 1998). And, there are seven notable shear zone in GSJ core from a depth of 530m to a depth of 710m (Tanaka et al. 1999).

### 2. Whole-rock geochemical analyses

We refer to results of whole-rock geochemical analyses. To investigate about income and expenditure of substance transfer of fault rocks, we examined whole-rock geochemical analysed data using by X-ray florescence. For that purpose, we adopted data of Tanaka et al. (1999)

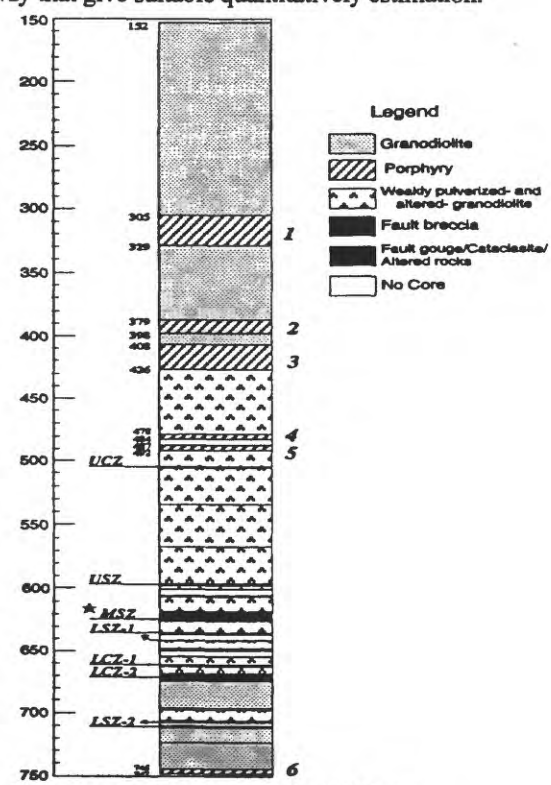


Fig.1 Geological columnar of GSJ core

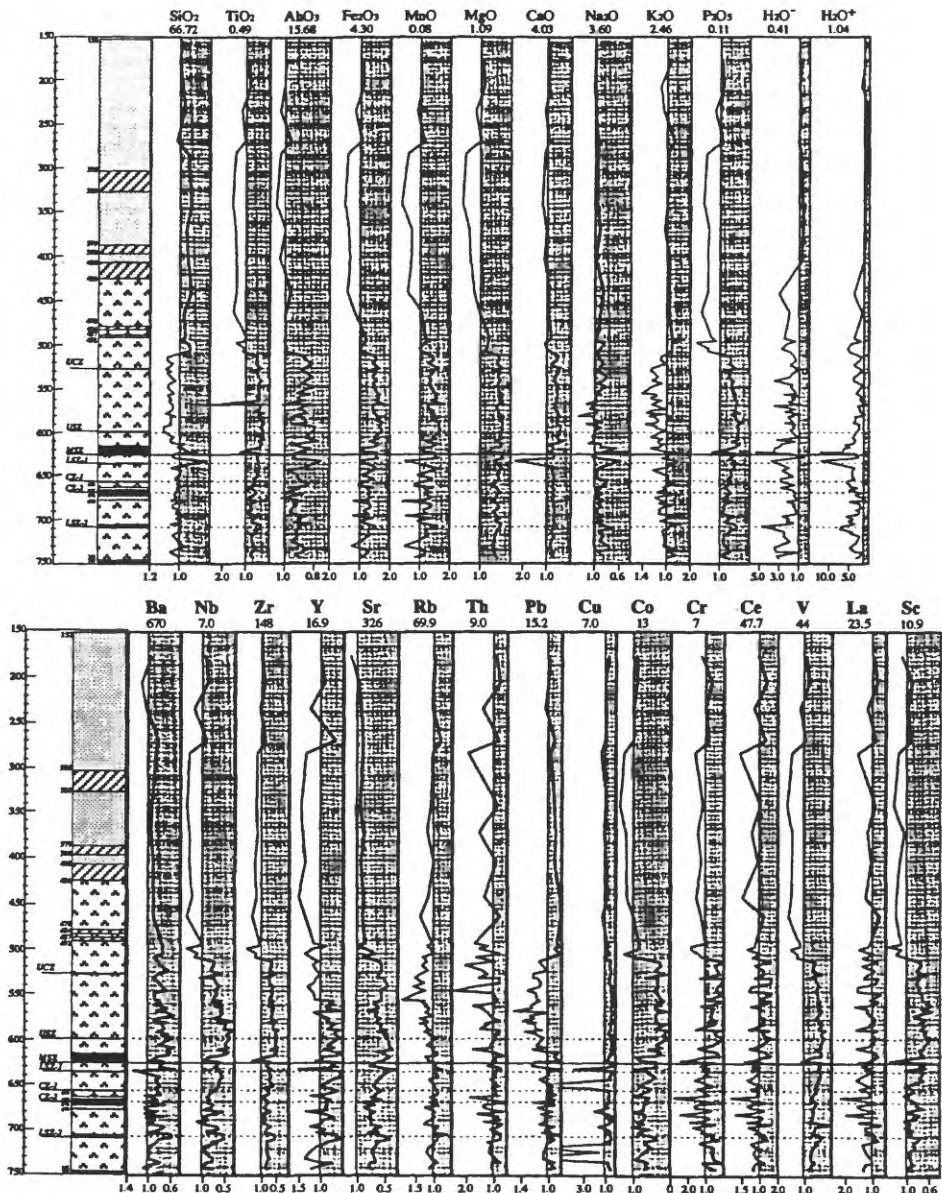


Fig.2 The data of whole - rock geochemical analyses

Major- and Trace- elements data were normalized by the standard data. Standard data are under chemical formulas or symbol of elements

In this research , they picked samples at intervals of 50m from a depth of 150m to main shear zone near by depth of 600m and at intervals of 2.5m from main shear zone to a depth of 710m. In all , they analyzed 94 samples.

In these analyzed data , we took the average of four samples within the shallow depth which have little deformation and alteration , and use it a standard data. And , we normalized all data by it.

As for major-element , 10 elements which

measured by X-ray flouorescence analysis and the Loss of ignition ( LOI ) (H<sub>2</sub>O- is adsorptive water , and H<sub>2</sub>O+ is water of crystallization ) compensate for 100%. We normalized these major- and trace- elements were by the standard data and compared with correspond the geologic columnar (Fig.2 ). According to the result , all elements vary from near a depth of 490m to more deeply parts. As to major-elements , all elements except SiO<sub>2</sub> , Na<sub>2</sub>O , K<sub>2</sub>O and H<sub>2</sub>O+ obviously decrease. And all elements show increase

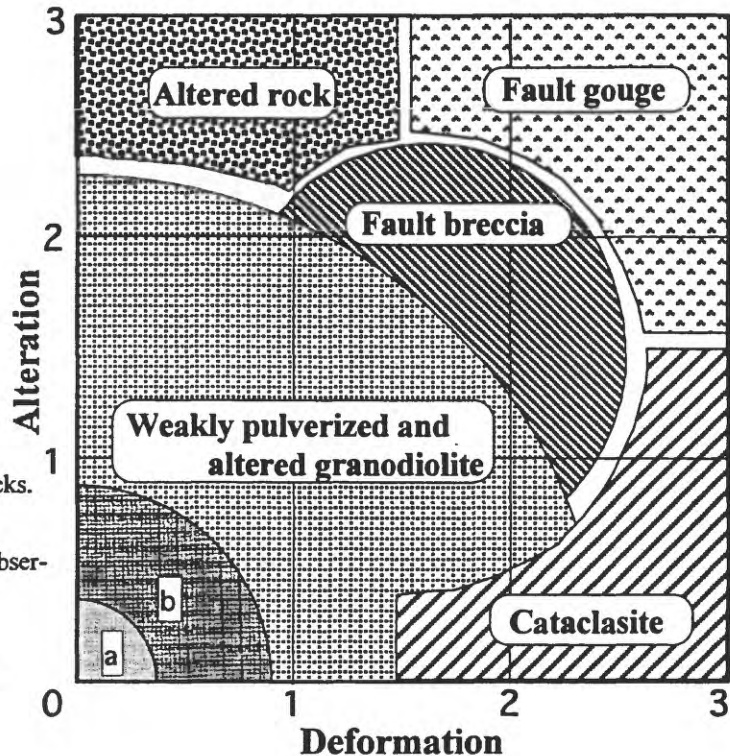


Fig.3 Diagram of division of fault rocks.

( Kobayashi , 1998 )

This diagram is based on the naked observation of the core.

a : Fresh granodiolite

b : Comparatively fresh granodiolite

and decrease trend at shear zones. As to trace-elements , all elements except Y , Rb , Th , Pb , Ce and La obviously decrease. As well as major-elements , all elements show increase and decrease trend at shear zones as for trace-element.  $H_2O^+$  has large increase at shear zones. In these results , it is considered that each elements transfer around shear zones by the medium of  $H_2O^+$ .

### 3. A fixed quantity of division of fault rocks

Fault rocks in GSJ core are divided semi-quantitatively based on the naked observation of the core ( Kobayashi , 1998 , Fig.3) On a discussion of chemical composition , it is important that we define clearly to division of fault rocks. And , these fault rocks were formed under influence of both of deformation and alteration , or either of them (Tanaka et al. 1999 ). However , this division of fault rocks is not quantitative. So we try to determine the quantity of GSJ core using two axes of deformation and alteration.

As deformation is action of destruction , we use the fracture density of surface of the core as an index of deformation. Fault gouge and altered rocks that have notable alteration contain plenty of clay minerals , carbonate minerals. Clay minerals contain

a large quantity  $H_2O$  , carbonate minerals contain  $CO_2$  in the structure , so we use the content of  $(H_2O + CO_2)$  of the core as an index of alteration. In this study , we consider LOI of samples is approximate value of the content of  $(H_2O + CO_2)$  , so we use the LOI of the core as an index of alteration.

#### 3-1.The method of measurement of the fracture density

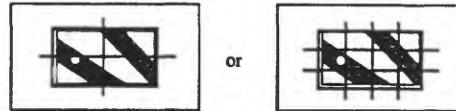
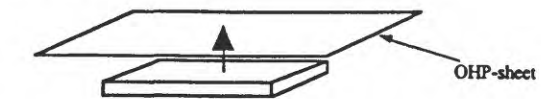
On measurement of the fracture density , we used 76 samples of GSJ core selected by the naked observation. We show the method of measurement ( Fig.4 )

##### 3-1-1.Trace of cores and draw several lines

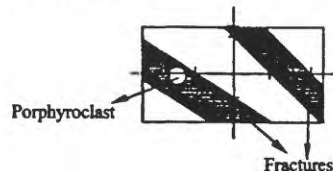
We put OHP-sheet on a core , and traced a figure of core. We drew several vertical and horizontal lines on the trace. The number of these lines depend on core size.

##### 3-1-2.Trace of fractures

We traced parts piled up fracture on the lines. In case there are fill minerals , we measured that width , and in case there are porphyroblast , we didn't trace there.



## 2, Trace of fractures



### 3. The calculation of fracture density

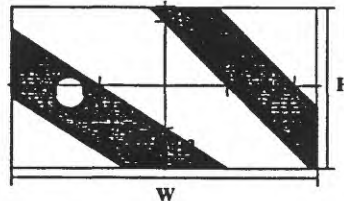


Fig.4 The method of measurement of the  $\Sigma Hn/H \times \Sigma Wn/W \times 100 (\%)$  Hn ( H1 , H2..... ) fracture density. Wn ( W1 , W2..... )

### 3-1-3.The calculation of fracture density

We suppose that vertical line length is  $H$ , horizontal line length is  $W$ , and vertical lines width on the line we trace are  $H_1, H_2, \dots$ , horizontal lines width are  $W_1, W_2, \dots$ . Next, we multiply the value  $(\sum H_n / H)$  that divided total of vertical lines width  $(\sum H_n)$  by vertical line length  $(H)$  by value  $(\sum W_n / W)$  that divided total of horizontal lines width  $(\sum W_n)$  by horizontal line length  $(W)$ . Then that value indicated percentage is fracture density. In case there are several vertical or several horizontal lines, we got an average.

$$\text{Fracture density} = (\sum H_n/H) \times (\sum W_n/W)$$

### 3-2. The calculation of LOI

On the calculation of shear density, we made powder samples from same samples calculated shear density. We show the method of measurement

### 3-2-1. Washing, crush, measurement of sample's weight

We pick up well-balanced point of samples , and for excepting mud water , wash them by super-sonic waves washer. After then , we made them dry at 60°C in the dry machine for one day. So , we crushed them by an agate-mortar. Lastly , measured sample's weight.

### 3-2-2.Exceptting adsorptive water

We excepted adsorptive water at 110°C in the dry machine for 3 hours. After then, we measured sample's weight ( weight after 110°C ) except adsorptive water.

### 3-2-3. Ignition

We excepted constitution water from samples excepted adsorptive water at 1000°C in the hearth for 3 hours. And then, we measured sample's weight ( weight after 1000°C. ) except water of crystallization.

### 3-2-4. The calculation of LOI

The value subtract weight after 1000°C from weight after 110°C is a loss in weight after 1000 °C.

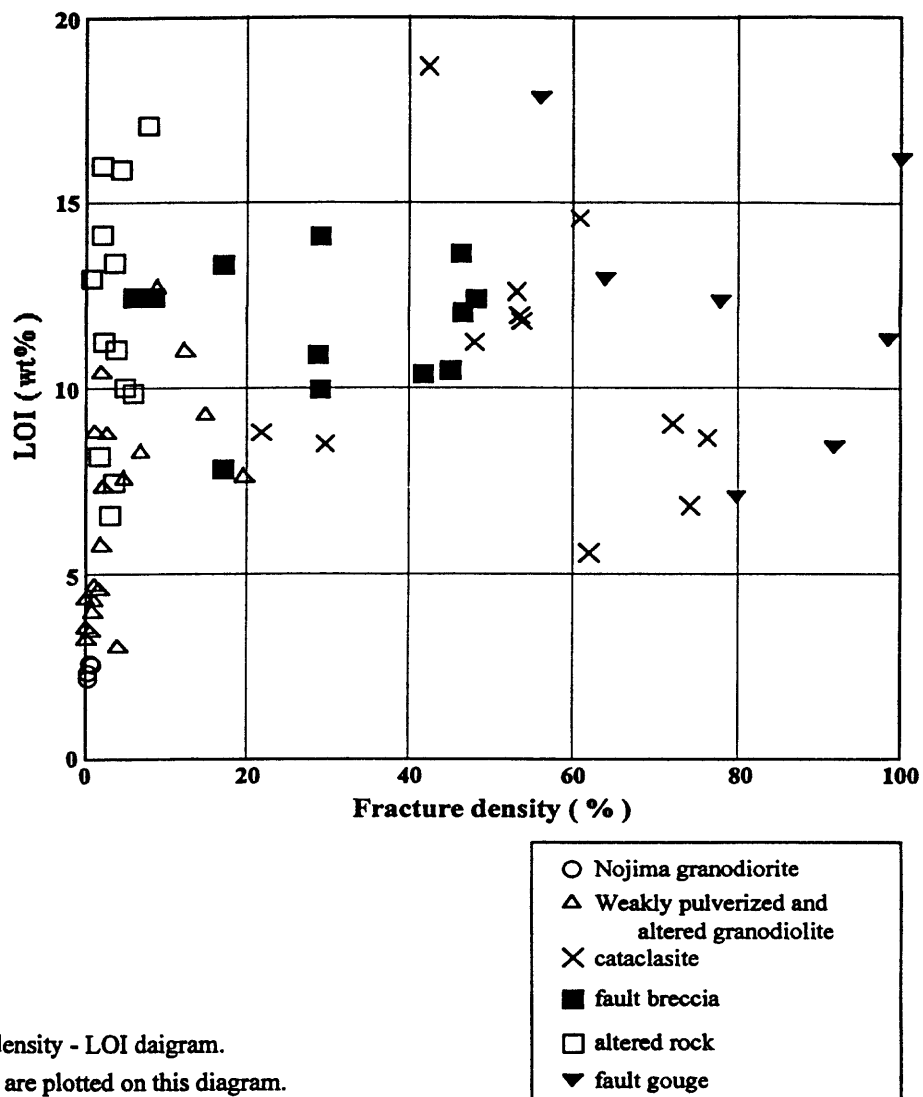


Fig.5 Fracture density - LOI daigram.  
70 samples datas are plotted on this diagram.

That value is weight of constitution water. We divided this weight of water of crystallization by weight after 110°C , and then that value indicated percentage is LOI.

$LOI (\text{ wt\% }) = \text{loss in weight after } 1000 \text{ }^{\circ}\text{C} / \text{ weight after } 110 \text{ }^{\circ}\text{C} \times 100$

#### 4.Results

We made Fracture density - LOI comparative figure ( Fig.5 ). We can look some character.

##### 4-1.The parent rock ( Granodiolite )

Both fracture density and LOI value indicate low.

##### 4-2. Weakly pulverized-and altered granodiolite

Fracture density value indicates low , LOI value indicates from comparatively low to high.

##### 4-3.Cataclasite

Fracture density value indicates comparatively high.

##### 4-4.Fault breccia

Both fracture density and LOI value indicate comparatively high.

##### 4-5.Altered rocks

Fracture density value indicates low , and LOI value indicates high.

##### 4-6.Fault gouge

Both fracture density and LOI value indicate high.

## 5.Discussion and conclusion

It is suspected that as deformation and alteration go by, fracture density and LOI indicate increase. It is considered that division of fault rocks by naked observation (Fig.3) and by measurement of the fracture density and LOI (Fig.5) are almost correspond.

However, we can not get clear border of division. It is suspected that we need increasing samples, and we must investigate the way that give suitable quantitatively estimation. So, we think we will analyze substance transfer minutely by whole-rock geochemical analyses.

## REFERENCES

Ito,H , Kuwahara,Y , Miyazaki,T , Nisizawa,O , Kiguchi,T , Fujimoto,K , Ohtani,T , Tanaka,H , Higuchi,T , Agar,S , Brie,A , Yamamoto,H 1996 , Structure and Physical Properties of the Nojima Fault by the Active Fault Drilling. *BUTSURI-TANSA* , Vol.49 , No.6 , p522-535

Kobayashi,K , Matsuda,T , Arai,T , Ikeda,R , Omura,K , Sano,H , Sawaguchi,T , Tanaka,H , Tomita,T , Tomida,N , Hirano,S , Yamazaki,A 1998 , Distribution of fault rocks, minerals, and elements at the deep depth of Nojima fault. *CHIKYU MONTHLY* , an extra No.21 , pp154-159

Tanaka,H , Higuchi,T , Tomida,N , Fujimoto,K , Ohtani,T , Ito,H , 1999 , Distribution, deformation and alteration of fault rocks along the GSJ core penetrating the Nojima Fault , Awaji Island , Southwest Japan. *THE JOURNAL OF THE GEOLOGICAL SOCIETY OF JAPAN* , Vol.105 , No.1 , pp72-85

Tanaka,H , Fujimoto,K , Tomida,N , Ohtani,T , Ito,H , 1998 , Fluid assisted material migration at shallow fault zone. *Abstract of The 105th Annual Meeting of the Geological Society of Japan* , pp135

# Permeability and Strength of Core Samples from the Nojima Fault of the 1995 Kobe Earthquake

David Lockner<sup>1</sup>, Hisanobu Naka<sup>2</sup>, Hidemi Tanaka<sup>2</sup>, Hisao Ito<sup>3</sup>, and Ryuji Ikeda<sup>4</sup>

<sup>1</sup> US Geological Survey, 345 Middlefield Rd MS977, Menlo Park, CA 94025, USA;  
[dlockner@usgs.gov](mailto:dlockner@usgs.gov)

<sup>2</sup> Ehime University, Matsuyama, Japan

<sup>3</sup> Geological Survey of Japan, Tsukuba, Japan

<sup>4</sup> National Research Institute for Earth Science and Disaster Prevention, Tsukuba, Japan

## ABSTRACT

The 1995 Hyogoken-Nanbu (Kobe) earthquake,  $M=7.2$ , ruptured the Nojima fault. We have studied core samples taken from two scientific drillholes which crossed the fault zone in the epicentral region on Awagi island. The shallower hole, drilled by the Geological Survey of Japan (GSJ), was started 75m to the SE of the surface trace of the Nojima fault and crossed the fault at a depth of 624m. A deeper hole, drilled by the National Research Institute for Earth Science and Disaster Prevention (NIED) was started 302m to the SE of the fault and crossed fault strands below a depth of 1140m. We have measured strength and matrix permeability of core samples taken from these two drillholes. We find a strong correlation between permeability and proximity to the fault zone shear axes. The width of the high permeability zone (approximately 20 to 40m) is in good agreement with fault zone width inferred from trapped wave analysis and other evidence. The fault zone core or shear axis contains clays with permeabilities of approximately 0.1 to 1 microdarcy at 50 MPa confining pressure. Within a few meters of the fault zone core, the rock is highly fractured but has sustained little net shear. Matrix permeability of this zone is approximately 100 microdarcy at 50 MPa confining pressure. Outside this damage zone, matrix permeability drops to sub-nanodarcy values. The clay-rich core material has the lowest strength with a coefficient of friction of approximately 0.55. Shear strength gradually increases with distance from the shear axis. These permeability and strength observations are consistent with fault zone models in which a highly localized core or shear zone is surrounded by a damage zone of fractured rock. In this case, the damage zone will act as a high-permeability conduit for vertical and horizontal flow in the

plane of the fault. The clay core region, however, will impede fluid flow across the fault.

## INTRODUCTION

The scientific drillholes crossing the Nojima fault at depth in the epicentral region of the 1995 Kobe earthquake,  $M=7.2$ , provide a unique opportunity to study the mechanical and fluid transport properties of an active fault immediately after a major rupture event. Most first hand evidence of the properties of active faults comes from examination of surface exposures which have typically undergone long and complicated histories of uplift and alteration. Examination of fault rock associated with rupture nucleation or significant energy release on strike-slip faults presents a particular problem since there is little vertical slip to bring deeper rocks to the surface. Seismic, gravity, electromagnetic and other remote sensing techniques can provide information about the deep structure of active faults, but a complete understanding of fault zone properties in the hypocentral regions of damaging earthquakes will require direct observation by the drilling of deep scientific boreholes.

Numerous laboratory and field observations have shown that earthquakes, representing the dynamic faulting process in the brittle crust, involve breaking and crushing of grains and the progressive growth of the fault zone. A typical fault zone structure, as suggested by studies of exhumed faults [Chester *et al.*, 1993; Caine *et al.*, 1996; Caine and Forster, 1999], includes a narrow clay-rich or fine-grained core surrounded by a damage zone of highly fractured rock. The bulk of the shear deformation associated with the fault occurs in the narrow core zone, implying that this is the weakest portion of the fault structure. However, due to the fine grain size of the clay or crushed material in the fault core, it is expected to have a relatively low permeability.

The surrounding damage zone contains a high density of microcracks, both within and between grains, but is likely to have sustained relatively little total strain. Similar structures have been observed in laboratory samples that have been loaded to failure [Moore and Lockner, 1995]. If the fault occurs in low-porosity crystalline rock (such as the Nojima fault), the high crack density in the damage zone results in significant pore volume increase and an increase in transport properties such as fluid permeability [Caine *et al.*, 1996; Caine and Forster, 1999] and electrical conductivity [Lockner and Byerlee, 1986]. The contrast in material properties between damage zones associated with active faults and the surrounding country rock can often be observed with remote geophysical techniques such as magnetotelluric and seismic profiling. Most recently, trapped seismic waves, in which the fault zone acts as a waveguide, have been observed in active faults [Li and Leary, 1990; Ben-Zion, 1998], and in particular on the Nojima fault [Li *et al.*, 1998].

In the present study, we report on laboratory tests of 22 core samples taken from the NIED and GSJ drillholes following the Kobe earthquake. Rock strength and matrix permeability measurements were carried out to provide fault zone properties for profiles across the fault at two depths. Due to the limited number of samples and the difficulties associated with sample preparation, this study was intended to be exploratory in nature. In fact, the permeability and strength measurements are in excellent agreement with the idealized fault structural model described above. The GSJ borehole showed a single clay-rich shear zone at a depth of 624 m. The NIED hole showed two clay-rich shear zones at depths of 1140 m and 1320 m. A more diffuse shear zone was also crossed at about 1800 m (see Fig. 1). These three zones are referred to, respectively, in this paper as the shallow, intermediate and deep NIED shear zones. Strength and permeability measurements reported here, as well as petrographic observations presented by Moore (this volume), all indicate that unlike the other shear zone crossings, the deep shear zone was not activated by the 1995 Kobe earthquake.

## EXPERIMENTAL TECHNIQUE

Protolith rock for the Nojima fault in the vicinity of the boreholes is a biotite-hornblende

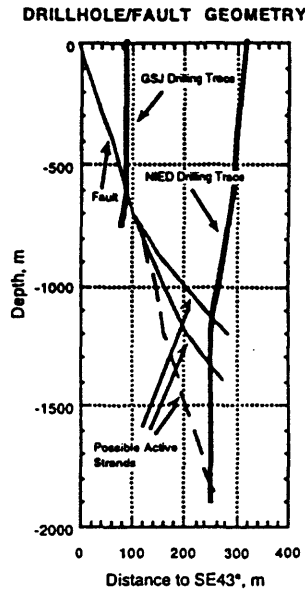


Figure 1. Schematic diagram of the Nojima fault in the vicinity of the JSG and NIED drillholes, showing the depths at which shear zones were intersected.

granodiorite (see, for example, Moore in this volume). A set of 22 samples were selected from the NIED and GSJ boreholes. Due to this limited number, sample selection was concentrated about the obvious shear zones in an attempt to obtain representative profiles across the fault zone structures. Significant variability of rock type exists in the shear zones and a more complete evaluation of fault zone properties would require a much denser and more systematic sampling of the core than was possible in this study. Preferred sample dimensions were nominally 25.4 mm-diameter by 50.8 mm-length cylinders. Much of the core (especially in the damage zones) had little or no cohesion and contained hard grain fragments. As a result, many samples were impossible to prepare to these preferred dimensions. Most samples that could not be prepared as cylinders were cut into rectangular prisms with 18.0 mm-square cross-sections. The clay-rich shear zone core samples were available in limited quantities and sliced to provide 2-mm-thick wafers. These were placed between porous sandstone driving blocks cut at an angle of 30° to the sample axis.

Samples were jacketed and loaded in a standard triaxial deformation apparatus. Each sample was evacuated and then saturated with

distilled, deionized water. Permeability was measured using a constant flow rate method at effective confining pressure of 10, 30, and 50 MPa. Test samples were oriented parallel to the original borehole cores so that the reported permeability and strength data are essentially for flow and maximum compressive stress oriented subvertically. No attempt was made to determine anisotropy in either permeability or strength. Following the hydrostatic permeability measurements, each sample was loaded incrementally at constant effective confining pressure of 50 MPa until failure occurred. Following each strain increment along the loading path, deformation was halted and permeability was determined as indicated in Fig. 2. After peak stress, deformation continued to 5 mm axial shortening at a rate of 1  $\mu\text{m/sec}$  with periodic pauses to repeat permeability measurements.

Accuracy of the permeability measurements is difficult to determine since some samples had less than ideal surface finishes and some permeabilities were near both the high and low limits of our measuring capabilities; sample permeabilities ranged from less than  $1 \times 10^{-9}$  to  $3 \times 10^{-3}$  Darcy ( $1 \text{ Darcy} = 10^{-12} \text{ m}^2$ ). The lower limit for our measuring system was  $\pm 0.3$  nDa. Absolute permeability uncertainties reported here are less than  $\pm 25\%$  while relative uncertainties in a single experiment are 5 to 10%.

## RESULTS

Permeability is plotted as a function of axial stress for a representative set of samples from the NIED borehole in Fig. 2. The first three measurements of each test at 10, 30, and 50 MPa were conducted without deviatoric stress and represent the permeability loss due to an increase in effective confining pressure. Permeability typically dropped by two orders of magnitude as microcracks closed in response to this hydrostatic loading. The remainder of the curves at axial stress above 50 MPa in Fig. 2 represent the deformation test at 50 MPa effective confining pressure. Initially, all samples showed loss of permeability with increasing deviatoric stress. By approximately 50% peak stress, most samples began to show increasing permeability with increasing deviatoric stress. This reversal from permeability decrease to permeability increase corresponds with the onset of dilatancy and the opening of microcracks within the sample (see,

for example, [Zoback and Byerlee, 1975] and similar trends in electrical conductivity [Lockner and Byerlee, 1986]). The clay-rich shear zone core sample did not show dilatant behavior. Instead, it showed a steady loss of permeability with continued shearing and strain hardening. The protolith granodiorite shown in the bottom curve, Fig. 2, is a dense crystalline rock with low matrix permeability. Application of deviatoric stress reduced the permeability below the measurement threshold of our test system. By 400 MPa axial load, however, new dilatant cracks had increased permeability to a measurable level which continued to increase to peak axial load of 483 MPa. Another trend observable in Fig. 2 is a systematic decrease in peak strength of samples from the intact protolith, through the damage zone samples to the shear zone core sample. The low strength of the shear zone core is consistent with the concentration of shear deformation in this zone.

## Rock Strength

Care was taken during sample preparation to preserve the intrinsic grain structure and cohesion as much as possible. Obvious changes did occur in the samples due to drying and decompression of the original cores. However, these changes

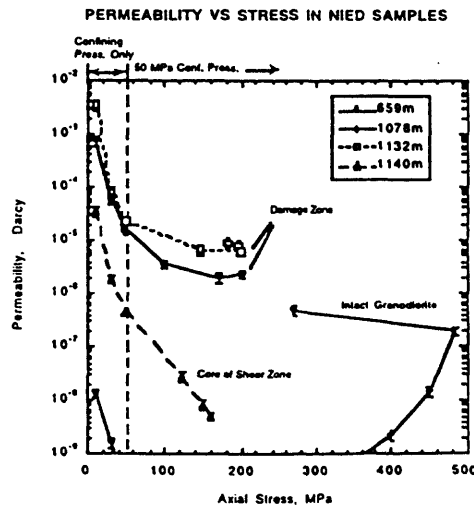


Figure 2. Permeability plotted versus axial load for selected NIED samples. Pressurization to 50 MPa is hydrostatic loading without deviatoric stress. Data above 50 MPa show permeability change in response to sample deformation at 50 MPa effective confining pressure.

were minimized as much as possible with the expectation that the *in situ* rock properties would be preserved to large extent. One way to evaluate this is to look for trends in the peak strength data for the various samples. Samples were tested at 50 MPa effective confining pressure, which is equivalent to approximately 3 km burial depth (assuming hydrostatic pore pressure gradient and average rock density of 2.7 g/cm<sup>3</sup>), to provide an easy means of comparing sample to sample strength. Peak strength data are presented in Fig. 3 as the ratio of shear to normal stress ( $\mu$ ) resolved on a plane inclined 30° to the sample axis. The actual inclination of the fracture plane was difficult to determine in many of the strength tests, so that 30° provides a satisfactory approximation for comparison of different samples. Peak differential stress,  $\sigma_d$ , which is the quantity measured directly in the experiments, can be recovered from the data in Fig. 3 by the formula  $\sigma_d = 200\mu/(1.732-\mu)$  (in MPa). Normalized strength for the intact granodiorite protolith is  $\mu_{intact} = 1.18$ .

The horizontal axis in Fig. 3 is the horizontal distance between the shear zone axis and the *in situ* location of each core sample. No distinct shear zone axis could be identified for the deep NIED shear zone so the horizontal axis in Fig. 3d could be shifted by a few meters. Notice that the three fault crossings with well-defined shear zone cores (Figs. 3a, 3b and 3c) all show a minimum in strength at the shear zone axis. This is consistent with the model described above in which nearly all displacement occurs in the narrow fault core (a zone that is only a few centimeters wide in all three examples). The general trend in these three examples is for strength to gradually increase with distance away from the shear zone axis. This gradual strength increase corresponds to a decrease in microcrack damage (*i.e.*, Moore this volume and [Moore and Lockner, 1995]). Damage zone half-width as suggested by the strength data in Figs. 3a - 3c is 15 to 25 m.

The deep NIED shear zone (Fig. 4d) is different from the other three examples. No distinct shear zone core was observed in the borehole samples. While three of the core samples showed strength significantly less than the protolith strength ( $\mu \sim 0.8$  as compared to 1.18), rock strength from this zone is significantly greater than the shallow shear zone core samples ( $\mu \sim 0.6$ ). Apparently this deep zone was not activated in the Kobe earthquake

and has, over time, been restrengthening by vein filling and mineral alteration.

#### Rock Matrix Permeability

We have already noted that the permeability of all samples tested shows a strong sensitivity to increases in effective confining pressure. The examples plotted in Fig. 2 all show a decrease of

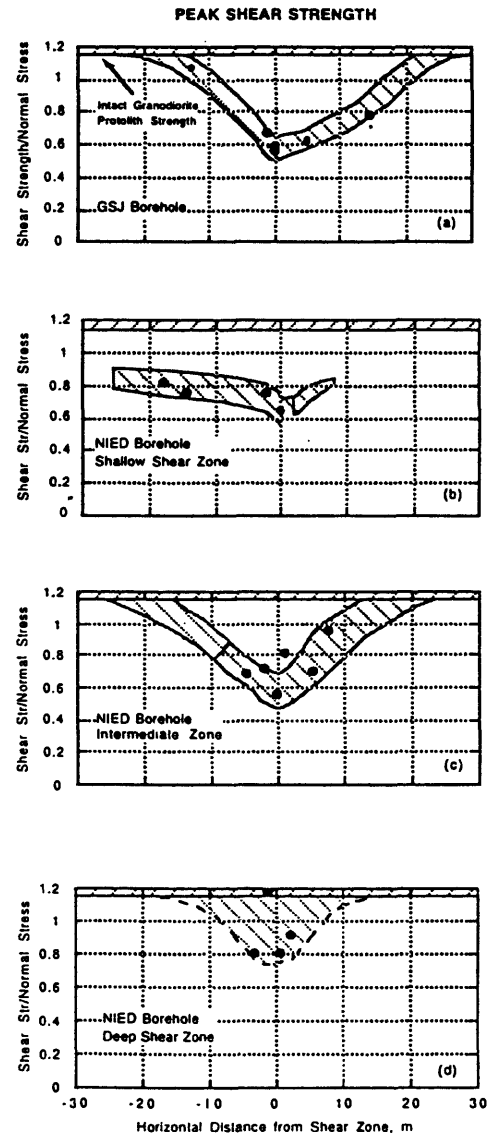


Figure 3. Profiles of peak shear strength divided by normal stress for the four shear zone crossings in the GSJ and NIED boreholes. Strength is lowest in the shear zone axis and recovers to the intact rock strength outside of the damage zone.

two orders of magnitude for a 50 MPa pressure increase. This pressure sensitivity is indicative of rocks in which flow is through low aspect ratio cracks (long, thin microcracks) which can open or close flow paths in response to small pressure changes. This type of microcrack is more susceptible to changes in permeability resulting from vein filling than the more equant pores that might be found, for example, in a porous sandstone.

Because of the strong pressure sensitivity of permeability in these samples, we expect that *in situ* permeability in the Nojima fault zone will decrease rapidly with depth. For example, the GSJ samples, with a fault crossing depth of 624 m would have an effective overburden pressure of approximately 11 MPa while the intermediate NIED crossing overburden pressure would be about 22 MPa. The peak damage zone permeabilities adjusted for these effective pressures would then be 3.3 mDa and 0.45 mDa, respectively.

To provide a more direct comparison of the different fault zone permeability measurements, we have plotted permeability profiles in Fig. 4 using values from 50 MPa effective confining pressure or 3 km burial depth. *In situ* permeabilities for the GSJ hole (at 11 MPa) would be about 50 times larger than the values shown in Fig. 4. As with the strength data, the three shallow crossings show permeability profiles similar to the idealized fault zone model described above. The shear zone axis, due to its high clay content and fine gouge grain size, has relatively low permeability in the microdarcy range. Flanking the shear zone axis, the highly fractured damage zone has permeabilities in the 50 to 100 microdarcy range. Farther away from the fault zone axis, grain damage and permeability decrease until permeability returns to the protolith permeability value. The damage zone half-width, as indicated by the permeability profiles ranges from 10 to 25 m. Based on trapped seismic wave analysis, Li *et al.* [1998] suggested a fault zone half width of approximately 15 m for the Nojima fault. Thus, direct measurements of both the permeability and strength of the fault zone indicate a damage zone half width that is consistent with the deeper seismic observations. The NIED borehole deep shear zone has permeability that is greater than the protolith permeability but significantly less

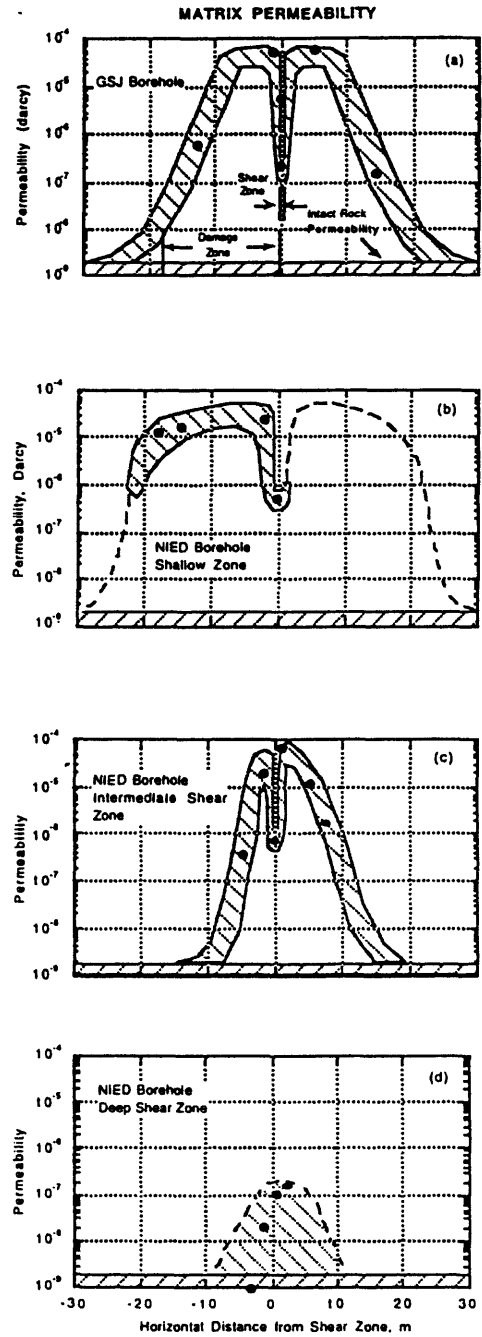


Figure 4. Profiles of matrix permeability measured at 50 MPa effective confining pressure. The three upper fault crossings show a low permeability shear zone axis surrounded by high permeability damage zones. The deep shear zone is partially sealed and was apparently not activated by the Kobe earthquake.

than the shallower shear zone values. Thus both strength and permeability data suggest that the deep shear zone was not activated in the Kobe earthquake and is now in the process of sealing and restrengthening.

## DISCUSSION

Our measurements of core sample strength and permeability are in good agreement with the idealized fault zone model described, for example, by [Chester *et al.*, 1993; Caine *et al.*, 1996; Evans *et al.*, 1997]. We observe a thin, low-strength, low-permeability fault zone core flanked by zones of high permeability rock that have undergone relatively limited total shear. These observations imply that to depths of as much as 3 to 5 km, the post-seismic fault zone will act as a high permeability fluid conduit for fluid flow in the plane of the fault. Because the fault core has low permeability it is likely to act as a barrier to fluid flow across the fault. However, this barrier is notably thin and may have a complex structure. For example, the Nojima fault zone appears to have branched into two shear zones between the GSJ and NIED borehole crossings. To the degree that this thin shear zone core is spatially discontinuous and anastomosed, its ability to act as a fluid barrier will be diminished.

The observations reported here provide a unique opportunity to understand fault zone properties at depth following a damaging earthquake. While we do not know the mechanical and hydraulic properties of the Nojima fault before the Kobe earthquake, it is likely that the violent rupture of the fault led to a sudden increase in permeability. This is consistent with observations following the 1989 Loma Prieta earthquake that enhanced fluid flow occurred in the epicentral region [Rojstaczer and Wolf, 1992]. One important question not addressed by this study is how rapidly the enhanced fault zone permeability structure will be reduced by sealing and crack healing processes. The observation of increased strength and decreased permeability in the deep NIED shear zone indicate that these processes can have significant influence on fault zone mechanics over the lifetime of an active fault. If this sealing and restrengthening process can occur over a single earthquake cycle, it could have an important influence on repeat time, stress drop and rupture nucleation.

## REFERENCES

Ben-Zion, Y., Properties of seismic fault zone waves and their utility for imaging low-velocity structures, *J. Geophys. Res.*, 103, 12,567-12,585, 1998.

Caine, J. S., J. P. Evans, and C. B. Forster, Fault zone architecture and permeability structure, *Geology*, 24, 1025-1028, 1996.

Caine, J. S., and C. B. Forster, Fault zone architecture and fluid flow: Insights from field data and numerical modeling, in *Faults and Subsurface Flow in the Shallow Crust: AGU Geophysical Monograph*, Vol. 113, edited by Haneberg, Amer. Geophys. Union, Washington, D.C., 1999.

Chester, F. M., J. P. Evans, and R. L. Biegel, Internal structure and weakening mechanisms of the San Andreas fault, *J. Geophys. Res.*, 98, 771-786, 1993.

Evans, J. P., C. B. Forster, and J. V. Goddard, Permeability of fault-related rocks, and implications for hydraulic structure of fault zones, *J. Structural Geol.*, 19, 1393-1404, 1997.

Li, Y.-G., K. Aki, J. E. Vidale, and M. G. Alvarez, A delineation of the Nojima fault ruptured in the M7.2 Kobe, Japan, earthquake of 1995 using fault zone trapped waves, *J. Geophys. Res.*, 103, 7247-7263, 1998.

Li, Y.-G., and P. Leary, Fault zone seismic trapped waves, *Bull. Seismol. Soc. Am.*, 80, 1245-1271, 1990.

Lockner, D. A., and J. D. Byerlee, Changes in complex resistivity during creep in granite, *Pure and Appl. Geophys.*, 124, 659-676, 1986.

Moore, D. E., and D. A. Lockner, The role of microcracking in shear-fracture propagation in granite, *J. Struct. Geol.*, 17, 95-114, 1995.

Rojstaczer, S., and S. Wolf, Permeability changes associated with large earthquakes: An example from Loma Prieta, California, *Geology*, 211-214, 1992.

Zoback, M. D., and J. D. Byerlee, The effect of microcrack dilatancy on the permeability of Westerly granite, *J. Geophys. Res.*, 80, 752-755, 1975.

# Permeability of Deep Drillhole Core Samples

Carolyn A. Morrow

U.S. Geological Survey, Menlo Park, CA 94025 U.S.A.

[cmorrow@usgs.gov](mailto:cmorrow@usgs.gov)

## ABSTRACT

The permeability of fault zone material is key to understanding fluid circulation and its role in earthquake generation. In this paper, permeability results from four different scientific drillholes are discussed in relation to recent studies on core samples from the Nojima Fault. This comparison illustrates the advantages and limitations of laboratory studies on extracted core samples. We observe that matrix permeability of core samples is extremely low, suggesting that most fluid flow at depth will occur through discrete joints and faults rather than through the bulk of the rock. The permeability of deep core samples is also more sensitive to pressure than equivalent rocks obtained from surface outcrops. In addition, stress-relief and thermal fractures due to coring and extraction may influence laboratory permeability measurements, most typically for deeper rocks and those containing abundant quartz.

## INTRODUCTION

Scientific drillholes through the Nojima Fault by the University Group, the Geological Survey of Japan (GSJ) and the National Research Institute for Earth Science and Disaster Prevention (NIED) provide unique information on the physical properties of rocks in an active fault zone. These drillholes cross the fault at depths of 389 m, 624 m, and below 1140 m respectively, sampling a variety of materials including a clay-rich fault core, a fractured zone adjacent to the fault and intact rock beyond the fracture zone. *Naka et al.* (1998) reported on the permeability and shear strength of core samples extracted from the GSJ and NIED drillholes at various distances from the fault zone. They found that permeability in the shear zone was low ( $\sim 10^{-18} \text{ m}^2$ ) due to the presence of the clay minerals; that the fractured zone had a higher permeability of around  $10^{-16} \text{ m}^2$ ; and that the intact zone more distant from the fault had permeability values of less than  $10^{-21} \text{ m}^2$ . These results suggest that the damaged zone on either side of the fault can act as a conduit for fluids parallel to the fault, but that the low permeability clay-rich shear zone will impede flow across the fault.

The core samples studied provide a picture of conditions in the upper crust adjacent to an active fault. However, because earthquakes can be generated at great depths and in many different environments, we are also interested in how the physical properties of extracted core samples depend on factors such as

depth of burial, *in situ* pressure, rock type, and the effects of weathering and stress-relief fracturing. This paper summarizes the permeability results of core samples from four other scientific drillholes, so that the lessons learned can be applied to the Nojima Fault studies. These drillhole sites include Cajon Pass in California, Kola in Russia, KTB in Germany, and Illinois UPH 3. Results show that (a), the matrix permeability of most crystalline rock samples is extremely low due to repeated episodes of hydrothermal healing and sealing, so that the bulk permeability of large rock masses is largely controlled by flow through fractures and joints; (b), weathering of near-surface rocks reduces the pressure sensitivity of permeability, so that permeability behavior determined from near-surface samples cannot be extrapolated to depth; and (c), in many cases, stress-relief fractures introduced during coring and extraction dominate the physical properties of the rocks, particularly for samples that contain quartz.

## SUMMARY OF CORE SAMPLE PERMEABILITIES

### Cajon Pass, California

At Cajon Pass in Southern California, a hole was drilled to a depth of 3500 m 4 km to the northeast of the San Andreas Fault to investigate the thermomechanical nature of this fault. Rocks selected for laboratory permeability studies included granodiorites, monzogranites and gneisses. Permeability measurements (Figure 1) were made on the core samples at confining and pore pressures that matched the *in situ* pressures for each sample depth (*Morrow and Byerlee, 1992*), so that each data point in Figure 1 represents a different sample. Permeability of unfractured samples (solid symbols, Figure 1) decreased systematically with depth from  $10^{-18}$  to  $10^{-22} \text{ m}^2$  at effective pressures of only 5 to 50 MPa, indicating a strong pressure sensitivity of permeability. Values for the relatively few specimens containing visible stress-relief fractures (open symbols, Figure 1) were one to two orders of magnitude higher than the unfractured samples, but still in the comparatively low permeability region of  $10^{-19}$  to  $10^{-20} \text{ m}^2$ . Petrographic observations indicate that repeated episodes of healing and sealing account for the overall low permeability values, which were several orders of magnitude below bulk downhole measurements. Accordingly, the laboratory measurements should be considered a lower limit to permeability. The results suggest that massive water

circulation through the mass of the rock is unlikely as a mechanism for obscuring the heat flow anomaly that would be expected if shear stresses acting on the San Andreas fault to cause slip were high. This finding is consistent with geochemical evidence (Kharaka *et al.*, 1988) of little mixing of the pore waters sampled from different sections of the borehole.

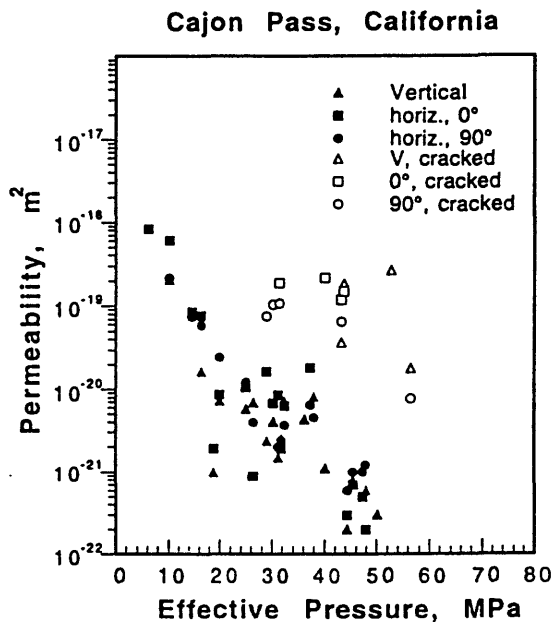


Figure 1. Permeability of intact (closed symbols) and fractured (open symbols) crystalline rock samples from the Cajon Pass drillhole in California under estimated *in situ* effective pressure conditions. Measurements in three mutually perpendicular orientations show the extent of permeability anisotropy.

#### Kola, Russia

Core samples from the 11 km deep Kola drillhole in Russia included granodiorite gneisses, basalts and amphibolites. Laboratory permeability tests were conducted to determine the pressure sensitivity of permeability and to compare the effects of stress-relief and thermal microcracking on the matrix permeability of different rock types (Morrow *et al.*, 1994). Permeability was measured on each sample under a series of increasing confining pressures. The permeability of the basaltic samples (Figure 2) was the lowest and most sensitive to pressure, ranging from  $10^{-20}$  to  $10^{-23}$  m<sup>2</sup> as effective pressure increased from 5 to only 60 MPa. Amphibolites and the granodiorite gneiss samples were more permeable and less sensitive to pressure than the basalts, with

permeability values ranging from  $10^{-17}$  to  $10^{-22}$  m<sup>2</sup> as effective pressures increased to 300 MPa. The weathered samples, a surface gneiss and a surface-derived Westerly Granite included for comparison, were the least sensitive of all rocks, with permeability trends that cut across those of the other samples. There was an abundance of microfractures in the quartz-rich rocks, but a relative paucity of cracks in the mafic rocks, suggesting that the observed differences in permeability were based on rock type and depth, and that stress-relief and thermal-cracking damage was correlated with quartz content.

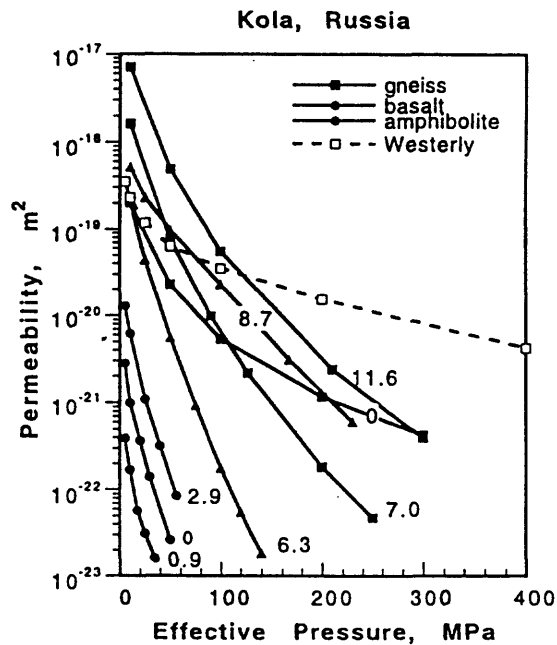


Figure 2. Permeability of core samples from the Kola well in Russia. Numbers indicate sample depth in km. Westerly granite (Brace *et al.*, 1968) included for comparison.

#### KTB, Germany

Amphibolite core samples from the 9 km deep KTB drillhole were tested under increasing confining pressures in mutually perpendicular directions to determine permeability anisotropy (Morrow *et al.*, 1994). Permeability values (Figure 3) for samples from 1252 and 3607 m were very low ( $10^{-19}$  to  $10^{-23}$  m<sup>2</sup> at pressures from 5 to 60 MPa), similar to the Kola mafic samples. This behavior appears to be due to the paucity of microfractures, either natural or induced through drilling and extraction, again most

likely related to the lack of quartz. Permeability anisotropy was over two orders of magnitude. Unlike most of the rocks described in this paper, permeability for many of the KTB samples followed the simple relation  $-\log k \propto P_e$ , where  $k$  is permeability and  $P_e$  is effective pressure. However, this may be a result of the limited pressure range over which permeability could be measured.

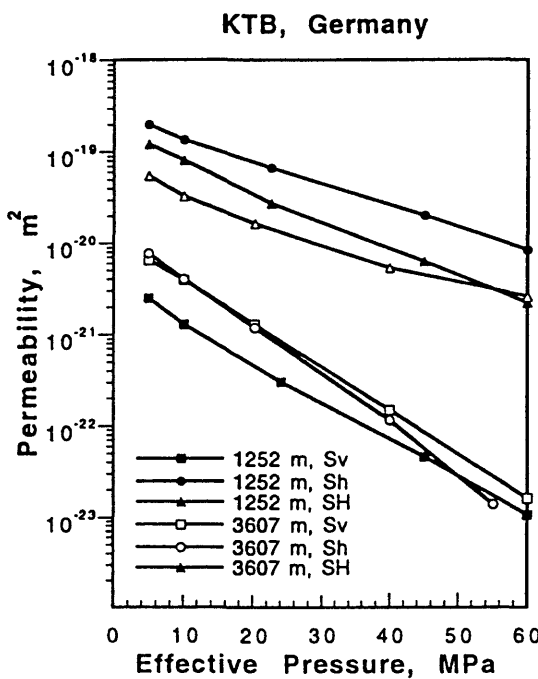


Figure 3. Permeability of amphibolite core samples from the KTB pilot hole in Germany, with cores oriented towards principal stresses.

#### Illinois UPH 3, Illinois, U.S.A.

Horizontal and vertically oriented granite cores were obtained from depths of 751 to 1605 m in the Illinois UPH 3 drillhole and tested in the laboratory at effective confining pressures from 5 to 100 MPa (Morrow and Lockner, 1997). Initial permeabilities (Figure 4) were in the range of  $10^{-16}$  to  $10^{-19}$  m<sup>2</sup> and dropped rapidly with applied pressure to values between  $10^{-18}$  and  $10^{-23}$  m<sup>2</sup>, typical of the strong pressure sensitivity of other core samples noted above. However, permeabilities of the Illinois cores were inversely related to sample depth in a systematic way. This suggests that stress-relief and thermal microfractures induced during core retrieval increased with depth and ultimately dominated the laboratory fluid flow measurements. In this case, our measurements give at best an upper bounds on matrix

permeability, and do not provide a realistic picture of *in situ* permeability conditions.

## DISCUSSION

### Crack-dominated fluid flow

The low matrix permeability ( $<10^{-16}$  m<sup>2</sup>) of core samples from the various drillholes cited above indicates that most fluid flow at depth will occur through discrete joints and faults rather than through the bulk of the rock. In addition, studies of both clay-rich and non-clay fault gouges from various active faults (Morrow *et al.*, 1984) show that gouge permeability is also extremely low ( $10^{-19}$  to  $10^{-22}$  m<sup>2</sup>) under *in situ* pressure conditions and during shearing. These findings are consistent with the results of Naka *et al.*, (1998) who determined that the fractured rocks adjacent to the Nojima Fault were many orders of magnitude more permeable than either the surrounding intact country rock or the clay-rich fault zone. This allows the damaged zone to serve as a conduit for fluids parallel to the fault in a horizontal or vertical direction but does not allow for free movement of fluids across the fault. This finding has important implications for the modeling of fluid circulation in the vicinity of the Nojima Fault.

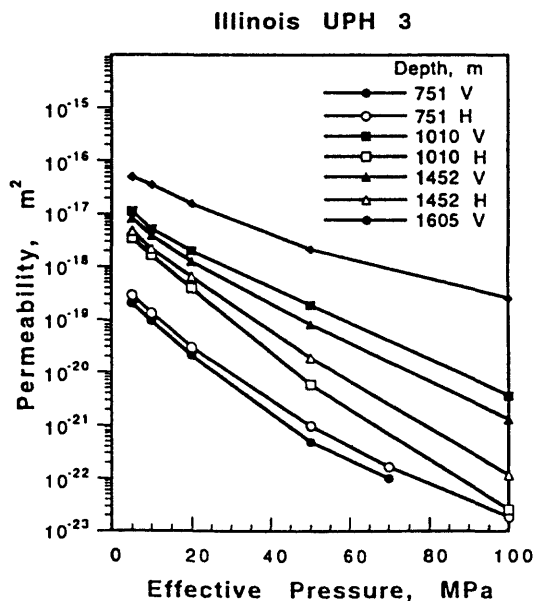


Figure 4. Permeability of granite core samples from the Illinois UPH 3 drillhole. Sample depth in meters for vertical (V) and horizontal (H) cores.

It is important to remember that the permeabilities of fault zone rocks are not fixed parameters with time. Petrographic evidence of repeated crack healing and sealing due to hydrothermal circulation in the various drillhole samples discussed above suggests that these rocks experienced cyclic permeability changes. This is consistent with current models of earthquake generation in which faults undergo repeated episodes of sealing, fluid pressurization, and finally rupture when fluid pressure exceeds the greatest principal stress, as discussed by Sibson (1992), Chester *et al.* (1993) and others.

#### Pressure sensitivity

An important finding from these diverse permeability studies is that permeability of deep core samples decreases more rapidly with applied pressure than equivalent surface-derived (quarried) or near-surface granites at comparable effective confining pressures. This is because weathering products in cracks and pores inhibit crack closure with applied pressure. In addition, stress-relief fractures that form from the release of triaxial *in situ* stresses may not completely close under the imposed hydrostatic pressure conditions of the laboratory. Such offset joints can become many orders of magnitude more hydraulically conductive than mated joints even at high stresses. This may explain why the deeper gneissic samples from the Kola well (7.0 and 11.6 km) which contained stress-relief fractures, were not as sensitive to pressure as the shallower (and hence less fractured) quartz-rich samples from Cajon Pass. Similarly, the largely unfractured mafic samples from the Kola and KTB drillholes reaches very low permeability values under only modest applied pressures. Differences in pressure sensitivity are illustrated in Figure 5 for intact, cracked and weathered samples from the Cajon Pass drillhole and also a sample of quarried Westerly Granite, which is often used as a standard in laboratory geophysical testing. The weathered and cracked samples (including weathered Westerly Granite) are more permeable and have a distinctly different pressure response from the intact samples. However, these less pressure-sensitive samples may not be representative of conditions at depth. This result has important implications for geophysical models that assume standard values for the transport properties of rock, such as models of heat transport or fluid pressure buildup. Other physical properties that are controlled by cracks and pores, such as seismic velocity and electrical resistivity, may be similarly affected by differences in pressure sensitivity between surface-derived rocks and deep core samples.

#### Stress-relief fracturing

While stress-relief fractures may affect the pressure sensitivity of permeability as described

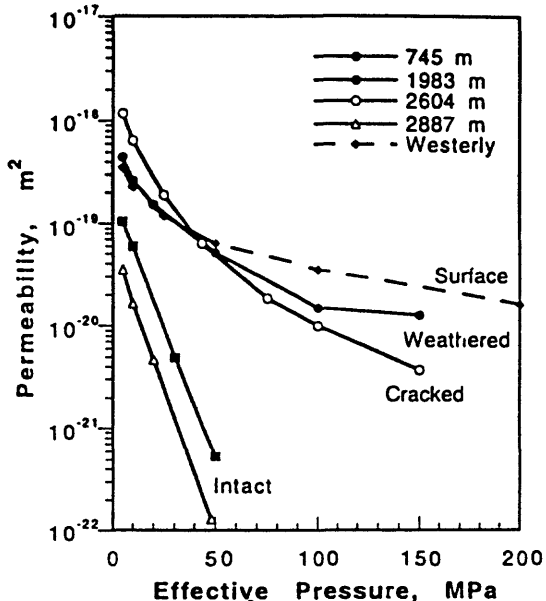


Figure 5. Permeability of selected Cajon Pass core samples showing differences in pressure sensitivity, with Westerly Granite (Brace *et al.*, 1968) included for comparison.

above, the most obvious influence is on the absolute value of permeability. Even on the small scale of these samples, flow in fractured samples was increased by several orders of magnitude. Stress-relief damage was generally more prominent in the quartz-rich rocks and in rocks from greater depths. However, as in the case of the Illinois UPH 3 cores, permeability was entirely dominated by stress-relief cracks even though the samples were from relatively shallow depths. This may result in a substantial overestimate of the *in situ* matrix permeability.

Stress-relief fractures can in some cases be useful for estimating *in situ* pressure conditions. For instance, we can apply the Equivalent Channel Model of Walsh and Brace (1984) to the permeability and porosity data to obtain analytical estimates of various parameters such as crack aperture, asperity height, and formation factor. Assuming that the physical characteristics of natural fractures are different than stress-relief fractures, the trend of these parameters with pressure should be different at *in situ* pressures above crack closure than below crack closure. From this change in physical characteristics with applied pressure we can estimate the closure pressure of the

stress-relief cracks, and thereby place bounds on the *in situ* effective pressure. This method proved successful for certain quartz-rich samples from the Kola drillhole, where the downhole fluid pressure was not well constrained and *in situ* effective pressures were unknown. However, the use of microcrack closure to estimate *in situ* pressure was not appropriate for the basalt and amphibolite samples from either the Kola or KTB drillholes, because they were relatively crack-free *in situ* (on the scale of our laboratory samples) and remained so even after core retrieval. As a result, their permeabilities were near or below the measurable lower limit of our apparatus at the estimated *in situ* pressures of the rocks, so that permeability measurements could not be made over the necessary spectrum of pressures.

## REFERENCES

Brace, W.F., Walsh, J.B., and Frangos, W.T., 1968, Permeability of granite under high pressure, *J. Geophy. Res.*, 73, 2225-2236.

Chester, F.M., Evans, J.P., and Biegel, R.L., 1993, Internal structure and weakening mechanisms of the San Andreas Fault, *J. Geophy. Res.*, 98, 771-786.

Kharaka, Y.K., White, L.D., Ambats, G., and White, A.F., 1988, Origin of subsurface water at Cajon Pass, *Geophy. Res. Lett.*, 15, 1049-1052.

Morrow, C.A., Shi, L.Q., and Byerlee, J.D., 1984, Permeability of fault gouge under confining pressure and shear stress, *J. Geophy. Res.*, 89, 3193-3200.

Morrow, C.A. and Byerlee, J.D., 1992, Permeability of core samples from Cajon Pass scientific drillhole: Results from 2100 to 3500 m depth, *J. Geophy. Res.*, 97, 5145-5151.

Morrow, C., Lockner, D., Hickman, S., Rusanov, M., and Röckel, T., 1994, Effects of lithology and depth on the permeability of core samples from the Kola and KTB drill holes, *J. Geophy. Res.*, 99, 7263-7274.

Morrow, C.A., and Lockner, D.A., 1997, Permeability and porosity of the Illinois UPH 3 drillhole granite and a comparison with other deep drillhole rocks, *J. Geophy. Res.*, 102, 3067-3075.

Naka, H., Lockner, D., Tanaka, H., Ikeda, R., and Ito, H., 1998, Strength and permeability of core samples taken from drillholes crossing the Nojima Fault of the 1995 Kobe earthquake, *EOS, Trans. Am. Geophy. Union*, 79, F823.

Sibson, R.H., 1992, Implications of fault valve behavior for rupture nucleation and recurrence, *Tectonophysics*, 211, 283-293.

Walsh, J.B., and Brace, W.F., 1984, The effect of pressure on porosity and the transport properties of rock, *J. Geophy. Res.*, 89, 9425-9431.

blank page

# Correlation of Deformation Textures with Laboratory Measurements of Permeability and Strength of Nojima Fault Zone Core Samples

Diane E. Moore<sup>1</sup>, David A. Lockner<sup>1</sup>, Hisao Ito<sup>2</sup>, and Ryuji Ikeda<sup>3</sup>

<sup>1</sup>*U. S. Geological Survey, MS977, 345 Middlefield Road, Menlo Park, CA, 94025 USA*

<sup>2</sup>*Geological Survey of Japan, Tsukuba, Japan*

<sup>3</sup>*National research Institute for Earth Science and Disaster Prevention, Tsukuba, Japan*

## ABSTRACT

The deformation textures observed in 22 core samples of intact and altered granodiorite from two drillholes into the Nojima fault zone are consistent with the permeability and strength data reported by Naka et al. (1998) for those samples. The highest measured permeability was in a sample subjected only to dilatational cracking. More intense fracturing accompanying microshear development also produces relatively high permeability, if the fragments generated by the deformation are relatively large. In these rocks, the fracturing intensity is directly correlated with the amount of strength reduction. Progressive granulation of the fragmented rock generates fine-grained gouge of low shear strength and moderately low permeability.

The deformation and mineralization features observed in the sample set have been combined into a general model for the evolution of a gouge layer relative to its permeability and strength. Of the four possible fault strands encountered in the two drillholes, the GSJ and shallowest NIED fault strands appear to be currently active, whereas the deepest NIED fault strand was abandoned and has since been thoroughly sealed with mineral deposits. The middle NIED strand also shows some evidence of recent shearing, although the two examined gouge samples are overprinted by dilatational cracking.

## INTRODUCTION

Core samples of biotite-hornblende granodiorite from two drillholes into the Nojima fault zone were measured for permeability and strength by Naka et al. (1998; see also Lockner, this volume) in the rock deformation laboratory at the U.S. Geological Survey in Menlo Park, California. The hole drilled by the Geological Survey of Japan (GSJ) crossed a gouge-bearing fault at about 624 m, whereas the hole drilled by the National Research Institute for Earth Science and Disaster Prevention (NIED) crossed three possible fault strands at depths of about 1140 m, 1320 m, and 1800 m. Four to six samples from each fault strand were examined by Naka et al. (1998) (Table 1), along with representative samples of the country rock.

In order to compare the degree of deformation with the strength and permeability values, a thin section was prepared from each sample for petrographic examination. All but two of the samples were cut perpendicular to the axis of the cylindrical core samples; NIED sample 81-22A and GSJ 99-4 were cut parallel to the axis. This report shows (1) the correlation of the deformation and mineralization textures to the strength and permeability values, and (2) the position of each fault strand in an evolutionary sequence for a gouge core zone that was constructed from the petrographic observations.

## FAULT ZONE STRUCTURE, PERMEABILITY, AND STRENGTH

The examination of exhumed faults (e.g., Chester and Logan, 1986; Chester et al., 1993; Evans et al., 1997), has shown that a fault zone commonly consists of a narrow ( $\leq 1$  m wide) core zone of fault gouge, where shear strain is concentrated. The core is embedded in a significantly wider zone of deformed rock, termed the damage zone, in which the intensity of deformation gradually decreases towards the undeformed country rock. Chester and Logan (1986) found that strength increases regularly from the fault core to the country rock (Chester and Logan, 1986), whereas permeability reaches a maximum within the zone of damaged rock (Evans et al., 1997). Depending on the initial permeability of the protolith — for example, a highly porous sandstone versus a low-permeability crystalline rock — the permeability of the gouge zone may be higher or lower than that of the country rock.

The strength and permeability data reported by Naka et al. (1998) and the textures of the Nojima fault rocks are consistent with this model of fault-zone structure and mechanical properties. The country rock has very low permeability and high strength. It contains few completely filled cracks and has little alteration. Naka et al. (1998) identified a 20–40 m-wide zone of high permeability associated with each fault strand that they correlated with the damage zone (the data are presented by Lockner, this volume). The range of deformation intensity associated with high permeability is illustrated by the two highest-permeability samples from the NIED drillhole (80-29,

Table 1. Samples examined in this study.

Sample #	Depth (m)	Description
<b>GSJ Drillhole</b>		
—	258.6	country rock; relict amphiboles
74-17	503.4	damage zone: microshear zones
91-6	582.0	2.5–10 mm-wide gouge-like band (old)*
98-31	623.6	banded gouge (old)
99-4	624.4	fine-grained gouge
101-2	634.1	two ≤6 mm-wide gouge-like bands
118-21	730.4	damage zone; relict amphiboles
<b>NIED Drillhole</b>		
12-1A	659.3	country rock; relict amphiboles
32-20	1063.7	damage zone: dilational fractures
34-27	1077.9	damage zone: microshear zones
43-37-1	1131.8	damage zone: gouge-like microshear zone
45-23	1140.1	fine-grained gouge
74-19	1278.6	damage zone: dilational fractures
76-17	1289.0	20 mm-wide gouge-like band
80-29	1307.5	damage zone: dilational fractures
81-22A	1312.0	coarse-grained banded gouge (old)
82-40	1320.3	damage zone: gouge-like microshear zones
85-15B	1332.2	coarse-grained gouge (old)
179-33	1798.2	old shear zone (see text)
181-34	1807.9	old shear zone
183-14C	1815.9	old shear zone
184-23	1821.9	old shear zone

\* The gouge in samples labelled (old) is cut by mineral-filled dilational ± shear fractures.

The narrow gouge-like bands in 91-6, 101-2, and 76-17 are bounded by damage-zone rock.

Figure 1a; 43-37-1, Figure 1b). Sample 80-29 is not highly deformed but does contain a set of elongate dilational fractures that are partly filled with a Ca-zeolite (probably laumontite) and carbonate minerals containing varying amounts of Fe, Mg, and Ca. Growth textures of the secondary minerals suggest that the fractures have remained open for at least two episodes of crystal growth. The more highly deformed damage-zone rocks, which are generally associated with some shear fracturing, also have high permeability if the fragments remain relatively large. The quartz crystal in Figure 1b has been thoroughly fractured, and the pieces form a high-permeability network of voids and cracks.

With further increases in the intensity of shearing, the rock loses cohesion and the fractured rock is replaced by dense, fine-grained gouge (Figure 1c) that has permeability intermediate between the undeformed granodiorite and the damage-zone rocks. The strength data of Naka et al. (1998) are directly correlated with the degree of cohesion, such that the sequence of samples in Figure 1a–c has progressively decreasing strength (see Lockner, this volume).

## GOUGE CORE EVOLUTION

Progressive deformation of the country rock to form a gouge layer destroys most traces of the layer's earlier history (e.g., Figure 1c). However, the variety of deformation and mineralization textures observable in the sample set of Table 1 can be combined into a generalized textural, permeability, and strength history of the gouge core zones. Overall, the first half of the sequence involves initial dilational fracturing of the granodiorite, followed by shear fracturing that increases in intensity and degree of localization until a gouge zone is formed. This part of the time sequence largely corresponds to the spatial sequence of deformation textures moving from the country rock through the damage zone to the gouge core. The second half of the time sequence is essentially the reverse of the first half, as the gouge zone is abandoned and eventually sealed.

The first deformation features to appear in damage-zone granodiorite are dilational cracks concentrated in quartz (see also Moore and Lockner, 1995) that typically consist of one prominent set of sub-parallel

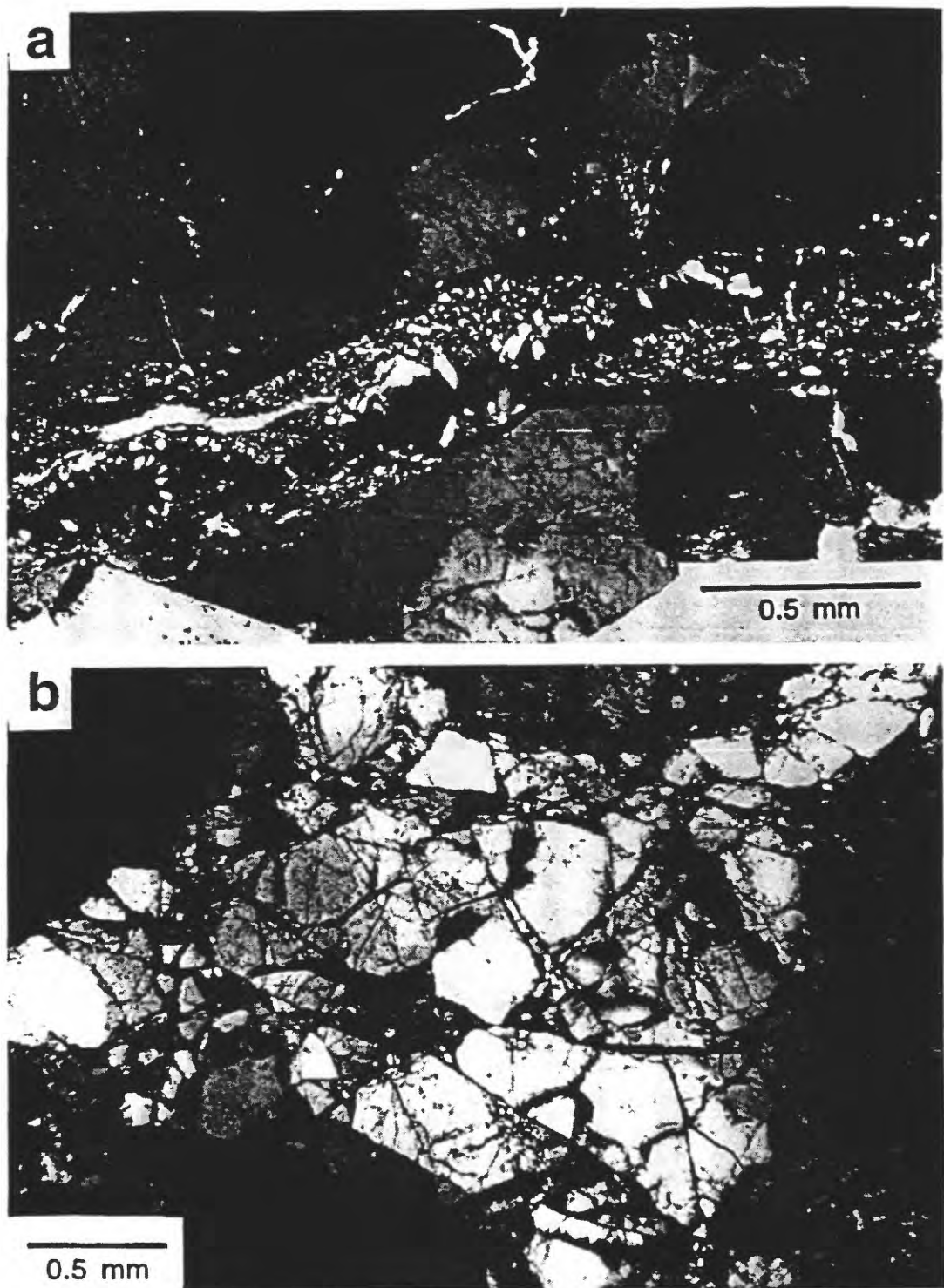


Figure 1. Photomicrographs of deformation and mineralization textures in core samples from the Nojima fault zone. a) The highest permeability measured by Naka et al. (1998) was in this NIED sample, 80-29, which contains a set of elongate dilatational cracks that are lined but not filled with laumontite and carbonate minerals (crossed polarizers). b) Heavily fractured quartz in high-permeability NIED sample 43-37-1.

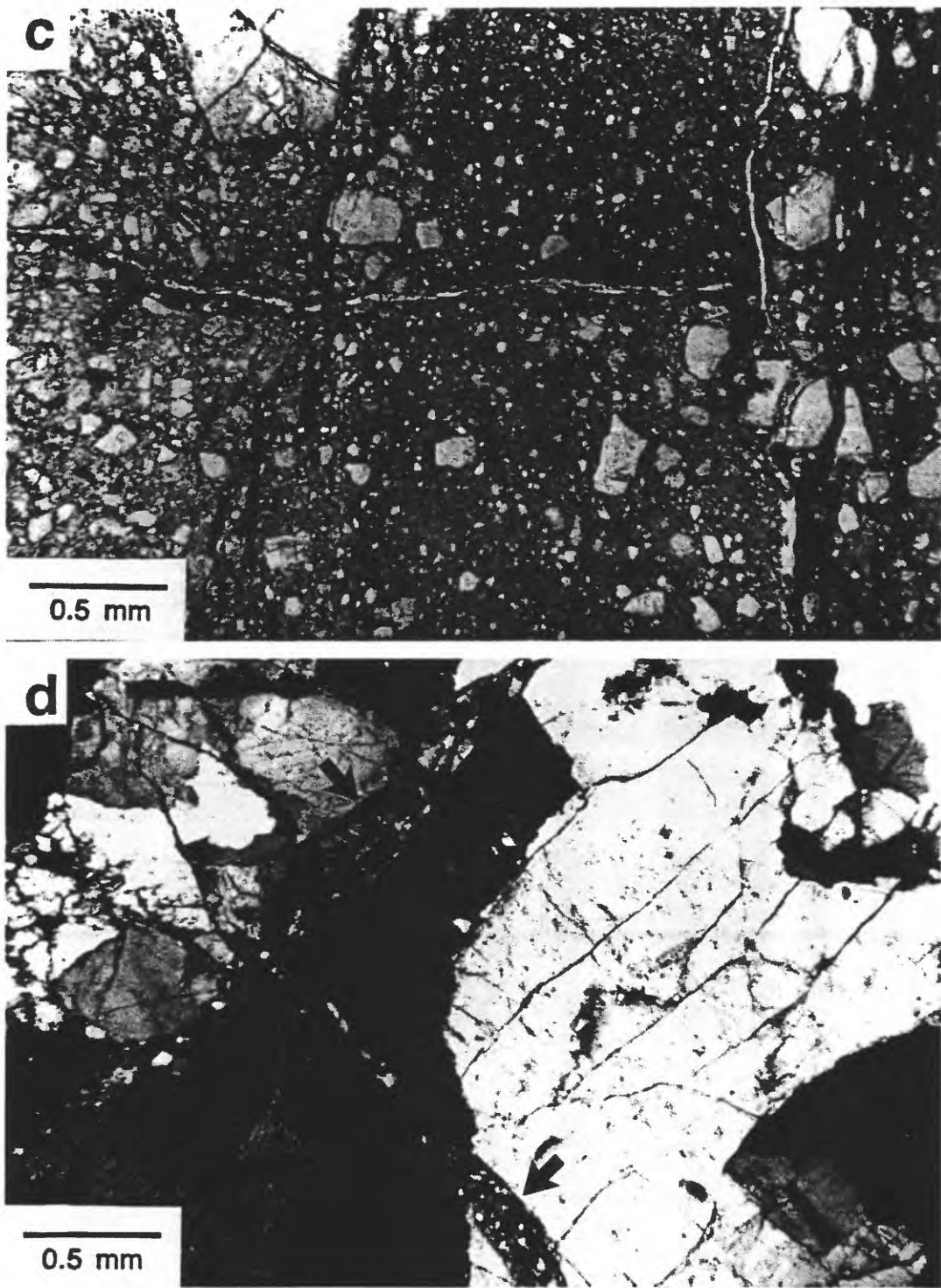
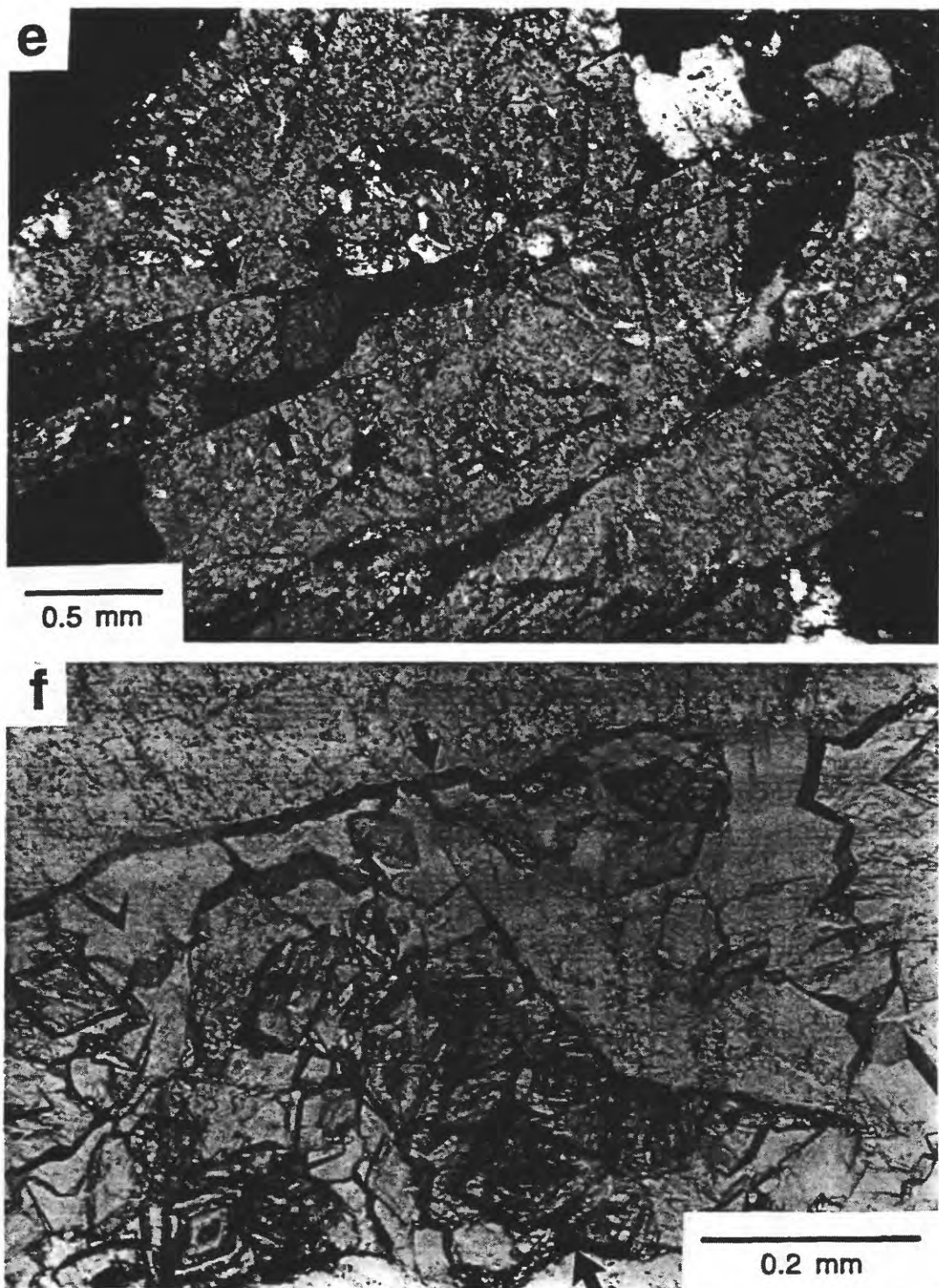


Figure 1, continued. c) Granulation of the igneous minerals leads to formation of fine-grained gouge of low strength and moderately low permeability. This gouge is cut by a dilational crack (indicated by arrow) filled with laumontite. The dark vertical lines contain carbonate minerals (GSJ 98-31, plane polarized light). d) Narrow microshears (indicated by arrows) parallel to the two prominent fracture orientations visible in the K-feldspar crystal at right (NIED 183-14C, crossed polarizers).



cracks (Figure 1a and d) and a subsidiary set that intersects the other at an angle of 60–90° (Figure 1d). Fluids flowing through the fractures after an earthquake cause some alteration of the igneous assemblage and deposit minerals on the fracture walls (Figure 1a). With increasing intensity of deformation, the igneous feldspars also begin to fracture extensively (Moore and Lockner, 1995). At this time, some of the earlier-formed dilational fractures undergo minor shear displacement. In Figure 1d the two intersecting shear fractures are parallel to the principal fracture sets visible in the large K-feldspar crystal. These two shears have developed from single fractures, but commonly closely spaced fractures pair up to form microshear zones (Figure 1e), with the fractures serving as boundary faults and the rock between them being more highly damaged than that outside the zone. Martel et al. (1988) and Segall and Pollard (1983) described similar fault-zone structures at outcrop scale in granitic rocks of the Sierra Nevada, California. In some of the Nojima fault samples, offsetting shears imply that the perpendicular shears were active at different times. However, most of them probably were active at the same time, leading to intensified fracturing of the granodiorite near their intersections.

As shearing becomes more heavily concentrated at one location, it becomes restricted to a single planar zone. Narrow gouge-bearing bands in NIED 76-17 and GSJ 101-2 intersect both sets of older

microshears; such cross-cutting relations may be typical of the gouge layers. Continued shearing within these single layers eventually generates gouge (Figure 1c). Among the remaining rock fragments in the gouge, clasts of medium-grained laumontite and of carbonate minerals are evidence of the gouge's earlier history of dilational fracturing and alteration. In addition, some of the gouge samples contain clasts of earlier-formed gouge, indicating multiple episodes of slip within the well-developed gouge layer.

Fault offset does not remain localized along the same gouge zone, but rather shifts to other gouge layers over time. If the new site of localized shear is within the same fault strand, then the abandoned gouge layer becomes part of the damage zone of the new gouge core. As such, the older gouge layer would be limited to dilational fracturing and minor shearing. For example, the banded gouge of GSJ 98-31 (Figure 1c) has been cut by a series of narrow laumontite and carbonate-filled cracks, such as the one extending from left to right across the middle of the photo. Eventually, fault motion may shift to a completely new strand, leaving the old strand outside the damage zone of the new one. In the absence of permeability-enhancing deformation, the old gouge layers, along with the rest of the abandoned fault strand, are gradually sealed with mineral deposits.

Figure 2 is a schematic summary of the general trends in permeability and strength that would accompany the deformation sequence described above,

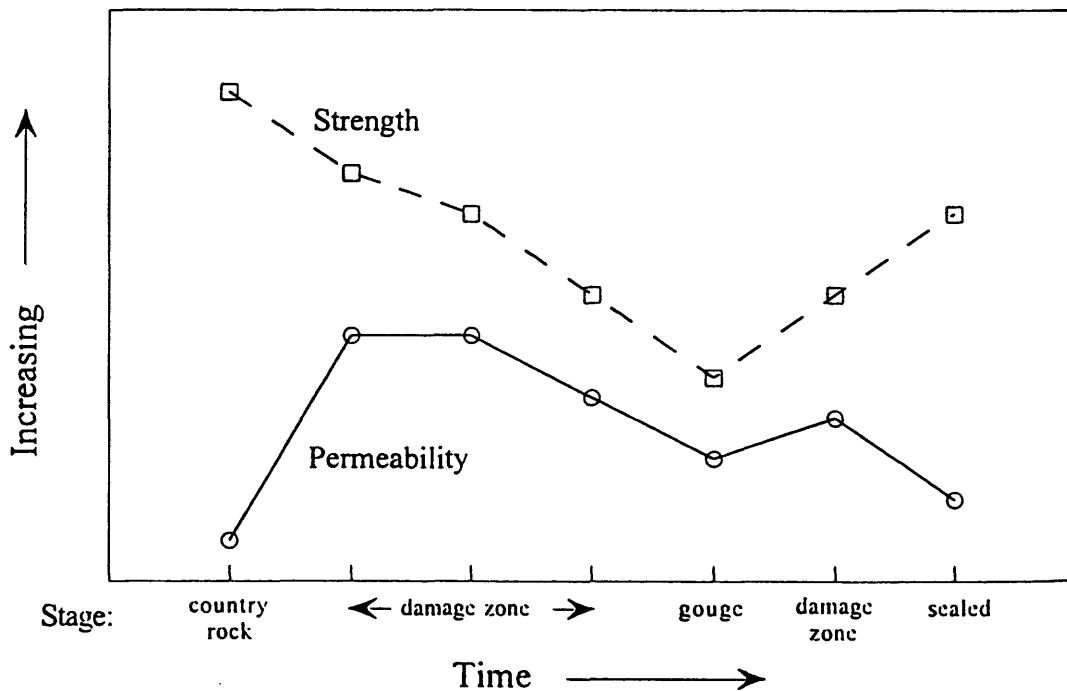


Figure 2. Relative changes in permeability and strength in the successive stages of the history of a gouge core zone (see text). The plots do not include the effects of individual earthquake cycles.

based on the data of Naka et al. (1998). The early stages leading up to gouge development correspond to the textural sequence in Figure 1a-c, and the accompanying changes in permeability and strength were described previously. When the gouge layer is abandoned as a site of localized shear, it becomes progressively indurated and strengthened as a result of sealing and alteration reactions. The two lines drawn in Figure 2 do not include the changes caused by individual seismic cycles (see Fig. 13 of Chester et al., 1993, p. 782). Sealing of fault rocks as a result of fluid-rock interaction will cause permeability to decrease and strength to increase between earthquakes.

#### POSITIONS OF THE FOUR FAULT STRANDS IN THE EVOLUTIONARY SEQUENCE

Of the four possible fault strands represented by the groups of samples in Table 1, the GSJ and the shallowest NIED strands are currently active. There have been some apparent shifts in the position of localized shear within the GJS strand, with one gouge sample (98-31) (Figure 1c) and a narrow band of gouge in a damage-zone sample (91-6) both being cut by mineral-filled dilatational cracks. These older gouge layers are now in the damage zone surrounding the new gouge core in that strand. The middle NIED fault strand also is active in at least a subsidiary sense, although both gouge samples (81-22A and 85-15B) are overprinted by dilatational cracks lined with mineral deposits. However, the narrow bands of gouge in 76-17 and 82-40 (Table 1) may have been sheared during the 1995 earthquake.

The deepest NIED fault strand is characterized by permeability and strength values approaching those of the country rock, and the mineralization textures suggest that it is an older, abandoned fault trace that would correspond to the final, sealed fault stage of Figure 2. This strand did not contain a gouge core; rather, shear may have been distributed among the many microshear zones (Figure 1d-e). Once shearing of this strand ceased, the extensive porosity in the microshears was gradually filled during several episodes of mineral growth (Figure 1f). The history of this strand would therefore lack the dip in permeability and strength corresponding to gouge formation in Figure 2; instead, the two parameters would change gradually from values characteristic of the first damage zone field to ones representative of the sealed fault.

#### REFERENCES

Chester, F. M., and Logan, J. M., 1986, Implications for mechanical properties of brittle faults from observations of the Punchbowl fault zone, California. In: Wang, C.-Y., (Ed.), Internal

Structure of Fault Zones, *Pure and Applied Geophysics*, 124: 79-106.

Chester, F. M., Evans, J. P., and Biegel, R. L., 1993, Internal structure and weakening mechanisms of the San Andreas fault, *Journal of Geophysical Research*, 98: 771-786.

Evans, J. P., Forster, C. B., and Goddard, J. V., 1997, Permeability of fault-related rocks, and implications for hydraulic structure of fault zones, *Journal of Structural Geology*, 19: 1393-1404.

Martel, S. J., Pollard, D. D., and Segall, P., 1988, Development of simple strike-slip fault zones, Mount Abbot quadrangle, Sierra Nevada, California, *Geological Society of America Bulletin*, 100: 1451-1465.

Moore, D. E., and Lockner, D. A., 1995, The role of microcracking in shear-fracture propagation in granite, *Journal of Structural Geology*, 17: 95-114.

Naka, H., Lockner, D., Tanaka, H., Ikeda, R., and Ito, H., 1998, Strength and permeability of core samples taken from drillholes crossing the Nojima fault of the 1995 Kobe earthquake, EOS, *Transactions American Geophysical Union*, Fall Supplement, 79: F823.

Segall, P., and Pollard, D. D., 1983, Nucleation and growth of strike-slip faults in granite, *Journal of Geophysical Research*, 88: 555-568.

blank page

# Laboratory Study of Fluid Migration and Fault Growth

Koji Masuda<sup>1</sup>, Mai Lihn Doan<sup>2</sup>, Osamu Nishizawa<sup>1</sup>, Xinglin Lei<sup>1</sup>, and Hisao Ito<sup>1</sup>

<sup>1</sup> Geological Survey of Japan, 1-1-3 Higashi, Tsukuba, 305-8567, Japan

<sup>2</sup> Ecole Normale Supérieure, 45 Rue d'Ulm 75230 Cedex, Paris 05 France

## ABSTRACT

Effects of the fluid migration on fracture process of inhomogeneous rock sample were investigated by using the Nojima core sample. Water was injected from the bottom surface of the rock under the confining pressure and the differential stress. X-ray CT images of the sample show the interior structure of the sample and revealed the relationship between the location of the fracture plane and foliation of the sample. Changes in P wave velocity measured along the six paths perpendicular to the sample axis show the upward migration of water. The distribution of the AE hypocenters reveals the development of fracture planes. The interior structure of the rock affects the location of fracture surface.

## INTRODUCTION

Water migration in the fault zone controls rupture process. Fluids in the fault zone play an important role in many aspects of earthquake faulting (ex. Masuda *et al.*, 1997). We investigate water-induced fracture processes using rock samples taken from the fault zone. We here focus on the effects of the pre-existing macro fractures of the rock on the water-induced fracturing.

## NOJIMA CORE SAMPLE

We used a core sample taken from the GSJ (Geological Survey of Japan) Hirabayashi borehole sample (depth 433.22m - 433.32m) penetrating the Nojima fault, which is a main fault of the 1995 Kobe earthquake, Japan (Ito *et al.*, 1996). This

sample was taken from the fault zone having coaxial zone of fault gouge at 623.3m to 635.1m, which is in the altered and deformed granodiorite rock in the depth from 426.1m to 746.6m (Tanaka *et al.*, 1998). Sample shape was a right cylinder of 50mm in diameter and 100mm in length. The sample contains pre-existing healed joints dipping 41 degree from the sample axis (Figure 1).

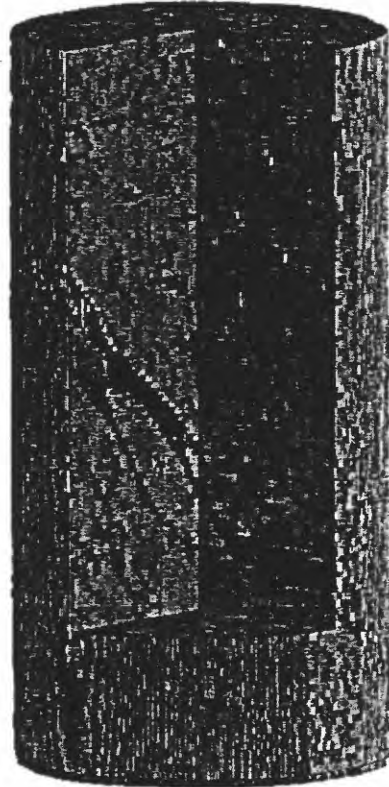


**Figure 1.** 3-D X-ray CT image of the sample. X-ray CT scanner, Hitachi CT-W2000, located at the Geological Survey of Japan was used to take the 2-D images of the sample. 3-D image was then constructed. CT value (gray scale) represents the density of the material.

## EXPERIMENTAL PROCEDURE

Under the confining pressure and the differential stress, we injected water from the bottom surface of the sample. Before the water injection, we took X-ray CT images of the sample to see the interior structure of the sample. During the water injection experiment, we monitored acoustic emission (AE) and measured surface strains and P-wave velocities (Figure 2). After the experiment, we took X-ray CT images of the sample to see the relationship between the location of the fault surface and the foliation of the sample. Figure 3 shows the locations of strain gages and PZT transducers. Thirty-two PZT transducers made a network for AE detection and an array for P wave velocity measurements. The AE hypocenter distribution was calculated by the same method used in seismology (*cf.* Masuda *et al.*, 1990, 1993).

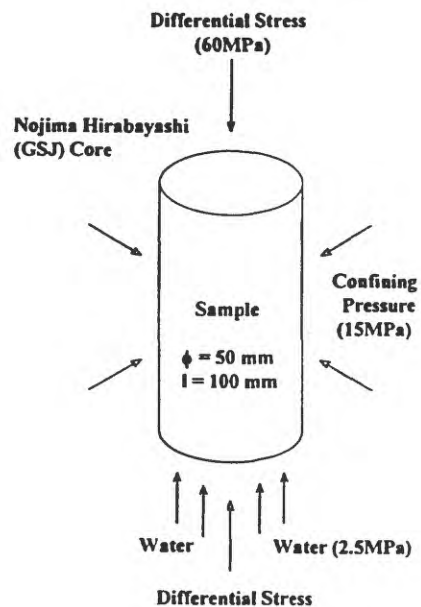


Figure 2. Experimental procedure. Sample was shaped as right cylinder of 50mm in diameter and 100mm in length. Water was uniformly injected from the bottom surface. We kept the stress condition constant during the water injection.

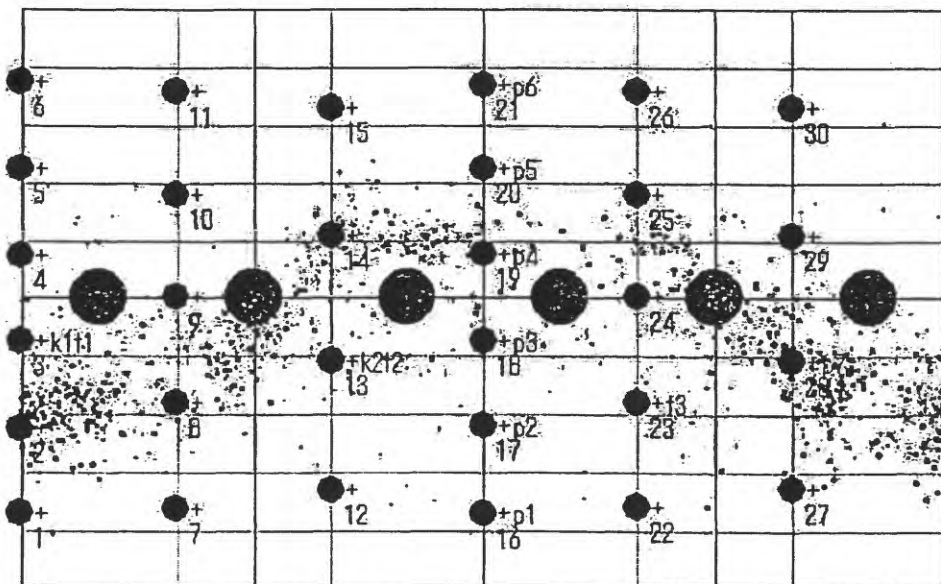


Figure 3. Locations of piezoelectric transducers and strain gages. Small circles indicate the piezoelectric transducers. Additional two transducers are placed in the end pieces attached at the top and the bottom of the sample. In P wave velocity measurements, elastic pulses were initiated from transducers No. 16 through No. 21 and received by No. 1 through No. 6. Large circles indicate the cross-strain gages which measure the axial and circumferential strains. AE locations projected to the sample surface are also plotted.

## STRESS CONDITION AND AE ACTIVITY

Figure 4 shows the changes in confining pressure, differential stress, water pressure, and AE activity. When we applied the confining pressure to the sample, AE activity increased and then decreased rapidly. These AE activities were caused by crush of the pre-existing cavities in the sample. We, then, applied the differential stress of 60 MPa, close to the fracture strength, to the sample under the confining pressure of 15 MPa. AE activity increased gradually in the first 20 min then decreased. When AE activity caused by the initial loading had ceased, we injected distilled water from the bottom end of the sample. Water-pressure measured at the injection point was 2.5 MPa and was kept constant for about 90 min, then increased to 5.0 MPa. When we increased water pressure from 2.5 MPa to 5.0 MPa, AE activity increased again and macroscopic fracture finally occurred after about 10 min from the water pressure increase.

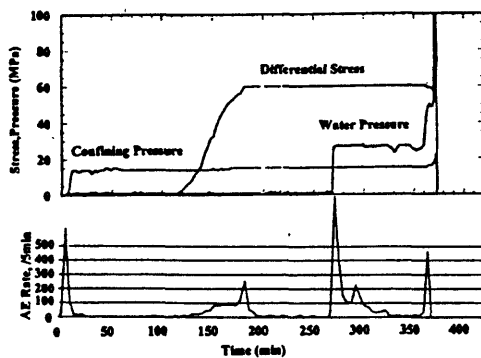


Figure 4. Changes of confining pressure, differential stress, injection water pressure, and AE rate. Water was injected at the duration time of 270 min. Injection water pressure was 2.5 MPa and then increased to 5.0 MPa. Macroscopic fracture occurred after about 10 min from the water pressure increase.

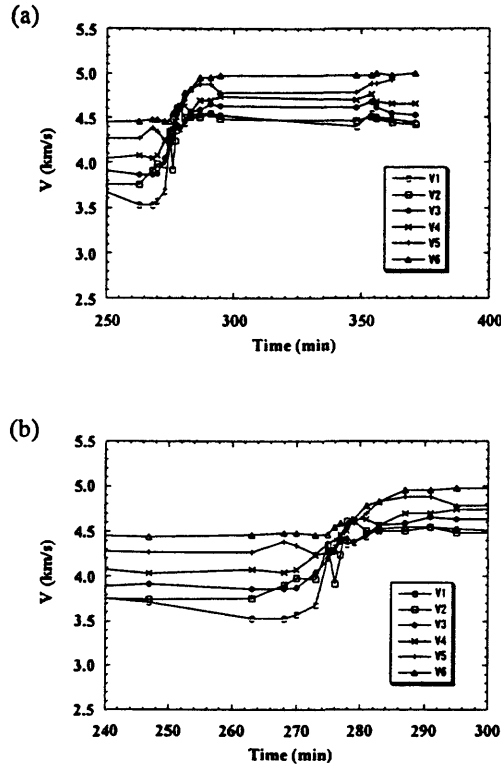
## P-WAVE VELOCITY

Figure 5 shows the changes in the P wave velocities along the six paths perpendicular to the sample axis. Figure 5a shows the P wave velocity from the time just before the water injection through the end of the experiment. Figure 5b shows the close up just before and after the water injection. When pre-existing cracks in a rock are filled with water, the P wave velocity is higher than that of the dry state. The variation of P wave velocity is a good indicator for monitoring the degree of saturation in rocks (eg, O'Connell and Budiansky, 1974, Masuda *et al.*, 1993, 1999). Figure 5a shows the increase of P wave velocities along the all paths measured after the water injection. Once the velocities of P wave reached to the peak values, they remain almost constant until the final failure. We infer that the water migrated upward in the sample and filled the cavities and cracks inside the sample in the short time and after that the degree of saturation didn't change so much. Figure 5b shows the close up of the P wave velocity data around the time of the beginning of water injection. The change in P wave velocity was very rapid. It means that the permeability of the Nojima core sample is very high, so that water migrated upward rapidly.

## AE HYPOCENTER DISTRIBUTION

We calculated the AE hypocenter distribution by using the wave form data. AE hypocenter locations projected to the sample surface were plotted in Figure 3. AE activity is located on the plane. This plane forms the final fracture plane of the sample, of which direction is parallel to the pre-existing healed joint of this Nojima core sample.

Figure 6 shows the AE hypocenter distribution for four time periods: Figure 6a, during the loading up (loading phase); Figure 6b, from the onset of creep to water injection (dry creep phase); Figure



**Figure 5.** P wave velocity change caused by the water injection. The horizontal axis represents the elapsed time. P wave velocities marked as V1, V2, V3, V4, V5, and V6 are the data from the receiver No.1, 2, 3, 4, 5, and 6 in Figure 3. Due to high permeability of the Nojima core sample, water migrated in the sample rapidly.

6c, from the water injection to just before the water pressure increase (water 2.5 MPa phase), and Figure 6d, from the increase of injection water pressure to macroscopic fracturing (water 5.0 MPa phase). During the loading phase, as shown in Figure 6a, clustering of AE hypocenters was not observed. AE activity during the dry creep phase was very low and clustering of AE hypocenter was not observed as shown in Figure 6b. After the water injection, AE events were located along the plane parallel to the pre-existing healed plane of the sample. During the water 5.0 MPa phase, AE activity was very high and AE hypocenters were

concentrated along the plane which formed the final fracture surface.

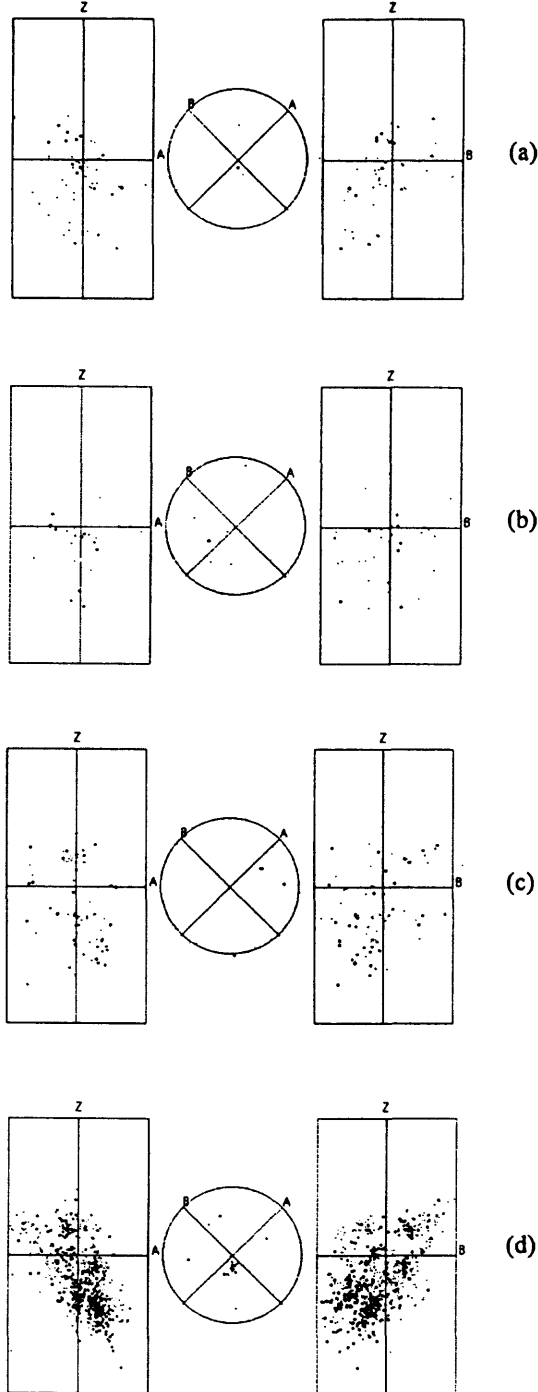


**Figure 6.** Spatial variation of AE hypocenter distribution. Hypocenter distribution of (a) loading phase, (b) dry creep phase, (c) water 2.5 MPa phase, and (d) water 5.0 MPa phase.

## FRACTURE PLANE AND FOLIATION

We took ninety-nine 2-D X-ray CT images perpendicular to the sample axis at every 1 mm along the sample axis. The thickness of each X-ray CT image was 1 mm. 3-D CT image (Fig.3) was constructed from these ninety-nine 2-D images. Figure 7 shows one of the 2-D X-ray CT images taken after the experiment. The direction of the foliation plane, from top left to bottom right, of the sample can be identified. The pre-existing healed joint, thick white portion, is also parallel to the foliation of the sample. Black line represents the location of the main fracture surface. The main fracture surface was formed parallel to the foliation plane of the sample.

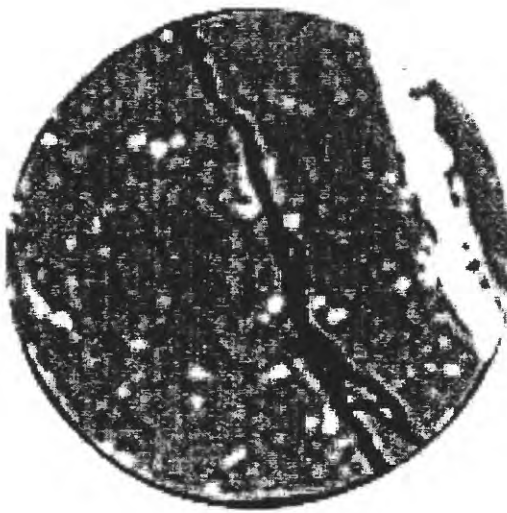


Figure 7.

2-D X-ray CT image of the sample after the experiment. Location of the image is 60mm from the top. Black line shows the fracture plane, white thick portion represents the pre-existing healed plane.

## CONCLUSION

We observed that the AE hypocenters were located in the plane which formed the fracture surface of the sample. The main fracture surface

was formed parallel to the foliation plane of the Nojima core sample. The interior structure of the rock affects the location of fracture surface.

## REFERENCES

Ito, H., Kuwahara, Y., Miyazaki, T., Nishizawa, O., Kiguchi, T., Fujimoto, K., Ohtani, T., Tanaka, H., Higuchi, T., Agar, S., Brie, A., and Yamamoto, H., 1996, Structure and physical properties of the Nojima fault by the active fault drilling, *Butsuri-Tansa*, **49**, 522-535. (In Japanese with English abstract).

Masuda, K., Nishizawa, O., Kusunose, K., Satoh, T., Takahashi, M., and Kranz, R., 1990, Positive feedback fracture process induced by nonuniform high-pressure water flow in dilatant granite, *J. Geophys. Res.*, **95**, 21583-21592.

Masuda, K., Nishizawa, O., Kusunose, K., and Satoh, T., 1993, Laboratory study of effects of in situ stress state and strength on fluid-induced seismicity, *Int. J. Rock Mech. Min. Sci. & Geomech. Abstr.*, **30**, 1-10.,

Masuda, K., Satoh, T., and Nishizawa, O., 1997, Effects of water on deformation and fracture process of rocks, *Bull. Geological Survey of Japan*, **48**, 475-485. (In Japanese with English abstract).

Masuda, K., Nishizawa, O., Lei, X., Satoh, T., and Ito, H., 1999, Laboratory study on fluid migration and fault growth in inhomogeneous rocks, *Geol. Surv. Japan Interim Report* no. EQ/99/1, 34-37.

O'Connell, R. J., and Budiansky, B., 1974, Seismic velocities in dry and saturated cracked solids, *J. Geophys. Res.*, **79**, 5412-5426.

Tanaka, H., Ikeda, R., Ito, H., Arai, T., Ohtani, T., Omura, K., Kobayashi, K., Sano, H., Sawaguchi, T., Tomita, T., Tomida, N., Higuchi, T., Hirano, S., Fujimoto, K., Matsuda, T., and Yamazaki, A., 1998, Mode of occurrence of fault rocks in the drilled

cores (GSJ and NIED) penetrating the Nojima  
earthquake Fault, *J. Geol. Soc. Japan*, 104,  
XIII-XVI.

# Hydraulic Properties at the GSJ Hirabayashi Borehole in the Nojima Fault from Analysis of Pump Test and Time Series Data

Evelyn A. Roeloffs<sup>1</sup>  
Norio Matsumoto<sup>1,2</sup>

<sup>1</sup>U.S. Geological Survey, 5400 MacArthur Blvd., Vancouver, WA 98661, USA, [evelynr@usgs.gov](mailto:evelynr@usgs.gov)

<sup>2</sup>Geological Survey of Japan, 1-1-3 Higashi, Tsukuba, Ibaraki 305-8567, Japan, [norio@gsj.go.jp](mailto:norio@gsj.go.jp)

## ABSTRACT

We analyzed groundwater-level data from the Hirabayashi borehole for the period from June, 1996 through October, 1999, as well as data from a pumping test conducted in March, 1998. The well is constructed so that groundwater-level variations represent fluid pressure fluctuations just below the major shear zone of the Nojima fault. Analysis of the pump test data yields a transmissivity that is consistent with a shear zone permeability obtained using a hydrophone VSP technique [Kiguchi *et al.*, 1999]. Flow during the pump test apparently was not from an area that is spatially limited, and we interpret this to mean that the pump test drew fluid from the near-vertical fault zone, rather than from large horizontal distances from the well. In this case, the transmissivity and storage coefficient from the pump test yield a vertical hydraulic diffusivity of 0.5 m<sup>2</sup>/s, which is consistent with the time constant of water-level increases in response to rainfall. Tidal variations in the groundwater level indicate strain sensitivities of 0.6 to 2.3 m/10<sup>-6</sup>, and tidal phases are suggestive of strains dominated by the deformation of planar fractures. The time series of water level in the Nojima Hirabayashi borehole should provide a means to monitor permeability changes associated with post-earthquake healing of the fault.

## BACKGROUND

The Hirabayashi borehole was completed with a casing that is perforated in the interval from 630 to 650 m below the land surface, about 5 m below where it intersects the main shear zone of the near-vertical Nojima fault at 623.3-625.1 m depth (Fig. 1). The shear zone consists of fault gouge, while the geology at the perforated interval is altered and deformed granodiorite [Tanaka *et al.*, 1999]. Interpretation of groundwater-level time series can place constraints on the hydraulic and mechanical properties of the formation, and also provides a way to monitor changes in these properties with time.

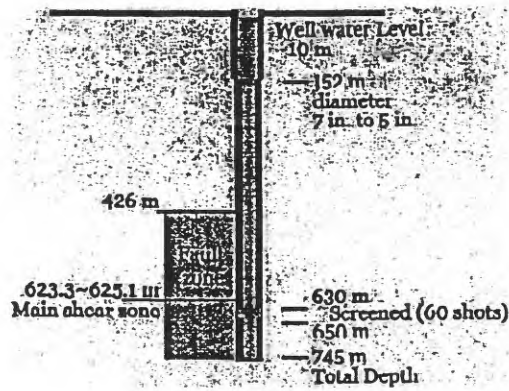


Figure 1. Diagram of GSJ Hirabayashi borehole.

## PUMP TEST ANALYSIS

The pump test sequence consisted of several short pumping intervals, followed by a constant-rate pumping test at a rate of 30 l/min (Fig. 2). We first analyzed the constant rate pumping test by matching the observed drawdowns to theoretical drawdowns for a well of non-negligible diameter that fully penetrates an aquifer of possibly limited width. The solution we used allowed for the possibility of a skin effect, which models the effect of a thin non-conductive zone at the wellbore wall such as might result from residual drilling mud or a clogged screen [Moench, 1985]. Models with aquifer widths of 500 m or more fit the data well, indicating that flow during the pump test came from distances at least this large. The best fit to the constant-rate pumping test was obtained for transmissivity,  $T$ , of  $1.5 \times 10^{-5} \text{ m}^2/\text{s}$ , storage coefficient,  $S$ , of  $3 \times 10^{-5}$  and a skin factor of 9.3. The non-zero skin factor indicates some resistance to flow at the borehole wall, possibly because only 0.05% of the perforated interval's area is actually open to the wellbore.

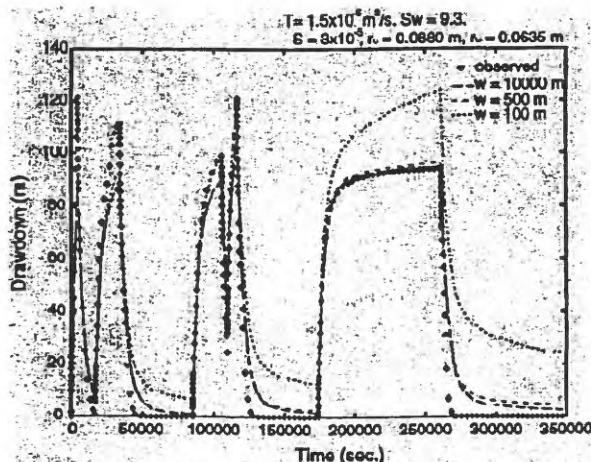


Figure 2. Observed drawdown during pumping tests and model simulations.

Kiguchi et al. [1999] used a hydrophone VSP technique to determine the permeability of fracture zones in the Hirabayashi borehole, and found that the gouge zone at 623-625 m depth had a

permeability of 2 darcies, corresponding to a hydraulic conductivity of  $1.9 \times 10^{-5} \text{ m/s}$ . Since the gouge zone is 1-2 m thick, their result agrees closely with the value obtained by dividing  $T = 1.5 \times 10^{-5} \text{ m}^2/\text{s}$  from the pump test by the aquifer thickness.

The structure of the Nojima fault zone is known to consist of a narrow fault core that is highly permeable relative to the surrounding rock. Thus, the result that the pump test data reveal no lateral limits to the aquifer is at first surprising. We interpret this result to indicate that the pump test is actually drawing fluid from the near-vertical fault zone, rather than from a horizontally extensive area around the well. The solution used to model the pump test data presumes only that flow around the well is essentially planar, but does not actually require that the plane be horizontal. Assuming that the pump test is primarily sampling the shear zone allows the vertical hydraulic diffusivity,  $c$ , to be calculated from the pump test data as  $c = T/S = 0.5 \text{ m}^2/\text{s}$ . This is a relatively high value, typical of fractured igneous rocks, and several orders of magnitude greater than hydraulic diffusivities for unsheared clay deposits [Roeloffs, 1996]. The high diffusivity suggests that a highly conductive pathway exists through the fault gouge, which is plausibly due to the recent fault rupture in the 1995 Hyogo-Ken-nanbu earthquake.

## RESPONSE TO RAINFALL

The groundwater-level record from the Hirabayashi well shows a strong influence of precipitation. Following periods of rainfall, water levels rise by as much as 2 m in a period of 4 to 5 days, returning to the pre-rain level after 3 to 5 weeks. There is no net rise or fall of groundwater level for the period of observation. The time constant of the water level increases due to rainfall is very similar to that obtained by assuming that the rainfall infiltrates as one-dimensional flow through a medium

that is 630 m thick and has a vertical hydraulic diffusivity of 0.5 m<sup>2</sup>/s, consistent with the results of the pump test analysis.

#### RESPONSE TO TIDES

The maximum amplitude of the tidal response in the Hirabayashi well is 9 cm peak to peak (Fig. 3). We analyzed the tidal signal to identify the major constituents M2 and O1. The amplitudes and phases of these tide constituents in water level data, when compared to a suitable reference, yield information about poroelastic and hydraulic properties of the aquifer.

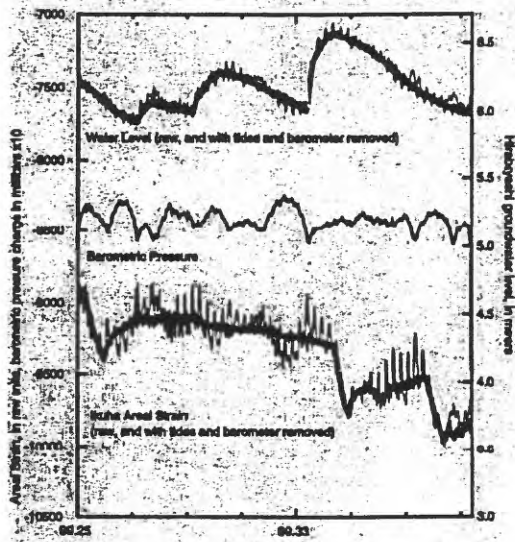


Figure 3. Water level, barometric pressure, and strain data at Hirabayashi for the period April 1 to June 1, 1999.

The location of the Hirabayashi well less than 0.5 km from the coastline of a small island presents a difficulty for the determination of in-situ tidal strain. Loads from ocean tides have a significant effect on tidal strain at Awaji Island, and are not readily calculated given the complex bathymetry around the island. We chose instead to compare water level tides at Hirabayashi to strain tides from a 3-component strainmeter at Ikuha, situated at a depth of 250-300 m and 5 km SW of the Hirabayashi

borehole. We summed the three components of strain at Ikuha to obtain a quantity proportional to either areal or volumetric strain. The absolute amplitude of the strain at Ikuha is not known, but we presume that the M2 constituent at Ikuha is within a factor of 2 of the calculated theoretical tide (neglecting ocean loads), which is  $13.4 \times 10^{-9}$  in volumetric strain.

Table 1 gives amplitudes and phases of M2 and O1 for the Hirabayashi groundwater level and for the Ikuha areal strain. Both time series have a larger O1 constituent than M2 constituent, indicating a large ocean load contribution. However, for the groundwater level data, the ratios of the observed M2 and O1 amplitudes to the amplitudes of the same constituents in the areal strain record, are nearly the same. For the assumed factor of 4 variation in the possible absolute amplitude of M2 at Ikuha, the strain sensitivity of the ground water level in the well is between  $0.6$  and  $2.3 \text{ m}/10^{-6}$  strain. The lower value is typical of a porous formation, but the higher values are unlikely unless the tidal variations are due to deformation of a permeable fracture. A better estimate of the absolute strain amplitude would be required in order to discriminate between these two possibilities.

The phases of the tidal constituents do suggest that the tidal response at Hirabayashi is governed by deformation of a fracture zone, rather than of a uniform porous material. The O1 constituent leads the areal strain, while the M2 constituent lags. Phases of opposite sign for these two constituents are not expected to result from fluid flow effects, but are consistent with phases calculated for the deformation of fractures [Bower, 1983]. The observed phase lag at M2,  $50.8^\circ$ , is larger than expected from the fracture deformation model, however.

Tidal analyses for several time periods indicate that the amplitudes and phases of M2 have remained relatively constant with time at Hirabayashi. However, the transmissivity of the interval is low enough that a decrease of hydraulic conductivity should produce detectable phase and amplitude changes in the M2 tide, allowing this technique to be used to monitor fault zone healing. It is necessary, however, to ensure that the wellbore is clean so that a change of skin factor does not introduce apparent changes of formation permeability.

## REFERENCES

Bower, D.R., Bedrock fracture parameters from the interpretation of well tides, *J. Geophys. Res.*, 88 (B6), 5025-5035, 1983.

Kiguchi, T., H. Ito, Y. Kuwahara, and T. Miyazaki, Estimate of the permeability of the Nojima fault by hydrophone VSP experiment, *Island Arc*, submitted, 1999.

Moench, A.F., Transient flow to a large-diameter well in an aquifer with storative semi-confining layers, *Water Resources Res.*, 21, 1121-1131, 1985.

Roeloffs, E.A., Poroelastic methods in the study of earthquake-related hydrologic phenomena, in *Advances in Geophysics*, edited by R. Dmowska, Academic Press, San Diego, 1996.

Tanaka, H., T. Higuchi, N. Tomida, K. Fujimoto, T. Ohtani, and H. Ito, Distribution, deformation, and alteration of fault rocks along the GSJ core penetrating the Nojima fault, Awaji Island, southwest Japan, *Jour. Geol. Soc. Japan*, 105 (1), 72-85, 1999.

	Period, hours	Ampli- tude in Ikuha areal strain	Phase in Ikuha areal strain, degrees	Amplitude in Hirabayashi water level, m	Phase in Hirabayashi water level, degrees	Amplitude Ratio, Hirabayashi /Ikuha	Phase difference, Hirabayashi -Ikuha, degrees
O1	25.8193	52.82	327.0	0.01898	134.0	3.59E-04	-13.0
M2	12.4206	40.56	332.1	0.01524	202.9	3.76E-04	50.8

Table 1. Results of tidal analysis of Ikuha areal strain and Hirabayashi groundwater level for the period April 1 through June 1, 1999. Areal strain amplitudes are in arbitrary units. Tidal phases are calculated with respect to 0000 on January 1, 1999, local time. A positive phase difference indicates a lag of peak water level behind peak contractional strain.

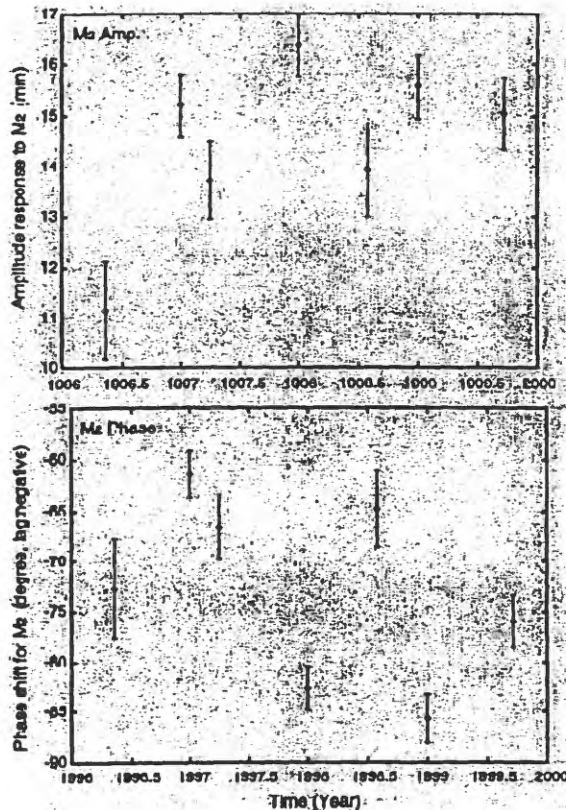


Figure 4. Amplitudes and phases of the M2 tidal constituent in the Hirabayashi groundwater level as functions of time.

blank page

# Earthquake-induced hydrological changes and possible permeability enhancement due to the January 17, 1995 Kobe Earthquake, Japan

Tomochika Tokunaga

Department of Geosystem Engineering, University of Tokyo

7-3-1 Hongo, Bunkyo-ku, Tokyo 113-8656, Japan

e-mail: tokunaga@geosys.t.u-tokyo.ac.jp

## ABSTRACT

Hydrologic changes associated with the January 17, 1995 Kobe Earthquake occurred in Awajishima Island very close to the epicenter. These included (1) large drop of water table in the mountainous area, (2) rapid increase of discharge along active faults, and (3) change of chemistry of discharged water. A simple horizontal flow model was constructed to explain the observed changes, and optimal sets of specific yield and change of hydraulic conductivity were estimated. Results suggest that this model can explain the observed phenomena consistently. The hydraulic conductivity is estimated to increase at least 5 times that before the Earthquake; however, quantitative measurement of the increase of discharge just after the earthquake would constrain better the change of the hydraulic conductivity. Specific yield of the unconfined aquifer is between 0.3 and 1.7 % depending on the assumed recharge rate but independent of the assumed depth to the impermeable basement. Change of chemical composition of discharged water could be explained by upward movement of deeper water due to invasion of saltwater into the aquifer.

## 1 INTRODUCTION

Hydrologic changes occur in response to large earthquakes, and various mechanisms have been postulated to explain them (e.g., Sibson, 1981; Muir-Wood and King, 1993; Rojstaczer et al., 1995). It has been reported that similar hydrologic fluctuations were associated with the Hyogo-ken Nanbu (Kobe) Earthquake in Awajishima Island (Fig. 1) (Sato et al., 1995; Groundwater Research Group, Osaka City University Investigation Team for the Hanshin-Awaji Great Earthquake Disaster (hereafter called GRG), 1996; Oshima et al., 1996; Sato and Takahashi, 1996). These can be summarized as follows: (1) A large amount of water was discharged in the mountainous area just after the Earthquake, and this effect ended within 4 months (Oshima et al., 1996). (2) The water table in the central part started to drop soon after the Earthquake (Fig. 2; Table 1), and water levels of small ponds also started to drop and some of them dried up (GRG, 1996; Oshima et al., 1996; Osada et al., 1997). (3) On the other hand, the volume of discharged water near active faults increased rapidly and this anomalous discharge has

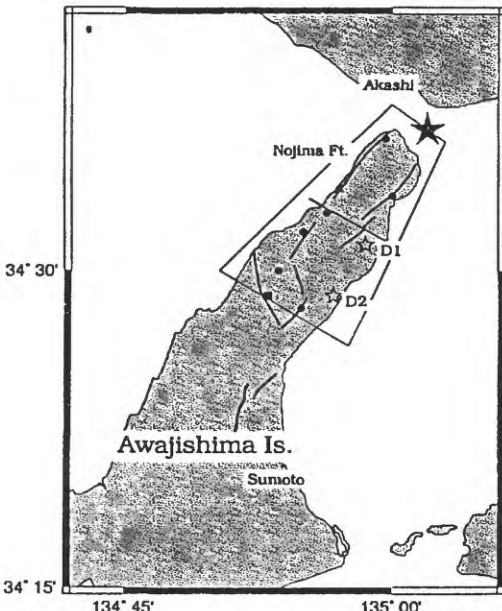


Fig. 1. Index map of the studied area. Filled star indicates the epicenter of the Kobe Earthquake, open stars the location of discharged water where the change of chemical composition was reported by Sato et al. (1995), filled square the location of a 1200 m deep well, dots the locations where Sato and Takahashi (1996) measured the relative discharge, a triangle the location where Oshima et al. (1996) measured the discharge rate, lines the location of active faults, and a straight line the location (estimated) of the cross section that appeared in GRG (1996).

continued for more than 1 year (Fig. 3) (Sato and Takahashi, 1996). (4) The chemical composition of discharged water has slightly increased in bicarbonate

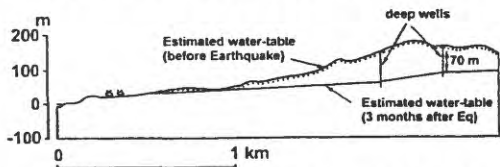


Fig. 2. Schematic cross section showing the possible water-table drop at the northern part of the Awajishima Island. The location of the section is shown in Fig. 1. Water-table at the western deep well before the Earthquake was not measured. Modified after GRG (1996).

Table 1. Water-table fluctuations of shallow wells in the central part of the Island (data after Oshima et al., 1996).

Well no.	Water table above well bottom (m)		Depth to well bottom (m)
	Before EQ	113 days after EQ <sup>a</sup>	
1	1.92	0.43	3.48
2	1.83	0.27	3.55
3	3.25	0.79	7.40
4	3.06	---	3.98
5	3.41	0.63	7.01
6	1.76	---	3.46
7	2.65	---	2.85
8	1.91	0.10	4.97
19	6.59	---	4.62
11	21.35	13.75	21.35
12	9.30	---	10.79
14	1.00	---	1.18
16	2.63	---	4.86
17	1.80	1.12	2.47
18	3.16	---	5.43
19	1.00	0.27	8.48

<sup>a</sup>: Dashes indicate that no water existed in the well.

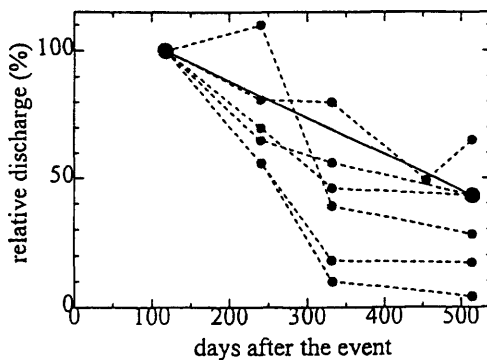


Fig. 3. Change of relative discharge (normalized by that in May, 1995) as a function of time. Small dots and dotted lines indicate each measurement and large dots and a line indicate the overall change between May 1995 and June 1996. Data after Sato and Takahashi (1996).

after the Earthquake (Fig. 4) (Sato et al., 1995;

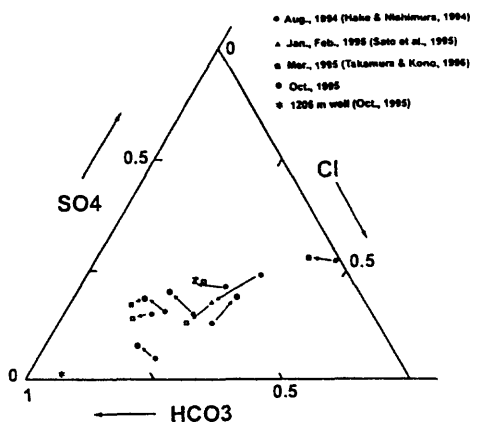


Fig. 4. Change of water chemistry (anions) due to the Earthquake.

Takamura and Kono, 1996), and it continued more than ten months. The observation (1) might be explained by the poroelastic response of the aquifer because the Island is situated in the compressional region of co-seismic strain field (King et al., 1995). The observations (2), (3), (4) are very similar with that reported after the Loma Prieta Earthquake (Rojstaczer and Wolf, 1992; Rojstaczer et al., 1995), and may be explained by the enhancement of the permeability due to the earthquake. The following discussion will be concentrated on a simple model to explain the latter observations because poroelastic deformation has contributed a minor amount of water discharge compared with that caused by permeability increase as discussed later.

## 2 HYDROLOGICAL CHANGES IN THE NORTHERN PART OF THE AWAJISHIMA ISLAND

Awajishima Island is situated very close to the epicenter (Fig. 1). Active faults run parallel and along the coastal lines (about 100 to 400 m far from the coast in the case of the Nojima Fault) of the northern part of the Island, and the Nojima Fault was ruptured by the Earthquake (Fig. 1). The central part of the Island consists mainly of weathered granite and a thin cover of Neogene marine sediments. The elevation of the central part is more or less constant at around 200 m above sea level (the highest point is 360 m at the southernmost part in the studied area).

The water table in the central part of the Island before the Earthquake was close to the topographic surface and dropped more than 70 m within 90 days after the Earthquake (GRG, 1996; H. Kumai, 1998 pers. comm.) (Fig. 2). The regional water table distribution at 90 days after the Earthquake was estimated from two deep wells and discharge points (GRG, 1996; H. Kumai, 1998 pers. comm.). Considering the spatial distribution of the wells and

discharge points, this estimation (Fig. 2) is reasonable. Shallow wells in the central part also dropped (Table 1) even though some of them still show the existence of water, which suggests the existence of local perched water systems. This water-table drop is significant compared with the possible magnitude of natural fluctuations. People have used shallow wells (less than 10 m in depth) (Table 1) for daily use, suggesting that the seasonal water table fluctuation is smaller than 10 m. The 70 m drop of water table cannot be explained by the annual fluctuation of recharge. Rainfall is largest in summer season and is about 4 times larger than that in the winter season. The Earthquake happened January 17 and the water table did not return after the summer season; instead it continued to drop except for 2 wells out of 16 measured shallow wells (Oshima et al., 1996). The annual rainfall is about 1400 mm, and assuming that one-third of annual rainfall is the recharge rate, it is necessary to consider more than 1 year of no rainfall for the water table to drop 70 m (assuming 1 % porosity). Thus, it is reasonable to assume that natural fluctuations are smaller than the observed water-table drop, and the water-table drop can be attributed to the Earthquake-related phenomenon.

Sato and Takahashi (1996) reported the volumetric change of discharge at 6 locations between May 1995 and June 1996 (Fig. 1). The overall discharge in June 1996 was 43 % that in May 1995 (Fig. 3). Although they did not measure the entire volume of discharge over the Island, their locations are all situated at the major discharge points and also cover the studied area; thus, it can be assumed that the ratio of their measurements represents the ratio of the whole volume of discharge. Oshima et al. (1996) measured stream flow of 4 locations, located about 250 m from the coast, whose catchment areas extend about 500 m to 600 m along the coast (Fig. 1). They measured an overall discharge of  $1.75 \text{ m}^3/\text{min}$ . 290 days after the Earthquake. This value is about 1.3 to 1.6 times larger than the steady state value (integrated over 500 to 600 m distance) obtained from the model which is described later, in the case where one-third of annual rainfall is assumed to be the recharge rate.

The increase of discharge also is significant compared with the annual fluctuations. Sato and Takahashi (1995) reported that the water level of one of the ponds, which is located where Oshima et al. (1996) measured discharge, increased very rapidly just after the Earthquake even though no water existed there before the Earthquake. Considering that the dam was artificially broken within a day after the Earthquake to prevent it from overflowing, the increase of discharge must have been significantly larger than the annual fluctuations.

The chemical composition of discharged water has increased in bicarbonate after the Earthquake (Fig. 4).

The change of chemical composition can be explained either by the mixing of discharged water at steady state and the deeper water represented by the 1205 m well, or by the discharge of water that had been side-tracked into dead-end pores and/or slow pathways through relatively less permeable rocks due to the possible earthquake-induced micro-fracturing, or some other reasons.

### 3 CONSTRUCTION OF A MODEL TO EXPLAIN THE HYDROLOGICAL CHANGES

GRG (1996) tried to estimate the increase in the permeability of the aquifer and reported that permeability increased 3.6 times after the Earthquake. However, they did not show the model and assumptions used to obtain the value and it is difficult to evaluate their result. Rojstaczek et al. (1995) used a simple diffusion model to explain the phenomenon following the 1989 Loma Prieta Earthquake. They adopted a confined aquifer model and discussed the water-table drop of the mountainous region.

Here, the Dupuit-Ghyben-Herzberg (D-G-H) model (Fetter, 1972; Bear, 1972; Vacher, 1988; Vacher and Wallis, 1992) was applied to the unconfined fluid flow in the Island. An infinite-strip island model can be applied due to the fact that the width of the northern part of the Island is around 5 km and more or less constant (Fig. 1). The D-G-H model results from combining (a) the Dupuit approximation of horizontal flow and (b) the Ghyben-Herzberg principle of proportionality between water-table elevation and depth to interface with (c) Darcy's law. The Dupuit approximation is violated near the coast where the thickness of the freshwater region narrows. However, this treatment might be acceptable because the relative change in discharge is used to estimate the relative change in the order of magnitude of the hydraulic properties by the earthquake. Although this earthquake may cause the increase of vertical flow along faults, Ishimaru (1997) showed that the increase of vertical permeability along faults alone could not explain any water-table drop in the central part of the Island, suggesting that the increase of horizontal permeability can be a possible reason for the observed water-table drop.

The resulting D-G-H version of Darcy's law is combined with the continuity equation to give a governing differential equation (Vacher, 1988). However, it is not appropriate to directly apply the model to the Island because the depth of the freshwater-saltwater interface at the central part before the Earthquake is calculated to be 6.6 km, assuming that the water-table is 165 m above sea level. This value is unrealistic considering the 5-km width of the Island. Instead, it is assumed that there is an impermeable basement below a specified depth and the fluid flow in the Island is governed by the

combination of the D-G-H model (where the water table is below  $z/G$ ) and the simple Dupuit model (where the water table is above  $z/G$ ) (Fig. 5), and the effect of the position of the impermeable basement is examined in this analysis. Here  $z$  and  $G(=\rho_w/(\rho_s - \rho_w))$

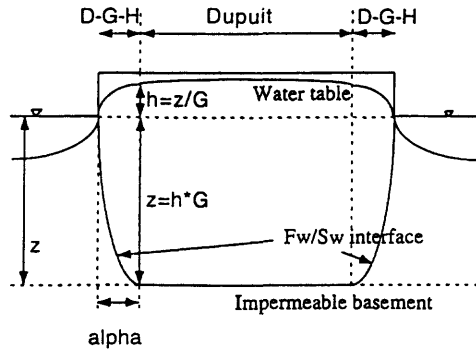


Fig. 5. A schematic figure of the model used in this study. D-G-H and Dupuit indicate the region where the Dupuit-Ghyben-Herzberg model and the simple Dupuit model are applied, respectively. See text for details.

represent the depth of the basement from sea level and the Ghyben-Herzberg constant, respectively, and  $\rho_w$  is the density of freshwater and  $\rho_s$  is that of saltwater. Assuming that the porosity of the unweathered granite at depth is very small compared with the specific yield of the highly weathered surficial granite, the governing equations for unconfined groundwater flow in the Island becomes

$$K(1+G)\frac{\partial}{\partial x}\left(h\frac{\partial h}{\partial x}\right) + w = S_y \frac{\partial h}{\partial t} \quad (1)$$

for the D-G-H region of the model, and

$$K\frac{\partial}{\partial x}\left((h+z)\frac{\partial h}{\partial x}\right) + w = S_y \frac{\partial h}{\partial t} \quad (2)$$

for the simple Dupuit region of the model, where  $K$  is the hydraulic conductivity,  $h$  is the height of the water table,  $w$  is the recharge rate,  $S_y$  is the specific yield. Because the boundary between the D-G-H and the simple Dupuit models moves with the change of water table height, this combined model tracks the boundary (the length 'alpha' in Fig. 5) and maintains conservation of mass during the transient calculations. The mass conservation is held at the boundary between the models because  $z=h^*G$  at the boundary (Fig. 5), and substituting this relationship into equation (2) shows that the same flux is obtained through the boundary from both equations (1) and (2).

A numerical code has been developed based on the finite-difference approximation. The validity of the code was checked by comparing 1) the numerical and analytical solutions of the Boussinesq problem (Bear, 1972; Polubarnova-Kochina, 1962) for the simple

Dupuit case and 2) the steady state results of both numerical and analytical solutions for the combined case.

#### 4 RESULTS OF NUMERICAL CALCULATION AND DISCUSSION

The observed quantitative data have been used to constrain the model. These are (1) the water table at the central part of the Island dropped from 165 m above sea level to 95 m within 90 days after the Earthquake (GRG, 1996; H. Kumai, 1998 pers. comm.) (Fig. 2). (2) the overall discharge in June 1996 was 43 % that in May 1995 (Fig. 3). (3) the depth to the impermeable basement is greater than 1205 m. This constraint comes from the chemical composition of the 1205 m well water, which does not show saltwater features ( $\text{Na}^+$  of 5.36 meq/l and  $\text{Cl}^-$  of 0.36 meq/l).

The initial condition is set as the steady state solution in which the water table at the center of the Island is 165 m above sea level, and is calculated using either the D-G-H model or the simple Dupuit model according to positions. The lower boundary is set as impermeable at the freshwater-saltwater interface for the D-G-H region and at the depth of the impermeable basement for the simple Dupuit region (Fig. 5). The condition for the lateral boundaries are set as 0 m height of water table at the coastal lines. Recharge is assumed to be constant and is assumed to be either half, one-third, or one-fifth of annual rainfall.

Using the above mentioned model and boundary conditions, the optimal sets of the change of hydraulic conductivity due to the Earthquake and the specific yield were estimated. Fig. 6 shows how calculated results change by changing these parameters. In this figure, solid contours show the absolute difference between the calculated and measured discharge ratio between May 1995 and June 1996, and dotted contours indicate the date when the water-table at the central part falls below 95 m. From constraint (1), the region above the 90 day contour is considered not to be optimal. Similarly, the region outside of the 0.05 solid contour is considered not to be optimal. Thus, the filled area is the region where the model is evaluated to be optimal.

It is found that the optimal specific yield is between 0.3 and 1.7 % depending on the recharge rate but independent of the assumed depth to the impermeable basement (Fig. 6). This result is noteworthy because the estimates of specific yield are usually not so well constrained. The hydraulic conductivity is estimated to increase at least 5 times after the Earthquake (Fig. 6). The increase of hydraulic conductivity should be interpreted as the geometric average of the increase of the conductivities in the fault zone and the surrounding rocks. The increase of hydraulic

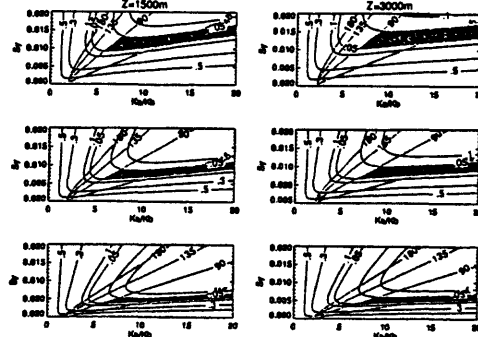


Fig. 6. Contour maps explaining how calculated results change due to changing parameters. Horizontal axis is the ratio between the hydraulic conductivity after ( $K_a$ ) and before ( $K_b$ ) the Earthquake, and vertical axis the specific yield. Recharge is assumed to be half of the annual rainfall for the upper, one-third for the middle, and one-fifth for the bottom figures. Lines indicate the absolute difference between the calculated and measured discharge ratio and dotted line the date when the water-table at the central part becomes below 95 m. Filled area is the region where the model is evaluated to be optimal.

conductivity in the fault zone might be larger than that of the surroundings. However, the thickness of the fault zone is very narrow compared with the thickness of the surrounding rocks considering the horizontal model used in this analysis, and it was not practical to explicitly account for faults as different hydraulic conductivity zones due to the scarcity of data sets. Thus, it was decided to estimate the geometric average of the change of hydraulic conductivity in this analysis.

Fig. 7a shows examples of the calculated change of discharge rate normalized by that at steady state as a function of time using the optimal sets of parameters. This result can be used to estimate the significance of poroelastic contribution to the discharge. Assuming a co-seismic volumetric strain of  $10^{-5}$ , a Biot-Willis coefficient of 0.85 (Berryman, 1992), and a deformation depth of 10 km, which are all very large estimates, the total discharge changes  $425 \text{ m}^3$  in a 1 m slice of the Island. This value is about 65 times larger than that of the assumed daily discharge at steady state condition (assuming one-third of rainfall as recharge). Even though this value is large, the increase of discharge due to the increase of hydraulic conductivity is an order of magnitude larger (integrate Fig. 7a); thus, the poroelastic contribution is considered to be very small.

It is obvious that the increase of the hydraulic conductivity is proportional to the increase of discharge just after the earthquake, and that it is difficult to estimate the increase of conductivity using

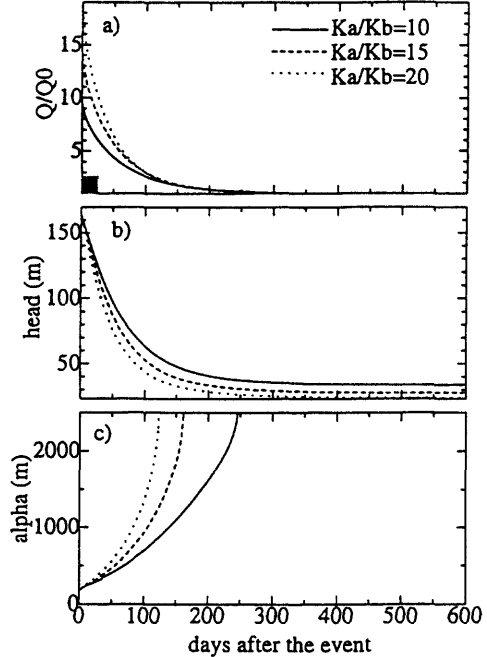


Fig. 7. Examples of calculated a) discharge rate normalized by that at steady state condition, b) water-table at the center of the Island, and c) location of freshwater-saltwater boundary at the depth of impermeable basement, from the optimal sets of hydraulic properties (in the case where  $z=1500$  m, recharge is one-third of rainfall). Solid box in a) indicates the equivalent volume of poroelastic contribution.

the discharge data 100 days after the earthquake, which is the case for this analysis (Fig. 3). This suggests that it is important to measure the change of discharge just after the earthquake to obtain a proper estimate of the change of hydraulic conductivity. Fig. 7b shows the calculated water table change as a function of time. This result tells us that it is also difficult to obtain the increase of the conductivity from the measurements of the water-table drop at the central part of the Island.

Fig. 7c shows the amount of saltwater invasion due to the drop of water table (see Fig. 5 for the definition of vertical axis). This result suggests that saltwater has intruded into the aquifer in accordance with the Ghyben-Herzberg principle. The saltwater intrusion could be the cause of the mixing of shallower and deeper water and could be the reason why the chemical composition has changed (Fig. 4). Note that this analysis does not necessarily support the interpretation because the flow direction is assumed to be horizontal and because the porosity of deeper granite is very small, neglecting the contribution of deeper groundwater to the calculated discharge. However, once the hydraulic conductivity is increased and approaches a new steady state condition, it is

suggested that the shape of freshwater zone narrows and deeper groundwater could discharge at around the coastal zone. More sophisticated modeling is necessary to fully take the contribution of the migration of deeper water into consideration.

## 5 CONCLUSIONS

Several hydrologic changes were observed in Awajishima Island caused by the Kobe Earthquake. A combined Dupuit-Ghyben-Herzberg and simple Dupuit model was constructed to test the ability to explain these phenomena. This model can explain the most of the phenomena consistently, and the following conclusions are obtained.

- 1) Increase of horizontal hydraulic conductivity by the Earthquake may be the main cause of hydrologic changes and the hydraulic conductivity is estimated to increase at least five-fold after the Earthquake.
- 2) It is necessary to measure the increase of discharge just after the earthquake to better constrain the increase of the hydraulic conductivity.
- 3) Contribution to discharge by co-seismic volumetric strain is calculated to be minor.
- 4) The specific yield of the unconfined aquifer is estimated to be 0.3 to 1.7 % depending on the recharge rate but independent of the assumed depth to the impermeable basement.
- 5) Change of chemical composition of discharged water could be caused by the movement of deeper water due to the intrusion of saltwater into the aquifer, however, more sophisticated analysis is necessary to prove this hypothesis.

## REFERENCES

Bear, J. (1972), Dynamics of fluids in porous media: New York, American Elsevier Publishing Company, 764 p.

Berryman, J. G. (1992), Effective stress for transport properties of inhomogeneous porous rock: *Journal of Geophysical Research*, 97, 17409-17424.

Fetter, Jr., C. W. (1972), Position of the saline water interface beneath oceanic islands: *Water Resources Research*, 8, 1307-1315.

Groundwater Research Group, Osaka City University Investigation Team for the Hanshin-Awaji Great Earthquake Disaster (GRG) (1996), Influence by the Hyogoken-Nanbu Earthquake to the groundwater including hot-spring water, in Shibasaki, T., Uemura, T. and Yoshimura T. eds., Great Earthquakes, Geologists' Roles in Time of Disaster: Tokai University Press, 133-147.

Hake, Y. and Nishimura, R. (1994), Visit to valuable water springs (27). Valuable water springs in Awaji island: *Journal of Groundwater Hydrology*, 36, 487-492.

Ishimaru, T. (1997), Study for long-term stability of geological environment -seismic effect on hydrogeological environment:- PNC Technical Review, 102, 39-46.

King, C. -Y., Koizumi, N. and Kitagawa, Y. (1995), Hydrogeochemical anomalies and the 1995 Kobe Earthquake: *Science*, 269, 38.

Muir-Wood, R. and King, G. C. P. (1993), Hydrological signatures of earthquake strain: *Journal of Geophysical Research*, 98, 22035-22068.

Osada, M., Tokunaga, T., Ishibashi, H. and Kayaki, T. (1997), Groundwater fluctuations in the northern part of Awaji Island after Hyogoken-Nanbu Earthquake: *Proceedings of 1997 Annual Meeting of the Japan Society of Engineering Geology*, 237-240.

Oshima, H., Tokunaga, T., Miyajima, K., Tanaka, K. and Ishibashi, H. (1996), Groundwater fluctuations caused by the earthquake: *Journal of the Japan Society of Engineering Geology*, 37, 351-358.

Polubarnova-Kochina, P. Ya. (1962), Theory of ground water movement: Princeton, Princeton University Press, 613 p.

Rojstaczer, S. and Wolf, S. (1992), Permeability changes associated with large earthquakes: An example from Loma Prieta, California: *Geology*, 20, 211-214.

Rojstaczer, S., Wolf, S. and Michel, R. (1995), Permeability enhancement in the shallow crust as a cause of earthquake induced hydrological changes: *Nature*, 373, 237-239.

Sato, T. and Takahashi, M. (1996), Anomalous ground water discharge after the 1995 Kobe (Hyogo-ken-nanbu) earthquake in the Awaji Island, Japan (part 2) Change of the discharge rate: *Chishitsu News*, 506, 24-28.

Sato, T., Takahashi, M., Matsumoto, N. and Tsukuda, E. (1995), Anomalous ground water discharge after the 1995 Kobe (Hyogo-ken-nanbu) earthquake in the Awaji Island, Japan: *Chishitsu News*, 496, 61-66.

Sibson, R. H. (1981), Fluid flow accompanying faulting: Field evidence and models, in Simpson, D. W. and Richards, P. G., eds., *Earthquake prediction: American Geophysical Union Maurice Ewing Series*, 593-603.

Takamura, H. and Kono, T. (1996), Trend of spring water and groundwater in the Awaji Island after the 1995 Hyogo-Nanbu Earthquake: *Journal of Groundwater Hydrology*, 38, 331-338.

Vacher, H. L. (1988), Dupuit-Ghyben-Herzberg analysis of strip-island lenses: *Geological Society of America Bulletin*, 100, 580-591.

Vacher, H. L. and Wallis, T. N. (1992), Comparative

hydrogeology of fresh-water lenses of  
Bermuda and Great Exuma Island,  
Bahamas. *Ground Water*, 30, 15-20.

blank page

# Chemical and isotopic compositions of groundwater obtained from the GSJ Hirabayashi well

Tsutomu Sato and Makoto Takahashi

*Geological Survey of Japan*

*Higashi 1-1-3, Tsukuba, Ibaraki 305-8567, Japan*

*sugar@gsj.go.jp*

**ABSTRACT** Chemical and isotopic compositions of groundwater obtained from the GSJ Hirabayashi well were analyzed. The well was constructed on the Nojima fault which moved at the time of the 1995 Kobe (Hyogo-ken nanbu) earthquake. Major cation and anion components of the groundwater are calcium and bicarbonate ions, respectively. The ionic characteristics is similar to that of local spring water in the northern part of Awaji Island. The isotopic characteristics is also similar to that of local meteoric water. The hydrogen and oxygen isotopic ratios indicate that the groundwater was recharged at the high altitude area of the island.

## Introduction

The Kobe (Hyogo-ken nanbu) earthquake occurred on January 17, 1995 with magnitude of M7.2 (Fig.1). At the northern part of Awaji Island, about 10 km long surface fault ruptures appeared along the Nojima fault (Awata et al., 1996).

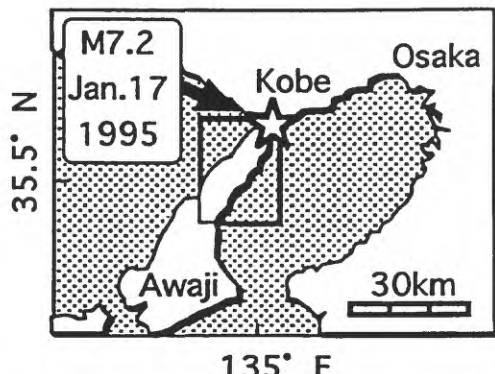


Fig.1 Location of Awaji Island. The 1995 Kobe (Hyogo-ken nanbu) earthquake occurred off the northern coast of the island on January 17, 1995.

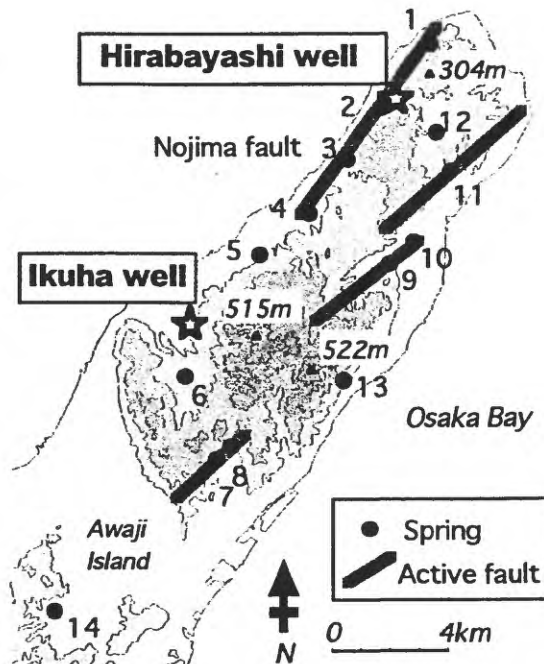


Fig.2 Location of the GSJ Hirabayashi and Ikuha wells. Local springs are also plotted by closed circles. An interval of the contour is 100 m.

Active fault drilling was performed at Nojima Hirabayashi by Geological Survey of Japan (GSJ) for the purpose of direct observation of physical and chemical processes operating in the fault zone (Ito et al., 1996). Groundwater was pumped up from the 747 m deep borehole, the Hirabayashi well (Fig.2). In this study, we analyzed chemical and isotopic compositions of the groundwater, and revealed the characteristics in comparison with local spring water and with groundwater obtained from the Ikuha well which was constructed for observation of crustal strain (Fig.2).

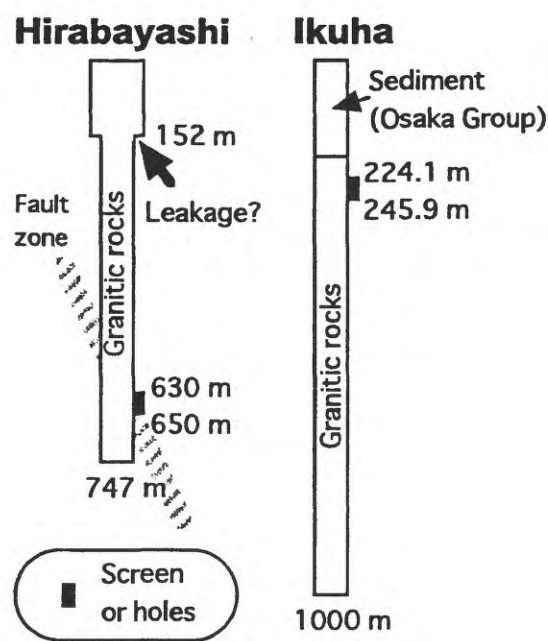


Fig.3 Structure of the GSJ Hirabayashi and Ikuha wells.

Table1 Chemical compositions of groundwater obtained from the GSJ Hirabayashi and Ikuha wells.

#### Samples

Groundwater of the both wells were obtained during pump test. A screen or holes of the wells are located at the depth from 630 m to 650 m at Hirabayashi and from 224.1 m to 245.9 m at Ikuha (Fig.3). However, there is a possible leakage of 152 m depth at Hirabayashi. Now we are checking the truth. In this study, we discussed our results in two cases that the leakage exists or not.

#### Temperature

Temperature of the Hirabayashi groundwater is lower than that of the Ikuha groundwater (Table1), which may indicate the depth of aquifer of the Hirabayashi groundwater is shallower than Ikuha. If the leakage exists, mixing ratio of the 152 m groundwater is thought to be very high. If no leakage, shallow groundwater might be sucked through the vertical fault zone tapping the borehole during pump test. In the latter case, the fault zone is thought to be permeable.

Table1

Well	Hirabayashi		Ikuha
	Sampling date	1996/4/4	1996/3/13
Temp.	°C	23.9	25.4
pH		7.8	8.6
E.C.	ms/m	60.3	60.5
HCO <sub>3</sub> <sup>-</sup>	mg/l	330	340
CO <sub>3</sub> <sup>2-</sup>	mg/l	<5	8.6
Cl <sup>-</sup>	mg/l	20.4	11.5
SO <sub>4</sub> <sup>2-</sup>	mg/l	5.1	1.3
NO <sub>3</sub> <sup>-</sup>	mg/l	<0.05	<0.05
F	mg/l	0.7	2.7
Br	mg/l	0.09	0.07
Li <sup>+</sup>	mg/l	<0.1	0
Na <sup>+</sup>	mg/l	36.2	124
K <sup>+</sup>	mg/l	4.7	1.1
Ca <sup>2+</sup>	mg/l	56.2	6.0
Mg <sup>2+</sup>	mg/l	20.0	3.6
Sr <sup>2+</sup>	mg/l	0.5	0.1
Mn <sup>2+</sup>	mg/l	0.16	0.07
Fe <sup>2+</sup>	mg/l	1.00	0.02
Fe <sup>3+</sup>	mg/l	0.94	0.37
CO <sub>2</sub>	mg/l	<0.001	<0.001
H <sub>2</sub> S	mg/l	<0.001	<0.001
H <sub>4</sub> SiO <sub>4</sub>	mg/l	57.2	23.4
HBO <sub>3</sub>	mg/l	1.20	3.80
HAsO <sub>4</sub> <sup>2-</sup>	mg/l	0.008	<0.001
Hg	mg/l	0.0003	<0.0002
Cd	mg/l	<0.005	<0.005
Pb	mg/l	<0.05	<0.05
Cr	mg/l	<0.01	<0.01
P	mg/l	0.01	<0.01
I	mg/l	<1	<1

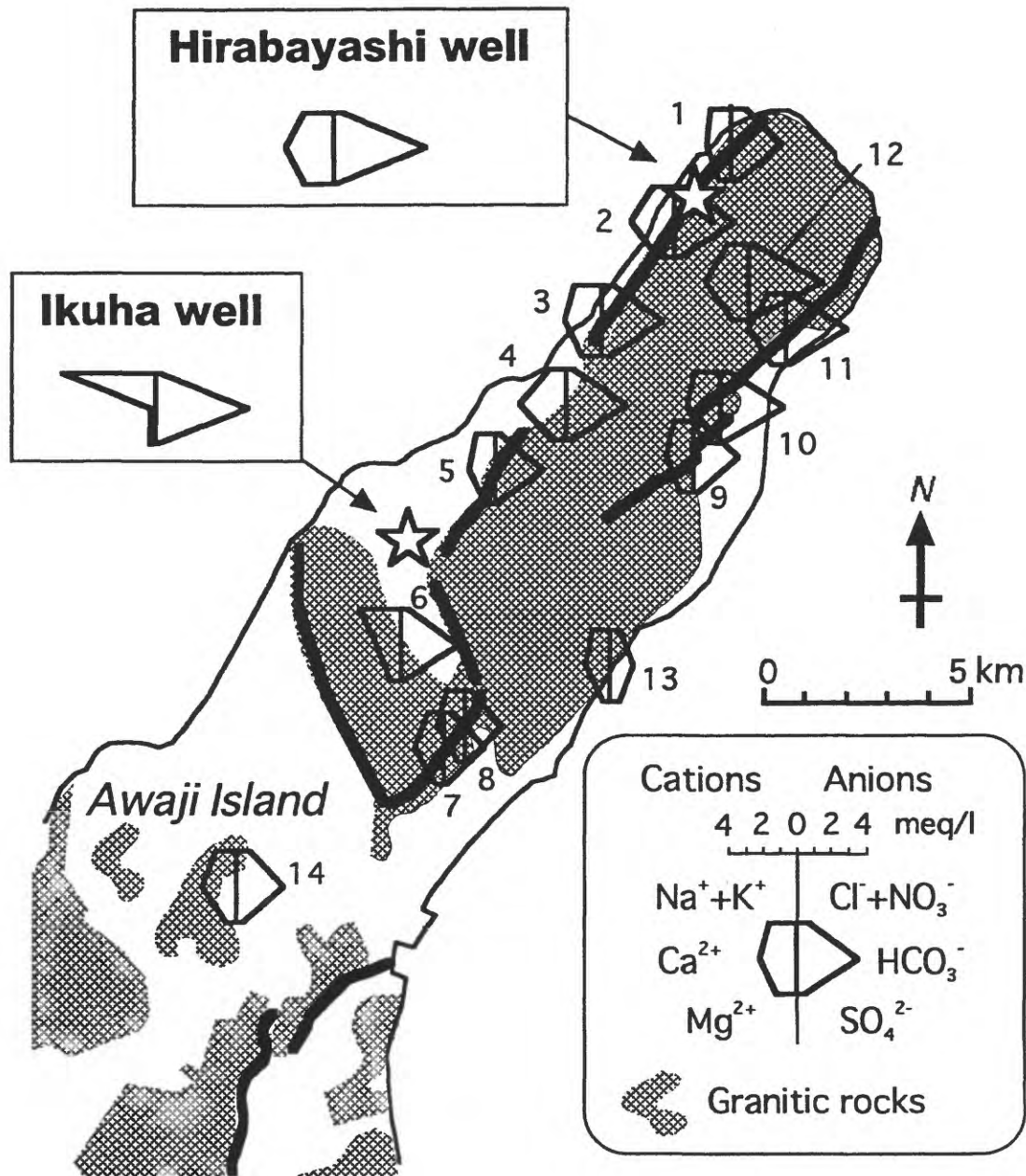


Fig.4 Stiff diagrams of groundwater obtained from the GSJ Hirabayashi and Ikuha wells in addition to local spring water. Analysis of major chemical compositions of local spring water was done by Sato and Takahashi (1997).

#### Chemical compositions

Concentrations of the major chemical compositions are shown in Fig. 4 as Stiff diagrams. Major cation and anion of the Hirabayashi groundwater are calcium and bicarbonate ions, respectively. Shape of the diagrams of the Hirabayashi groundwater is very similar to local spring water, which supports the

possibility that the Hirabayashi groundwater is shallow groundwater. Aquifer of the local spring water is estimated to be fractures in granitic rocks widely distributed at the northern part of Awaji Island (Sato and Takahashi, 1997). Similarly, aquifer of the Hirabayashi groundwater is thought to be located in the granitic rocks.

### Isotopic compositions

Isotopic compositions of the Hirabayashi and Ikuha groundwater are shown in Table 2. First, the hydrogen and oxygen isotopic ratios are same as the local meteoric water, because the both groundwater are plotted on the "meteoric water line" in Fig. 5. The meteoric water line was calculated by using isotopic data of local spring water (Sato et al., 1999). Thus, the Hirabayashi groundwater is thought to be the local groundwater and not stay for a long time on condition that water - rock interaction occurred.

Second, in the other stable isotopic compositions in Table 2, we can not detect remarkably different characteristics from local meteoric water. The helium isotopic ratio of the Hirabayashi groundwater is same as that of atmosphere.

Finally, the tritium concentrations of the both groundwater were lower than 1 TU (Table 2). Such low tritium concentration indicates that the groundwater was recharged before 1953 (Freeze and Cherry, 1979).

Table 2 Isotopic compositions of groundwater obtained from the GSJ Hirabayashi and Ikuha wells.

Well	Hirabayashi	Ikuha
Sampling date	1996/4/4	1996/3/13
$\delta D$ (SMOW)	‰	-50.0
$\delta^{18}\text{O}$ (SMOW)	‰	-7.9
$\delta^{13}\text{C}$ (PDB)	‰	-12.0
$\delta^{34}\text{S}$ (CDT)	‰	+8.9
$^{3}\text{He}/^{4}\text{He}$	$\times 10^{-6}$	$1.40 \pm 0.05$
$^{3}\text{H}$	TU	<1

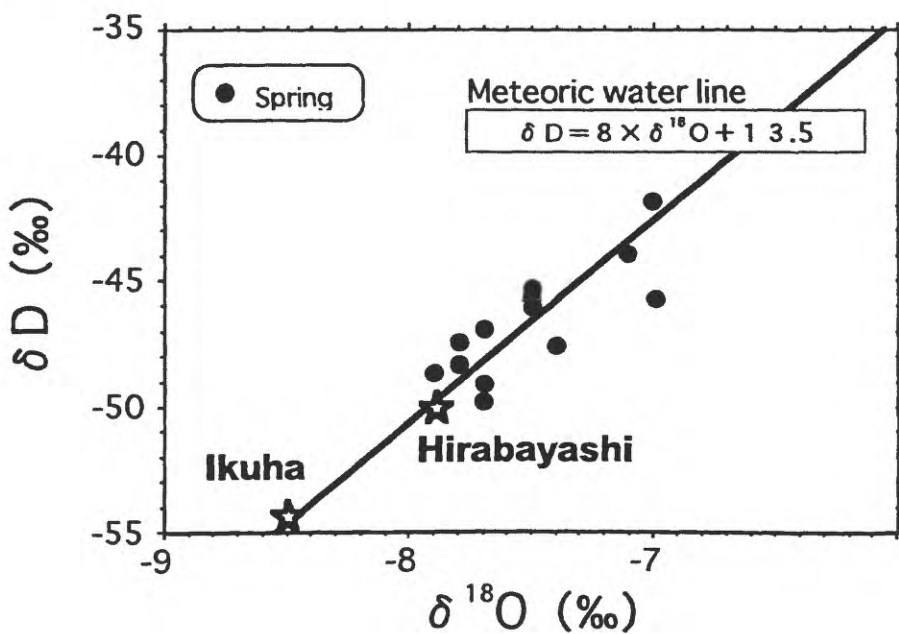


Fig.5  $\delta D$ - $\delta^{18}\text{O}$  diagram of groundwater obtained from the Hirabayashi and Ikuha wells. Data of local spring water are from Sato et al. (1999). The meteoric water line was calculated by using data of the local spring water.

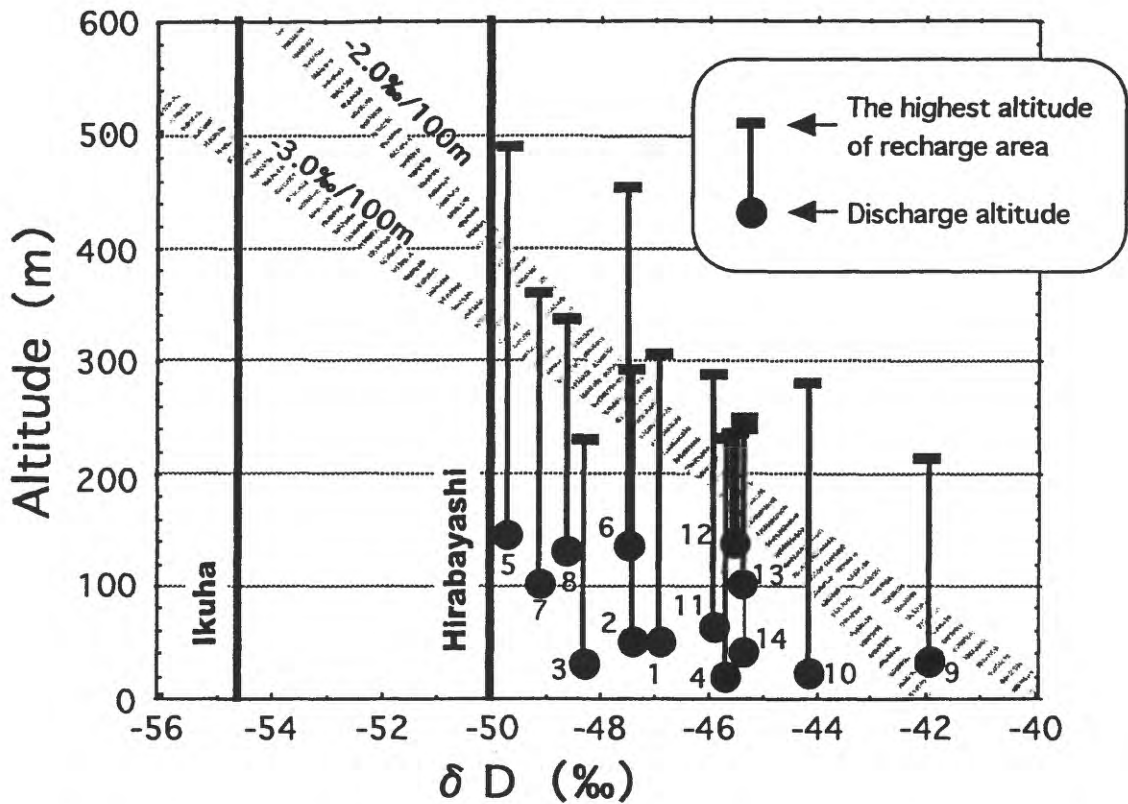


Fig.6 Altitude -  $\delta$  D diagram of local spring water (Sato et al., 1999). Dotted lines show groundwater recharge lines with the slopes of  $-2.0\text{ ‰} / 100\text{ m}$  and  $-3.0\text{ ‰} / 100\text{ m}$ .

#### Estimation of the recharge altitude

Fig.6 shows the groundwater recharge lines estimated by using data of local spring water (Sato et al., 1999). If the larger slope of  $-3.0\text{ ‰} / 100\text{ m}$  is chosen, the recharge altitude of the Hirabayashi and Ikuha groundwater are estimated at about 350 m and 500 m, respectively. These altitudes are almost same as that of top of mountains near each well. Therefore, the both groundwater are thought to be recharged at high altitude area of the island.

#### Discussion

In this section, we discuss the characteristics of the Hirabayashi groundwater using Fig. 7. First, the recharge altitude of the groundwater was estimated at high altitude area by hydrogen and oxygen isotopic data. The period of the groundwater flow may be over 40 years because of the low tritium concentration.

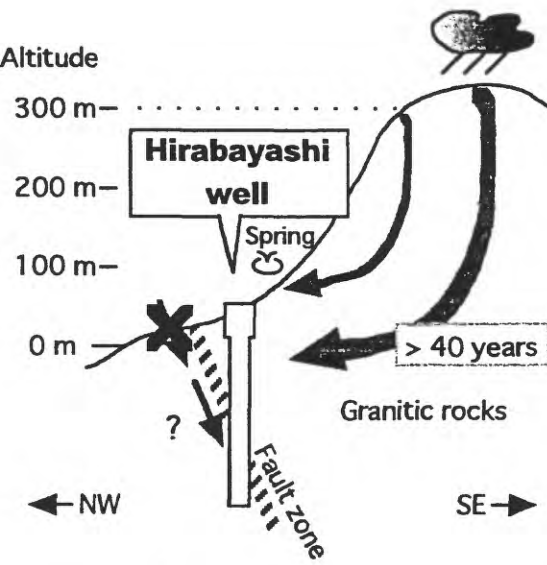


Fig.7 Schematic diagram of the groundwater flow at Hirabayashi.

Flow path of the groundwater is thought to be located in granitic rocks based on local geology and major chemical compositions. Second, the depth of aquifer of groundwater obtained from the Hirabayashi well may be shallower than that of screen of Ikuha (224.1 m) because of lower temperature than Ikuha. If the leakage exists at 152 m depth, the most part of the Hirabayashi groundwater may be groundwater coming from the leakage. If no leakage, shallow groundwater might be sucked by pump test through the fault zone of the Nojima fault.

#### Reference

Awata, Y., Mizuno, K., Sugiyama, Y., Imura R., Shimokawa, K., Okumura, K. and Tsukuda, E., 1996, Surface fault ruptures on the northwest coast of Awaji Island associated with the Hyogo-ken nanbu earthquake of 1995, Japan, *J. Seismol. Soc. Japan*, 2nd series, **49**, No.1, 113-124. (in Japanese with English abstract).

Freeze, R. and Cherry, J., 1979, *Groundwater*, Prentice Hall, New Jersey, p136.

Ito, H., Kuwahara, Y., Miyazaki, T., Nishizawa, O., Kiguchi, T., Fujimoto, K., Ohtani, T., Tanaka, H., Higuchi, T., Agar, S., Brie, A. and Yamamoto, H., 1996, Structure and physical properties of the Nojima fault by the active fault drilling, *Butsuri-tansa*, **49**, 522-535 (in Japanese with English abstract).

Sato, T. and Takahashi, M., 1997, Geochemical changes in anomalously discharged groundwater in Awaji Island -after the 1995 Kobe earthquake-, *Chikyukagaku*, **31**, 89-98 (in Japanese with English abstract).

Sato, T., Sakai, R., Ōsawa, H., Furuya, K. and Kodama, T., 1999, Oxygen and Hydrogen isotopic ratios of the anomalously discharged groundwater after the 1995 Kobe earthquake in Awaji Island, Japan, *J. Japanese Assoc. Hydrol. Sci.*, **29**, 113-24 (in Japanese with English abstract).

# DEEP SURFACE-WATER FLOW NEAR THE NOJIMA EARTHQUAKE FAULT

Shinichi UDA 1\*, Aiming LIN 2\*, Keiji TAKEMURA 3\*

1\*Earthquak Reserch Institute, University of Tokyo, Bunkkyoku, Tokyo, 113-0032, Japan

2\*Faculty of Science, Kobe University, Nadaku, Kobe, 657-8501, Japan

3\*Graduate school of Science, Kyoto University, Sakyouku, Kyoto, 606-8502, Japan

**ABSTRACT** The Nojima earthquake fault for the Southern- Hyogo Prefecture Earthquake runs almost parallel to the northwest coastline of Awaji Island. It is several hundred meters inside from the coast, stretching from northeast to southwest. The cores were taken from the 1800m University drilling hole at Ogura to survey the fault, in which were recognized to the bottom of the hole many weathered cracks. Several of unconsolidated brown clay veins which filled opening cracks were also recognized. In 747m and 1839m cores taken by Geological Survey of Japan ,and National Reserch Institute for Earth Science and Disaster Prevention respectively at Hirabayashi ,consolidated brown colored veins are also recognized. As a result of the X-ray powder diffraction these clays are composed of clay minerals and carbonates such as siderite and calcite. Thin sections of consolidated veins clarified that these veins are composed of carbonate materials. The top of the University drilling hole was about 45m above the sea level, therefore most of the core was far below from the stable groundwater table. Then these phenomena are very rare. We think that the cause of these cracks and clay veins was the rapid flowing- in of groundwater near the ground surface along well cracked zone near the Nojima fault fractured zone before and after the earthquake, and that the consolidated veins are formed from injected clay veins above mentioned. These phenomena suggests the process of recovery of impermeability and strength of the fractured zone.

key words: crack-filling clay, weathered crack, consolidated carbonate vein, groundwater fluctuation, carbonate, Nojima earthquake fault, Southern-Hyogo Prefecture Earthquake (Hyogoken Nanbu Earthquake), drilling core

## INTRODUCTION

Usually there are cracks in the hard rock mass whether they are many of a few. Near the surface of the ground, the rock mass becomes loose, these cracks open, and groundwater easily comes

into these cracks. It is well-known that there exists a weathered zone in the underground from the surface to some depth, usually from a dozen meters deep to several tens meters deep. Deeper than this zone, weathering becomes less and less and at last the rock mass becomes fresh. But the drilling cores of the 1800m university hole ,GSJ and NIED hole dose not show the ordinary appearance. There are many weathered cracks and crack-filling clays and consolidated carbonate veins. We would like to examine these phenomena and fathom their causes.

#### DRILLING SITE AND GROUNDWATER LEVEL

The Nojima earthquake fault runs almost parallel to the northwest coastline of Awaji Island. It is several hundred meters inside from the coast, stretching from northeast to southwest (Lin and Uda 1996). The 1800m University drilling hole at Ogura is drilled almost vertically till the depth of 800m and below this depth dipping about 75° (from the horizontal), directing to the northwest to make the right angle with the fault. The distance of the bore hole bottom from the seacoast is about 550m. Usually at a place near the sea like this site, the groundwater level is higher than the sea water level. The elevation of the groundwater table of this hole is 5.8m from the hole top.

#### GROUNDWATER FLUCTUATION AFTER THE EARTHQUAKE

As for the groundwater fluctuation at Awaji Island immediately after the earthquake, many discharges of groundwater near the Nojima fault and at many places in Awaji Island are reported by Touda (1995). These discharges dried up 4 months later and that the ground water level of wells also lower down compared with the level before the earthquake at Nuruyu district, northern Awaji(The Japan Society of engineering Geology Edited(1996). Osada(1997) reports that the water level of irrigation ponds in the Kobe Group and the Osaka Group distributing areas was restored, while the water level of the irrigation ponds in the granite areas is not restored even 2 years after the earthquake. As a reason for this difference he says there occurred some change inside of the granite area which include the Nojima fault.

#### WEATHERING OF THE CRACKS

We observed all of the cores of university hole. All the rock mass was relatively solid except in the fractured zone. Many of the cracks were reddish brown in color through oxidization (Fig. 1). It is surprising to see many of oxidized cracks at this depth far below the groundwater table. The angles of these cracks are various from high to low. There is not any particular angle which is

peculiarly oxidized. Because the bore hole is almost vertical, the chance to come across a high-angled crack (from the core axis) is bigger than to come across a low-angled crack. Therefore we can not say definitely whether there is a relationship between the oxidization and the crack angle. The directions of the cracks are unclear, because they are in the drilling core.

#### WEATHERING CONDITION OF THE CRACKS IN THE ORDINARY ROCK

Usually there are cracks in the hard rock mass whether they are many or a few. Near the surface of the ground, the rock mass becomes loose, these cracks open, and groundwater easily comes into these cracks. It is well-known that there exists a weathered zone in the underground from the surface to some depth, usually from a dozen meters deep to several tens meters deep. Deeper than this zone, weathering becomes less and less and at last the rock mass becomes fresh and many of the cracks are closed. Permeability is also high in the weathered zone and small in the fresh zone. Rock itself is impermeable, so permeability here means the permeability of the cracks. The level of the groundwater is logically decided by the balance between the flow-in and flow-out of the groundwater, but generally it is often placed about the borderline between the weathered zone and the fresh zone. The groundwater level is almost always tilted and the water is flowing from the high potential to the lower potential. With this flow of the groundwater containing rich O<sub>2</sub>, cracks are oxidized. Deep in the underground, however, the groundwater flow is slow and the oxidized cracks are fewer. For example, in the 1000m deep core, which was drilled by Geological Survey of Japan at Inagawa-machi, Hyogo Prefecture, none of the cracks were oxidized (Fig.2).

#### UNCOSOLIDATED BROWN CLAY (CRACK-FILLING CLAY)

We have already said in Section WEATHERING OF THE CRACKS that the cracks of the 1800m University hole were highly oxidized. Inside of these oxidized cracks we often found out unconsolidated clays sticking to the surface of the cracks. These clays are of high water content and their color was from yellowish brown to reddish brown. The clays we found out were very fine that we scarcely felt the grain between our fingers, and it was quite similar to the filling clay which fills the opening cracks in loosened rock mass near the ground surface which is often found in the inspection adits of damsites. Filling clay here means the clay which flows in from outside as was suggested by Tsunoda, Miyakoshi and Ogata (1979). They describes the characteristics of it as follows:

Grain size is very small (50% grain size is less than 20  $\mu$ m).

It contains minerals which do not exist in the host rock .

It has a close relationship with the loosening of the rock .

Naked eye can easily discern it from its grain size, color and water content.

It works as an indicator to show the high permeability of the rock.

In addition to these characteristics, Wakizaka, et al.(1997), Wakizaka,et al.(1998) give us other characteristics as below (many of the samples in these reports are taken from several tens meters deep from the ground surface):

It contains more of  $Fe_2O_3$  compared with the clay of other origins.

Weathered origin, such as halloysite, gibbsite and goethite are seen.

The rate of amorphous content is high.

Brownish color is one of the characteristic indicator to discriminate from other origin.

We use the term of crack-filling clay in the same meaning as that defined by Tsunoda et al.(1979) and Wakizak et al.(1998).The width of the clay veins we see in the university core is almost all less than a few millimeters. Most of the host rocks these clay veins are hosted are hard and are not softend through hydrothermal alteration. We took three samples of clay from comparatively wide clay veins and made analysis of them with X-ray powder diffraction. The depths of the samples are 1320.80m, 1323.60m and 1665.15m. The 1320.80m sample was from a caly vein which was 1-2mm wide, in a hard host rock and was 70° from the boring axis(Fig. 3a). The 1323.60m sample clay was soft and of high water content The clay clung into a crack of 40° from the drilling axis, and it still kept a tip of its host rock. This clay seemed to be the thickest and the most typical crack-filling clay in the whole bore hole(Fig. 3b). The 1665.15m clay was 3mm wide, caught in a crack at the angle of 30° from the drilling axis. The lower part of its host rock was hard but the upper part was soft and white (Fig.3c). In order to make comparisons, we made the same analysis on the fault gouges (Hirabayashi outcrop and 388.42m deep gouge in the 500m University hole), and also on the host rock (1545.60m deep in the 1800m University hole). The drilling mud is also analyzed in order to eliminate the influence to the clays.

The result is in the Fig.4. The figure shows that the difference between the fault gouges and the host rock lies whether biolite is contained or not. But there is a big difference of the components between the fault gouges and the crack-filling clays. Crack-filling clays are of carbonates, such as calcite ( $CaCO_3$ ) and siderite ( $FeCO_3$ ), and of montmorillonite, quartz, feldspar. Especially the 1320m and the 1665m clays are composed of almost the same components. The 1323m clay contains more of calcite than the other two. The drilling mud consists mainly of quartz ,montmorillonite and calcite. Therefore some of montmorillonite in the crack-filling clay and fault

gouges may come from the drilling mud. But montmorillonite is also observed in the sample from Hirabayashi outcrop where is not affected by the drilling mud. The content of calcite in the drilling mud is so small that influence to the crack-filling clays is negligible. When we consider the characteristics we examined before in this section, these three samples of crack-filling clay may be said to contain more of carbonates than the typical crack-filling clay. The crack-filling clay distributed near the ground surface has generally high content of  $Fe_2O_3$  in rich  $O_2$  environment (Wakizaka et al. 1997, 1998). On the other hand, siderite can be formed from  $Fe_2O_3$  in the water which contains  $CO_2$  under the condition of low Eh(oxidation potential) (Garrels and Christ 1965). Sato and Takahashi (1997) report that chemical composition of deep well water at Hrabayashi of GSJ is composed of high content of  $HCO_3^-$ . Arai, Okusawa and Tsukahara (1998) also report high content of  $CO_2$  in the drilling core of the 1800m university hole and high content of  $H_2$  in lower part. Therefore the condition is satisfied. Then crack-filling clay appears as  $Fe_2O_3$  in shallow zone where  $O_2$  is rich, however, appears as siderite ( $FeCO_3$ ) in deep zone where  $CO_2$  is rich and poor in  $O_2$ .

#### CONSOLIDATED CARBONATE VEIN

In the cores taken by GSJ and NIED at Hirabayashi many consolidated hard veins are recognized. Some veins make no discontinuity in the cores (Fig. 5 a, b), tightly connect the host rock. Some veins make discontinuity (Fig. 5 c). Other veins have sometimes cavities, which diameter are about 10–15mm (Fig. 5 d, e). Thin sections of these veins clarified that these are composed of carbonate materials (Fig. 6 a, b). These carbonate veins are considered to be formed from unconsolidated clay veins above mentioned.

#### FLOWING-IN MODEL OF THE GROUNDWATER AND PROCESS OF RECOVERING THE IMPERMEABILITY AND STRENGTH OF FRACTURED ZONE

In former Sections we checked the characteristics of weathered cracks, the distribution of crack-filling clays and consolidated hard carbonate veins. On the basis of these, here we can say almost certainly that the groundwater which had been near the earth surface came down rapidly onto this level along the cracks near the Nojima fault. If the velocity is slow  $O_2$  in the water should have been consumed during the infiltration to deep zone. Arai, Okusawa and Tsukahara (1998) describe that origin of C is from the surface of the ground. But this phenomenon — the ground water flowing down far deeper than the stable ground water table — is rare as we said in the former Section. The difference of potential is necessary. For that deeper flow, following models

are possible.

- 1) Far below the bore hole of our sampling, many new cracks had generated and flows of groundwater occurred in order to fill these cracks before or simultaneously earthquake.
- 2) The rock mass both near and below the bore hole had been saturated. When the great earthquake occurred, groundwater flew up to or near the ground surface. The rock mass became unsaturated and new groundwater came down from the ground surface to saturate the rock mass.
- 3) Model 1) and model 2) occurred simultaneously.

With the data we have at present, we can not decide which model is the most appropriate. As for the model 2), however, there is scarcely any doubt about it as we said in former Section. After the flow-in of the groundwater, crack-filling clays consolidate and seal the cracks. These sealed cracks should have contributed to recover the impermeability and strength of rock.

As carbonate materials are discovered in the fault gouges (Fujimoto et al. 1998), the possibility which they contribute also to recover the impermeability and strength of fault fractured zone is suggested.

#### ACKNOWLEDGEMENT

We thank Professor Masataka Ando and Toshihiko Shimamoto of Kyoto University for their encouragement throughout this study, and Dr. Hidemi Tanaka of Ehime University and Dr. Masahiro Taniguchi of Geological Survey of Japan for their discussion in the powder X-ray diffraction analysis. Thanks are also due to Dr. Shun-ichi Nakai of Earthquake Research Institute, University of Tokyo for his assisting in the Eh-Ph diagram analysis. This work was partially supported by the Science Research Project (No.09640544) of the Ministry of Education and Culture of Japan.

## REFERENCES

ARAI T., OKUSAWA T. & TSUKAHARA H. 1998. Variation with depth in chemical composition and carbon isotope ratio of gas extracted from drilling cores.  
*GekkanChikyu* 21, 165-170.\*\*

FUJIMOTO K., OHTANI T., TANAKA H., HIGUCHI T., TOMIDA N., ITOH H., AGAR M. S., 1998  
Characteristics of fault fractured zone immedeately after the earthquake  
*GekkanChikyu* 21, 149-153.\*\*

GARRELS R. M. & CHRIST C. L. 1965. Solutions, Minerals, and Equilibria.  
*Harper & Row, New York*, pp. 450.

JAPAN SOCIETY OF ENGINEERING GEOLOGY (edited), 1996 Groundwater fluctuationcaused by the earthquake.  
*Journal of Japan Society of Engeering Geology* 37, 351-358.

LIN A. & UDA S. 1996. Morphological characteristics of the earthquake surface ruptures on Awaji Island, associated with the 1995 Southern Hyogo Prefecture Earthquake. *The Island Arc* 5, 1-15.

OSADA T., TOKUNAGA T., ISHIBASHI H. & KAYAKI T. 1997. Groundwater fluctuations in the northern part of Awaji Island after Hyogoken-Nanbu Earthquake. *Annual meeting Proceedings, Japan Society of Engineering Geology* 237-240. \*

SATO T. & TAKAHASHI M. 1997. Geochemical changes in anomalously discharged groundwater in Awaji Island after the 1995 Kobe earthquake.  
*Chikyukagaku(Geochemistry)* 31, 89-98. \*

SCHOLZ C. H. 1990. The mechanics of earthquake faulting.  
*Cambridge University Press*, pp.438.

TOUDA S., TANAKA K., CHIGIRA M., MIYAKAWA K. & HASEGAWA T. 1995  
Coseismic behavior of groundwater by the 1995 Hyogo-ken Nanbu Earthquake. *Zisin, Journal of the Seismological Society of Japan* 48, 547-553. \*\*

TSUNODA T., MIYAKOSHI K. & OGATA M. 1979. Crack-filling clay in fault fractured zone. *Annual meeting Proceedings, Japan Society of Engineering Geology* 56-59. \*\*

WAKIZAKA Y., OHARA M., TAKAHASHI T., HARADA M. 1997 What is so-called "Ryunyu-nendo(clay)" *Abstract the 104 th Annual meeting of the Geological society of Japan* 294.\*\*

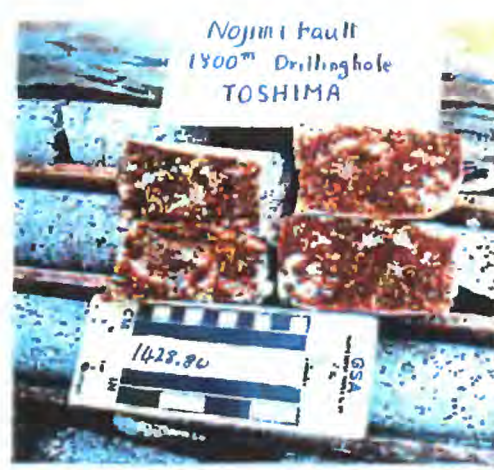
WAKIZAKA Y., OHARA M., TAKAHASHI T., HURUICHI H., HARADA M.  
TANAKA M. 1998. MineralogIcal and chemical properties of clays for discrimination of weak zone type. *Proceedings of 8th International IAEG Congressa* 359-367

\* in Japanese with English abstract

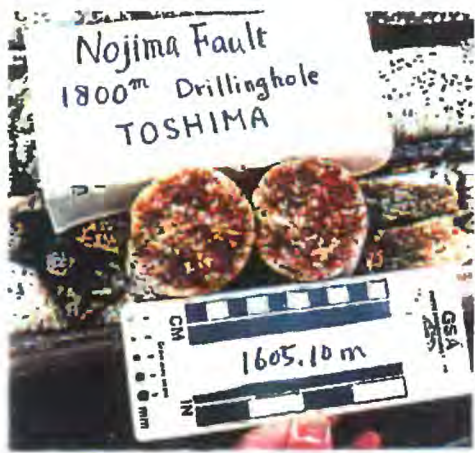
\*\* in Japanese



a)



b)



c)

Figure 1. Photographs showing the occurrence of the brown-colored weathered cracks found in the Ogura 1800m cores.

- a) The depth is 1317-1322m.
- b) 1428.8m
- c) 1605.1m

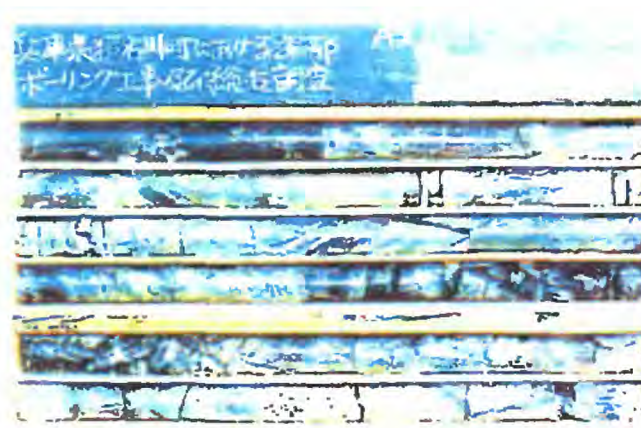


Figure 2. Photograph showing the occurrence of the cracks in the ordinary rock. Cracks are not oxidized. This core was taken by GSJ at Inagawamachi Hyougo Pref. The depth is 960m



a)



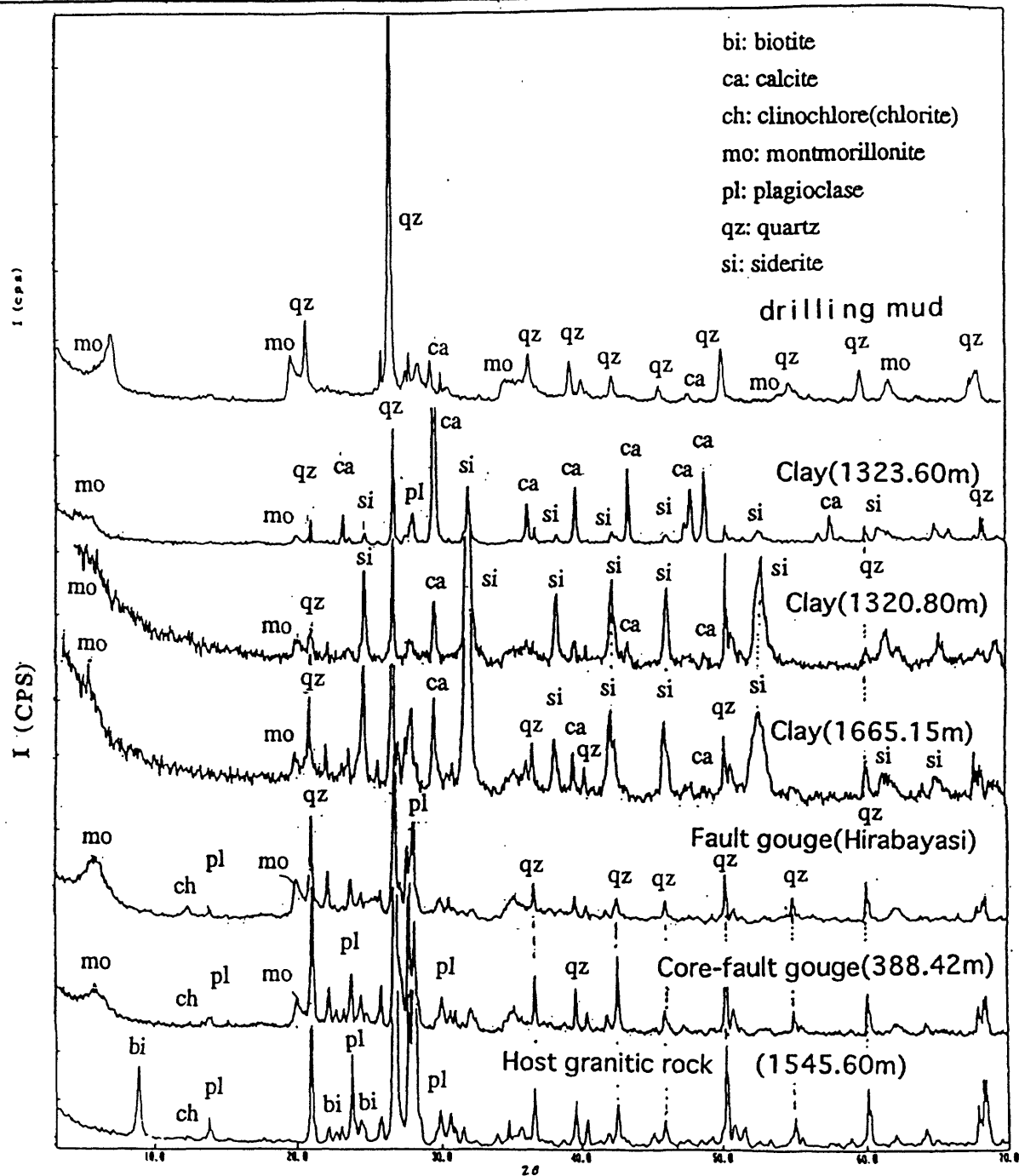
b)



c)

Figure 3. Photographs showing the occurrence of the crack-filling clays found in the Ogura 1800m cores.

- a) Weathered opening crack filled by unconsolidated clay. This figure shows the feature after removing the clay, but at the left end of the core crack-filling clay is observed. Note no shear textures can be found in the granitic rock at both sides of the crack.
- b)&c) Crack-filling clay deposited in the opening cracks at the depth of 1323.6m(b) and 1665.1m(c). The crack-filling clay contains high water content, which is unconsolidated in the fresh cores. Note some pieces of the host rock stick to the crack-filling clay(b). The crack-filling clay which is brown filled oblique crack. The width of the clay is 3mm(c).

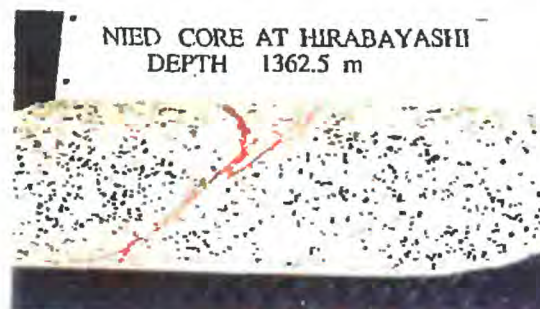


Sample	Nojima-core-132080	File name	tempd/Nc132080	[1]:Smooth	Original [0]:Raw
X-ray generator	: 30k	Divergence Slit	: 1.00	deg	Smoothing
Target	: 1.54050 Å (Cu)	Scattering Slit	: 1.00	deg	Peak Search
Monochromator	: use	Receiving Slit	: 0.15	mm	Data points : 5
KV	: 40.0 KV	Attachment	: no use		Threshold : 2.00
mA	: 20.0 mA	Rotating Speed			Background subtraction
Sampling Width	: 0.020 deg				Operator
Scanning Speed	: 2.000 deg/min				Data points : 0
					Repeating time: 0
					Measuring Date : 97. 9. 7 17:54:46
					Operating Date : 97. 9. 7 18:33:37
		Comment	:		

Figure 4. Powder X-ray diffraction spectra of the crack-filling clay samples taken from the 1800 m cores and fault gouges taken from the 500 m cores and the outcrop at Hirabayashi. Drilling mud is also analysed. The crack-filling clays differ from fault gouges and are characterized by carbonate materials such as calcite and siderite.



a)



b)



c)

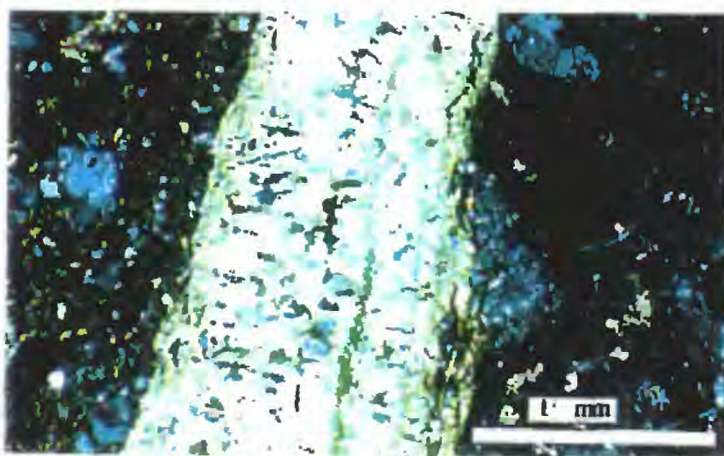


d)

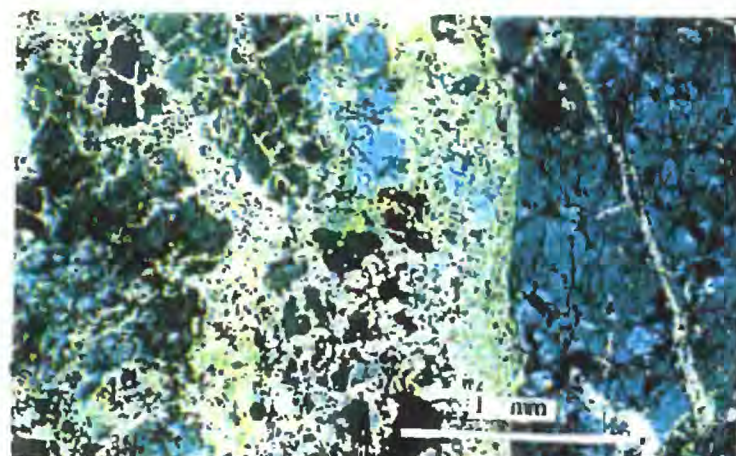


e)

Figure 5. Photographs showing the occurrence of the consolidated carbonate veins. a) Hard 1-2mm width vein. b) Hard vein connecting tightly host rock taken by NIED at Hirabayashi. c) Consolidated hard carbonate vein forming the sharp discontinuity. d),e) Cavities in the consolidated carbonate veins. Diameter of the cavities is 10-15mm.



a)



b)

Figure 6. Photographs showing the thin sections of the consolidated carbonate veins. a) The same sample as Fig.5a). Coarse grained calcite crystals grow from the wall, and very fine grained siderite crystals fill up the space(crossed polarizers). b) The same sample as Fig.5c). Fine grained calcite and siderite crystals fill up the space(crossed polarizers).

# Thermal history analysis of the Nojima fault borehole samples by fission-track thermochronology

Takahiro Tagami<sup>1</sup>, Masaki Murakami<sup>1</sup>, Noriko Hasebe<sup>2</sup>, Hidenori Kamohara<sup>2</sup> and Keiji Takemura<sup>1</sup>

<sup>1</sup>Div. Earth Planet. Sci., Grad. Sch. Sci., Kyoto Univ., Kyoto 606-8502, Japan,

*ttagami@ip.media.kyoto-u.ac.jp*; <sup>2</sup>Dept. Earth Sci., Faculty Sci., Kanazawa Univ., Kanazawa 920-1192, Japan.

## ABSTRACT

To better understand the heat generation and transfer along earthquake fault, this paper presents preliminary zircon fission-track (FT) length data from Nojima fault, Awaji-shima Island, Japan, which was activated during the 1995 Kobe earthquake (Hyogo-ken Nanbu earthquake). Samples were collected from Cretaceous granitic rocks at depths using the Ogura 500 m borehole and Geological Survey of Japan (GSJ) borehole, as well as at outcrops nearby the boring sites. The Nojima fault plane was drilled at 389.4 m depth (along-core apparent depth) for Ogura and at about 625 m for GSJ. For Ogura samples, FT lengths in zircons from localities >60 m away from the fault plane as well as those from outcrops are characterized by the mean values of ~10-11  $\mu\text{m}$  and unimodal distributions with positive skewness, showing no signs of appreciable reduction of FT length. In contrast, those from nearby the fault at depths show significantly reduced mean of ~7-8  $\mu\text{m}$  and distributions having a peak around 6-7  $\mu\text{m}$  with rather negative skewness. A similar trend was observed for GSJ samples, in which the peak around 6-7  $\mu\text{m}$  is less dominant however. In conjunction with other geological constraints, these results are best interpreted by the recent thermal anomaly around the fault, which is attributable to the frictional heating of fault motion and/or heat transfer via fluids from the deep interior of the crust.

## INTRODUCTION

Quantitative assessment of heat generation and transfer along earthquake fault is of primary importance in understanding the dynamics and geohistory of faulting, as well as in constraining the heat budget and thermo-tectonic evolution of mobile belts. Although the laboratory rock deformation experiments predict general occurrences of frictional heating in fault motions, the magnitude and extent of the resultant heating in nature has been a subject of long controversy concerned with the assessment of shear stresses on faults (e.g., Hanks & Raleigh 1980; Scholz 1996), due primarily to (a) lack of clear heat-flow anomaly near the San Andreas fault (Brune et al. 1969) and (b) rare occurrence of pseudotachylite along geological faults, the existence of which suggests substantial heat generation (Sibson 1975). Heat

transfer processes around a fault zone may, however, be complex involving fluid flow, which can disperse the generated heat rapidly and may obscure the expected local thermal anomaly (O'Neil & Hanks 1980).

One of useful approach to tackle this problem is the thermal history analysis using radiometric dating methods. In fact, apparent age reduction towards a fault was found for the Alpine fault, New Zealand (Scholz 1979), and Median Tectonic Line, SW Japan (Tagami et al. 1988b), and those patterns were initially interpreted by frictional heating and resultant temperature increase that caused the age resetting. Such observed age reduction, however, is two-dimensional and thus allows alternative interpretations. New data set from the Alpine fault were reinterpreted by the recent differential uplift giving young cooling ages (Kamp et al. 1989). To reduce such ambiguity in data interpretation, thermochronologic analysis is needed using a well-documented vertical section across a fault.

This paper reports preliminary zircon fission-track (FT) length data from the Ogura 500 m and Geological Survey of Japan (GSJ) boreholes in addition to the outcrops near the boring sites. The boreholes intersect at different depths the Nojima fault, Awaji-shima Island, Japan, which was activated during the 1995 Kobe earthquake (Figure 1). The observed track length distributions near the fault suggests the existence of recent thermal anomaly around the fault, which is attributable to frictional heating of fault motion and/or heat transfer via fluids from the deep interior of the crust.

## SAMPLE AND EXPERIMENTAL OUTLINES

Following geological outlines for the Ogura site are after Murata et al. (1999). The Ogura 500m borehole primarily comprises in the descending order: (1) sands and gravels (0 - 118.0 m; apparent depth along the core), correlative to the Plio-Pleistocene Osaka Group, (2) arkose sandstones and silty sandstones (118.0 - 191.6 m), correlative to the Miocene Kobe Group and (3) granitic rocks (191.6 - 389.4 m), consisting mainly of granodiorite, correlative to the Cretaceous Ryoke Granitic Rocks, cropping out widely on the eastern side of the Nojima fault.

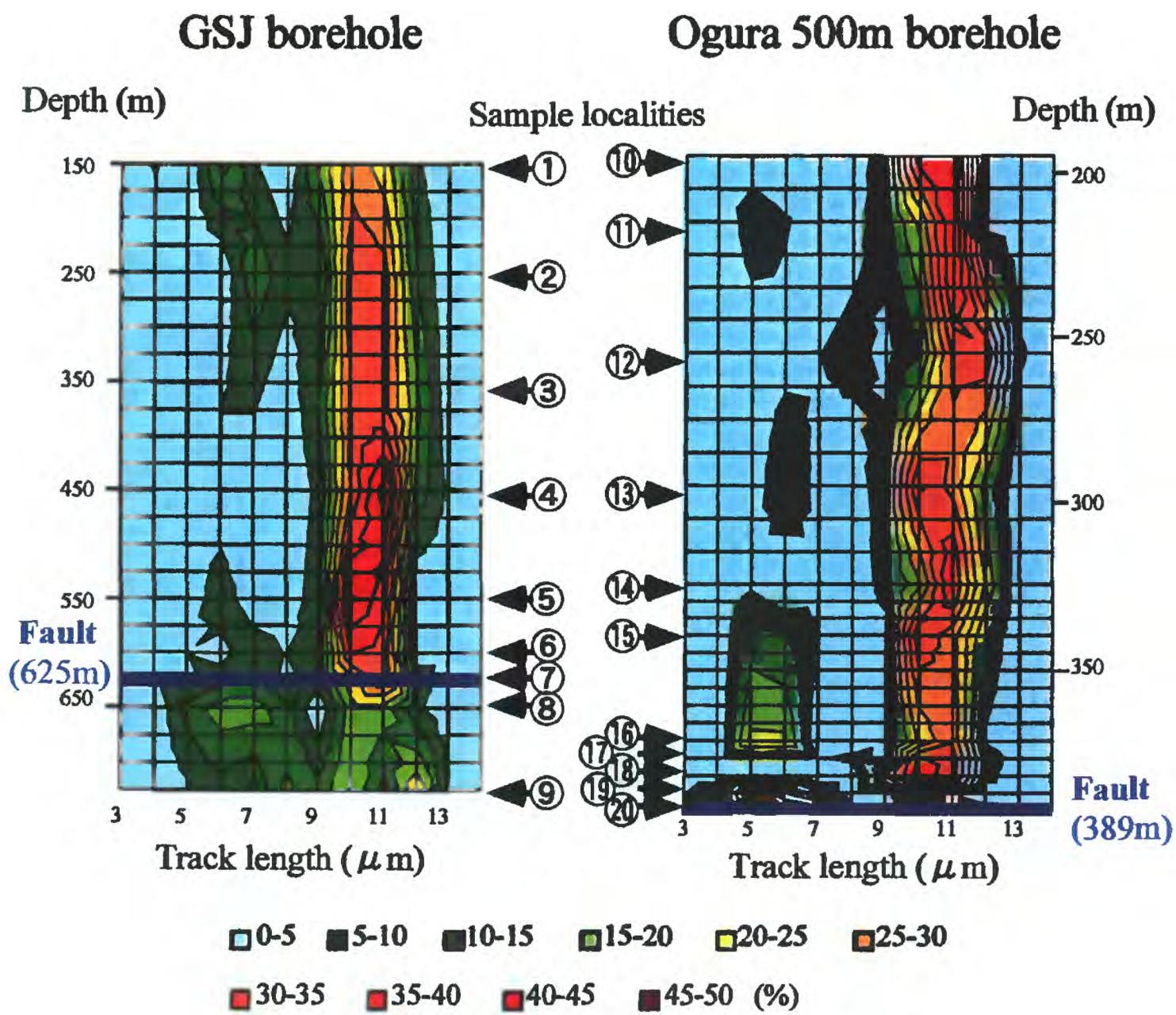


**Fig. 1** Relative frequency distribution of fission track lengths in zircon

### Sample localities:

### GSJ borehole

①GSJ-TH01 ②23 ③47 ④64 ⑤84 ⑥93 ⑦99

⑧103 ⑨119

### 500m borehole

⑩NFS1-FTG01 ⑪02 ⑫04 ⑬06 ⑭19 ⑮08

¶11 ¶12 ¶13 ¶14 ¶16, 17

These sequence is observed again beneath the fault at 389.4 m depth: sands and gravels (389.4 - 410.7 m), arkose sandstones and silty sandstones (410.7 - 494.2 m), and granitic rocks (494.2 - 550.7 m). Boundaries between the Osaka Group and Kobe Group (118.0 m and 410.7 m) as well as those between the Kobe Group and the Ryoke Granitic Rocks (191.6 m and 494.2 m) are considered to be unconformable.

All samples used for analysis were collected from granitic rocks. For comparison, samples were also taken from two surface outcrops of granitic rocks; one adjacent (<30 cm) to the Nojima fault ("branched fault") nearby the boring site (NFL02) and the other 30 m away to the southeast of the fault (NFL03).

Samples collected from the GSJ borehole (Ito et al., 1996; Tanaka et al., 1999) were granitic rocks throughout. As for the case of the Ogura 500m borehole, a sample was also taken from a surface outcrop of the granitic rock adjacent (<30 cm) to the Nojima fault nearby the boring site (NF-HB1).

Zircon and apatite crystals were separated using conventional mineral separation procedures. Zircon mounts were etched in KOH-NaOH eutectic etchant at  $250^{\circ} \pm 1^{\circ}\text{C}$  for about 13 hours. Under this condition, the maximum widths of surface tracks reached  $2.0 \pm 0.5 \mu\text{m}$  in most grains of the samples (for this etching criterion, see Yamada et al. 1995a). Track lengths and angles to the c axis were analyzed on horizontal confined tracks (Laslett et al. 1982) revealed both as tracks in tracks (TINTs: Lal et al. 1969) and as tracks in cleavages (TINCLES). Tracks with widths of  $1.0 \pm 0.5 \mu\text{m}$  were selected for measurement to reduce the influences of different etching states on measured lengths (Yamada et al. 1993, 1995a). In the second-series of analyses (i.e., all GSJ samples and three Ogura borehole samples NF51-FTG12, NF51-FTG13 and NF52-FTG01), samples were repolished to reduce the optical perturbation by surface tracks. This facilitated the observation of confined tracks at the interior of crystals and thus improved the efficiency of measurement.

Apatite mounts prior to etching were irradiated by  $^{58}\text{Ni}$  ion using a tandem van de Graaff accelerator (Watanabe et al. 1991; see also Yamada et al. 1998) to increase artificially number of host tracks (i.e., tracks that cut the etched mineral surface and accordingly give a pathway of etchant to TINTs) because spontaneous track densities in the samples were expected to be generally too low to measure sufficient number of confined tracks. The apatite samples were etched in 0.6%  $\text{HNO}_3$  at  $32.5^{\circ} \pm 0.5^{\circ}\text{C}$  for 2 minutes, and then served for track length analysis.

For the Ogura 500m borehole and outcrop samples, confined track lengths were measured at a fission-track laboratory newly setup in Kanazawa University, using a Nikon Optiphot microscope with 100x dry objective connected with a digital camera and image analysis system. Track images

were monitored on TV screen where lengths were measured using a mouse at a marked position in the center. Measured lengths were calibrated 100 times with the help of a microscale having a minimum scale of  $0.1 \mu\text{m}$ . As a result, data acquisition precision was as good as less than 1%. GSJ borehole and outcrop samples as well as three additional Ogura borehole samples (i.e., NF51-FTG12, NF51-FTG13 and NF52-FTG01) were analyzed at the fission-track laboratory of Kyoto University. See Yamada et al. (1995a) and Tagami et al. (1988a) for the details of experimental procedures employed.

#### DETECTION OF SECONDARY HEATING OF ROCKS USING FISSION-TRACK THERMOCHRONOLOGY

The FT method is useful for thermal history analysis of the upper crust because fission tracks in minerals are annealed at temperatures of  $\sim 100^{\circ}$  to  $300^{\circ}\text{C}$ . Figure 2 illustrates how the secondary heating of rocks is detected by the single-grain age and track length distributions, using data from the contact metamorphic aureole in the Cretaceous Shimanto Belt formed by the intrusion of the Takatsukiyama Granite at 15 Ma (Tagami & Shimada 1996). Figure 2a shows representative examples of single-grain age distributions using age spectra (Hurford et al. 1984) and track length histograms. Sample SMTZ56, 10.6 km away from the contact, yields single-grain ages predominantly predating the depositional age, with no sign of partial resetting due to heating at 15 Ma. Approaching the contact, single-grain ages increasingly postdate the time of deposition as a result of their partial resetting due to the paleotemperature increase (SMTZ39). Single-grain ages show a spread between the depositional age and 15 Ma time of heating, with an overall younging as the paleotemperature increases (SMTZ19). Eventually, ages converge to around the 15 Ma heating and become statistically concordant with each other (SMTZ07 to 03).

Track length distributions also show variations consistent with increasing resetting due to the heating at 15 Ma. In unreset samples, e.g., SMTZ56, track lengths show a unimodal distribution with a small number of tracks shorter than  $9 \mu\text{m}$ . Their average lengths are  $\sim 10 \mu\text{m}$  and close to the reference value of  $10.5 \pm 0.1 \mu\text{m}$  (1 standard error) determined for zircon age standards from rapidly cooled volcanics (Hasebe et al. 1994) (note that this reference is for tracks  $>60^{\circ}$  to c axis). Approaching the contact, samples that experienced higher paleotemperature have tracks which were significantly annealed and shortened with a greater number of tracks  $<9 \mu\text{m}$  and mean lengths  $<10 \mu\text{m}$  (SMTZ39). In the more advanced stage of track annealing, track lengths are characterized by both bimodal distributions and shorter mean lengths of  $9-7 \mu\text{m}$  (SMTZ19). They comprise two components; (1) preexisting tracks shortened to various degrees by the Miocene

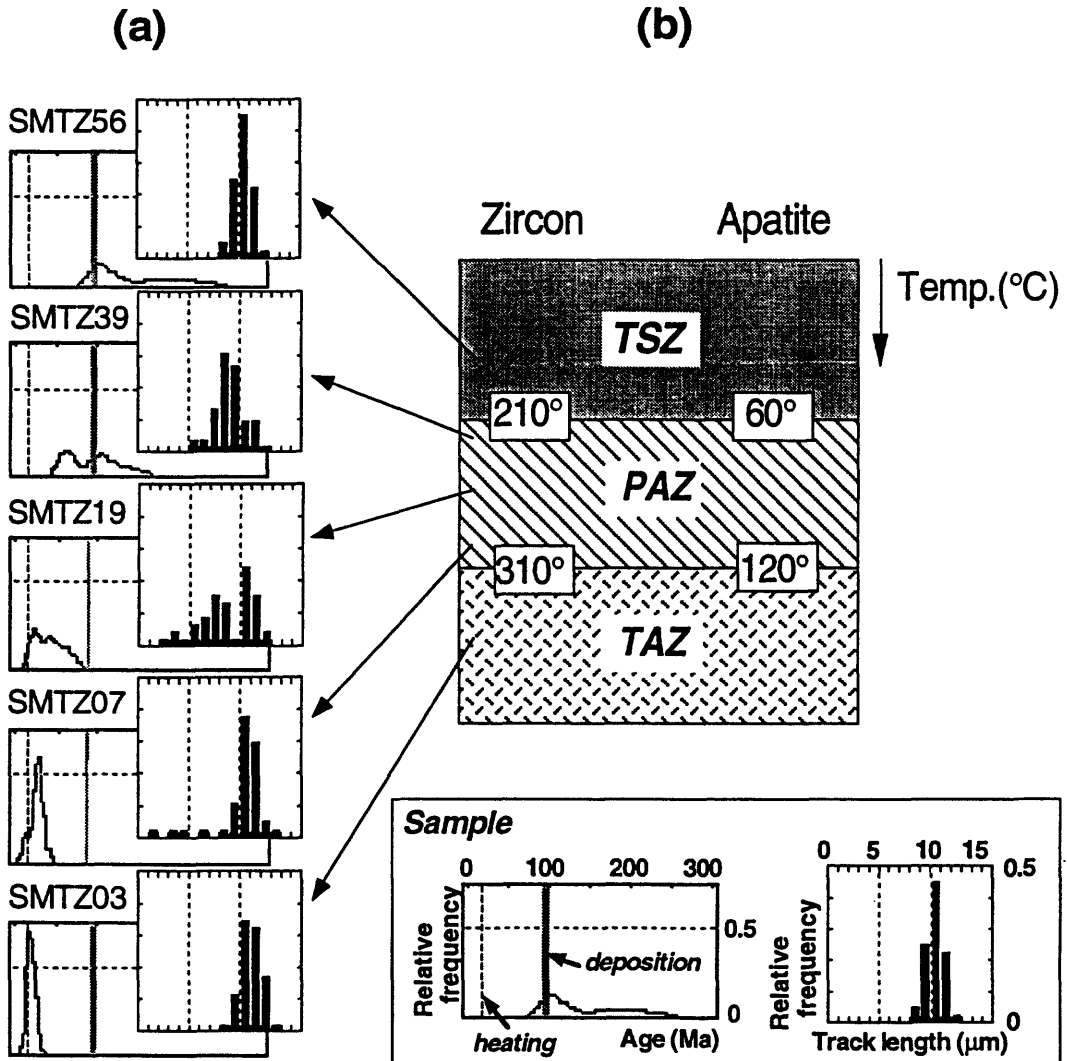


Figure 2. Thermal annealing characteristics of fission tracks at geological timescales. (a) Zircon single-grain age and track length distributions formed by the long-term heating of Cretaceous Shimanto sandstones due to the thermal influence of the intrusion of Miocene Takatsukiyama Granite (Tagami & Shimada 1996). Approaching the contact (i.e. from SMTZ56 to 03), the ages exhibit a systematic reduction from  $\sim 120$  Ma detrital ages to  $\sim 15$  Ma total reset ages, which is concordant with the zircon age of the granite ( $15.0 \pm 0.8$  Ma) that reflects post-emplacement cooling. Accordingly, track length distributions show a systematic variation from the initial unimodal distribution (i.e. SMTZ56), through the bimodal one with a significant number of tracks shorter than  $9 \mu\text{m}$  (SMTZ19), to the unimodal one (SMTZ03). (b) Thermal stability of fission tracks in apatite and zircon. TSZ = total stability zone, PAZ = partial annealing zone, TAZ = total annealing zone. The upper and lower temperature limits of PAZ are given as total fading and 5% length reduction of spontaneous tracks, respectively. The temperature values are after Green et al. (1989) for apatite and Tagami & Shimada (1996) for zircon: the latter was adjusted for a heating duration of 10 m.y using the kinetic functions of Yamada et al. (1995b).

heating and (2) unannealed tracks with original, long lengths formed and accumulated after intrusion. Initially, component 1 is dominant in the distributions (SMTZ56 to 39), followed by the emergence and increasing overlap of component 2 (SMTZ19). Finally, as resetting approaches completion, component 1 greatly diminishes and eventually disappears, leaving behind component 2 with a unimodal distribution (SMTZ07 to 03). Mean lengths in such samples are similar to the reference value of standards (Hasebe et al. 1994).

Figure 2b summarizes the temperature ranges that can be analyzed by the FT method. Three temperature zones can be defined as first-order approximation for apatite and zircon FT systems, respectively: the total stability zone (TSZ) where tracks are thermally stable and hence accumulated as time elapsed; the partial annealing zone (PAZ) where tracks are partially stable and slowly annealed and shortened; and the total annealing zone (TAZ) where tracks are unstable and thus removed soon after their formation. Also shown is the approximate correlation between those temperature zones (Figure 2b) and the track age-length distributions (Figure 2a). We accordingly can reconstruct the secondary heating of host rocks using single-grain age and track length distributions, both of which are characteristic of degree of heating. In particular, track length data is useful for a preliminary study because of greater resolution to degree of annealing in addition to a prompt analysis without neutron irradiation.

## RESULTS AND INTERPRETATION

Apatites exhibited few confined tracks in each sample despite of the  $^{58}\text{Ni}$  ion irradiation, and thus were not employed for thermal history analysis. In contrast, zircon samples yielded spontaneous track densities sufficiently high ( $>106\text{cm}^{-2}$ ) for reliable track length analysis. Sixteen samples were analyzed on the outcrops and borehole section for the Ogura locality and ten samples for the GSJ locality (Figure 1; which shows data only from successive parts of borehole sections around the fault).

It is found from the Ogura borehole that FT lengths in zircons from localities  $>60\text{ m}$  away from the fault plane as well as those from outcrops are characterized by the mean values of  $\sim 10\text{-}11\text{ }\mu\text{m}$  and unimodal distributions with positive skewness. In contrast, those from nearby the fault at depths (i.e., NF51-FTG14, 16 and 17) show significantly reduced mean of  $\sim 7\text{-}8\text{ }\mu\text{m}$  and distributions having a peak around  $6\text{-}7\text{ }\mu\text{m}$  with rather negative skewness. The former pattern is similar in the mean length to spontaneous tracks in unannealed zircons (i.e.,  $10.8\text{ }\mu\text{m}$  for all azimuth angles; Hasebe et al. 1994), and thus is interpreted by the cooling through the temperature zone of track shortening (i.e., the zircon PAZ in Figure 2b) after the emplacement of granite, with the absence of effective secondary heating into the

PAZ in more recent times. The latter indicates substantial track shortening due to partial annealing and is interpreted either by the existence within the zircon PAZ for an extended period of time during the initial cooling of granite down to within the PAZ, or by the secondary heating up to within the PAZ after the initial cooling of granite below the PAZ (i.e., the zircon TSZ in Figure 2b). In either case, the samples were finally cooled below the PAZ as indicated by the modern environmental geothermal temperature of  $<40^\circ\text{C}$  around the boring site (Yamano et al., 1999), which is much lower than the lower temperature limit of zircon PAZ, i.e.,  $\sim 230^\circ\text{C}$ .

A similar trend was observed for GSJ samples, in which the peak around  $6\text{-}7\text{ }\mu\text{m}$  is less dominant however. A notable feature of the obtained track length profile is that tracks are more intensely annealed at localities significantly below the main shear zone. Further, we found a large proportion of preserved, long tracks with a small number of shortened ones at localities of around 150-300 m depth.

## DISCUSSION

Although the zircon age determination is needed to specify the time of final cooling, we can roughly deduce the time using the shape of observed track length distributions with significant number of shortened tracks (e.g., NF51-FTG14): in which, the longer, unannealed tracks with lengths  $>9\text{ }\mu\text{m}$  (i.e., tracks accumulated during a period from the final cooling to the present) are less than the shorter, annealed ones with lengths  $\sim 5\text{-}8\text{ }\mu\text{m}$  (i.e., accumulated from the initial cooling of granite to the final cooling). In addition, the shorter component in the distributions is relatively more dominant than the case of  $\sim 15\text{ Ma}$  secondary heating on  $\sim 120\text{ Ma}$  zircons (e.g., SMTZ19 in Figure 2a; see also the discussion in Tagami & Shimada (1996)), suggesting a relatively shorter period of time from the last cooling to the present than SMTZ19. As the zircon FT age of the initial cooling is around 60 Ma in the Ryoke belt (Tagami et al. 1988b, 1995), it is likely that the samples were finally cooled at  $<7\text{-}8\text{ Ma}$ , possibly in Quaternary.

The region of high paleotemperature observed in the Ogura 500m borehole ranges  $>5\text{ m}$  in apparent along-core depth from the fault, which is equal to  $>3\text{ m}$  in the distance from the fault. In addition, such region was not found from the outcrop sample (NFL02), and thus likely restricted to the crustal interior. To further constrain the formation of the region, here we consider the variations in mean track length vs. depth that are generally expected for the borehole section across the fault. Three models would be plausible that accompanies the significant change in mean track length: (a) thermal anomaly along the fault, in which case the mean track length shows local reduction around the fault, (b) local uplift of the fossil zircon PAZ by the thrust motion of the fault,

in which the downward gradual reduction in mean length (which was formed as a consequence of the downhole increase in geothermal temperature at depth) may emerge repeatedly in the section, and (c) regional uplift of the fossil PAZ, in which the mean track length shows monotonous downward reduction without any sudden change across the fault.

The model (a) corresponds to the secondary heating mentioned in the last paragraph: whereas, the models (b) and (c) to the existence within the PAZ for an extended period of time. Since samples below the fault in the Ogura 500m section (i.e., NF52-FTG01 and NF52-FTG02 from 497 and 550 m depths, respectively) yield no significant reduction in the mean length, the model (c) is not applicable to the present case. The width of high paleotemperature region is as narrow as < 63 m above the fault (Figure 3) and hence the region cannot be explained by the fossil PAZ under subnormal island-arc geothermal conditions. (Note that there is no geological signs of magmatism-related thermal anomalies around the boring site in the recent past.) In addition, the region is ~200 m beneath the base of Miocene Kobe Group, and this indicates that the total amount of post-Miocene uplift is of limited near the boring site. These facts are not compatible with the models (b) and (c). Based on these considerations, therefore, the present track length data are best explained by the model (a). The deduced thermal anomaly is likely attributable to the frictional heating of fault motion and/or heat transfer via fluids from the deep interior of crust. To resolve these two factors, it is necessary to compare and contrast the observed FT length profile with that of rock deformation and alteration being accumulated. In addition, more detailed FT thermochronological analysis involving age determinations is currently undertaken on the present borehole as well as on other deeper boreholes across the Nojima fault, with a particular focus on the rocks nearby the fault.

#### ACKNOWLEDGMENTS

We thankfully acknowledge Drs. Hisao Ito and Hidemi Tanaka for their helps on collecting borehole samples. Thanks are due to Dr. Koichiro Watanabe for the irradiation using a tandem van de Graaff accelerator at Kyushu University and Mr. Hidehiro Hoshino for his help on track length analysis. This study was supported by a Grant-in-Aid No. 09640507 and 08308005 from the Japanese Ministry of Education, Science, Culture and Sports and by a research fund from Institute of Geosphere Assessment.

#### REFERENCES

Brune, J.N., Henyey, T.L. & Roy, R.F. 1969. Heat flow, stress, and rate of slip along the San Andreas fault, California. *J. Geophys. Res.* 74, 3821-3827.

Green, P.F., Duddy, I.R., Gleadow, A.J.W. & Lovering, J.F. 1989. Apatite fission-track analysis as a paleotemperature indicator for hydrocarbon exploration. In N.D. Naeser & T.H. McCulloch eds. *Thermal history of sedimentary basins. Methods and case histories.* 181-195. Springer-Verlag, New York.

Hanks, T.C. & Raleigh, C.B. 1980. The conference on magnitude of deviatoric stresses in the earth's crust and uppermost mantle. *J. Geophys. Res.* 85, 6083-6085.

Hasebe, N., Tagami, T. & Nishimura, S. 1994. Towards zircon fission-track thermochronology: Reference framework for confined track length measurements. *Chem. Geol. (Isot. Geosci. Sec.)* 112, 169-178.

Hurford, A.J., Fitch, F.J. & Clarke, A. 1984. Resolution of the age structure of the detrital zircon populations of two Lower Cretaceous sandstones from the Weald of England by fission track dating. *Geol. Mag.* 121, 269-396.

Ito, H., et al., 1996. Structure and physical properties of the Nojima fault by the active fault drilling. *SEGJ J.* 49, 522-535.

Kamp, P.J.J., Green, P.F. & White, S.H. 1989. Fission track analysis reveals character of collisional tectonics in New Zealand. *Tectonics* 8, 169-195.

Lal, D., Rajan, R.S. & Tamhane, A.S. 1969. Chemical composition of nuclei of  $Z > 22$  in cosmic rays using meteoritic minerals as detectors. *Nature* 221, 33-37.

Laslett, G.M., Kendall, W.S., Gleadow, A.J.W. & Duddy, I.R. 1982. Bias in measurement of fission-track length distributions. *Nucl. Tracks* 6, 79-85.

Murata, A., Takemura, K., Miyata, T. & Lin, A. 1999. Quaternary vertical displacement and average slip rate of the Nojima fault in Awaji Island, Japan. *The Island Arc*, in press.

O'Neil, J.R. & Hanks, T.C. 1980. Geochemical evidence for water-rock interaction along the San Andreas and Garlock faults of California. *J. Geophys. Res.* 85, 6286-6292.

Scholz, C.H. 1979. Frictional metamorphism, argon depletion, and tectonic stress on the Alpine Fault, New Zealand. *J. Geophys. Res.* 84, 6770-6782.

Scholz, C.H. 1996. Faults without friction? *Nature* 381, 556-557.

Sibson, R.H. 1975. Generation of pseudotachylite by ancient seismic faulting. *Geophys. J. R. astr. Soc.* 43, 775-794.

Tagami, T., Lal, N., Sorkhabi, R.B., Ito, H. & Nishimura, S. 1988a. Fission track dating using external detector method: A laboratory procedure. *Mem. Fac. Sci., Kyoto Univ.* 53, 14-30.

Tagami, T., Lal, N., Sorkhabi, R.B. & Nishimura, S. 1988b. Fission track thermochronologic analysis of the Ryoke Belt and the Median Tectonic Line, Southwest Japan. *J. Geophys. Res.* 93, 13705-13715.

Tagami, T. & Shimada, C. 1996. Natural long-term annealing of the zircon fission track system around a granitic pluton. *J. Geophys. Res.* 101, 8245-8255.

Tanaka, H., et al., 1999. Distribution, deformation and alteration of fault rocks along the GSJ core penetrating the Nojima fault, Awaji island, southwest Japan. *J. Geol. Soc. Japan* 105, 72-85.

Watanabe, K., Izawa, E., Kuroki, K., Honda, T. & Nakamura, H. 1991. Detection of confined  $^{238}\text{U}$  fission tracks in minerals and its application to geothermal geology. *Ann. Rep. Tandem Accelerator Lab., Kyushu Univ.* 3, 151-155.

Yamada, R., Tagami, T. & Nishimura, S. 1993. Assessment of overetching factor for confined fission track length measurement in zircon. *Chem. Geol. (Isot. Geosci. Sec.)* 104, 251-259.

Yamada, R., Tagami, T. & Nishimura, S. 1995a. Confined fission-track length measurement of zircon: assessment of factors affecting the paleotemperature estimate. *Chem. Geol. (Isot. Geosci. Sec.)* 119, 293-306.

Yamada, R., Tagami, T., Nishimura, S. & Ito, H. 1995b. Annealing kinetics of fission tracks in zircon: an experimental study. *Chem. Geol. (Isot. Geosci. Sec.)* 122, 249-258.

Yamada, R. et al. 1998. Comparison of experimental techniques to increase the number of measurable confined fission tracks in zircon. *Chem. Geol.* 149, 99-107.

blank page

# Inspection of resetting state of ESR signals and elucidation of radioactive disequilibria in the fault gouge zone using the Nojima Fault GSJ 750m drilling core samples

Tatsuro Fukuchi<sup>1</sup>, Noboru Imai<sup>2</sup> and Natsumi Tanaka<sup>3</sup>

<sup>1</sup> Department of Earth Sciences, Faculty of Science, Yamaguchi University, 1677-1 Yoshida, Yamaguchi 753-8512, JAPAN

<sup>2</sup> Geochemistry Department, Geological Survey of Japan, 1-1-3 Higashi, Tsukuba 305-8567, JAPAN

<sup>3</sup> Department of Earth and Planetary Science, Graduate School of Science and Technology, Kobe University, 1-1 Rokkodai-cho, Nada-ku, Kobe 657-8501, JAPAN

## ABSTRACT

The fault gouge zone in the Nojima Fault GSJ 750m drilling core samples has been analyzed by ESR, ICP-AES/MS and XRD. By ESR measurement, E', peroxy and Al centers in quartz and quartet ESR signals in montmorillonite are detected from the fault gouge, and they had hardly been affected by the faulting in the 1995 Kobe Earthquake. In addition, strong Mn<sup>2+</sup> ion signals also are detected from the fault gouge just on the fault surface. The existence of Mn<sup>2+</sup> ion signals suggests that reduction once occurred along the fault surface. On the other hand, high concentrations of CaO and rare earth elements in the yttrium group are detected from the fault gouge just on the fault surface by ICP-AES/MS. No prominent change of Ca-rich minerals are detected from the fault surface by XRD analysis. The high CaO may be attributed to anomalously discharged groundwater with large amounts of Ca ions, which occurred along the Nojima Fault just after the Kobe Earthquake. Furthermore, the ICP-MS data on U, Th and Pb isotopes indicates that no Rn anomaly occurred along this fault gouge zone, and that the U- and Th-series in the fault gouge zone have been in disequilibrium

states. The disequilibria of U- and Th-series are probably attributable to the migration of <sup>238</sup>U and <sup>232</sup>Th, and/or the whole Pb isotopes. According to XRD analysis of the fault gouge, the peaks of smectites and laumontite in the lower fault block extremely decrease with approaching the fault surface. These peaks are hardly detected from the foliated gouge in the upper fault block. These results show that smectites and laumontite with H<sub>2</sub>O molecules may have been decomposed and dehydrated by frictional heat in previous faulting.

## INTRODUCTION

In the 1995 Kobe Earthquake, many natural phenomena accompanied with the Earthquake were observed. In order to clarify the mechanism of these earthquake-related phenomena, it is probably effective to analyze by various analytical techniques the fault-related materials collected from deep positions just after the Earthquake. In this work, we inspect the resetting state of ESR signals and elucidate radioactive disequilibria in the fault gouge zone for the purpose of the clarification of the earthquake-related phenomena such as water discharge or radon anomaly along the Nojima Fault. The samples used for ESR, ICP-AES/MS and XRD

analyses are the fault gouge zone (623.3~625.1m in depth) in the Nojima Fault 750m drilling core samples collected from Nojima-Hirabayashi by Geological Survey of Japan (Ito et al., 1996; Tanaka et al., 1998; 1999).

## SAMPLE PREPARATION

The fault gouge generated along the fault surface is divided into two parts; gray or dark gray foliated gouge in the upper fault block and white gray or rusty gouge with fault breccia in the lower fault block (Tanaka et al., 1998; 1999). The foliated gouge has been cut and displaced by many cracks, so that it is clear that the foliated gouge had been formed before the 1995 Earthquake.

Before ESR, ICP-AES/MS and XRD analyses, the fault gouge was treated as follows: First, epoxy resin on the surface around the fault gouge was chipped by a diamond cutter. Next, the fault gouge was separated into 16 sheet parts along the fault surface ( $d=0\text{mm}$ ) and foliation with a resolution of 6mm. Each sheet part was twice washed in pure water using a supersonic washer and then separated from the supernatant solution by centrifugation and Millipore filters ( $0.45\text{ }\mu\text{m}$ ). We did not carry out any other sample treatments. Each bulk sample obtained by these treatments was used for ESR, ICP-AES/MS and XRD analyses.

## ESR ANALYSIS

Figure 1 shows ESR spectra obtained from each sheet part of the fault gouge at room and low (77K) temperatures. ESR measurements were carried out using an X-Band ESR spectrometer (JEOL RE-2X and RE-3X) with a 100kHz modulation width. ESR spectrum data were accumulated 3 times using a computer system. The sample weight used for the ESR measurements is 100mg. In the spectra, we can

observe an E' center derived from an oxygen vacancy ( $g=2.001$ : McMorris, 1970; Griscom, 1979), a peroxy center derived from an oxygen interstitial ( $g_1=2.067(\text{av.})$ ,  $g_2=2.0078$ ,  $g_3=2.0016$ : Stapelbroek et al., 1979; Griscom, 1979), and an Al center derived from an aluminum ion which has replaced a silicon ion (Schnadt and Rauber, 1971) in quartz, and a quartet ESR signal derived from montmorillonite ( $g_a=2.048$ ,  $g_b=2.0102$ ,  $g_c=1.9956$ ,  $g_d=1.981$ : Fukuchi, 1996). These ESR signal intensities are almost unchanged, so that they had hardly been affected by the faulting in the 1995 Kobe Earthquake. Especially, the Al center has its intrinsic hyperfine structure (hfs) by the interaction between a nuclear spin and an electron spin, which can be easily annihilated by heating. However the hfs remains almost unchanged even in the 0~6mm or -6~0mm sheet parts of the fault gouge just on the fault surface. This result indicates that heat did not rise so much along the fault surface in the 1995 Kobe Earthquake.

In addition to these ESR signals, strong six ESR signals are detectable from the fault gouge just on the fault surface. These signals are derived from  $\text{Mn}^{2+}$  ions in the fault gouge. A  $\text{Mn}^{2+}$  ion signal is splitted into six hyperfine lines by the interaction between a nuclear spin and an electron spin. According to the result from ICP-AES (Fig.2), high  $\text{MnO}$  is undetectable from the fault gouge just on the fault surface, so that once reduction may have occurred along the fault surface.

## ICP ANALYSIS

Figure 2 shows the results from each sheet part of the fault gouge by ICP-AES and MS. As shown in the figures, the concentrations of  $\text{CaO}$  and rare earth elements of the yttrium group become prominently high over measurement errors ( $1\text{ }\sigma=5$

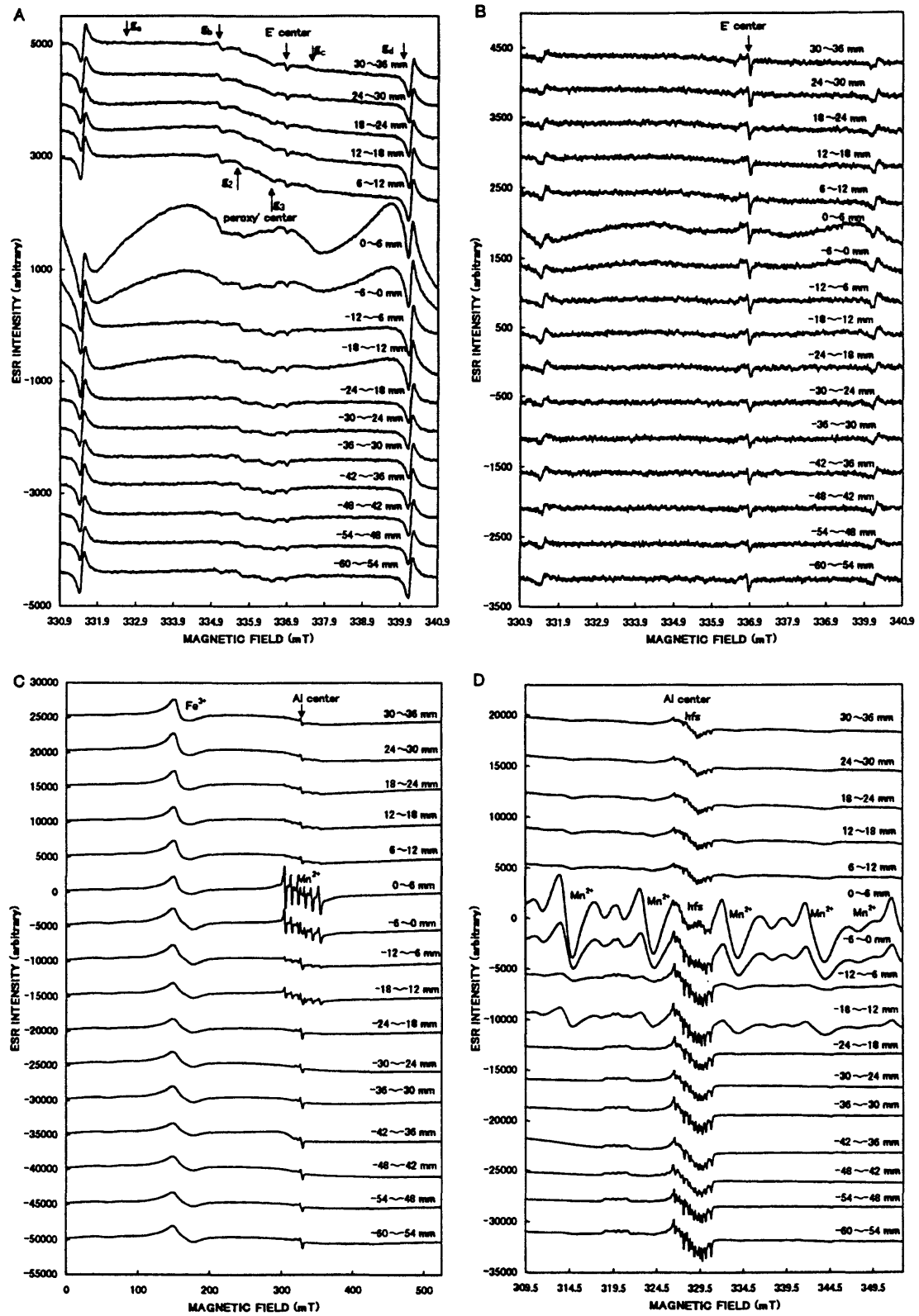


Figure 1 ESR spectra obtained from the fault gouge in the GSJ 750m drilling core samples. Measurement conditions:  
 A) Microwave frequency 9.44GHz, Temperature RT, Microwave power 1mW, Modulation width 100kHz 0.05mT, Response 0.3s, Sweep time 8min; B) 9.44GHz, RT, 0.01mW, 100kHz 0.05mT, 0.3s, 8min; C,D) 9.22GHz, 77K, 1mW, 100kHz 0.05mT, 0.3s, 8min.

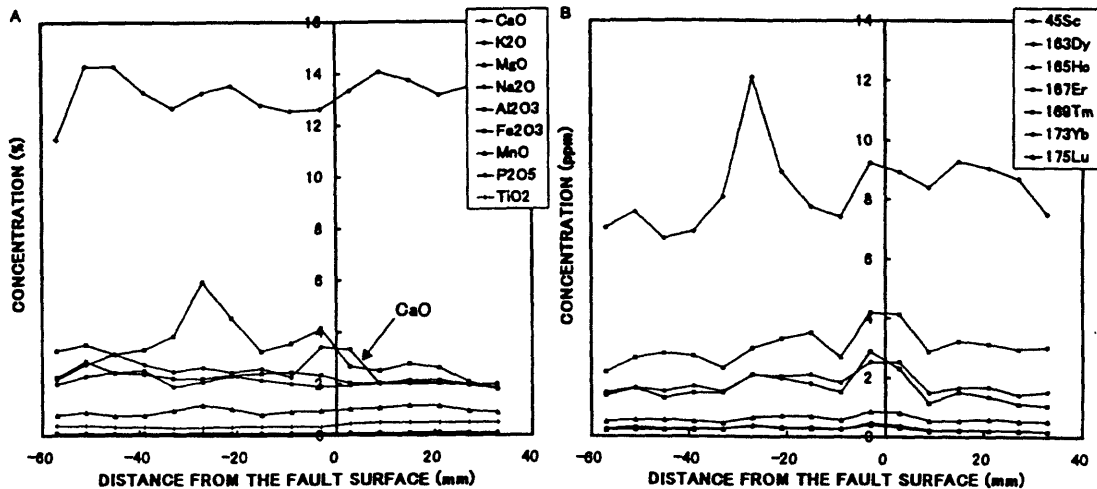


Figure 2 Variations of major (A) and rare earth (yttrium group) (B) elements in the fault gouge detected by ICP-AES and MS. The distance from the fault surface was measured at the center of each sheet part of the fault gouge.

~15%) in the 0~6mm and -6~0mm sheet parts of the fault gouge just on the fault surface. No prominent change of Ca-rich minerals are detected from around the fault surface even by XRD analysis (Fig.5). Sato and Takahashi (1997) reported that the anomalously discharged groundwater which occurred along the Nojima Fault just after the Kobe Earthquake contained large amounts of Ca ions, and that the groundwater collected from the bottom of the GSJ 750m drilling hole also contained high CaO. Therefore, the high CaO detected from the fault gouge just on the fault surface may be attributed to the anomalously discharged groundwater in the Kobe Earthquake. The rare earth elements in the yttrium group also are carried and concentrated into the fault gouge along the fault surface with the anomalously discharged groundwater. The origin of the anomalously discharged groundwater is still unclear.

Figure 3 shows the ratios of  $^{206}\text{Pb}/^{238}\text{U}$  and  $^{208}\text{Pb}/^{232}\text{Th}$  in the fault gouge and its source rock obtained by ICP-MS. As shown in the figure, the anomalies of  $^{206}\text{Pb}/^{238}\text{U}$  and  $^{208}\text{Pb}/^{232}\text{Th}$  ratios are undetectable from the fault gouge. If Rn anomaly caused along the fault surface in the Kobe

Earthquake,  $^{206}\text{Pb}$  and  $^{208}\text{Pb}$  which are the finally stable daughter nuclei in the U- and Th-series may concentrate in the fault gouge near the fault surface. Therefore, these ICP-MS data indicates that Rn anomaly did not occur along this fault surface. As a result of ICP-MS analysis of the Nojima Fault 500m drilling core samples (Fukuchi and Imai, 1998; 1999), Pb anomaly was detected along the fault plane, however the ICP data in this work indicate that the Rn anomaly does not always occur throughout the whole fault plane of the Nojima Fault. In addition, the drilling hole is more or less 10cm in diameter and a very small spot, so that it may be very difficult to detect by such a pin spot the Rn anomaly on the fault plane of the order of 100km<sup>2</sup> in area.

Figure 4 shows the U-Pb, Th-Pb and Pb-Pb isochrons obtained from the fault gouge and its source rock. There exist no linear relationship between  $^{206}\text{Pb}/^{204}\text{Pb}$  and  $^{238}\text{U}/^{204}\text{Pb}$  or  $^{208}\text{Pb}/^{204}\text{Pb}$  and  $^{232}\text{Th}/^{204}\text{Pb}$ . This result indicates that the U- and Th-series in the fault gouge zone have been in radioactive disequilibrium states. On the other hand, there exist linear relationships with high correlation coefficients ( $R=0.951, 0.961$ ) between

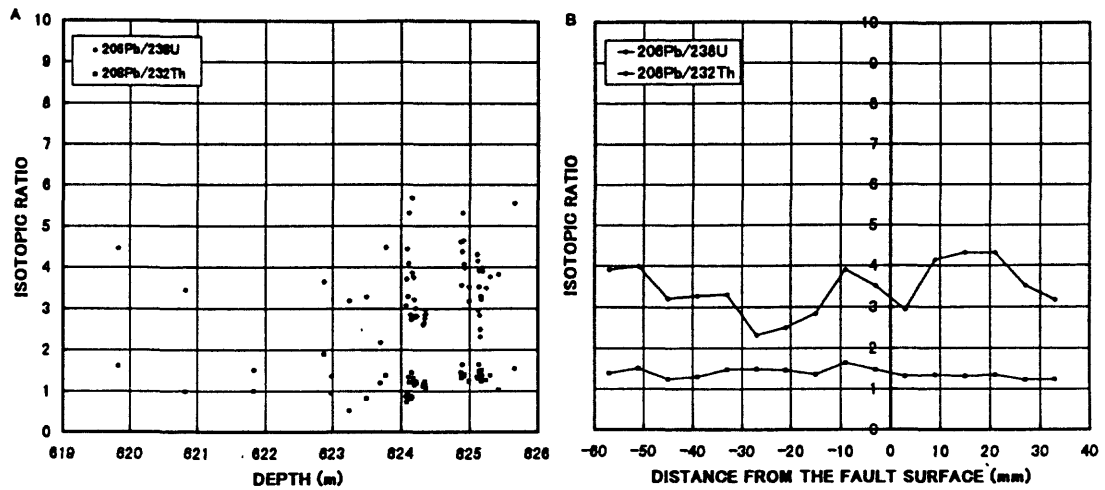


Figure 3 Isotopic ratios of the U- and Th-series in the GSJ 750m drilling core samples. A) The fault gouge and its source rock (Nojima Granitoid), B) The fault gouge around the fault surface. The distance from the fault surface was measured at the center of each sheet part of the fault gouge. The fault surface is located at 625.13m in depth.

$^{207}\text{Pb}/^{204}\text{Pb}$  and  $^{206}\text{Pb}/^{204}\text{Pb}$ , and  $^{207}\text{Pb}/^{204}\text{Pb}$  and  $^{208}\text{Pb}/^{204}\text{Pb}$ . If the radioactive disequilibria in the fault gouge zone are attributed to the migration of the daughter nuclei of  $^{238}\text{U}$  and  $^{232}\text{Th}$ , the ratios of Pb isotopes must change. Therefore, the radioactive disequilibria are probably attributable to the migration of  $^{238}\text{U}$  and  $^{232}\text{Th}$ , and/or the whole Pb isotopes.

#### XRD ANALYSIS

Figure 5 shows X-ray diffraction (XRD) patterns obtained from the fault gouge. In addition to quartz, feldspars and carbonate minerals, the peaks of smectites and laumontite are detected from the fault gouge in the lower fault block, but they extremely decrease in the -6~0mm sheet part just on the fault surface. On the other and, these peaks are hardly detected from the foliated gouge in the upper fault block. Smectites and laumontite with  $\text{H}_2\text{O}$  molecules may have been decomposed and dehydrated by frictional heat in previous faulting. By the dehydration, hot water should have been generated and injected into the upper fault gouge along the fault surface.

Fukuchi and Imai (1998, 1999) proposed that hot fluids may have passed through the fault plane in the Kobe Earthquake, on the basis of the results from ESR, ICP and XRD analyses of the Nojima Fault 500m drilling core samples. The origin of the hot fluids may be attributable to the dehydration of the fault gouge at deeper positions.

#### CONCLUSIONS

The fault gouge zone in the Nojima Fault GSJ 750m drilling core samples was analyzed by ESR, ICP-AES/MS and XRD. ESR signals in the fault gouge had hardly been affected by the faulting in the 1995 Kobe Earthquake. In addition, strong  $\text{Mn}^{2+}$  ion signals were detected from the fault gouge just on the fault surface, and suggest that reduction once occurred along the fault surface.

From the fault gouge just on the fault surface, high concentrations of  $\text{CaO}$  and rare earth elements in the yttrium group were detected. Since no prominent change of  $\text{Ca}$ -rich minerals were detected from the fault surface, the high  $\text{CaO}$  may be attributed to  $\text{Ca}$ -rich discharged groundwater, which occurred along the Nojima Fault just after

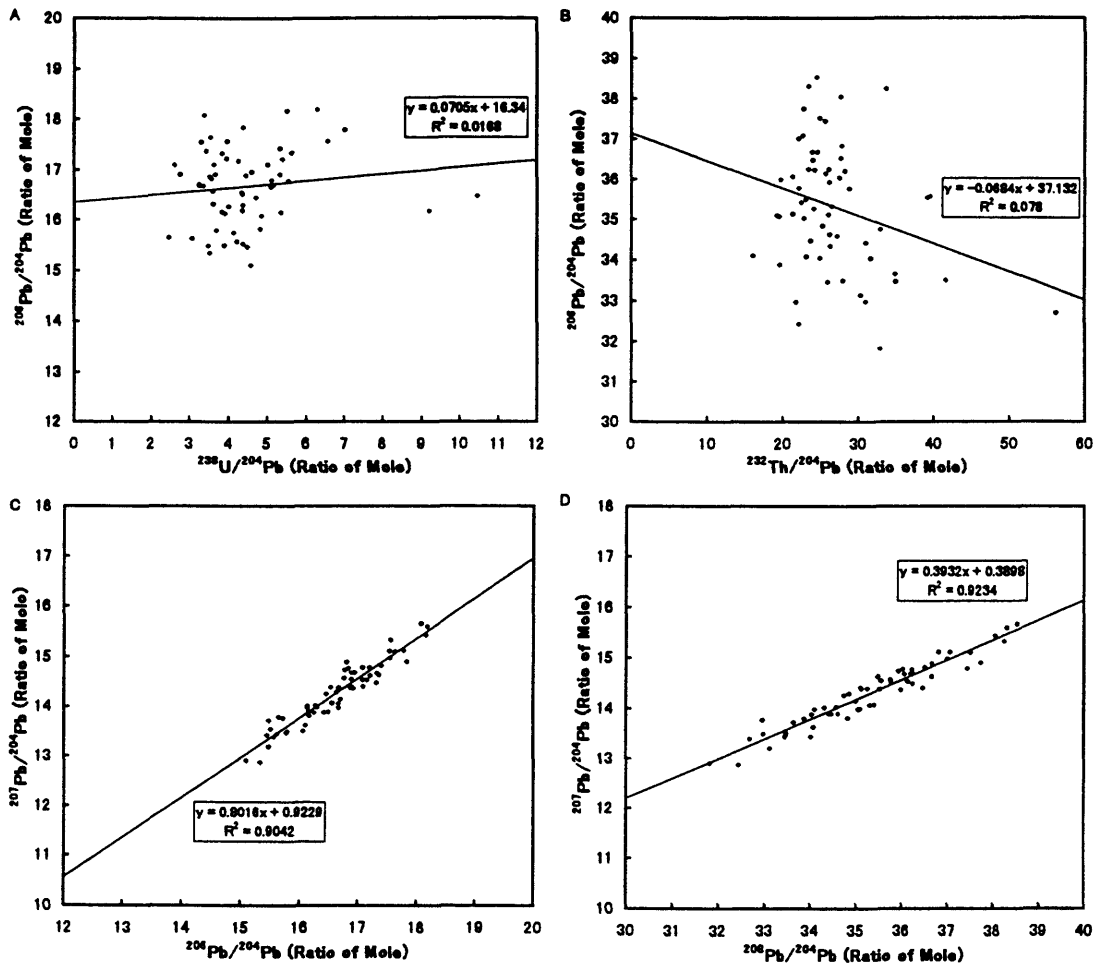


Figure 4 U-Pb (A), Th-Pb (B) and Pb-Pb (C,D) isochrons obtained from the fault rocks (fault gouge and host rocks) in the GSJ 750m drilling core samples.

the 1995 Kobe Earthquake. Furthermore, the relationships between Pb isotopic ratios in the fault gouge remain linear and do not support the existence of Rn anomaly along the fault surface. Whereas, the relationship between U/Pb and Pb/Pb ratios or Th/Pb and Pb/Pb ratios is random and the U- and Th-series in the fault gouge zone have been in radioactive disequilibrium states. The radioactive disequilibria are probably caused by the migration of  $^{238}\text{U}$  and  $^{232}\text{Th}$ , and/or the whole Pb isotopes.

The XRD data indicates that the peaks of smectites and laumontite are hardly detected from the foliated gouge in the upper fault block. These minerals with  $\text{H}_2\text{O}$  molecules may have been

decomposed and dehydrated by frictional heat in previous faulting.

#### ACKNOWLEDGMENTS

We wish to thank Drs. H. Ito, K. Fujimoto and T. Ohtani for their offer of the GSJ 750 drilling core samples and their cooperation in sampling. This work has been supported by a Grant-in-Aid for Scientific Research (No.10640441) from the Ministry of Education, Science and Culture of Japan, by the Inter-University Program for the Joint Use of JAERI Facilities (No.8123 and 9127) and by the scholarship from Tokiwa Engineering Society (No.103042).

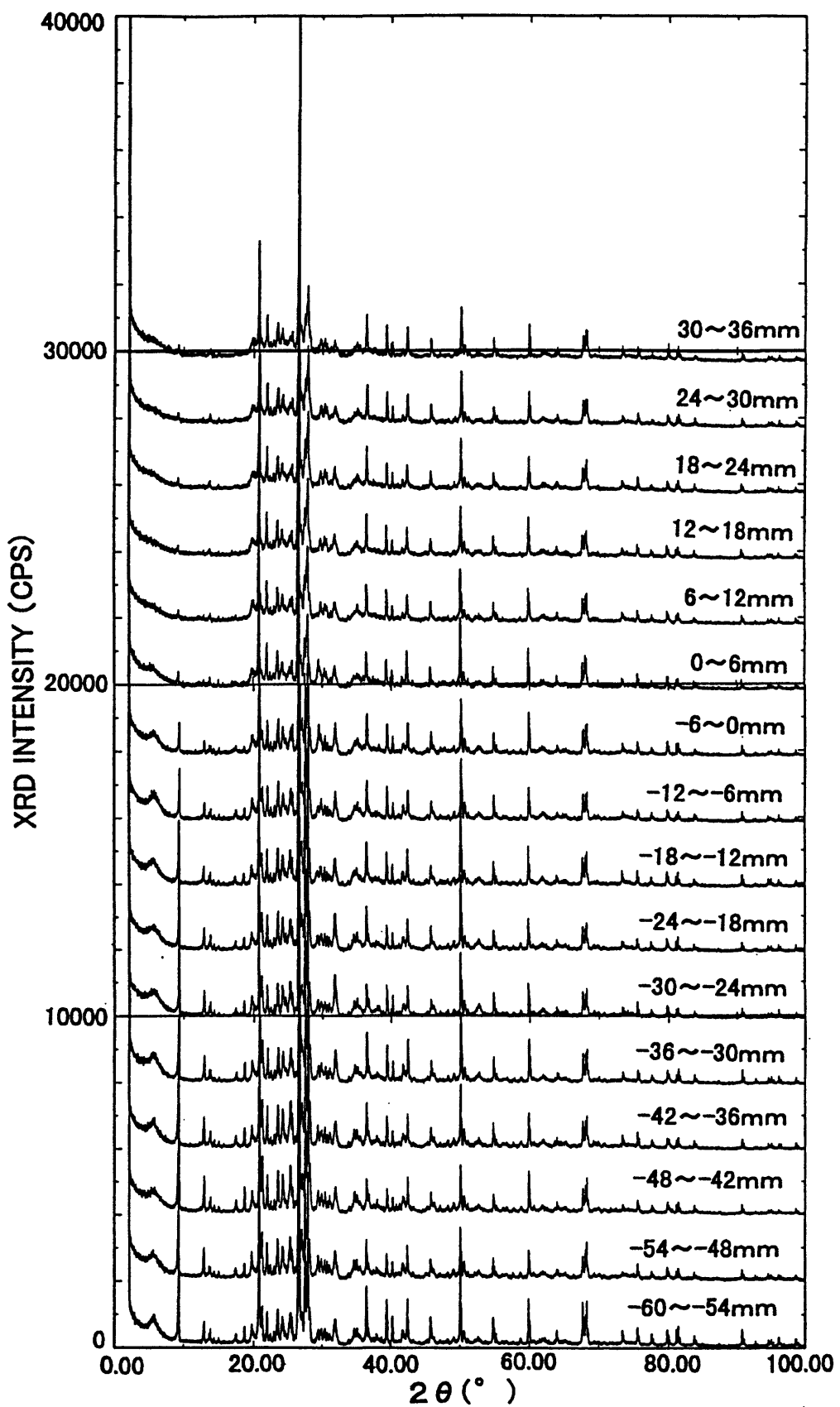


Figure 5 X-ray diffraction patterns obtained from the fault gouge in the GSJ 750m drilling core samples.

## REFERENCES

Fukuchi, T., 1996, Quartet ESR signals detected from natural clay minerals and their applicability to radiation dosimetry and dating. *Japanese Journal of Applied Physics*, 35, 1977-1982.

Fukuchi, T. and Imai, N., 1998, ICP-MS and ESR dating of the 500m Nojima drilling core samples. *The Chikyu Monthly*, 21, 180-185.

Fukuchi, T. and Imai, N., 1999, ESR and ICP analyses of the Ogura 500m core samples drilled into the Nojima Fault, Japan: Evidence for hot fluids through the fault plane. *The Island Arc* (in review)

Griscom, D.L., 1979, Point defect and radiation damage processes in  $\alpha$ -quartz. *Proceeding of the 33rd Frequency Control Symposium*, 98-109.

Ito, H., Kuwahara, Y., Miyazaki, T., Nishizawa, O., Kiguchi, T., Fujimoto, K., Ohtani, T., Tanaka, H., Higuchi, T., Agar, S., Brie, A. and Yamamoto, H., 1996, Structure and physical properties of the Nojima Fault by the active fault drilling. *BUTSURI-TANSA*, 49, 522-535.

McMorris, D.W., 1970, ESR detection of fossil alpha damage in quartz. *Nature*, 226, 146-148.

Schnadt, R. and Rauber, A., 1971, Motional effects in the trapped-hole center in smoky quartz. *Solid State Communication*, 9, 159-161.

Stapelbroek, M., Griscom, D.L., Friebele, E.J. and Sigel,Jr. G.H., 1979, Oxygen-associated trapped-hole centers in high purity fused silica. *Journal of Non-Crystalline Solids*, 32, 313-326.

Tanaka, H., Ikeda, R., Ito, H., Arai, T., Ohtani, T., Omura, K., Kobayashi, K., Sano, H., Sawaguchi, T., Tomita, T., Tomida, N., Higuchi, T., Hirano, S., Fujimoto, K., Matsuda, T. and Yamazaki, A., 1998, Mode of occurrence of fault rocks in the drilled cores (GSJ and NIED) penetrating the Nojima Earthquake Fault. *Journal of the Geological Society of Japan*, 104, XIII-XVI

Tanaka, H., Higuchi, T., Tomida, N., Fujimoto, K., Ohtani, T. and Ito, H., Distribution, deformation and alteration of fault rocks along the GSJ core penetrating the Nojima Fault, Awaji Island, Southwest Japan. *Journal of the Geological Society of Japan*, 105, 72-85.

# Decay of $E_1'$ Center in Quartz from the Nojima Fault Gouge by the Contact of $H_2$ Gas — Possible Indicator for $H_2$ Generation and Seismic Activity

Hiroshi MATSUMOTO, Makoto HIRAI, Chihiro YAMANAKA and Motoji IKEYA

Department of Earth and Space Science, Graduate School of Science, Osaka University,

1-1 Machikaneyama, Toyonaka, Osaka 560-0043, Japan

e-mail: matsu@ess.sci.osaka-u.ac.jp

## Abstract

The changes of ESR signals of quartz by contact with  $H_2$  gas were studied. Grains taken from four core samples of the fracture zone of the Nojima fault at the depth of 625m were exposed to  $H_2$  gas and changes of their ESR signals ( $E_1'$  and peroxy centers) were observed. One out of four samples without etching treatment showed small decrease of the  $E_1'$  center while other three samples didn't give any change. Quartz grains selected by etching with 6N HCl and 10% HF were also exposed to  $H_2$  gas and all of samples showed large decrease of the  $E_1'$  center. The decrease was suggested as substitution of an unpaired electron at the  $E_1'$  center by  $H^-$ . Large decrease for etched sample, in contrast to small or no decrease for nonetched sample, might be explained by exposure of dislocations and defects by the cleavage during etching. The decrease of the  $E_1'$  center might be used as indicator of  $H_2$  generation.

## Introduction

ESR signals found in quartz have been studied and applied for dating using their sensitivity of radiation (Ikeya 1988, Fukuchi 1991, Buhay *et al.* 1988, Imai and Shimokawa 1988) or survey of heating history (Tani *et al.* 1997, Fukuchi 1998, Yamanaka *et al.* 1998). Some of the ESR centers are also sensitive of environmental gas. ESR can be used to investigate molecules adsorbed on materials, or structure induced by chemical reaction with environmental gas. Fubini (1989) found that the ESR signals in artificially crushed quartz are subjective to the environmental gas at crushing and referred to gaseous environment at production of industrial dust.

The amount of degassing has been monitored at fault area and anomalous generation of  $H_2$  gas especially

Table 1. Samples used for experiments.

sample	core number	depth(m)	description
A, A'	98-25	623.3	Fault breccia
B, B'	99-6	624	light grayish green fault gouge
C, C'	99-10	624	weakly altered and deformed granodiorite
D, D'	99-22	625.5	weakly altered and deformed granodiorite

\*X' indicates that samples were etched by 12N HCl for 1h and 10% HF for 30 min.

related to major earthquakes are reported (Ito 1999, Sato 1984). Wakita (1989) found the production of  $H_2$  gas around the Nojima fault and suggested that  $H_2$  gas was produced by reaction of  $H_2O$  and the fresh surface of quartz formed by crushing, which was certified experimentally by Kita (1982). Thus concentration of  $H_2$  is monitored trying to utilize it as indicator of activity of faults.

In this paper the effect of  $H_2$  was studied by ESR for core sample taken by drilling at the Nojima fault (Ito *et al.* 1996), aiming to detect trace of  $H_2$  once present inside fault.

## Experimental

Four core samples were measured as summarized in Table 1. Samples were mildly crushed and sieved to select grains of the size less than 100  $\mu m$ . Part of the grains were etched by using 6N HCl for 1hour and then by 10% HF for about 30 min. Samples were checked by using microscope after etching and drying. Samples were then put in a small polystyrene case which is filled with  $H_2$  and kept for two hours. ESR measurements were carried out and the spectra before and after contact with  $H_2$  gas were compared. ESR measurements were performed at room temperature using modulation field of 0.05 mT, microwave power of 0.01mW and microwave frequency about 9.4 GHz using X-band ESR spectrometer (GEOL RE-1X).

## Result

Figure 1 shows the ESR spectrum of sample A'.  $E_1'$  peroxy centers were observed. Samples without etching treatment showed ESR signal of  $Mn^{2+}$  and  $Fe^{3+}$  together with  $E_1'$  and peroxy centers. The contact of  $H_2$  with samples without etching gave

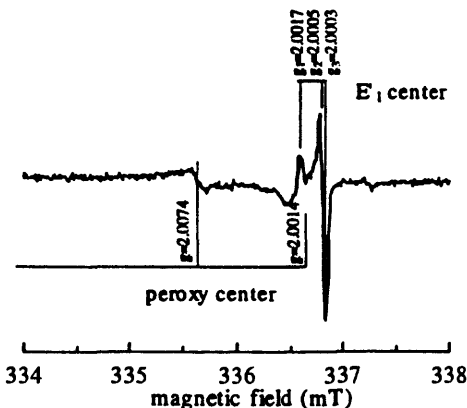


Figure 1. ESR signal measured for sample A'. Peroxy  $E_1'$  centers were observed. Measurement were done at microwave power  $10^{-2}$  mW and modulation field 0.05mT.

no signal change for B, C, D and small change for A as shown in Fig.2 (a) and (c). Contact of  $H_2$  with etched samples, however, resulted in clear decrease of the  $E_1'$  center for all samples as Fig.2 (b) and (d).

### Discussion

The  $E_1'$  center is an oxygen vacancy trapping a hole. Oxygen vacancy is created by mechanical deformation or  $\alpha$ -recoil breaking Si-O bond as

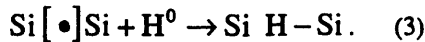


where  $[ ]$  and  $\bullet$  indicate an oxygen vacancy and an electron respectively. Irradiation ionizes oxygen vacancy to create the  $E_1'$  center.



An oxygen vacancy with paired electrons is not detected by ESR while the  $E_1'$  center is detectable.

We propose a model of decay of the  $E_1'$  center by  $H_2$  gas as follows. When quartz is exposed to  $H_2$  gas, atomic hydrogen comes to the  $E_1'$  center and substitutes with an unpaired electron as



Quartz grains of the fracture zone often get fine grained during etching with HF. This phenomenon is not observed in the case of samples of bed rock. This implies that dislocation or point defects would reside in quartz grains in the fracture zone. If  $E_1'$  and oxygen vacancies are abundant along dislocations and cleavage occurs along dislocations, quartz grains after etching will have a large amount of the  $E_1'$  center or oxygen vacancies on its surface, and the  $E_1'$  center would be more subjective to  $H_2$ . This may be why decay of the  $E_1'$  center is dominant in etched sample, and not in nonetched sample.

The decrease of the  $E_1'$  center by contact with  $H_2$  would imply that sample have not been exposed to  $H_2$  gas if the  $E_1'$  center decreased by  $H_2$  do not recover. No signal change in sample B, C and D indicates that these samples were already exposed to  $H_2$  gas and small decrease of the  $E_1'$  center in sample A suggests that the sample was less exposed to  $H_2$  gas.

The source of  $H_2$  gas is still questioned. It might have been produced by the contact of  $H_2O$  with crushed quartz surface created by crushing, as Kita (1982) suggested. It might have been produced somewhere at more depth than the fracture zone and come up to the fracture zone. The latter model

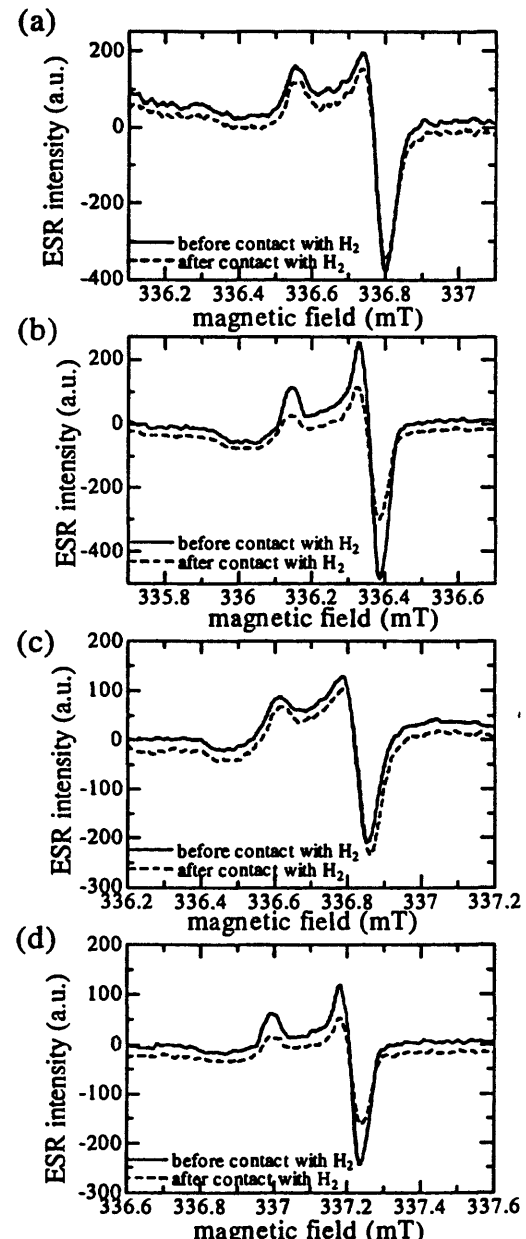


Figure 2. Change of ESR signal of the  $E_1'$  center by the contact with  $H_2$ . (a), (b), (c) and (d) shows results for sample A, A', B and B' respectively.

might seem to be more reasonable because sample A, which was located upper side of B, C and D were less affected by H<sub>2</sub> than other three samples.

Anyhow, further study is necessary for detailed discussion. The stability of decreased of the E<sub>1</sub>' center and kinetics of decreasing the E<sub>1</sub>' center should be studied.

### Conclusion

The change of ESR signals in quartz by the contact with H<sub>2</sub> were studied using four core samples taken by drilling of the Nojima fault. Samples at the fracture zone (98-25, 99-6, 99-10 and 99-22) were studied. One sample (98-25) showed decrease of the E<sub>1</sub>' center by exposure to H<sub>2</sub> gas while other three samples didn't show any change if samples were not etched. Samples after etching by 6N HCl and 10% HF were also exposed to H<sub>2</sub> gas and all samples showed clear decrease of the E<sub>1</sub>' center. The decrease of the E<sub>1</sub>' center was tentatively suggested as substitution of an unpaired electron at the E<sub>1</sub>' center by H<sub>2</sub> gas and implies that sample was less exposed to H<sub>2</sub> gas.

### Acknowledgment

We thank Dr H. Ito, Dr. T. Ohtani, Dr. K. Fujimoto at Geological Survey of Japan (GSJ), and all people involved drilling for offering us a core sample and valuable help.

### References

Buhay, W.M., Schwarcz, H.P., Grun, R. 1988. ESR dating of fault gouge: the effect of grain size. *Quat. Sci. Rev.* **7**, 515-22.

Fubini, B., Giamello, E., Pugliese, L. and Volante, M. 1988. Mechanically induced defects in quartz and their impact on pathogenicity. *Solid State Ionics* **32/33**, 334-343.

Fukuchi T. 1998. Analysis of core sample of Nojima fault by ICP-MS and ESR dating. *Chikyu Monthly*. **21**, 180-5.

Fukuchi, T. 1991. The Itoigawa-Shizuoka tectonic line at the western edge of the South Fossa Magna, Japan. *Mod. Geol.* **15**, 347-66.

Ikeya M. 1993. *New Applications of Electron Spin Resonance*. World Scientific, Singapore.

Imai, N., Shimokawa, K. 1988. ESR dating of Quaternary tephra from Mt. Osore-zan using Al and Ti centres in quartz. *Quat. Sci. Rev.* **7**, 529-32.

Ito, H., Kuwahara, Y., Miyazaki, T., Nishizawa, O., Kiguchi, T., Fujimoto, K., Ohtani, T., Tanaka, H., Higuchi, T., Agar, S., Brie, A. and Yamamoto, H. 1996. Structure and physical properties of the Nojima fault by the active fault drilling. *BUTSURU-TANSA* **49**, 522-535.

Ito, T., Nagamine, K., Yamamoto, K., Adachi, M., Kawabe, I. 1999. Preseismic hydrogen gas anomalies caused by stress-corrosion process preceding earthquakes. *Geophys. Res. Lett.* **26**, 2009-12.

Kita, I. and Matsuo, S. 1982. H<sub>2</sub> Generation by Reaction Between H<sub>2</sub>O and Crushed Rock: An Experimental Study on H<sub>2</sub> Degassing From the Active Fault Zone. *J. Geophys. Res.* **87**, 10789-10795.

Sato, M., Sutton, A.J., McGee, K.A. 1984-1985. Anomalous hydrogen emissions from the San Andreas fault observed at the Cienega Winery, central California. *Pure & Appl. Geophys.* **122**, 376-91.

Tani, A., Bartoll, J., Ikeya, M., Komura, K., Kajiwara, H., Fujimura, S., Kamada, T., and Yokoyama, Y. 1997. ESR study of thermal history and dating of a stone tool. *Appl. Magn. Reson.* **13**, 561-569.

Toyoda, S. and Ikeya, M. 1991. Thermal stabilities of paramagnetic defect and impurity centers in quartz: Basis for ESR dating of thermal history. *Geochem. J.* **25**, 437-445.

Yamanaka, C., Matsumoto, H. and Ikeya, M. 1998. ESR Analysis of a core sample of Nojima fault. *Chikyu Monthly*. **21**, 186-190.

Wakita, H., Nakamura, Y., Kita, I., Fujii, N., Notsu, K. 1980. Hydrogen release: new indicator of fault activity. *Science* **210**, 188-90.

blank page

# A Survey of Thermal Disturbance on the GSJ Nojima Core Sample by Electron Spin Resonance (ESR)

Atsushi Tani, Hiroshi Matsumoto and Motoji Ikeya

Department of Earth and Space Science, Graduate School of Science, Osaka University

1-1 Machikaneyama Toyonaka, Osaka, 560-0043, JAPAN

Corresponding e-mail address: [atani@ess.sci.osaka-u.ac.jp](mailto:atani@ess.sci.osaka-u.ac.jp)

## Abstract

Quartz grains extracted from the GSJ Nojima core sample were measured by electron spin resonance (ESR) to survey thermal disturbance on the whole drilling core. Signal intensity of Ti center decreased in the region of fault zone around 625 m while E' and Al centers increased. This is consistent with the result that Ti center is less stable than Al and E' centers in Mannari granite, Okayama Japan. The intensity of Al center in samples near fault zone may be related to aluminum contents in quartz grains because of no growth by  $\gamma$ -ray irradiation. This might indicate that aluminum atoms could be trapped into deformed quartz grains where many cracks were formed during fault activity. The intensity of E' center increased after heating samples at 250 °C for 30 minutes, which implies that the sample may not be affected recently by heat around 200 °C or higher. In addition, Ti and Al centers show thermal disturbance around 250 m, which is concordant with the results of fission-track analysis.

## Introduction

Radiation-induced defects are produced in minerals by natural radiation and accumulated for a few hundred thousand years if they are stable enough. Those defects can be measured by thermoluminescence (TL), optically stimulated luminescence (OSL) or electron spin resonance (ESR). An ESR measurement has an advantage to

detect signals repeatedly since trapped electrons and holes do not recombine by measurements. This technique can be applied to quartz, carbonates like coral and stalactite, phosphates like fossil bones and teeth and so on (Ikeya 1993).

The ESR study of fault material was started by Ikeya *et. al.* in 1982 for dating the latest fault activity. After that, several groups have investigated fault material by ESR (e.g. Buhay *et. al.* 1988, Fukuchi 1991, Lee and Schwarcz 1993). Recent drilling core projects in the Nojima fault gave an opportunity to get the fault sample at great depth. The possibility to anneal ESR signals by faulting in drilling core samples were reported by Yamanaka *et. al.* (1998) and Fukuchi (1998).

We developed the way to assess storage temperature, cooling rate and denudation rate from ESR signal intensity using quartz grains in core samples of intrusive Eldzhurtinskiy granite, Caucasus (Grün *et. al.* 1999). For example, the ratio of E' center before ( $I_1$ ) and after heating ( $I_2$ ) shows the beautiful correlation of the signal intensity with storage temperature (Fig. 1) (see also Chen *et. al.* 1997). On the other hand, impurity centers (Al and Ti centers) decreased monotonically (Fig. 2) and the cooling rate and denudation rate can be assessed by computer simulation of the signal growth.

In this paper, we study changes of ESR signal intensities in depth and the effect of thermal activity to ESR signals in the Nojima core samples.

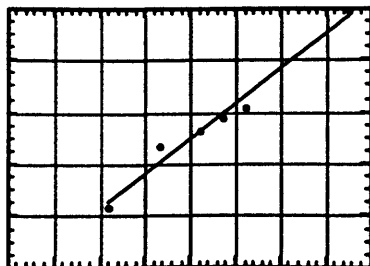


Figure 1. The signal intensity ratio of E' center before and after heating quartz samples in Caucasus (Grün *et. al.* 1999).

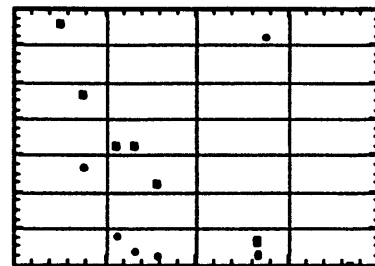


Figure 2. ESR signal intensities of Al and Ti centers in quartz of intrusive granite (Grün *et. al.* 1999).

Table 1. Samples and their descriptions. The marker '\*' indicates contamination of resin in samples.

Core & Sample No.	Depth [m]	Description	Etc.
#1	156	Granodiorite	
#11	203	Granodiorite	
#21	251	Granodiorite	
#32	303	Granodiorite	
#42	347	Granodiorite	
#53	402	Granodiorite	
#65	459	Granodiorite	
#75-7A	507	Weakly altered and deformed granodiorite	
#84-11	550	Weakly altered and deformed granodiorite	
#97-14	617	Fault breccia	
#99-06	625	Light grayish green fault gouge	*
#99-22	625	Weakly altered and deformed granodiorite	*
#100-08	630	Weakly altered and deformed granodiorite	
#103-17	656	Weakly altered and deformed granodiorite	*
#105-24	669	Weakly altered and deformed granodiorite	*
#106-13	676	Granodiorite	
#111-15	696	Weakly altered and deformed granodiorite	
#121-16	743	Weakly altered and deformed granodiorite	

### Sample and Experimental

All samples used in this study are summarized in Table 1. Most samples are granodiorite or weakly altered and deformed granodiorite (Ito *et. al.* 1996). The samples near 625 m are mostly deformed and do not remain the original structure of granodiorite at all.

A piece of about 1 cm in thickness was taken out by saw in the middle of each full or half-cut core. The surface of the piece was cut off about 3-5 mm to remove resin keeping the figure of the core structure. The obtained piece was gently crushed into small grains in an alumina mortar and sieved into four aliquots based on grain size of 0-100, 100-250, 250-500 and more than 500  $\mu\text{m}$ . We used only the aliquot of 100-250  $\mu\text{m}$  because small grains were easily dissolved in HF acid and large grains gave a huge angular dependence on ESR

signals.

Those samples were washed with 35 % HCl to dissolve carbonate and some other minerals and put in 10 % HF solution for 30-90 minutes to remove other minerals like feldspar and mica. This solution can also remove surface of quartz grains that were damaged by external  $\alpha$ -rays.

Samples were measured by JEOL RE-2X ESR spectrometer with a 100 kHz field modulation of 0.1 mT for oxygen hole center (OHC), Al and Ti centers and of 0.05 mT for E' center. Al and Ti centers were detected at 77 K with a finger dewar while E' and OHC were detected at room temperature. Magnesium oxide with Mn<sup>2+</sup> impurity was also measured simultaneously for calibration of signal intensities. Microwave power was 5 mW for Al and Ti centers, 1 mW for OHC and 0.001 mW for E' center. After measurements, all were heated in an oven at 250 °C for 30

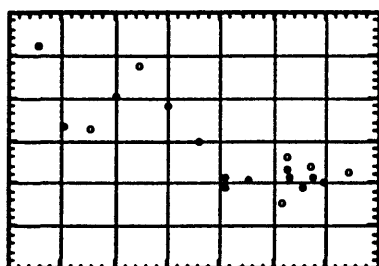


Figure 3. Ti center in the GSJ core sample. The intensity decreased around the fault zone as well as 200-300 m.

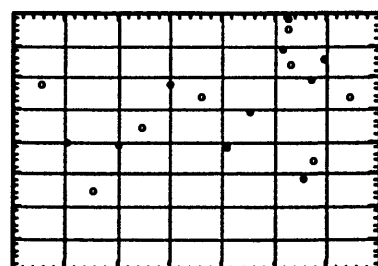


Figure 4. Al center in the GSJ core sample. The intensity decreased around 250 m but increased around the fault zone.

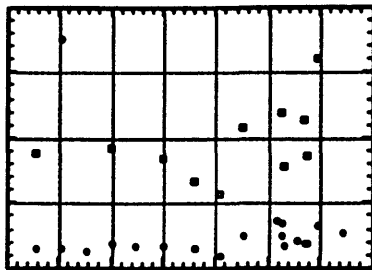


Figure 5. E' center before and after heating in the GSJ core sample.

minutes. A  $^{60}\text{Co}$  source of the  $\gamma$ -rays was used for irradiation.

### Results and Discussions

#### Ti Center

The results of Ti center in Fig. 3 are close to the results on the study of the intrusive granite. Signal intensity decreased around the deformed granodiorite zone below 500 m. This may be due to the thermal effects. The samples around 200-300 m also show small intensities. This is concordant with the results of fission-track study on the GSJ core sample (Murakami *et. al.* 1999).

#### Al Center

The intensities of Al center were plotted in Fig. 4. The results indicate that the signal intensities did not decrease but increased in the fault zone around 625 m. Toyoda and Ikeya (1991) reported that Al center was much stable than Ti center using quartz samples from Mannari granite, Japan. Assuming the same thermal stability, thermal disturbance was not enough to affect to Al center in these samples. As Al center in the samples near 625 m did not increase by artificial  $\gamma$ -ray irradiation, those signals have been already saturated and the intensity may be related to aluminum content.

Quartz in fault zone is crushed by fault activity and many cracks should be involved into quartz grains. Water containing aluminum ions dissolved from feldspar or clay minerals will surround quartz grains. Those aluminum ions may be attached on fresh surface or go into cracks in quartz grains. Silica in water will precipitate at the surface of the grains and rearrangement of  $\text{SiO}_2$  network may include such aluminum atoms inside. This model might be the reason why the intensity of Al center increased in the region of fault zone.

The intensity decreased around 250 °C, which is concordant with the results of Ti center and may

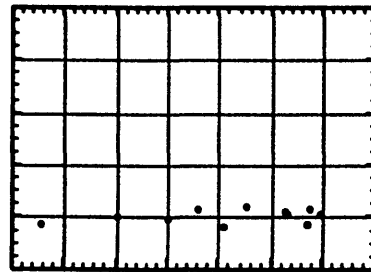


Figure 6. The ratio of signal intensities of the E' center before ( $I_1$ ) and after heating ( $I_2$ ).

be an evidence of the thermal effect.

#### E' Center

The results of the E' center are shown in Fig. 5. The intensities of the natural signals were almost the same except for a few samples in fault zone around 625 m. This no change of natural signal intensities is the same result as the Caucasus sample. The data of E' center in several samples after heating were also plotted in Fig. 5.

Figure 6 shows the ratio of E' center signal intensity before and after heating. ( $I_1$  is before and  $I_2$  is after). The all obtained ratio were around 0.2. The study in Fig. 1 has been tested above 40 °C. Chen *et. al.* (1997) also investigated the relation between the ratio  $I_1/I_2$  and storage temperature up to 20 °C but it is not clear at this stage. The difference of the E' center intensity may depend on the number of precursors, oxygen vacancies due to the similar ratio  $I_1/I_2$  for all samples. Further study of thermal stability and change of E' center is necessary to discuss more details.

### Summary

Thermal effects near fault zone have not been observed clearly by ESR in this sample because of the intensive signal of Al center and increase of E' center after heating. The large signal of Al center might be due to aluminum contents in quartz. The intensities of Al and Ti centers around 250 m were smaller than the others and may indicate thermal disturbance. The intensity of E' center is almost the same except for the samples near fault zone but the ratio of the intensity before and after heating is the same for whole samples.

### Acknowledgements

The authors thank Dr. H. Ito, T. Ohtani, K. Fujimoto at Geological Survey of Japan (GSJ) and all people involved in Nojima drilling project for

sample provide and valuable discussions. This work was supported by a grant from Research Fellowship of the Japan Society for the Promotion of Science for Young Scientists (No. 5083, 1997-2000).

## REFERENCES

Buhay W.M. and Schwarcz H.P. 1988. ESR dating of fault gouge: the effect of grain size. *Quat. Sci. Rev.* 7, 515-522.

Chen Y., Feng J., Gao J. and Grün R. 1997. Investigation of the potential use of ESR signals in quartz for palaeothermometry. *Quat. Sci. Rev.* 16, 495-499.

Fukuchi T. 1991. The Itoigawa-Shizuoka tectonic line at the western edge of the South Fossa Magna. *Jpn. Mod. Geol.*, 15, 347-366.

Fukuchi T. 1998. Analysis of core sample of the Nojima fault by ICP-MS and ESR dating. *Chikyu Monthly* 21, 180-185.

Grün R., Tani A., Gurbanov A., Koshchug D., Williams I. and Braun J. 1999. A new method for the estimation of cooling and denudation rates using paramagnetic centers in quartz: a case study on the Eldzhurtinskiy Granite, Caucasus. *J. Geophys. Res.*, 104, 17531-17549.

Ikeya M., Miki T. and Tanaka K. 1982. Dating of a fault by ESR on intrafault materials. *Science* 215, 1392-1393.

Ikeya M. 1993. New applications of electron spin resonance - dating, dosimetry and microscopy. World Scientific, Singapore.

Ito H., Kuwahara Y., Miyazaki T., Nishizawa O., Kiguchi T., Fujimoto K., Ohtani T., Tanaka H., Higuchi T., Agar S., Brie A. and Yamanamoto H. 1996. Structure and physical properties of the Nojima fault by the active fault drilling, *Butsuri-tansa*, 49, 522-535.

Lee H.K. and Schwarcz H.P. 1993. An experimental study of shear-induced zeroing of ESR signals in quartz. *Appl. Radiat. Isot.* 44, 191-195.

Murakami M., Tagami T. and Hasebe N. 1999. Fission-track thermochronology of Nojima fault borehole samples. *Godo-taikai* in 1999.

Toyoda S. and Ikeya M. 1991. Thermal stabilities of paramagnetic defect and impurity centers: basis for ESR dating of thermal history. *Geochem. J.* 25, 186-190.

Yamanaka C., Matsumoto H. and Ikeya M. 1998. ESR analysis of a core sample of Nojima fault. *Chikyu Monthly*, 21, 186-190.

# Anisotropy of elastic and anelastic properties of granites from the Hirabayashi hole, Japan.

Maria Zamora<sup>1</sup>, Philippe A. Pezard<sup>2</sup>, and Hisao Ito<sup>3</sup>.

<sup>1</sup>*Institut de Physique du Globe de paris (CNRS ESA7046), 4 place Jussieu 75252 Paris cedex 05, France (zamora@ipgp.jussieu.fr)*

<sup>2</sup>*CEREGE(CNRS), BP 80, 13545 Aix-en-Provence cedex 4, France (pezard@cerege.fr),*

<sup>3</sup>*Geological Survey of Japan, Earthquake Research Department, 1-1-3, Higashi, Tsukuba, Ibaraki, 305-8567, Japan (g0193@gjrstn.gsj.go.jp).*

## ABSTRACT

The ultrasonic P-wave velocities have been measured, in different directions, in 20 cores collected from the GSJ Hirabayashi hole, Japan. The cores offer a large range of fracturation and alteration. We have investigated the effect of the alteration and the fracturing intensity on the velocity and anisotropy of P-waves. The measurements were successively performed on dry samples and fully water-saturated samples. P-wave velocities strongly decrease when porosity increases. The reduction attains 50 % for 3 % of porosity. Anisotropy of  $V_p$  increases with porosity, indicating that the porosity of the samples is principally a thin cracks porosity type. A good agreement between sonic log and laboratory data is observed.

## INTRODUCTION

Cores and downhole measurements were collected in 1996 from the GSJ Hirabayashi hole, south-west Japan, about one year after the devastating Nanbu Earthquake (Fujimoto et al. 1999; Ito et al. 1998). The hole penetrated the most recent rupture of the Nohima fault zone near 625 m of depth and the core recovery was higher than 90 %. In the core, the host rock was found intensely fractured and altered over more than 300 m (about 30 m of true thickness due to the relative orientation of the drillhole with respect to this near-vertical fault). The penetrated lithology is mostly constituted with granodiorites, with rare intrusions of porphyry. The granodiorites are altered and deformed to varying degrees. This tendency appears to reflect a macroscopic increase in the rate of fracturing and alteration of the granodiorites towards the most recent rupture of the fault. The Hirabayashi hole offers a unique opportunity to study the relationship between deformation, alteration and physical properties of the penetrated rocks. In particular, because the penetrated lithology is relatively constant, it offers the possibility of quantify the effect of alteration and degree of fracturation on P- and S-wave velocities and attenuation.

The elastic properties of cracked rocks depends much more on the density, aspect ratio, and spatial distribution of cracks, and on whether they are dry or

saturated, than on the elastic moduli of the constituent minerals (Kuster and Toksöz, 1974). Information on these parameters is contained in the anisotropy of P- and S-wave velocities and the birefringence of S waves (Crampin, 1987). Ideally, knowing  $V_p$  and  $V_s$  in several directions, we would like to infer the geometry of the cracks population and the state of saturation (Zamora and Poirier, 1990). Unfortunately, if some theoretical models connecting elastic or anelastic properties to the state of fracturing of the rock exist (Hudson, 1981, 1988; O'Connell and Budiansky, 1977) the experimental works allowing the test of these models are scarce (Nur and Simmons, 1969; Rai, and Hanson, 1988; Zamora and Poirier, 1990).

The objective of this experimental study is to quantify the effect of alteration and fracturing intensity on velocity and attenuation of compressional and shear waves. With this aim, ultrasonic P and S wave velocity and attenuation are measured in different directions, in order to study the anisotropy of these parameters, of a selected samples coming from different depth of the Hirabayashi hole. These samples cover a wide range of degree of alteration and fracturing intensity. We report here preliminary results concerning compressional wave velocities and anisotropy of 20 cores coming from 205 to 500 m depth of the Hirabayashi hole. The data concerning the S-wave velocities and P- and S-wave attenuation are in processing.

## EXPERIMENTAL PROCEDURE

### DESCRIPTION OF THE CORES

For this study, 20 cores from the Hirabayashi hole were selected. The cores were sampled uniformly between 205 m and 490 m depth. The sampling was constituted from granodiorites (16 samples) and porphyry dikes (4 samples). They offer a large range of fracturation and alteration, since unaltered and weakly deformed samples until considerably altered and extremely macrofractured samples.

The mineralogical composition and state of alteration of the samples have been studied by Ohtani et al., 1999.

## THE SAMPLES PREPARATION

Cylindrical samples, 57 mm in diameter and 50-70 mm length, were sawn out of cores. The faces of the samples are ground to a good finish and kept parallel to within 0.004 radian. The axis of the cylinder corresponds to the vertical (Z), while the two horizontal directions (X and Y) were chosen independently for each sample.

## CORE MEASUREMENTS

The connected porosity of the samples is measured with the triple weighing method.

P and S wave velocities are measured with an ultrasonic pulse transmission technique. Two pairs of Panametrics transducers (500 kHz) are used. The signal is delivered by a Panametrics 5055PR pulse generator. The output signals are displayed and stored in a Tektronix 7603 oscilloscope with a digital programmable rack. The transit time of compressional (P) and shear waves (S) was measured at atmospheric pressure and room temperature.

Different measurements were successively performed on each sample:

a) measurements of P- and S-wave velocities along the vertical direction. S-waves were measured with 18 different polarizations in order to observe the possible shear-wave birefringence (dependence of shear-wave velocities with the polarization of the particle motion).

b) measurements of P-wave velocities along of 12 different directions in the horizontal plane in order to quantify the P-wave anisotropy of the rock.

All these measurements were successively performed on dry samples and fully water-saturated samples. The measurement errors associated with velocities are less than 2% for P waves and 4% for S waves.

## EXPERIMENTAL RESULTS

Only the results concerning P-wave velocities and anisotropy will be discussed in this paper. Figure 1 display three examples illustrating the different behaviors observed. As a general rule, P-wave velocities measured in the Z (vertical) direction are higher than those measured in the horizontal plane.

Depending on the degree of alteration and fracturation two different behaviors have been observed:

a) unaltered and uncracked granodiorite and porphyry samples (samples 232 and 305) present high P-wave velocities, close to the quartz's velocity (quartz is the principal constituent of these rocks). The anisotropy is weak (< 5%) and the effect of the saturation is also unimportant.

b) altered or fractured granodiorite samples (sample 249) display small  $V_p$  velocities. The anisotropy may be important, attaining 40%, and the increasing of P-waves velocities with water-saturation may be also important and can reach 50%.

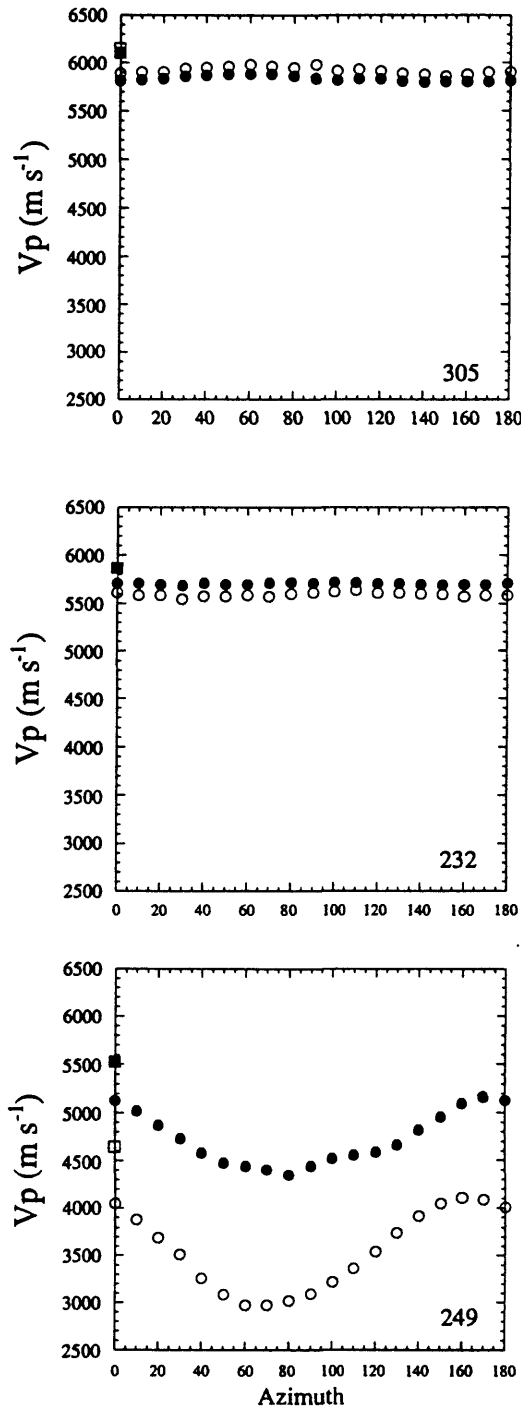


Figure 1. P-wave velocities as a function of azimuth for three the samples from the GSJ Hirabayashi hole. The squares symbolize the vertical velocities and the circles the velocities obtained in the horizontal plane. The open and closed symbols represent respectively the dry and water-saturated velocities. Top: porphyry sample; middle: unaltered granodiorite sample; bottom: intensely altered and cracked granodiorite sample.

Depth m	$\Phi$ %	$V_p$ Dry km s <sup>-1</sup>	$V_p$ Sat km s <sup>-1</sup>	A Dry %	A Sat %
204.0	1.0	5.32	5.87	5	4
220.0	1.2	4.95	5.59	14	9
224.0	1.2	5.28	5.43	7	4
232.0	0.3	5.73	5.79	6	3
240.0	0.4	5.51	5.77	9	2
242.5	0.7	5.40	5.69	8	5
244.4	1.9	—	5.39	—	5
249.9	2.3	4.10	5.13	41	23
250.5	2.2	—	5.06	—	9
251.5	2.0	4.35	5.36	22	7
256.2	0.5	5.36	5.52	9	3
261.0	0.7	5.35	5.61	11	7
271.8	0.6	5.40	5.88	6	3
305.7	0.2	6.04	5.97	5	5
316.2	0.5	5.60	5.81	3	5
348.1	0.4	5.61	5.69	10	6
362.4	0.7	5.18	5.86	9	7
409.6	0.4	5.74	5.78	6	5
429.6	2.6	4.35	5.05	9	7
441.2	2.7	3.48	5.20	16	12
487.6	2.7	4.69	4.81	10	8

Table 1. Porosity ( $\Phi$ ), mean P-wave velocities, in dry ( $V_p$  Dry) and water-saturated conditions ( $V_p$  Sat), P-waves anisotropy, in dry (A Dry) and water-saturated conditions (A Sat).

Table 1 shows porosity, mean P-wave velocity and anisotropy, in dry and water-saturated conditions.

The anisotropy, A, is defined by:

$$A = \frac{V_{P\text{Max}} - V_{P\text{Min}}}{V_{P\text{Mean}}} \quad (1)$$

We observe that:

- the porosity of the samples ranges from 0.3 % to 2.7 %.
- P-wave velocities cover a large scale of values, in contrast with the weak porosity of the samples, ranging from 6.04 km/s to 3.48 km/s in dry samples and from 5.97 km/s to 4.81 km/s in saturated samples.

Figure 2 presents the evolution of P-wave velocities with porosity. We see that  $V_p$  decreases quickly when porosity increases. The diminution is more important in dry samples, where it can reach 50%.

The comparison of our data with the predictions of the Kuster and Toksöz (1974) model shows that mean aspect ratio of the pores ranging from  $10^{-2}$  to  $10^{-1}$  are compatible with our results.

For granodiorite samples, water saturation implies always higher P-wave velocities, while for porphyry samples, water saturation implies slightly higher or slightly lower  $V_p$ . The augmentation of  $V_p$  with

saturation increases with porosity (figure 3), it is larger than to 20% in the most porous samples. The variation of the effect of the saturation with the porosity is more important in the granodiorite samples than the porphyry samples.

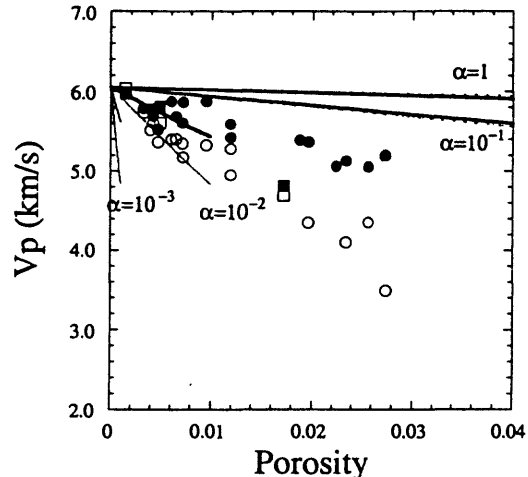


Figure 2. P-wave velocities as a function of porosity for the measured samples. The squares and the circles correspond, respectively, to porphyry and granodiorite samples. The open and closed symbols represent respectively the dry and water-saturated velocities. The lines are the predictions of the Kuster and Toksöz (1974) model for different values of the aspect ratio,  $\alpha$ , of the pores. Continuous lines correspond to the saturated case and dotted lines to the dry case.

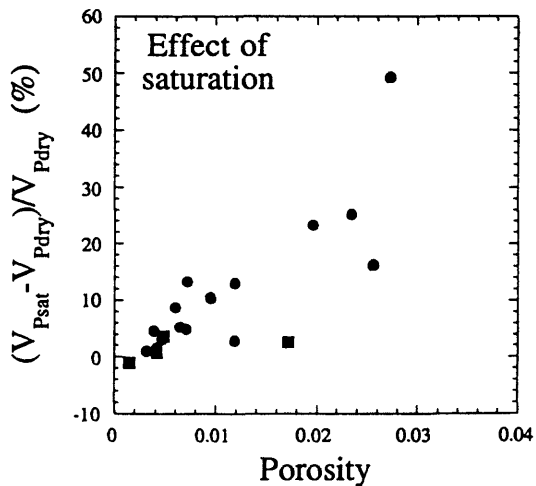


Figure 3. Effect of water saturation (defined by:  $(V_{P\text{Sat}} - V_{P\text{Dry}}) / V_{P\text{Dry}}$ ) as a function of porosity. The squares and the circles correspond, respectively, to porphyry and granodiorite samples.

The anisotropy is important in dry samples, where it reaches 41%. Water saturation decreases the anisotropy, which is, in this case, generally smaller than 10 %. As the effect of saturation, the anisotropy increases with porosity (figure 4).

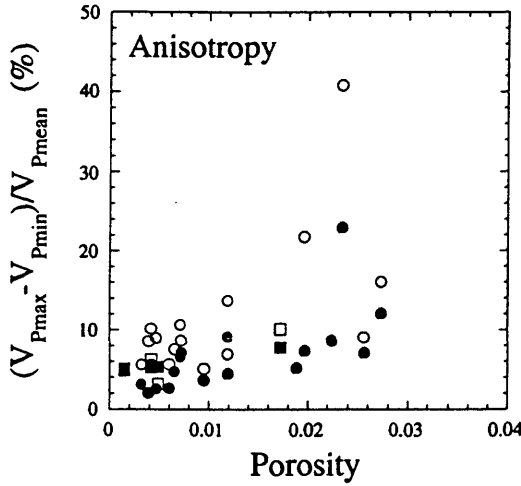


Figure 4. Anisotropy as a function of porosity. The open and closed symbols represent respectively the dry and water-saturated cases.

#### COMPARISON WITH FIELD DATA

In the GSJ Hirabayashi hole, P-wave velocities were determined by sonic log. The values obtained are reported in Figure 5 together with those obtained in laboratory. In granodiorite samples the sonic log velocities, at given depth, are generally located between dry and saturated values of  $V_p$  obtained in the laboratory, on samples collected at the same depth. In porphyry samples the sonic log velocities are equivalent, or slightly inferior, to the laboratory values.

On the whole, the agreement between sonic log and laboratory data is very good, especially if we take into account the fact that the frequencies utilized in situ and in laboratory are different. Laboratory measurements were made at 500 kHz, as compared to  $\approx 10$  kHz for sonic log. Assuming a compressional velocity of 5 km/s, the corresponding wavelengths are  $5 \cdot 10^{-3}$  and 0.5 m respectively. Thus field experiments sample much larger volumes of rock than laboratory ultrasonic experiments. The correspondence between these two scales is not well understood, but it is often assumed that the microcracks and fractures have approximately same effect on the propagation of ultrasonic and sonic waves in dry rocks (Spencer and Nur, 1976; Murphy, 1984; Han and Nur, 1987). This assumption is also supported by the fact that velocity dispersion is usually small (of the order of a few percent) in dry rocks (Winkler, 1983). In water-saturated rocks, dispersion effects are stronger and acoustic velocities are increasing functions of frequency (Winkler, 1985).

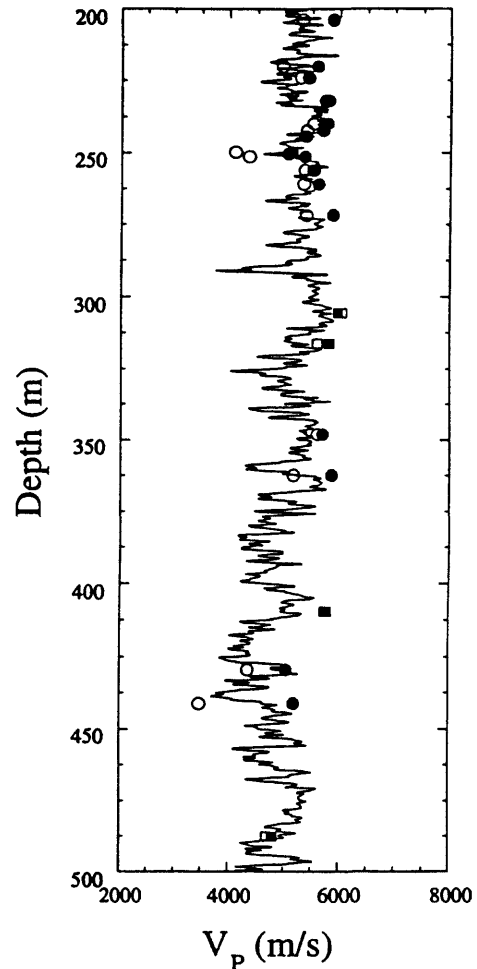


Figure 5. P-wave velocity as a function of depth obtained in laboratory and in-situ by sonic log. The open and closed symbols represent respectively the dry and water-saturated laboratory measurements and the continuous line the sonic log values.

#### DISCUSSION AND PERSPECTIVES

In the studied samples, P-wave velocities strongly reduce when porosity increases. This reduction is very spectacular, especially if we take into account the small porosity of our samples ( $< 3\%$ ). For instance, in sedimentary rocks, a reduction of 50 %, as those obtained in granodiorite samples for an augmentation of porosity of 3 %, is observed for an increase of about 20 % of porosity. According to the theoretical model of Kuster and Toksöz (1974) this strong reduction of  $V_p$  with porosity may be only explained if we assume that the porosity is of the fissural type. The comparison of our data with the predictions of this model shows that mean aspect ratio of the pores ranging from  $10^{-2}$  to  $10^{-1}$  are compatible with our results. This is confirmed by the strong effect of the water saturation on  $V_p$ . Actually, for very thin pores and cracks,  $V_p$  velocities are higher in water saturated

samples. Even porosity of less than 1% of thin pores may increase the velocities in saturated rocks by more than 10%, the increase being much more pronounced for very thin cracks.

Anisotropy of P-waves velocities strongly increase with porosity. That is also the consequence of the augmentation of the percentage of thin cracks, if the cracks are not randomly distributed, when porosity increases. Figure 6 shows that  $V_p$ , anisotropy and effect of water saturation are well correlated.

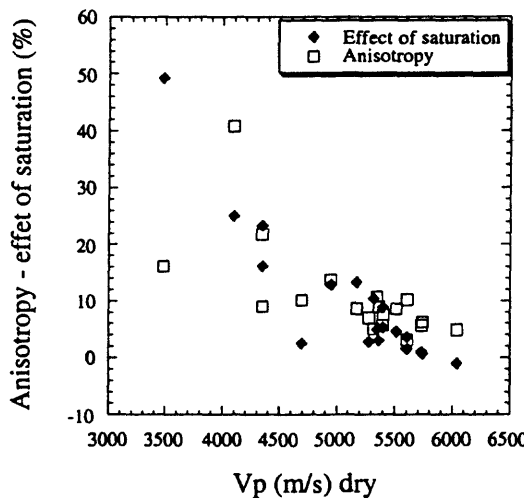


Figure 6. Anisotropy and effect of saturation as a function of P-wave velocities. The open and closed symbols represent respectively anisotropy and effect of saturation.

These preliminary results show that, in rocks that are not very porous, like granitic rocks, the effect of the deformation or fracturation on P-wave velocities is very important and that P-wave velocity and anisotropy are a good indicators of the degree of fracturation of the rock.

We have limited our study here to the P-wave velocity. Including S-wave velocity and attenuation would allow to better understand the relations of these parameter with fracturing intensity and alteration.

#### ACKNOWLEDGMENTS

This study was financed by CNRS and ANDRA through the GdR FORPRO (Research Action 99.V) and corresponds to the GdR FORPRO contribution number FORPRO 99/007 B.

#### REFERENCES

Fujimoto K., Tanaka H., Higuchi T., Tomida N., Ohtani T., et Ito H. Alteration and mass transfer along the GSJ Hirabayashi borehole penetrating

the Nojima earthquake fault, Japan. Submitted to *Island Arc.*

Han, D.H. and A. Nur, 1987, Velocity dispersion in sandstones, *Annu. Int. Meet. Soc. Explor. Geophys. Expanded Abstr.*, 57, 5-8.

Hudson, J. A., 1981, Wave speeds and attenuation of elastic waves in material containing cracks, *Geophys. J. R. Astr. Soc.*, 64, 133-150.

Hudson, J. A., 1988, Seismic wave propagation through material containing partially saturated cracks, *Geophys. J.*, 92, 33-37.

Ito H., Kuwahara T., Kiguchi T., Fujimoto K., Ohtani T., Tanaka H., Brie A., Endo T., Yamamoto H. Permeability structure of the Nojima Fault from borehole measurements in the GSJ borehole crossing the Nojima Fault on Awaji Island, Japan. AGU Fall meeting, San Francisco, *EOS transactions*, 1998.

Kuster G.T. and Toksöz M.N., 1974, Velocity and attenuation of seismic waves in two-phase media : Part I. Theoretical formulations, *Geophysics*, 39, 587-606.

Murphy W.F., 1984, Seismic to ultrasonic velocity drift: Intrinsic absorption and dispersion in crystalline rock, *Geophys. Res. Lett.*, 11, 1239-1242.

Nur A. and Simmons G, 1969, Stress induced velocity anisotropy in rock : an experimental study, *J. Geophys. Res.*, 74 (27), 6667-6674.

O'Connell R. and Budiansky B., 1977, Viscoelastic properties of fluid-saturated cracked solids, *J. Geophys. Res.*, 82, 5719-5735.

Ohtani T., Fujimoto K., Ito H., Tanaka H., Higuchi T., Tomida N. Subsurface internal structure of the Nojima Fault from the GSJ borehole survey. Submitted to *Island Arc.*

Rai, C.S., and Hanson, K.E., 1988, Shear-wave velocity anisotropy in sedimentary rocks: A laboratory study, *Geophysics*, 53, 800-806.

Spencer J.W. and A. Nur, 1976, The effect of pressure, temperature, and pore water on velocities in Westerly granite, *J. Geophys. Res.*, 81, 899-904.

Winkler K.W., 1983, Frequency dependent ultrasonic properties of high porosity sandstone, *J. Geophys. Res.*, 88, 9493-9499.

Winkler K.W., 1985, Dispersion analysis of velocity and attenuation in Berea sandstone, *J. Geophys. Res.*, 90, 6793-6800.

Winkler K.W. and Nur A., 1979, Pore fluid and seismic attenuation in rocks, *Geophys. Res. Lett.*, 6, 1-4.

Zamora M. and Poirier J.P., 1990, Experimental study of acoustic anisotropy and birefringence in dry and saturated Fontainebleau sandstone *Geophysics*, 55, 1455-1465.

blank page

# BOREHOLE WALL GEOMETRY ACROSS THE NOJIMA FAULT: BHTV ACOUSTIC SCANS ANALYSIS FROM THE GSJ HIRABAYASHI HOLE, JAPAN.

Bernard P. Célérier<sup>1</sup>, Philippe A. Pezard<sup>2</sup>, Hisao Ito<sup>3</sup>, Tsutomu Kiguchi<sup>4</sup>

<sup>1</sup> ISTEEM (Université Montpellier 2 - CNRS), cc57, 34095 Montpellier Cedex 5, France,  
*Bernard.Celerier@dsu.univ-montp2.fr;*

<sup>2</sup> CEREGE (CNRS), BP 80, 13545 Aix en Provence Cedex 4, France, *Pezard@cerege.fr.*

<sup>3</sup> Earthquake research Department, Geological Survey of Japan, Tsukuba, Ibaraki 305-8567, Japan,  
*g0193@gsj.go.jp.*

<sup>4</sup> Earthquake research Department, Geological Survey of Japan, Tsukuba, Ibaraki 305-8567, Japan,  
*kig@gsj.go.jp*

## ABSTRACT

The Borehole Televiewer acoustic scans in the Hirabayashi hole reveal a few deformed cross sections in an otherwise very much in gauge borehole. A recent interpretation suggests that slip on pre-existing fractures is one of the many possible causes that can lead to enlarged boreholes which is often overlooked. Given the dynamic context of the Nojima fault, we investigate such possibility by looking for offsets on irregular borehole cross sections that remain circular by piece. Only 37 locations satisfy these criteria, among which 24 are in the 1995 earthquake rupture zone (623-635 m depth). Each of these events is associated with a fault plane that intersects the borehole. The fault plane is identified on the BHTV image when possible, or on the FMI images when the acoustic reflectivity is low, as near the rupture zone. The fault slip vector can be inferred from the offset of the circular pieces of the borehole wall. In this preliminary analysis, interpretation of some of these borehole wall deformations can however be ambiguous. In a few cases, slip on a pre-existing fault plane may be confused with incipient breakouts or spalling around a pre-existing discontinuity. Further analysis of the detailed three-dimensional geometry of these deformations may help resolve such uncertainties.

## INTRODUCTION

The Geological Survey of Japan (GSJ) Hirabayashi borehole is drilled mainly within granodiorite and intersects the 1995 rupture zone of the Nojima fault at 623-625 m depth (Ito et al., 1996). The hole was drilled with a 11.43 cm (4.5 inches) drill bit, then logged with a suite of tools including a Borehole Televiewer (BHTV), then enlarged with a 15.88 cm (6.25 inches) drill bit and logged with the Formation Micro Imager (FMI) and Digital Sonic Imager (DSI).

Both BHTV and FMI logs provide detailed images of the borehole wall and precise diameter measurements (Fig. 1 and 2). The work presented here proposes to interpret some of the diameter anomalies shown in these measurements.

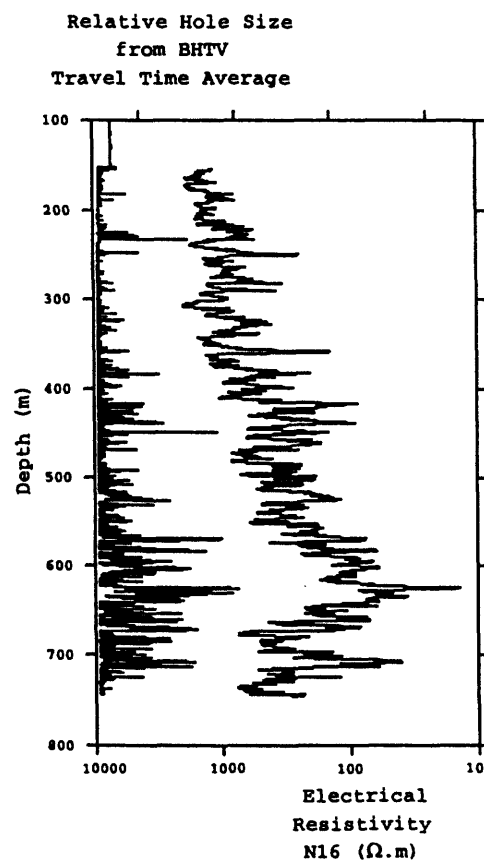


Figure 1. Left: relative hole size derived by averaging BHTV travel time for each scan. Note that these averages contain values that correspond to an absence of arrival detection, and therefore include some noise. Right: electrical resistivity from the N16 measurement. Note the correlation between hole enlargements and low resistivity.

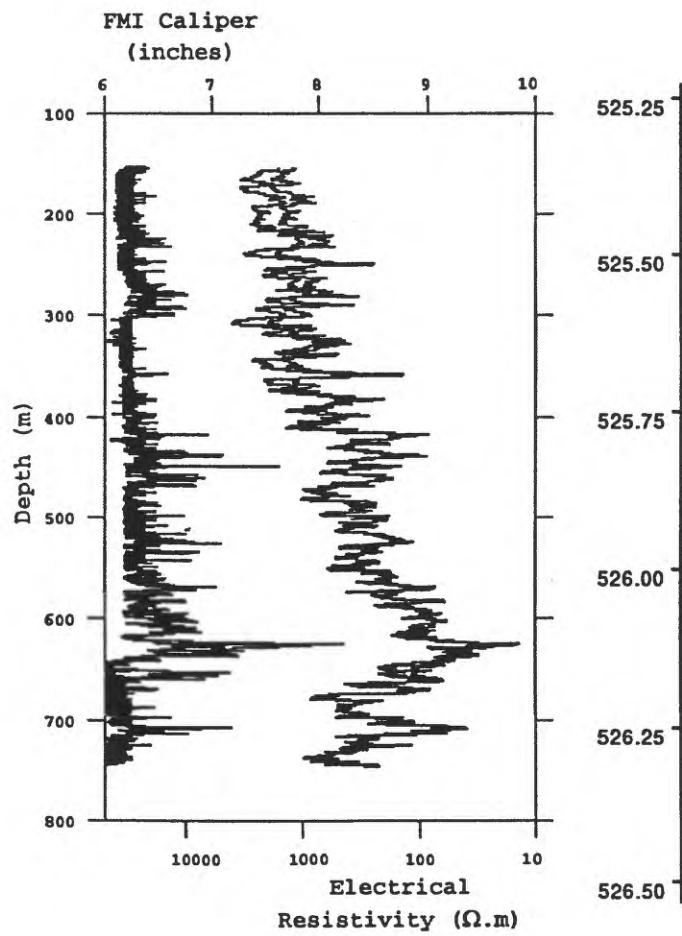


Figure 2. Left: hole diameter measured by FMI caliper C1 and C2. Right: electrical resistivity from the N16 and N64 measurements. Note the correlation between hole enlargements and low resistivity.

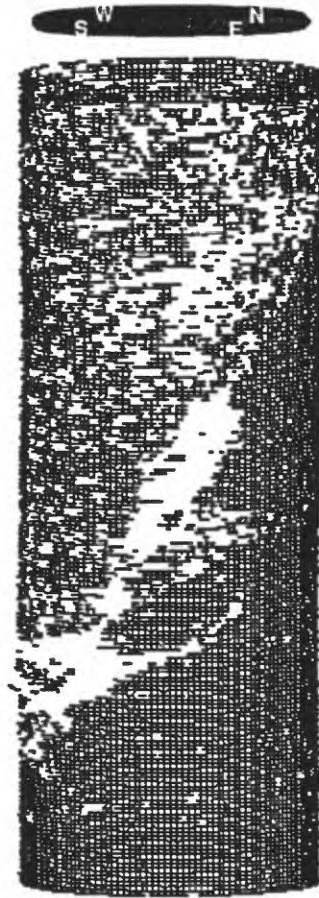


Figure 3. Perspective plot of BHTV travel time data around 526 m depth. Empty spots correspond to areas where no arrivals were detected by the tool resulting in a default high value of travel time. Note the numerous missing arrivals along a main SW dipping fractures as well as within the hanging wall.

## BOREHOLE SHAPE

These caliper measurements show that most of the borehole is in gauge and that the enlargements correlate with low electrical resistivities (Fig. 1 and 2), suggesting the presence of fractures and alteration (Pezard et al., this volume). This is usually confirmed by BHTV or FMI images, as shown for the enlargement at 526 m by the BHTV travel time data: a SW dipping fault is underlined by the absence of arrival detection (Fig. 3). This fault corresponds to low BHTV amplitude and is also visible on FMI images as a conductive feature. One can note an asymmetry between the hanging wall and the footwall, which is more reflective, and corresponds to higher borehole wall impedance.

## INTERPRETATION OF ENLARGEMENTS

It has recently been realized that slip on a pre-existing fault need to be considered among the numerous causes that can lead to borehole enlargements (Heliot et al., 1990; Maury and Sauzay, 1989; Maury and Etchecopar, 1992; Maury and Zurdo, 1994; Etchecopar et al., 1997; Cornet et al. 1997; Maury et al., 1999). According to this interpretation, a small amount of slip shears the cylindrical borehole resulting in a restriction (Fig. 4, left). If the slip occurs during drilling operations, the resulting restriction is reamed, often along the low side of the hole, and transformed in an elongation (Fig. 4, right).

The elongation resulting from a reamed sheared zone is not easily distinguishable from that resulting from other causes such as breakouts or spalling around fractures. To differentiate these causes requires the high-resolution diameter measurements provided by the BHTV. In the case of shear, the borehole cross section should be composed of arcs of circles with same diameter but different centers. The center offset is the component of slip perpendicular to the borehole axis.

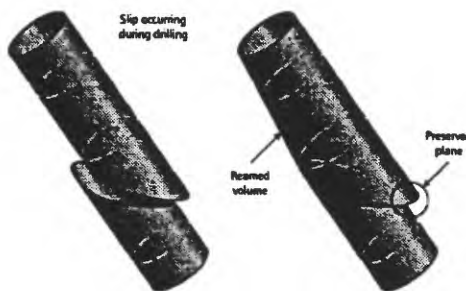


Figure 4. Borehole sheared by slip on a fault (after Etchecopar et al., 1997). Left: geometry after slip resulting in restriction. Right: geometry after reaming resulting in an elongation. The reaming is usually associated with the drill bit cutting its way out of the hole.

## APPLICATION TO THE HIRABAYASHI BOREHOLE

To check for possible slip in the borehole, we analyzed BHTV travel time cross sections built by stacking up to three consecutive acoustic scans. In normal, "in gauge" intervals, these cross-sections are circular (Fig. 5). A complementary representation, called the telescopic view, plots consecutive acoustic scans while reducing their size so as to create a downhole perspective (Fig. 6). This representation was proposed by Heliot et al. (1990) to verify the vertical continuity of intersected features. Fig. 5 and 6 show a surprisingly undeformed borehole located around 50 cm vertically above, i.e. around 5 cm in distance from, the 1995 main rupture plane.

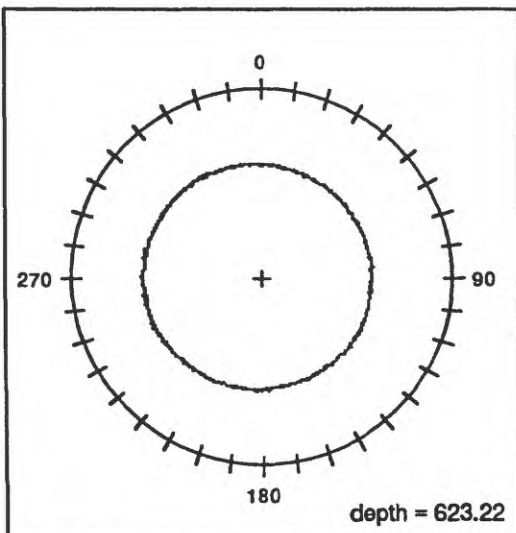


Figure 5. BHTV travel time cross section. Three consecutive acoustic scans are stacked.

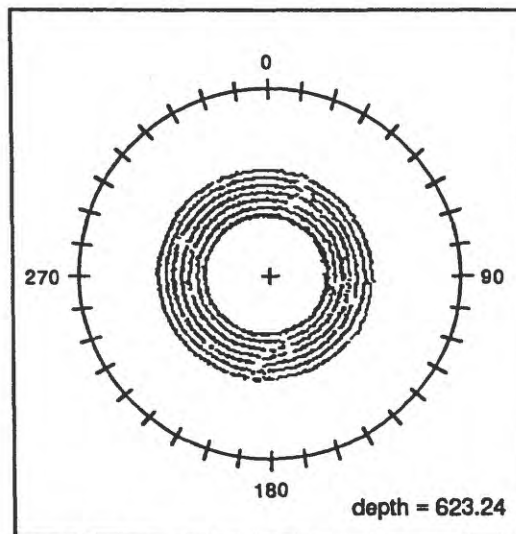


Figure 6. BHTV travel time telescopic cross section. Seven consecutive acoustic scans are presented.

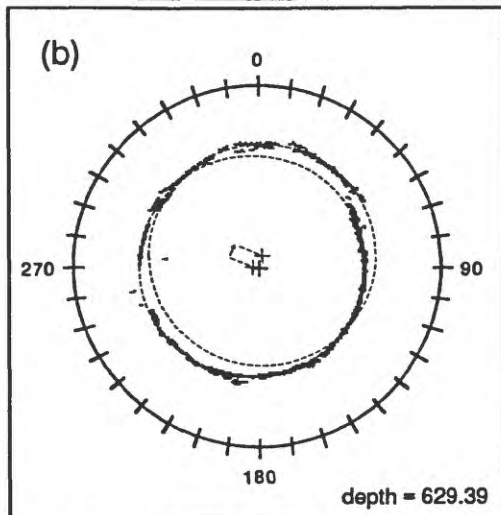
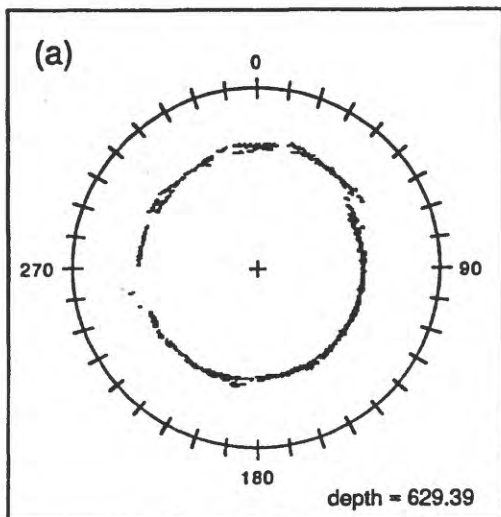


Figure. 7. BHTV travel time cross section. (a) Raw data. (b) Interpretation in terms of shear displacement. The circles centers offset represents the horizontal component of slip.

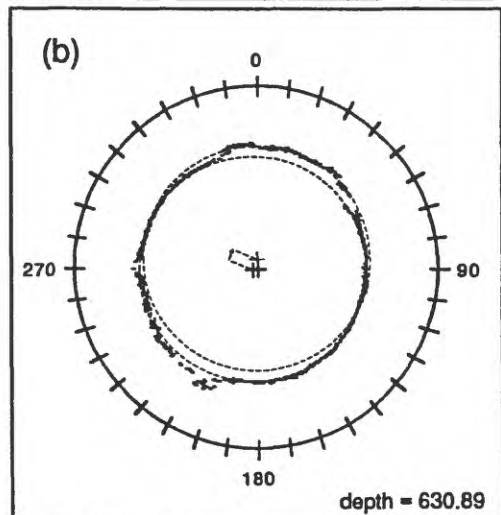
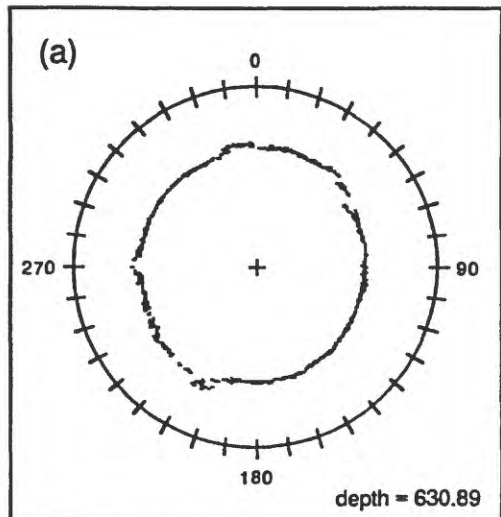


Figure. 9. BHTV travel time cross section. (a) Raw data. (b) Interpretation in terms of shear displacement. Note that an alternate interpretation in terms of incipient breakout is possible.

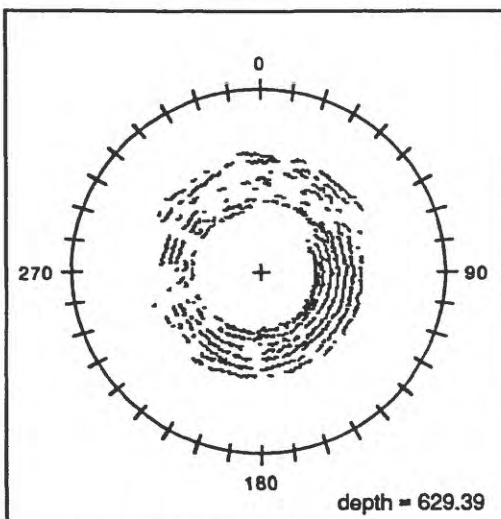


Figure. 8. BHTV travel time telescopic cross section.

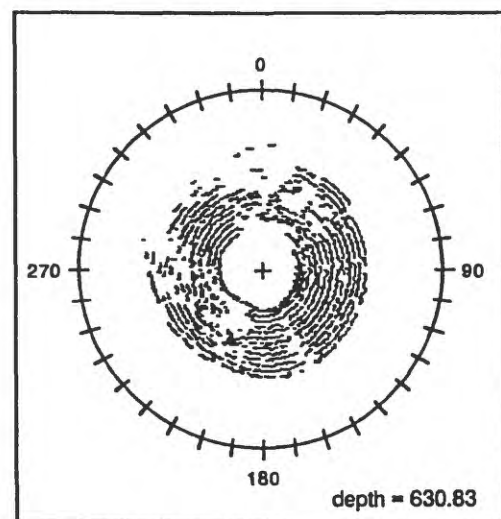


Figure. 10. BHTV travel time telescopic cross section.

An example of anomalous cross section is found a few meters below, within the fault zone, at a depth of 629.39 (Fig. 7). The borehole is elongated in the NE direction in relation with a NE offset of the borehole wall (Fig. 7a). If a circle of diameter equal to that of the drill bit is superposed to the cross section, it fits only part of the data (Fig. 7b). A second offset circle is required to fit the data in the NE quadrant. The offset between the two circle centers represents the horizontal component of the inferred slip vector. The fault plane, which is identified either on the BHTV or on the FMI images, is striking NE and dipping SE so that the displacement is mainly strike-slip. The inferred fault plane and displacement are therefore consistent with that of the large-scale main fault zone (Ito et al., 1996). The telescopic view shows that this offset is continuous vertically (Fig. 8). However this telescopic view also shows that the data are sparse because the low reflectivity of irregular wall makes the arrival time detection difficult.

A more ambiguous situation arises 1.5 m below: the elongation becomes symmetrical and suggests either strike-slip on a similarly oriented plane or incipient breakout in the NE direction (Fig. 9 and 10). This second interpretation would be consistent

with the stress directions inferred from breakout observations in the Ikuha borehole (Ito et al., 1997). The elongation is also subparallel to the main fault strike but the FMI images show that, if the 627-634 depth interval displays numerous NE striking and SE dipping faults, none dips more than 60°, which makes them distinct from the 84° dip of the main fault.

This analysis revealed 37 locations where elongations could be interpreted as possible shear zones (Fig. 11): 12 locations in the hanging wall of the main fault, 24 locations within the fault zone between 623 and 635 m (Fig. 12) and one location in the footwall. The corresponding fault plane orientations are varied but dominated by a trend with a NE strike, which is similar to that of the main fault, and a 50-70° dip, which is markedly lower than that of the main fault (Fig. 13 & 14).

The inferred slip directions show diverse type of movements (Fig. 13 & 15) that are not compatible with a single homogeneous stress system. The slip direction, however, is determined from a small offset vector (Fig. 7b) and is therefore sensitive to small errors. Direct numerical computations of the offset vectors from the data are expected to improve the precision.

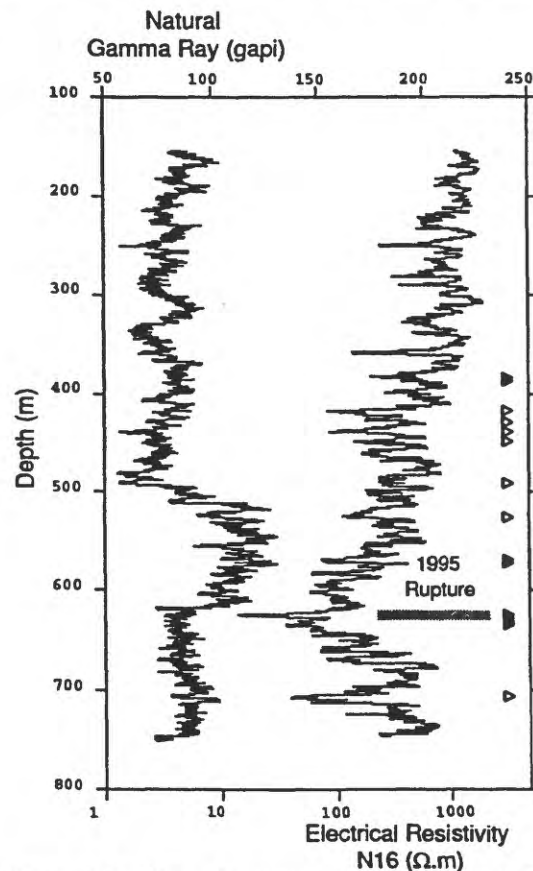


Figure 11. Natural gamma ray, N16 resistivity measurement and location of possible borehole shear zones (triangle symbols).

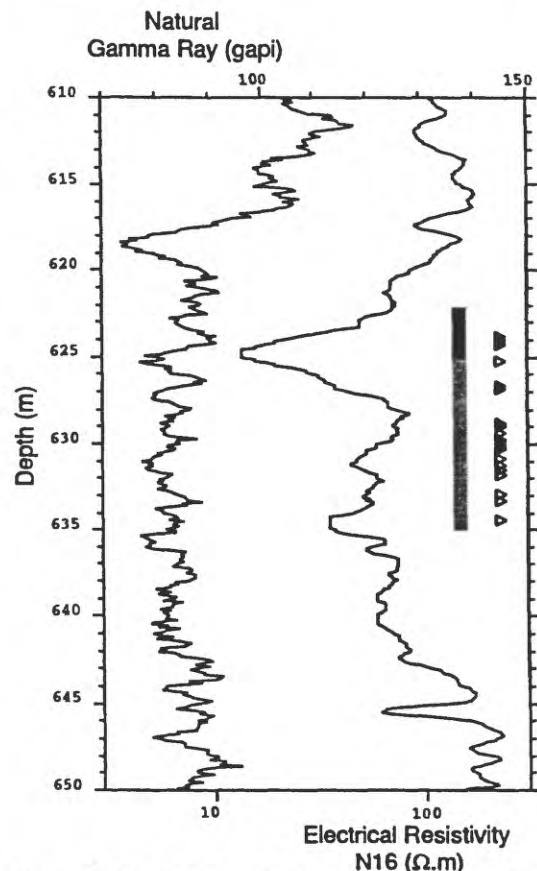


Figure 12. The Nojima fault zone. The main fault zone is marked by the grey bar and the gouge by the black bar. Natural gamma ray, N16 resistivity measurement and location of possible borehole shear zones (triangle symbols).

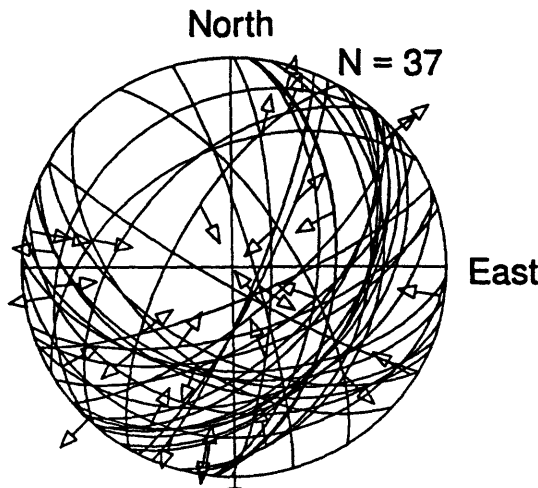


Figure 13. Stereographic projection of the inferred fault planes and slip vectors. Equal area Schmidt projection of the lower hemisphere.

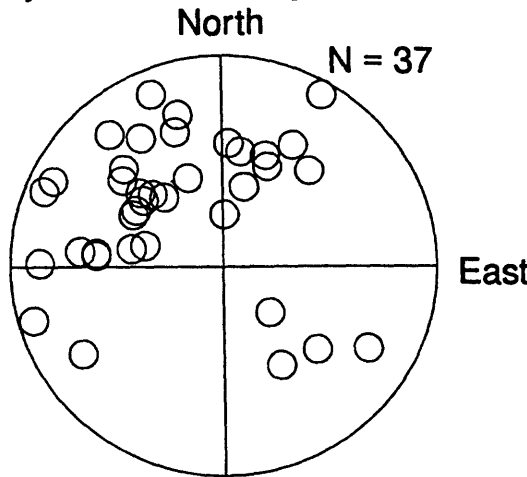


Figure 14. Stereographic projection of the poles of the inferred fault planes. Equal area Schmidt projection of the lower hemisphere.

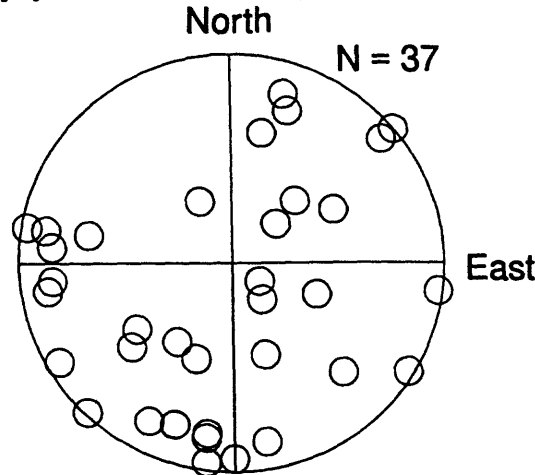


Figure 15. Stereographic projection of the inferred slip vectors. Equal area Schmidt projection of the lower hemisphere.

## CONCLUSIONS

The walls of the GSJ Hirabayashi borehole shows offsets associated with elongations that can be interpreted as the result of slip on pre-existing fault planes. However this interpretation is neither unique nor unambiguous at this point. A more quantitative analysis of the geometry of the wall, such as determination of radius of curvature and of vertical extent may help clear some of the present ambiguities.

## ACKNOWLEDGMENTS

The BHTV analysis used the BHTVImage2.2 software written by Colleen Barton (1995). This work was supported by the GdR FORPRO (contribution FORPRO 99/011 B).

## REFERENCES

Barton, C., 1995. BHTVImage, version 2.2, software.

Cornet, F.H., Helm, J., Poitrenaud, H. & Etchecopar, A. 1997. Seismic and aseismic slips induced by large-scale fluid injections. *Pure and applied geophysics*, **150**, 563-583.

Etchecopar, A., Cheung, P., Cesaro, M. & Gonfalini, M. 1997. Shaping up to stress in the Appenines ITALY 2000. In: *Value added reservoir characterization*.

Héliot, D., Etchecopar, A. & Cheung, P. 1990. New developments in fracture characterisation from logs. In: *Rock at great depth* (edited by V. Maury and D. Fourmaintraux). Balkema, Rotterdam, 1471-1478.

Ito, H., Kuwahara, Y., Miyazaki, T., Nishizawa, O., Kiguchi, T., Fujimoto, K., Ohtani, T., Tanaka, H., Higuchi, T., Agar, S., Brie, A., & Yamamoto, H., 1996. Structure and physical properties of the Nojima Fault. *Butsuri-Tansa*, **49**, 522-535.

Ito, H., Kuwahara, Y. & Nishizawa, O. 1997. Stress measurements by the hydraufracturing in the Hyogo-ken Nanbu earthquake source region. In: *International symposium on rock stress*, Kumamoto, Japan, 7-10 October 1997.

Maury, V.M. & Sauzay, J.M. 1989. Oil well collapse due to fault shearing: a case study and some comments. In: *Rock at great depth* (edited by V. Maury and D. Fourmaintraux). Balkema, Rotterdam, 871-880.

Maury, V.M. & Etchecopar, A. 1992. Shear induced by oil and gas wells drilling and production along faults and discontinuities. In: *International Geological Congress*, Kyoto, 1992.

Maury, V.M. & Zurdo, C. 1994. Wellbore instability due to shear displacements along preexisting fractures: are we overlooking a common cause of drilling problem? In: *IADC/SPE Drilling conference*, 1994. 553-562.

Maury, V.M., Etchecopar, A. & Pezard, P.A. 1999. New borehole imagery techniques: an aid for failure modes and in situ stress analysis and for minimizing drilling incidents. *SPWLA Transactions*, Oslo, Norway.

# STRESS STATE AROUND THE NOJIMA FAULT ESTIMATED FROM CORE MEASUREMENTS

Kiyohiko Yamamoto<sup>1)</sup>, Namiko Sato, and Yasuo Yabe

Graduate School of Science, Tohoku University, Sendai 980-8578, Japan

<sup>1)</sup>e-mail: [yama@aob.geophys.tohoku.ac.jp](mailto:yama@aob.geophys.tohoku.ac.jp)

## ABSTRACT

The Nojima earthquake fault in Awaji, Hyogo prefecture, Japan, ruptured accompanied by the 1995 Hyogo-ken Nanbu earthquake ( $M_{JMA}=7.2$ ). The *in-situ* stresses have been measured on boring core samples by deformation rate analysis (DRA) for the sites close to the fault, Hirabayashi (HRB), Toshima (TSM), and Ikuha (IKH). HRB and TSM locate along the fault segment of large dislocation observed on the ground. IKH is near the southern end of the buried fault extended from the earthquake fault. The stresses have been obtained for 343 and 350m depth of HRB, 310, 312, and 415m depth of TSM, and 5 depths from 351 to 720m of IKH. The stresses show strike-slip regime for all the sites, although the compression is predominant at TSM. The maximum horizontal stress lies in NW-SE direction at HRB and TSM. The direction rotates counterclockwise by about 120° at IKH with an increase in depth from 544m to 720m. The direction at 720m in depth is identical to that of the other sites. These directions are almost perpendicular to the fault plane. Since DRA is based on the rock property of long-term memory of stress, this result implies that the friction coefficient of fault is small even before the earthquake. The NW-SE direction is close to the direction of the largest contraction during about 100 years for the Osaka bay area adjacent to the fault. Defining  $r$ -value as the maximum shear stress divided by the normal stress on the maximum shear plane, the value is large at TSM and small at HRB. The reason for the small  $r$ -value at HRB is inferred to be the small distance of the measuring points from the fault plane that is about 50m.

## INTRODUCTION

The Byerlee's law for frictional strength states that frictional sliding and/or slip occurs when shear stress on a fault plane exceeds the frictional strength, which

is determined by the normal stress and the coefficient of friction for the fault plane (Byerlee, 1978). The law was established by laboratory experiments performed on the faults simulated in rock specimens. When fracturing or sliding occurs on a simulated fault, shear stress drop takes place uniformly in the specimen and the strain energy in the specimen probably decreases. Therefore, it is reasonable to consider that the law holds on the condition that applied shear stress decreases by failure. The seismogenic field, for example the earth's crust, appears to be infinite in size, while the faulting or the shear fracture to generate an earthquake occurs in an area of finite size. If the shear fracture or the sliding occurs in the crust on the condition that the average stress in the crust is invariable with the fracture, the fracture may make the stress field more non-uniform and the strain energy in the crust increase. These circumstances appear to be different from that for laboratory experiments. It is thus one of the problems if the faulting in the crust can be represented in terms of the Byerlee's law. The solution may be obtained by field observations.

According to the Byerlee's law, the coefficient of friction is about 0.85 for small normal stress to the fault plane and about 0.60 for larger normal stress. The strength of intact rock specimens for stress of compression is approximately represented by the Coulomb criterion. The criterion is represented to be the sum of cohesion force and the frictional strength that is the product of the internal friction coefficient and the normal stress to the fault plane, provided that the plane is formed when the specimen fractures. Here, the frictional strength is called the internal frictional strength for discrimination from the frictional strength for simulated faults. The internal friction coefficient has the magnitude of 0.5 – 1.5 (e.g. Paterson, 1978). The internal frictional strength is thus almost comparable in magnitude to the frictional strength. This means that the strength of intact rock specimens is larger only by the amount of cohesive strength. It is known further that the strength of intact rock de-

creases with an increase in specimen size (e.g. Pratt *et al.*, 1972). Therefore, if the frictional strength did not decrease with an increase in specimen size, the frictional strength for faults would exceed the shear strength of intact rocks. For this reason, it should be considered that the frictional strength or the friction coefficient is variable as well as the strength of intact rock specimens (Yamamoto, 1999).

There may be three problems that should be investigated by stress measurement in field. One of them is to reveal the conditions for faulting in the crust or earthquake occurrence imposed on the stress field. Another is to clarify whether or not the value of the friction coefficient obtained for the simulated faults can be taken as that for faults in nature. The other is to clarify the role of faults on forming the stress field in the crust. Although there are not sufficient number of data, Yamamoto *et al.* (1998) has briefly discussed on the first problem. The second is the basic problem, which has been discussed in comparison with the results of laboratory experiments. The last problem may be important for the discussions on the formation of 'stress provinces' and 'characteristic earthquakes', because small friction coefficient of fault can de-couple the stress fields of the blocks on both sides of a fault. This paper is rather focusing on the last two problems.

Hydraulic fracturing measurements of stresses in the Cajon Pass Research Bore-hole close to the San Andreas Fault has shown that the direction of the largest horizontal stress is almost perpendicular to the fault strike (e.g. Zoback and Healy 1992). This means that the frictional stress of the fault is very small compared with that estimated from the friction coefficient in laboratory experiment. Many researchers have tried to explain the smallness of the frictional strength by the reduction of effective normal stress due to pressurized fluid around the fault. Coyle and Zoback (1988) have found however that pore fluid pressure in the fractured rock mass drilled at Cajon Pass is very close to hydrostatic. This may imply that it is possible for friction coefficients to have magnitudes much smaller than 0.6. The number of the data is not sufficient to conclude that the small friction coefficient is not unusual. It is thus the problem today to increase the number of data for *in-situ* stress near faults.

Yamamoto H. *et al.* (1990) measured *in-situ* stresses by deformation rate analysis (DRA) in the vicinity of the inferred fault of the 1984 Nagano-ken Seibu Earthquake, which is a shallow intraplate earth-

earthquake of  $M_{JMA}=6.8$ . DRA has been proposed as a method to measure *in-situ* stresses on rock specimens in laboratories (Yamamoto *et al.*, 1990; Yamamoto, 1995). This method is based on the rock property of *in-situ* stress memory briefly explained in the next section. From the measurement, the followings have been suggested: 1) The relative shear stress, that is the maximum shear stress divided by the normal stress on the maximum shear plane, can be taken as an index of potential for earthquake occurrence. 2) There are the areas in the vicinity of faults where shear stress concentrates and stress field around a fault is highly non-uniform. 3) The relative shear stress closely correlates to the thermal state of the sites. However, the friction coefficients for the fault were not determined, because the cores were not oriented.

The Hyougo-ken Nanbu earthquake of  $M_{JMA}=7.2$  occurred January 17, 1995. The Nojima fault and the Ogura fault in Awaji, Hyougo prefecture, were ruptured accompanied by the earthquake (Awata *et al.* 1996). These two faults altogether are called the Nojima earthquake fault, here. Immediately after the earthquake, Kyoto University (UNV), Geological Survey of Japan (GSJ), and National Research Institute for Earth Science and Disaster Prevention (NIED), respectively, conducted the drillings at Toshima, Ikuha, Hirabayashi, and some sites close to and near the fault. Yamamoto *et al.* (1998) and Sato *et al.* (1999) measured the stresses by DRA on the cores of two depths at Hirabayashi (GSJ), three depths at Toshima (UNV) and five depths at Ikuha (GSJ). This paper will review their results. It has been known that the stresses can be determined by DRA even from the rock specimens recovered from a few years ago (e.g. Yamamoto *et al.* 1997). For the reason, the measured stresses in the present paper are expected to be the stresses before the earthquake.

## METHOD OF STRESS MEASUREMENT

### DEFORMATION RATE ANALYSIS

The property of stress memory is found in inelastic strain behavior of rock specimens under uni-axial loading of compression. According to Kuwahara *et al.* (1990), the change in micro-fracturing activity produces the change in the increasing rate of inelastic strain. When the rate change reflects the stress that has been previously applied to the specimen, the change is generally called the memory of the previous stress or the stress memory. The rate change is detected by us-

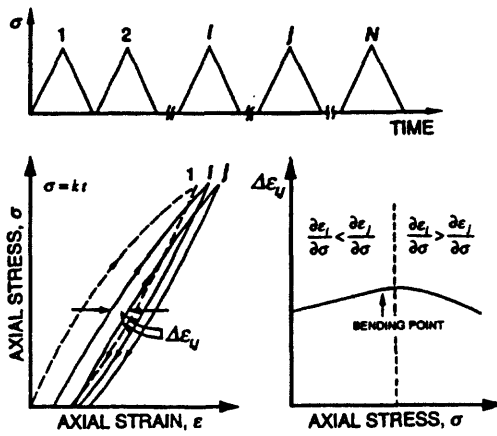


Figure 1. Schematic illustration for DRA. The upper figure shows the loading history for the detection of stress memory. The lower figure illustrates the definition of strain difference function  $\Delta\epsilon_{j,i}(\sigma)$  and the bending point.

ing the strain difference function  $\Delta\epsilon_{j,i}(\sigma)$  obtained by cyclic loading of compression to a specimen. The function is defined by

$$\Delta\epsilon_{j,i}(\sigma) = \epsilon_j(\sigma) - \epsilon_i(\sigma), \quad j > i, \quad (1)$$

Here,  $\epsilon_j(\sigma)$  is axial strain of a specimen at an applied stress  $\sigma$  for the  $j^{\text{th}}$  loading. The strain difference function mainly represents the difference in inelastic strain between the  $i^{\text{th}}$  and the  $j^{\text{th}}$  loading. When contraction and compression are defined to be positive in sign, negative derivative of  $\Delta\epsilon_{j,i}(\sigma)$  with respect to  $\sigma$  means that inelastic strain rate is larger in the  $i^{\text{th}}$  than in the  $j^{\text{th}}$  loading. Strain difference function is schematically illustrated in Fig. 1. Bending point means the point in the function at which the continuous decrease in its derivative starts. Bending stress is the axial stress at the bending point. Especially when the bending point is observed as the stress memory, the bending stress is called the memory stress.

The followings have been confirmed for the stress memory observed for the specimens from core samples: The magnitudes of the bending stress can be taken as the *in-situ* stress magnitudes, where *in-situ* stress means the normal component of *in-situ* stress in the direction of loading axis. *In-situ*

stress memory is detected in the strain difference functions from the pair of loading cycles after the first cycle in most cases. On the basis of this result, uni-axial loading of four or five cycles is performed on each specimen for DRA. Yamamoto (1995) has shown that the property of *in-situ* stress memory is explained by assuming that stress field in rocks is the most uniform under the *in-situ* stresses. The property of *in-situ* stress memory should be discriminated from the Kaiser effect.

#### MEASUREMENT OF STRAIN

Specimens used for the stress measurement are of rectangular prism in shape of about  $15 \times 15 \times 38$  (mm) in size. They are sawed in the vertical and the four horizontal directions at an interval of  $45^\circ$  from boring cores, as shown in Fig. 2. Uni-axial stress of compression is cyclically applied in the direction of the longer axis for DRA. The loading is performed at a constant stress rate between 3 and 5 MPa a minute using a servo-controlled apparatus. The peak applied-stress is usually taken to be 1.5 to 2.5 times of the target memory stress. Bending point is generally identified by eye as the point that shows the largest bend or the fold in a strain difference function. The bend can be not always uniquely fixed. The measurement is repeated on the same specimen or on the different ones of the same direction to fix the identification. If the bending points for horizontal specimens are correctly identified as the *in-situ* stress memory, the dependence of the bending stresses should be expressed by a sinusoidal function

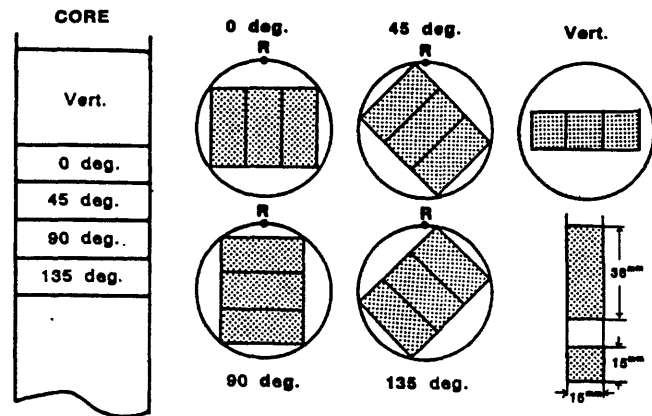


Figure 2. Orientation of specimens in a core sample. Specimens are sawed out of a core sample in order that their longer axes respectively direct to the vertical and one of the four horizontal directions at an interval of  $45^\circ$  in general.

of azimuth as follows;

$$\sigma_0(\theta) = (\tau_{xx} + \tau_{yy})/2 + (\tau_{xx} - \tau_{yy})\cos 2\theta/2 + \tau_{xy}\sin 2\theta \quad (2)$$

where  $\sigma_0(\theta)$  is the bending stress or the normal component of *in-situ* stress to the plane perpendicular to the loading direction,  $\theta$  is the azimuth and  $\tau_{xx}$ ,  $\tau_{yy}$ , and  $\tau_{xy}$  are *in-situ* stress components when  $x$  and  $y$  axes are taken in a horizontal plane. The distribution of horizontal stress for azimuth expressed by (2) is used as an additional condition to determine the bending point, especially when the bending stress cannot be determined only from the specimens of the same azimuth.

The maximum and the minimum horizontal stress are obtained by fitting the sinusoidal function  $\sigma_0(\theta)$  expressed by (2) to the bending stresses observed for the horizontal specimens. A parameter  $r$  is defined by assuming that one of the principal direc-

$$r = (\sigma_1 - \sigma_3)/(\sigma_1 + \sigma_3)$$

tions is in the vertical as follows;

where  $\sigma_1$  and  $\sigma_3$  are the largest and the smallest principal stress of compression. Usually, the frictional strength of a surface increases proportionally to an increase in the normal component of stress on the surface. Thus,  $r$  may be thought as an index of the potential for frictional sliding. The parameter  $r$  is here called relative shear stress. In the present paper,  $r$  is used to characterize the stress field in relation to seismic activity and earthquake occurrence.

## STRESSES NEAR THE FAULT

### SITES AND SPECIMENS

The 1995 Hyogo-ken Nanbu earthquake ( $M_{JMA}=7.2$ ) exposed surface rupture more than 10 km long along the Nojima earthquake fault (Awata, *et al.*, 1996). The stress measurements were performed on cores recovered from the holes at Hirabayashi, Toshima and Ikuha close to the fault system (see Fig. 5). Hirabayashi (HRB) is located in the central part of the Nojima fault, where the largest surface displacement is observed. Toshima (TSM) is located near the southern end of the surface rupture exposed along the fault. The surface rupture was not found around Ikuha (IKH). Ikuha is located about 1 km southeast from the Mizukoshi flexure on the line extended from the Ogura fault. According to Satoh and Sugihara (1995), the buried fault has reached near the site. The site is inferred to be a few kilometers northeast from the end of

Table 1 Rock types and Young's moduli of specimens (After Sato *et al.*, 1999).

Site	Depth m	Rock type	E GPa
HRB	343	granodiorite	46.1±6.7
	350	granodiorite	47.2±4.8
TSM	310	granodiorite	82.5±2.6
	312	granodiorite	78.5±2.8
IKH	415	granodiorite	70.2±3.8
	351	granodiorite	61.3±5.4
IKH	465	porphyrite	32.1±2.0
	544	granodiorite	34.6±4.4
	639	granodiorite	10.8±1.2
	720	porphyrite	52.4±4.8

Young's modulus is determined from the axial stress at  $10^{-4}$  in axial strain.

the buried fault, referring to the fault estimated from the geodetic and seismological data (*e.g.* Yoshida *et al.*, 1996; Wald, 1996).

The sampling points, that is, the sites and the depths, are shown in Table 1 together with rock type and Young's modulus of specimen. The points are at a distance from the fault surface smaller than 50m for HRB and at a distance more than 200m for TSM. The distance is not clear for IKH. The value of  $E$  in the table demotes the Young's modulus averaged over the specimens of the depth. Each modulus is calculated from the axial stresses at 0 and about  $100\times 10^{-6}$  in axial strain on loading. The Young's modulus at 639 m depth at IKH is very small. It is inferred that there is fracture zone around the depth (Personal communication, Ito and Kuwahara). This small Young's modulus seems to be in relation to the fracture zone.

### VERTICAL STRESSES

Fig. 3 shows the strain difference functions measured on the two vertical specimens of 351 m depth of IKH (IKH351). The notation  $(i, j)$  stands for  $\Delta_{ij}(\sigma)$ . S11 and S21 mean the 1<sup>st</sup> measurement on the specimens No. 1 and No. 2. The bending points we have chosen are marked with arrows. Although the behavior of the strain difference functions is different between the two specimens, the bending points are found at almost the same axial stress of about 9.0 MPa. This stress corresponds to the overburden pressure calculated for about  $2.6\times 10^3$  kg/m<sup>3</sup> in the density of overburden rocks.

The bending stresses at other sites have been determined by the similar way. The vertical stresses thus determined at all the sites are shown in Fig. 4. The lines in the figure show the relation of overburden pressure to depth calculated for the assumed densities

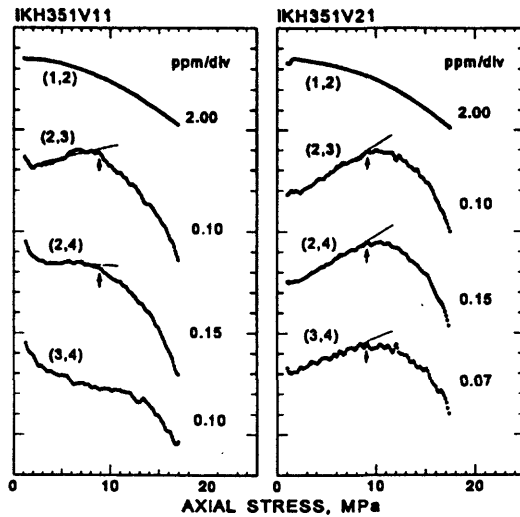


Figure 3. The records of strain difference functions  $\Delta\epsilon_{i,j}(\sigma)$  for the vertical specimens 351m depth of IKH. The notation  $(i, j)$  stands for  $\Delta\epsilon_{i,j}(\sigma)$ . Sensitivity of strain is indicated near each curve in  $10^{-6}$  a division (ppm/div).

of overburden rocks indicated in the figure. The linear relation best fitted to the data is obtained for  $2.55 \pm 0.10 \times 10^3 \text{ kg/m}^3$  of the average density of overburden rocks. This value seems to be suitable for the rocks around the sites. This result suggests the deviations of the data are estimated to be about 5 %.

#### HORIZONTAL STRESSES

The bending stresses are determined by the same way for the determination of the vertical stresses. When the determination is difficult for a direction, the determination is performed on the condition that the horizontal stresses are represented by a sinusoidal function, as described before. The bending stresses are thus determined. The largest and the smallest horizontal stress

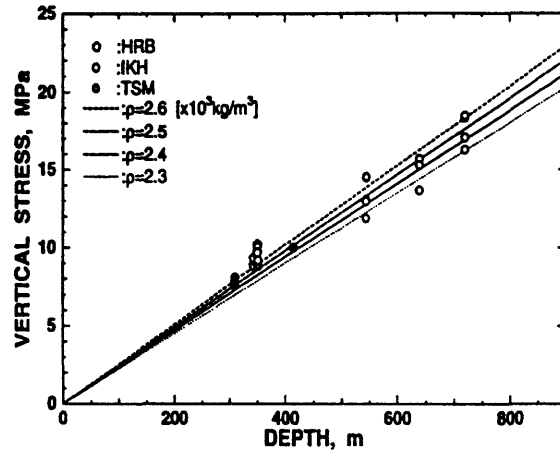


Figure 4. Relationship between the bending stresses read for the vertical specimens and the sampling depth of the specimens. (Data after Yamamoto *et al.* (1998) and Sato *et al.* (1999)).

of compression are obtained by fitting the function of (2) to the relation of the bending stress to the azimuth. The largest and the smallest horizontal stress thus obtained are listed in Table 2.

#### Stress Change in Depth Direction

The directions  $\theta_{h\max}$  for the largest horizontal stress of compression are shown in Fig. 5 by arrows. The largest and the smallest horizontal stresses ( $\sigma_{h\max}$  and  $\sigma_{h\min}$ ) at IKH are plotted for depths in Fig. 6. Sato *et al.* (1999) have pointed out that the direction  $\theta_{h\max}$  rotates counterclockwise by about 120° while the depth increases from 544m to 720m at IKH. The direction  $\theta_{h\max}$  is approximately along the fault strike for shallow depth and nearly perpendicular to the strike for larger depth. This direction of NW-SE at the larger depth is almost identical to that reported by Ito *et al.*

Table 2. The vertical stress  $\sigma_{\text{vert}}$ , the largest and the smallest horizontal stress,  $\sigma_{h\max}$  and  $\sigma_{h\min}$ , together with the azimuth for the largest horizontal stress  $\theta_{h\max}$ , measured by Yamamoto *et al.* (1998) and by Sato *et al.* (1999).  $r$  means relative shear stress. See text for the definition of  $r$ .

Site	Depth m	$\sigma_{\text{vert}}$ MPa	$\sigma_{h\max}$ MPa	$\sigma_{h\min}$ MPa	$r$	$\theta_{h\max}$ (N°E)
IKH	351	$9.0 \pm 0.2$	$13.9 \pm 0.5$	$7.1 \pm 0.5$	0.32	$73.7 \pm 1.4$
	465		$14.3 \pm 0.5$	$6.8 \pm 0.5$	0.36	$80.0 \pm 1.1$
	544	$13.1 \pm 1.0$	$15.1 \pm 0.6$	$6.7 \pm 0.6$	0.39	$41.7 \pm 2.7$
	639	$14.9 \pm 0.9$	$16.9 \pm 0.6$	$11.7 \pm 0.6$	0.18	$159.7 \pm 4.3$
	720	$17.8 \pm 0.6$	$20.5 \pm 0.9$	$14.0 \pm 0.9$	0.19	$133.5 \pm 3.2$
TSM	310	$7.8 \pm 0.2$	$17.1 \pm 0.4$	$5.34 \pm 0.4$	0.54	(* $\pm 0.8$ )
	312	---	$16.7 \pm 0.6$	$6.8 \pm 0.6$	0.42	$113.3 \pm 1.3$
	415	$10.1 \pm 0.0$	$18.6 \pm 0.5$	$6.3 \pm 0.5$	0.49	$139.4 \pm 0.8$
HRB	343	$9.0 \pm 0.3$	$11.6 \pm 0.5$	$7.8 \pm 0.5$	0.20	$153.5 \pm 3.4$
	350	$9.7 \pm 0.3$	$11.0 \pm 0.5$	$7.2 \pm 0.5$	0.21	$146.5 \pm 5.1$

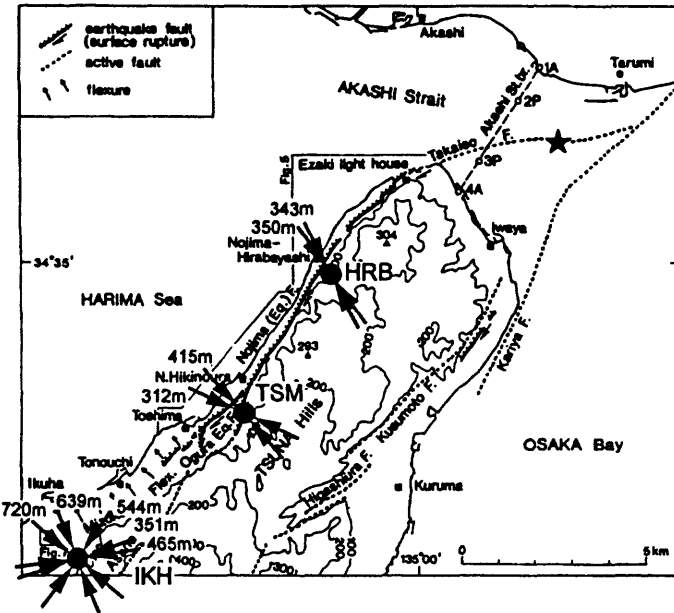


Figure 5. The location of the sites for the stress measurements plotted on the map by Awata *et al.* (1996). Arrows show the directions of the largest horizontal stresses (Yamamoto *et al.*, 1998; Sato *et al.*, 1999).

(1997) and to that for the other sites. Sato *et al.* further have found that  $\sigma_{h\max}$  and  $\sigma_{h\min}$  are almost constant without regards to depth and  $\sigma_{h\max}$  for the shallow depth are almost equal to  $\sigma_{h\min}$  at larger depths, as seen in Fig. 6. As stated before, it is inferred that there is fracture zone around the depth. The rotation of  $\theta_{h\max}$  and the continuity of  $\sigma_{h\max}$  for small depth to  $\sigma_{h\min}$  for large depths may be explained by assuming the near vertical fracture zone between the upper and the lower block, of which the strike lies along the direction of the largest horizontal stress of the upper block and the friction coefficient is very small.

The stresses in Table 2 show that TSM is in the strike-slip regime, but compression is predominant. The *r*-values more than 0.4 are large comparably to those at some sites in the focal region of the 1984 Nagano-ken Seibu earthquake (Yamamoto H., *et al.*, 1994). Tsukahara *et al.* (1998) performed hydraulic fracturing measurement at two depths near 1,500m. The stresses at the depths are of almost pure strike-slip. The *r*-values of about 0.16 at the depths are very small compared with those at small depths by DRA. They proposed the stress drop due to faulting as one of the explanations for this difference. Ikeda *et al.* (1998) carried out hydraulic fracturing measurement in a hole near HRB drilled by NIED (HRB<sub>NIED</sub>). Their meas-

urement revealed that the site is in the reverse fault regime, although the largest horizontal stresses for depths of about 300 m and 400m appear to be close to those at TSM. The *r*-values of about 0.3 for depths smaller than 850 m appear moderate. On the other hand, the small *r*-values have been obtained at depths near 1,200m similarly to the large depths at HRB<sub>NIED</sub>.

Sato *et al.* (1999) recently obtained the stresses by DRA for the depths about 350m at HRB. The stresses are characterized with the strike slip regime and the relatively small *r*-values. These characteristics are different from those for shallow depth at HRB<sub>NIED</sub>. The small *r*-value may be caused not by the stress drop due to faulting, because the small values by DRA are considered to be for the stresses before the earthquake. The characteristics seem to be rather similar to those of the stresses at larger

depths of other sites. The HRB hole locates at a distant of about 100m, while HRB<sub>NIED</sub> at a distance of about 300 m on ground surface. Referring to the trajectories of the boreholes in relation to the fault for HRB, HRB<sub>NIED</sub>, TSM, respectively, given by Ito

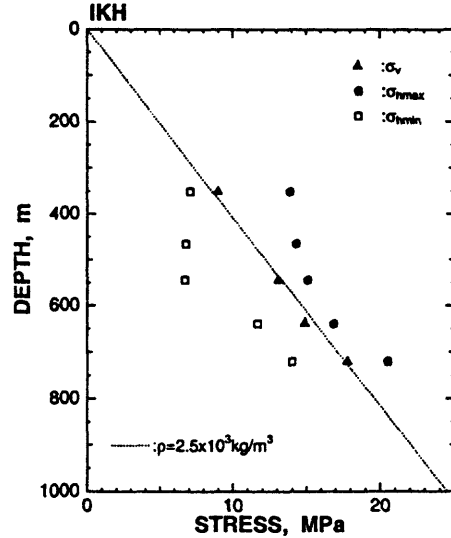


Figure 6. The changes in the vertical, the largest and the smallest horizontal stress with depth at IKH (Data after Sato *et al.*, 1999).

(1996), Ikeda *et al.* (1998), and Shimazaki *et al.* (1998), the characteristics appear to be of the points at a horizontal distance smaller than 100 m at largest from the fault surface (Sato *et al.*, 1999). Therefore, the small magnitude of shear stress may be one of the characteristics of the stress state in fault zone.

#### *Stresses along The Fault*

The directions  $\theta_{h\max}$  are shown in Fig. 5. The depths of the measurement are denoted near the respective arrows. Their directions approximately lie along the NW-SE except for shallow depths of IKH. The directions are almost perpendicular to the fault strike as has been observed at Cajon Pass near the San Andreas Fault. Since the fault surface is near vertical (Takemura *et al.*, 1997), the shear stress resolved on the fault surface may be very small. The friction coefficient is estimated to be not larger than 0.3 from the stresses for small depth at TSM by Yamamoto *et al.* (1998). The directions at HRB, which might be of the stresses in the fault zone, appear to resist the right lateral motion of the fault. This may also imply the small frictional stress on the fault. The directions determined by hydraulic fracturing technique are reported to lie in the NW-SE direction, too (Tsukahara *et al.*, 1998, Ikeda *et al.*, 1998). Referring to the horizontal strain between 1885 and 1985 observed by Geographical Survey Institute, Japan (Geographical Survey Institute, 1997), the direction  $\theta_{h\max}$  is nearly equal to that of the largest contraction of the Osaka bay area adjacent to the sites. This implies that the NW-SE direction for  $\theta_{h\max}$  has not been formed after the faulting. The stress may be governed by the tectonic situation even in the vicinity of the fault.

The direction  $\theta_{h\max}$  is approximately in the direction of the strike of the fault at small depths of IKH. The reason for this has not been clarified. One of the possible reasons is that the site is close to the end of the surface break. Unfortunately, there are no data to be compared with the results for shallow part at IKH.

The relative shear stress  $r$  is generally about 0.3 for the areas of moderate seismic activity (Yamamoto *et al.*, 1997). The value near 0.5 at TSM is very large compared with those of the areas, while the inferred friction coefficient is small. Yamamoto H. *et al.* (1990) obtained the values larger than 0.4 near the epicenter of 1984 Nagano-ken Seibu Earthquake ( $M_{JMA}=6.8$ ). The  $r$ -value at TSM together with that for 1984 Nagano-ken Seibu earthquake may imply that there are the areas in focal regions, where the  $r$ -value

is large independently of friction coefficient of fault.

#### **SUMMARY**

The Nojima earthquake fault in Awaji, Hyogo prefecture, Japan, has ruptured accompanied by the 1995 Hyogo-ken Nanbu earthquake ( $M_{JMA}=7.2$ ). The *in-situ* stresses near the fault have been measured by deformation rate analysis (DRA). This method is based on the rock property of *in-situ* stress memory of long term. Therefore, the method is expected to yield the stresses before the earthquake.

The measurements have been performed for 343 and 350m in depth at Hirabayashi (HRB), 310, 312, and 415m in depth at Toshima (TSM), and 5 depths from 351 to 720m at Ikuha (IKH) sites. HRB and TSM locate along the fault segment of large dislocation observed on the ground. IKH is near the southern end of the buried fault extended from the earthquake fault. The stresses show strike-slip regime for all the sites. However, the compression is predominant at TSM. The maximum horizontal stress lies in the NW-SE direction at HRB and TSM. The direction at IKH rotates counter-clockwise by about 120° with an increase in depth from 544m to 720m. The direction at 720m in depth is almost identical to that for the other sites. The NW-SE direction is almost perpendicular to the fault plane and is consistent with that obtained by hydraulic fracturing technique after the earthquake.

The estimated stresses are considered to be the stresses before the earthquake. The direction suggests thus that the friction coefficient of fault is small even before the earthquake. The direction of NW-SE is close to the largest contraction direction during about 100 years obtained for the adjacent area by the geodesic survey. The results support the concept that the fault is a preexisting weak plane and further seem to suggest that the fault plane orients as if to make the frictional stress on the plane small.

Defining  $r$ -value as the maximum shear stress divided by the normal stress on the maximum shear plane, the value is large at the depths smaller than about 500 m for the sites except for HRB. Taking account of the small  $r$ -values obtained for great depths of TSM and HRB<sub>NIED</sub> by hydraulic fracturing technique, it is inferred that the small  $r$ -value is not caused due to the depths of the measuring points but due to their small horizontal distance from the fault plane. The small  $r$ -values are obtained for the points at the distances of 100 m at largest from the fault plane,

while the other points are at the distances more than about 200 m.

**ACKNOWLEDGEMENT:** Prof. M. Ando, Kyoto University, provided this stress measurement in the program for the research of earthquake fault by drilling. Dr. K. Takemura, Kyoto University, prepared core samples for this measurement. Dr. H. Ito and Dr. Y. Kuwahara, Geological Survey of Japan, readily permit us to use the core samples of Ikuha and Hirabayashi for our measurement and further the discussions with them and the suggestions from them are very useful to prepare this manuscript. We have to thank all of them for their helpful support to this study.

We would like to express special thanks to Prof. Hirasawa, Tohoku University, for his suggestive comments and introductions on the problems included in the process of faulting.

#### REFERENCES

Awarta Y., K. Mizuno, Y. Sugiyama, R. Imura, K. Shimokawa, K. Okumura, and E. Tsukuda, 1996. Surface fault ruptures on the northwest coast of Awaji Island associated with the Hyogo-ken Nanbu Earthquake of 1995, Japan, *Zisin* 2, 49, 113-124 (in Japanese with English abstract).

Byerlee, J., 1978. Friction of rocks. *Pure and Appl. Geophys.*, 116, 615-626.

Geographical Survey Institute, 1997. The horizontal strain in Japan, 1994 - 1883, *Geographical Survey Institute* (Maps).

Coyle B.J., and M.D. Zoback, 1988. In situ permeability and fluid pressure measurements at ~ 2km depth in the Cajon Pass research well, *Geophys. Res. Lett.*, 15, 1,029-1,032.

Ikeda, R., Y. Iio, and K. Omura, 1998. Scientific drilling and in-situ stress measurements in the vicinity of active faults, *Chikyu Manthly*, Suppl. No. 21, 91-96 (in Japanese).

Ito, H., 1997. Structure and physical properties of the Nojima fault, *Proc. Symp. on Drilling Project of Faults*, (ed.) Shimazaki, Kyoto Univ., 37-59.

Ito, H., Y. Kuwahara, and O. Nishizawa, 1997. Stress measurements by the hydraulic fracturing in the 1995 Hyogoken-nanbu earthquake source region, In K. Sugawara and Y. Obara (ed.), *Rock Stress*, A. A. Balkema., 351-354.

Kuwahara, Y., K. Yamamoto, and T. Hirasawa, 1990. An experimental and theoretical study of inelastic deformation of brittle rocks under cyclic uniaxial loading, *Tohoku Geophys. J. (Sci. Rep. Tohoku Univ., Ser 5)*, 33, 1-21.

Paterson, 1978. *Experimental rock deformation-Brittle Field*, Springer-Verlag, pp. 254.

Pratt, H.R., A.D. Black, W.S. Brown, and W.F. Brace, 1972, The effect of specimen size on the mechanical properties of unjointed diorite, *Int. J. Rock Mech. Min. Sci.*, 9, 513 - 529.

Sato N., Y. Yabe, K. Yamamoto, and T. Hirasawa, 1999. Stresses at sites close to the Nojima earthquake fault estimated from core samples: III, *Prog. Abst. Seism. Soc. Japan*, 1999 Fall Meeting, C14. (in Japanese)

Satoh, T., and M. Sugihara, 1995. A GPS survey of triangulation points for crustal deformation associated with the 1995 southern Hyogo prefecture earthquake, *Chishitsu News*, No. 490, 41-43 (in Japanese).

Shimazaki, K., M. Ando, K. Nishigami, and N. Oshiman, 1998, Water injection test at Ogura site along the Nojima earthquake fault, *Chikyu Manthly*, Suppl. No. 21, 33-37 (in Japanese).

Takemura K., A. Murata, T. Miyata, A. Lin, and T. Sotoda, 1997 Description on the cores recovered by drilling, *Proc. Symp. on Drilling Project of Faults*, (ed.) Shimazaki, Kyoto Univ., 115-125 (in Japanese).

Tsukahara, H., R. Ikeda, and K. Yamamoto, 1998. *In-situ* stress measurement at points close to Nojima fault at the depths about 1500m -The maximum compressive stress perpendicular to the fault strike-, *Chikyu Manthly*, Suppl. No. 21, 66-69 (in Japanese).

Wald, D. J., 1997. Slip history of the 1995 Kobe, Japan, earthquake determined from strong motion, teleseismic, and geodetic data, *J. Phys., Earth*, 44, 489-503.

Yamamoto, H., K. Yamamoto, N. Kato, T. Hirasawa and Y. Iio, 1994. *In situ* stresses in the epicentral area of the Naganoken-Seibu earthquake of 1984 (II), *Prog. Abst. Seism. Soc. Japan*, 1990, No. 1, 24 (in Japanese).

Yamamoto K., 1995. The rock property of in-situ stress memory: Discussions on its mechanism. In Matsuki & Sugawara (eds.), *Proc. Int. Work Shop on Rock Stress Meas. at Great Depth*, Tokyo, 1995: 46-51.

Yamamoto, K., 1999. A model for fracturing process of intact rocks under axial loading of compression: The size-effect on strength for fracture of specimens, IUGG99, Birmingham, ST1/W12.

Yamamoto K., Kuwahara, N. Kato and T. Hirasawa, 1990. Deformation rate analysis: A new method for in situ stress estimation from inelastic deformation of rock samples under uni-axial compressions. *Tohoku Geophys. J (Sci. Rep. Tohoku Univ., Ser 5)*, 33: 127-147.

Yamamoto, K., H. Yamamoto, and Y. Yabe, 1997. Relation of in-situ stress field to seismic activity as inferred from the stresses measured on core samples, In K. Sugawara and Y. Obara (ed.), *Rock Stress*, A. A. Balkema, 375-380.

Yamamoto, K., Y. Yabe, and N. Sato, 1998, Stresses at sites close to the Nojima earthquake fault estimated from core samples: I, *Prog. Abst. Seism. Soc. Japan*, 1998 Fall Meeting, B13.

Yoshida, S., K. Koketsu, B. Shibasaki, T. Sagiya, T. Kato, and Y. Yoshida, 1996. Joint inversion of near- and far-field waveforms and geodetic data for the rupture process of the 1995 Kobe earthquake, *J. Phys. Earth*, 44, 437-454.

Zoback, M. D., and J. H. Healy, 1992, In situ stress measurements to 3.5 km depth in the Cajon Pass Scientific Research Borehole: Implications for the mechanics of crustal faulting, *J. Geophys. Res.*, 97, 5039-5057.

# Estimation of in-situ stress on cores retrieved from a deep borehole at the Arima - Takatsuki tectonic line

Ziqiu XUE<sup>1</sup>, Hisao ITO<sup>2</sup> and Osamu NISHIZAWA<sup>2</sup>

<sup>1</sup> Kiso-Jiban Consultants Co., 3-12-21 Tatsuno-Minami, Sango-Cho, Ikoma-Gun, Nara, 636-0822, Japan, Email:xue.ziqiu@kiso.co.jp

<sup>2</sup> Geological Survey of Japan, 1-1-3 Higashi, Tsukuba, Ibaraki, 305-8567, Japan

## ABSTRACT

We performed Anelastic Strain Recovery (ASR) measurements and Differential Strain Curve Analysis (DSCA) on freshly drilled cores to estimate in situ crustal stress. Geological Survey of Japan drilled a borehole at the intersection of the aftershock zone and the Arima-Takatsuki tectonic line. ASR and DSCA techniques were employed to estimate in situ stress state around the well by using the core sample retrieved from the depth about 600m. Both results show that the maximum principal stress orient to NE-SW, and the maximum and the intermediate principal stresses lie close to the horizontal plane. This is consistent with the occurrence of the borehole breakouts observed in the well. These results are in good agreement with the in situ stress measured by hydraulic fracturing. Although ASR and DSCA are convenient and economical methods to estimate in situ stress condition, the reliability of both methods is still unclear because the relationship between the microcracks due to stress relief and the in situ stress condition are still unknown. To evaluate applicability of both methods to stress measurements, we discuss some problems of microcracks relevant to ASR and DSCA.

## INTRODUCTION

After the Hyogoken-nanbu earthquake of January 17, 1995 (M7.2), Geological Survey of Japan drilled a 1000m-deep well at the intersection of the aftershock zone and the Arima-Takatsuki tectonic line located about 50km northeast of the Nojima Fault (Fig.1). One of the purposes of this drilling project is to investigate the crustal stress state. We carried out two kinds of core-based stress measurements: Anelastic Strain Recovery (Voight, 1968; Teufel and Warpinski, 1984) and Differential Strain Curve Analysis (Strickland and Ren, 1980; Dey and Brown, 1986).

Hereafter these two techniques are denoted as ASR and DSCA, respectively. The core-based stress measurement methods could be useful, when the borehole wall condition is not suitable for the hydraulic fracturing method.

A lot of studies have been carried out over the last two decades on core-based stress measurement techniques, such as ASR and DSCA, to estimate in situ stress conveniently and economically. However, the mechanisms of microcrack generation during the stress relaxation in the core sample and the relationship between the microcracks and the in-situ stress are still unclear. Since ASR and DSCA use the same core sample, it is possible to investigate the characteristics of microcracks that are of basic importance in two methods. Stress measurements by ASR and DSCA are based on assumptions that the core sample is originally isotropic and that the stress release inside the core sample results in microcracks that open against the principal stress with their crack planes perpendicular to the stress axis.

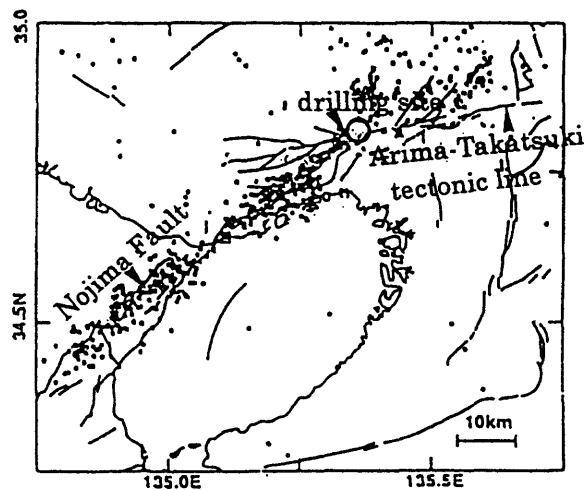


Fig.1 The location of the borehole (open circles) and aftershock distribution (solid circles).

In this paper, we discuss the results obtained by ASR and DSCA methods, which were performed on three core samples retrieved from the depth about 600m, and compare the results with the in situ stress data obtained by hydraulic fracturing (Ito et al., 1997). Our purpose is to assess the feasibility of stress measurements by ASR and DSCA as a method of determining stress directions and magnitudes. We also aim to increase the reliability for measuring and interpreting of in situ stress conditions.

## MEASUREMENTS

### ASR (Anelastic Strain Recovery)

The drilling site is located at Arima-Takatsuki tectonic line of which major fault oriented ENE-WSW. The borehole is drilled vertical and the depth is 1000m. 66mm-diameter cores were retrieved from the rhyolite formation at the depth 590-615m. After removing the drilled core from the wireline corebarrel, a core sample of 20-40cm in length was cut from the lowest part of the core and marked with a scribe line. Anelastic strain measurements started from 2-2.5 hours after coring.

ASR technique measures the stress relaxation in the fresh core retrieved from deep borehole using linear variable differential transformers (LVDTs) or strain gages, which are instrumented immediately after retrieval from the core barrel (Wolter and Berckhemer, 1989; Xue et al., 1998). The core sample needs to be retrieved within several hours after core cutting, instrumented quickly, and then monitored for an interval from several days to several weeks. In this study, we mounted five strain gage rosettes (#1 – #5) directly on the core side-surface at each 72° in azimuth (Fig.2a). We used strain gages for strain measurements in stead of LVDT, because we use strain gages for DSCA and the measurement methods should be same for the two methods. Instrumented cores were wrapped with thin films and inserted into an isolated container to prevent moisture loss inside the cores.

Both strain and temperature were measured by a portable data acquisition system, and data were recorded every ten minutes for periods of about one day to several weeks. A platinum temperature probe is placed directly on the surface of the core. During ASR measurements,

the room temperature was kept constant at 25°C to avoid thermal effects on core samples. It takes about 5 hours for core sample to reach the thermal equilibrium. The temperature of the sample surface shows periodical change between 20 °C and 23°C, corresponding to the daily temperature variation of outer atmosphere. We minimize the effect of the daily variation on data analysis by collecting the temperature effect. The method of strain analysis used for ASR is similar to that described in Kato et al. (1994).

### DSCA (Differential Strain Curve Analysis)

DSCA technique measures the strains of rock sample under hydrostatic pressures. A cubic sample was cut from the same core used for ASR measurement, of which orientation is temporally assigned with a scribe line marked on the position of gage #1 in ASR measurement. All measurements and analysis of the present study were performed on the basis of the direction assigned by this line. Three single-component strain gages (0, 45, 90 degree) were mounted in a rosette pattern on each surface of the cubic sample (Fig.2b). The entire sample was sealed with silicon rubber to prevent immersion of pressure medium oil. As suggested by Siegfried and Simmons (1978), the instrumented sample was set inside the pressure vessel with a same-instrumented fused silica, which was used as a reference for reducing thermal effects and electrical drifts. The sample and the reference are then pressured up to 150MPa by stepwise increasing of confining pressure. The strain data of rock sample and fused silica were recorded by using a portable data acquisition system. The data analysis method used for DSCA in this study is similar to that described by Dey and Brown (1986).

DSCA provides additional information on rock anisotropy resulted from microcracks, by observing the closure of microcracks under hydrostatic pressure. If the microcracks in core samples are opened as a result of stress relief, the microcrack-planes will preferentially orient perpendicular to the in situ principal stresses. Since we use the same core sample for ASR and DSCA. The DSCA principal strain directions should coincide with those indicated by ASR.

True orientations of the cores were determined later by assigning the prominent fractures in the cores to the fractures seen in

the ultrasonic borehole televiwer of which true orientations are accurately known.

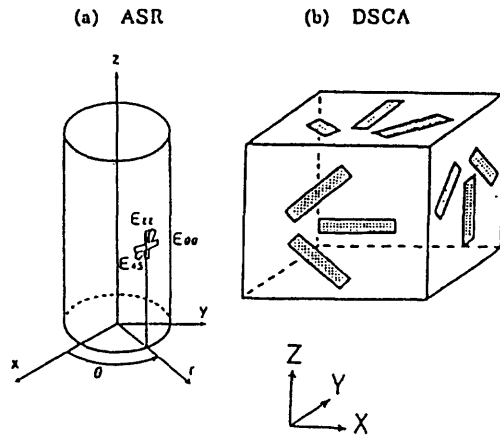


Fig. 2 Configurations of strain gages for ASR and DSCA. The cubic DSCA sample was cut from the same core used for ASR measurement.

## RESULTS

Fig. 3a-5a show the principal strain recovery of ASR, calculated from the anelastic strains measured by strain gages. Strain recovery was monitored about 20 hours for sample No.1 and No.2, and 170 hours for sample No.5, respectively. Time-dependent strain recovery continues for several days. In sample No.1 and No.2, the anelastic strains are still increasing after 25 hours. To confirm that the strain recovery curve reaches an asymptotic value, strain measurement should continue for more than 100 hours.

The intermediate strain and the minimum strain in sample No.1 show much smaller values than those of the maximum principal strain. In sample No.2, a part of strain data is lacking because of a system trouble. Typical anelastic strain recovery curves appear in sample No.5, whose strains increase rapidly at the initial stage and then approach constant values asymptotically.

At the beginning of the strain measurements, all the recovery curves indicate slight shrinkage of core samples, but after 10 hours they indicate expansion. The initial shrinkage is due to reduction of pore fluid pressure resulted from pore-fluid diffusion (Sarda and Perreau, 1989). Thus two processes are competing during ASR measurements: shrinkage caused by pore-fluid diffusion and

expansion by anelastic strain recovery. Since the permeability of our sample is very low (microdarcy order), the time interval of several hours may be insufficient for relaxation of pore pressure by fluid diffusion throughout the sample.

Fig. 3b-5b show the stereographic projections of the principal strain directions for each sample. In all samples the maximum principal strains orient at NE-SW. Two principal strains, the maximum and the intermediate, lie close to the horizontal plane.

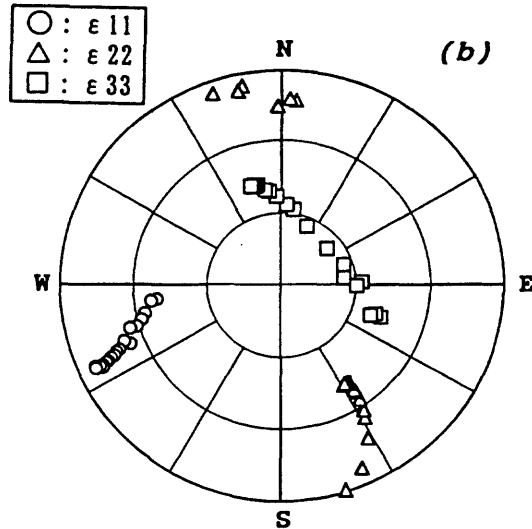
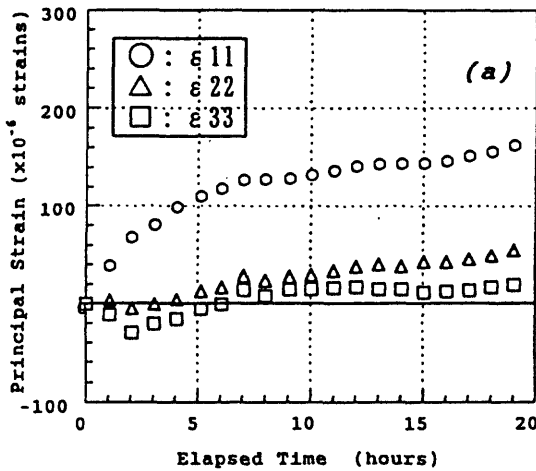


Fig. 3 ASR measurement results for sample No.1 (depth: 590m). (a) The principal anelastic strains recovery. (b) Estimated orientations of the principal anelastic strains (upper hemisphere stereonet).

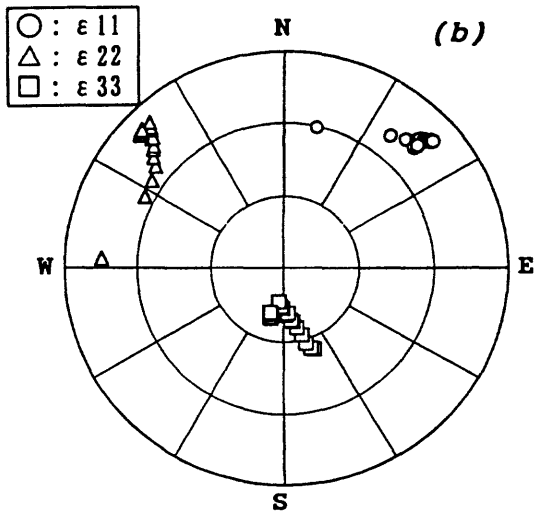
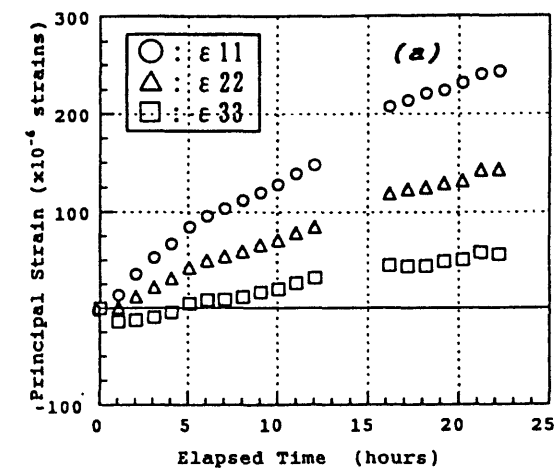


Fig.4 ASR measurement results for sample No.2 (depth: 593m). (a)The principal anelastic strains recovery. (b)Estimated orientations of the principal anelastic strains (upper hemisphere stereonet).

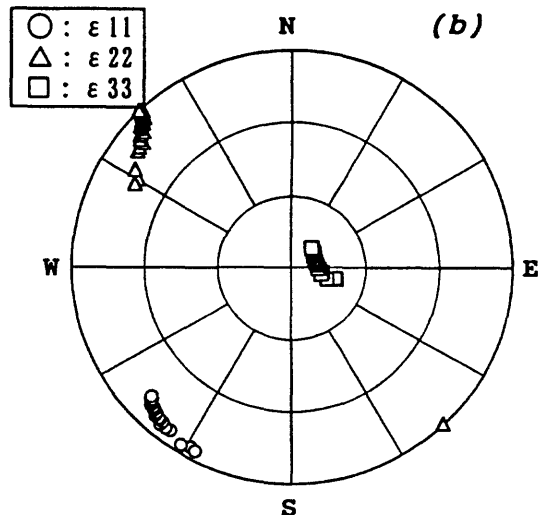
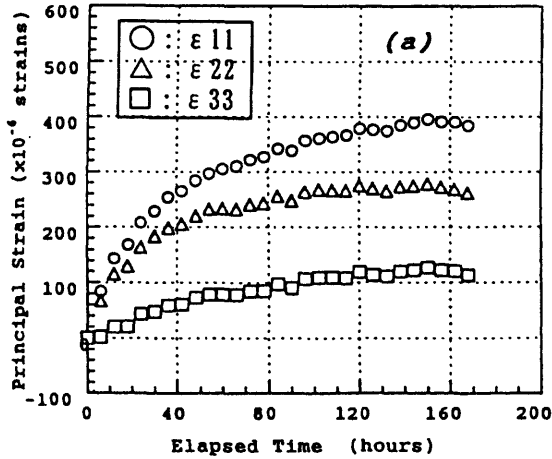
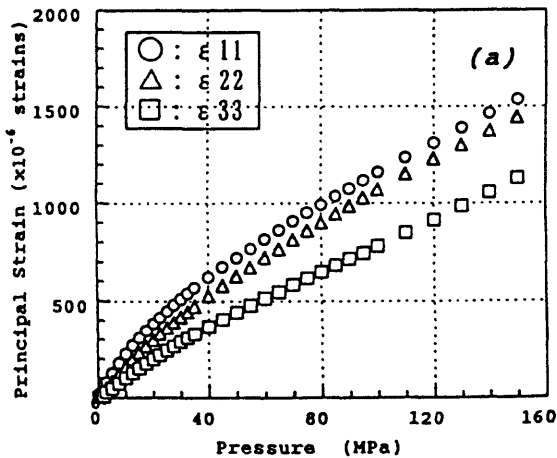


Fig.5 ASR measurement results for sample No.5 (depth: 614m). (a)The principal anelastic strains recovery. (b)Estimated orientations of the principal anelastic strains (upper hemisphere stereonet).

Figs.6, 7, and 8 show the results of DSCA: (a) the principal strain curves, (b) the stereographic projections of the principal strain directions.

When hydrostatic pressure is applied to rock samples, the strains increase rapidly at the initial low-pressure stage. Then the strains increase gradually, and finally the strains increase almost linear above 100MPa. The non-linearity of the strain-increment curves in the low-pressure range is generally interpreted as closure of microcracks in rock samples.



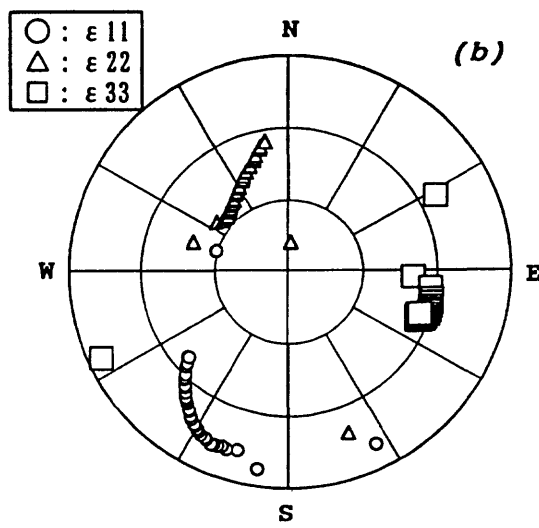


Fig.6 DSCA results for sample No.1 (depth: 590m). (a)The principal anelastic strains recovery. (b)Estimated orientations of the principal anelastic strains (upper hemisphere stereonet).

The principal strain directions are almost equal for the three samples, indicating all results of DSCA are consistent. It is important to note that the principal strain directions in DSCA show only a little change with pressure, whereas those of ASR show considerable changes with time. Closure of microcracks under hydrostatic pressure depends on aspect ratio of microcrack (Walsh, 1965). The DSCA results (Figs. 6b-8b) suggest that the predominant orientations of microcracks are almost same for all cracks, irrelevant to their aspect ratios. Thus the predominant cracks are quite uniform in studied samples.

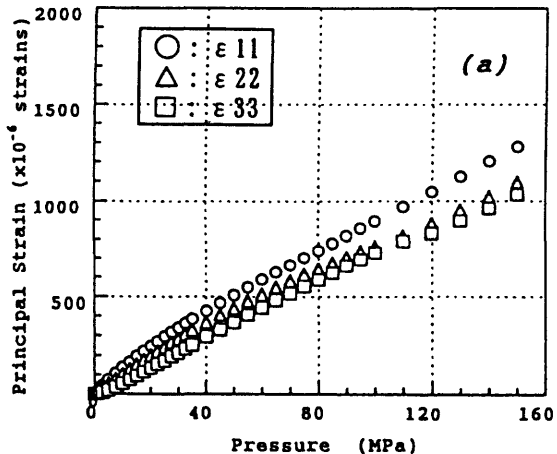


Fig.7 DSCA results for sample No.2 (depth: 593m). (a)The principal anelastic strains recovery. (b)Estimated orientations of the principal anelastic strains (upper hemisphere stereonet).

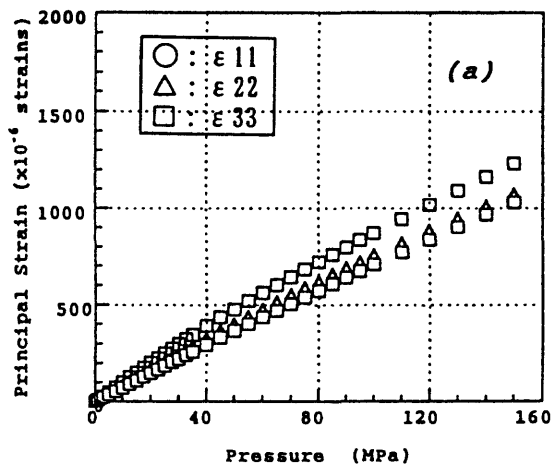


Fig.8 DSCA results for sample No.5 (depth:

614m). (a)The principal anelastic strains recovery. (b)Estimated orientations of the principal anelastic strains (upper hemisphere stereonet).

## DISCUSSION

Microcracks in crystalline rocks appear in a variety of forms as reviewed by Kranz (1983). To find a relationship between the characteristics of microcracks in drilled cores and the in situ stress conditions, it is necessary to investigate the mechanism of the stress relief during ASR measurements. Experimental measurements of the elastic wave velocity and permeability on drilled cores show that P-wave velocity decreases and permeability increases as the core depth becomes deeper (Morrow and Byerlee, 1992; Morrow et al., 1997). These results strongly suggest that the microcracks are generated by the stress relief inside the core sample due to the removal from the stressed rock mass to the stress-free state.

To investigate the mechanism of stress relief, Wolter and Berckhemer (1989) measured acoustic emission on drilled cores, and found a strong correspondence between the overall characteristics of the acoustic emission and the strain recovery. They concluded that the occurrence of each acoustic emission marks a tensile microcrack formation. In the meantime, Engelder (1984) suggested that the time-dependent behavior of strain caused by stress relief is controlled by healed cracks in Algerie Granite. Open cracks and healed cracks could exist simultaneously in cores. It is still unclear which is dominant, and which one mainly generates the anelastic strain. Applying ASR and DSCA on the same sample may give an answer to these problems.

Kowallis and Wang (1983) studied the microcracks in granite from Illinois borehole UPH-3, and found that most of the microcracks are due to stress relief, and healed cracks have higher aspect ratio than that of open cracks. Thus it seems that there could be some distinct sets of healed and open cracks, having different role in ASR and DSCA.

Our measurements show that both principal strain directions in ASR and DSCA are very close each other for all the samples, and their principal strain directions are in good agreement with the maximum stress direction determined by hydraulic fracturing and the

borehole breakouts. These results indicate that the open microcracks of studied rock samples are not greatly different in aspect ratio and predominant crack directions. The open crack hypothesis is also supported by the results of crack spectrum analysis by Dey and Brown (1986); they showed spectra of crack aspect ratio by analyzing the population of cracks closing under hydrostatic pressure. Only one peak was observed in crack spectra of our sample. We believe that open cracks probably play a main role in ASR and DSCA.

## CONCLUSIONS

ASR and DSCA on the same drilled cores retrieved from the Arima-Takatsuki Tectonic Line show consistent results on the principal strain directions for all samples. This enables a prediction of the principal stress direction.

The ASR and DSCA methods in its simplest form appear to provide an economical and convenient method for measuring both stress magnitudes and directions. Most of the microcracks in studied samples are probably produced from stress relief. However, the reliable mechanism of the microcrack occurrence during stress relief is still unclear. Further work is necessary to allow us to calculate reliable stress tensor. Application of ASR and DSCA methods for the same core sample will be greatly useful for improving the reliability of the stress measurements.

## REFERENCES

Dey, T.N. and D.W. Brown: Stress measurements in a deep granitic rock mass using hydraulic fracturing and differential strain curve analysis, *Proc. Int. Symposium on Rock Stress and Rock Stress Measurements*, pp.351-357, 1986

Engelder, T.: The time-dependent strain relaxation of Algerie granite, *Int. J. Rock Mech. Sci. & Geomech. Abstr.*, Vol.21, pp.63-73, 1984

Ito, H., Y. Kuwahara and O. Nishizawa: Stress measurements by the hydraulic fracturing in the 1995 Hyogoken-nanbu earthquake source region, *Rock Stress, Sugawara & Obara (eds)*, p.351-354, 1997

Kato, H., Y. Mizuta and O. Sano: On the relationship between time-dependent strain variations on core surface and in-situ stress, *Shigen-to-Sozai*, Vol.110,

pp.80-86, 1994 (in Japanese with English abstract)

Kowallis, B.J. and H.F. Wang: Microcrack study of granitic cores from Illinois deep borehole UPH-3, *J. Geophys. Res.*, Vol.88, p.7373-7380, 1983

Kranz, R.L.: Microcracks, A review, *Tectonophysics*, Vol.100, p.449-480, 1983

Morrow, C.A. and J.D. Byerlee: Permeability of core samples from Cajon Pass scientific drillhole, results from 2100 to 3500m depth, *J. Geophys. Res.*, Vol.97, p.5145-5151, 1992

Morrow, C. and D. Lockner: Permeability and porosity of the Illinois UPH 3 drillhole granite and a comparison with other deep drillhole rocks, *J. Geophys. Res.*, Vol.102, p.3067-3075, 1997

Sard, J.P. and P.J. Perreau: Determination of in situ stress parameters from measurements on cores, *Commision of the European Communities Rept.* 12514, 1989

Siegfried, R. and G. Simmons: Characterization of oriented cracks with differential strain analysis, *J. Geophys. Res.*, Vol.83, pp.1269-1278, 1978

Strickland, F.G. and N.K. Ren: Use of differential strain curve analysis in predicting in-situ stress state for deep wells, *Proc. 21th U.S. Symposium on Rock Mech.*, pp.523-532, 1980

Teufel, L.W. and N.R. Warpinski: Determination of in-situ stress from anelastic strain recovery measurements of oriented core: Comparison to hydraulic fracture stress measurements in the Rollins sandstone, Piceance Basin, Colorado, *Proc. 25th U.S. Symposium on Rock Mech.*, pp.176-185, 1984

Voight, B.: Determination of the virgin state of stress in the vicinity of a borehole from measurements of a partial anelastic strain tensor in drill cores, *Rock Mech. Eng. Geo.* Vol.6, pp.210-215, 1968

Walsh, J.B.: The effect of cracks on the compressibility of rock, *J. Geophys. Res.*, Vol.70, p.381-389, 1965

Warpinski, N.R. and L.W. Teufel: A viscoelastic constitutive model determining in-situ stress magnitudes from anelastic strain recovery of core, *SPE*, 15368, pp.1-12, 1986

Wolter, K.E. and H. Berckhemer: Time dependent strain recovery of core from the KTB deep drill hole, *Rock Mech. and Rock Eng.* Vol.22, pp.273-287, 1989

Xue, Z.Q., H. Ito and O. Nishizawa: Estimations of in-situ stresses from ASR and DSCA measurements on drilled cores, *Proc. 10th National Symposium on Rock Mechanics*, p.671-676, 1998 (in Japanese with English abstract)

blank page

# ELECTRICAL PROPERTIES AND ALTERATION OF GRANODIORITES FROM THE GSJ HIRABAYASHI HOLE, JAPAN.

PHILIPPE A. PEZARD<sup>1</sup>, HISAO ITO<sup>2</sup>, DANIEL HERMITTE<sup>1</sup>, AND ANDRE REVIL<sup>1</sup>.

<sup>1</sup>CEREGE(CNRS), BP 80, 13545 AIX-EN-PROVENCE CEDEX 4, FRANCE (pezard@cerege.fr),

<sup>2</sup>GEOLOGICAL SURVEY OF JAPAN, EARTHQUAKE RESEARCH DEPARTMENT, 1-1-3, HIGASHI, TSUKUBA, IBARAKI, 305-8567, JAPAN (g0193@gsjrsn.gsj.go.jp).

## ABSTRACT

Cores and downhole measurements collected from the GSJ Hirabayashi hole, Japan, after the devastating Nanbu Earthquake ( $M = 7.2$ ) are analyzed to study the relationship between deformation, alteration and physical properties of the penetrated granodiorite.

In particular, the electrical properties of 24 samples are analyzed in order to derive the effective formation factor ( $F$ ) as well as the electrical surface properties. These are analyzed in terms of structure of the pore space such as porosity ( $\emptyset$ ), tortuosity and altered matrix fraction. While  $\emptyset$  and  $F$  are, as expected, inversely related, tortuosity is also found (for 92 % of the samples) to be inversely related to porosity and altered matrix fraction.

The physical properties measured in-situ seem to be related, in this transpressional context, to changes in alteration and fracturing intensity. A low-frequency, monotonic decrease in electrical resistivity is recorded between fresher granodiorites in the upper part of the hole and the recent rupture (or "co-axial" zone), near 625 m. This tendency appears to reflect, over tens of m (in terms of true fault thickness), a macroscopic increase in the intensity of fracturing and alteration of the granodiorites towards the most recent rupture of the fault. Variations in saturating fluid salinity in the hanging wall might also contribute to this monotonic electrical resistivity trend. The central, cataclastic part of the fault is also described from in-situ measurements of physical properties and measured as 30 cm-thick. In-situ intrinsic of the fault gouge might be derived in the future from the numerical modeling of electrical logs.

## INTRODUCTION

While lithospheric rupture processes have been studied for many decades (in the field, in the laboratory, or from modelling), detailed in-situ studies of a major fault zone in terms of structure and dynamics has never been performed. While downhole geophysical methods now allow one to image the borehole wall at cm-scale, the in-situ

analysis in the vicinity of the fault of dynamic parameters such as heat-flow, spontaneous potential, or stress field is now of scientific concern. While the presence of core is vital for such analyses, continuous borehole geophysical images do not necessarily require continuous coring anymore. Such is actually difficult to achieve in faulted environments.

Numerous projects of drilling active lithospheric faults have however been proposed over the last decade. Attempts have, for example, been made to drill at sea, either though an active normal fault in the Woodlark basin (ODP Leg 180), or in less active structures on the flank of mid-ocean ridges (Pezard et al., 1997). On land, projects to drill either through the San Andreas Fault (California), or one of the normal faults associated with rifting in the Gulf of Corinth (Greece) are now in the planning phase.

In this framework, the hole drilled in 1996 at Hirabayashi by the Geological Survey of Japan (GSJ) is among the very first to penetrate an active segment of a seismogenic fault. In a fairly uniform lithological context, the impact of deformation and alteration in the near vicinity of the fault may be evaluated from the very complete set of geophysical and geological data obtained. We have chosen here to study the relationship between deformation, alteration and physical properties through the analysis of electrical properties of the Awaji granodiorites. The preliminary results are presented below.

## NANBU EARTHQUAKE - NOJIMA FAULT.

In January 1995, the Hyogo-ken/Nanbu Earthquake (or "Kobe" Earthquake, with  $M=7.2$ ) was for Japan one of the most destructive since the great Kanto (or "Tokyo") Earthquake in 1923. The epicentre was located about 20 km to the south-west of Kobe, and to the north-east of Awaji island, along a tectonic line oriented NE-SW. A 10,5 km-long surface rupture was observed along the Nojima Fault, with both dextral and reverse sense of motion, and displacement amplitudes on the order of 2 m (Awata et al., 1996; Tanaka et al., 1999).

## GSJ HIRABAYASHI HOLE

Five hole were drilled along the Nojima Fault in 1996 under the split responsibility, according to site, of GSJ and the University of Ehime (Tanaka et al., 1999). Two of these, located on Awaji island (at Ikuha and Hirabayashi), intersected a major fault. The Hirabayashi drill site was located close to the surface rupture of the Nojima Fault, where the largest displacement values were measured. The hole reaches a total depth of 746 m while penetrating the fault over more than 300 m, hence less than 30 m in true thickness due to the relative inclination of the hole with respect to the structure. The most recent rupture was identified at 625 m in the hole from core, downhole "Stoneley" wave attenuation, as well as borehole wall images (Ito et al., 1998).

Between 152 and 746 m, the core recovery from the GSJ Hirabayashi hole was larger than 95 %. The penetrated lithology is mostly constituted with granodiorites, with rare intrusions of porphyry. The granodiorites are altered and deformed to varying degrees, as illustrated in downhole physical properties measurements (Figure 1).

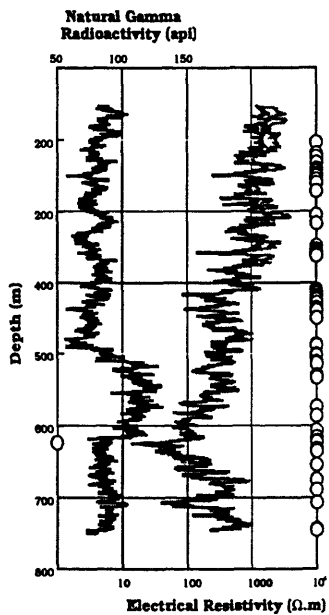


Figure 1. Electrical resistivity logs recorded with a Normal sonde (16" and 64"; to the right-hand side), with gamma ray log (to the left-hand side) and sample locations (open circles to the far right).

## DOWNHOLE MEASUREMENTS

A low-frequency, monotonic decrease in electrical resistivity is, for example, recorded between less altered and fractured granodiorites in the upper part

of the hole (between 150 and 300 m) and the recent rupture (or "co-axial" zone) near 625 m. This trend appears to reflect, over tens of m (in terms of true fault thickness), a macroscopic increase in the rate of fracturing and alteration of the granodiorites, elsewhere considered as fairly uniform from chemical analyses (Fujimoto et al., submitted). Variations in saturating fluid nature and salinity might also contribute to this monotonic resistivity trend.

The increase in natural gamma ray radioactivity (GR) over the 100 m-long section located above the recent rupture (Figure 1) indicates the precipitation of K/Th/U-rich minerals in relation to fluid circulation and the seismogenic process. Away from the co-axial zone, smaller fracture zones tend to be associated with a GR decrease. In the core, the deformation was described as more intense in the hanging-wall than in the foot-wall (Ito et al., 1998; Ohtani et al., soumis).

At a smaller scale, that of a few meters, a similar behavior is identified from other downhole measurements in front of small fracture zones (with dm-scale true thickness) such as those located near 250 or 360 m. While physical properties variations are gradual in the hanging-wall of these dm-scale structures, an abrupt change is often recorded at the base, locally reflecting the assymetrical tendency obtained over the entire length of the hole. In order to study the relationship between physical properties, alteration and fracturing intensity, a set of 60 cores with varying degrees of deformation and alteration was sampled. Preliminary results from core analyses are presented in the following, then compared to in-situ measurements.

## ELECTRICAL CONDUCTIVITY

The sensitivity of electrical properties of porous media to fluid-content provides a powerful means to detect conductive horizons such as fractures in a resistive matrix (Walsh & Brace, 1984; Katsube & Hume, 1987; Pezard et al., 1988). At a m-scale, *in situ* measurements of electrical resistivity are usually analyzed to derive porosity (Archie, 1942; Brace et al., 1965). The possibility to identify in the laboratory the different modes by which the current is being transported also provides, with the analysis of surface electrical conduction (Waxman & Smits, 1968; Pezard, 1990; Revil & Glover, 1998), insights into the degree of alteration of the rock.

## BACKGROUND

In a porous media constituted with a matrix considered as infinitely resistive and a connected

pore space saturated with a conductive electrolyte, two main mechanisms for electrical conduction appear: an electrolytic conduction mechanism in pore volumes as well as a "surface" conduction mechanism at the interface between the electrolyte and minerals. The latter is due to the presence of charges present to conserve the electroneutrality of the interface and constituting a diffuse layer through which cations migrate to contribute to the overall conduction.

When the surface conduction component is negligible with respect to the electrolytic component, the total conductivity of the pore space ( $C_o$ ) can be considered as proportional to that of the saturating fluid ( $C_w$ ). The proportionality coefficient  $F$  is the dimensionless electrical "formation factor":

$$C_o = C_w / F \quad (1)$$

$F$  has often been considered to characterize the 3D topology of the pore space.

**Surface conductivity.** When surface processes cannot be neglected with respect to electrolytic conduction, which is generally the case in the presence of alteration phases or clays, (1) does not hold anymore. Waxman et Smits (1968; WS) have proposed an empirical model to take into account the excess conductivity ( $C_s$ ) due to surface processes, with:

$$C_o = C_w / F + C_s \quad (2)$$

This added conductivity ( $C_s$ ) is attributed to the circulation of hydrolized cations within a so-called diffuse layer located at the fluid-grain interface.  $C_s$  is hence related to the notion of cations exchange capacity (CEC) of the altered phase in the pore space. The CEC represents the number of cations considered as mobile per unit weight, and is expressed in meq/100 g (or in cmole/kg). Per unit volume, the CEC is noted  $Q_v$  (and expressed in meq/ml), with:

$$Q_v = CEC \cdot \rho_m \cdot (1 - \emptyset) / \emptyset \quad (3)$$

where  $\rho_m$  is the grain density. The electrical conductivity of the pore space may then be written, after Waxman & Smits (1968):

$$C_o = (C_w + \mu \cdot Q_v) / F^* \quad (4)$$

where  $\mu$  is the mobility of cations in the diffuse layer, and  $F^*$  the global electrical formation factor of the sample. This model is considered as satisfactory at high fluid salinity (HS), but poor at low fluid salinity (LS), with a tendency to overestimate surface conductivity processes outlined in laboratory measurements. For example, the

Waxman & Smits (WS) model is based on a constant  $Q_v$  and  $\mu$  decreasing at low salinity while cations mobility tends to increase at low salinity.

A new approach based on the pore space microgeometry is proposed by Revil & Glover (1998), with:

$$C_o = (C_w / F) [1 - t_{(+)}^f + F\xi + f(F, \xi)] \quad (5)$$

where  $t_{(+)}^f$  is the Hittorf number of cations in the electrolyte, and  $\xi$  is a dimensionless parameter defined by Kan and Sen (1987), with:

$$\xi = C_s / C_w \approx (2/3) [\emptyset / (1 - \emptyset)] B_s Q_v / C_w = (2/3) B_s \rho_m CEC / C_w \quad (6)$$

and  $B_s$  is the ionic mobility determined by Revil & Glover (RG) from a database including 129 samples with different types of clay content. For a monovalent solute with  $Na^+$  ions, RG propose  $B_s = 5.14 \cdot 10^{-9} m^2 \cdot s^{-1} \cdot V^{-1}$  at 25 °C, and  $t_{(+)}^f (Na^+) \approx 0.38$ .  $f(F, \xi)$  is a complex function of  $F$  and  $\xi$  detailed by RG. The predictive capacity of this model covers the adequate salinity range. While WS propose:

$$\begin{aligned} C_o &= (C_w / F) [1 + F\xi] && (HS), \\ C_o &= \xi C_w && (LS) \end{aligned} \quad (7)$$

From the single approach of (5), the RG model is more precise yielding the following high and low salinity end-members with:

$$\begin{aligned} C_o &= (C_w / F) [1 + 2 \xi (F-1)] && (HS) \\ C_o &= \xi C_w [1 - (\xi - 1) / \xi F] && (LS) \end{aligned} \quad (8)$$

In the following, the electrical resistivity of a set of samples from the GSJ Hirabayashi hole has been measured at 100 Hz with a variable saturating fluid salinity. The intrinsic electrical "formation factor"  $F$  of each sample, as well as surface conductivity parameters have been extracted with the RG model, then converted in terms of 3D topology of the pore space.

**Altered fraction.** On the basis of surface electrical properties, an estimate for the altered weight fraction ( $\Phi_w$ ) of the matrix has been derived. After Waxman et Smits (1968), or equations (3) & (4) here, the surface conductivity ( $C_s$ ) and cation exchange capacity (CEC) are related. In the case of clay-sand mixtures, Revil et al. (1998) propose to relate the effective or "mean" CEC of the porous media to the clay weight-fraction ( $\Phi_w$ ) defined as follows:

$$CEC = \Phi_w \cdot \sum \chi_i CEC_i \quad (9)$$

where  $CEC_i$  are the respective values of CEC for the different clay fractions, and  $\chi_i$  the relative fractions for each of the clay components.

In the following, the notion of alteration is related to the surface electrical properties of alteration phases of granodiorites, but also to the (small) size of clay particles with respect to that of primary phases such as quartz. The notion of altered fraction ( $\phi_\omega$ ) is here extended to that of granodiorites from the Nojima fault zone, keeping only in our model one alteration phase per sample. Equation (9) consequently becomes:

$$CEC = \phi_\omega \cdot CEC_{alt} \quad (10)$$

Where the  $CEC_{alt}$  is that measured from cobalthexamine titration on the fraction  $< 150 \mu\text{m}$  for each sample. As the effective CEC is related to the effective surface conductivity ( $C_s$ ) by (6), the altered fraction ( $\phi_\omega$ ) is obtained from (11), yielding:

$$C_s = (2/3) \phi_\omega \beta_s \rho_M CEC_{alt} \quad (11)$$

With  $\beta_s$  as above for an electrolyte with sodium cations only, while  $C_s$ ,  $\rho_M$  and the  $CEC_{alt}$  are measured in the laboratory on the same sample.  $\phi_\omega$  is then computed for each sample. In summary, this new method a quantitative evaluation of the altered weight fraction of the matrix in a crystalline rock offers on the basis of electrical properties.

## CORE MEASUREMENTS

At this stage of the project, 24 samples from the GSJ Hirabayashi hole have been subjected in series to eight different saturating fluids with salinities ranging from 0.5 to 100 g/l. This set corresponds to some of the less fractured and altered facies of the fault zone. The more damaged samples will be treated in the near future in a separate manner. Particular attention will be taken to avoid damaging the samples during the electrical measurements.

The effective formation factor  $F$  and surface conductivity ( $C_s$ ) of each 24 samples has been computed here from the RG model, giving for the derivation the same weight to each of the measurements. This justifies the use of a logarithmic scale (Figure 2). Among this set, two samples corresponding respectively to the freshest and more porous rocks are presented here to illustrate the method. All the samples are 25 mm long cylinders cut with a 25 mm diameter and with the axis in the horizontal plane.

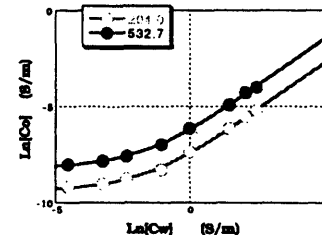


Figure 2. Neperian logarithm of fluid and core conductivities for two of the samples from the GSJ Hirabayashi hole. The less conductive sample (open symbols) is from 204.0 m, that is more than 30 m away from the main trace of the fault, while the more conductive one (closed symbols) is from 532.7 m, that is within 10 m from the main fault.

While  $F$  values from core provide a range similar to that deduced from in-situ measurements (Figure 3), the porosity measurements from logs are, on average, up to an order of magnitude too high. This is due to the presence of high-capture cross-section elements for neutrons in the granite such as Sm, Gd or Eu, which tends to increase the apparent porosity of the rock (Harvey et al., 1996; Pezard et al., 1999).

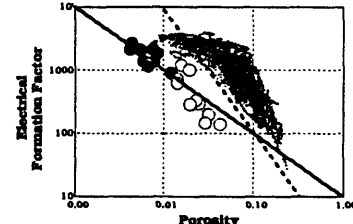


Figure 3. Effective formation factors  $F$  derived from the RG model with samples located above 410 m (closed symbols) and below (open symbols), close to the main fault zone. The porosity on core was determined from triple weighting. The small dots are points computed from downhole logs, with porosity values deduced from neutron activation, and  $F$  obtained from the 16" Normal curve, assuming a mean and constant pore fluid conductivity of 2.0 S/m. Archie (1942) formula: dashed line, and Pezard (1990) inverse relationship for basalts: solid line, are drawn for reference.

The fresher, less altered samples (closed symbols) located away from the fault tend to follow an inverse relationship such as:

$$F = T / \phi \quad (12)$$

with  $T=10$  in this case, representing the volume tortuosity of the pore space (Katsube and Hume, 1987; Pezard, 1990). The more porous, possibly more altered samples from the fault zone (open symbols) diverge from the previous trend and require a different law than Archie's to explain the dataset. An exponential fit to the measurements made on core (Figure 4) appears to cover the entire range, with:  $m_0 \approx 2900$  and  $m_1 \approx -85$  (assuming in this case  $F = m_0 \cdot e^{m_1 \theta}$ ).

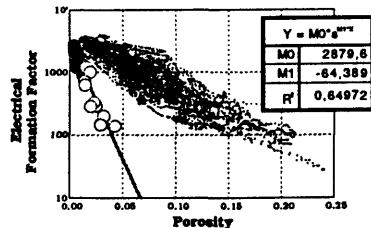


Figure 4. Effective formation factors  $F$  and porosity for core samples from the GSJ Hirabayashi hole (symbols as in Fig. 3). The continuous line represents an exponential fit to the 24 measurements made on core.

As the in-situ dataset tends to follow a similar trend (with a different slope but a similar origin), further analyses will be made in the near future to test the validity of this result. While the samples obtained in the near vicinity of the fault appear as more porous than more distant ones (Figures 3 and 5), the electrical tortuosity computed from (13) as a simple product ( $T = F \cdot \theta$ ) offers a more complex behavior.

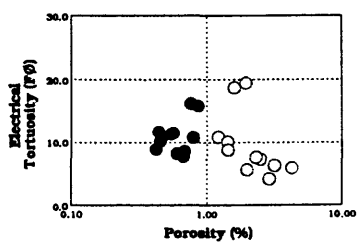


Figure 5. Electrical tortuosity ( $F\theta$ ) as a function of porosity for core samples from the GSJ Hirabayashi hole. Symbols as in Fig. 3.

While the low tortuosity samples exhibit a trend with decreasing tortuosity at higher porosity (Figure 5), the higher tortuosity samples follow an inverse relationship. Such a bimodal attitude has already been reported (Pezard et al., 1999) for granites from the Vienne area (France). In the latter case, the high- $T$  trend corresponded to slow and low-temperature

matrix alteration, while the low- $T$  trend equated to samples from hydrothermally altered horizons.

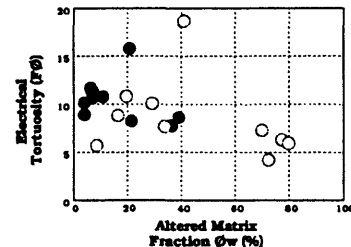


Figure 6. Electrical tortuosity ( $F\theta$ ) as a function of altered matrix fraction for core samples from the GSJ Hirabayashi hole. Symbols as in Fig. 3.

A similar attitude is provided by the plot of electrical tortuosity ( $F\theta$ ) versus altered matrix fraction (Figure 6). Values as low as a few percent and as high as 80 % for  $\theta_w$  are obtained. These results now need to be compared with that from traditional methods such as X-ray mineralogy.

## DISCUSSION AND PERSPECTIVES

**Electrical properties.** In a very uniform and electrically resistive setting in terms of lithology, changes in the electrical resistivity signal may originate from three different although related sources with: either (1) changes in the degree of fracturing of the rock, or (2) changes in the nature of fracture fillings, or (3) changes in the degree of alteration of the rock, or else (4) changes in the pore space fluid salinity.

The degree of fracturing can be described almost directly down to mm-scale from downhole FMI electrical images of the borehole wall (Ito et al., 1998). However, changes in alteration are more difficult to apprehend. As the natural gamma radioactivity signal (GR) provides insights into integrated alteration mechanisms, the first order signal appears to be complex. For example, a 50 % increase in GR is obtained in the hanging wall of the main fault zone only (Figure 7), in a very assymetrical pattern. To the contrary, a slight GR decrease is recorded in front of smaller fracture zones such as those located at 250, 370 and 435 m. The identification of proxies for matrix alteration in relation to deformation and associated fluid-circulation is hence necessary to the unfolding of the in-situ resistivity signal (Figure 7).

The determination of whether fluid circulation, hence alteration in the main fault zone traced in the GR signal is confined to the hanging wall is, for example, one of the main objectives of these

analyses. If a valid proxy for matrix alteration can be identified, then fluid-salinity changes through this active fault zone may be traced.

A fair to excellent fit is obtained between laboratory and in-situ (using for this first-order comparison a constant  $C_w = 2.0 \Omega \cdot \text{m}$ ) estimates of formation factor ( $F$ ), with decreasing  $F$  values close to the main fault zone (Figure 7).

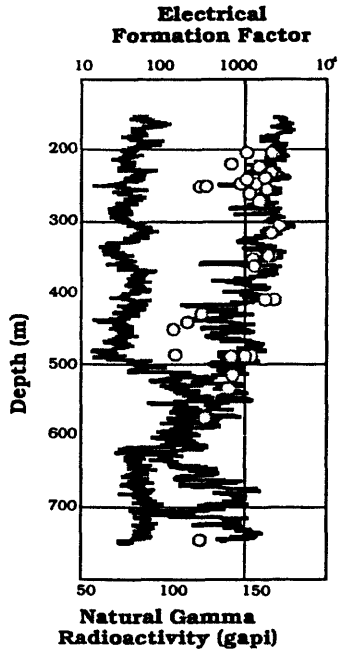


Figure 7. Electrical formation factor  $F$  derived from a resistivity logs recorded with a 16" Normal sonde (with  $C_w = 2.0 \Omega \cdot \text{m}$ ; to the right-hand side) compared with a gamma ray log (to the left-hand side).  $F$  values derived from core with the RG model are also presented versus depth (open symbols).

**Alteration.** Besides GR data, other proxies might originate from the bulk density signal (Figure 8), or

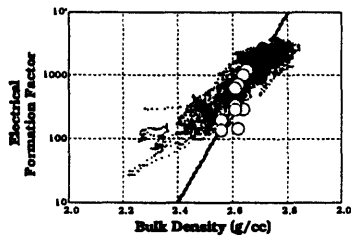


Figure 8.  $F$  as a function of bulk density for core samples from the GSJ Hirabayashi hole (symbols as in Fig. 3). The in-situ density data are obtained from gamma activation. An exponential fit through the core data is presented.

the magnetic susceptibility (Figure 9). The direct relationship between  $F$  and bulk density might be related to both porosity (hence fracturing) and alteration of the matrix.

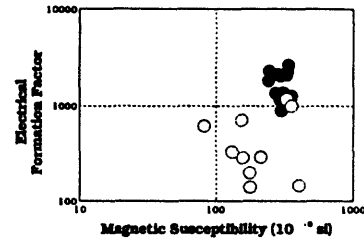


Figure 9.  $F$  as a function of magnetic susceptibility for core samples from the GSJ Hirabayashi hole (symbols as in Fig. 3).

As no magnetic susceptibility data were recorded in the hole, continuous measurements on core will be necessary if this property is to be used as a proxy for alteration. A significant decrease in magnetic susceptibility is obtained for the samples from the main fault zone (Figure 9) with respect to the fresher samples.

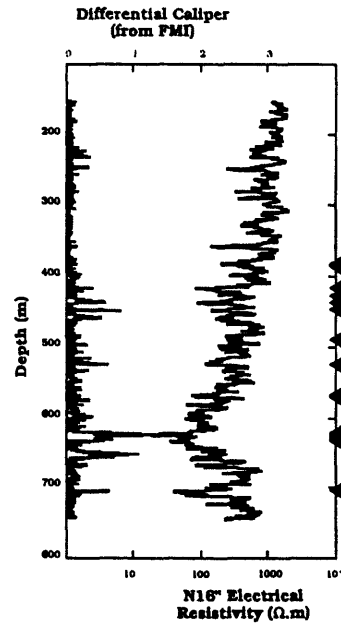


Figure 10. Electrical resistivity log recorded with a 16" Normal sonde (to the right-hand side) compared with a differential caliper from orthogonal mechanical measurements of the FMI (to the left-hand side) and location of active faults identified from the analysis of BHTV images (closed triangles to the far right; Célérier et al., this issue).

Once continuous alteration and fluid conductivity ( $C_w$ ) logs obtained from the combined analysis of laboratory and downhole measurements, an attempt at identifying the signal related to the last seismic event should be made.

**Active faulting.** In particular, a comparison between electrical anomalies and zones identified from BHTV images as mechanically weak or active during drilling in 1996, that is one year after the Nanbu earthquake, should be made. Each active fault and differential caliper anomaly is found here to be the site of a resistivity drop (Figure 10).

The 24 active horizons detected from BHTV images over a 12-m-long interval (Célérier et al., this issue), described elsewhere as the inner part of the main fault zone (Ito et al., 1998), define a zone where sharp hole size and electrical resistivity anomalies are recorded. In the upper 3 m of this zone, and in order to determine the intrinsic electrical properties of the 30-cm-thick gouge where the most intense deformation has been found (Fujimoto et al., this issue), 3D numerical modeling of the scalar resistivity logs (Normal 16" and 64") should be performed on the basis of the geometry derived from FMI images, as well as from measurements on core.

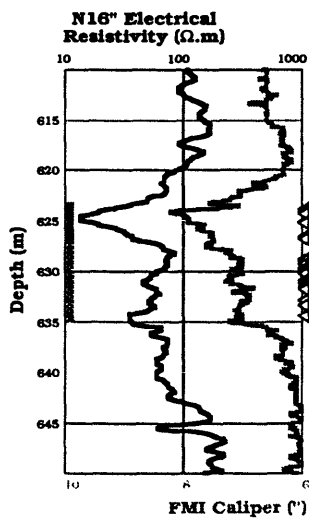


Figure 12. Electrical resistivity log recorded with a 16" Normal sonde (to the right-hand side) compared with a caliper measurement from the FMI (to the left-hand side) and location of active faults identified from the analysis of BHTV images (open triangles to the far right; Célérier et al., this issue). The location of the 12-m-thick, inner part of the main fault zone is underlined to the far left of the diagram, from 623 to 635 m.

In summary, the physical properties measured in-situ seems to be related, in this transpressional context,

to alteration and fracturing intensity. This relationship might be tested with a set of coherent petrological, mineralogical and petrophysical measurements on cylindrical mini-cores. The samples have been chosen in order to analyse, from cm- to 100 m-scale, a set of rocks with varying degrees of deformation and alteration. A thin section will be cut for each of the samples in order to identify the modes of deformation and alteration to which the rocks were submitted.

## ACKNOWLEDGEMENTS

This study was financed by CNRS and ANDRA through the GdR FORPRO (Research Action 99.V - FORPRO contribution 99/006 B).

## REFERENCES

Archie G.E., 1942. The electrical resistivity log as an aid in determining some reservoir characteristics, *J. Pet. Techn.*, 5, 1-8.

Awata Y., Mizuno K., Sugiyama Y., Imura R., Shimokawa K., Okumura K., Tsukuda E., 1996. Surface fault ruptures on the north-west coast of Awaji Island associated with the Hyogo-ken Nanbu earthquake of 1995, Japan. *Zisin2*, 49, 113-124 (in Japanese with English abstract).

Brace W.F., Orange A.S., and Madden T.R., 1965. The effect of pressure on the electrical resistivity of water-saturated crystalline rocks, *J. Geophys. Res.*, 70, 5669-5678.

Fujimoto K., Tanaka H., Higuchi T., Tomida N., Ohtani T., et Ito H. Alteration and mass transfer along the GSJ Hirabayashi borehole penetrating the Nojima earthquake fault, Japan. Submitted to *Island Arc*.

Ito H., Kuwahara T., Kiguchi T., Fujimoto K., Ohtani T., Tanaka H., Brie A., Endo T., Yamamoto H., 1998. Permeability structure of the Nojima Fault from borehole measurements in the GSJ borehole crossing the Nojima Fault on Awaji Island, Japan. AGU Fall meeting, San Francisco, *EOS transactions*.

Harvey P.K., Lovell M.A., Brewer T.S., Locke J., and Mansley E. 1996. Measurement of thermal neutron absorption cross section in selected geochemical reference materials. *Geostandards Newsletter*, 20, 1, 79-85.

Katsube T.J., and Hume J.P., 1987. Permeability determination in crystalline rocks by standard geophysical logs, *Geophysics*, 52, 342-352.

Kan R., and Sen P.N., 1987. Electrolytic conduction in periodic arrays of insulators with charges. *J. Chem. Phys.*, 86, 5748-5756.

Pezard P.A., and Luthi S.M., 1988. Borehole Electrical Images in the Basement of the Cajon Pass Scientific Drillhole, California; Fractures

Identification and Tectonic Implications. *Geophys. Res. Lett.*, 15, 1017-1020.

Pezard P.A., 1990. Electrical Properties of MORB, and Structure of the Upper Oceanic Crust at Site 504. *J. Geophys. Res.*, 95, 9237-9264.

Pezard P.A., Ayadi M., Revil A., Bronner G., and Wilkens R., 1997. Detailed structure of an oceanic normal fault: a multi-scalar approach at DSDP/ODP Site 504. *Geophys. Res. Lett.*, 24, 337-340.

Pezard P.A., Hermitte D., Revil A., Virlogeux D., Leutsch Y., and Harvey P.K., 1999. Physical Properties of Granite, with Applications to Nuclear Waste Storage in the Subsurface. Extended abstract, Texture and Physical Properties of Rock, Oct 13-16, IGDL, University of Göttingen.

Ohtani T., Fujimoto K., Ito H., Tanaka H., Higuchi T., Tomida N. Subsurface internal structure of the Nojima Fault from the GSJ borehole survey. Submitted to *Island Arc*.

Revil A. and Glover P.W.J., 1998. Nature of surface electrical conductivity in natural sands, sandstones and clays. *Geophys. Res. Lett.*, 25: 691-694.

Revil A., Cathles L.M. III, Losh S., and Nunn, J.A., 1998. Electrical conductivity in shaly sands with geophysical applications. *J. Geophys. Res.*, 103, B10, 23925-23936.

Tanaka H., Higuchi T., Tomida N., Fujimoto K., Ohtani T., and Ito H., 1999. Distribution, deformation and alteration of fault rocks along the GSJ core penetrating the Nojima Fault, Awaji Island, Southwest Japan. *Geological Society of Japan*, 105, 1, 72-75.

Walsh J.B., and Brace W.F., 1984. The effect of pressure on porosity and the transport properties of rocks, *J. Geophys. Res.*, 89, 9425-9431.

Waxman M.H., and Smits L.J.M., 1968. Electrical conductivities in oil-bearing shaly sands. *Soc. Pet. Eng. J.*, 8, 107-122.

# Fracture system in the Nojima fault

Tsutomu Kiguchi<sup>1</sup>, Hisao Ito<sup>2</sup>, Yasuto Kuwahara<sup>3</sup> and Tomoyuki Ohtani<sup>4</sup>

<sup>1</sup> Geophysics Department, Geological Survey of Japan, Higashi 1-1-3, Tsukuba, Ibaraki, 305-8567, Japan.  
kig@gsj.go.jp

<sup>2</sup> Earthquake Research Department, Geological Survey of Japan, Higashi 1-1-3, Tsukuba, Ibaraki, 305-8567, Japan.  
g0193@gsj.go.jp

<sup>3</sup> Earthquake Research Department, Geological Survey of Japan, Higashi 1-1-3, Tsukuba, Ibaraki, 305-8567, Japan.  
g8702@gsj.go.jp

<sup>4</sup> Geothermal Research Department, Geological Survey of Japan, Higashi 1-1-3, Tsukuba, Ibaraki, 305-8567, Japan.  
ohtani@gsj.go.jp

## ABSTRACT

The borehole was drilled by the Geological Survey of Japan to penetrate the Nojima fault. The coring, borehole logging and hydrophone VSP experiment were carried out. The fault zone is characterized by altered and deformed rocks from 426.1 m to 746 m, with coaxial zone of fault gouge at 623.3 m to 625.1 m. We detected a few thousands of fractures from FMI images. The trend of the fracture strike at the depth range where the conventional logging data showed extreme anomaly in the fault zone almost parallel to the surface strike of the Nojima fault, although the strike of all fractures inside of the fault zone is rather dispersed. Seismic anisotropy outside of the fault zone estimated from the DSI data is considered to be caused by the aligned fracture with NW - SE trend. It is noteworthy that almost all the resistive fractures are distributed in the shallower depth than the coaxial zone. The strike and dip of some fractures at coaxial zone are consistent with the surface strike of the Nojima fault and the dip estimated from the depth of coaxial zone. The fractures at coaxial zone are considered to be permeable from the results of hydrophone VSP analysis.

## INTRODUCTION

Subsurface fracture systems have an essential influence on rock strength, seismic velocities, seismic anisotropy and permeability. It is very important to characterize the orientation, frequency and permeability of fractures in the fault zone in order to understand the earthquake fault mechanics.

The Geological Survey of Japan drilled a 746.7 m deep borehole at Nojima Hirabayashi on the northwest-

ern coast of Awaji Island to penetrate the Nojima fault. Cores were recovered for almost entire depth interval from 152 m to 746 m. In addition to conventional logging, FMI\* (Fullbore Formation Microlmager) and DSI\* (Dipole Shear Sonic Imager) were conducted (Ito et al., 1996).

FMI images provided the detailed distribution of fractures. In this study, we analyzed the FMI fracture data inside and outside of the fault zone in order to characterize the fracture system in the Nojima fault.

## BOREHOLE DATA

The drilling site was 74.6 m from the surface break of the Nojima fault. The borehole was drilled through 300 m of granodiorite at the surface. The borehole then penetrated layers of protolith granodiorite and porphyry and the fault zone from 426 m to the bottom of the hole, which was characterized by deformed and altered rocks (Ito et al., 1996, Tanaka et al., 1999). The coaxial zone of the Nojima fault, which consists of a fault gouge, was found at 623.3-625.1 m. In the fault zone (426-746 m), fault gouges and cataclasite were detected. Fig.1 shows the geological structure of the borehole.

We conducted the borehole logging including FMI and DSI. The fault zone observed by core inspection is characterized by low velocity, low electrical resistivity and low density. Especially, the logging data showed extremely large anomaly at the depth range from 623 m to 650 m. DSI tool can measure differences in shear slowness in different directions in a plane perpendicular to the tool axis. Therefore we analyzed seismic anisotropy along the borehole from the DSI data. FMI tool provides micro-resistivity images of the borehole wall. We were able to detect a few thousands of conductive fractures and resistive ones

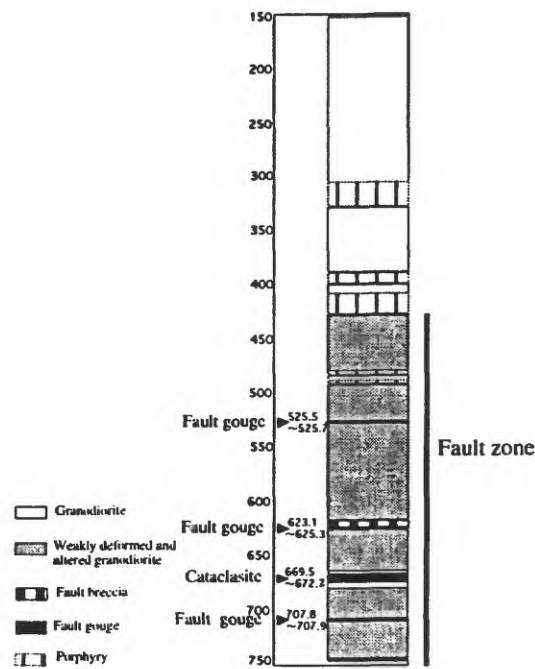


Fig1. The geological structure of the Nojima Hirabayashi borehole (modified from Ito et al., 1996).

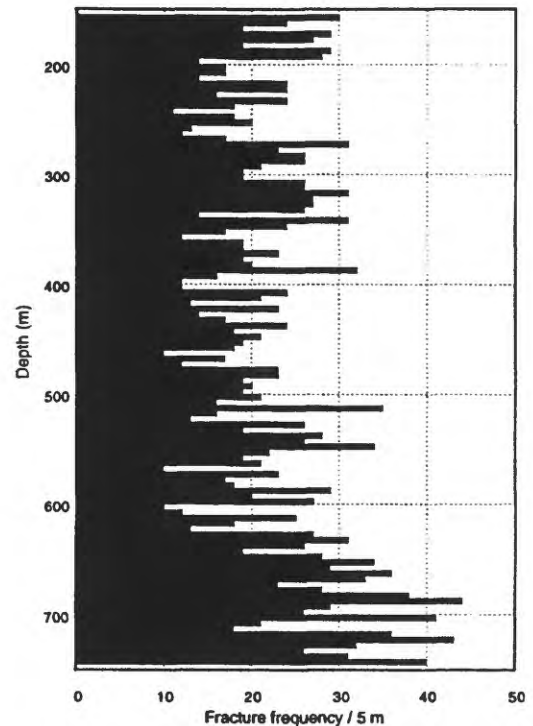


Fig2. Distribution of the fracture frequency per 5 m.

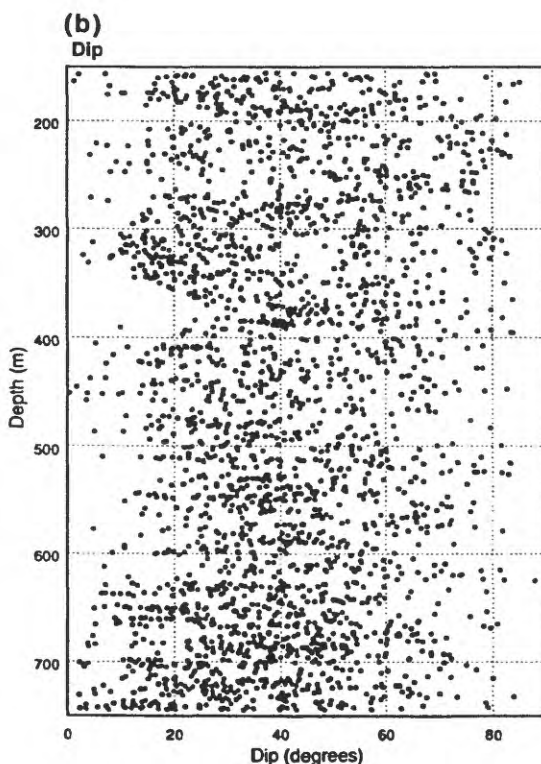
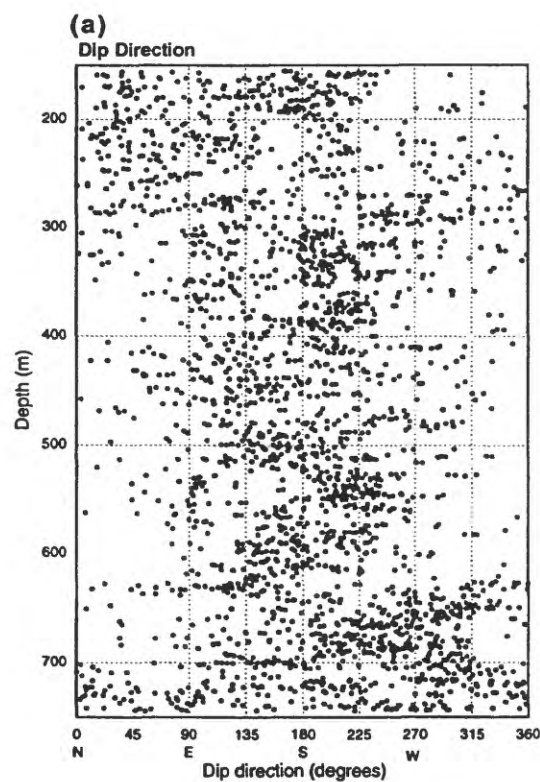


Fig3. Distribution of the dip direction (a) and dip (b) of fractures.

from FMI images. Fig. 2 shows the frequency of the all fractures detected from FMI images. Fracture dips and dip directions with depth is presented in Fig. 3.

We also carried out hydrophone VSP experiment at this borehole. Kiguchi et al. (1998) analyzed tube waves obtained by the VSP in order to detected permeable fractures and to estimate the parameter of the permeable fractures, such as permeability, dip and strike.

## RESULTS OF FRACTURE ANALYSIS

### *Orientation of the fractures inside and outside of the fault zone*

The fault zone from 426 m to the bottom of the

hole was characterized by deformed and altered rocks by core inspection. A few thousands of fractures were detected inside and outside of the fault zone (Fig. 2). We compared the fracture trend inside of the fault zone with one outside of the fault zone.

Orientations of all fractures inside of the fault zone are shown in Fig. 4 (a) in a lower hemisphere equal-area projection. Shading pattern gives the standard deviation from a random distribution. Fig. 4 (b) and (c) are presented as the distribution of strike and dip of all fractures inside of the fault zone, respectively. Fig 5 is the same plot as Fig. 4 for the fractures outside of the fault zone. As shown in Fig. 4 (b), strike of the fractures inside of the fault zone is rather dispersed and the major trend of strike

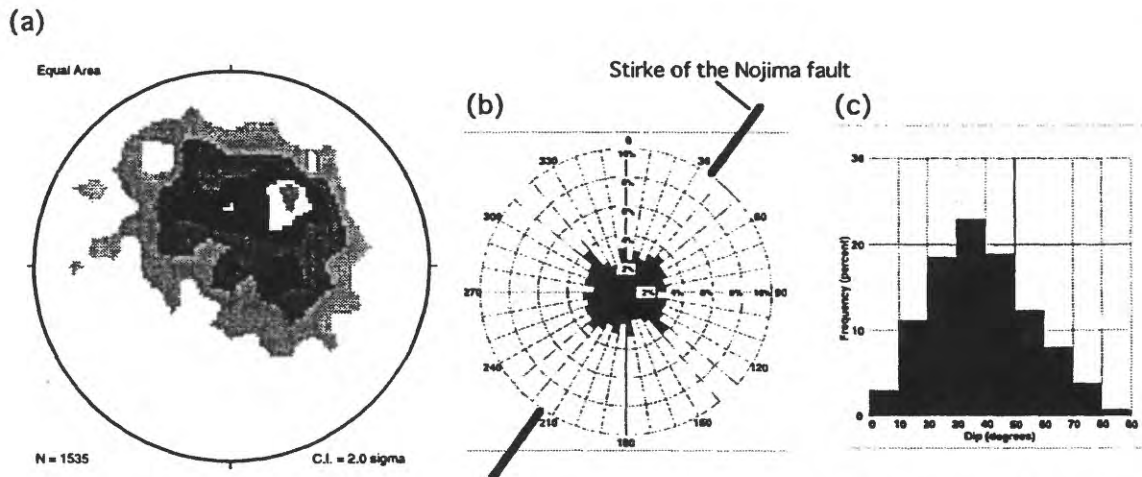


Fig 4. (a) Lower hemisphere equal-area projection for the fractures inside of the fault zone (426 - 745 m). Contour interval is  $2\sigma$ . The distribution of strike (b) and dip (c) of the fractures inside of the fault zone. The surface strike of the Nojima fault are indicated.

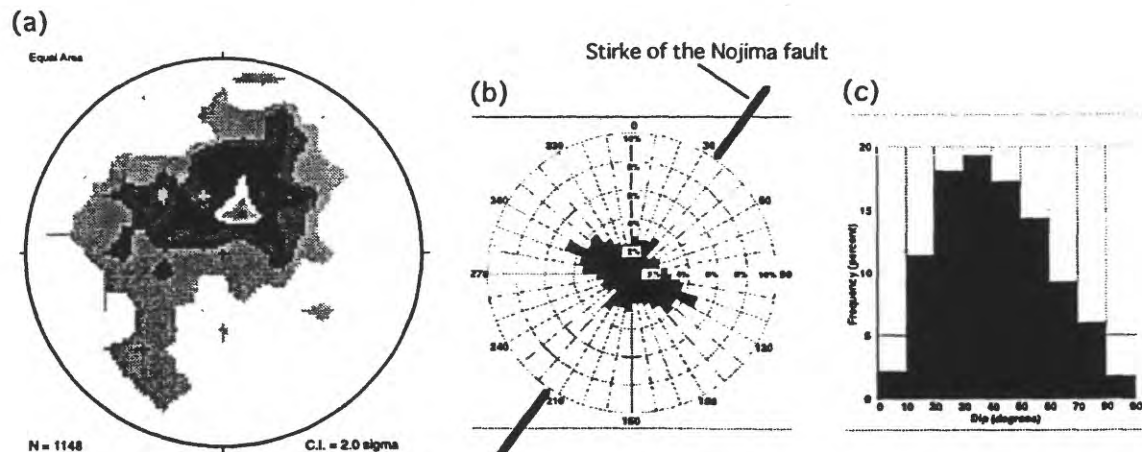


Fig 5. Same as Fig 4 for the fractures outside of the fault zone (152 - 426 m).

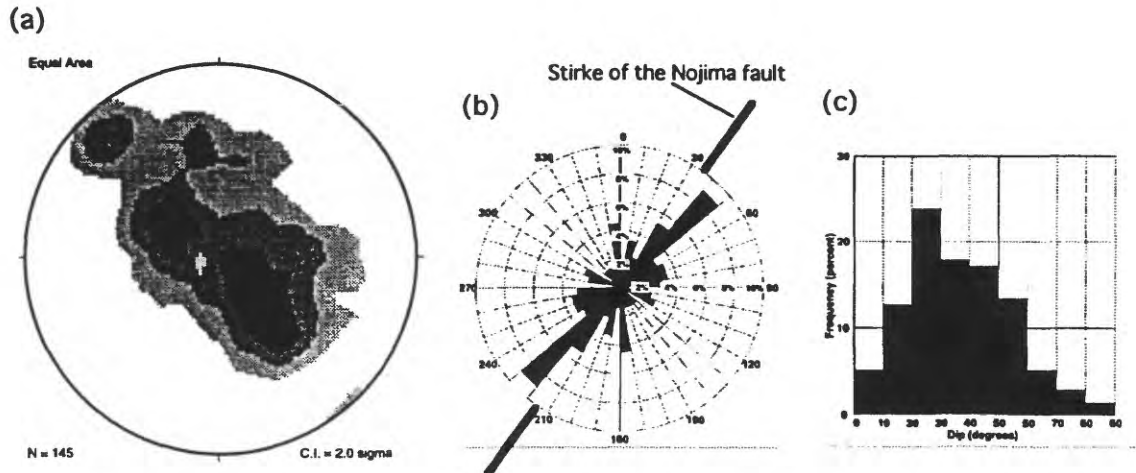


Fig 6. Same as Fig 4 for the fractures at the depth range from 623 m to 650 m, where the logging data shows extremely large anomaly.

is not clear. On the other hand, the concentration of the fractures outside of the fault zone strikes as NW - SE (Fig. 5 (b)). Although the trend of the all fracture strike inside of the fault zone is not clear, the concentration of the fracture at the depth range from 623 m to 650 m, where the logging data showed extremely large anomaly, strikes as NE - SW. Orientation of the fractures at the depth range from 623 m to 650 m and the distribution of strike and dip are shown in Fig. 6. There is no significant difference of the trend of fracture dip between inside and outside of the fault zone.

#### *Distribution of the resistive fractures*

We were able to detect resistive fractures as resistive sinusoids observed on the FMI image. The filling materials in fracture are considered to cause resistive on the FMI image. Fig. 7 shows the distribution of the resistive fractures. The number of the resistive fractures is remarkably less than one of the conductive fractures. It is noteworthy that most resistive fractures are distributed in the shallower zone than the coaxial zone of fault gouge at 623.3-625.1 m and there is only one resistive fracture at the depth range from 600 m to the bottom of the hole. The trend of the strike of the resistive fractures is NE - SW.

#### *Seismic anisotropy and fracture trend*

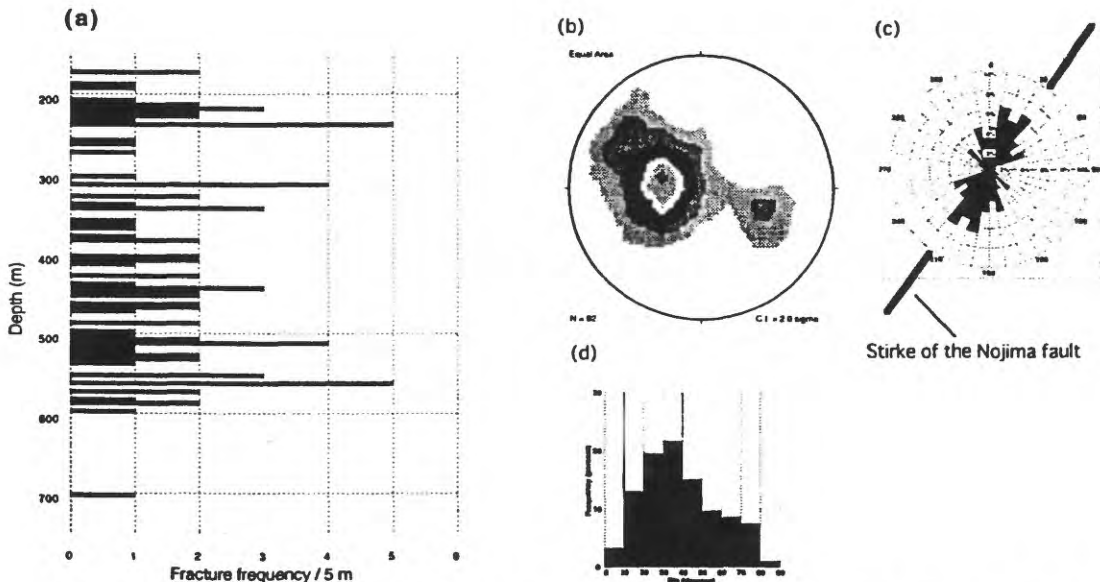


Fig 7. (a) Distribution of the frequency of the resistive fractures per 5 m. (b) Lower hemisphere equal-area projection for the resistive fractures. The distribution of strike (c) and dip (d) of the resistive fractures.

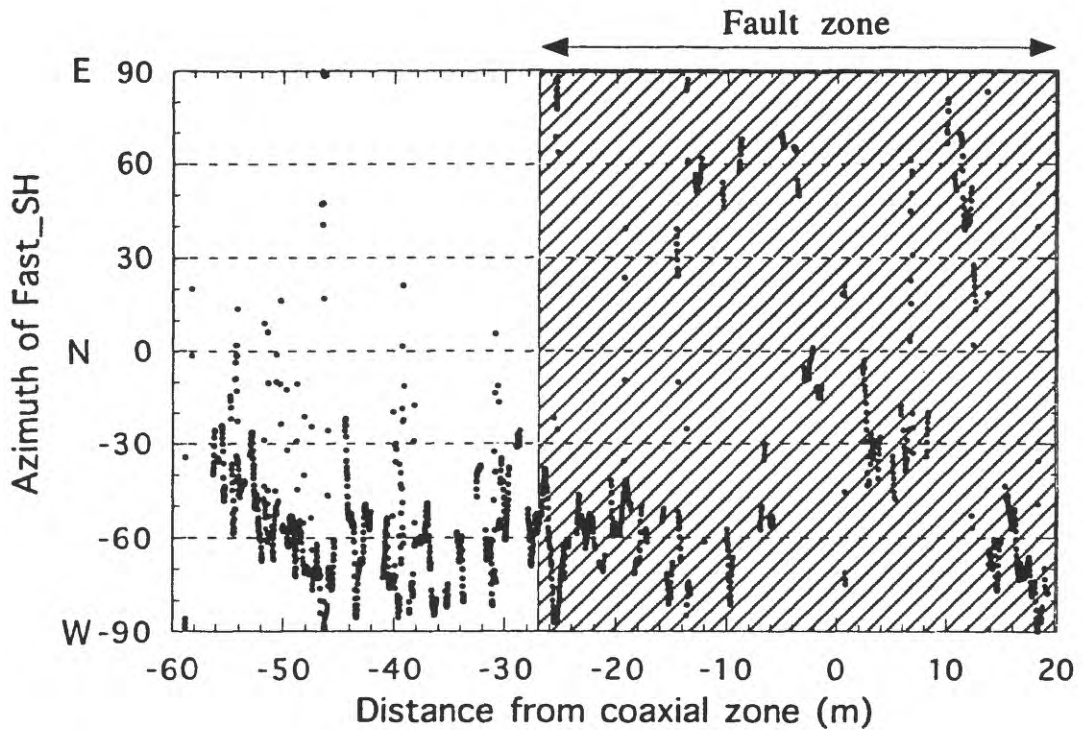


Fig 8. Azimuth of the fast shear wave estimated from the DS1 data as a function of distance from the coaxial zone of the fault. Negative value in the horizontal axis indicates shallower depth than coaxial zone. The shading zone indicates the fault zone.

We analyzed seismic anisotropy along the bore-hole from the DS1 data. The azimuth of the fast shear wave estimated from the DS1 data is shown in Fig. 8. The horizontal axis in Fig. 8 is the distance from coaxial zone(623.3-625.1 m) and negative value in the axis implies shallower depth than coaxial zone. At outside of the fault zone, the fast shear azimuth is localized in NW direction. The result that the concentration of the fractures outside of the fault zone strikes as NW - SE implies that seismic anisotropy outside of the fault zone is caused by the aligned fractures. Inside of the fault zone, the fast shear azimuth is rather dispersed in the same manner as the fracture trend.

#### *Characterization of the fractures at coaxial zone (623.3-625.1 m)*

The fractures at coaxial zone of fault gouge (623.3-625.1 m) are detected as shown in Fig. 9. The following are major finding in characterizing the fractures:

(1) The dip direction of almost all the fractures is about

S50° E. This is in good agreement with the surface strike of the Nojima fault.

(2) The fractures have higher dip angle than 65 degrees except one fracture. The dip of some fractures is consistent with the one which is estimated from the angle between the surface trace and the depth of the fault gouge; about 80 degrees.

(3) Several fractures seem to have parallel structure, because these fractures have the almost same strike and dip. These fractures are considered to correspond to a foliation of the fault gouge.

From the hydrophone VSP data, the coaxial zone has very high permeability and the estimated dip of the permeable fracture is about 80 degrees (Kiguchi et al., 1998). Therefore we think that there are permeable fractures at coaxial zone.

#### CONCLUSIONS

We detected and analyzed the fractures from the FMI data at the borehole which was drilled to penetrates the Nojima fault. The fractures outside of the fault zone

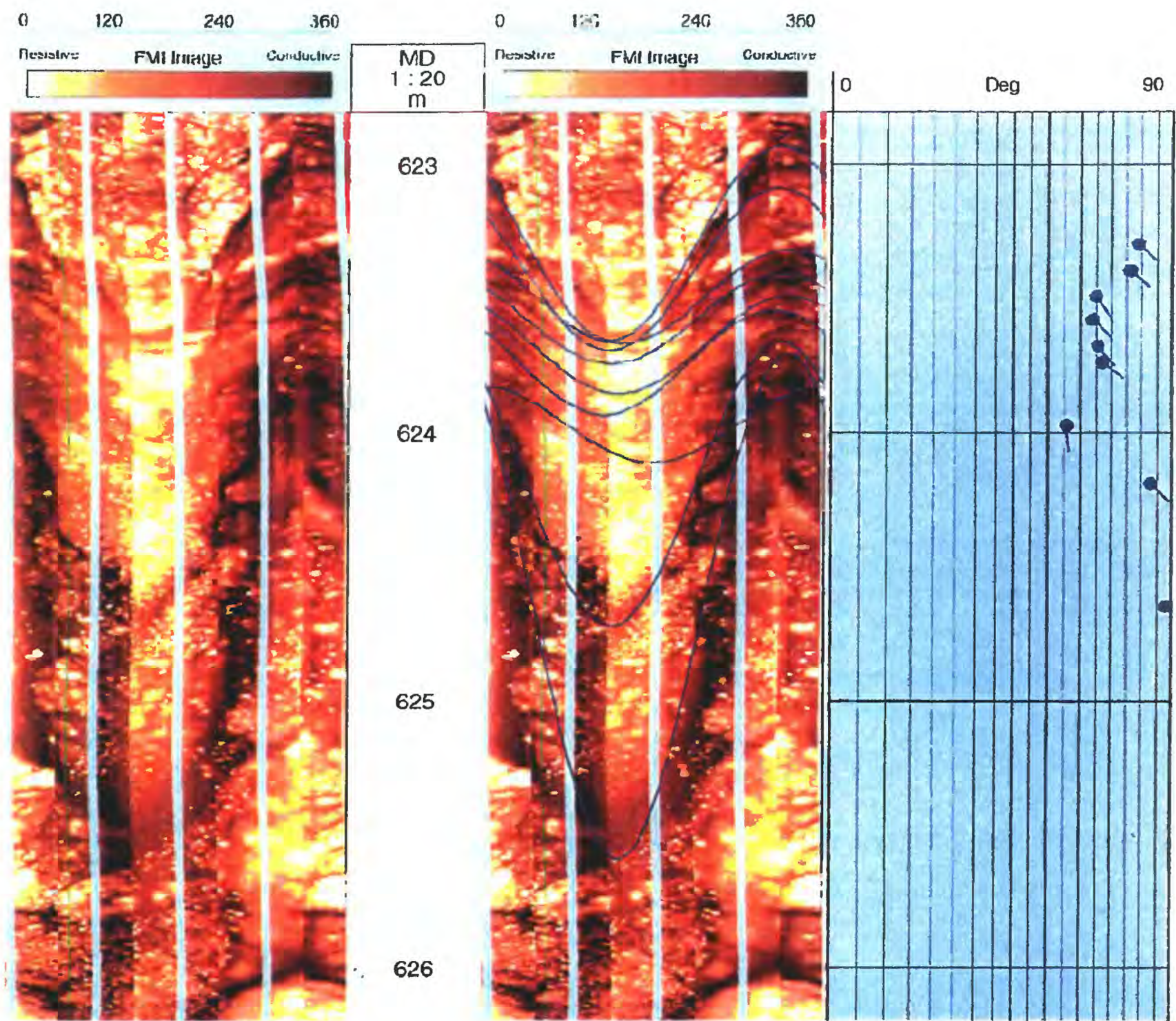


Fig 9. FMI image at coaxial zone (623.3 - 625.1 m) of the Nojima fault.  
Sinusoidal curves indicate fractures.

have the dominant trend of strike as NW-SE. This fracture trend is consistent with the azimuth of the fast shear wave estimated from the DS1 data. Therefore seismic anisotropy at outside of the fault zone is considered to be caused by the aligned fractures. The fracture strike inside of the fault zone is widely dispersed. However, the concentration of the fractures at the depth range, where the logging data showed extremely large anomaly in the fault zone, strikes as NE - SW. This fracture trend is roughly parallels the surface strike of the Nojima fault. It is important to note that almost all the resistive fractures are distributed in the shallower depth than the coaxial zone (623.3 - 625.1 m) and the trend of the resistive fractures is NE - SW. Most of the fractures at coaxial zone have the same strike and high dip angle. This strike and dip are good agreement with the surface strike of the Nojima fault and the dip estimated from the depth of the fault gouge, respectively. From the tube wave analysis of hydrophone VSP, there are permeable fractures at coaxial zone.

For the future study, we will characterize the permeable fracture system in the Nojima fault by using the hydrophone VSP data and the logging data.

## REFERENCES

Ito, H., Kuwahara, Y., Miyazaki, T., Nishizawa, O., Kiguchi, T., Fujimoto, K., Ohtani, T., Tanaka, H., Higuchi, T., Agar, S., Brie A. & Yamamoto, H. 1996. Structure and physical properties of the Nojima Fault, BUTSURI-TANSA, 49, 522-535 (in Japanese with English abstract).

Kiguchi, T., Ito, H., Kuwahara, Y. & Miyazaki, T. 1998. Estimation of permeability of Nojima fault by hydrophone VSP experiment, Proceedings of the 4th SEGJ International Symposium, 335 - 342.

Tanaka, H., Higuchi, T., Tomida, N., Fujimoto, K., Ohtani, T. & Ito, H. 1999. Distribution, deformation and alteration of fault rocks along the GSJ core penetrating the Nojima Fault, Awaji Island, Southwest Japan. Jour. Geol. Soc. Japan, 105, 72-85 (in Japanese with English abstract).

blank page

# Reorientation of cores and distribution of macroscopic fractures along the GSJ borehole penetrating the Nojima fault zone

Tomoyuki Ohtani<sup>1</sup>, Teruki Miyazaki<sup>1</sup>, Hidemi Tanaka<sup>2</sup>, Takayuki Higuchi<sup>2</sup>, Koichiro Fujimoto<sup>1</sup>, and Hisao Ito<sup>1</sup>

*1: Geological Survey of Japan, Tsukuba, 305-8567 Ibaraki, Japan. TEL: +81-298-54-3706, FAX: +81-298-54-3702. E-mail: ohtani@gsj.go.jp*

*2: Department of Earth Sciences, Ehime University, 2-5 Bunkyo-cho, Matsuyama, Ehime 790-8577, Japan*

## ABSTRACT

Reorientation of cores from the GSJ borehole penetrating the Nojima fault zone was attempted by the comparison of the core scanner and the Fullbore Formation Microimager (FMI) images, and the distribution and orientation of macroscopic fractures from core scanner images were measured. Although more than half of cores above 350 m depth were reoriented, the cores in the fault zone were difficult to orient by the comparison of the core scanner and FMI images. Open fractures with shallow dipping are developed irrespective of depth along the borehole. Distribution of sealed fractures is consistent with that of the porphyry intrusives and the fault core of the Nojima fault zone. The orientation of the sealed fractures is NE-SW with steeply NW dipping and NNE-SSW with steeply ESE dipping. NNE-SSW sealed fractures are almost parallel to the fault core of the Nojima fault zone. These two types of the sealed fractures might be a conjugate set. As open fractures were formed after the development of the sealed fracture, both open and sealed fractures are probably related to the activity of the Nojima fault.

## INTRODUCTION

After the 1995 Kobe (Hyogo-ken Nanbu) earthquake (M7.2), southwest Japan, Geological Survey of Japan (GSJ) drilled a 746.7 m borehole to clarify the nature of the fault zone just after the large earthquake. The borehole penetrated the fault zone and provided samples of brittle fault rocks. This enabled us to perform continuous observation of the unweathered fault rocks in the Nojima fault zone. This fault drilling by GSJ (Ito et al. 1996) is one of the first experiences of direct observation of subsurface fault zones just after a large earthquake.

Although the orientation of the deformational features of the fault rocks is important for the structural study, the cores from the borehole are generally not oriented. A few cores from the GSJ borehole were oriented during the drilling, and most cores were not oriented. To estimate the

orientation of cores, the core scanner images were compared with the Fullbore Formation Microimager (FMI, trademark of Schlumberger) images.

Fracture distribution along faults is important for fault strength, fluid flow in fault zones. These are related to not only earthquake generation but also the problem of the nuclear waste deposit. Borehole survey enables us to understand the underground fracture distribution along the active faults. To estimate the fracture distribution, we measured the orientation of fractures on the core scanner images. Although the orientation of fractures could be measured only on the reoriented core scanner images, open and sealed fractures could be distinguished on the images.

## REORIENTATION OF CORES

Core scanner images are compared with FMI images to estimate the orientation of cores. Core images were captured using DMT corescan system (Miyazaki et al., 1997). This consists of a CCD camera and core rotation unit. Cores are rotated on the rotation unit and a CCD camera captures whole core surface images. FMI is a logging tool to visualize the borehole wall based on the resistivity contrast. They enable to observe the fracture distribution continuously along boreholes. FMI images reflect not only open fractures but also minor shear zones (Fig. 1). In general, it is difficult to detect mineralized veins from FMI images and to distinguish between open fractures and minor shear zones. Aplite veins are a good indicator to estimate the orientation of cores.

The success rate of core reorientation is very low in and around the fault core (Fig. 2). This results in discontinuity of recovered core samples. As the continuity of cores is good outside of the fault zone, some reorientation markers such as open fractures and aplite veins are included on a core scanner image. In contrast, few markers are included on an image in the fault zone. This makes difficult to estimate the orientation of cores.

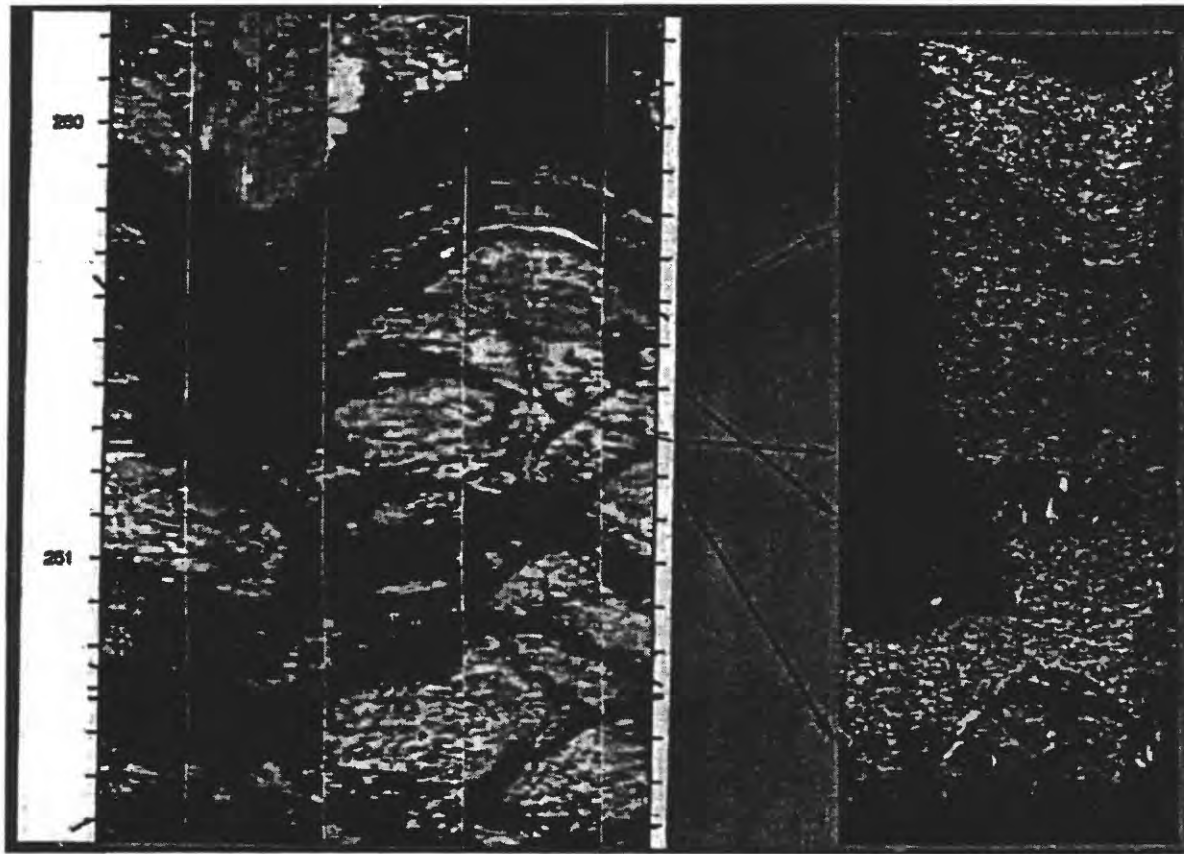


Fig. 1 FMI (left) and core scanner (right) images.

#### FRACTURE DISTRIBUTION ALONG THE GSJ BOREHOLE

Fracture distribution along the GSJ borehole was estimated, no matter what the success of reorientation (Fig. 3). Distribution of open fractures is almost constant from 150 to 650 m depth. The number of open fractures increases below 650 m depth. Distribution of sealed fractures such as zeolite and carbonate veins and minor shear zones is changed according to depth. The number of sealed fractures is small above 300 m depth. From 350 to 500 m depth, many sealed fractures are distributed. This depth interval is consistent with the distribution of the porphyry intrusives. Sealed fractures increase again in and near the fault core of the Nojima fault zone from 600 to 650 m depth.

The tendency of dip angle of open fractures (Fig. 4) is greatly different from that of sealed fractures (Fig. 5). Dip angle of open fractures is characterized by shallow angle. In contrast, that of sealed fractures is high angle.

Dip direction of open fractures concentrates to 180-240°. This trend is changed according to depth (Fig. 6). That of sealed fractures trends to 90-150° and 300-330°. This is remarkable trend of sealed

fractures above 500 m depth (Fig. 7). Sealed fractures below 500 m depth do not have a marked tendency.

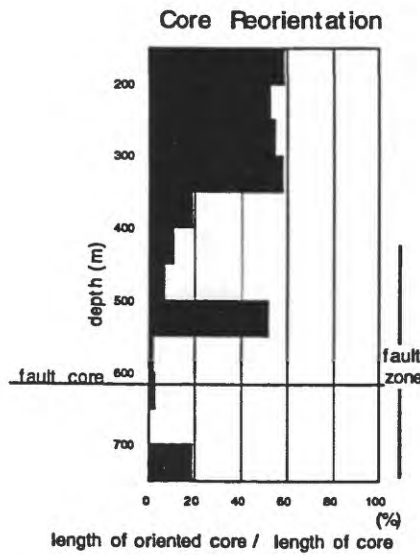


Fig. 2 Success rate of core reorientation

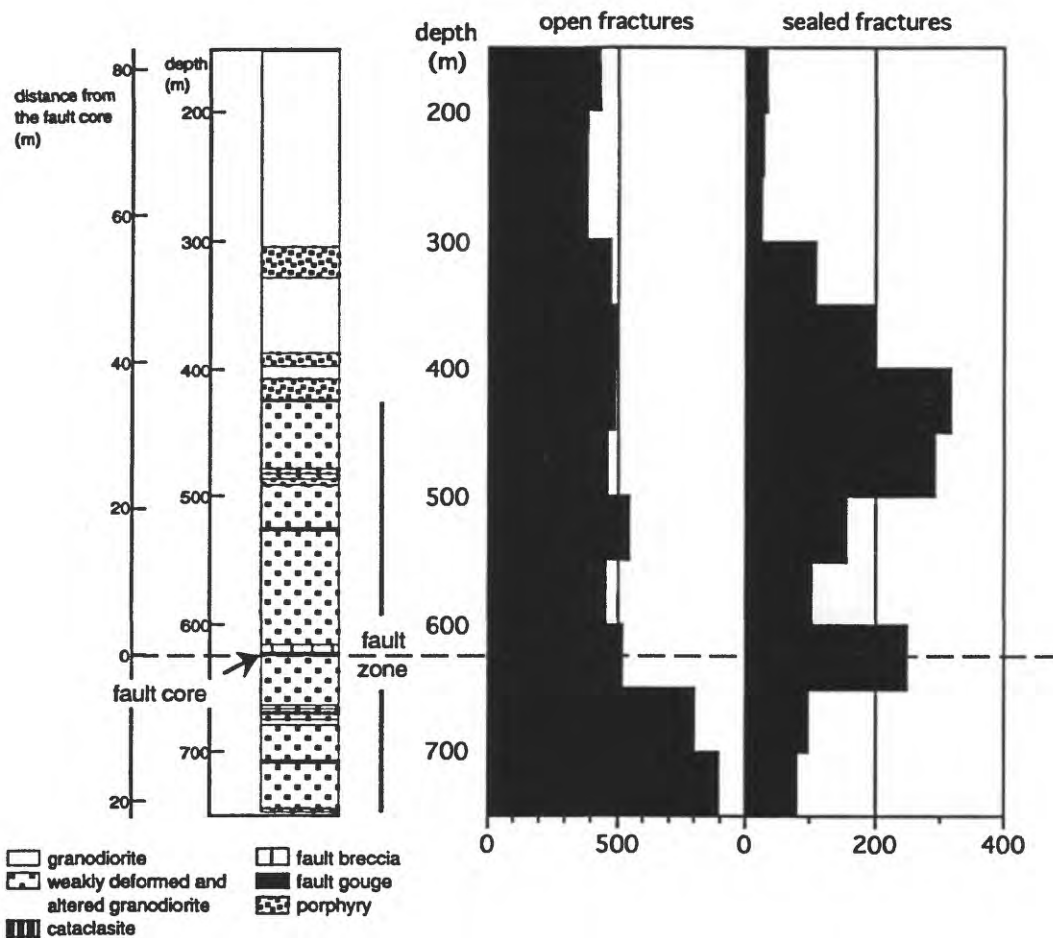


Fig. 3 Distribution of open and sealed fractures

## DISCUSSION

Reorientation of cores by the comparison of the core scanner and FMI images is the first experience for cores from the borehole penetrating the active

fault zone. This will provide a future active fault drilling with useful information. Reorientation of cores was difficult in the Nojima fault zone. One reason is that the length of each core is short in the fault zone. Another reason is that the GSJ borehole

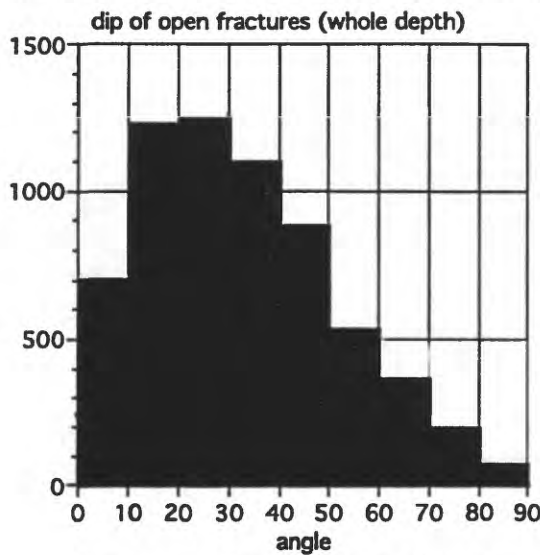


Fig. 4

Dip angle of open fractures

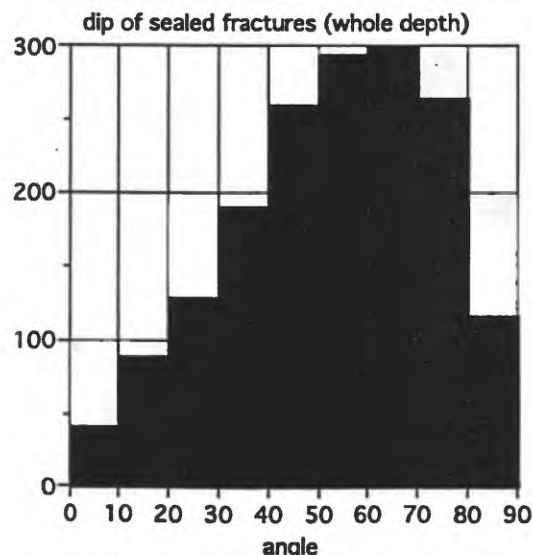


Fig. 5

Dip angle of sealed fractures

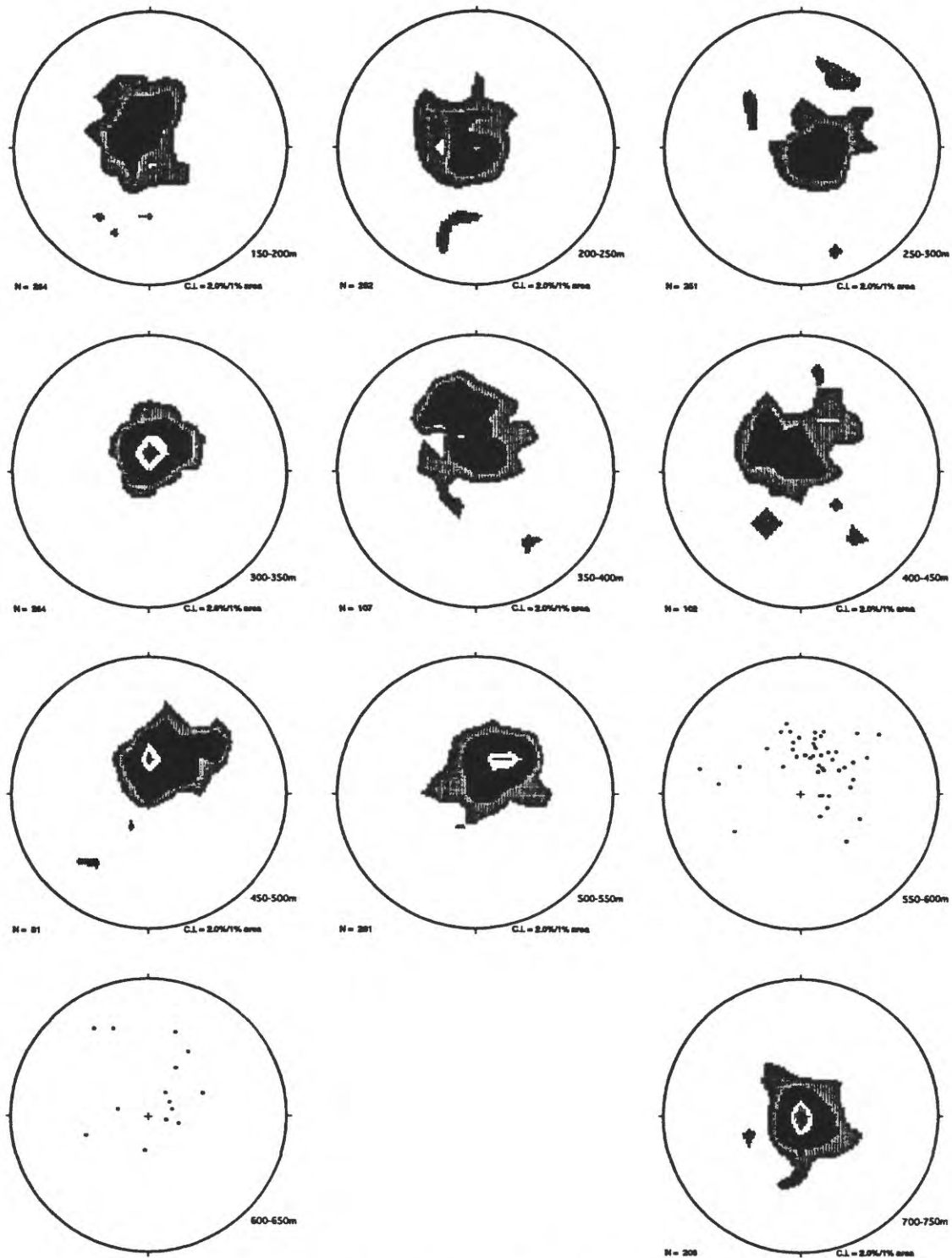


Fig. 6 Stereonet projection of open fractures. Equal area and lower hemisphere projection.

penetrated the fault rocks originated from granodiorite and porphyry intrusives. These rocks have few good markers for core reorientation. Foliated rocks such as sedimentary rocks and metamorphic rocks have an advantage for core

reorientation, because foliation is often detectable by FMI and it becomes a good marker. Generally, it is difficult to reorient cores in the fault zones. Oriented coring is necessary to recover the oriented cores.

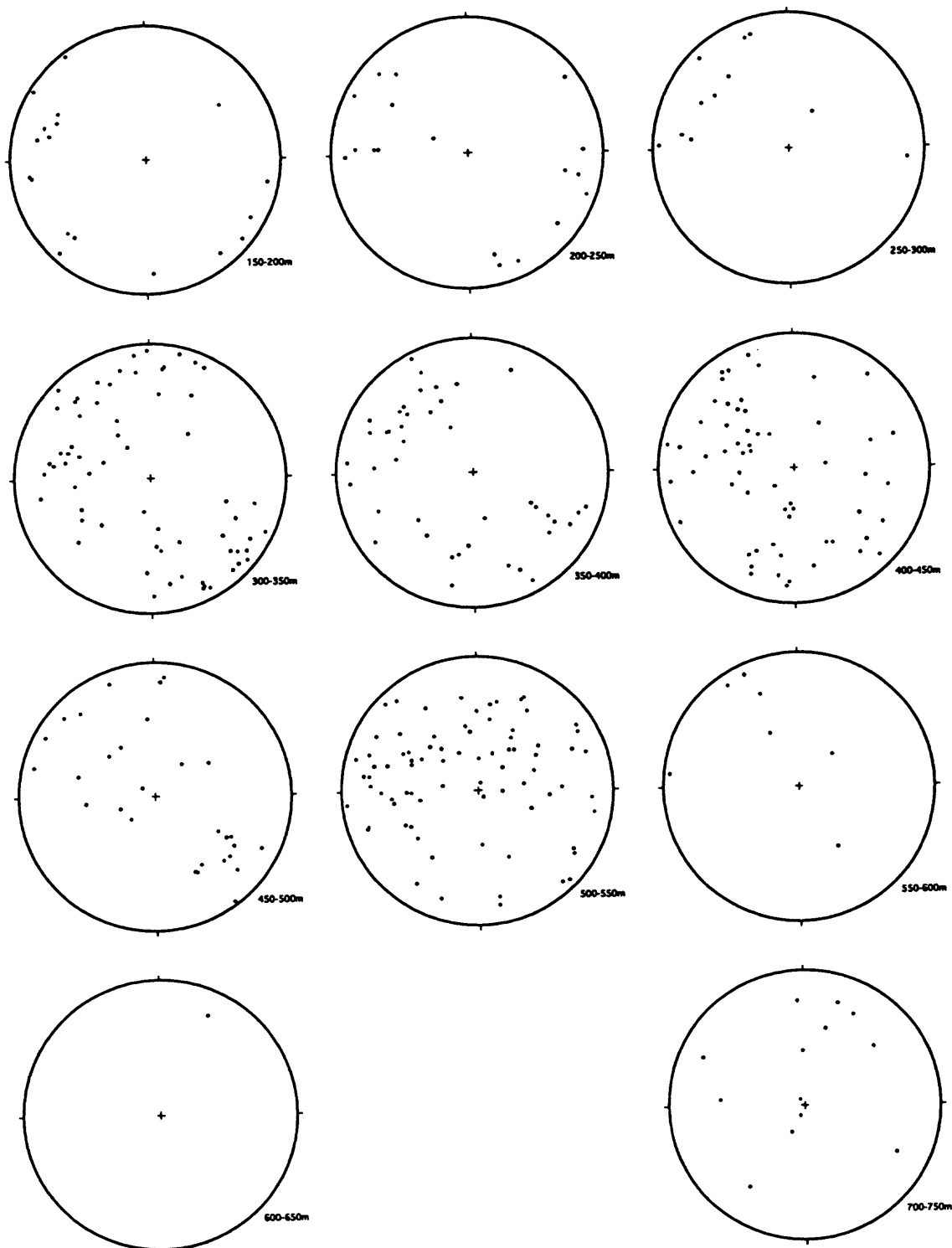


Fig. 7      Stereonet projection of sealed fractures. Equal area and lower hemisphere projection.

Distribution of the open fractures is greatly different from that of the sealed fractures. The open fractures seem to be distributed irrespective of the Nojima fault zone. They gently dip, and they are

almost normal to the fault core of the Nojima fault zone. In contrast, the sealed fractures are distributed in connection with the porphyry intrusives and the fault core. This suggests that the

sealed fractures are related to the porphyry intrusion and the activity of the Nojima fault. The porphyry intrusion is expected to enhance the hydrothermal activity around the porphyry intrusives during the intrusion. The difference of physical property between the granodiorite and the porphyry intrusives, however, may cause the difference of the sealed fracture distribution. Because the porphyry consists of finer grains rather than the granodiorite, the porphyry may be fractured into the smaller pieces than the granodiorite. As there are no porphyry intrusives close to the fault core, the sealed fractures from 600 to 650 m depth is probably related to the activity of the Nojima fault. After a large earthquake, the fault core is expected to be a conduit of fluids. If the hydrothermal fluid flows along the fault core from the deeper part, the sealed fractures would be developed in and close to the fault core. The orientation of the sealed fractures is NE-SW with steeply NW dipping and NNE-SSW with steeply ESE dipping. The sealed fractures which trend NNE-SSW with steeply ESE dipping are almost parallel to the fault core of the Nojima fault zone. Those which trend NNE-SSW with steeply ESE dipping might be a conjugate set of NE-SW with steeply NW dipping. If these two types of sealed fractures are a conjugate set, these sealed fractures are suggested to be related to the activity of the Nojima fault. This also means that the porphyry intrusion might be related to the activity of the Nojima fault.

As open fractures are generated after the sealed fractures, they are not a primary structure of the granodiorite. The characteristics of the open fractures may suggest the fracture development in the shallower zone or recent fracture development in the fault zone rather than the sealed fractures.

## CONCLUSIONS

1. The success rate of the core reorientation by the

comparison of core scanner and FMI images is more than 50 percent above 350 m depth and quite low in the Nojima fault zone

2. The number of open fractures is developed irrespective of depth along the borehole. Open fractures have shallow dipping.
3. The number of sealed fractures increases from 350 to 500 m and 600 to 650 m depth. The former is consistent with the distribution of the porphyry intrusives, and the latter is the fault core of the Nojima fault zone. The orientation of the sealed fractures is NE-SW with steeply NW dipping and NNE-SSW with steeply ESE dipping. NNE-SSW sealed fractures are almost parallel to the fault core of the Nojima fault zone. These two types of the sealed fractures might be a conjugate set.

## REFERENCES

Ito, H., Kuwahara, Y., Miyazaki, T., Nishizawa, O., Kiguchi, T., Fujimoto, K., Ohtani, T., Tanaka, H., Higuchi, T., Agar, S., Brie, A. & Yamamoto, H. 1996. Structure and Physical Properties of the Nojima Fault. *BUTSURI-TANSA* 49, 522-535\*

Miyazaki, T., Ito, H., Tanaka, H. & Higuchi, T. 1997. Core image data of Nojima-Hirabayashi borehole (v.1.0). Geol. Surv. Japan Open-file Rep., no. 1997-306.\*\*

Tanaka, H., Higuchi, T., Tomida, N., Fujimoto, K., Ohtani, T. & Ito, H. 1999. Mode of fault rocks distribution and their mode of deformation and alteration along GSJ drilling core penetrating the Nojima earthquake fault, northwest of Awaji Island, Southwest Japan. *Journal of Geological Society of Japan* 105, 72-85.\*

\* in Japanese with English abstract

\*\* in Japanese

# Temperature Monitoring in a Borehole Drilled into the Nojima Fault and Radioactive Heat Production of Core Samples

Tohru Yamaguchi<sup>1</sup>, Makoto Yamano<sup>2</sup>, Toshiyasu Nagao<sup>3</sup>, and Shusaku Goto<sup>4</sup>

<sup>1</sup>*RIKEN International Frontier Program on Earthquake Research, c/o Earthquake Prediction Research Center, Tokai University, 3-20-1 Orido, Shimizu, Shizuoka 424-8610, Japan*

<sup>2</sup>*Earthquake Research Institute, University of Tokyo, 1-1-1 Yayoi, Bunkyo-ku, Tokyo 113-0032, Japan*

<sup>3</sup>*Earthquake Prediction Research Center, Tokai University, 3-20-1 Orido, Shimizu, Shizuoka 424-8610, Japan*

<sup>4</sup>*School of Marine Science and Technology, Tokai University, 3-20-1 Orido, Shimizu, Shizuoka 424-8610, Japan*

## ABSTRACT

Long-term monitoring of the temperature distribution in a borehole drilled into the Nojima fault was conducted using the optical fiber temperature sensing technique. The temperature profile down to a depth of 1470 m has been measured over two years with a spatial resolution of 1 m and the temperature resolution of about 0.1 K. Distinct local temperature anomalies were observed at three depths in the upper part of the hole (above 500 m). They may be attributed to localized groundwater flows in the surrounding formations and some of them seem to correspond to fractured zones. One of the anomaly was very stable, while the other two were of transient nature. The water level in the borehole can be estimated from the diurnal temperature variations in the uppermost part of the hole and may provide information on the pore pressure in the fault zone. Thermal conductivity and radioactive heat production were measured on core samples and the obtained values are well correlated with the lithology. The conductive heat flow calculated from the overall temperature profile appears to increase with depth. It probably result from errors in thermal conductivity due to sampling problems and/or from advective heat transfer by regional groundwater flow. Assuming that the middle part of the hole (less fractured granite layer) is least affected by these factors, heat flow at this site is estimated to be  $70 \pm 15 \text{ mW/m}^2$ .

## INTRODUCTION

Terrestrial heat flow, an important constraint on the subsurface thermal structure, is determined from the geothermal gradient and the thermal conductivity. On land, the geothermal gradient is usually obtained through temperature logging in boreholes.

As the temperature profiles are disturbed by drilling effects, we need to log the temperature long after the drilling or to extrapolate repeated temperature logs to the equilibrium for determination of the undisturbed geothermal gradient. This problem can be avoided if temperature sensors are installed in a borehole for long-term measurements. Long-term monitoring of the borehole temperature profile is also useful for detection of temporal variations of fluid flows in and around the hole.

We have been monitoring the temperature profile in a borehole drilled into the Nojima fault in Awaji island, southwest Japan since July, 1997, as part of the "Nojima Fault-zone Probe" project for geophysical and geological investigations of an earthquake fault (Ando, 1997). We also measured thermal properties of core samples (thermal conductivity and radioactive heat production). The purposes of these works are: 1) to determine the terrestrial heat flow precisely; and 2) to detect possible effects of fluid flows on the temperature profile. A reliable heat flow data is necessary for estimation of the thermal structure in the crust, which is important for studies of geophysical and geochemical processes around the fault. Extensively fractured and highly permeable zones are expected to exist around the Nojima fault and they would act as conduits for groundwater flows. Such flows may be temporally variable, especially right after the earthquake, and might affect the distribution of heat producing elements.

## TEMPERATURE MONITORING WITH AN OPTIC FIBER CABLE

We used the distributed optical fiber temperature sensing technique for temperature monitoring. It determines the temperature distribution continu-

ously along an optic fiber by sending a pulsed laser into the fiber and measuring the spectrum of the backscattered light. This relatively new technology is widely used in industry and can be a unique tool for temperature measurements in boreholes as well (Hurtig et al., 1993). Once an optic fiber cable has been installed in the hole, the temperature profile can be measured at any time, though the temperature resolution is much lower than that of ordinary thermistor or quartz sensors. For the system used in the present study, the spatial resolution is 1 m and the temperature resolution is about 0.3 K.

We installed an optic fiber together with three seismometers in a 1740 m deep borehole at 34° 33.0' N, 134° 56.8' E (Ogura 1800-m hole). The hole did not penetrate through the Nojima fault, but the bottom part is highly fractured and thought to be in the fault zone. It was cased from the ground surface to the bottom with perforations between 1596 m and 1671 m for water injection experiments. The bottom end of the fiber cable is located just above the topmost seismometer, at 1470 m. We started monitoring the temperature distribution on July 15, 1997. A single measurement is made through integration of a large number of pulses for 18 min. We can attain a better temperature resolution of about 0.1 K by averaging data for 90 min. or more. The temperature data presented in the following are 180 min. averages.

Examples of temperature variations with time (at 200, 800, and 1400 m) are shown in Figure 1 (there is an interruption for about 180 days due to a trouble with the measurement system). Rapid (sudden) changes and gradual variations by up to 0.8 K are observed, but the variation patterns at different depths are very to each other, though the amplitudes are different. We therefore believe they represent drifts of the measurement system, not real temperature variations in the hole. There is a tendency for the temperature to become more stable with time, indicating stabilization of the system.

#### GROUNDWATER FLOW

The obtained temperature profile is generally smooth (cf. Fig. 3), but several minor kinks are found mainly in the upper part of the hole, indicating the existence of localized groundwater flow around the hole. Most distinct ones are at around 80 m, 380 m, and 500 m (Fig. 2). The location of

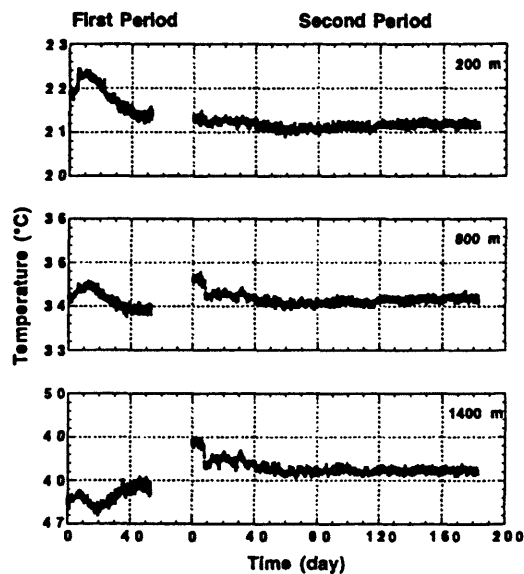


Figure 1. Temperatures (180 min. running averages) at 200, 800, and 1400 m plotted against time. The actual interval of the first and second measurement periods is about 6 months.

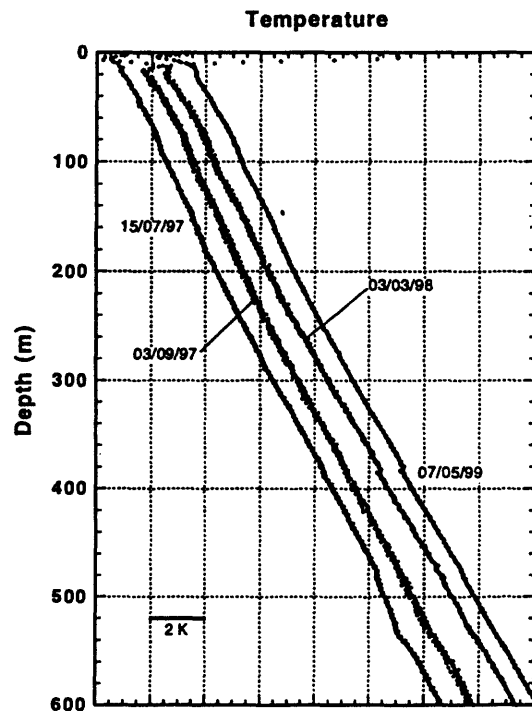


Figure 2. Temporal variations of local temperature anomalies demonstrated by temperature profiles at four different times (July 15 and September 3 in 1997, March 3 in 1998, and May 7 in 1998). The temperature origin of each profile is shifted on the temperature axis so that the shapes of the profiles can be easily compared.

the anomaly around 80 m coincide with a fractured zone detected while drilling the hole. The anomaly around 380 m is possibly related to a fractured zone between 396 m and 400 m, but the one around 500 m does not seem to correspond to any fractured zone.

The anomaly around 80 m appears to be stable as the shape of the temperature profile has not changed to the present, while the other two anomalies varied with time. The temporal changes suggest that groundwater flows around the hole have some transient components. Except for these localized anomalies and the drifts in the measurement system, the temperature profile has been quite stable.

The temperature profile of the topmost part of the hole shows diurnal variations and the depth above which the diurnal variation is significant has changed with time. This depth is thought to correspond to the water level in the hole, which can be an indicator of the pore pressure in formations of the perforated zone from 1596 to 1671 m. Monitoring of the temperature profiles may therefore provide information on the temporal variation of the pore water pressure in the Nojima fault zone.

A series of water injection experiments will be

carried out early in 2000 and we expect to obtain more information on the hydrological characteristics around the hole by monitoring the temperature profile during and after the experiments.

## THERMAL CONDUCTIVITY AND HEAT PRODUCTION

We measured thermal conductivity on relatively unfractured rock samples selected from the recovered cores in wet (water-saturated) conditions using the transient line-source probe method (Sass et al., 1984). The obtained values are plotted versus depth in Figure 3 together with the lithology and the temperature. It appears that granite, which mainly lies below 560 m, have higher thermal conductivity than other types of rocks (andesite, diorite and granodiorite) composing the most part of the layers above 560 m. The mean conductivity with the standard deviation is  $3.10 \pm 0.19 \text{ W/m/K}$  for granite and  $2.48 \pm 0.16 \text{ W/m/K}$  for other rocks.

We also measured radioactive heat production on the same core samples (Fig. 3). The heat production rates were calculated from the uranium, thorium and potassium contents determined with the  $\gamma$ -ray spectrometry technique (Rybäch, 1989). The

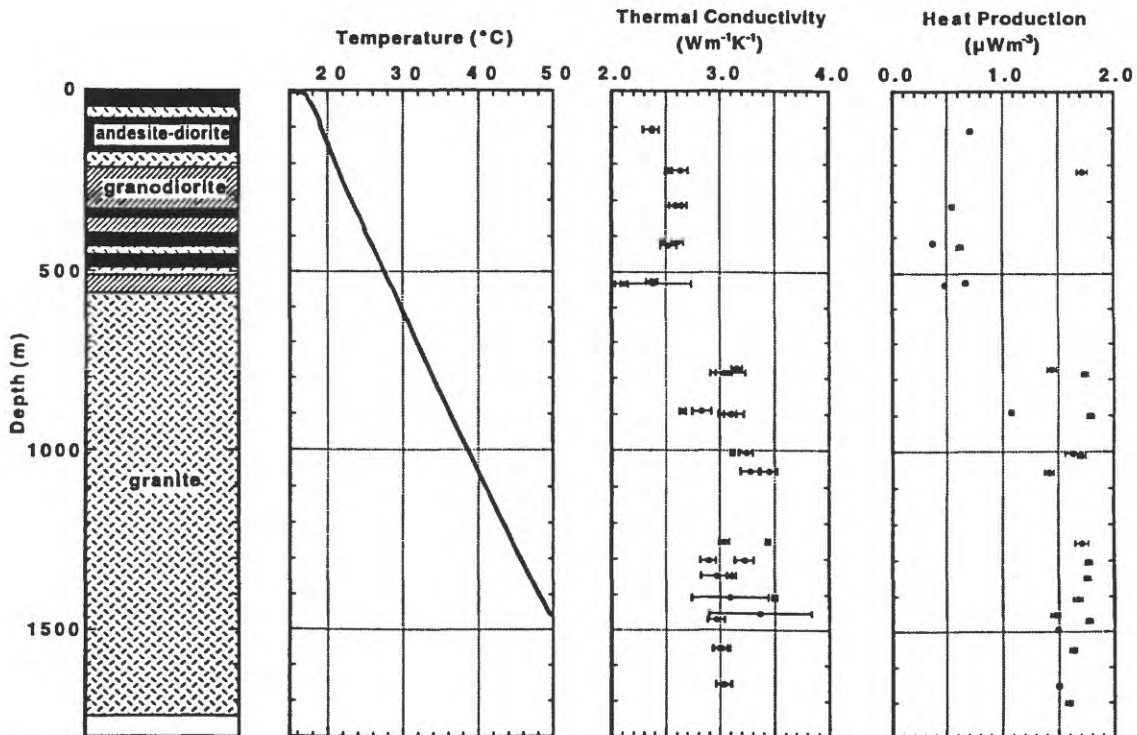


Figure 3. Simplified lithology of the Ogura 1800-m hole, temperature profile on April 22, 1998, and thermal conductivity and radioactive heat production measured on core samples.

average of heat production is  $1.60 \mu\text{W}/\text{m}^3$  in the granite layer below 560 m, while it is relatively low,  $0.57 \mu\text{W}/\text{m}^3$ , in the above layers. A good correlation between the thermal conductivity and the heat production is apparently due to the difference in mineral composition between the upper part and the lower part of the hole. The heat production of granite is consistent with the values reported for granitic rocks in the surrounding area (Miyake et al., 1975).

The distributions of three radioactive elements

(U, Th, and K) are generally similar to that of the total heat production, but the uranium content seems to decrease with depth around 1300 m (Fig. 4). Since uranium has a higher solubility than the other two elements, the lower uranium content in the deeper part may be attributed to groundwater circulation in highly fractured layers, though such a distribution may also be a result of the differentiation process during crystallization of the granite. We need to make more dense measurements in deeper layers in order to examine a possible correlation.

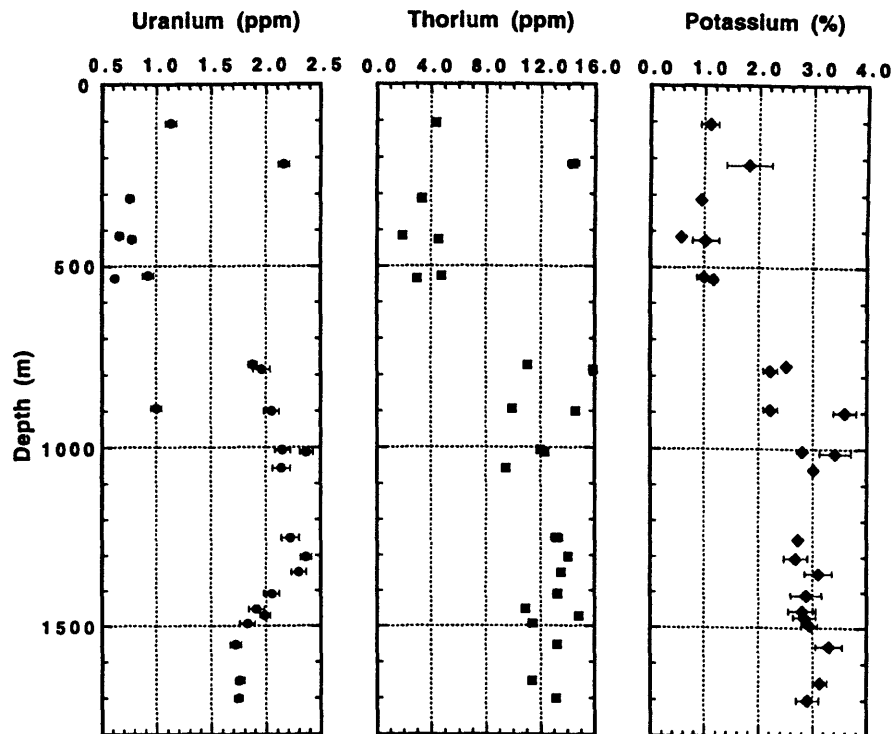


Figure 4. U, Th and K contents of the Ogura 1800-m hole samples plotted versus depth.

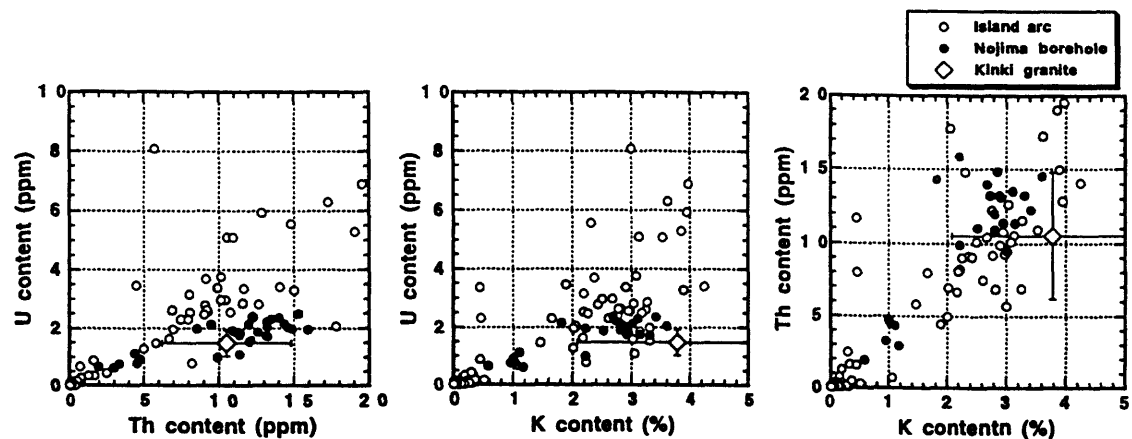


Figure 5. U-Th, U-K and Th-K relations for Nojima borehole samples and typical island arc crustal rocks (Mukai et al., 1999) with the average for granite in the Kinki district (Miyake et al., 1975).

tion between the concentration of radioactive elements and the fractured zones.

The relationships among the contents of U, Th, and K for the samples measured in this study and typical island arc crustal rocks (Mukai et al., 1999) are shown in Figure 5. The U/K and U/Th ratios of the Nojima borehole samples are relatively low, but similar to the average values for granite in the Kinki district (Miyake et al., 1975), in which the borehole is located. The low uranium content may be a common feature of granite in the Kinki district.

#### TERRRESTRIAL HEAT FLOW

Although there are some temperature anomalies probably due to localized groundwater flows, the terrestrial heat flow can be calculated from the overall temperature profile, which has been very stable for the last two years. We plotted the temperature against the thermal resistance between the ground surface and the measurement depth calculated from the above mean conductivity values (Fig. 6). The conductive heat flow, which is given by the slope of this plot, seems to increase with

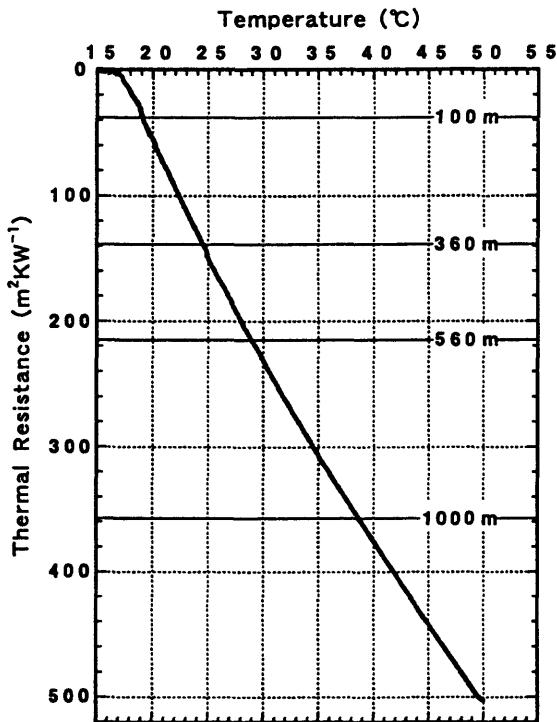


Figure 6. Temperature measured on April 22, 1998 plotted against the thermal resistance for determination of the conductive heat flow. Horizontal lines are the boundaries used for calculation of heat flow in specific depth intervals.

depth. The average heat flow for the andesite-diorite-granodiorite layer above 560 m (excluding the top 20 m) and for the underlying granite layer is 55 and 73 mW/m<sup>2</sup> respectively. Excluding zones with local temperature anomalies in the upper layer, it is 54 mW/m<sup>2</sup> for a zone from 100 to 360 m.

The apparent increase in heat flow with depth may result partly from problems in sampling of cores for thermal conductivity measurements. While we made measurements on "good" samples with no significant cracks, the formations drilled through contain many fractured zones. Since the fractures must be filled with water in natural condition, the thermal conductivity of the fractured formation is expected to be lower than the conductivity measured on solid rocks. If the granite layer is sub-divided at 1000 m, below which more fractured zones exist, the average heat flow is 68 mW/m<sup>2</sup> for 560 to 1000 m and 76 mW/m<sup>2</sup> below 1000 m. This difference might be attributed to the effect of fractures.

It is also possible that the variation of conductive heat flow is an indication of advective heat flux by diffuse pore fluid flow. As the most simple model, a uniform downward flow with a Darcy velocity of  $2 - 3 \times 10^{-10}$  m/s can reproduce the observed temperature profile quite well, though the actual flow regime must be much more complicated.

The third possibility is that we observed a thermal effect of the 1995 Hyogoken-Nanbu earthquake (January 17, 1995). Frictional heating in the shear zone or advective heat transfer by fluid movement associated with the fault rupture could be the heat source. The temperature profile, however, has not significantly changed for over two years, suggesting that the effect of the earthquake, which must be intrinsically transient, is small.

Based on the above discussion, we estimate the heat flow from the deep to be  $70 \pm 15$  mW/m<sup>2</sup>, supposing that the value for granite layers with less fractured zones and with no local temperature anomalies (560 to 1000 m) is most reliable. In the Hirabayashi 1800-m hole, located about 4 km northeast of the present site, heat flow was determined to be 57 mW/m<sup>2</sup> (Kitajima et al., 1998). In a 1200 m deep hole about 10 km to the southwest, a value of 47 mW/m<sup>2</sup> is reported but the temperature gradient is slightly higher in the deeper part of the hole (Furukawa et al., 1998). These data indicate that the regional heat flow in the northern part of the

Awaji island is 50 to 70 mW/m<sup>2</sup>. It is consistent with the surface heat flow distribution given by a thermal model of subduction for the southwest Japan arc (Wang et al., 1995).

The subsurface temperature structure can be calculated based on the surface heat flow and radioactive heat production data obtained by this study. We assume that the thermal regime is one-dimensional, steady-state and purely conductive. With the thermal conductivity and the depth scale of exponential distribution of the heat production typical of the upper continental crust, the temperature at the maximum depth of aftershocks of the 1995 Hyogoken-Nanbu earthquake (17 km) is estimated to be 300 to 450 °C. It is consistent with the temperature of the cutoff depth of crustal earthquakes previously reported for other areas (e.g. Chen and Molnar, 1983; Ito, 1990; Kitajima et al., 1997).

#### REFERENCES

Ando, M., 1997, Geophysical and geological drilling into the Nojima fault – the 1995 Hyogoken Nanbu earthquake fault in Awaji island, Japan, *Eos, Transactions, Am. Geophys. Un.*, **78**, F492 (abstract).

Chen, W.P. and Molnar, P., 1983, Focal depths of intracontinental and interplate earthquakes and its interpretations for the thermal and mechanical properties of the lithosphere, *J. Geophys. Res.*, **88**, 4183-4214.

Furukawa, Y., Shinjoe, H. and Nishimura, S., 1998, Heat flow in the southwest Japan arc and its implication for thermal processes under arcs, *Geophys. Res. Lett.*, **25**, 1087-1090.

Hurtig, E., Schröter, J., Großwig, S., Kühn, K., Harjes, B., Wieferig, W. and Orrell, R.P., 1993, Borehole temperature measurements using distributed fibre optic sensing, *Scientific Drilling*, **3**, 283-286.

Ito, K., 1990, Regional variations of the cutoff depth of seismicity in the crust and their relation to heat flow and large inland-earthquakes, *J. Phys. Earth*, **38**, 223-250.

Kitajima, T., Kobayashi, Y., Suzuki, H., Ikeda, R., Omura, K., Kasahara, K. and Okada, Y., 1997, Thermal structure and earthquakes beneath the Kanto district, *1997 Japan Earth and Planetary Science Joint Meeting, Abstracts*, 247 (in Japanese).

Kitajima, T., Kobayashi, Y., Ikeda, R., Iio, Y. and Omura, K., 1998, Heat flow measurement in Nojima-Hirabayashi, Awaji Island, *Chikyu Monthly Extra*, No. 21, 108-113 (in Japanese).

Miyake, Y., Sugimura, Y., and Hirao, Y., 1975, Uranium, thorium, and potassium contents in granitic and basaltic rocks in Japan, *The Natural Radiotaion Environment II* (J.A.S. Adams, W.M. Lowder, and T.F. Gesell eds.), U.S. Energy Research & Development Admin., Washington, D.C., 535-558.

Mukai M., Yamaguchi, T., Komura, K., Furumoto, M., and Nagao, T., 1999, Measurement of radioactive heat generation in rocks by means of gamma ray spectrometry, *Proc. Japan Acad.*, **75**, Ser. B, 181-185.

Rybäch, L., Determination of heat production rate, 1989, *Handbook of Terrestrial Heat-flow Density Determination* (R. Haenel, L. Rybäch and L. Stegenga, eds.), Kluwer Academic Publ., Dordrecht, 125-142.

Sass, J.H., Stone, C. and Munroe, R.J., 1984, Thermal conductivity determinations on solid rocks - a comparison between a steady-state divided-bar apparatus and a commercial transient line-source device, *J. Volcanol. Geothermal Res.*, **20**, 145-153.

Wang, K., Hyndman R.D. and Yamano, M., 1995, Thermal regime of the southwest Japan subduction zone: effects of age history of the subducting plate, *Tectonophysics*, **248**, 53-69.

# Deep Structure of the Nojima Fault by Trapped Wave Analysis

Yasuto Kuwahara and Hisao Ito

*Earthquake Research Department, Geological Survey of Japan  
1-1-3 Higashi, Tsukuba, Ibaraki 305-8567, Japan*

## ABSTRACT

Fault zone trapped waves have been demonstrated to be useful for studying segmentation of faults and for studying physical properties, such as width, Q, and velocities, of fault zones. We observed the fault zone trapped waves using surface seismometer arrays on the Nojima fault immediately after the 1995 Kobe earthquake. In order to study physical properties; such as velocity, width and Q values of fault zones, we have installed 3 borehole seismometers at the depths of 400m, 500m and 600m. The borehole seismometer at the depth of 600m is almost at the center of the low velocity zone of the Nojima fault. The seismometer at the depth of 400m is outside the low velocity zone. The surface array observations have also been conducted simultaneously. The results are follows: 1) The trapped waves observed in the borehole have much higher frequency (about 30 Hz) than those observed at the surface (about 5 Hz). 2) The velocity amplitudes of wave trains following direct S waves at the depth of 600m are larger than those at the depth of 400m when the trapped waves are observed at the surface seismometer array. These indicate that the results of the physical properties of the fault zone from the surface observation must be changed to generate trapped waves of higher frequency. We demonstrated that the characters of the trapped wave observed at the surface are consistent with those of synthetic trapped waves for the model of 50% deduction of S-wave velocity comparing the surrounding materials and low Q ( $Q=10$ ) in the fault zone whose width is 50m. However, the present study shows that the surface waveforms are affected by shallow structure and are not adequate for estimating deep physical properties. With the borehole data, we infer more low S wave velocity contrast and/or

more narrower fault zone width.

## INTRODUCTION

After the 1995 Hyogoken-nanbu earthquake ( $M_s = 7.2$ ) on January 17, about 10 km long distinguished surface breaks of the Nojima fault in Awaji island, Japan, appeared (Awata et al., 1996). Detailed structures of Nojima fault were delineated by fault drilling to the depth of 746.7 m (Ito et al., 1996). Ito et al. (1996) and Tanaka et al. (1998) elucidate the lithology by core inspection and the physical properties such as electric resistivity, density, and seismic velocities through the borehole by borehole logging. They find the fault zone with a width of a few tens of meters characterized by altered and deformed granodiorite with fault gouge, low resistivity, low density, and low velocities.

Recent studies have established that seismic waves from small earthquakes are trapped in the low velocity zones of faults (Li and Leary, 1990; Li et al., 1994; Li et al., 1994a; Li et al., 1994b). It has been demonstrated that fault zone trapped wave is useful for studying the fault zone property, three dimensional geometry to seismogenic depths. The fault zone trapped waves have characteristics related to the velocity, attenuation, thickness and geometry of the fault zones. Thus, observations of trapped waves can reveal a fine structure of the fault zone in deeper parts to seismogenic depths.

Ito et al. (1995) estimate the width of a low velocity zone of the Nojima fault is less than 100 m from the trapped wave observation of surface seismic arrays, being consistent with the results of fault drilling. However, the wave forms of trapped seems to be contaminated by shallow fault structures, in which the foot wall side of the fault has sedimentary structure, the

hanging wall side has hard rock. In order to distinguish the effect of shallow structure on the trapped waveforms, we have conducted a downhole observation with a multi-level downhole seismometer array.

In this paper, we describe a surface seismic array observation on the Nojima fault just after the 1995 Kobe earthquake, and the downhole observation. We compare the results of deep structure from the surface and downhole observations.

## SURFACE ARRAY OBSERVATION

Ito and Kuwahara(1996) deployed a temporal seismic array to observe aftershocks of the 1995 Kobe earthquake in the north part of the Nojima fault in Awaji island for about two weeks from February 14, 1995. The array is perpendicular to the Nojima fault at Nojima Hirabayashi, where maximum right-lateral slip of about 2 m was observed (Awata et al, 1996). Fig. 1 shows a schematic view of the array observation. The array consists of 12 velocity type 3-component seismometers (Mark Products L-28B, 4.5 Hz). The total length of the array is about 250 m. Intervals of seismometer are about 5 m close to the fault , and about 35 m at the end of the array. It is noted that the soft sediments of the Osaka group are distributed in the west side of the Nojima fault, while the hard rock of granodiorite is distributed in the east side of the fault.

We found two types of waveforms among the recorded as shown in Fig. 2. First is the type of waveforms with fault zone trapped wave, and then second is that without trapped wave. We have observed distinct low frequency phase (the peak frequency is about 5 Hz) following the S wave only for the stations close to the fault surface break. The stations that are apart more than 50 m from the surface break did not show this low frequency phase. We have also found that this low frequency phase was observed only for the earthquakes occurred along the Nojima fault. These strongly suggest that these low frequency phases after S wave are fault zone trapped waves. We estimate the width of the Nojima fault is less than 100 m, because the

low frequency phase is observed only for the station less than 50 m apart from the fault.

Although we found distinct low frequency phases that are considered as fault zone trapped waves with surface seismic array, it is still difficult to analyze the data qualitatively with the surface array data. The soft sediment of the Osaka group are distributed in the west side of the Nojima fault, while the hard rock of granodiorite is distributed in the east side of the fault. Especially for the seismic stations on the soft sediment of the Osaka group, the waveforms are contaminated with low frequency noises.

## OBSERVATION WITH MULTI-LEVEL SEISMOMETERS IN THE BOREHOLE

After the fault drilling (Ito et al., 1997) has completed(Fig. 3), we have been using the multi-level digital borehole seismometer system (Fig. 4) that were developed by Ito et al.(1995)....The purposes and advantages of installing downhole seismometer array are 1) to reduce the seismic noises, 2) to increase high frequency sensitivity, 3) to avoid the effects of site geology and topography, 4) to avoid the changes in the condition of the array for the long term monitoring to detect the changes in trapped wave characteristics, for example, due to the fault healing process with time, and 5) to observe the trapped wave characteristics within the fault zone and outside of the fault zone.

The borehole seismometer system has three level seismometers with three-component sensors and a unit to digitize the data with 16 bits resolution at the maximum of 2 kHz. The sensors are 4.5 Hz velocity sensor and each satellite seismometers are fixed with the locking arm against the borehole wall. The waveform data are acquired by trigger mode. The directions of the two horizontal sensors were determined by analyzing the particle motion from the surface shots.

The three satellites were installed at the depth of 400 m (satellite 1), 500 m (satellite 2) and 600 m (satellite 1); The satellite 1 is outside of the fault zone, the satellite 2 is in the fault zone and the satellite 3 is very

close to the fault core. We are also deploying a surface seismic array to compare the waveforms at the surface and in the borehole.

Fig. 5 shows an example of the waveforms at the surface (upper) and in the borehole (lower) for the earthquake with the epicenter near the Nojima fault. The "PARA", "PERP" and "Z" show the horizontal components parallel and perpendicular to the surface strike of the Nojima fault, and vertical component, respectively. Fig. 5 shows distinct low frequency phases close to the fault for the surface array data, and waveforms with much higher frequency for the downhole data. It is noteworthy that the amplitudes of P and S waves at the depth of 600m are larger than those at the depth of 400m when the trapped waves are observed for the surface array. Fig. 6 shows the power spectrum of the waveforms of the surface seismometer (a), and downhole seismometer (b). It is shown that the spectrum of the downhole seismometer has much higher frequency component of about 35Hz, while the surface array has peak frequency of 6-7 Hz.

Fig. 7 shows the 10Hz low-pass filtered seismograms of event shown in Fig.5. It is clear that the seismic energy with the frequencies less than 10Hz is sufficient in the borehole. Only the energy with these low frequencies is observable at the surface array because the higher frequency energy is considered to be strong attenuated at the shallower parts of the fault zone than the depth of 400m.

#### DEEP STRUCTURE OF THE NOJIMA FAULT

It was demonstrated that the characters of the trapped wave observed at the surface are consistent with those of synthetic trapped waves for the model of 33% deduction of S-wave velocity comparing the surrounding materials and low Q ( $Q=10$ ) in the fault zone whose width is 50m. However, the results of the borehole observation indicate that the physical properties of the fault zone from the surface observation must be changed to generate trapped waves of higher frequency. We simulated fault zone trapped wave using a simple model

composed of a low-velocity, low-Q layer sandwiched between two half spaces with relatively high velocity and high Q by the method of Ben-Zion(1989). Fig. 8 shows examples of the simulations for various low velocity zone models. The SH line dislocation is positioned at the left interface of the low velocity zone and the source depth is 5km. The synthetic seismograms are calculated for the surface array with 50m sensor spacing. The model A is the best fitted model for the surface array observation. In order to generate higher frequencies than those of the model A, we test the models of the low velocity zone with a higher velocity, with a narrower width, and with higher Q as shown in the models B, C and D, respectively. The dominant frequency and the duration of the simulated trapped wave for the model D is about 30Hz and 0.3s, respectively, being consistent with the borehole observation, while the frequencies for the other models are much lower. It is, thus, shown that the characters of the trapped wave observed in the borehole are consistent with those of synthetic trapped waves for the model D of 33% deduction of S-wave velocity comparing the surrounding materials and low Q ( $Q=50$ ) in the fault zone whose width is 20m. The present study shows that the surface waveforms are affected by shallow structure and are not adequate for estimating deep physical properties by comparing observed waveforms with synthetic calculations. With the borehole data, we infer higher Q and/or narrower fault zone width than those estimated from the surface observation.

#### REFERENCES

Awata, Y., K. Mizuno, Y. Sugiyama, R. Imura, K. Shimokawa, K. Okumura, E. Tsukuda and K. Kimura, 1996, Surface fault ruptures on the northwest coast of Awaji Island associated with the Hyogo-ken Nanbu earthquake of 1995, Japan, *Zisin*, Suppl. 2, 49, 113-124, 1996.

Ben-Zion, Y and K. Aki, 1990, Seismic radiation from an SH line source in a laterally heterogeneous planar fault zone, *Bull. Seis. Soc. Am.* 80, 971-994.

Ito, H and Y. Kuwahara, 1996, Proceedings of VIIth International Symposium on the observation of the Continental Crust through Drilling, 399-403.

Ito, H., Y. Kuwahara, T. Ohminato, S. Nakao and T. Kiguchi, 1995, Development of multi-level digital borehole seismometer system, Rep. Geol. Surv. Japan, No. 282, 163-175.

Ito, H., Y. Kuwahara, T. Miyazaki, O. Nishizawa, T. Kiguchi, K. Fujimoto, T. Ohtani, H. Tanaka, T. Higuchi, S. Agar, A. Brie and H. Yamamoto, 1997, Structure and physical properties of the Nojima Fault, BUTSURI-TANSA, 49, 522-535.

Li, Y.-G., and P.C. Leary, 1990, Fault zone trapped seismic waves, Bull. Seism. Soc. Amer., 80, 1245-1271.

Li, Y.-G., K. Aki, D. Adams, A., Hasemi and W. H. K. Lee, 1994a, Seismic guided waves trapped in the fault zone of the Landers, California, earthquake of 1992, J. Geophys. Res., 99, 11705-11722.

Li, Y.-G., J. E. Vidale, K. Aki, C. J. Marone and W. H. K. Lee, 1994b, Fine structure of the Landers fault zone: segmentation and the rupture process, Science, 265, 367-370.

Tanaka, H., T. Higuchi, N. Tomida, K. Fujimoto, T. Ohtani and H. Ito, 1999, Distribution, deformation and alteration of fault rocks along the GSJ core penetrating the Nojima Fault, Awaji Island, Southwest Japan, Jour. Geol. Soc. Japan, 105, 1, 72-85.

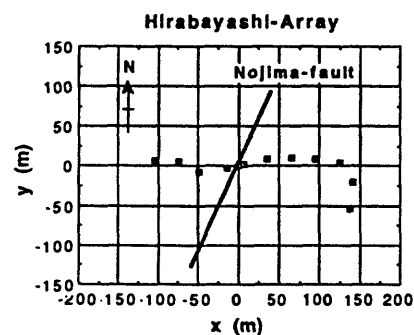
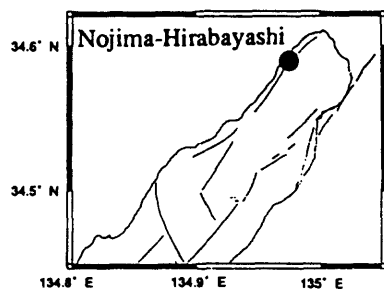


Fig. 1 Configuration of the surface array observation.

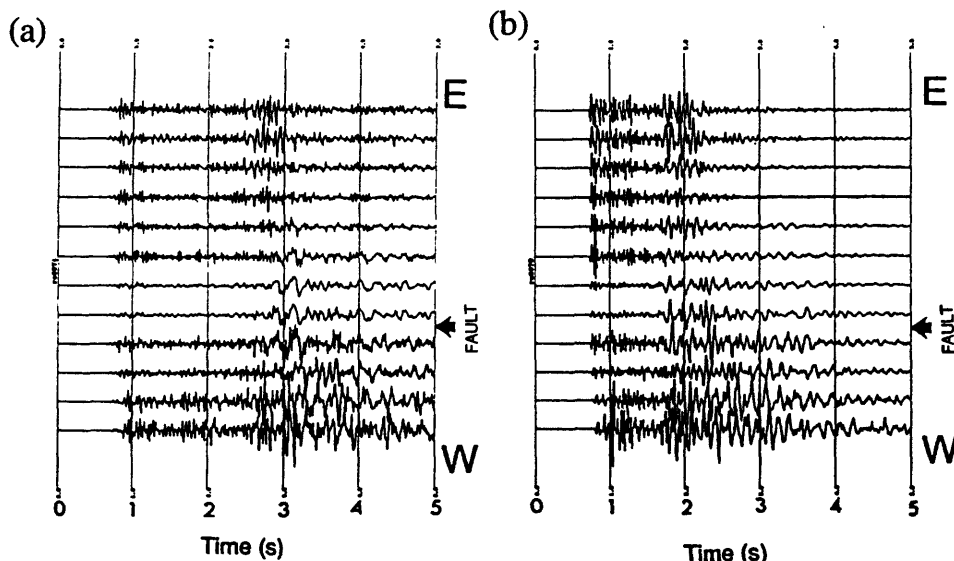


Fig. 2 Two types of waveforms observed at the surface array.  
 (a) Example of fault zone trapped wave. (b) Waveform without trapped wave.

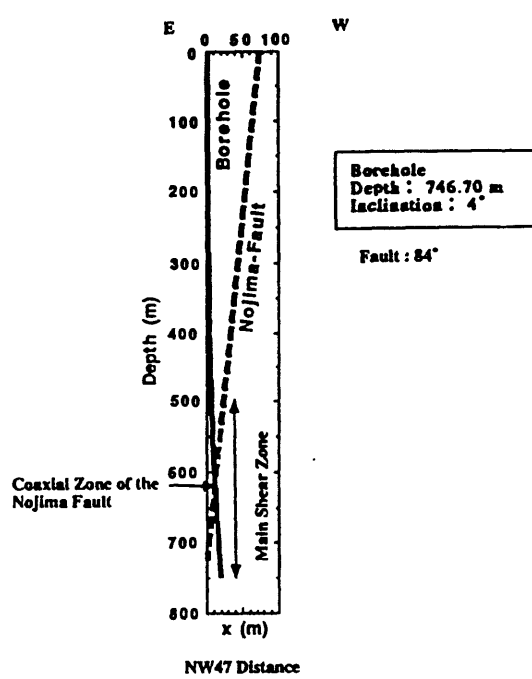


Fig. 3 The trajectory of the borehole.

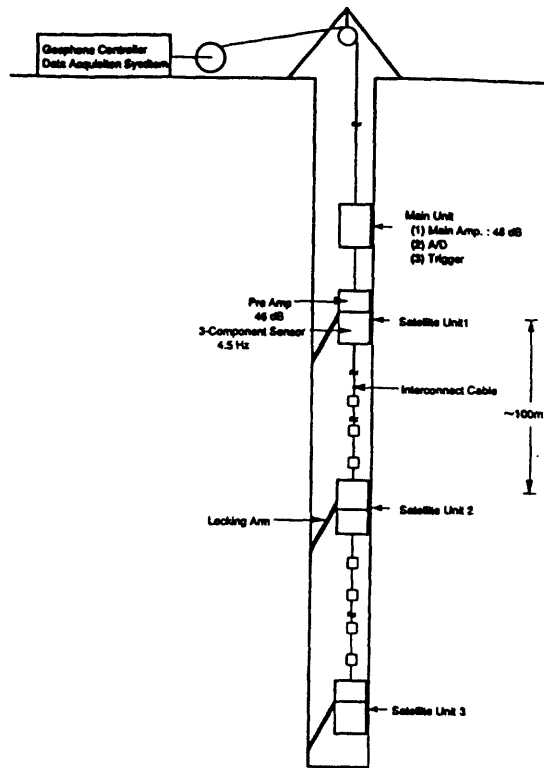


Fig. 4 Schematic diagram of the multi-level digital borehole seismometersystem.

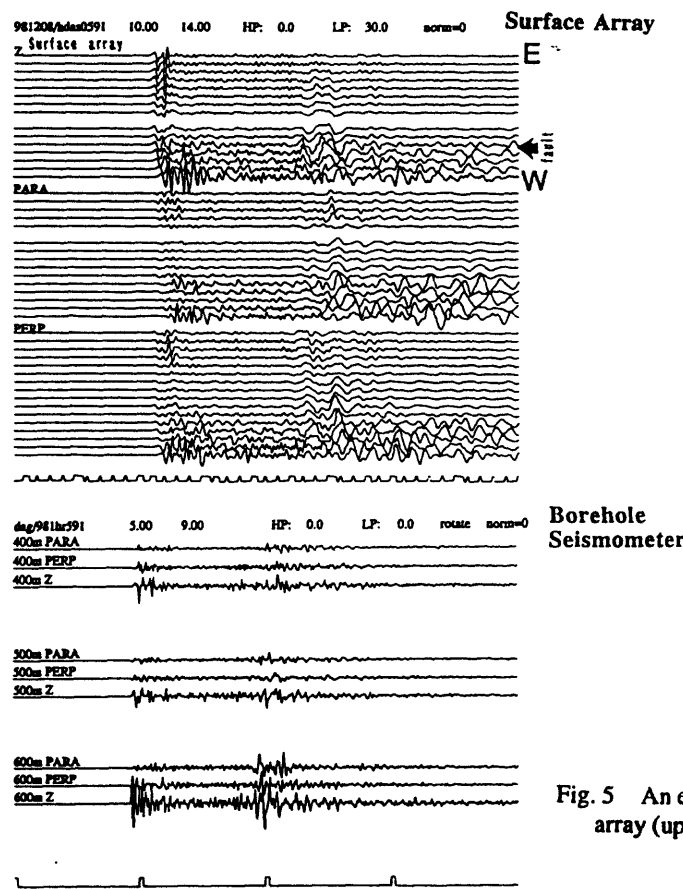


Fig. 5 An example of the waveform of the surface array (upper) and the borehole seismometer (lower).

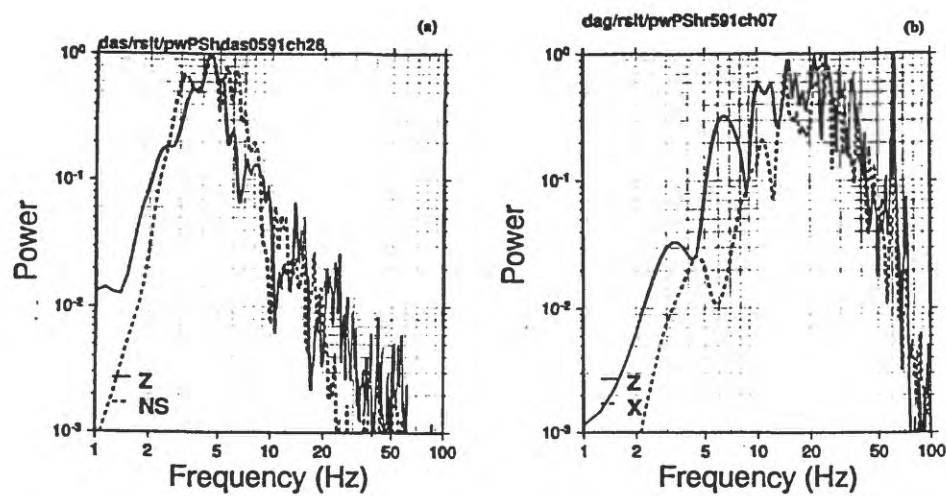


Fig. 6 Power spectrum of one of the surface array (a) and downhole data (b).

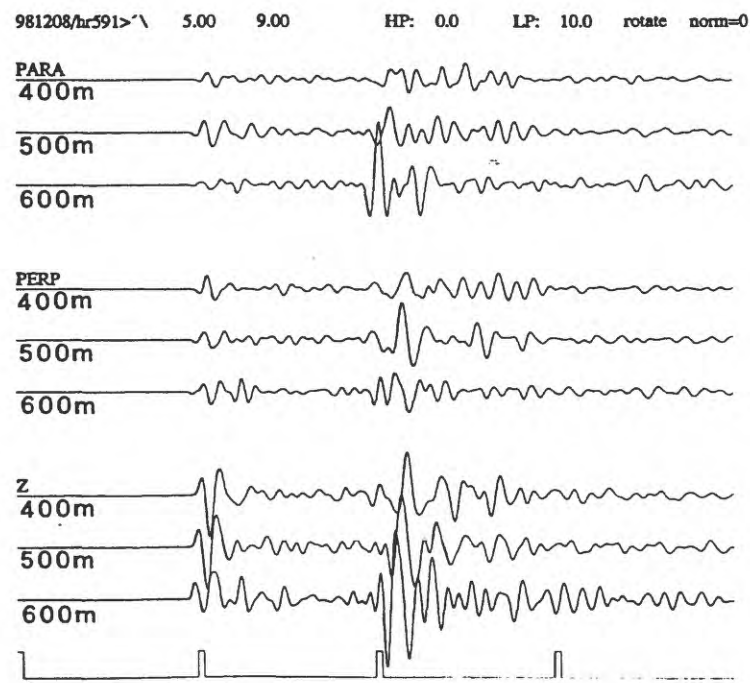


Fig. 7 10 Hz low-pass filtered seismogram for the event shown in Fig.5

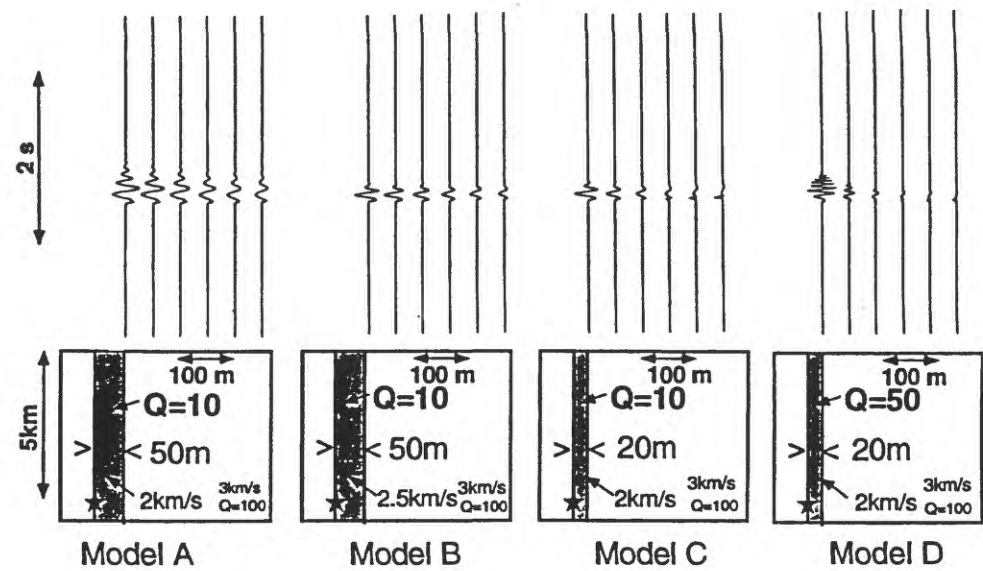


Fig.8 Synthetic waveforms of trapped waves for various models of fault structure.